METALS. SUPERCONDUCTORS

Hydrogen in amorphous and crystalline ytterbium films

V. M. Kuz'menko and A. N. Vladychkin

Khar'kov Physicotechnical Institute, 310108 Khar'kov, Ukraine
(Submitted May 29, 1998)
Fiz. Tverd. Tela (St. Petersburg) **41**, 177–182 (February 1999)

Ytterbium vapor condensation on a liquid-helium cooled substrate in a hydrogen atmosphere is used to obtain Yb–H films containing up to 55 at. % hydrogen. Various thermodynamic and kinetic parameters of the transition of these films from the amorphous to the crystalline state ($a \rightarrow c$ transition) are investigated along with the electrical conductivity of these states. It is shown that the investigated properties of Yb–H films containing up to 40 at. % hydrogen are essentially indistinguishable from those of pure Yb films in the temperature interval 4.2 $-$ 293 K. Increasing the hydrogen concentration to 55 at. % leads to an insignificant increase in the electrical resistivity, the kinetic temperature, and the activation energy of the $a \rightarrow c$ transition, and also to a decrease of the propagation speed of self-maintaining avalanche (explosive) crystallization. Reasons for the observed influence of hydrogen on the properties of Yb–H films are analyzed. The examined low-temperature Yb–H condensates can be characterized as a ''frozen'' solid solution of hydrogen in ytterbium in the temperature interval 4.2 $-$ 293 K. Storing such films at room temperature leads to the formation of ionic ytterbium dihydride YbH_2. © *1999 American Institute of Physics.* [S1063-7834(99)00102-1]

The condensation of ytterbium vapors in a superhigh vacuum onto a liquid-helium cooled substrate leads to the formation of amorphous films of this metal.[1,2] Upon heating the films to $T_{a \rightarrow c} = 13 - 20$ K, a transition from the amorphous to the crystalline state ($a \rightarrow c$ transition) occurs. At room temperature, no other phases besides *fcc* Yb were detected in the examined films.[1]

It is well known that all lanthanides, including ytterbium, form hydrides easily. Pure samples of metals under the appropriate conditions hydrogenate at room temperature in hydrogen at atmospheric pressure.[3] In particular, ytterbium forms a ionic orthorhombic hydride YbH_2 by direct reaction of pure ytterbium with hydrogen under ordinary conditions.[3,4] In addition, two metastable hydrides of ytterbium with *fcc* lattices are well known: $YbH_{2.55}$, formed at elevated temperatures and hydrogen pressures, and YbH_2 as the result of decomposition of $YbH_{2.55}$ at $T = 473 - 573$ K (Ref. 5). Orthorhombic YbH_2 has also been detected in thin films prepared by evaporating Yb in an ordinary vacuum chamber at a pressure $p \approx 1.33 \times 10^{-4}$ Pa at room temperature.[6]

To date, amorphous hydrides have been obtained by various methods;[7–9] however, we do not know of any instances in which they have been formed by low-temperature condensation of pure metals in a residual hydrogen atmosphere.

The aim of the present paper is to determine whether it is possible to form amorphous ytterbium hydride by condensation of ytterbium vapors in a hydrogen atmosphere onto a liquid-helium cooled substrate. If this is impossible, then the aim is to determine how hydrogen influences the electrical conductivity of amorphous and crystalline Yb films at temperatures from 4.2 K to room temperature and how it influences the thermodynamics and kinetics of the $a \rightarrow c$ transition.

1. EXPERIMENTAL TECHNIQUE

The only technique for obtaining amorphous films of pure monoatomic metals is vapor condensation in superhigh vacuum onto a liquid-helium cooled substrate. In this process, if the substrate is capable of absorbing the heat of condensation without noticeable heating, cooling rates as high as 10^{15} K/s can be reached.[10]

The principle of the design of the device used to prepare and study pure metallic amorphous films in the present work was first proposed by Shal'nikov.[11] The main component of the device is a glass ampoule [Fig. 1(a)], in which evaporation and condensation of the investigated metals takes place. Leads *1* of platinum wire (diameter ≈ 0.3 mm) were soldered onto a flat polished substrate *4*, which is the floor of the tumbler *3*. These served for electrical measurements of the metallic layer condensed on the substrate. In the lower part of the ampoule, platinum leads *9* were soldered to the glass as mounts for the tungsten evaporators *7* and to supply them with electric current.

Before each measurement, the ampoule, cut along the line *cc*, is carefully washed with an alkali solution, with acid, and with a jet of water vapor. After drying the ampoule, a mask *5* with cuts to produce one or two films (of a suitable form for the measurements) is placed over the substrate and evaporators with starting charges of the appropriate metal are

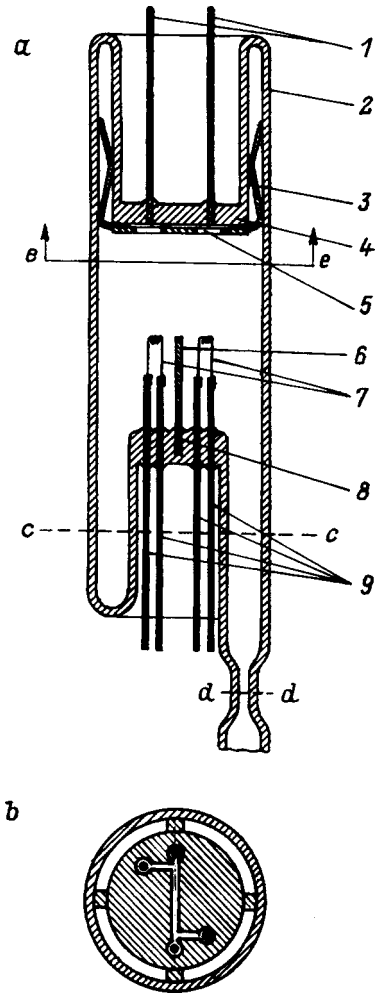

FIG. 1. Diagram of a functional ampoule for preparing and investigating the films *a*: *1* — platinum leads for the electrical measurements; *2* — housing; *3* — tumbler; *4* — polished substrate; *5* — mask for obtaining films of the required geometry; *6* — divider screen; *7* — tungsten evaporators; *8* — platinum wire mount for the divider screen; *9* — platinum leads for mounting the evaporators and supplying them with current. *b* — view of the mask from *ee*.

mounted. The mounted ampoule is soldered shut along the cut *cc* and through the glass adapter is connected to the vacuum setup for pumping. The ampoule, pumped down to a pressure of approximately 1.33×10^{-4} Pa, is unsoldered by a gas blow-torch along the line *dd* and is mounted in a cryostat in preparation for the experiment. As liquid helium is poured into the cryostat, the residual gas condenses mainly in the tail of the ampoule (in the region *dd*), which is the first part to be cooled. The pressure in the ampoule thereupon falls to $\approx 10^{-10}$ Pa (with the helium). The design of the ampoule and the technique of the experiment essentially prevent condensation of the residual gas onto the substrate and walls of the ampoule in the region of the evaporators. Thus, evaporation and condensation of the investigated metals take place under conditions of superhigh vacuum which are difficult to achieve using other techniques. To obtain purer films, part of the charge is evaporated with the substrate enclosed by a screen. A nickel screen is held in place on the substrate by a permanent magnet lowered into the tumbler *3*. When the magnet is removed, the screen falls to the bottom of the ampoule, uncovering the substrate for film condensation.

The technique we used to obtain low-temperature metal–hydrogen condensates is analogous to the technique described above. The ampoule, after being pumped down to $p\cong1.33\times10^{-4}$ Pa, is filled with gaseous hydrogen at atmospheric pressure, hermetically sealed (soldered shut) and mounted in the cryostat. As liquid helium is poured into the cryostat, hydrogen condenses in the tail of the ampoule, where the temperature is kept ≈ 4.2 K during the entire process of film preparation. The hydrogen pressure corresponds to the vapor pressure above solid hydrogen at $T\cong4.2$ K and is $\approx 4.67\times10^{-5}$ Pa. The mean temperature of the Yb–H films during their condensation onto the glass substrate did not exceed 4.5 K.

The ratio of the number of hydrogen atoms n' to the number of Yb atoms n in the films was estimated from the relation[12]

$$\frac{n'}{n}=4.365\times10^{-4}\frac{M}{\delta}(M'T)^{-1/2}\frac{p}{v}\gamma, \tag{1}$$

where M and M' are the molecular weights of Yb and H, respectively, δ is the density of the Yb film, p is the hydrogen pressure (in Pa), v is the ytterbium condensation rate (cm/s), γ is the sticking coefficient (at a substrate temperature of 4.5 K $\gamma\approx0.02$, Ref. 13).

As was noted above, to obtain a film of the required geometry, a mask *5* of stainless steel is placed over the substrate *4* (looking down on the substrate) and is kept in place on the substrate with the help of spring-loaded ''feet'' extending into the space between the tumbler *3* and the housing *2* of the ampoule. Depending on the purpose of the measurement, the masks can have various shapes. Figure 1(b) shows a mask used in the present work for measurements of the electrical resistance of the films by the four-probe method. To study the films in the temperature range 4.2–300 K, we used the method of the inverted dewar[14]: the ampoule is covered by a dewar and the substrate temperature is regulated with the help of a heater wound around the housing of the ampoule. The temperature (in the interval 4.2–293 K) was measured with a platinum resistance thermometer located in the tumbler *3*.

2. EXPERIMENTAL RESULTS

We found that, for a hydrogen content in the Yb films up to 40 at. %, their electrical parameters and the stability parameters of the amorphous state were essentially indistinguishable from those of pure Yb films (see Table I).

Table I displays averaged values of the parameters for 15 pure Yb films (first row) and six Yb–H films (second row), of which two had hydrogen content ≈ 17 at. % H; two had hydrogen content, ≈ 25 at. % H, and two had a hydrogen content of 40 at. % H. The condensation rate of these films varied from 0.07 to 0.24 nm/s, and their thickness—from 50 to 70 nm. The spread in the parameter values listed in the table for individual samples was $\pm10\%$, which is within the error limits for determining these parameters. As can be seen in the table, the transition from the amorphous to the crystalline state occurs roughly at the same kinetic tem-

TABLE I. Averaged parameters of Yb and Yb–H films.

Composition	$\frac{n'}{n}$	$T_{a\to c}$, K	$\frac{\Delta\rho_{a\to c}}{\rho_a}$, %	ρ_a, $\mu\Omega\cdot$cm	$\rho_{a\to c}$, $\mu\Omega\cdot$cm	ρ_{300}, $\mu\Omega\cdot$cm	U_f, m/s	E, kJ/mol
Yb	–	13.5	86	125	17	23	9.0	3.4±0.4
Yb–H	0.2–0.7	14.5	85	127	19	26→∞	8.3	3.4±0.4
Yb–H	1.2	18	72	140	36	31→∞	5.4	4.4±0.4

Note: Here ρ_a, $\rho_{a\to c}$, and ρ_{300} are the resistivities of the films in the amorphous state, directly after the $a\to c$ transition, and at $T\cong 300$ K, respectively; U_f is the propagation speed of the avalanche crystallization front; E is the activation energy of the $a\to c$ transition.

perature $T_{a\to c}$ for Yb and Yb–H films, and the corresponding relative difference in the resistivity ($\Delta\rho_{a\to c}/\rho_a=(\rho_a-\rho_{a\to c})/\rho_a$) is 85–86%.

The ninth column gives values of the activation energy of the passage of atoms through the interface of the amorphous and crystalline phases. They were determined by the ''ratio of angular coefficients'' method[15] from the isothermal dependences of ρ on time for different heating temperatures of the same sample.

The eighth column records the speed of the avalanche crystallization (AC) front of the Yb and Yb–H films. Avalanche crystallization of the films was initiated at $T=4.2$ K by a local current pulse and propagated along the sample in a self-sustaining manner due to liberation of the latent heat of the transition. The nature of the avalanche crystallization and the technique for determining the speed of its propagation front were described in Refs. 16 and 17. Note that, for individual samples of both Yb and Yb–H, the speed of the avalanche crystallization front varied from 7.5 to 10 m/s and depended, in particular, on the amount of random impurities (besides hydrogen) winding up the film upon condensation. The temperature dependences of the resistivities of the crystallized Yb and Yb–H films, recorded in a heating regime of 1–1.5 K/min, were essentially indistinguishable up to room temperature. The resistivities of both series of films played into the reversible metallic dependence $\rho(T)$ somewhere around 200 K, which is evidence of a playout of relaxation processes taking place in the Yb films at temperatures below room temperature. Hydrogen was not observed to have any noticeable effect on the ytterbium films even against a background of low $\rho_{a\to c}$ values (see Table I). For comparison, we note that the absolute increase of ρ in vanadium, niobium, and tantalum at room temperature lies between 0.7 and 1.2 $\mu\Omega\cdot$cm/at. % H (Ref. 18).

Increasing the hydrogen concentration in the Yb films to ≈ 50 at. % has a noticeable effect on their electrical properties and stability. The third row of the table presents results for two Yb–H films of ≈ 93 nm thickness, prepared simultaneously in the same ampoule with a condensation rate ≈ 0.04 nm/s and containing roughly about 55 at. % hydrogen. As can be seen in the table, the resistivities increase in both the amorphous and the crystalline state (in comparison with pure Yb films), the kinetic temperature of crystallization upon heating rises and the propagation speed of the avalanche crystallization front decreases. The heating curve of one of the Yb–H films containing ≈ 55 at. % H, is shown in Fig. 2, curve *1*. However, even here, the departure from the behavior of pure Yb films is only quantitative, and there is essentially no difference in the parameter values or the behavior upon heating (or avalanche crystallization) for Yb films containing an increased quantity of impurity atoms (but not hydrogen) (see Fig. 2, curve *2*). In our experiments a small quantity of external impurities can wind up in the film due to inadequate preliminary cleaning of the starting charges of metal or of the substrate.

Abrupt qualitative changes in all the investigated Yb–H films take place when they are stored at room temperature in the hydrogen atmosphere remaining in the ampoules after film condensation. Thus, whereas the resistivity decreases a little due to a continuation of relaxation processes in films of pure Yb and films of Yb containing an increased quantity of random impurities (besides H) when stored at room temperature, the resistivity of Yb–H films begins rapidly to grow and during a few hours reaches values exceeding nominally $10^4\ \Omega\cdot$cm. This is no longer the resistivity of a metal, but of a semiconductor or insulator. The films acquire a blue color and become translucent. For example, while the optical density of pure Yb films of thickness ≈ 70 nm tends to infinity, the optical thickness of Yb–H films of thickness 93 nm is only ≈ 50. Sometimes when the ampoule is opened to air,

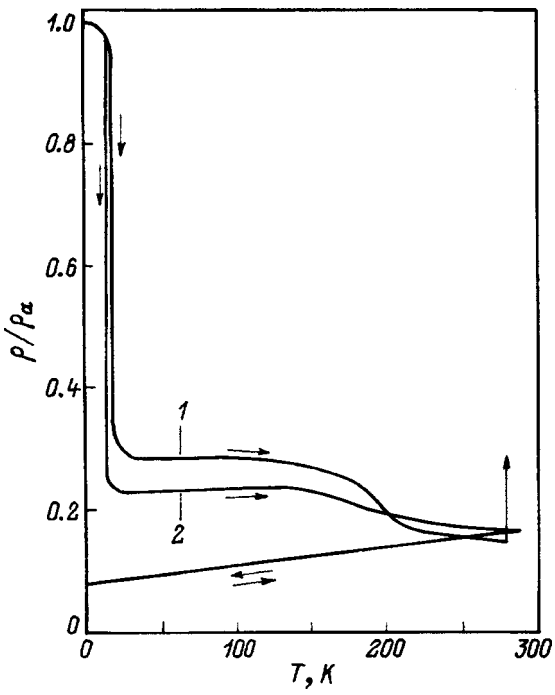

FIG. 2. Dependence of the reduced resistance of Yb–H films (*1*) and Yb films (*2*) on the temperature.

the Yb–H films underwent spontaneous combustion. Pure Yb films are ductile: the metal is easily smeared over the glass upon scraping the film with a sharp-edge. Yb–H films stored at room temperature are characterized by a high degree of brittleness. In contrast to pure Yb, they react only weakly with nitric acid, but react vigorously with sulfuric acid.

3. DISCUSSION OF RESULTS

It is well known that amorphous films of pure metals usually exhibit an insignificant resistance to crystal growth, but the addition of impurities frequently retards this growth.[19] Some hypotheses have been formulated attempting to explain the stabilization mechanisms of the amorphous state of a metal upon the addition of a second component.[2,20,21] In the opinion of Bennet, Polk, and Turnbull,[20] to realize crystallization the impurity atoms filling the pores of the amorphous structure of the metal must be displaced at least one interatomic distance. Thus, crystal growth will be limited by the frequency of jumps of impurity atoms from one equilibrium site to another, which leads, for example, to a higher degree of local order. The time constant of this process τ should be of the order of the time constant of diffusion or of viscous flow.[21] Bennet *et al.*[20] claim that the value of τ in this case must be much larger than for motion of the interphase surface ''amorphous solid – crystal'' in pure systems, which can proceed by much smaller atomic displacements (by a nondiffusion mechanism).[17] Their hypothesis probably explains the high stabilizing power of such large (in comparison with hydrogen) implantation atoms as O, N, C, and B (Refs. 21 and 22), especially when they interact strongly with the metal atoms.

Hydrogen is unique among the elements forming solid solutions of implantation type. Even if it is present in the metal lattice in atomic form, its dimensions are similar to those of the lattice interstices even without mentioning the possibility of the existence of hydrogen in proton form in the metal. In this regard, the diffusion coefficient of hydrogen in metals, as a rule, is extraordinarily large. For example, in vanadium at room temperature, a hydrogen atom completes 15–20 orders more jumps per second than heavy interstitial impurities such as oxygen and nitrogen at the same temperature.[22] At low temperatures (<100 K) the diffusion mobility of hydrogen in comparison with other implantation impurities is still higher since non-activation migration of its atoms becomes possible (sub-barrier tunneling).[22–24] Indeed, the similarity of the parameters $T_{a\rightarrow c}$ and E for Yb and Yb–H films and their small values are an indication of the high mobility of hydrogen atoms. The latter manage to redistribute themselves over the ytterbium lattice even during the brief time of such a rapid process as avalanche crystallization. The observed decrease in the speed of the front of avalanche crystallization in Yb–H amorphous films containing a high concentration of hydrogen (see Table I) may be due, according to the theory expounded in Ref. 17, to an increase in the activation energy E. On this basis, we conclude that its weak interaction with ytterbium and the high diffusion mobility of hydrogen at low temperatures are the main reason for the weak stabilizing power of hydrogen in the amorphous system Yb–H.

Analyzing the weak effect of hydrogen on the electrical conductivity of amorphous and crystalline films of ytterbium, it may be assumed that, at low temperatures (and during condensation onto a cold substrate), hydrogen does not react chemically with ytterbium, but rather forms a solid solution with it. It is very difficult theoretically to explain a change in the electrical resistivity as a result of implantation of dissolved H atoms, especially for transition metals. On the one hand, an increase in the number of scattering centers for a significant difference in the scattering potentials of H and Yb atoms should lead to an increase in ρ with growth of the hydrogen concentration. On the other hand, electrons can transfer from the implanted hydrogen atoms to an unfilled d shell of ytterbium. In this case, $s-d$ scattering can be reduced for significant hydrogen concentrations, which facilitates a negative contribution to the resistivity. It seems that the determining factor influencing the resistivity of Yb–H films is scattering of conduction electrons by structural defects, and not a change in the electron spectrum of ytterbium under the influence of hydrogen. Indeed, the size of the crystallites in films of pure metals immediately after an $a\rightarrow c$ transition is ≈ 10 nm (Ref. 2) and the defect density is very large (not even speaking of the amorphous state). The defect level in the structure of Yb–H films for hydrogen concentration <40 at. %, below room temperature, apparently differs only slightly from the defect level in pure Yb films, for which reason the resistivities of such films also differ only slightly.

Hydrogen atoms can not only populate interstices of the metal lattice, but also accumulate near structural defects, thereby forming various ''atmospheres,'' and by recombining into molecules also induce large strains in the crystal leading sometimes to the formation of macroscopic defects.[24] This can be the cause, in particular, of the marked influence of hydrogen on the electrical resistivity and the stability characteristics of Yb–H films containing more than 50 at. % hydrogen.

The marked qualitative changes in the state of Yb–H films when stored at room temperature are due to the emergence of hydride conversion. It is well known that the reaction of ytterbium with hydrogen at atmospheric pressure and room temperature only gives the dihydride YbH_2 having an orthorhombic lattice. Two metastable hydrides of ytterbium—$YbH_{2.55}$ and YbH_2—are also known. The higher hydride of ytterbium $YbH_{2.55}$, prepared in high-pressure experiments,[5] is a black powder having face-centered cubic structure. When heated to $T=473-573$ K it decomposes, transforming to a face-centered cubic modification of YbH_2, which upon quenching is metastable at room temperature. Annealing of *fcc* YbH_2 causes it to convert to the stable orthorhombic form.

The orthorhombic YbH_2 ionic hydride, consisting of Yb^{2+} ions and H, is also isostructural with the ionic hydride CaH_2.[3,5] Characteristic properties of our Yb–H films, stored at room temperatures—the almost complete absence of conductivity, a small optical density, and high brittleness, typical indicators of an ionic hydride, show that storage at room

temperature causes a phase transition to take place wherein the solid solution of hydrogen in *fcc* ytterbium transforms into the ionic hydride YbH_2. In this phase transition almost all the ytterbium conduction electrons are used up in the formation of hydride ions H^-, forming ionic bonds with the Yb^{2+} ions.

A generally accepted picture of the nature and mechanism of hydride conversions has still not been assembled. According to current hypotheses,[25] it may be assumed that the conversion $(Yb–H) \rightarrow YbH_2$ has a diffusion–nondiffusion character. This means that hydrogen transport to the growing hydride nucleus and its redistribution and ordering in the implantation sublattice are realized via a diffusion path. At the same time, small (on the order of interatomic) displacements of the atoms of the metallic matrix taking place during the conversion have a cooperative character and are apparently produced by a nondiffusion mechanism of martensite type.[25] The blue color of ytterbium dihydride in our experiments may be due to the presence of F centers,[3–26] which indicates the presence of a metal excess. Preliminary x-ray studies confirm that, in addition to orthorhombic YbH_2, the films contain some quantity of unbonded metal.

We found that a more complete conversion occurs not only with participation of hydrogen dissolved in the ytterbium but also thanks to an additional influx of hydrogen into the metal from inside the ampoule. This was demonstrated with the aid of the following additional experiment. After obtaining Yb–H films containing ≈ 35 at. %, followed by their crystallization, the ampoule was opened up at $T \cong 80$ K in a helium atmosphere. After multiple ''washings'' of the ampoule with gaseous helium[1)] the Yb–H films were stored in a helium atmosphere at room temperature for 24 h. A rapid growth of the resistivity as well as characteristic changes in the color and transparency of the films testify to the formation in them of ytterbium dihydride. However, the hydrogen dissolved in the films was insufficient, and they preserved their metallic conductivity. What probably took place here was a distribution of inclusions of the dihydride YbH_2 throughout the *fcc* Yb matrix. It seems that if the hydrogen concentration in the film corresponds to the stoichiometry of the dihydride, then the hydride conversion takes place over the entire volume of the film without additional influx of hydrogen from outside.

It is interesting to note that a pure Yb film immersed in a hydrogen atmosphere after being kept for two hours in air did not exhibit any noticeable signs of hydride formation after 24 hours storage at room temperature in this atmosphere. Probably, penetration of hydrogen into the sample was hindered by the oxide film forming on its surface.

[1)]The ampoule was run through several cycles: pumping down to $p \cong 0.133$ Pa followed by pumping helium into the ampoule at atmospheric pressure.

[1] B. G. Lazarev, V. M. Kuz'menko, A. I. Sudovtsov, and R. F. Bulatova, Dokl. Akad. Nauk SSSR **184**, *3*, 587 (1969).
[2] Yu. F. Komnik, Fiz. Nizk. Temp. **8**, *1*, 3 (1982) [Sov. J. Low Temp. Phys. **8**, 1 (1982)].
[3] K. Makkeĭ, *Hydrogen Compounds of Metals* [in Russian] (Moscow, 1968), 244 pp.
[4] W. L. Korst and J. C. Warf, Acta Crystallogr. **9**, 452 (1956).
[5] J. C. Warf and K. J. Hardcastle, Inorg. Chem. **5**, 1736 (1966).
[6] A. E. Curzon and O. J. Singh, Less-Common Metals **39**, 227 (1975).
[7] X. L. Yeh, K. Samwer, and W. L. Johnson, Appl. Phys. Lett. **42**, 242 (1983).
[8] R. A. Andrievskiĭ, *Material Science of Hydrides* [in Russian] (Moscow, 1986), 128 pp.
[9] *Abstracts of the Fifth International Conference on Hydrogen Materials Science and Chemistry of Metal Hydrides*, Valta, 1997, p. 21.
[10] A. S. Nowick, Comments Solid State Phys. **2**, 155 (1970).
[11] A. J. Shal'nikov, Nature (London) **142**, 74 (1938).
[12] H. L. Caswell, in *Physics of Thin Films*, edited by G. Hass, Vol. 1, Ch. 1 (Moscow, 1967), 343 pp.
[13] E. Trendelenburg, *Superhigh Vacuum* (Moscow, 1966), 286 pp.
[14] N. V. Zavaritskiĭ, Prib. Tekh. Éksp., *2*, 140 (1956).
[15] S. Mader and A. S. Nowick, Acta Metall. **15**, *2*, 215 (1967).
[16] V. M. Kuz'menko and V. I. Mel'nikov, Zh. Éksp. Teor. Fiz. **82**, *3*, 802 (1982) [Sov. Phys. JETP **55**, 474 (1982)].
[17] V. A. Shklovskiĭ and V. M. Kuz'menko, Usp. Fiz. Nauk **157**, *2*, 311 (1989) [Sov. Phys. Usp. **32**, 163 (1989)].
[18] E. Fromm and E. Gebhardt, *Gase und Kohlenstoff in Metallen* [*Gases and Carbon in Metals*, in German] (Springer-Verlag, Berlin, 1976; Moscow, 1980), 712 pp.
[19] V. M. Kuz'menko, B. G. Lazarev, V. I. Mel'nikov, and A. I. Sudovtsov, Ukr. Fiz. Zh. **21**, *6*, 883 (1976).
[20] C. H. Bennet, D. E. Polk, and D. Turnbull, Acta Metall. **19**, *12*, 1295 (1971).
[21] K. Suzuki, H. Fujimori, and K. Hasimoto, *Amorphous Metals* (Moscow, 1987), 328 pp.
[22] J. Völkl and G. Alefeld, in *Hydrogen in Metals*, edited by G. Alefeld and J. Völk, Vol. I, Ch. 12 (Springer-Verlag, New York, 1978; Moscow, 1981), 478 pp.
[23] V. A. Gol'tsov, V. V. Latyshev, and L. I. Smirnov, in *Interaction of Hydrogen with Metals* [in Russian], edited by A. P. Zakharov (Moscow, 1987), Ch. 4, 296 pp.
[24] P. V. Gel'd, R. A. Ryabov, and L. P. Mokhracheva, *Hydrogen and the Physical Properties of Metals and Alloys* [in Russian], (Moscow, 1985), 232 pp.
[25] V. A. Gol'tsov, in *Interaction of Hydrogen with Metals* [in Russian], edited by A. P. Zakharov (Moscow, 1987), Ch. 9, 232 pp.
[26] C. A. Wert and R. M. Thomson, *Physics of Solids*, 2nd ed. (McGraw-Hill, New York, 1970; Moscow, 1969), 560 pp.

Translated by Paul F. Schippnick

SEMICONDUCTORS, DIELECTRICS

Differences in the atomic environment of nonequivalent sites in SiC-polytype structures

A. E. Madison

St. Petersburg State Electrical Engineering University, 197376 St. Petersburg, Russia
(Submitted February 18, 1998; accepted for publication July 10, 1998)
Fiz. Tverd. Tela (St. Petersburg) **41**, 183–186 (February 1999)

A general algorithm is proposed for calculating the Θ series of SiC polytypes. The obtained Θ series of the main SiC polytypes can be useful in calculating lattice sums, in particular when using the Mellin transform of the Θ series. By expanding the Θ series in the Jacobi parameter, one obtains sequences of coordination numbers for crystallographically nonequivalent atomic sites in the main SiC polytypes. A nontrivial interrelationship is demonstrated between these numerical sequences and the local symmetry of the nonequivalent sites. © *1999 American Institute of Physics.* [S1063-7834(99)00202-6]

DIFFERENCES IN THE ATOMIC ENVIRONMENT OF NONEQUIVALENT SITES IN SIC-POLYTYPE STRUCTURES

SiC polytypes are of great practical significance as a class of promising semiconductor materials having a range of band gap widths.[1–6] In addition, they have definite academic interest as natural superlattices and as a models for a proper study of polytypism.[7–9] ZnS also crystallizes in analogous structures.

A characteristic of polytypes is the presence in their structures of crystallographically nonequivalent sites differing in the local symmetry of their immediate environment, and also the number and mutual arrangement of the atoms in the distant coordination spheres. Their existence has a serious effect, in particular, on the kinetics of impurity capture during crystal growth,[10,11] the multiplet structure of the impurity states,[12,13] and the optical, electrical, and some other properties of SiC polytypes.

All polytype structures differ from one another by the stacking sequence of double Si–C layers along some preferred direction (the c axis). Structural characteristics of the main polytypes of SiC and our notation for nonequivalent sites are depicted in Fig. 1. We find it necessary to draw attention to the strict 1–1 correspondence of nonequivalent sites of atoms of different sublattices. In particular, for the polytype $6H$ the ordering of nonequivalent sites $(h,c_1,c_2,\dots)$ along the c axis in the silicon sublattice corresponds to the ordering of nonequivalent sites $(h,c_2,c_1,\dots)$ in the carbon sublattice.

We investigated differences in the atomic environment of nonequivalent sites using the method of Θ series. Besides the fact that use of Θ series can substantially expedite the task of calculating lattice sums, they are of independent interest in crystallography. As a result of expanding them in a series in the Jacobi parameter, the coordination numbers for successive coordination spheres can be obtained without especial effort.[14–17]

Such information is useful, for example, in the analysis of the stability of atomic clusters in the initial stages of crystal growth,[16] the study of fine structures of impurity states,[13] and in some other problems.

Of all the SiC and ZnS polytypes, the Θ series are known only for the simplest structures—sphalerite and würzite.[16,17] With this fact in mind, the main task of the present work was to determine the Θ series of the basic polytypes of silicon carbide, and also to determine the coordination numbers for crystallographically nonequivalent atomic sites in the structures of the most important polytypes.

To obtain the Θ series of polytypes of SiC and ZnS we used a general approach rigorously developed in Refs. 17 and 18. First it is necessary to note the following fact. We assume that the Θ series is already known for a case in which the origin coincides with one of the sites of one of the sublattices. If we then translate the origin to one of the atoms of the other sublattice, the fundamental picture of the atomic environment does not change and it is sufficient to replace all the Si atoms by C atoms and conversely. Thus, it suffices to consider the Θ series by successively locating the origin at nonequivalent sites of just one of the sublattices. For the case in which the origin coincides with one of the sites of the other sublattice, the Θ series can be obtained by a formal substitution of atoms, and it is necessary just to bear in mind the strict 1–1 correspondence of the nonequivalent sites of the different sublattices. This conclusion is valid for almost all the main polytypes of SiC and ZnS. As an exception we may cite the example of the quite rarely encountered polytype $21R$-ZnS or $(2311)_3$ in Zhdanov symbols.[7] For it, the Θ series of the zinc sublattice in the $(2311)_3$ structure are equivalent to the series of the sulfur sublattice in the structure $(3211)_3$, and the converse.

All Θ series can be expressed in terms of Jacobi Θ functions.[16,19] After substantial simplifications thanks to the use of some of their properties, and introducing the α, β and φ functions derived in the Appendix, we succeeded in showing that the Θ series of any nonequivalent site in the struc-

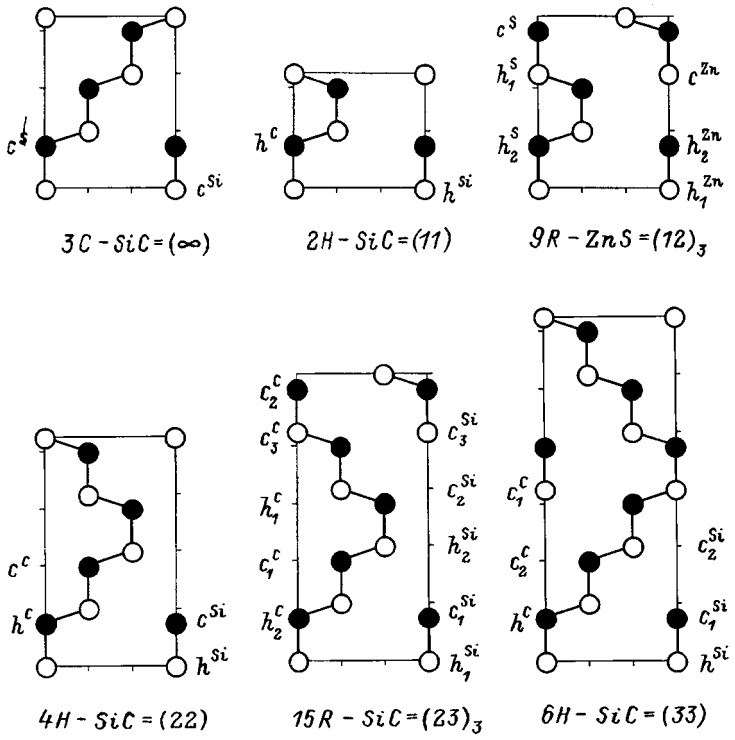

FIG. 1. Arrangement of atoms in the $(11\bar{2}0)$ planes for the main SiC polytypes using a hexagonal unit cell. For rhombohedral polytypes, only one-third of the unit cell is shown. In view of the absence in the literature of common notation for crystallographically nonequivalent sites, here we use our own notation. The rhombohedral polytype $9R$-ZnS is hardly ever encountered for silicon carbide, but it is one of the common polytypes of zinc sulfide.

ture of any polytype can be obtained using relations of general form. In particular, if we place the origin at one of the nonequivalent sites in the silicon sublattice, then the relative positions of all the remaining silicon atoms will be determined by the Θ series

$$\Theta_{\mathrm{Si-Si}}(z)=\alpha(z)\sum_{k\in\mathbf{A}}\varphi\left(\frac{2}{3}n^2z,\frac{k}{n}\right)+\beta(z)\sum_{k\in\mathbf{B}}\varphi\left(\frac{2}{3}n^2z,\frac{k}{n}\right),\qquad(1)$$

and the Θ series defining the relative positions of the carbon atoms can be obtained using

$$\Theta_{\mathrm{Si-C}}(z)=\alpha(z)\sum_{k\in\mathbf{A}}\varphi\left(\frac{2}{3}n^2z,\frac{k+\frac{3}{4}}{n}\right)+\beta(z)\sum_{k\in\mathbf{B}}\varphi\left(\frac{2}{3}n^2z,\frac{k+\frac{3}{4}}{n}\right).\qquad(2)$$

In these equations, n is the number of layers per unit cell of given polytype and the argument k successively takes all values of some set A, for the first sum, and from some set B, for the second sum. Placing the origin now at one of the nonequivalent sites, we consider atoms in successive layers $0\leqslant k\leqslant n-1$. If the atoms in the kth layer are located directly above the atoms of the zeroth layer, then the corresponding value of k is assigned to the set A and, in the opposite case, to the set B. Using the ABC polytype notation,[7] this procedure becomes elementary. In deriving Eqs. (1) and (2), the lattice constant of the hexagonal lattice a was taken as the unit of measurement of all the linear dimensions, the coordination tetrahedra were assumed to be ideal, and the ratio of dimensions of the unit cell was also taken to be equal to its ideal value $c/a=n(\sqrt{6}/3)$ for all polytypes.

Utilizing the hexagonal arrangement of axes and the above-described method for analyzing the cubic polytype $3C$ (sphalerite), we obtained the Θ series for the Si sublattice which, to within a scale factor, coincides with the series of the PZK lattice published in Ref. 16, where a cubic arrangement of the coordinate axes was used. The carbon sublattice corresponds to an analogous series found by translating the origin to one of the tetrhedral voids.[16] After expanding the Θ series of the $2H$–SiC structure (würzite) in powers of the Jacobi parameter it is clear that our results also agree with the results of Ref. 17.

The coordination numbers of the most important SiC polytypes for the first 43 coordination spheres are listed in Table I. The first column gives the square of the radius of the coordination sphere, expressed in units of the lattice constant a. This number can be considered as an index of the coordination sphere m, which can be fractional. The following columns give the number of atoms in it S_m for the most important polytypes, including the structures $2H$ and $3C$. The last column indicate the kind of atom (Si or C) of which this spheres is composed.

The most widespread polytype of SiC is $6H$. Like $2H$, it belongs to the space group $P6_3mc$, but this structure has three crystallographically nonequivalent sites—one hexagonal and two cubic (see Fig. 1). The Θ series for them can be obtained from Eqs. (1) and (2) if we set $n=6$ in them. An analysis of the coordination numbers given in the table for $6H$-SiC points up their nontrivial interrelationship with the site (hexagonal or cubic) at which the atom is found. In particular, an atom at a hexagonal site has the same local

TABLE I. Sequences of coordination numbers for nonequivalent sites of SiC polytypes.

	3*C*	2*H*	4*H*		6*H*			15*R*					
r^2	*c*	*h*	*h*	*c*	*h*	c_1	c_2	h_1	c_1	h_2	c_2	c_3	
0	1	1	1	1	1	1	1	1	1	1	1	1	Si
3/8	4	4	4	4	4	4	4	4	4	4	4	4	C
1	12	12	12	12	12	12	12	12	12	12	12	12	Si
$1\frac{1}{24}$	–	1	–	1	–	1	–	–	1	–	1	–	C
$1\frac{3}{8}$	12	9	12	9	12	9	12	12	9	12	9	12	C
2	6	6	6	6	6	6	6	6	6	6	6	6	Si
$2\frac{1}{24}$	–	6	–	6	–	6	–	–	6	–	6	–	C
$2\frac{3}{8}$	12	9	12	9	12	9	12	12	9	12	9	12	C
$2\frac{2}{3}$	–	2	–	2	–	1	1	–	2	–	1	1	Si
3	24	18	24	18	24	21	21	24	18	24	21	21	Si
$3\frac{3}{8}$	16	9	15	9	16	9	16	16	9	15	9	15	C
$3\frac{2}{3}$	–	12	–	12	–	6	6	–	12	–	6	6	Si
$3\frac{17}{24}$	–	3	3	3	–	3	–	–	3	3	3	3	C
4	12	6	12	6	12	9	9	12	6	12	9	9	Si
$4\frac{1}{24}$	–	6	–	6	–	6	–	–	6	–	6	–	C
$4\frac{3}{8}$	24	18	18	18	24	18	24	24	18	18	18	18	C
$4\frac{17}{24}$	–	3	3	3	–	3	–	–	3	3	3	3	C
5	24	12	24	12	24	18	18	24	12	24	18	18	Si
$5\frac{1}{24}$	–	7	–	7	–	6	–	–	7	–	6	1	C
$5\frac{3}{8}$	12	3	12	3	12	6	12	12	3	12	6	9	C
$5\frac{2}{3}$	–	12	–	12	–	6	6	–	12	–	6	6	Si
$5\frac{17}{24}$	–	6	6	6	–	6	–	–	6	6	6	6	C
6	8	6	6	6	8	6	6	7	6	7	6	6	Si
$6\frac{1}{24}$	–	6	–	6	–	–	–	–	6	–	–	6	C
$6\frac{1}{3}$	–	6	6	6	–	6	6	3	6	3	6	6	Si
$6\frac{3}{8}$	24	12	18	12	24	15	24	24	12	18	15	15	C
$6\frac{2}{3}$	–	12	–	12	–	6	6	–	12	–	6	6	Si
7	48	24	36	24	48	30	30	42	24	42	30	30	Si
$7\frac{1}{24}$	–	1	1	1	–	–	–	–	–	1	1	1	C
$7\frac{1}{3}$	–	6	6	6	–	6	6	3	6	3	6	6	Si
$7\frac{3}{8}$	36	15	27	15	36	24	36	36	18	27	21	21	C
$7\frac{17}{24}$	–	6	6	6	–	6	–	–	6	6	6	6	C
8	6	–	6	–	6	3	3	6	–	6	3	3	Si
$8\frac{1}{24}$	–	24	6	24	–	12	–	–	18	6	18	12	C
$8\frac{1}{3}$	–	12	12	12	–	12	12	6	12	6	12	12	Si
$8\frac{3}{8}$	12	9	9	9	12	12	12	12	12	9	9	9	C
$8\frac{17}{24}$	–	3	3	3	–	3	–	–	3	3	3	3	C
9	36	12	24	12	36	18	18	30	12	30	18	18	Si
$9\frac{1}{24}$	–	6	–	6	–	–	–	–	6	–	–	6	C
$9\frac{3}{8}$	28	12	21	12	28	24	28	27	18	22	18	15	C
$9\frac{2}{3}$	–	24	–	24	–	12	12	–	24	–	12	12	Si
$9\frac{17}{24}$	–	9	9	9	–	9	–	3	9	6	9	9	C
10	24	12	12	12	24	12	12	18	12	18	12	12	Si

symmetry of its first two coordination spheres as in würzite, and the number of atoms in the far coordination spheres coincides exactly with the corresponding numbers for sphalerite (i.e., the cubic modification). The identity of the corresponding Θ series graphically illustrates the fact that fundamentally different structures can have identical Θ series. For one of the two cubic sites, the sequence of coordination numbers differs not too greatly from the corresponding sequence for sphalerite and, for the second cubic site, it differs not too greatly from the corresponding sequence for würzite. The first differences from the ideal sequences show up starting at the eighth coordination sphere, which corresponds to ≈ 267 nearest interatomic distances. Such results are entirely unexpected at first glance.

The 4*H*-SiC structure has two nonequivalent sites: hexagonal and cubic (see Fig. 1). The sequence of coordination numbers for the hexagonal site differs only insignificantly from the corresponding sequence for sphalerite, and the differences appear starting from the tenth coordination sphere (3 nearest interatomic distances). The analogous sequence for the cubic site coincides with the sequence of coordination numbers of würzite (i.e., the hexagonal modification).

The 15*R*-SiC structure has five nonequivalent sites: two hexagonal and three cubic (see Fig. 1). The coordination numbers for them are also listed in the table. The nontrivial interrelationship between the coordination numbers and the local symmetry of the site noted by us for the 6*H* and 4*H*-SiC structures also holds for the other two polytypes.

In conclusion we note the following salient points. A general algorithm for calculating the Θ series of SiC and ZnS polytypes has been proposed. The Θ series have been analyzed in detail for the most important SiC polytypes. The sequences of coordination numbers so obtained for all the crystallographically nonequivalent atomic sites in the main SiC polytypes allow us to conclude that there is a nontrivial interrelationship between these sequences and the local symmetry of their immediate environment.

APPENDIX

In general, a Θ series is defined as a holomorphic function of a complex variable

$$\Theta_\Lambda(z)=\sum_{\mathbf{r}\in\Lambda} q^{N(\mathbf{r})}=\sum_m S_m q^m,$$

where $q=e^{i\pi z}$ is the Jacobi parameter, $N(\mathbf{r})=r^2$ is the lattice vector norm, and S_m is the number of vectors in the lattice Λ with norm equal to m. The expansion coefficients of the Θ series in powers of the parameter q give the coordination numbers in the successively considered coordination spheres with radius $\sqrt{m}$.

The structures of all SiC polytypes can be considered as a union of several primitive hexagonal sublattices Λ_0, shifted relative to one other by the vector **u**. In this case, for the kth nonequivalent site, the Θ series is defined as the sum of the series of sublattices[18]

$$\Theta_\Lambda(z)=\sum_{j=1}^{n}\sum_{\mathbf{r}\in\Lambda_0} q^{N(\mathbf{r}+\mathbf{u}_j-\mathbf{u}_k)}.$$

All Θ series can be expressed in terms of the Jacobi Θ functions.[16,19] To avoid the alternative interpretations encountered in the literature, we are forced to give specific equations

$$\vartheta_3(\xi,z)=\sum_{m=-\infty}^{+\infty} e^{i(2m\xi+\pi m^2 z)}, \quad \mathrm{Im}(z)>0;$$

$$\vartheta_3(z)=\vartheta_3(0,z)=\sum_{m=-\infty}^{+\infty} q^{m^2};$$

$$\vartheta_2(z)=e^{i\frac{\pi}{4}z}\,\vartheta_3\left(\frac{\pi}{2}z,z\right)=\sum_{m=-\infty}^{+\infty} q^{\left(m+\frac{1}{2}\right)^2}.$$

Developing the approach in Ref. 16, we deem it useful to introduce the function

$$\varphi(z,\tau)=e^{i\pi z\tau^2}\,\vartheta_3(\pi\tau z,z)=\sum_{m=-\infty}^{+\infty} q^{(m+\tau)^2}.$$

It is easy to show that the parameter τ can always be selected from the interval $0\leqslant\tau\leqslant 1/2$. It is also clear that the standard Jacobi functions $\vartheta_2(z)$ and $\vartheta_3(z)$ are particular cases of the function φ introduced above, specifically $\vartheta_3(z)=\varphi(z,0)$ and $\vartheta_2(z)=\varphi(z,\frac{1}{2})$. For the function φ it is possible to prove the identity

$$\sum_{j=1}^{k-1}\varphi\left(z,\tau+\frac{j}{k}\right)=\varphi\left(\frac{z}{k^2},\tau k\right),$$

where k is an arbitrary integer. The Jacobi functions are interrelated by an entire labyrinth of useful relations,[19] many of which are special cases of the last equation. Making use of it, it is possible to show that the Θ series obtained by analysis of the polytype structures can be expressed in terms of a combination of Jacobi functions, for which it is convenient to introduce separate notations

$$\alpha(z)=\vartheta_2(z)\vartheta_2(3z)+\vartheta_3(z)\vartheta_3(3z),$$

$$\beta(z)=\frac{1}{2}\left[\vartheta_2(z)\vartheta_2\left(\frac{z}{3}\right)+\vartheta_3(z)\vartheta_3\left(\frac{z}{3}\right)\right]-\frac{1}{2}\alpha(z).$$

[1] Yu. M. Tairov, Mater. Sci. Eng., B **29**, 83 (1995).
[2] R. F. Davis, G. Kelner, M. Shur, J. W. Palmour, and J. A. Edmond, Proc. IEEE **79**, 677 (1991).
[3] R. F. Davis, J. W. Palmour, and J. A. Edmond, Diamond Relat. Mater. **1**, 109 (1992).
[4] J. H. Edgar, J. Mater. Res. **7**, *1*, 235 (1992).
[5] R. F. Davis, J. Vac. Sci. Technol. A **11**, *4*, 829 (1993).
[6] C. M. Venvliet, G. Bosman, and L. L. Hench, Ann. Res. Mater. **18**, 381 (1988).
[7] A. R. Verma, P. Krishna, Polymorphism and polytypism in crystals, (John Wiley & Sons, N.Y. 1966; Mir, Moscow, 1969).
[8] Yu. M. Tairov and V. F. Tsvetkov, Prog. Cryst. Growth Charact. **7**, 111 (1983).
[9] M. Dubey, U. Shanker Ram, K. Nath Rai, and G. Singh, Phys. Status Solidi A **18**, *2*, 689 (1973).
[10] G. B. Dubrovskii and E. I. Radovanova, Phys. Status Solidi **48**, 875 (1971).
[11] D. J. Larkin, P. G. Neudeck, J. A. Powell, and L. G. Matus, Appl. Phys. Lett. **65**, 1659 (1994).
[12] G. Pensl and W. J. Choyke, Physica B **185**, 264 (1993).
[13] Y. A. Vodakov, G. A. Lomakina, E. N. Mokhov, E. I. Radovanova, V. I. Sokolov, M. M. Usmanova, G. F. Yuldashev, and B. S. Machmudov, Phys. Status Solidi A **35**, 37 (1976).
[14] I. J. Zucker, J. Math. Phys. **16**, *11*, 2189 (1975).
[15] M. L. Glasser and I. J. Zucker, Theor. Chem.: Adv. Persp. **5**, 67 (1980).
[16] N. J. A. Sloane and B. K. Teo, J. Chem. Phys. **83**, 6520 (1985).
[17] N. J. A. Sloane, J. Math. Phys. **28**, 1653 (1987).
[18] A. M. Odlyzko and N. J. A. Sloane, Stud. Sci. Math. Hung. **15**, *4*, 461 (1980).
[19] *Handbook of Mathematical Functions with Formulas, Graphs and Mathematical Tables*, edited by M. Abramowitz and I. A. Stegun, National Bureau of Standards, Appl. Math. Series-55 (1964).

Translated by Paul F. Schippnick

Effect of constant-energy surface anisotropy on the thermoelectric figure-of-merit of the *n*-$Bi_2(Te,Se,S)_3$ solid solutions

V. A. Kutasov, L. N. Luk'yanova, and P. P. Konstantinov

A. F. Ioffe Physicotechnical Institute, Russian Academy of Sciences, 194021 St. Petersburg, Russia
(Submitted July 10, 1998)
Fiz. Tverd. Tela (St. Petersburg) **41**, 187–192 (February 1999)

A study is reported of the thermoelectric and galvanomagnetic properties of n-$Bi_2Te_{3-x-y}Se_xSe_y$ solid solutions for $0.12 \leqslant x \leqslant 0.36$ and $0.12 \leqslant y \leqslant 0.21$ within the 80–300 K temperature region. The thermoelectric figure-of-merit Z has been found to correlate with the parameters of the many-valley energy-band model including anisotropic carrier scattering. It is shown that a decrease in the constant-energy surface anisotropy and scattering anisotropy results in a growth of Z for optimum carrier concentrations in the solid solution. © *1999 American Institute of Physics.* [S1063-7834(99)00302-0]

A number of problems of practical significance require finding ways of reaching temperatures below 150 K by thermoelectric methods. This makes development of materials with a high figure-of-merit Z in this temperature region particularly urgent. In this connection, there is considerable interest to carry out a comprehensive analysis of the parameters determining Z

$$Z = \mu_0 (m/m_0)^{3/2} / \kappa_L , \tag{1}$$

where m is the effective density-of-states mass, μ_0 is the carrier mobility with inclusion of degeneracy, and κ_L is the lattice heat conductivity.

The quantities entering Eq. (1) are connected with the constant-energy-surface parameters and carrier scattering processes, enabling establishing the relation between the figure-of-merit, these parameters, and the scattering processes under variation of temperature, carrier concentration, and solid-solution composition.

The most comprehensive studies of the constant-energy-surface were performed for n-Bi_2Te_3, both in weak[1–5] and strong[6,7] magnetic fields. Studies of Bi_2Te_3-based n-type solid solutions were performed on $Bi_2Te_{3-x}Se_x$ ($x<0.1$; $x>0.8$) using the Shubnikov-de Haas effect,[8] as well as by the present authors on n-$Bi_{2-x}Sb_xTe_{3-y}Se_y$ solid solutions in weak magnetic fields for isotropic carrier scattering,[9] and on $Bi_{2-x}In_xTe_3$ for anisotropic scattering[10]. At the same time the effect of changes in the constant-energy surface on the thermoelectric figure-of-merit Z has not been investigated up to now.

1. GALVANOMAGNETIC EFFECTS

The n-$Bi_2(Te,Se,S)_3$ solid solutions have rhombohedral symmetry with space group $R\bar{3}m$ and exhibit a strong anisotropy in transport properties due to characteristics of the crystal structure and the nature of their chemical bonds. The constant-energy surface of these Bi_2Te_3-based solid solutions is described by a many-valley band model, in which the resistivity, Hall effect, and magnetoresistance tensor components (ρ_{ii}, ρ_{ijk}, and ρ_{ijkl}, respectively) are related to the parameters determining the shape of the constant-energy ellipsoids u, v, w through[1,3]

$$\frac{\rho_{312}}{\rho_{123}} = \frac{(w+uv)(1+u)}{4uv}, \tag{2}$$

$$\frac{\rho_{11}\rho_{1133}}{\rho_{123}^2} = \frac{1+u^2}{4u\beta} - 1 , \tag{3}$$

$$\rho_{11}\rho_{1122}/\rho_{123}^2 = \frac{(3w+uw+uv+3u^2v)(1+u)}{16\beta u^2} - \frac{2v}{a^2(1+u)}, \tag{4}$$

$$\rho_{11}\rho_{1111}/\rho_{123}^2 = (w-5uw+3uv+u^2v)(1+u/16\beta u^2) , \tag{5}$$

where $a = \rho_{312}/\rho_{123}$.

The u, v, w parameters are connected with the components of the inverse effective-mass tensor $\alpha^{\leftrightarrow}$ by

$$u = \alpha_{11}/\alpha_{22}, \quad v = \alpha_{33}/\alpha_{22}, \quad v - w = \alpha_{23}/\alpha_{22} . \tag{6}$$

The rotation angle of the major axes of the constant-energy ellipsoids relative to the crystal axes is defined by

$$\tan 2\theta = 2\alpha_{23}/(\alpha_{22} - \alpha_{33}) . \tag{7}$$

The degeneracy parameter β can be written

$$\beta = \frac{I_1^2}{I_0 I_2},$$

$$I_n = \left(\frac{e}{m}\right)^n \frac{e^2}{3\pi^2 m}\left(\frac{2m}{\pi^2}\right)^{3/2} \frac{1}{|\alpha_{ij}|^{1/2}} \int_0^\infty \tau^{n+1}\varepsilon^{3/2}\frac{\partial f_0}{\partial \varepsilon} d\varepsilon . \tag{8}$$

Figure 1 presents temperature dependences of ρ_{312}/ρ_{123} (curves *1–9*) and of $\rho_{11}\rho_{1133}/\rho_{123}^2$ (curves *10–17*) measured in weak magnetic fields on single-crystal samples of the n-type $Bi_2Te_{3-x}Se_x$ and $Bi_2Te_{3-y}S_y$ solid solutions for

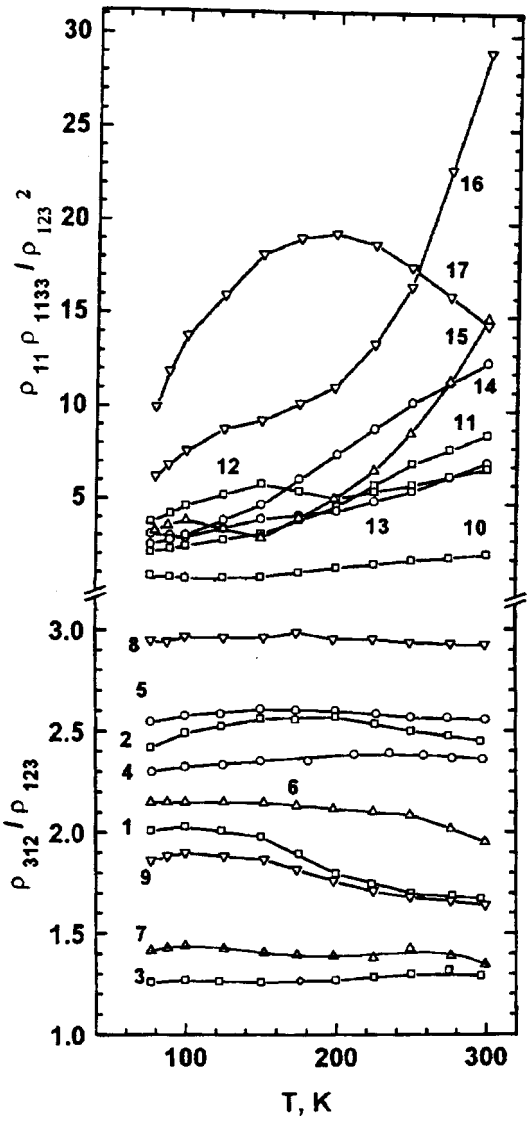

FIG. 1. Temperature dependences of the ratios ρ_{312}/ρ_{123} (*1–9*) and $\rho_{11}\rho_{1133}/\rho_{123}^2$ (*10–17*) for the $Bi_2Te_{3-x}Se_x$ and $Bi_2Te_{3-y}S_y$ solid solutions. n (10^{19} cm^{-3}): ($x=0.12$) *1, 10* — 0.25; *2, 11* — 0.9; *3, 12* — 3; ($x=0.3$) *4, 13* — 0.35; *5, 14* — 1.5; ($y=0.12$) *6* — 0.7; *7, 15* — 1.8; ($y=0.21$) *8, 16* — 0.5; *9, 17* — 2.6.

$x=0.12, 0.3$ and $y=0.12, 0.21$. As follows from Eq. (2), the variation of ρ_{312}/ρ_{123} with carrier concentration and temperature is determined only by that of u, v, w and does not depend on the actual scattering mechanism involved. The variation of ρ_{312}/ρ_{123} with carrier concentration indicates the need to use the two-band energy-spectrum model,[3,4] because these ratios remain constant within a one-band model.

As seen from Eqs. (3)–(5), the $\rho_{ii}\rho_{ijkl}/\rho_{ijk}^2$ ratios are determined not only by the quantities u, v, and w but by the form of the relaxation time τ as well and, therefore, the variation of these ratios is affected by two factors, namely, the influence of the second band and the carrier scattering anisotropy. Because the (3)–(5) relations have identical temperature and concentration dependences, we shall consider in what follows only the $\rho_{11}\rho_{1133}/\rho_{123}^2$ ratio.

It is known that the second band in the conduction band of Bi_2Te_3-based solid solutions fills at carrier concentrations $n\approx 3\times 10^{18}$ cm^{-3}.[3–5] Therefore the small increase in the $\rho_{11}\rho_{1133}/\rho_{123}^2$ ratios at low n (curve *10* in Fig. 1), where the existence of the additional band is still not felt, can be associated with anisotropic carrier scattering in the main band. The $\rho_{11}\rho_{1133}/\rho_{123}^2$ ratios increase with increasing carrier concentration, which can be accounted for by the presence of the second additional band, as well as because of anisotropy in carrier scattering (curves *11, 14, 16* in Fig. 1). The difference in the contributions due to these effects with further increase of carrier concentration may affect the shape of the temperature dependence of the $\rho_{11}\rho_{1133}/\rho_{123}^2$ ratio (curves *12, 15, 17* in Fig. 1).

2. EFFECTIVE MASS AND MOBILITY IN THE ISOTROPIC-SCATTERING MODEL

When analyzing the material parameters determining the thermoelectric figure-of-merit, one usually does not take into account the specific features of the complex band structure and of the scattering mechanisms. In such a model, the carrier scattering is isotropic and described by a scalar relaxation time depending only on energy by a power law relation

$$\tau=\tau_0 E^r, \tag{9}$$

where τ_0 is an energy-independent factor, and r is a scattering parameter; for the acoustic scattering mechanism that is dominant in the materials of interest here $r=-0.5$. The constant-energy surface in this case is spherical, and it corresponds to an average effective density-of-states mass m/m_0. The specific features in the band structure and scattering mechanisms can be included in calculations of the effective mass, (m/m_0), concentration (n), and mobility (μ_0) through an effective scattering parameter r_{eff}.[11] The quantities μ_0 and m/m_0 were derived from experimental data on electrical conductivity σ and Seebeck coefficient α for r_{eff} using the relations[12] for the carrier concentration and mobility valid for a semiconductor in the extrinsic conduction region.

The carrier concentration needed for calculation of μ_0 and m/m_0 in anisotropic materials was determined from

$$n=A(r_{\text{eff}},\eta)\,B/\rho_{ijk}e, \tag{10}$$

where η is the reduced Fermi level, $A(r_{\text{eff}},\eta)$ is the Hall factor, and B is the anisotropy parameter:

$$B=[(\rho_{11}\rho_{1133}/\rho_{123}^2+1)\beta(r_{\text{eff}},\eta)]^{-1}. \tag{11}$$

The Fermi level η was calculated from the Seebeck coefficient α derived in accordance with Ref. 13 for different values of r_{eff}. Figure 2 presents the concentration dependence of the Seebeck coefficient α obtained for the solid solutions under study at 300 and 77 K. For $Bi_2Te_{3-x-y}Se_xS_y$ measured for $y=0$ and at 300 K, α follows the same dependence on carrier concentration with x varying from 0.12 to 0.36 (points *1–4*). For $x=0, y=0.12$ and 0.21 the $\alpha=f(n)$ dependence becomes smoother (points *5* and *6*). At 77 K, the $\alpha=f(n)$ dependence similarly is weaker for $y=0.12, 0.21$ (points *11, 12*) and, in addition, for $x=0.12$ (points *7*).

Figures 3 and 4 plot characteristic temperature dependences of μ_0 and m/m_0 for $Bi_2Te_{3-x}Se_x$ and $Bi_2Te_{3-y}S_y$.

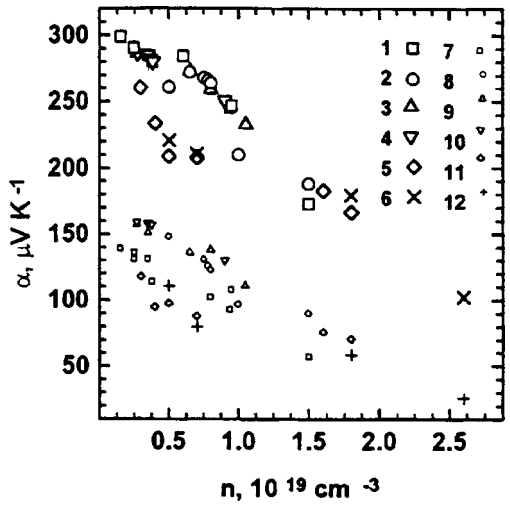

FIG. 2. Dependence of the Seebeck coefficient α on carrier concentration in the $Bi_2Te_{3-x}Se_x$ and $Bi_2Te_{3-y}S_y$ solid solutions measured at 300 K (*1–6*) and 77 K (*7–12*). *x*: *1*, *7* — 0.12; *2*, *8* — 0.21; *3*, *9* — 0.3; *4*, *10* — 0.36; *y*: *5*, *11* — 0.12; *6*, *12* — 0.21.

The carrier concentration n was varied by introducing Te in excess of the stoichiometric composition. The mobility μ_0 and the slopes $|s|=d\ln\mu_0/d\ln T$ decreased with increasing n and x in the solid solution because of the increasing number of scattering centers. In the low-temperature region ($80\,\mathrm{K}<T<150$ K) and for low carrier concentrations $n=(0.25-0.35)\times10^{19}$ cm^{-3}, $|s|$ decreases from 1.7 to 1.3 with x increasing from 0.12 to 0.36. For $y=0.12$ and 0.21, $|s|$ decreases from 1.6 to 0.8, respectively. The decrease of the slope in $Bi_2Te_{3-y}S_y$ compared to $Bi_2Te_{3-x}Se_x$ is due to the S atoms producing substantially larger distortions than Se when substituting for Te in the Bi_2Te_3 lattice.

As follows from the temperature dependence of the effective mass m/m_0 (curves *1–10* in Fig. 4), m/m_0 increases with n in samples with the same content of the second component, which can be assigned to the influence of the second additional band characterized by a larger effective mass than that in the main band (curves *1*, *2* and *5*, *6* in Fig. 4). As x and y increase, m/m_0 increases in samples with close carrier concentrations (curves *1*, *4*; *5*, *2*; *3*, *8*; and *9*). Such changes in m/m_0 with solid-solution composition are in agreement with the gap width E_g, because E_g increases with increasing x and y in the solid solution[14].

It should be pointed out that in the low-temperature domain m/m_0 decreases with decreasing temperature for $x=0.3$ and 0.36. This dependence of m/m_0 on T for a carrier concentration $n=0.35\times10^{19}$ cm^{-3} results in an increase of the thermoelectric figure-of-merit Z (curves *12* and *14* in Fig. 4), particularly at low temperatures. This carrier concentration is optimum for the low-temperature region and is close to the concentration at which the second band in the conduction band of Bi_2Te_3-based solid solutions starts filling. The largest increase of Z was observed in the $Bi_2Te_{3-x}Se_x$ solid solution with $x=0.3$ (curve *12* in Fig. 4) for low temperatures. At $x=0.3$, the decrease in mobility (curve *2* in Fig. 3) is compensated compared to the $x=0.12$ case (curve *1* in

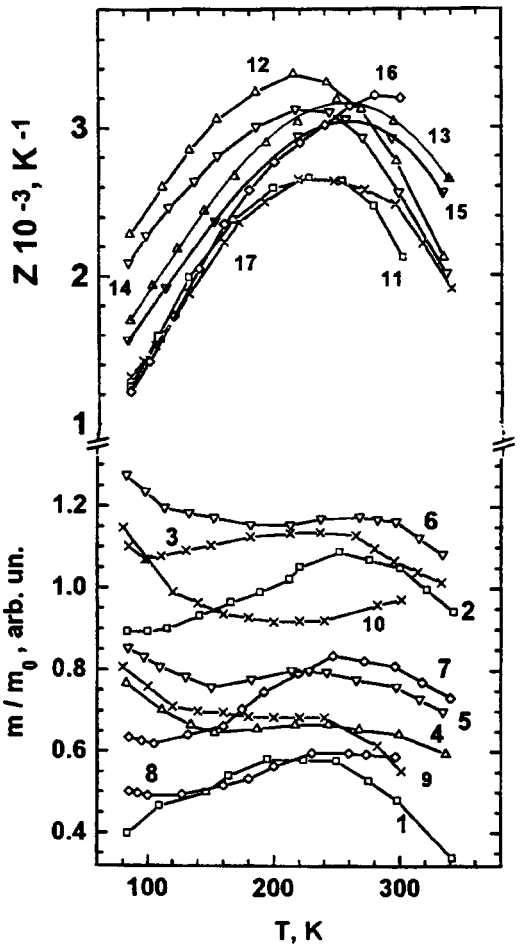

FIG. 4. Temperature dependences of the DOS effective masses m/m_0 (*1–10*) and thermoelectric figure-of-merit Z (*11–17*) in the $Bi_2Te_{3-x}Se_x$ and $Bi_2Te_{3-y}S_y$ solid solutions. n (10^{19} cm^{-3}): ($x=0.12$) *1*, *11* — 0.25; *2* — 0.8; ($x=0.21$) *3* — 0.8; ($x=0.3$) *4*, *12* — 0.35; *13* — 0.65; ($x=0.36$) *5*, *14* — 0.35; *6*, *15* — 0.9; ($y=0.12$) *7* — 0.4; *8*, *16* — 0.7; ($y=0.21$) *9* — 0.7; *10*, *17* — 1.8.

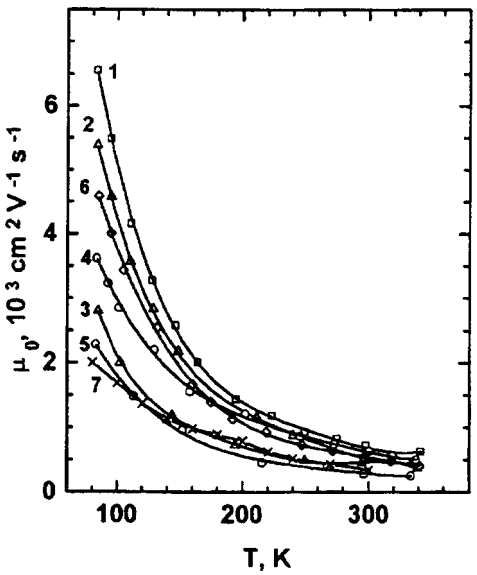

FIG. 3. Temperature dependence of mobility μ_0 in the $Bi_2Te_{3-x}Se_x$ and $Bi_2Te_{3-y}S_y$ solid solutions. n (10^{19} cm^{-3}): ($x=0.12$) *1* — 0.25; ($x=0.3$) *2* — 0.35; *3* — 0.65; ($x=0.36$) *4* — 0.35; *5* — 0.9; ($y=0.12$) *6* — 0.4; ($y=0.21$) *7* — 1.8.

Fig. 3) not only because m/m_0 increases with x but also because of the additional growth of m/m_0 with decreasing temperature which results from the increasing impurity-scattering contribution. At $x=0.36$ one also observes a high figure-of-merit at low T (curve *14* in Fig. 4). But the decrease in mobility was not completely compensated by the increase in effective mass (curve *4* in Fig. 3). The decrease in the lattice heat conductivity κ_L observed to occur in $Bi_2Te_{3-x}Se_x$ with increasing concentration of Se atoms[15] is likewise not large enough to increase Z. For higher carrier concentrations at $x=0.36$ (curve *6* in Fig. 4) and $y=0.21$ (curves *9* and *10* in Fig. 4), where m/m_0 also grows at low temperatures, the corresponding values of the figure-of-merit Z likewise decreased because of the decrease in mobility (curves *14* and *16* in Fig. 4).

3. ANISOTROPIC SCATTERING

The anisotropy in the transport properties of Bi_2Te_3-based solid solutions, which is caused by that in the elastic vibrations of the crystal, requires taking into account the anisotropy in carrier scattering. Therefore the most appropriate model for the constant-energy surface is a many-valley band approach, where the scattering is described by a tensor $\tau\leftrightarrow$ [with τ_0 in Eq. (9) being replaced by τ_{0ij}]. The corresponding changes in the expressions for the galvanomagnetic coefficients obtained without taking into account the scattering anisotropy reduce to substituting matrix products $(\alpha\tau)_{ij}$ for the inverse effective-mass tensor components α_{ij}.[16,17]

We use here the orientation of the Cartesian system relative to the crystal axes[3,4,6,18] in which the Z or (3) axis is along the three-fold axis C, the $X(1)$ axes are along the two-fold axes (binary directions $\langle 2110\rangle$), and the $Y(2)$ axes lie in the mirror planes (bisector directions $\langle 1010\rangle$).

Taking into account the Onsager principle, the expressions relating the components of tensor $\alpha^{\leftrightarrow}$ for the anisotropic and isotropic relaxation times can be written[4]

$$\alpha'_{11}=\gamma_1, \quad \alpha'_{22}=c^2\gamma_2+s^2\gamma_3, \tag{12}$$

$$\alpha'_{33}=s^2\gamma_2+c^2\gamma_3, \tag{13}$$

$$\alpha'_{23}=sc(\gamma_2-\gamma_3)+(c^2-s^2)\gamma_4, \tag{14}$$

where

$$\gamma_1=\alpha_1\tau_{11}, \quad \gamma_2=\alpha_2\tau_{22}, \quad \gamma_3=\alpha_3\tau_{33}, \quad \gamma_4=\alpha_2\tau_{23},$$
$$c=\cos\theta, \quad s=\sin\theta. \tag{15}$$

In view of Eq. (6), we obtain from Eqs. (12)–(14)

$$\gamma_2/\gamma_1=(c^2+s^2v)/u+2sc(v-w)^{1/2}u, \tag{16}$$

$$\gamma_3/\gamma_1=(s^2+c^2v-2sc(v-w)^{1/2})/u, \tag{17}$$

$$\gamma_4/\gamma_1=[-sc(1-v)+(c^2-s^2)(v-w)^{1/2}]/u. \tag{18}$$

As seen from Fig. 5, the γ_i/γ_j ratios calculated using Eqs. (15)–(18) depend on carrier concentration. It should be noted that the γ_2/γ_1 ratio increases more than tenfold as one crosses over from a sample with a low carrier concentration

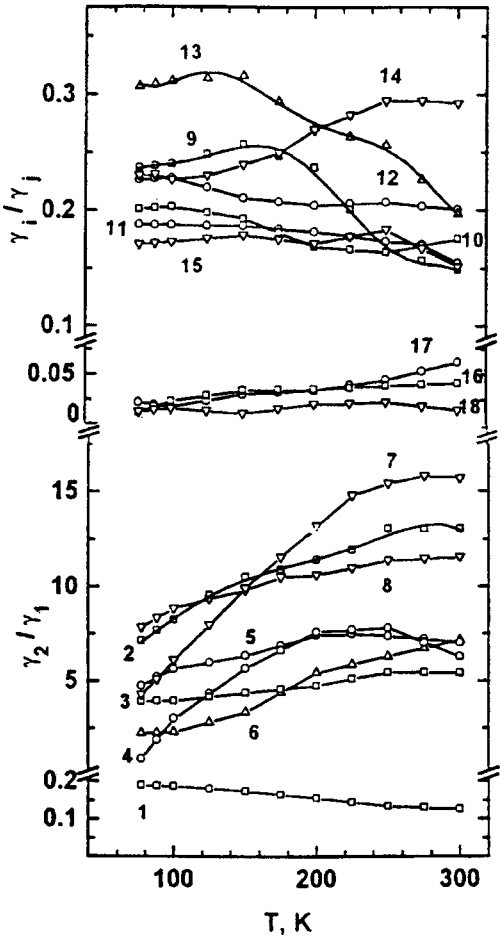

FIG. 5. Temperature dependences of the matrix-product ratios γ_i/γ_j in the $Bi_2Te_{3-x}Se_x$ and $Bi_2Te_{3-y}S_y$ solid solutions. n (10^{19} cm^{-3}): γ_2/γ_1 ($x=0.12$): *1* — 0.25; *2* — 1.5; *3* — 3; ($x=0.3$) *4* — 0.35; *5* — 1; ($y=0.12$) *6* — 1.8; ($y=0.21$) *7* — 0.4; *8* — 2.6. γ_3/γ_1 ($x=0.12$): *9* — 0.25; *10* — 1.5; ($x=0.3$) *11* — 0.35; *12* — 1; ($y=0.12$) *13* — 1.8; ($y=0.21$) *14* — 0.4; *15* — 2.6. γ_4/γ_1 ($x=0.12$) *16* — 0.25; ($x=0.3$) *17* — 0.35; ($y=0.21$) *18* — 0.4.

($n=0.25\times10^{19}$ cm^{-3}), at which the second band in the conduction band of the $Bi_2Te_{3-x}Se_x$ solid solutions has not yet started filling (curve *1* in Fig. 5), to samples with higher carrier concentrations ($n>0.35\times10^{19}$ cm^{-3}). This is followed by a growth of γ_2/γ_1 with increasing carrier concentration. At the highest carrier concentrations, similarly to the $\rho_{11}\rho_{1133}/\rho_{123}^2$ ratio (curves *12* and *17* in Fig. 1), the γ_i/γ_j ratios were observed to decrease compared to their values for lower carrier concentrations for $Bi_2Te_{3-x}Se_x$ and $Bi_2Te_{3-y}S_y$ (curves *2*, *3* and *7*, *8* in Fig. 5, respectively). This behavior of $\gamma_i/\gamma_j=f(n)$ can be explained by a narrowing of the gap between the bands in the solid-solution conduction band with increasing carrier concentration[18] until they finally overlap, which manifests itself in a change of the γ_2/γ_1 *vs* n dependence. The γ_i/γ ratios for $Bi_2Te_{3-y}S_y$ are larger than those for $Bi_2Te_{3-x}Se_x$ for comparable carrier concentrations and Se and S contents in the solid solution (curves *4* and *7* in Fig. 5).

Because the γ_i/γ_j ratios depend both on α_i/α_j and τ_{ij}/τ_{ii}, the concentration dependence of γ_i/γ_j can be associated not only with the constant-energy surface of the solid solutions under study becoming more anisotropic (curves *4*,

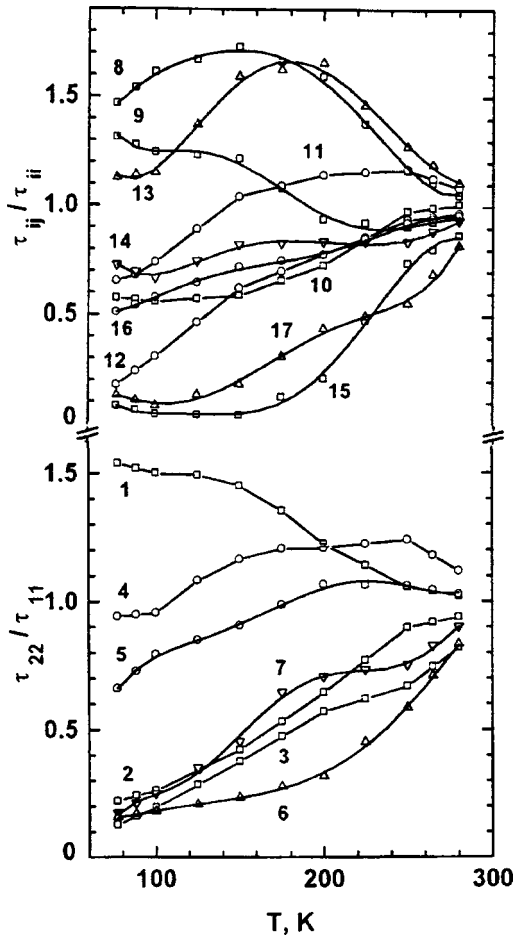

FIG. 6. Temperature dependences of the relaxation-time tensor component ratios τ_{ij}/τ_{ii} in the $Bi_2Te_{3-x}Se_x$ and $Bi_2Te_{3-y}S_y$ solid solutions. n (10^{19} cm^{-3}): (τ_{22}/τ_{11}) ($x=0.12$) *1* — 0.25; *2* — 0.6; *3* — 1; ($x=0.3$) *4* — 0.35; *5* — 1; ($y=0.12$) *6* — 0.7; ($y=0.21$) *7* — 0.4. (τ_{33}/τ_{11}) ($x=0.12$) *8* — 0.25; *9* — 0.6; *10* — 1; ($x=0.3$) *11* — 0.35; *12* — 1.5; ($y=0.12$) *13* — 0.7; ($y=0.21$) *14* — 2.6. (τ_{23}/τ_{11}) ($x=0.12$) *15* — 1.5; ($x=0.3$) *16* — 1.5; ($y=0.12$) *17* — 0.7.

5 and *6*, *7* in Fig. 5) but also with a change in the scattering anisotropy. The values of the γ_i/γ_j ratios were used to calculate the ratios of the inverse effective-mass and relaxation-time tensor components (α_i/α_j and τ_{ij}/τ_{ii}, respectively). Using galvanomagnetic coefficients, measured only in a weak magnetic field, to determine the τ_{ij}/τ_{ii} ratios is justified if one assumes that the room-temperature carrier scattering is close to isotropic, which is conceivable because of the anisotropy in phonon scattering being compensated by that of the phonon energy spectrum.[2,16,17] At low temperatures the impurity scattering contribution increases, and the anisotropy in phonon scattering is no longer compensated, making it necessary to include anisotropic scattering. The $\alpha^{\leftrightarrow}$ tensor component ratios were calculated under the assumption of α_i/α_j being temperature independent.

The temperature dependences of τ_{ij}/τ_{ii} (Fig. 6) show for low concentrations and temperatures that the τ_{22}/τ_{11} and τ_{33}/τ_{11} ratios for $Bi_2Te_{3-x}Se_x$ (curves *1*, *9* and *4*, *11* in Fig. 6) have close values, which suggests that scattering in the mirror plane is isotropic. For $x=0.3$, the scattering is nearly isotropic in both two-fold and bisector directions (curve *4* in Fig. 4). In $Bi_2Te_{3-x}Se_x$ ($x=0.12$) and $Bi_2Te_{3-y}S_y$ ($y=0.21$), the anisotropy in τ_{22}/τ_{11} at low carrier concentrations is larger; note that for $x=0.12$ (curve *1* in Fig. 6) the relaxation time increases in the bisector directions, and for $y=0.21$ (curve *7* in Fig. 6), in the binary directions because the scattering from Se and S atoms follows different patterns, as this was pointed out when discussing the variation of the slopes of the temperature dependences of mobility. The higher anisotropy in the scattering mechanism and the constant-energy surface may account also for the low figure-of-merit of the $Bi_2Te_{3-y}S_y$ solid solution (curve *7* in Fig. 4).

TABLE I. Ratios of the inverse effective-mass tensor components α_i/α_j for the $Bi_2Te_{3-x}Se_x$ and $Bi_2Te_{3-y}S_y$ solid solutions at 77 K.

$Bi_2Te_{3-x-y}Se_xS_y$				
x	y	n, 10^{19} cm^{-3}	α_2/α_1	α_3/α_1
0.12	0	0.25	0.12	0.16
		0.6	30.6	0.18
		1	35.5	0.32
		1.5	20.3	0.29
		3	5.6	0.06
0.3	0	0.35	8	0.18
		1	7	0.2
		1.5	6.3	0.15
0	0.12	0.7	15.5	0.38
		1.8	8.3	0.34
0	0.21	0.4	21.9	0.15
		2.6	8.5	0.04

The τ_{ij}/τ_{ii} ratios decrease with increasing carrier concentration, and the relaxation time in the binary directions increases (curves *1–3* and *4*, and *5*, *7* and *6* in Fig. 6). As the Se and S contents in the solid solution increase, the anisotropy in τ also increases along the binary directions (curves *1*, *4* and *9*, *12* in Fig. 6). The τ_{23}/τ_{11} ratios responsible for impurity scattering[4] are larger at $x=0.3$ (curve *17* in Fig. 5) than those for $x=y=0.12$ (curves *16* and *18* in Fig. 5). The τ_{ij}/τ_{ii} ratio decreases with increasing carrier concentration, which implies an increase of the relaxation time also along the binary directions.

The α_i/α_j ratios derived from the data on γ_i/γ_j (see Table I) depend on carrier concentration in such a way that the anisotropy in the constant-energy surface increases with carrier concentration and the content of Se and S atoms in the solid solution. The values thus obtained are in agreement with the available data[4] on α_i/α_j in n-Bi_2Te_3.

Thus our study of the thermoelectric and galvanomagnetic effects in $Bi_2Te_{3-x-y}Se_xS_y$ solid solutions made within the many-valley model showed the increase of the figure-of-merit at low temperatures to be the largest in $Bi_2Te_{3-x}Se_x$ ($x=0.3$), whose constant-energy surface and carrier scattering mechanisms are only weakly anisotropic. The optimum carrier concentration $n\cong 0.35\times 10^{19}$ cm^{-3} corresponding to the weakest anisotropy is close to complete filling of the second band in the conduction band of the $Bi_2Te_{3-x}Se_x$ ($x=0.3$) solid solution.

[1] J. R. Drabble, R. D. Groves, and R. Wolfe, Proc. Phys. Soc. London **71**, 430 (1958).
[2] B. A. Efimova, V. I. Novikov, and A. G. Ostroumov, Fiz. Tverd. Tela (Leningrad) **4**, 302 (1962) [Sov. Phys. Solid State **4**, 218 (1962)].
[3] L. P. Caywood and G. R. Miller, Phys. Rev. B **2**, 3210 (1970).
[4] H. A. Ashworth, J. A. Rayne, and R. W. Ure, Phys. Rev. B **3**, 2646 (1971).
[5] H. Kaibe, Y. Tanaka, M. Sakata, and I. Nishida, J. Phys. Chem. Solids **50**, 945 (1989).
[6] H. Köhler, Phys. Status Solidi B **73**, 95 (1976).
[7] R. B. Malinson, J. A. Rayne, and R. W. Ure, Phys. Rev. **175**, 1049 (1968).
[8] H. Köhler, W. Haigis, and A. Middendorff, Phys. Status Solidi B **78**, 637 (1976).
[9] V. A. Kutasov and L. N. Luk'yanova, Phys. Status Solidi B **154**, 669 (1989).
[10] V. A. Kutasov and L. N. Luk'yanova, Fiz. Tverd. Tela (Leningrad) **32**, 488 (1990) [Sov. Phys. Solid State **32**, 282 (1990)].
[11] V. A. Kutasov and L. N. Luk'yanova, Fiz. Tverd. Tela (Leningrad) **26**, 2501 (1984) [Sov. Phys. Solid State **26**, 1515 (1984)].
[12] A. I. Ansel'm, *Introduction to the Physics of Semiconductors* [in Russian] (Nauka, Moscow, 1978), 615 pp.
[13] V. A. Kutasov and L. N. Luk'yanova, Fiz. Tverd. Tela (Leningrad) **28**, 899 (1986) [Sov. Phys. Solid State **28**, 502 (1986)].
[14] D. L. Greenaway and G. J. Harbeke, J. Phys. Chem. Solids **26**, 1585 (1965).
[15] V. A. Kutasov and L. N. Luk'yanova, Fiz. Tverd. Tela (St. Petersburg) **38**, 2366 (1996) [Phys. Solid State **38**, 1302 (1996)].
[16] G. Herring and E. Vogt, Phys. Rev. **101**, 944 (1956).
[17] I. Ya. Korenblit, Fiz. Tverd. Tela (Leningrad) **2**, 3083 (1960) [Sov. Phys. Solid State **2**, 2738 (1960)].
[18] L. R. Testardi and E. Burstein, Phys. Rev. B **6**, 460 (1972).

Translated by G. Skrebtsov

Excitons in monoclinic zinc diphosphide. Longitudinal exciton and the mixed mode

I. S. Gorban', A. P. Krokhmal', and Z. Z. Yanchuk

Kiev State (T. Shevchenko) University, 252022 Kiev, Ukraine
(Submitted March 2, 1998; resubmitted July 20, 1998)
Fiz. Tverd. Tela (St. Petersburg) **41**, 193–202 (February 1999)

Exciton absorption spectra in high-quality $\beta-ZnP_2$ single crystals have been investigated at $T=1.7$ K for various directions of the wave vector and various polarization states of the radiation. It has been unambiguously established that the additional high-energy *A* series, which in some works has been called a *D* series and ascribed to ZnP_2 crystals, of so-called ''rhombic'' symmetry,[1,8,10,11] is an intrinsic exciton of the $\beta-ZnP_2$ series. A mixed mode has been detected for the first time, and the energy of the longitudinal exciton has been determined. The selection rules for the exciton transitions have been analyzed by a group-theoretical approach, and the symmetry of the nS states of the single exciton has been established on the basis of the experimental data — $\Gamma_2^-(z)$. © *1999 American Institute of Physics.* [S1063-7834(99)00402-5]

Monoclinic zinc diphosphide $\beta-ZnP_2$, with the space group $P2_1/c$ (C_{2h}^5), a direct-bandgap, optically biaxial semiconductor, in which dipole-forbidden electronic transitions as well as electric dipole transitions ($E1$) are realized,[1–4] is a beautiful model material for studying Wannier–Mott excitons and associated effects of spatial dispersion in low-symmetry crystals. In addition, the exciton states in monoclinic crystals should be influenced both by the anisotropy of the crystal field and by the dependence of the directions of the principal axes of the exciton polarizability and effective mass tensors on the direction of the wave vectors. But up to the present, exciton states in $\beta-ZnP_2$ have been examined insufficiently. This is due, first of all, to the incompleteness of the experimental data that has been obtained on high-quality single crystals for various directions of the wave vector of the exciton, the lack of quantitative calculations of the band structure, and also the absence of theoretical studies of exciton states in crystals whose symmetry is lower than rhombic.[5]

For normal incidence of radiation on one of the principal crystal-forming faces **bc** or the (100) plane of $\beta-ZnP_2$ crystals (and the overwhelming majority of studies have been performed in this geometry) the two well-known hydrogen-like exciton series are observed. The electric-dipole nS series of the singlet exciton, called the *C* series, is manifested in the exciton reflection spectra for the radiation polarized parallel to the crystallographic **c** axis ($\mathbf{E}\|\mathbf{c}$) and has a pronounced polariton character of its dispersion contours.[1–4] Because of the large oscillator strength of the exciton transition,[1–3] it has been possible to observe this series in the absorption spectra only in specially prepared thin samples.[4] For $\mathbf{E}\|\mathbf{b}$ the relative weak *B* series is observed in the absorption spectra. The authors of Ref. 1 identify the $n=1$ line, the so-called *B* line, with the $1S$ state of the ortho-exciton, and the authors of Refs. 6 and 7 identify the entire *B* series with high-energy components of the doublet lines for $n\geqslant 3$ with transitions to the nS ortho-states. The authors of Ref. 4 consider the lines with $n\geqslant 2$ to be due to transitions to the nP states of the exciton.

Sometimes an additional higher-energy series of absorption bands is observed simultaneously with the *B* series, whose nature has also not been determined.[4,8–10] The authors of Ref. 9 consider it to be the intrinsic exciton series that is observed for the polarization $\mathbf{E}\|\mathbf{a}$ while the authors of Refs. 8, 10, and 11 treat it as an exciton *D* series belonging to ZnP_2 crystals with rhombic symmetry.

Thus, a study of exciton spectra for various directions of the wave vector and various polarization states in high-quality oriented $\beta-ZnP_2$ single crystals is of urgent importance, and the present paper[1)] represents an attempt to fill this gap.

1. CRYSTAL GROWTH, AND EXPERIMENT

Quantities of $\beta-ZnP_2$ were synthesized from the ingredients phosphorus and zinc of 99.999% purity in quartz ampoules evacuated to $p=2\times10^{-5}$ mm Hg in twelve-zone tubular furnaces. Such furnaces make it easy to select and stably maintain the optimal temperature gradient along the ampoule axis. For total mass of the starting mixture equal to 15 g (with the mass of phosphorus 2 at. % larger than its stoichiometric amount) complete synthesis took roughly 100 h at temperatures in the zinc zone $\approx$1000 °C and in the phosphorus zone $\approx$480 °C. After double cleaning by resublimation in vacuum, the product was loaded into ampoules in $5-6$ g amounts to commence the growth phase. In ampoules of length $\approx$160 mm and inner diameter $\approx$18 mm, at a temperature in the zone with the charge $\cong$960 °C and in the growth zone $\cong$940 °C, complete mass transfer took place after $100-150$ h, where the transfer rate was determined mainly by the amount of surface of the charge. The crystals had well-developed, specular faces, as a rule of the types (100) and (110), and also $(\bar{1}01)$ and (102), with distance between the (100) and $(\bar{1}00)$ faces from 1 to 6 mm. The crystals were easily cleaved along the (110) planes. X-ray

studies of the crystals using the method of powder diffraction in a DRON-3 diffractometer with filtered copper radiation[12] revealed 100% phase composition of $\beta-ZnP_2$ with lattice periods $a=0.88752(24)$ nm, $b=0.72864(15)$ nm, and $c=0.75590(13)$ nm and monoclinic angle $\beta=102.407(20)°$. Our data are in good agreement with the $\beta-ZnP_2$ lattice parameters obtained on single-crystal wafers in Ref. 13. Laue diffraction patterns, taken with the primary beam collinear with the **b** (Y) and **c** (Z) axes and the crystallophysical X axis (**b**×**c**) and showing sharp reflections, revealed the presence of symmetry elements belonging to the group $P2_1/c$. The twinning at the microlevel in the (100) plane noted in Refs. 1, 10, and 13 was not observed. Using the thermal probe method it was determined that the as-grown single crystals have p-type conductivity.

In the present work we investigated the low-temperature exciton absorption spectra of $\beta-ZnP_2$ for various propagation directions of the incident radiation in the crystal $\mathbf{s}=\mathbf{q}/|\mathbf{q}|$ (where **q** is the wave vector of the electromagnetic wave and **k** is the wave vector of the exciton) and polarizations **E** relative to the crystal and crystal axes. We use the set of crystal axes customary for the monoclinic system. In this set[14] the monoclinic C_2 axis is parallel to the crystallophysical **b** axis, which is aligned with the Y axis of the crystallophysical coordinate system, the **c** axis is aligned with the Z axis, and the **a** axis makes an angle $\beta=102.3°$ (Refs. 12 and 13) with the **c** axis in the mirror plane m (XZ).

The absorption spectra were measured by transmission on an improved and automated DFS-12 spectrometer.[15] In the reported measurements, which had a spectral resolution of 0.05 meV, the spectrometer error in determining the photon energies corresponding to wavelengths in vacuum, and in the conversion factor 1239.852 eV·nm, did not exceed 4×10^{-5} eV. The cryosystem allows one to achieve fixed temperatures from 1.7 K on up with deviation from the prescribed value not greater than 0.1 K.

2. SYMMETRY OF THE EXCITON STATES, AND SELECTION RULES

According to Ref. 16, the absolute extrema[2)] of the bands in $\beta-ZnP_2$ can be located at the points Γ, A, R and D of the Brillouin zone (BZ). Since $E1$ transitions to S-type exciton states occur in $\beta-ZnP_2$,[1–4] but the group of the crystal class contains an inversion, the wave functions of the bottom of the conduction band (CB) and the top of the valence band (VB) have opposite parity if the corresponding group of the wave vector also contains an inversion. The valence band in $\beta-ZnP_2$, is formed by the $3p$ states of phosphorus,[17] whereas the conduction band is most probably formed by the $4s$ states of zinc. In Ref. 18 the parity of the conduction-band wave functions was assumed *a priori* to be negative. It is significant that the triply orbital-degenerate valence band formed by the $3p$ states of phosphorus in a monoclinic $\beta-ZnP_2$ crystal is completely split by the anisotropic crystal field with symmetry $2/m$ (C_{2h}), while the magnetic moments associated with the orbital motion are to first order equal to zero (the so-called ''freezing'' of orbital angular momenta by the crystal field[19]) and the relativistic interaction is expected to be weak.[3)] Data on the transmission spectra of thin crystals[4] indicate, in all probability, that the largest value of the crystal splitting of the valence band in $\beta-ZnP_2$ is around 0.15 eV. In Refs. 6 and 7 on the basis of magneto-optical measurements of the B series it was also concluded that the crystal splitting of the valence band in $\beta-ZnP_2$ significantly exceeds the spin–orbit splitting.

Since the monoclinic C_2 axis is aligned with the Y axis, for a correct group-theoretical analysis of the selection rules, it is necessary correspondingly to align the symmetry elements in the point group of the crystal class $2/m$, specifically, the C_2 axis should be aligned with the Y axis, not with the Z axis as is customary in group theory. In this case, the z and y coordinates change places in the basis functions of the irreducible representations. In the basis functions of the irreducible spinor representations the projections of the total angular momentum **J** onto the quantization axis, which is now the Y axis, changes sign since in the new representation the matrix $\sigma_y'=-\sigma_z$ becomes the diagonal Pauli matrix. In the double group $2/m$ the one-dimensional spinor representations Γ_3^+ and Γ_4^+, and also Γ_3^- and Γ_4^-, belong to the case ''b'' according to their symmetry to time inversion;[20] therefore they are combined and in what follows denoted as Γ_{34}^+ and Γ_{34}^-.

Assuming that the extrema of the bands are found in the center of the BZ, i.e., at $\mathbf{k}=0$, four one-dimensional terms arise for the nS states of the exciton for the fully symmetric envelope wave function: $\Gamma_e\times\Gamma_v\times\Gamma_{env}=\Gamma_{34}^+\times\Gamma_{34}^-\times\Gamma_1^+=2\Gamma_1^-+2\Gamma_2^-$. The group symmetry of the wave function in the Γ and A points of the BZ does not allow degenerate states with integer spin except for the points R and D, where a double degeneracy exists, associated with the spatial symmetry.[21,22] The analytical part of the short-range exchange interaction leads to singlet and triplet excitons, or para- and ortho-excitons. The non-analytical part of the exchange interaction with its long-range character taken into account can lead to removal of degeneracy of the ortho-state and to a dependence of the energy on the wave vector.[22]

$E1$ transitions to singlet nS states of symmetry Γ_1^- are allowed in the polarization $\mathbf{E}\|\mathbf{b}\|Y$, and to states with symmetry Γ_2^- in the polarization $\mathbf{E}\|\mathbf{b},\mathbf{c}\|X$ or $\mathbf{E}\|\mathbf{c}\|Z$ according to the orientation of the dipole moment $\mathbf{P}_m(\mathbf{s})$ for the given exciton band. Our data[23], which were presented in detail below, unambiguously indicate that $\mathbf{P}_m(\mathbf{s})$ is aligned with the **c** (Z) axis for the lowest exciton band in $\beta-ZnP_2$. Consequently, the singlet nS states have symmetry Γ_2^- with basis functions transforming in z. The three remaining symmetry states $2\Gamma_1^-+\Gamma_2^-$ must belong to the ortho-exciton, and in this case the basis functions of the Γ_2^- state most likely transform in x. Optical transitions to the ortho-states for systems with spherical symmetry are intercombinationally forbidden. This prohibition can be relaxed by the spin–orbit interaction and—this is especially important—in systems with a noncentral field, such as, probably, excitons in crystals with low symmetry. Transitions to ortho-states with symmetry $2\Gamma_1^-(y)+\Gamma_2^-(x)$ are forbidden in the electric quadrupole and magnetic dipole approximations by parity ($PP'=-1$).

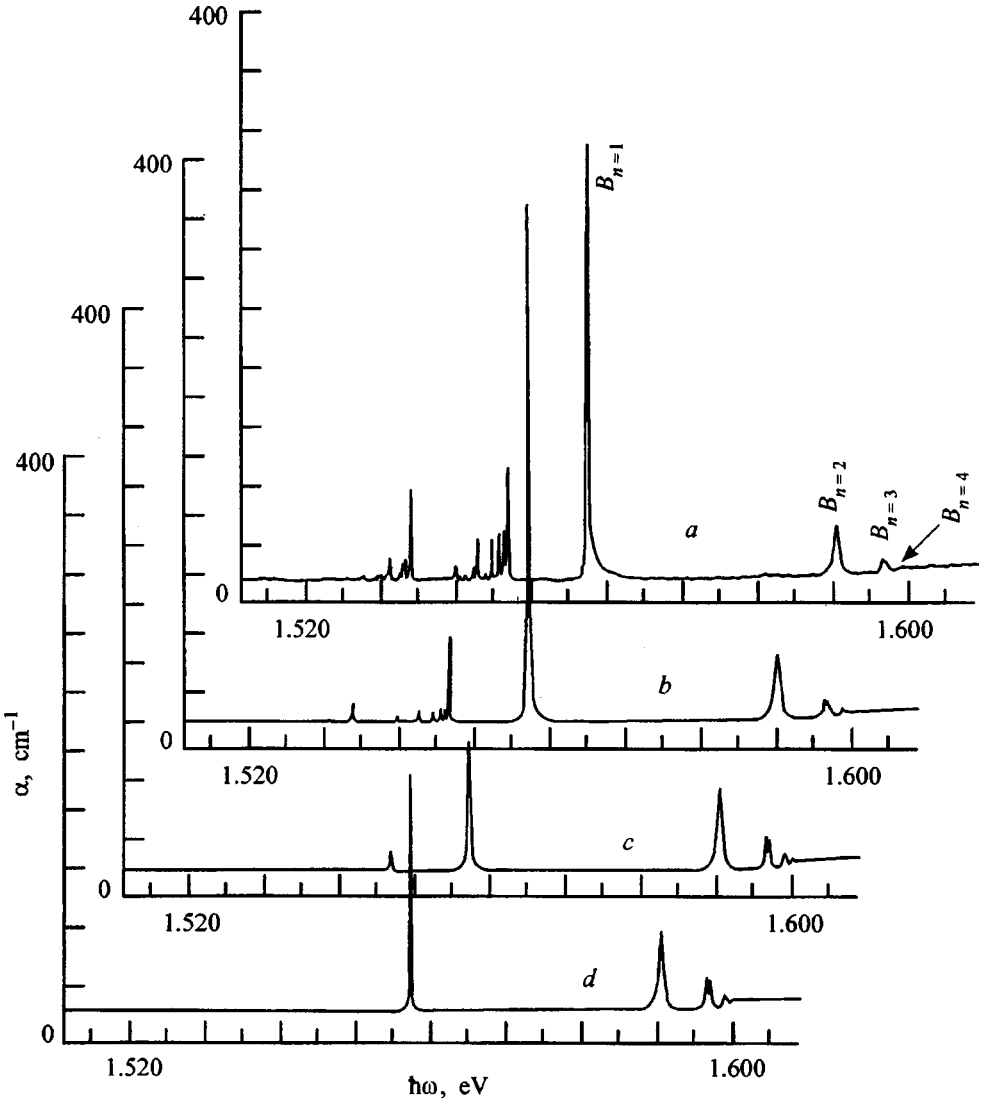

FIG. 1. Absorption spectra of $\beta-ZnP_2$ crystals grown under different conditions. $\mathbf{s}\perp(100)$, $\mathbf{E}\|\mathbf{b}$ and $T=1.7$ K. Sample thickness d, mm: a — 0.1206, b — 0.0988, c — 0.453, d — 0.205.

For $\mathbf{s}\|\mathbf{P}_m(z)$ the long-range nature and the non-analytical part of the exchange interaction[5,24] lead to the appearance of a longitudinal exciton, also with symmetry $\Gamma_2^-(z)$.

Let us consider other possible excited states of an exciton. For nP states 12 terms arise: $\Gamma_{34}^+\times\Gamma_{34}^-\times(\Gamma_1^-+2\Gamma_2^-)=6\Gamma_1^++6\Gamma_2^+$. But for excitons with ''p-like'' envelope wave functions the exchange interaction at zero can be neglected; therefore only three states are of interest: $\Gamma_2^-\times(\Gamma_1^-+2\Gamma_2^-)=2\Gamma_1^-+\Gamma_2^+$. These states do not have a simple analog, as is the case for crystals with axial symmetry, i.e., p_0 and $p_\pm$, but are completely split by the anisotropic crystal field into states of the type $P_a-\Gamma_1^+(xz)$, $P_b-\Gamma_2^+(yz)$ and $P_c-\Gamma_1^+(zz)$, where the coordinates indicated in parentheses are the coordinates in which the wave functions of the irreducible representations transform. Transitions to the nP states are split in the quadrupole approximation for scalar and magnetic-dipole ($M1$) and electric quadrupole ($E2$) transitions. However, the transition probabilities here may be expected to be several orders of magnitude smaller than for $E1$ transitions to nP states.[25,26] Optical transitions to nP exciton states of $\beta-ZnP_2$ have recently been observed for two-photon absorption.[18]

For nD exciton states 20 terms arise

$$\Gamma_{34}^+\times\Gamma_{34}^-\times(3\Gamma_1^++2\Gamma_2^+)=10\Gamma_1^-+10\Gamma_2^-,$$

of which only five turn out to be of interest: $\Gamma_2^-\times(3\Gamma_1^++2\Gamma_2^+)=2\Gamma_1^-+3\Gamma_2^-$, transitions to which are symmetrically allowed in the dipole approximation.

3. EXPERIMENTAL RESULTS AND DISCUSSION

Figure 1 displays absorption spectra of four $\beta-ZnP_2$ samples grown under different conditions for $\mathbf{s}\perp(100)$ and $\mathbf{E}\|\mathbf{b}$. It is clear from Fig. 1(a) that in one of the samples, besides the B series not less than two groups from the set of narrow lines with half-width $H=0.10-0.16$ meV are observed in the low-energy region, which are due to exciton-impurity (EI) complexes.[2,27] In the spectrum of the other sample [Fig. 1(b)] there are noticeably fewer EI lines, but in the spectrum of the sample shown in Fig. 1(c) there is only one very intense high-energy EI line at the photon energy 1.54732 eV. In the spectrum of the sample shown in Fig. 1(d) the 1.54732 eV line is absent even for a sample thickness $d=0.78$ mm, whereas two very weak ($\alpha\leqslant 1$ cm^{-1}) and very

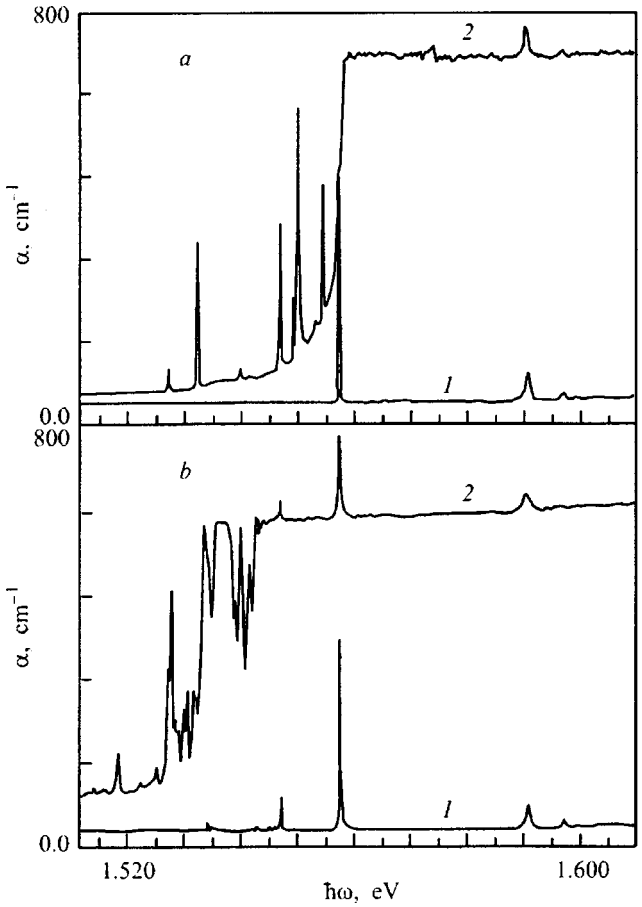

FIG. 2. Absorption spectra of two $\beta-ZnP_2$ samples for $\mathbf{s}\perp(100)$ for $\mathbf{E}\|\mathbf{b}$ (*1*) and $\mathbf{E}\|\mathbf{c}$ (*2*). $T=1.7$ K. *a* — sample *d* (Fig. 1) for $d=0.076$ mm, *b* — sample *b* (Fig. 1) $d=0.0988$ mm. Because of the large thickness of the samples the absorption coefficients for horizontal segments for $\mathbf{E}\|\mathbf{c}$ do not correspond to physical reality and are shown for comparison with the spectra in the exciton-impurity (EI) region..

high-energy lines are observed at 1.55065 eV and 1.55495 eV, obviously of a different EI nature. The intense and rich narrow-line spectrum with its strongest line at 1.54732 eV is observed in crystals grown with enhanced rates of mass transport and is probably due to structural defects, probably phosphorus vacancies or antistructural defects. The presence of EI lines due to phosphorus vacancies was also indicated in Refs. 8 and 28.

It is significant that in high-quality samples on which further studies were performed, a weak ($\alpha\leqslant 1-2$ cm^{-1}) EI line showed up at 1.54732 eV for sample thickness in the $\langle 100\rangle$ direction $d=1-2$ mm or did not show up at all.

Figure 2(a) shows absorption spectra in two polarizations. For $\mathbf{E}\|\mathbf{c}$ in one of the high-quality samples of thickness $d=0.076$ mm, in which no narrow-line EI spectrum is observed for $\mathbf{E}\|\mathbf{b}$, even for a thickness one order of magnitude layer, 0.78 mm, continuous absorption due to the *C* series starts up beyond the *B* line (1.55775 eV). On the long-wavelength wing of the powerful $C_{n=1}$ line several narrow lines of the EI complexes are observed. Figure 2(b) shows the absorption spectrum of another $\beta-ZnP_2$ sample, of thickness $d=0.098$ mm, having a relatively developed EI spectrum for $\mathbf{E}\|\mathbf{b}$ [Fig. 1(b)]. In the allowed polarization (curve *2*), the closely spaced EI lines overlap because of the giant oscillator strength[29] and continuous absorption arises already at ≈ 1.545 eV, which is significantly lower in energy than the *B* line. In some crystals an EI-absorption line is observed at 1.5506 eV. The strong absorption at this line in low-quality crystals leads to another resonance in the reflection spectra, which the authors of Refs. 1, 8, 19, and 30 ascribe to the intrinsic exciton series *A*, ''belonging'' only to the monoclinic modification of black ZnP_2.

It should be noted that, with decrease of the uncontrolled impurities and/or structural defects, the lines of the *B* series with $n=2-5$ become more intense while the doublet lines with $n\geqslant 3$ become sharper and a line with $n=6$ appears. With decrease of the intensity of the lines of the EI spectrum the total absorption coefficient of the *B* line decreases. Thus the shape of the *B* line with asymmetric high-energy wing in the impurity-laden samples becomes symmetric in the high-quality samples, and its half-width narrows from $H=0.27$ meV in an impurity-laden crystal [Fig. 1(a)] to $H=0.18$ meV in the high-quality crystal [Fig. 1(d)]. Consequently, the asymmetric high-energy wing of the *B* line observed by many authors in low-quality crystals is not due to intraband scattering of excitons by phonons as is supposed in Ref. 6, but is more likely caused by scattering of exciton polaritons by charged defects.[31] The properties of the *B* line will be considered in more detail in a subsequent work. Here we only note that in the hydrogenlike approximation for the *B* series the following exciton Rydberg energies and series convergence energies obtain: $R_y=45.87$ meV and $E_\infty=1.60279$ meV. In order to reduce to a minimum the distortion of the hydrogenlike trend caused by ''corrections for the central cell'' and by the anisotropic part of the Hamiltonian,[6,18] we used photon energies for the lines with $n=3$ and $n=4$ in the calculations.

As was already noted in some works,[4,8–11,32] another, higher-energy series of bands with dominant line around 1.575 eV has sometimes been observed in the absorption spectra of $\beta-ZnP_2$ together with the *B* series. The authors of Refs. 8 and 10 call it an exciton *D* series and ascribe it to crystals with so-called ''type-II rhombic symmetry,'' and the authors of Refs. 4 and 32 do not exclude the possibility of an impurity origin. The authors of Refs. 9 and 28 believe this series to be the exciton series that is observed in $\beta-ZnP_2$ for $\mathbf{E}\|\mathbf{a}$.

In some $\beta-ZnP_2$ samples we also observed the indicated series. X-ray diffraction identification of the most developed face in such samples showed that it has Miller indices (110), i.e., in the given case we recorded the spectrum for $\mathbf{s}\perp(110)$ and $\mathbf{E}\perp\mathbf{c}$. To confirm this result, we performed a direct experimental check: from a single crystal with well-developed faces and $d=2.5$ mm in the $\langle 100\rangle$ direction, in whose absorption spectrum for $\mathbf{s}\perp(100)$ and $\mathbf{E}\|\mathbf{b}$, i.e., in the traditional geometry only the *B* series is observed, we cleaved off a wafer parallel to the (110) plane. Figure 3 shows its spectrum, in which, in addition to the *B* series, a more intense high-energy series is observed. The $n=1$ line of this series is located at 1.57531 eV and has a half-width $H=0.43$ meV at a sample thickness of 0.062 mm. It is significant that the given line series decreases in intensity when

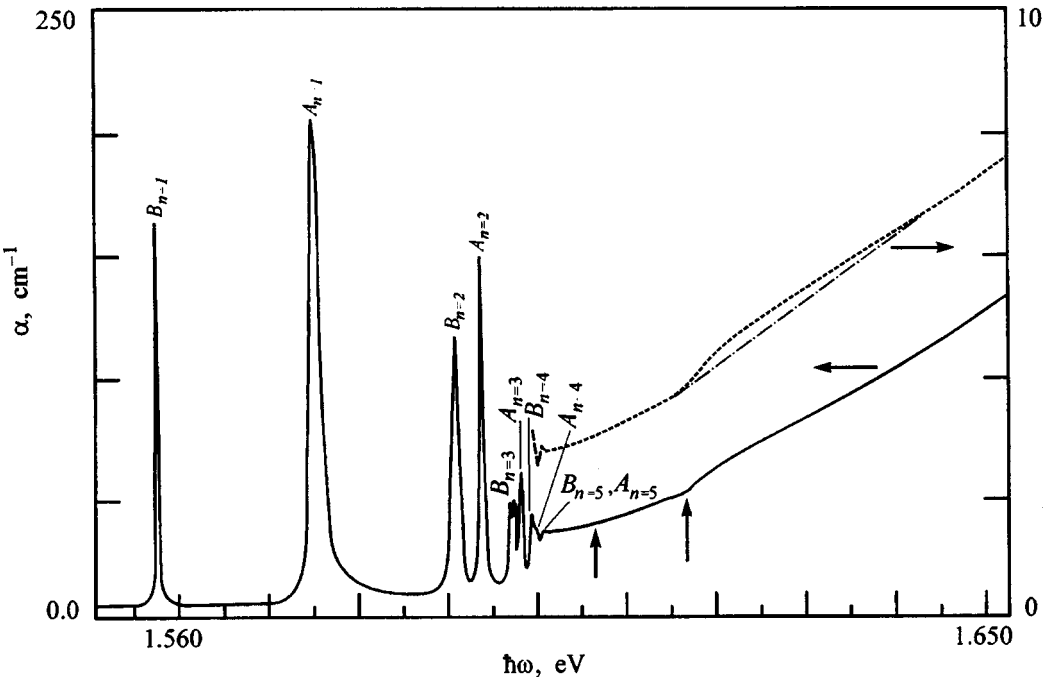

FIG. 3. Absorption spectrum of a $\beta-ZnP_2$ crystal for $\mathbf{s}\perp(110)$, $\mathbf{E}\perp\mathbf{c}$, and $T=1.7$ K. $d=0.30$ mm. *1* — ordinate axis scaled in cm^{-1}, *2* — in $cm^{-1/2}$. Arrows pointing up indicate the band-gap energy E_g and salient points in the continuous spectrum.

the sample plane is rotated about the **c** axis, upon which the refracted beam approaches the normal to the (100) plane and, conversely, increases if the refracted beam approaches the normal to the (010) plane. In the geometry with $\mathbf{s}\perp(010)$ and $\mathbf{E}\|\mathbf{b},\mathbf{c}\|X$ the *A* spectrum[4)] in its overall form is almost indistinguishable from the spectrum for $\mathbf{s}\perp(110)$ and $\mathbf{E}\perp\mathbf{c}$, but is more intense and its series of lines is insignificantly shifted toward higher energies. The half-width of the $A_{n=1}$ line $H=0.64$ meV is greater, as is its short-wavelength asymmetry.

Table I gives the energies of the lines of the *A* spectrum for $\mathbf{s}\perp(110)$ and $\mathbf{E}\perp\mathbf{c}$ and their values calculated in the hydrogenlike approximation. The *A* series follows the hydrogenlike trend with noticeable deviation for the $n=1$ line, and insignificant deviation for the $n=2$ line. The deviation of the $n=1,2$ lines can be explained by the corrections for the central cell, i.e., deviation of the potential from a Coulomb potential for an electron in the field of a hole. It is interesting to note that the positive value of the correction[4] either indicates the existence of a repulsive part of the non-Coulomb potential for the exciton ground state or is mainly due to another interaction, e.g., an exchange interaction. The Rydberg energy $R_y=35.38$ meV of the *A* series for $\mathbf{s}\perp(110)$ differs considerably from the Rydberg energy for the *B* series, but the convergence energy of the *A* series $E_\infty=1.60243$ eV is very close to its value for the *B* series. This leads us to the thought that the *A* series probably arises from the same pair of bands as the *B* series. The properties of the *A* series will be considered in detail in a subsequent work.

TABLE I. Energies of the lines of the *A* spectrum in the geometry $\mathbf{s}\perp(110)$ and $\mathbf{E}\perp\mathbf{c}$, their values calculated in the hydrogenlike approximation, and the corresponding discrepancies.

	E_{exp}	E_H	$\Delta E=E_{exp}-E_H$
n	(eV)	(eV)	(eV)
1	1.57531	1.56705	0.00826
2	1.59409	1.59359	0.00050
3	1.59850	1.59850	0
4	1.60022	1.60022	0
5	1.60107	1.60102	0.00005

As was noted in Ref. 9, the *A* series for $\mathbf{E}\|\mathbf{a}$ has been successfully observed either on cleaved wafers or, more rarely, on naturally grown wafers containing the **a** and **c** axes. Now it is obvious that the authors of Ref. 9 observed the *A* spectrum in the geometry $\mathbf{s}\perp(110)$ and $\mathbf{E}\perp\mathbf{c}$, and not $\mathbf{E}\|\mathbf{a}$, since $\beta-ZnP_2$ crystals do not have (010) faces, rather they cleave along (110) planes.

In the absorption spectrum for $\mathbf{s}\perp(110)$ and $\mathbf{E}\perp\mathbf{c}$, in addition to the discrete *A* and *B* series in the region of the continuum of the band-to-band transitions, a distinct salient point at $\hbar\omega=1.6064$ eV and a more intense step at 1.6170 eV are observed (Fig. 3). These features are observed 46.15 meV and 56.75 meV above the energy of the $C_{n=1}$ transverse exciton (see below). The indicated energies coincide with the energies of the *LO* phonons $\hbar\Omega=46.12$ meV and $\hbar\Omega=56.79$ meV found in Ref. 10, and and $\hbar\Omega=56.54$ meV, found in Ref. 33. Consequently, the observed features can be tentatively associated with indirect transitions to the $n=1$ band of the singlet exciton with emission of *LO* phonons.

Thus, the experimental results obtained on high-quality $\beta-ZnP_2$ crystals are at variance with the classification of exciton spectra observed in Refs. 1, 8, and 10 as belonging to monoclinic and various types of so-called ''rhombic'' crystals of black ZnP_2. All the spectra belong to the monoclinic

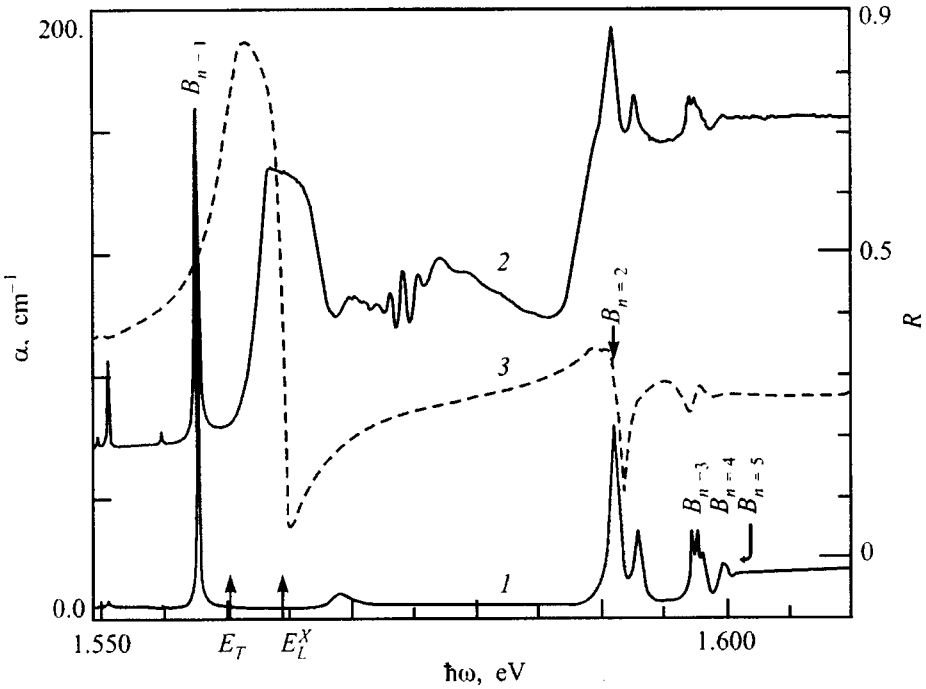

FIG. 4. Absorption spectrum of a $\beta-ZnP_2$ crystal for $\mathbf{s}\perp(001)$ for two polarizations: *1* — $\mathbf{E}\|\mathbf{b}$, *2* — $\mathbf{E}\|\mathbf{a}$ (shifted upward by $50\,cm^{-1}$). Curve *3* is the $\beta-ZnP_2$ reflection spectrum for $\mathbf{s}\perp(100)$ and $\mathbf{E}\|\mathbf{c}$. The arrows indicate the energies of the transverse exciton and longitudinal exciton for the given geometry. $T=1.7$ K, $d=0.386$ mm.

modification of $\beta-ZnP_2$. The presence of a large quantity of uncontrolled impurities and/or structural defects not only alters the lattice constants, but also distorts the exciton spectrum in a substantial way because of scattering (capture) of excitons by defects and also because of a shift and broadening of exciton states by screening effects as well as local fields of charged impurities and ionization in them of states with high n [Fig. 1(a)].

It is significant that for the polarization $\mathbf{E}\|\mathbf{c}$ for $\mathbf{s}\perp(110)$ and $\mathbf{s}\perp(010)$, as in the case $\mathbf{s}\perp(100)$, there is a powerful absorption of the dipole-allowed *C* series.

Figure 4 shows the spectrum of $\beta-ZnP_2$ for $\mathbf{s}\perp(001)$ and $\mathbf{E}\|\mathbf{b}$. In this spectrum two series of lines are again observed. One of them is the *B* series, whose line intensities for $n\geqslant 2$ are roughly the same as for $\mathbf{s}\perp(100)$ and $\mathbf{E}\|\mathbf{b}$. The second, of much lower intensity, with the $n'=1$ line at 1.56906 eV has a comparatively large half-width ($H\cong 2$ meV) and asymmetric lineshape with a high-energy tail. An important feature of this series is the significant and nonlinear shift that it undergoes attendant to rotations of the sample plane **ab** (001) about the **b** (C_2) axis by some angle i relative to the incident radiation. As the direction of the refracted beam approaches the **c** axis, i.e., the angle between **s** and **c** decreases from its initial value $\varphi_0=12.3°$, it shifts toward lower energies and the intensity of the given series grows. As the angle of incidence increases to $i\approx 32°$, the $n'=1$ line shifts to the photon energy 1.5649 eV, and its half-width narrows to 1 meV while preserving its original asymmetry. When the (001) plane is rotated in the opposite direction, i.e., as the angle φ_0 increases, the series shifts toward higher energies and its intensity falls. For this series $R_y'=37.65$ meV and $E_\infty=1.60230$ eV, i.e., they are close to the values obtained for the *A* series. Note that the intensity and position of the lines of the *B* spectrum remain essentially unchanged as the sample is rotated.

For $\mathbf{E}\|\mathbf{a}$ (Fig. 4) and $\mathbf{s}\perp(001)$, beyond the *B* line a wide and attenuated absorption band is observed in the region of the dispersion contour of the exciton reflection of the $C_{n=1}$ exciton, having a shape characteristic of $n=1$ dipole excitons. It is followed by a window of transparency, beyond which absorption to the states $n\geqslant 2$ arises, transitioning into the continuum. These data indicate that for $\mathbf{s}\perp(001)$ there is a small projection of the dipole moment of the transition matrix element onto the vector **E**. It is interesting to note that around 1.575 eV interference of the birefringence can arise when the vector **E** is not parallel to one of the two vectors: **a** and **b**.

Figure 5 shows the spectrum of $\beta-ZnP_2$ for the radiation incident on the plane of the cut normal to **c**, i.e., in the geometry $\mathbf{s}\|\mathbf{c}\|Z$ for $\mathbf{E}\|\mathbf{b}$ and $\mathbf{E}\|\mathbf{b}\times\mathbf{c}\|X$. For $\mathbf{E}\|X$ two series of lines are observed: the *B* series and a new, less intense high-energy series with dominant line $n'=1$ at 1.56481 eV. In different samples its position can shift by up to ≈ 0.1 meV toward either higher or lower energies, which is probably due to internal strains in the samples. Table II lists the line energies for this series. The series follows a hydrogenlike trend. A noticeable deviation toward higher energies is observed only for the line $n'=1$. For the given series, for $\mathbf{E}\|X$ $R_y'=42.38$ meV and $E_\infty=1.60263$ eV.

Two series are also observed for $\mathbf{E}\|\mathbf{b}$: a *B* series and a higher-energy series, one with $n''=1$ at 1.56491 eV, which is shifted by $\Delta E=0.1$ meV toward higher energies in comparison with the series for $\mathbf{E}\|X$. This difference can vary from sample to sample and even become zero under certain conditions, e.g., for $T\approx 100$ K, which is obviously due to the biaxialilty of the crystal. The absorption coefficients of the lines n, $n''\geqslant 2$ of the *B* series and the additional series are roughly the same. Table III lists the line energies of this series. The series closely follows a hydrogenlike trend. A noticeable deviation toward higher energies is observed only

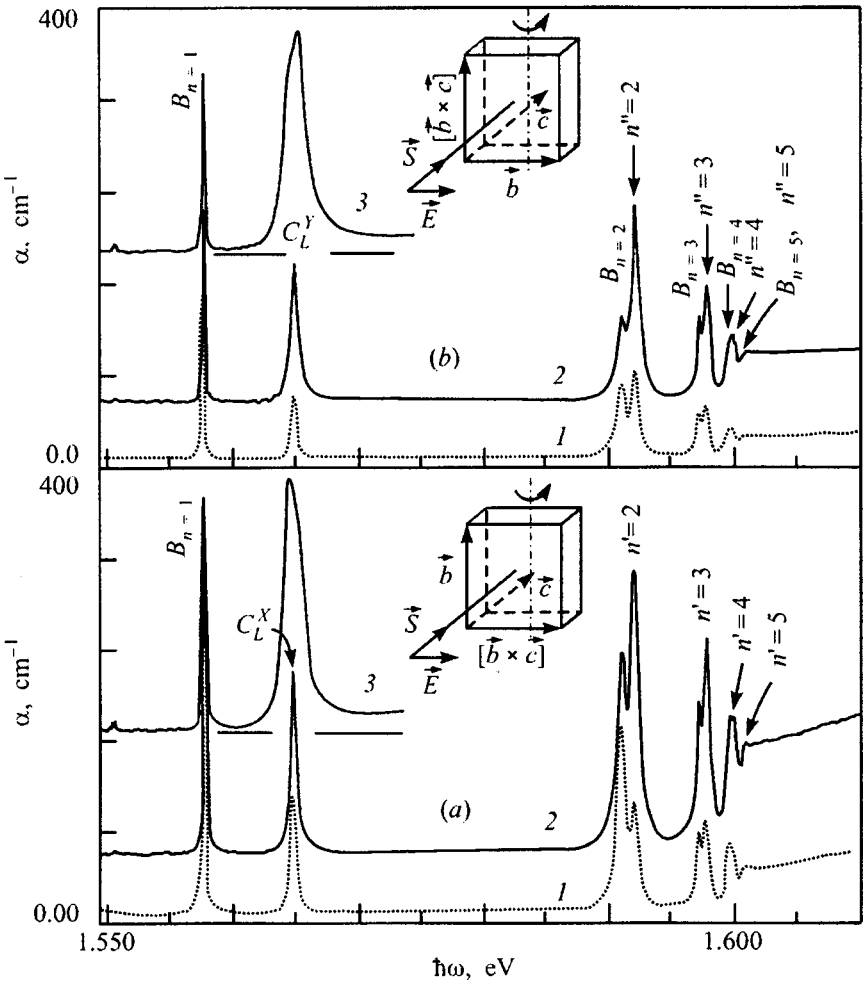

FIG. 5. Absorption spectrum of $\beta-ZnP_2$ for radiation incident on the cleavage plane normal to the **c** (z) axis for two polarizations: *a* — $\mathbf{E}\|\mathbf{b}\times\mathbf{c}\|X$, *b* — $\mathbf{E}\|\mathbf{b}\|Y$, and several angles of incidence: *i*: *1* — 0°, *2* — 5°, *3* — 15°. $T=1.7$ K, $d=0.168$ mm. Curves *2* and *3* are shifted upward. Insets show the geometry of the experiment.

for the line $n''=1$. For this series we also have $R_y''=42.38$ meV and $E_\infty=1.60263$ eV. It is significant that in the geometry $\mathbf{s}\|\mathbf{c}\|Z$ for $\mathbf{E}\|X$ and $\mathbf{E}\|\mathbf{b}$ the strong absorption due to dipole-allowed exciton transitions is not observed.

Thus, analyzing the polarization properties of the absorption spectra for various directions of propagation in $\beta-ZnP_2$, we arrive at the conclusion that $E1$ transitions to exciton states occur in the case when the vector **E** has a component along the **c** axis. Consequently, the specific dipole moment $\mathbf{P}_m$ for the lowest exciton band is aligned with the crystallographic axis **c** or Z.

It is well known[5,34] that only along a principal direction of the exciton polarizability tensor κ (for the total field **E**) for which the dipole moment $\mathbf{P}_m(\mathbf{s})$ is nonzero are longitudinal polarization waves excited having $\mathbf{E}\|\mathbf{s}$ and frequency ω_L determined by the dispersion law of the longitudinal wave $\det|\varepsilon_{ij}(\omega,\mathbf{k})|=0$, which is equivalent to excitation of a longitudinal Schrödinger exciton with energy E_L. The longitudinal wave of exciton polarization does not interact with a transverse electromagnetic wave; for this reason the so-called ''mixed mode'' is a characteristic indicator of the existence of a longitudinal exciton.[26,35]

For normal incidence of radiation with $\mathbf{E}\|X$ onto the plane of the **b**, $\mathbf{b}\times\mathbf{c}$ or XY cut of a $\beta-ZnP_2$ crystal, the line of the additional series at 1.56481 eV, which we shall call the C_L^X line, is observed in the ordinary ray upon a small rotation of the sample about the **b** (C_2) axis[5)] and grows considerably in intensity even for a small increase in the angle of incidence *i* from zero [curves *2* and *3* in Fig. 5(a)]. Lines of the series with $n'\geqslant 2$ also grow substantially under these condi-

TABLE II. Energies of the mixed mode for $\mathbf{s}\|\mathbf{c}$ and $\mathbf{E}\|X$, $E_{nT(H)}^X$, their values calculated in the hydrogenlike approximation for the direction $\mathbf{s}\|X$, and the corresponding discrepancies.

n'	$E_{\exp}$ (eV)	$E_{T(H)}^X$ (eV)	$\Delta E=E_{\exp}-E_H$ (eV)
1	1.56481	1.56025	0.00456
2	1.59218	1.59204	0.00014
3	1.59792	1.59792	0
4	1.59998	1.59998	0
5	1.60095	1.60093	0.00002

TABLE III. Energies of the lines for the additional series for $\mathbf{s}\|\mathbf{c}$ and $\mathbf{E}\|\mathbf{b}$, their values calculated in the hydrogenlike approximation, and the corresponding discrepancies.

n''	$E_{\exp}$ (eV)	E_H (eV)	$\Delta E=E_{\exp}-E_H$ (eV)
1	1.56491	1.56025	0.00466
2	1.59221	1.59203	0.00018
3	1.59792	1.59792	0
4	1.59998	1.59998	0
5	1.60097	1.60093	0.00004

tions, whereby the line C_L^X shifts toward lower energies. This shift is in accord with the theoretical predictions in Ref. 5.

Thus, for $\mathbf{s}\|\mathbf{c}$ and $\mathbf{E}\|X$ we have all the indicators of a mixed mode in the X direction at the frequency of the longitudinal exciton $E_L=1.56481$ eV. The series with $n'\geqslant 2$ for $\mathbf{E}\|X$ should be considered as the series of the mixed mode of hydrogenlike states of the longitudinal exciton with the corresponding states of the transverse exciton E_{nT} for $\mathbf{s}\|X$. Since the magnitude of the longitudinal splitting of the exciton is proportional to the oscillator strength of the transition $\Delta E_{LT}\cong 2\pi\kappa_0 E_T/\langle\varepsilon_0\rangle$ and the oscillator strength falls off as n^{-3} for the nS states, for high n the splitting ΔE_{LT} can be neglected. Therefore the energies of the states, $E_{n'}$, of the mixed mode approach E_{nT} with growth of n'. Because $\Delta_{LT}\propto n^{-3}$, mixing of longitudinal and transverse states of the exciton grows dramatically for the higher terms of the series, which is the cause of the above-noted faster increase of the lines $n'\geqslant 2$ in comparison with the $n'=1$ line. Thus, the $E_{n'}$ values calculated in the hydrogenlike approximation for $n'=3$ and $n'=4$ of the mixed mode are very close to the E_{nT}^X values of the C series of the transverse exciton in the X direction.

For $\mathbf{s}\|\mathbf{c}$ and $\mathbf{E}\|\mathbf{b}$ the 1.56491 eV line, which we denote as C_L^Y, is also observed in the extraordinary ray for a small rotation of the sample plane (the XY plane) about the direction $\mathbf{b}\times\mathbf{c}$ (the X direction) and increases noticeably in intensity with growth of the angle of incidence i from zero [curve *2* in Fig. 5(b)]. The intensity of the lines with $n''\geqslant 2$ also undergoes substantial growth. But with increase of the incidence angle i the C_L^Y line and the terms of the series with $n''\geqslant 2$ are shifted toward higher energies. With further increase of i above 10° the C_L^X line also clearly exhibits a low-energy component, which is shifted toward lower energies [curve *3* in Fig. 5(b)]. Thus, it appears that in the given case two spectra are manifested. One of these is the mixed mode of a longitudinal and a transverse exciton, in the $\langle 010\rangle\|\mathbf{b}\|Y$ direction, E_T^Y, and the other, shifted toward higher energies, is probably the A spectrum.

Consequently, the above-obtained Rydberg energies $R_y=42.38$ meV are the Rydberg constant for the exciton, and E_∞ is the width of the band gap $E_g=1.60263$ eV. The energy of the $n'=1$ line, found in the hydrogenlike approximation, corresponds to the energy of the transverse exciton $E_T^X=(1.56025\pm 0.00015)$ eV without allowance for the corrections for the central cell or the nonspherical part of the Hamiltonian.[6] The value of E_T^X obtained coincides with the value $E_T=1.5603$ eV (Ref. 2) and is close to the value $E_T=1.5606$ eV (Refs. 1 and 3), both of which were found by fitting the theoretical exciton reflection spectrum to the experimental spectrum with allowance for spatial dispersion.

In crystals of the monoclinic system the dielectric tensor $\varepsilon_{ij}(\omega)$ is equivalent to two real tensors $\varepsilon_{ij}(\omega)=\varepsilon'_{ij}(\omega)+i\varepsilon''_{ij}(\omega)$. The existence of a longitudinal exciton in the Z direction indicates[34] that in $\beta-ZnP_2$ the principal axes of the tensors $\varepsilon'_{ij}(\omega)$ and $\varepsilon''_{ij}(\omega)$ coincide not only in the Y direction, but also in the Z and X directions. Consequently, frequency dispersion of the axes is absent in $\beta-ZnP_2$, in any case, at low temperatures.

Monoclinic crystals are conveniently distinguished by the fact that their symmetry does not allow excitation of $E1$ excitons with the same polarization, since each exciton band in correspondence with a split p-valence band has its own specific dipole moment of exciton polarization $\mathbf{P}_m(\mathbf{s})$. We found that in $\beta-ZnP_2$ for the lowest exciton band $\mathbf{P}_m(\mathbf{s})$ is aligned with the $\mathbf{c}$ axis (Z axis), the direction in which the mixed mode of the hydrogenlike states is observed. This circumstance allowed us to determine with high accuracy not only the energy of the longitudinal exciton E_L^X and E_L^Y, but also important parameters in $\beta-ZnP_2$ such as E_g and R_y, and also the energies E_{nT} for the singlet exciton without resorting to a study of superthin crystal wafers.

If we assume that the extrema of the bands are not located at the center of the Brillouin zone, but at some other point whose wave-vector symmetry group does not contain an inversion,[16] then it is hard to explain to presence of exciton spectra, especially the B series, for all directions of the wave vector. We thank V. Ya. Markiv for doing the x-ray analysis of the $\beta-ZnP_2$ and V. A. Gubanov for fruitful discussions.

This work was carried out with the support of the State Foundation of the Ukraine for Basic Research (Grant No. 2.4/311).

[1)] The results of this work were reported in part at the Eleventh and Twelfth Republic School–Seminars on Spectroscopy of Molecules and Crystals, Khar'kov (May 1993), Nezhin (July 1995), and the Sixteenth Pekar International Conference on the Theory of Semiconductors, Odessa (October 1994).

[2)] The term 'absolute extremum' means: in all three directions k_x, k_y, k_z.

[3)] Spin–orbit splitting of the $^2P_{1/2}-{}^2P_{3/2}$ states in the phosphorus atom is 3.13 meV, and of the $^3P_0-{}^3P_1$ states in the zinc atom is 23.5 meV. Consequently, in ZnP_2 spin–orbit splitting of the valence band can be expected to be $\Delta_{so}\approx 8.5$ meV.

[4)] The vector $\mathbf{b}\times\mathbf{c}$ makes an angle of 12.3° with the crystallographic **a** axis, wherefore this additional series has acquired the designation A series.[9,23,28]

[5)] If the surface of refractive indices of $\beta-ZnP_2$ is determined by the principal values ε_a, ε_b, and ε_c, also obtained at helium temperatures from an analysis of the magneto-optical data on the B series in Ref. 6.

E-mail: expdept@expphys.ups.kiev.ua

[1] A. B. Pevtsov, S. A. Permogorov, A. V. Sel'kin, and N. N. Syrbu, Fiz. Tekh. Poluprovodn. **16**, 1399 (1982) [Sov. Phys. Semicond. **16**, 897 (1982)].
[2] R. S. Berg, P. Y. Yu, and Th. Mowles, Solid State Commun. **46**, *2*, 101 (1983).
[3] O. Arimoto, M. Tachiki, and K. Nakamura, J. Phys. Soc. Jpn. **60**, *12*, 4351 (1991).
[4] I. S. Gorban', N. M. Belyĭ, V. A. Borbat, V. A. Gubanov, I. N. Dmitruk, and Z. Z. Yanchuk, Dokl. Akad. Nauk USSR. Ser. A, *4*, 48 (1988).
[5] S. I. Pekar, *Crystal Optics and Booster Light Waves* [in Russian] (Naukova Dumka, Kiev, 1982).
[6] S. Taguchi, T. Goto, M. Takeda, and G. Kido, J. Phys. Soc. Jpn. **57**, *9*, 3256 (1988).
[7] T. Goto, S. Taguchi, K. Cho, Y. Nagamune, S. Takeyama, and N. Miura, J. Phys. Soc. Jpn. **59**, *2*, 773 (1990).
[8] N. N. Syrbu and V. M. Mamaev, Fiz. Tekh. Poluprovodn. **17**, 694 (1983) [Sov. Phys. Semicond. **17**, 433 (1983)].
[9] V. V. Sobolev and A. I. Kozlov, Phys. Status Solidi B **126**, *1*, K59 (1984).
[10] N. N. Syrbu, Fiz. Tekh. Poluprovodn. **26**, 1069 (1992) [Sov. Phys. Semicond. **26**, 599 (1992)].
[11] M. Sugisaki, O. Arimoto, and K. Nakamura, J. Phys. Soc. Jpn. **65**, *1*, 23 (1996).

[12] V. Markiv and N. Belyavina, in *Proceedings of the Second International Conference on Constructive and Functional Materials* [in Ukrainian] (Nauk. T-vo im. T. Shevchenko, L'viv, 1997), p. 260.
[13] M. E. Flett and Th. A. Mowles, Acta Crystallogr. **40**, 1778 (1984).
[14] Yu. I. Sirotin and M. P. Shaskol'skaya, *Fundamentals of Crystal Physics* [in Russian] (Nauka, Moscow, 1979), 639 pp.
[15] S. I. Boĭko, I. S. Gorban', A. P. Krokhmal', V. I. Osinskiĭ, and I. A. Rozhko, Fiz. Tekh. Poluprovodn. **27**, 822 (1993) [Semiconductors **27**, 1447 (1993)].
[16] T. N. Sushkevich, Ukr. Fiz. Zh. **11**, *7*, 744 (1966).
[17] É. P. Domashevskaya, V. A. Terekhov, Ya. A. Ugaĭ, V. I. Nefedov, N. P. Sergushin, and G. N. Dolenko, Fiz. Tverd. Tela (Leningrad) **19**, 3670 (1977) [*sic*].
[18] D. Fröhlich, M. Schlierkamp, J. Schubert, S. Spitzer, O. Arimoto, and K. Nakamura, Phys. Rev. B **49**, 10 337 (1994-I).
[19] R. M. White, *The Quantum Theory of Magnetism* (McGraw-Hill, New York, 1970; Mir, Moscow, 1985) 303 pp.
[20] F. Koster, J. O. Dimmock, R. C. Wheeler, and H. Statz, *Properties of Thirty-Two Point Groups* (MIT Press, Cambridge, Massachusetts, 1963) 105 pp.
[21] O. V. Kovalev, Fiz. Tverd. Tela (Leningrad) **2**, 2557 (1960) [Sov. Phys. Solid State **2**, 2279 (1960)].
[22] G. L. Bir and G. E. Pikus, *Symmetry and Deformation Effects in Semiconductors* [in Russian] (Nauka, Moscow, 1972) 584 pp.
[23] I. S. Gorban', A. P. Krokhmal', and Z. Z. Yanchuk, in *Abstracts of the Eleventh Republic School–Seminar on the Spectroscopy of Molecules and Crystals* [in Ukrainian] (Khar'kiv, 10–16 May 1993, Kiev), p. 22.
[24] J. Floher, E. Jahne, and M. Porsch, Phys. Status Solidi B **91**, *2*, 467 (1979).
[25] P. W. Baumeister, Proc. R. Soc. Med. **121**, 359 (1961).
[26] J. J. Hopfield and D. G. Thomas, Phys. Rev. **122**, 35 (1961).
[27] I. S. Gorban', V. V. Lugovskiĭ, I. I. Tychina, and A. V. Fedotovskiĭ, JETP Lett. **17**, 137 (1973).
[28] V. V. Sobolev, A. I. Kozlov, M. M. Markus, L. A. Bityutskaya, and E. N. Bormontov, Ukr. Fiz. Zh. **30**, *1*, 36 (1985).
[29] É. I. Rashba and G. I. Gurgenishvili, Fiz. Tverd. Tela (Leningrad) **4**, 1029 (1962) [Sov. Phys. Solid State **4**, 759 (1962)].
[30] O. Arimoto, S. Okamoto, and K. Nakamura, J. Phys. Soc. Jpn. **59**, *10*, 3490 (1990).
[31] V. N. Ermakov, V. M. Nitsovich, and N. V. Tkach, Ukr. Fiz. Zh. **22**, *4*, 653 (1977).
[32] I. S. Gorban', V. V. Lugovskiĭ, A. P. Makovetskiĭ, I. I. Tychina, and A. V. Fedotovskiĭ, Fiz. Tekh. Poluprovodn. **8**, 436 (1974) [Sov. Phys. Semicond. **8**, 283 (1974)].
[33] I. M. Dmitruk, M. M. Bilyi, I. S. Gorban, and Z. Z. Yanchuk, in *Proceedings of the Fifteenth International Conference on Raman Spectroscopy* (August 11–16, Pittsburgh, USA) Chichester–N.Y., Brisbane–Toronto–Singapore (1996), p. 874.
[34] V. M. Agranovich and V. L. Ginzburg, *Crystal Optics with Spatial Dispersion, and Excitons* (Springer-Verlag, New York, 1984; Nauka, Moscow, 1979] 432 pp.
[35] F. Gross and B. S. Razbirin, Fiz. Tverd. Tela (Leningrad) **4**, *1*, 207 (1962) [Sov. Phys. Solid State **4**, 146 (1962)].

Translated by Paul F. Schippnick

Unusual temperature dependences of the photoconductivity and recombination luminescence of amorphous molecular semiconductors doped with ionic dyes

N. A. Davidenko, A. A. Ishchenko, A. K. Kadashchuk, N. G. Kuvshinskiĭ, N. I. Ostapenko, and Yu. A. Skryshevskiĭ

T. G. Shevchenko Kiev State University, 252033 Kiev, Ukraine
(Submitted April 17, 1998; resubmitted July 22, 1998)
Fiz. Tverd. Tela (St. Petersburg) **41**, 203–209 (February 1999)

A nonexponential increase in photoconductivity with increasing temperature is discovered for poly(N-epoxypropylcarbazole) (PEPK) films doped with polymethine dyes. It is postulated that traps for nonequilibrium charge carriers form in these films during irradiation and are destroyed as the temperature is raised. Such traps are manifested by broadening of the high-temperature shoulder on the thermally stimulated luminescence (TSL) curves following the preliminary irradiation of PEPK films doped with polymethine and xanthene ionic dyes in the visible or UV range at 250–320 K and by the appearance of a new narrow TSL maximum near the preliminary irradiation temperature. These TSL features disappear after prolonged storage of the films in the dark or heating to higher temperatures. © *1999 American Institute of Physics.* [S1063-7834(99)00502-X]

Films of photoconductive amorphous molecular semiconductors (AMS's) are employed as optical recording media in electrography and holography,[1] as well as in elements of electroluminescent displays.[2] The internal photoeffect in such AMS's is sensitized by introducing special additions, which absorb visible light and act as centers for the photogeneration of charge carriers. The photophysical properties of AMS's based on poly(N-vinylcarbazole) (PVK) and poly(N-epoxypropylcarbazole) (PEPK) doped with organic electron acceptors [for example, 2,4,7-trinitro-9-fluorenone (TNF)] or intramolecular charge-transfer compounds (ICTC's) have been studied most thoroughly.[3,4] In AMS's with TNF the carrier photogeneration centers are intermolecular charge-transfer (CT) complexes formed between carbazole ring systems and TNF molecules, and in AMS's with ICTC's they are molecules of the ICTC. The mechanism for the photogeneration of charge carriers consists of two steps. After a photon is absorbed in a photogeneration center, a Coulomb-bound electron-hole pair forms, in which the hole is localized on a carbazole ring system and the electron is localized on a molecule of TNF or the ICTC. In the second photogeneration step the charge carriers in the electron-hole pair either separate or recombine. One characteristic feature of the AMS's under discussion is the exponential dependence of the photogeneration quantum yield η of carriers on the square root of the external electric field intensity E and the temperature T in the ranges $E=1\times10^7-2\times10^8$ V/m and $T=290-340$ K. The value of η is determined experimentally from measurements of the steady-state direct photocurrent j during uniform bulk carrier photogeneration. In this case the dependence of η on E and T can be represented by the analytic expression

$$j\sim\eta\sim\exp\{-(W_{\mathrm{OPH}}-\beta E^{1/2})/kT_{\mathrm{eff}}\}, \tag{1}$$

where W_{OPH} is the activation energy for photoconduction, β is a constant close to the Poole–Frenkel constant, $T_{\mathrm{eff}}^{-1}=T^{-1}-T_0^{-1}$, and T_0 is the temperature at which the plots of $\log j(T^{-1})$ measured for different values of E and extrapolated to large T intersect.

The dependences of the type (1) for AMS's based on PEPK with CT complexes and ICTC's could be considered universal, since they remain unchanged even in the presence of traps for charge carriers formed when dopants are introduced. For example, it was shown in Ref. 5 that the introduction of molecules of an ICTC into PEPK leads to broadening of the energy spectrum of localized states which trap photogenerated charge carriers. Displacement of the temperature dependence of the thermally stimulated recombination luminescence (TSL) of the AMS toward higher T is then observed, and j and the photogeneration quantum yield of carriers decrease, but the functional dependence of $j(E,T)$ of the type (1) remains unchanged.

From a practical standpoint, ionic dyes can be more effective photosensitizers of the internal photoeffect in AMS's, since they have a high absorption coefficient due to the high degree of charge transfer in the ground and excited states and are successfully employed as photosensitizers of redox reactions involving electrons.[6] Such dyes include the polymethine dyes, whose photophysical properties have been thoroughly studied.[7] However, the presence of stable ions within the dyes can induce significant changes in the local electric fields in the bulk of an AMS and cause the appearance of new electronic states. This is evidenced by the unusual temperature dependences of the photoconductivity and TSL of films of AMS's based on carbazole-containing polymers doped with ionic dyes, which are the object of investigation in the present work.

1. SAMPLES AND EXPERIMENTAL METHOD

The cationic polymethine dye 1,3,3,1′,3′,3′-hexamethylindocarbocyanine (HIC), the xanthene dye

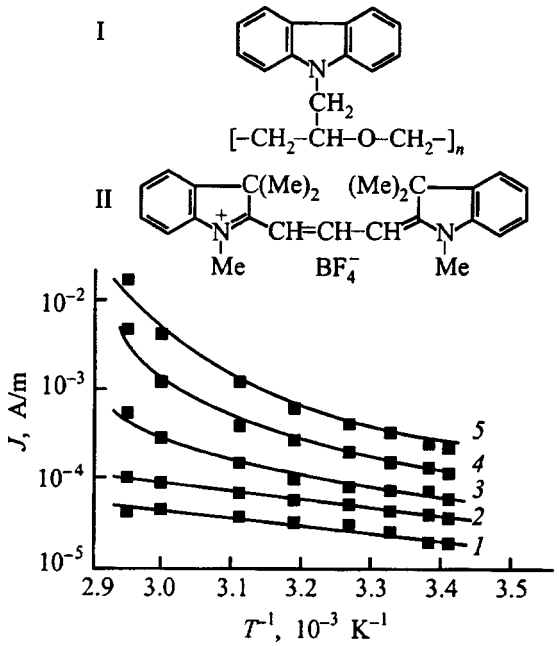

FIG. 1. Plots of $j(T)$ in a sample of Al-PEPK+0.5 mole % HIC-SnO_2 upon irradiation by light with a wavelength $\lambda=540$ nm and an intensity equal to 1.5 W/m^2 for external electric field intensities $E=1.8\times10^7$ V/m (*1*), 2.7×10^7 V/m (*2*), 4.5×10^7 V/m (*3*), 6.4×10^7 V/m (*4*), and 8.2×10^7 V/m (*5*). The thickness of the AMS film was 1.1 μm. The inset shows the structural formulas of the PEPK (I) and HIC (II) molecules.

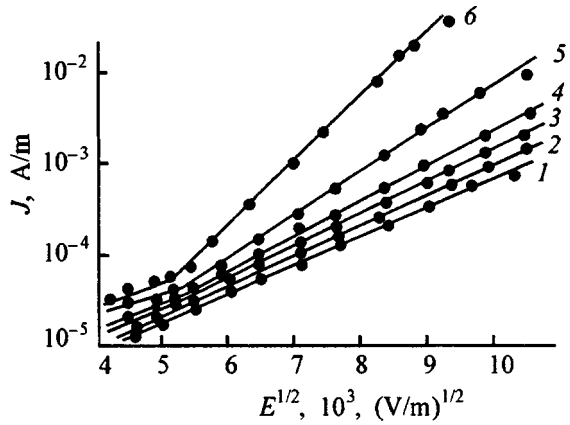

FIG. 2. Plots of $j(E)$ in a sample of Al-PEPK+0.5 mole % HIC-SnO_2 upon irradiation by light with a wavelength $\lambda=540$ nm and an intensity equal to 1.5 W/m^2 for temperatures equal to 295 K (curve *1*), 305 K (*2*), 313 K (*3*), 323 K (*4*), 330 K (*5*), and 337 K (*6*). The thickness of the AMS film was 1.1 μm.

Rhodamine 6G (R6G), the intramolecular charge-transfer compound 9-(4-methoxyphenylmethylene)-2,5,7-trinitrofluorene-4-carboxylic acid (ICTC1), and TNF were used in the experiments. The concentration of the dopants in PEPK was varied in the range 0−15 mole %. The structural formulas of PEPK and HIC are presented in the inset in Fig. 1. The samples for the experiments were prepared either in the form of structures with a free surface (quartz substrate/AMS film) or in the form of sandwich structures (quartz substrate/SnO_2/AMS film/Al). The AMS films were prepared by pouring solutions of the original components in dichloroethane onto the substrates and drying in a heated desiccator at +75 °C. The thickness of the AMS films in the sandwich-structure samples was 1−2 μm. The aluminum electrodes were deposited on the AMS films by thermal sputtering in a vacuum chamber.

The value of j was measured in the sandwich-structure samples in the photoresistance regime with the positive polarity of the electric voltage on the Al electrode using a storage oscillograph during irradiation on the SnO_2 electrode side by monochromatic light with a wavelength $\lambda>500$ nm in the absorption region of the photogeneration centers and outside the absorption region of PEPK. The electric field intensity and the temperature were varied in these experiments in the ranges $E=2\times10^7-2\times10^8$ V/m and $T=290-345$ K. The TSL measurements were performed by an automated system, in which the integrated intensity I_{TL} was recorded by a photomultiplier, which operated in the photon-counting mode and was placed in direct proximity to the cryostat window. The temperature of the sample investigated was varied in the range 4.2−330 K according to a linear law at the rate of 0.1 K/s. For the measurements of the dependence of I_{TL} on T, the cooled sample was irradiated in the cryostat by light with either $\lambda=365$ nm (in the absorption region of PEPK) or $\lambda>500$ nm, the sample was held in the dark until the isothermal recombination luminescence decayed, and linear heating of the sample was started. The irradiation time was 60 s and corresponded to the saturation of I_{TL} from the irradiation dose. A DRSh-500M mercury lamp with a set of light filters served as the light source.

2. RESULTS

Photoconduction of the doped AMS's was observed in all the sandwich-structure samples investigated upon irradiation by light in the absorption region of the photogeneration centers. The behavior of $j(E,T)$ for the samples with PEPK:TNF and PEPK:ICTC1 can be represented by the analytical expression (1) with $\beta=(4.2\mp0.1)\times10^{-5}$ eV $\cdot(V/m)^{-1/2}$ and $T_0=490\mp15$ K, which correlate well with the known literature data.[3,4,8,9] The behavior of $j(E,T)$ for the samples with PEPK:HIC films differs significantly from (1). Figure 1 presents plots of $j(T)$ in $\log j$ vs T^{-1} coordinates measured for various values of E. The plots for $E>3\times10^7$ V/m are significantly nonlinear, and the dependence of j on T becomes stronger as E is increased. Figure 2 presents plots of $j(E)$ in $\log j$ vs $E^{1/2}$ coordinates measured at various values of T. Although these plots can be approximated by straight lines, the slope of these straight lines increases with increasing T. In Fig. 3 curve *1* is a plot of $\beta(T)$, where β was calculated as the quantity $(\Delta\log j/\Delta E^{1/2})\cdot kT$ from the results of measurements of the slope of the corresponding plot of $\log j(E^{1/2})$ in Fig. 2. Curve *2* in Fig. 3 is a plot of $\beta(T)$ calculated by the same method, but from the results of measurements of $j(E,T)$ in samples with PEPK:TNF films. Curve *3* in Fig. 3 is a plot of $\beta(T)$ calculated as $(\Delta\log j/\Delta E^{1/2})\cdot kT_{\text{eff}}$ as a function of T in PEPK:TNF samples.

Figure 4 presents the TSL curves after irradiation of the samples at $T=5$ K. Curves *1–4* were obtained with samples which were held in the dark at room temperature for more

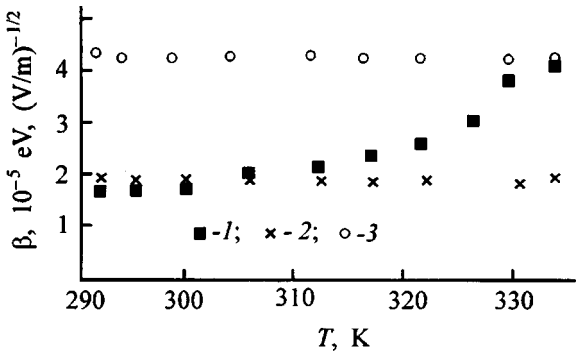

FIG. 3. Plots of $\beta(T)$ in samples of Al-PEPK+0.5 mole % HIC-SnO_2 (curve *1*) and Al-PEPK+1 mole % TNF-SnO_2 (*2*, *3*) upon irradiation by light with a wavelength $\lambda=540$ nm.

than 48 h. Curves *1′–4′* were obtained with samples which were irradiated by light with $\lambda=365$ nm for 60 s at $T_{irr}=300$ K before being cooled. It can be seen that the TSL of the PEPK and PEPK:TNF films exhibit little sensitivity to irradiation at room temperature. After irradiation by UV light at room temperature, the TSL curves of PEPK:ICTC1 and PEPK:HIC films exhibit a high-temperature TSL shoulder in the temperature range 200−300 K.

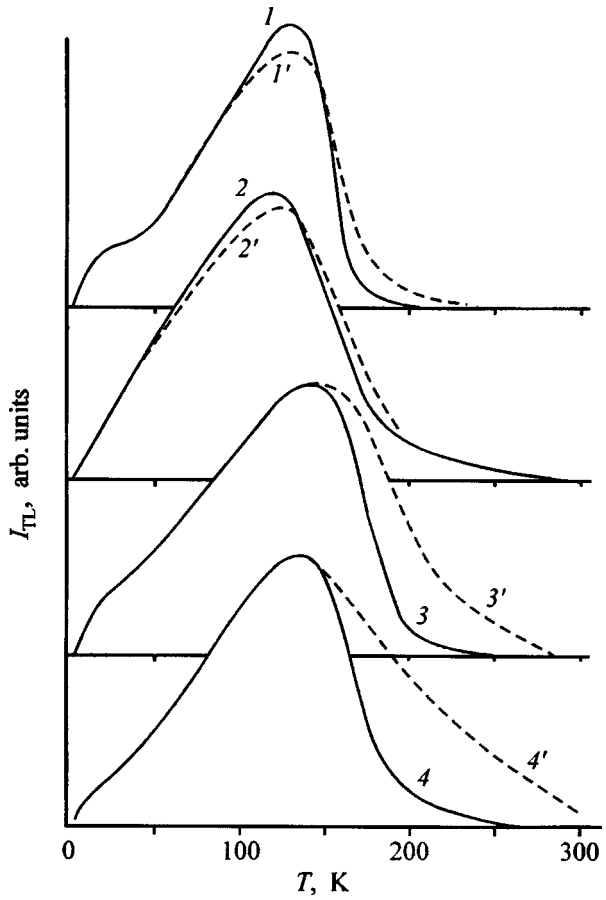

FIG. 4. TSL curves of samples of PEPK (*1*, *1′*), PEPK+0.1 mole % TNF (*2*, *2′*), PEPK+0.1 mole % ICTC1 (*3*, *3′*), and PEPK+0.5 mole % HIC (*4*, *4′*) with the excitation of TSL by light with a wavelength $\lambda=365$ nm for 60 s at $T=5$ K. To obtain curves *1′–4′* the samples were irradiated by light with $\lambda=365$ nm for 60 s at $T_{irr}=300$ K before cooling.

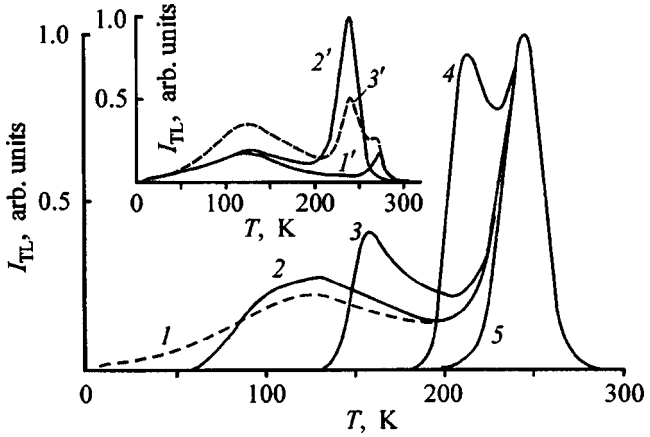

FIG. 5. TSL curves of a sample of PEPK+0.1 mole % HIC for the excitation of TSL by light with a wavelength $\lambda=546$ nm at 5 K (curve *1*), 50 K (*2*), 150 K (*3*), 200 K (*4*), and 250 K (*5*) after preliminary irradiation by light with $\lambda=365$ nm for 60 s at $T_{irr}=250$ K. Inset: TSL curves of the same sample for the excitation of TSL by light with $\lambda=546$ nm at $T=5$ K following preliminary irradiation by light with $\lambda=365$ nm for 60 s at $T_{irr}=280$ K (*1′*), 250 K (*2′*), 280 K and 250 K (*3′*).

If a sample of PEPK:HIC is irradiated by light with $\lambda=365$ nm or $\lambda>500$ nm at $T_{irr}=290$ K and rapidly cooled to $T=5$ K (with a cooling rate equal to 5−10 K/s), and then the sample is irradiated by light to excite the TSL, the TSL curve displays an additional narrow band with a maximum at $T_{max2}=T_{irr}\mp7$ K. This new TSL band appears for $250<T_{irr}<320$ K, the intensity of the TSL maximum at T_{max2} increases with decreasing T_{irr} and reaches its highest value for $T_{irr}=250$ K, and the equality $T_{max2}=T_{irr}\mp7$ K does not depend on the wavelength of the light or the temperature at which the TSL was excited (Fig. 5).

Another special feature of the TSL of the PEPK:HIC samples is that in the temperature range 250−320 K we can obtain not just one additional TSL maximum near T_{irr}, but two or even three new maxima near the temperatures at which additional irradiation of the sample is carried out during cooling to the TSL excitation temperature (inset in Fig. 5).

Figure 6 presents the TSL curves of PEPK:HIC samples with various concentrations of HIC, which were irradiated at $T_{irr}=290$ K before cooling prior to the excitation of TSL.

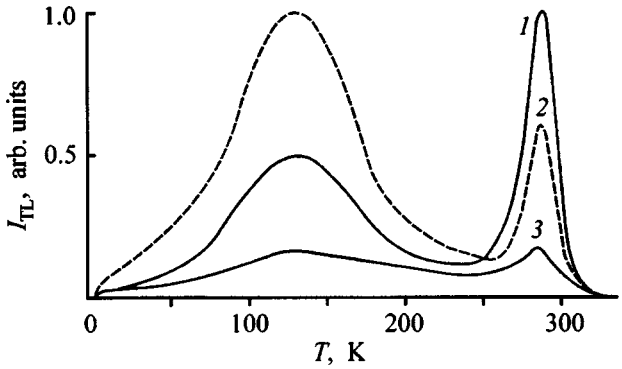

FIG. 6. TSL curves of PEPK:HIC samples with a concentration of HIC in PEPK equal to 0.1 mole % (curve *1*), 0.5 mole % (*2*), and 5 mole % (*3*) following excitation by light with a wavelength $\lambda=546$ nm at 5 K.

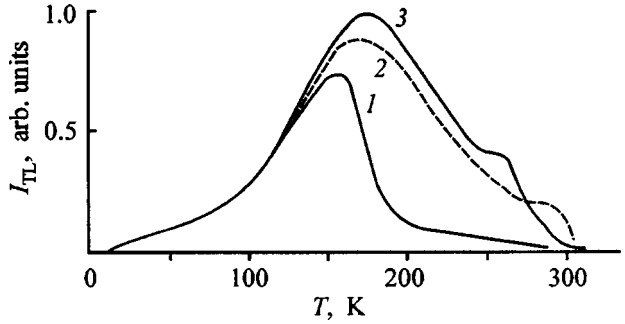

FIG. 7. TSL curves of a sample of PEPK+0.1 mole % ICTC1 following the excitation of TSL by light with $\lambda > 500$ nm at $T=5$ K, storage for more than 48 h in the dark (curve *1*), preliminary irradiation by light with a wavelength $\lambda > 500$ nm at $T_{irr}=290$ K (*2*), 250 K (*3*), and rapid cooling (at the rate of 5−10 K/s) to $T=5$ K.

One special feature of these TSL curves is that the intensity of the TSL maximum at T_{max2} decreases more rapidly as the dye concentration is increased than does the intensity of the TSL maximum at T_{max1}.

Similar TSL features were discovered for the AMS's based on PEPK doped by HIC with different anions (BF_4^-, Cl^-) and R6G, as well as on PEPK+0.1 mole % ICTC1 (Fig. 7). The activation energy for thermal release of carriers from traps W_{TL} was determined for these samples over the entire temperature range investigated by fractional heating with the measurement of I_{TL}. It was found that, regardless of the parameters of the preliminary irradiation at high temperatures, the value of W_{TL} is linearly dependent on T and this dependence does not change near T_{irr}. Near $T_{irr}=250$ we obtained $W_{TL}=0.82\mp0.01$ eV, and this value is close to the value of the activation energy for the β relaxation of PEPK previously measured by an independent method.[10]

3. DISCUSSION OF RESULTS

Several assumptions can be made to analyze the unusual $j(T,E)$ curves for PEPK:HIC and their deviations from the analytical representation by expression (1).

1) Since in the carrier photogeneration model (1), which was used in Refs. 3 and 4 to explain the dependence of η and j on E and T, the coefficient $\beta=(q^3/\pi\varepsilon\varepsilon_0)^{1/2}$, where q is the charge of an electron and ε is the dielectric constant of the sample, the increase in β with increasing temperature (Fig. 3) can associated with a decrease in ε. It follows from the results in Fig. 3 that as the temperature is raised from 295 K to 330 K, the value of ε should decrease by a factor of 3 and approach $\varepsilon=1$ in this case. However, it is known that the implantation of polar additions in the form of ionic dyes in AMS's can lead to an increase in ε. In addition, we found experimentally that the changes in the refractive index of the PEPK:HIC films in this temperature range do not exceed 2% and there is no basis to allow for the variation of ε.

2) In the carrier photogeneration model in Refs. 3 and 4 the activation energy for photogeneration W_{OPH} in (1) is equivalent to the energy of the Coulomb interaction between charges for an initial distance r_0 in photogenerated electron-hole pairs. Then the deviation from linearity of the plots of $j(T)$ in $\log j$ vs T^{-1} coordinates (Fig. 1) could be attributed to a decrease in W_{OPH} with increasing T due to an increase in r_0. In fact, electron-hole pairs are photogenerated in PEPK:HIC films according to the scheme

$$Cz+(An^-..r_{dye}..HIC^+)\xrightarrow{h\nu}(Cz^+..r_0..An^-)+HIC^{\cdot}, \quad (2)$$

where Cz represents a carbazole moiety of PEPK near a photogeneration center consisting of a photoactive HIC^+ dye cation and an An^- anion at a distance r_{dye} from it, $h\nu$ is the energy of the photon absorbed by HIC^+, $HIC^{\cdot}$ is an electroneutral radical of the dye cation formed after the transition of a positive charge from HIC^+ to Cz, and $(Cz^+..r_0..An^-)$ is an electron-hole pair formed by the cation radical of the PEPK carbazole moiety and the dye anion. Then it could be presumed that an increase in r_0 with increasing temperature occurs because of an increase in the molecular diffusion of An^-. However, in this case, the distances r_{dye} and r_0 after heating and cooling of the AMS should have differed from the values before heating, and repeated measurements of the $j(T,E)$ curves should have revealed an increase in j after heating and the measurement of j at high values of T followed by cooling. Such effects were not observed in our experiments, and the values of j did not depend on preliminary heating and cooling of the samples in the presence or absence of an electric field.

3) The decrease in W_{OPH} with increasing temperature might have been attributed to an increase in r_0 due to alteration of the conditions for transfer of the energy released from a hole photogeneration center to the environment. It follows from scheme (2) that after photogeneration, a hot hole interacts mainly with the carbazole moieties of PEPK. It is presumed that the same process occurs following the photogeneration of holes in PEPK with TNF or ICTC1. However, the relation (1) holds in PEPK with TNF or ICTC1.

4) It can be presumed that in (1) the parameter T_0 increases with increasing temperature. However, in the carrier photogeneration model in AMS's in Ref. 4 the parameter T_0 reflects features of the transport of a mobile charge carrier among localized states upon the dissociation of electron-hole pairs. At low dopant concentrations in PEPK the dissociation of photogenerated electron-hole pairs occurs as a result of transitions of holes between carbazole moieties of PEPK, and the electrons can be considered quasistationary in the dissociation step. Therefore, the value of T_0 depends weakly on the type of photogeneration center,[4] and there are no apparent reasons for its variation in PEPK with ionic dyes.

5) The unusual increase in j with increasing T (Fig. 1) might have been attributed to an increase in the photogeneration quantum yield of electron-hole pairs with increasing T. However, the temperature dependence of the initial concentration of electron-hole pairs should not influence the dependence of j on E (Fig. 2) or of β on T (Fig. 3), in contradiction to our results.

It can be postulated that the deviation of the behavior of $j(T,E)$ from the analytical representation (1) is a result of a decrease in the influence of the charged traps on the steps in the dissociation of electron-hole pairs. In fact, in AMS's with ionic dyes there are many stable ions capable of creating new local energy levels not present in undoped PEPK, and release

from these traps should be facilitated by an external electric field. The hypothesis that there are new charged traps in PEPK:HIC is confirmed by the results of the TSL experiments.

Let us turn to Fig. 4. The increase in the intensity of the high-temperature TSL shoulder of the PEPK:HIC films following irradiation at room temperature and the preservation of this high-temperature TSL shoulder following various TSL excitation procedures at low temperatures and heating to room temperature provide evidence that the concentration of the deeper carrier-trapping levels increases in the PEPK films with a dye after light irradiation. These trapping levels can be populated by photogenerated charges at both high and low temperatures. The release of charge carriers from these levels has an activation character. It can be theorized that these new localized states are located near electrons previously photogenerated at room temperature. In other words, if a PEPK sample contains long-lived electrons (for example, anions of cationic dyes or electrons of long-lived electron-hole pairs in PEPK films with an ICTC), the photogeneration of charge carriers is followed by self-trapping of the photogenerated electrons, which form trapping centers. The hypothesis that trapped electrons have such an effect is based on the fact that no increase in the intensity of the high-temperature TSL shoulder is observed in PEPK without additions, for example, in PEPK:TNF. In these AMS's trapped charges do not manage to accumulate in large numbers following irradiation at room temperature due to the short lifetimes of the electron-hole pairs. However, such an increase in the intensity of the high-temperature TSL shoulder occurs in PEPK:ICTC1 (curves *3* and *3′* in Fig. 4), where electron-hole pairs with lifetimes as long as several hours form after irradiation at room temperature.[11–13]

As the temperature is increased, trapped carriers are released from the charged traps, and the concentration of such traps also decreases because of an increase in the mobility the localized charges and a decrease in the concentration of trapped electrons. The latter is confirmed by the fact that, after the TSL is recorded (curve *4′* in Fig. 4), the original TSL curve (curve *4* in Fig. 4) can be recovered, if the sample is stored in the dark at room temperature for 24 h or heated to a temperature close to the glass-transition point.

However, the charged traps appearing after the photogeneration and self-trapping of electrons are not the only type of traps which form upon the irradiation of PEPK containing ionic dyes and whose concentration decreases with increasing temperature. Let us turn to Fig. 5. If the sample is irradiated in the range $250<T<320$ K by light which causes the photogeneration of charge carriers, a certain fraction of these charges will be trapped for a long time and released only at the temperature at which the sample was irradiated. This is evidenced by the experimental observation that after a sample is irradiated at a temperature in the range indicated and held in the dark at the same temperature for several tens of minutes or even hours and then the sample is cooled and subjected to heating, a narrow maximum appears on the TSL curve at the temperature at which the sample was irradiated (see, for example, curve *5* in Fig. 5). In addition, irradiation near T_{max2} does not lead to the formation of empty trapping sites for newly photogenerated charge carriers, and the ''memory'' of such irradiation is lost after the sample is heated to $T>T_{irr}$. The conclusion that the accumulation of charges in the traps occurs only in response to such irradiation and that new unfilled traps do not form is based on the fact that the intensity of the recombination luminescence near T_{irr} on the TSL curves does not depend on whether or not the sample was light-irradiated after it was cooled to lower temperatures (a comparison of curve *5* and curves *1–4* in Fig. 5 reveals that the values of I_{TL} at $T=250$ K are identical for all the curves). It is important to note that the trapping of photogenerated carriers takes place near dye monomers and not near aggregates of dye molecules, since the concentration quenching of the TSL intensity occurs sooner near T_{max2} than near T_{max1} (Fig. 6).

The release of trapped carriers from such photoinduced traps is not associated with overcoming the potential barrier created by the difference between the ionization potentials of the recombination center and the PEPK carbazole moiety in which the hole is located. The latter follows from the results of the TSL measurements in PEPK+0.1 mole % ICTC1 (Fig. 7), where the activation energy for TSL near T_{max2} equals 0.82 ∓ 0.01 eV, while the difference between the ionization potentials of ICTC1 and the carbazole ring systems of PEPK equals 0.38 ∓ 0.01 eV according to the data in Ref. 11.

Thus, two types of traps for photogenerated charge carriers appear in PEPK:HIC after light irradiation. The following features are characteristic of the photoinduced traps of the first type.

1) In PEPK these traps appear in the presence of stable localized ions (for example, An^-) and are manifested by broadening of the high-temperature TSL shoulder after preliminary irradiation of the samples at high temperatures (near room temperature) followed by the excitation of TSL at low temperatures.

2) Self-trapped electronic states similar to charged traps appear after the photogeneration of electrons at high temperatures and the trapping of those electrons.

3) The lifetime of these self-trapped electronic states is equal to the lifetime of trapped electrons and decreases with increasing temperature. To increase the concentration of self-trapped electronic states, the sample must be irradiated repeatedly at high temperatures.

The following features are characteristic of the photoinduced traps of the second type appearing in PEPK with ionic dyes.

1) These traps appear in the presence of stable localized anions (An^-) of dye monomers and are not detected in PEPK with other additions (ICTC's, TNF) that do not contain such ions.

2) These traps appear during the photogeneration of charge carriers and exist only in the filled state. We refer to a trap of the second type as a photoinduced charged conformer and assume that it forms as a result of alignment of the PEPK carbazole ring systems appearing in predimer states near a stable ion (for example, near An^-) upon the photogeneration of a hole in these carbazole ring systems from a photogeneration center (upon the passage of a hole from HIC^+ to Cz).

3) The formation of a trap of this type, the trapping of a charge carrier in it, its annihilation, and release of the charge carrier occur at the same temperature, and the activation energy of these processes is close to the activation energy for β relaxation. At the same temperature the rate of annihilation of this trap is far smaller than the rate of its generation because PEPK already has predimer states, which transform into dimer states at different temperatures (there is a spread of formation energies of dimers in the carbazole moieties). The dimer states are hole traps. Photogenerated holes can find their way into predimer states located near An^-, and in the electrostatic field of An^- they can promote the conversion of the predimer states into dimer states by aligning the carbazole ring systems (β relaxation). A filled dimeric hole trap thus appears, and the energy deficiency for its formation at a given temperature is offset by polarization of the medium by the trapped hole and the electrostatic interaction of the hole with An^-. If the temperature is raised, the hole leaves the trap, but dissociation of the dimer then occurs as a result of a loss of alignment of the carbazole ring systems, and a predimer state, which is now empty, forms from the dimer state. However, because of the energy spread of the dimer states at these higher temperatures, PEPK contains other predimer states, which can also transform into filled dimeric trap states when photogenerated holes enter them. Therefore, for each temperature there are specific photoinduced charged conformers, which are manifested by the appearance of narrow high-temperature TSL maxima near the irradiation temperatures (see the inset in Fig. 5).

4) Such traps are manifested in the TSL by the appearance of a new narrow TSL maximum near the light-irradiation temperature of the sample, and the amplitude of this maximum and its position on the temperature scale do not depend on the subsequent excitation of TSL.

Thus, the unusual $j(T,E)$ and TSL curves for PEPK with anionic dyes can be attributed to the influence of photoinduced traps of two types, which are destroyed as the temperature is raised. These traps are characteristic of AMS's containing stable ions.

[1] R. M. Schaffert, *Electrophotography*, Wiley, New York (1981) 420 pp.
[2] D. Neher, M. Remmers, and V. Cimrova, in *Electrical and Related Properties of Organic Solids*, R. W. Munn *et al.* (Eds.), Kluwer, Dordrecht–Boston (1997), pp. 79–99.
[3] M. Pope and C. E. Swenberg, *Electronic Processes in Organic Crystals*, Clarendon Press, Oxford (1982) 725 pp.
[4] N. G. Kuvshinskiĭ, N. A. Davidenko, and V. M. Komko, *Physics of Amorphous Molecular Semiconductors* [in Russian], Lybid', Kiev (1994) 176 pp.
[5] N. A. Davidenko, A. K. Kadashchuk, N. G. Kuvshinsky, N. I. Ostapenko, and N. V. Lukashenko, J. Inf. Rec. Mater. **24**, 327 (1996).
[6] A. N. Terenin, *Photonics of Dye Molecules* [in Russian], Nauka, Leningrad (1967) 616 pp.
[7] A. A. Ishchenko, *Structure and Luminescence-Spectral Properties of Polymethine Dyes* [in Russian], Naukova Dumka, Kiev (1994) 232 pp.
[8] P. J. Melz, J. Chem. Phys. **5**, 1694 (1972).
[9] A. Halperin, A. A. Braner, A. Ben-Zvi, and N. Kristianpoller, Phys. Rev. **117**, 416 (1960).
[10] J. M. Pochan, D. F. Hinman, and R. Nash, J. Appl. Phys. **46**, 4115 (1975).
[11] N. A. Davidenko and N. G. Kuvshinsky, J. Inf. Rec. Mater. **21**, 185 (1993).
[12] A. K. Kadashchuk, N. I. Ostapenko, N. A. Davidenko, N. G. Kuvshinskiĭ, and N. V. Lukashenko, Fiz. Tverd. Tela (St. Petersburg). **39**, 1183 (1997) [Phys. Solid State **39**, 1047 (1997)].
[13] N. A. Davidenko and N. G. Kuvshinsky, J. Inf. Rec. Mater. **22**, 37 (1994).

Translated by P. Shelnitz

Erbium electroluminescence excitation in amorphous hydrogenated silicon under thermally stimulated deep-center tunneling ionization

O. B. Gusev, M. S. Bresler, B. P. Zakharchenya, A. N. Kuznetsov, P. E. Pak, E. I. Terukov, K. D. Tséndin, and I. N. Yassievich

A. F. Ioffe Physicotechnical Institute, Russian Academy of Sciences, 194021 St. Petersburg, Russia
(Submitted July 31, 1998)
Fiz. Tverd. Tela (St. Petersburg) **41**, 210–217 (February 1999)

A study of the electroluminescence of erbium-doped, amorphous hydrogenated silicon, *a*–Si:H $\langle$Er$\rangle$, is reported. It has been found that the electroluminescence intensity at the wavelength $\lambda = 1.54\ \mu$m corresponding to the $^4I_{13/2} \rightarrow {}^4I_{15/2}$ intra-$4f$ shell transition in Er passes through a maximum near room temperature. The unusual temperature and field dependences of the electroluminescence indicate electric-field induced multi-phonon tunneling emission of electrons from deep centers. The electroluminescence of Er^{3+} ions is due to their becoming excited as conduction-band electrons are captured by neutral dangling bonds (D^0 centers), which form when erbium is incorporated into the amorphous matrix. This Auger process transforms the center from its neutral state, D^0, to a negatively charged state, D^-, and the energy released in the capture is transferred by Coulomb interaction into the erbium-ion $4f$ shell. The steady-state current through the electroluminescent structure is supported by the reverse process of multi-phonon tunneling-electron emission from the D^- center to the conduction band. The proposed theoretical model is in a good agreement with experimental data. © *1999 American Institute of Physics.* [S1063-7834(99)00602-4]

The recent intensive studies of erbium luminescence in semiconducting matrices[1] are stimulated by the fact that the erbium-luminescence wavelength of 1.54 μm corresponding to the intra-$4f$ transition of the Er^{3+} ion from the first excited state $^4I_{13/2}$ to the ground state $^4I_{15/2}$ falls into the minimum in optical fiber absorption.

Recent investigations announced observation of efficient photoluminescence[2–4] (PL) and electroluminescence[5] (EL) of erbium ions in amorphous hydrogenated silicon (*a*-Si:H $\langle$Er$\rangle$). The interest in this semiconducting matrix is initiated by both the simple and inexpensive method of erbium incorporation used presently, i.e., magnetron sputtering of metallic erbium in a SiH_4 ambient, and the comparatively weak temperature quenching of the erbium photoluminescence, which makes it a promising material for developing light-emitting diodes capable of operating at room temperature.

It was suggested[5] that erbium ions in *a*–Si:H$\langle$Er$\rangle$ are excited by an Auger process, in which a conduction-band electron is captured by a dangling-bond–type neutral defect D^0 to form the D^- state. The transition energy is transferred through Coulomb interaction to the erbium-ion inner $4f$ shell and promotes the ion from the ground state, $^4I_{15/2}$, to the first excited state, $^4I_{13/2}$. The efficiency of this process results from the similar energies of the $D^0 + e \rightarrow D^-$ and the $^4I_{15/2} \rightarrow {}^4I_{13/2}$ transitions. To sustain stationary electroluminescence, there should exist a reverse process transferring the defects from the D^- to D^0 state.

The object of this work is to show that this process is the multi-phonon tunneling ionization of D^- centers in an electric field. This ionization accounts for the high field-dependent electron concentration in the conduction band and, accordingly, for the shape of the *I*–*V* characteristic and the field and temperature dependences of the erbium electroluminescence.

1. EXPERIMENTAL RESULTS

The structures used to study the electroluminescence, as in Ref. 5, were *a*–Si:H$\langle$Er$\rangle$ films with thickness $d \approx 1\ \mu$m and diameter 1 mm deposited on 300-μm thick *n*-type single-crystal silicon substrates. The electric contacts to the film and the substrate were prepared by aluminum deposition. The EL studies were performed under pulsed excitation-current stabilization at 100 Hz with a slope of 1:2 for both forward- and reverse-biased substrates. The emitted light was collected by a lens system from the back side of the silicon substrate and analyzed by a double-grating spectrometer with a cooled germanium photodetector. A typical *I*–*V* characteristic of the structure studied is displayed in Fig. 1 (the inset shows schematically the electroluminescent structure). A forward-biased structure (with the upper aluminum contact positive, and the *n*-type single-crystal substrate, negative) produced at room temperature only free-exciton EL ($\lambda \approx 1.16\ \mu$m) from the single-crystal silicon substrate (Fig. 2a). Under reverse bias one observed erbium ($\lambda \approx 1.54\ \mu$m) and defect-induced luminescence ($\lambda \approx 1.34\ \mu$m) (Fig. 2b).

The erbium luminescence intensity grows rapidly with temperature within the interval from 200 K to room temperature (see the temperature dependence of the signal intensity at the wavelength of 1.54 μm displayed for several excitation currents in Fig. 3). All curves in Fig. 3 exhibit a maximum in the erbium luminescence. Note that erbium PL obtained on the same structures is temperature-independent

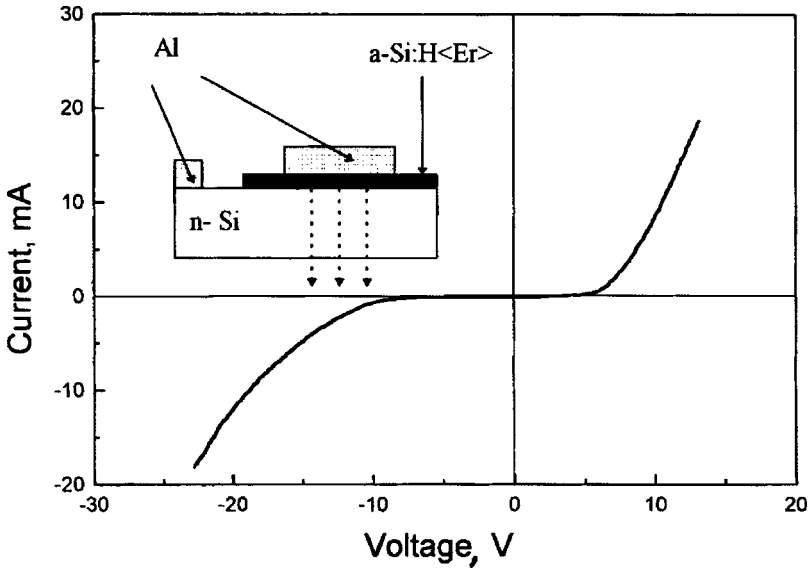

FIG. 1. I–V characteristic of an a–Si:H⟨Er⟩-based electroluminescent structure. $T=300$ K. The inset shows a schematic diagram of the structure.

from the nitrogen to room temperature. The erbium EL intensity depends practically linearly on excitation current (Fig. 4).

Figure 5 presents oscillographic traces of the voltage across a reverse-biased structure. One readily sees a voltage peak at the leading edge of the pulse. The peak amplitude increases, and the characteristic decay time decreases with increasing current through the structure. The relative height of the peak decreases with decreasing temperature. Passing currents approximately in excess of 30 mA through the structure results in an irreversible disappearance of erbium EL (while the broad luminescence band due to defects persists). The spikes on the oscillographic traces of the reverse voltage applied to the structure also disappear.

2. DISCUSSION OF RESULTS

The electroluminescent samples studied by us are Al/a–Si:H⟨Er⟩/n^+–c–Si/Al structures. The Schottky barrier height ϕ at the metal/semiconductor interface should be equal to the difference between the work function of the metal, A, and the electron affinity of the semiconductor, χ, i.e., $\phi=A-\chi$. Because A(Al) and χ(a-Si:H) practically coincide,[6] the value of ϕ should not exceed 0.1–0.2 eV. At the same time the values of ϕ measured both in a–Si:H and c–Si are considerably in excess of the value calculated from $\phi=A-\chi$, and are reported to be $\sim 0.7-0.8$ eV.[6] This discrepancy was assigned[6] to the existence of surface states with a concentration of $\sim 10^{13}$ cm^{-2}, and it is these states that are responsible for the interface barrier. The built-in Schottky-barrier field is, in order of magnitude, $\sim 2\times 10^4$ V/cm, and it is $<0.1\,\mu$m in size (Fig. 6b).

The 1.54 μm erbium EL was observed starting with currents ≈ 3 mA (the corresponding voltage on the reverse branch $V\approx 10$ V). For the 1-mm diameter of the diode structure, the current density $j_V=4\times 10^{-1}$ A/cm^2, which is considerably in excess of the saturation current density characteristic of the reverse branch of an aluminum-contact Schottky diode, which may be considered equal to $j_0=10^{-7}-10^{-6}$ A/cm^2. No special study was made of the nonlinearity of the I–V characteristic from j_0 to j_V. Because $j_V \gg j_0$, it can be assumed that the Schottky barrier forming at the Al/a–Si:H⟨Er⟩ interface is no longer rectifying, and that the applied electric field is approximately the same throughout the thickness of the a–Si:H⟨Er⟩ layer. In the con-

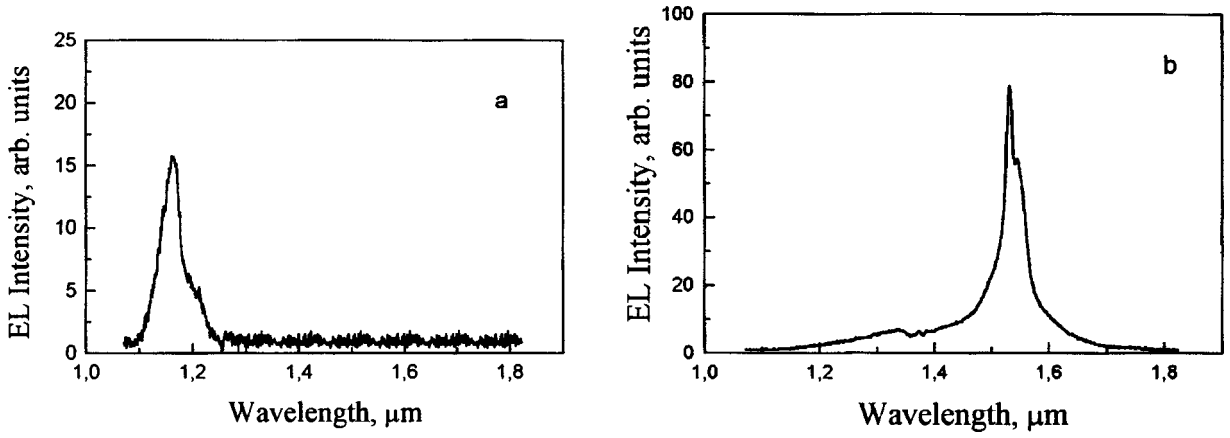

FIG. 2. EL spectra of an a–Si:H⟨Er⟩-based structure under (a) forward and (b) reverse bias. $T=300$ K.

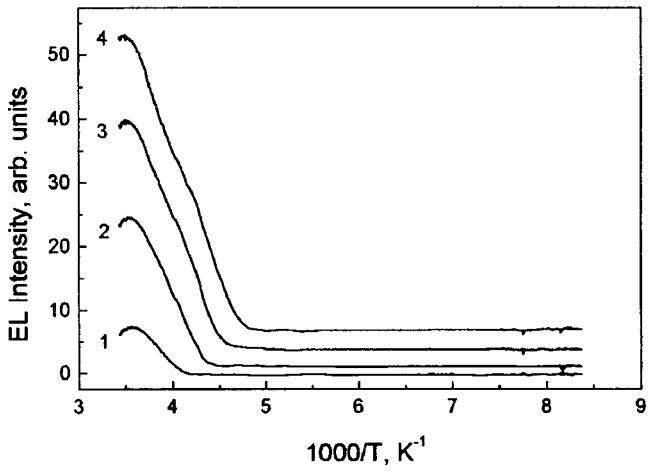

FIG. 3. Erbium EL intensity at 1.54 μm *vs* temperature measured under reverse bias. Current (mA): (1) 5, (2) 10, (3) 15, (4) 20.

ditions of effective erbium luminescence, this average field is $\sim 2\times 10^5$ V/cm.

The band diagrams of the electroluminescent structures studied are shown schematically in Fig. 6a for no bias applied, and in Fig. 7a and 7b for the cases of forward and reverse bias, respectively. Figure 7b presents also a diagram illustrating erbium ion excitation. When the structure is forward biased, the holes transfer into the crystalline-silicon substrate through the layer of amorphous silicon (Fig. 7a), and one observes free-exciton luminescence from the *n*-type substrate (Fig. 2a). An EL spectrum of the same structure but under reverse bias (Fig. 7b) is displayed in Fig. 2b. We readily see in this case the 1.54-μm erbium luminescence corresponding to the transition from the first excited state $^4I_{13/2}$ to the ground state $^4I_{15/2}$ in the inner $4f$ shell of the Er^{3+} ion. Besides the erbium luminescence, one observes also a broad band due to the defect-induced luminescence.

PL studies of *a*-Si:H⟨Er⟩ showed[7] that erbium ions in an amorphous matrix are excited primarily through the Auger process by which conduction-band electrons transfer to D^0 centers ($D^0+e\rightarrow D^-$), and that the energy released in this transition is expended through Coulomb interaction in exciting the erbium ion from the ground, $^4I_{15/2}$, to the first excited, $^4I_{13/2}$, state. It appears natural to assume that erbium excitation in EL occurs by the same process. As will be seen later on, this assumption permits one to explain the totality of experimental data, as well as to reconstruct the band diagram of *a*–Si:H⟨Er⟩ presented in Fig. 6a.

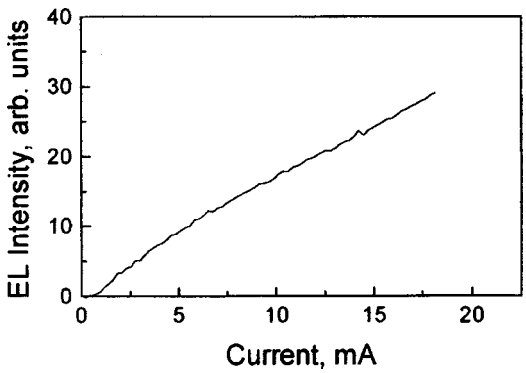

FIG. 4. Erbium EL intensity at 1.54 μm *vs* current. $T=300$ K.

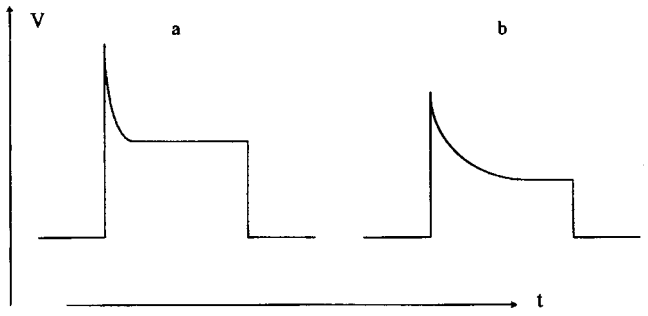

FIG. 5. Oscillographic traces of voltage across a reverse-biased electroluminescent structure. (a) $I=20$ mA, (b) $I=10$ mA.

When reverse biased, the conduction-band electrons moving in the amorphous layer can be trapped by D^0 centers (Fig. 7b), as a result of which the center transfers to the D^- state ($e+D^0\rightarrow D^-$). The trapping of free electrons by D^0 centers can be either a radiative (defect-induced luminescence) or nonradiative process. This can be either a multiphonon capture or an Auger process involving energy transfer to the $4f$ shell of erbium ions by the Coulomb interaction between the electron trapped by a D^0 center and a $4f$ electron of a ground-state erbium ion. The defect-assisted Auger

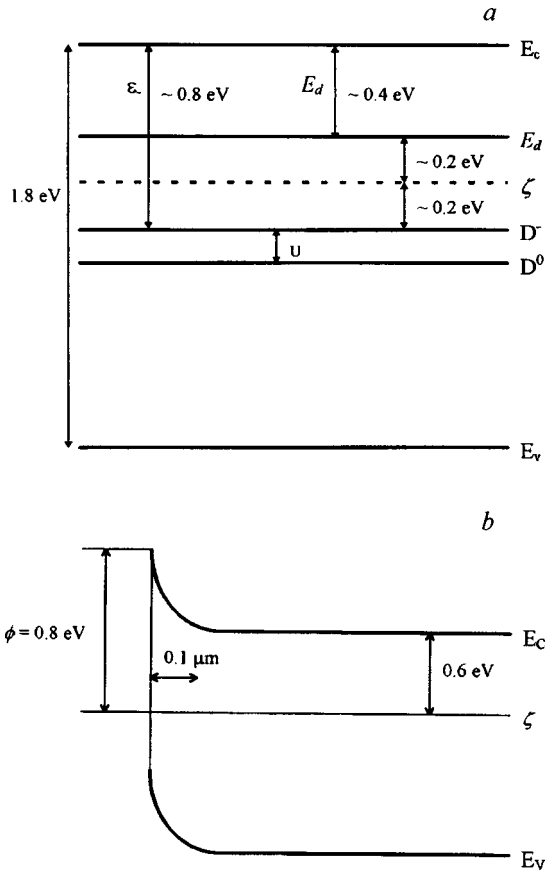

FIG. 6. Energy band diagram of *a*–Si:H⟨Er⟩ under zero bias. (a) *U* is the correlation energy, (b) Schottky barrier at the Al/*a*–Si:H⟨Er⟩ interface at equilibrium.

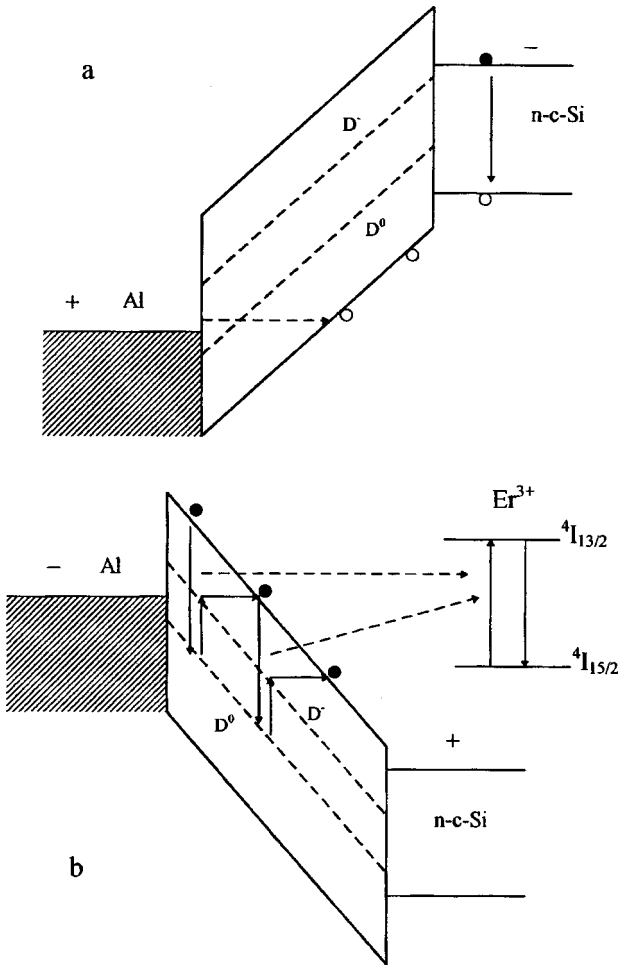

FIG. 7. Energy band diagrams of an electroluminescent structure (a) under forward bias, (b) under reverse bias.

excitation (DRAE process[7]) is an efficient process due to its nearly resonant character. The energy of the $e+D^0 \rightarrow D^-$ transition is close to that of the intra-$4f$ Er^{3+} ion transition from the ground, $^4I_{15/2}$, to the first excited, $^4I_{15/2}$, state. The excess energy is transferred to local phonons.

Consider these processes in more detail within the proposed energy-band diagram (Fig. 6a). It is known that incorporation of erbium and oxygen into crystalline silicon creates deep donors with an energy of 150–200 meV. Erbium doping of amorphous silicon, which contains large amounts of oxygen, can be also expected to produce donor states depicted in Fig. 6a by level E_d, because impurity donor and acceptor states in amorphous silicon form basically in the same way as this occurs in crystalline silicon. This viewpoint[8] is borne out by the results of a Mössbauer study, which showed the optically active erbium center in amorphous silicon to be actually an erbium-oxygen complex similar to the one observed in crystalline silicon.

It is also well known that doping amorphous silicon results in formation of dangling bonds,[9] which in an *n*-type semiconductor can be in two charge states, D^0 and D^-. The dangling silicon bonds in amorphous hydrogenated silicon containing 10% and even more hydrogen are known to undergo passivation. As this was shown in an EPR study[10] of the dangling-bond concentration, however, doping amorphous hydrogenated silicon with an impurity whose concentration is several orders of magnitude lower than that of hydrogen creates dangling bonds which are not hydrogen passivated.

We believe that because the dangling bonds appearing in our case are primarily due to erbium doping, their concentration N_D is approximately equal to the donor concentration N. As a result of the nearly complete compensation of D^- centers by donors, the Fermi level ζ in this case lies in between the donor level E_d and the D^- center level (Fig. 6a). Thus we have an analog of a classical intrinsic semiconductor, in which the part of the valence band is played by the D^- center level, and the donor level E_d acts as a conduction band. Then the concentration of neutral donors N is equal to that of neutral dangling bonds (D^0 centers).

We assume that, in an electric field, the electron concentration in the conduction band n and the changes in the concentrations of charged centers, $\delta N_{D^-}=N_{D^-}-N^0_{D^-}$, and of neutral centers, $\delta N_{D^0}=N_{D^0}-N^0_{D^0}$, are much smaller than the equilibrium values $N^0_{D^-}$ and $N^0_{D^0}$, i.e.,

$$N^0_{D^-}, N^0_{D^0} \gg \delta N_{D^-}, \delta N_{D^0}, n. \tag{1}$$

Because the mechanism of erbium excitation in EL is the $D^0+e \rightarrow D^-$ Auger process involving energy transfer to the inner $4f$ shell, observation of EL under steady-state conditions requires operation of the reverse process of D^--center ionization ($D^- \rightarrow D^0+e$).

A study of electric-field–induced deep-center ionization in crystalline matrices showed that the probability of multiphonon deep-center tunneling ionization in an electric field E can be written[11]

$$e(E)=e_T \exp\left(\frac{E^2}{E_c^2}\right), \tag{2}$$

$$E_c=(3m^*\hbar/\tau_2^3 q^2)^{1/2}, \tag{2a}$$

where e_T is the thermal-ionization probability, E_c is a characteristic electric field, m^* is the carrier effective mass, q is the electronic charge, and τ_2 is the defect tunneling time:[11]

$$\tau_2=\tau_1+\frac{\hbar}{2kT}, \quad \tau_1=\frac{1}{2\omega}\ln\frac{\varepsilon_T}{\varepsilon_{\rm opt}-\varepsilon_T}. \tag{2b}$$

Here ω is the local-vibration frequency, and ε_T and $\varepsilon_{\rm opt}$ are the thermal and optical ionization energies of the D^- center, respectively.

We use Eq. (2) to consider the static interaction of electrons in the conduction band and at deep centers (at donors and D centers) in an amorphous matrix. We shall assume this interaction to occur only through ionization of electrons into the band and their reverse capture by donors and D centers. This scenario can be described by the following coupled equations

$$\frac{nN_{D^0}}{N_{D^-}}=N_c e^{-\frac{\varepsilon_-}{kT}+\left(\frac{E}{E_{c1}}\right)^2}, \tag{3}$$

$$\frac{nN_+}{N_0}=N_c e^{-\frac{E_d}{kT}+\left(\frac{E}{E_{c2}}\right)^2}, \tag{4}$$

$$n+N_{D^-}=N_+, \tag{5}$$

$$N=N_0+N_+, \tag{6}$$

$$N_D=N_{D^-}+N_{D^0}, \tag{7}$$

where n is the electron concentration, N_0 and N_+ are, respectively, the concentrations of neutral and ionized donors, N_{D^-} and N_{D^0} are the concentrations of D centers in different charge states, N_c is the effective density of states at the conduction-band edge, and ε_- is the D^--center ionization energy.

Equations (3) and (4) describe the charge exchange of D centers ($D^0+e\rightarrow D^-$) and donors ($N_++e\rightarrow N_0$), which in zero field require energy expenditures ε_- and E_d, respectively. Eq. (5) is the charge neutrality condition, and Eqs. (6) and (7) give the total concentration of the donors and D centers.

The first term in the exponent in Eq. (5) relates to the D^--center ionization with an ionization energy ε_-, which occurs in a zero electric field. In an electric field $E\approx V/d$, where V is the applied voltage and d is the thickness of the a–Si:H⟨Er⟩ layer, multi-phonon tunneling ionization takes place, and it accounts for the second term in the exponent, $(E/E_{c1})^2$, where E_{c1} is a characteristic field determined by the D-center tunneling time τ_2. E_{c2} is the characteristic time for deep centers with energy E_d. Taking into account that $N\approx N_D$, Eqs. (3)–(7) yield for equilibrium values in zero electric field

$$n_0=N_c\exp\left(-\frac{\varepsilon_-+E_d}{2kT}\right)\equiv N_c\exp\left(-\frac{\zeta}{kT}\right), \tag{8}$$

$$N_+^0\approx N_{D^-}^0\approx N, \tag{9}$$

$$N_{D^0}^0\approx N_D\exp\left(-\frac{\varepsilon_--\zeta}{kT}\right). \tag{10}$$

The Fermi-level position ζ corresponding to the solution of Eqs. (8)–(10) is shown in Fig. 6a. Assuming $N=N_D\approx 10^{19}$ cm^{-3} in zero electric field, which corresponds to the erbium concentration, we obtain from Eqs. (8)–(10) for the concentration of neutral D^0 centers $N_{D^0}^0\approx 10^{16}$ cm^{-3} for $\varepsilon_--\zeta=0.2$ eV, the value derived from the temperature dependence of EL in Fig. 3 for the equilibrium electron concentration in the band $n_0\approx 10^9$ cm^{-3}.

Consider now the case of a strong electric field assuming the changes in concentrations δN_{D^0} and δN_0 to be much smaller than the equilibrium values $N_{D^0}^0$ and N_0^0. Equations (3)–(7) yield

$$n=N_c e^{-\frac{\zeta}{kT}+\left(\frac{E}{E_c}\right)^2}\equiv n_0 e^{\left(\frac{E}{E_c}\right)^2}, \tag{11}$$

where $n_0=N_c\exp(-\zeta/kT)$. We have assumed here for the sake of simplicity that the characteristic fields E_{c1} and E_{c2} are approximately equal. This can be substantiated by the fact that τ_2 turns out quite frequently to be the same for different defects in the same semiconducting matrix.[11]

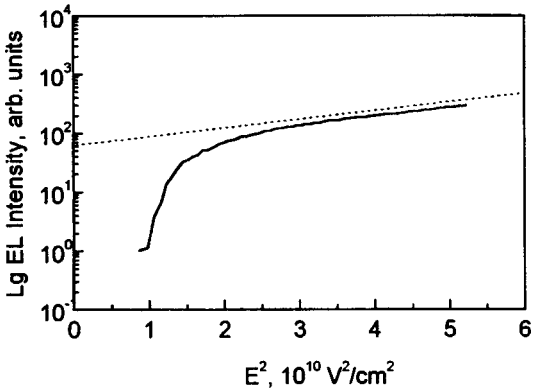

FIG. 8. Log erbium EL intensity at 1.54 μm plotted against the square of electric field applied across the amorphous silicon layer.

Thus, according to Eq. (11), the dependence of the current flowing through the structure on electric field at a given temperature (i.e., the reverse branch of the I–V characteristic, Fig. 1) should be determined primarily by the exponential growth of the electron concentration in the conduction band caused by multi-phonon tunneling ionization.

Electron capture from the conduction band by the D^0 centers can take place in three channels:[7] by radiative capture, by the Auger excitation of erbium ions, or through a nonradiative multi-phonon process

$$c=c_R+c_A+c_{mp},$$

where c_R, c_A, and c_{mp} are the coefficients of radiative recombination, Auger process, and multi-phonon nonradiative capture by a D^0 center, respectively. The erbium luminescence intensity will be determined not by the total probability of electron capture by a D^0 center but rather by that of the Auger process, which yields, taking into account condition (1), the following expression for the electroluminescence intensity I_L:

$$I_L=c_A n_0 N_{D^0}^0\exp\left(\frac{E^2}{E_c^2}\right)\frac{\tau}{\tau_r}, \tag{12}$$

where τ and τ_r are the total and radiative erbium lifetimes in excited state, respectively.

Because the electric-field dependences of both the current and the erbium luminescence intensity are dominated by the exponential in Eqs. (11) and (12), these dependences are practically the same, and the luminescence intensity, in full agreement with experiment, depends linearly on current (Fig. 4). To test the theory, one should, however, confirm the dependence of erbium luminescence intensity on electric field following from Eq. (12). Figure 8 plots the dependence of the log erbium EL intensity against the square of the electric field applied to the amorphous silicon layer. For voltages $V<12$ V, the electric-field dependence of $\ln I_L$ is determined apparently by the combined action of delocalization of shallow tail states and the donor-state Poole-Frenkel effect. As the voltage is increased, the $\ln I_L\propto E^2$ dependence is seen to be met starting from $V\approx 15$ V, which provides support for the theory [Eq. (12)] and permits one to determine the characteristic electric field E_c. Assuming the field to be uniform

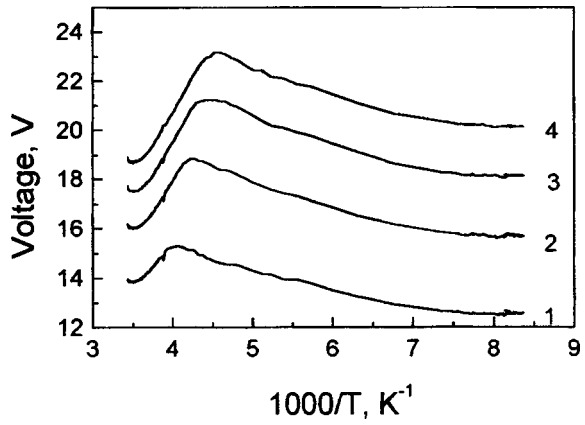

FIG. 9. Voltage V across the structure vs temperature for currents (mA): (1) 5, (2) 10, (3) 15, and (4) 20.

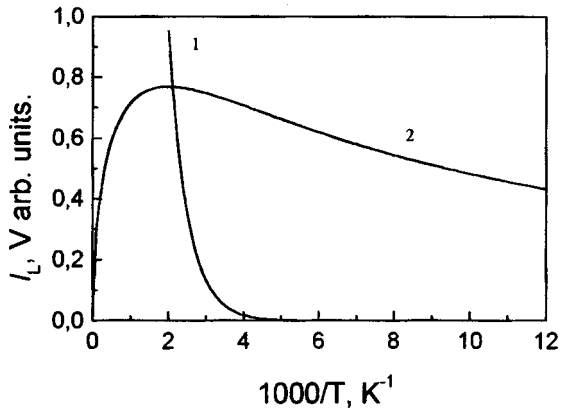

FIG. 10. Theoretical temperature dependences of (1) erbium EL intensity and (2) voltage across the structure in the dc current regime.

throughout the thickness of the amorphous layer ($\approx 1\ \mu$m), one obtains $E_c \approx 1.6\times 10^5$ V/cm. This yields an estimate for the tunneling time $\tau_2 \sim 3\times 10^{-14}$ s. This figure agrees in order of magnitude with the data obtained for other defects and in other semiconductors.[11]

The temperature dependence of erbium EL intensity I_L at 1.54 μm displayed in Fig. 3 was measured with dc current. To facilitate comparison with experimental data, one can conveniently express I_L through the current density $j = q\mu nE$ and make use of the relation

$$N_{D^0}^0 = N_D \exp\left(-\frac{\varepsilon_- - \zeta}{kT}\right). \tag{13}$$

Then for the temperature dependence of erbium EL intensity in the dc current regime we can write

$$I_L = c_A N_D \exp\left(-\frac{\varepsilon_- - \zeta}{kT}\right)\frac{j}{q\mu E_j}\frac{\tau}{\tau_r}, \tag{14}$$

where E_j, the electric field applied to the structure at current j, is only weakly temperature dependent, q is the electronic charge, and μ is the electron mobility. A comparison of Eq. (14) with the data in Fig. 3 shows that the ε_- level lies ~ 0.2 eV below the Fermi level. By our model, the donor level E_d is 0.2 eV above the Fermi level. Thus the donor level, as can be readily seen from Fig. 6a, is located ~ 0.4 eV below the conduction-band bottom E_c. One could attempt to reconcile the above results also with the band-structure model in which ζ coincides with E_d ($N > N_D$), but then one would have to assume the deep-donor energy to be still larger ($E_d \approx 0.5$ eV). Therefore we preferred the model displayed in Fig. 6a.

Let us discuss now the relation connecting the temperature dependences of EL intensity I_L (Fig. 3) and of the voltage across the sample $V = E/d$ (Fig. 9) measured in the dc current regime. As seen from these figures, the $V(T)$ relation passes through a maximum in the temperature region where one observes an increase of EL with temperature. This case can be described readily in terms of our model. Indeed, expressing the electric field (the voltage at the sample) through current density yields

$$E = E_c\sqrt{\ln\frac{j}{q\mu n_0 E}}, \tag{15}$$

where one can make an approximate substitution of E for E_c within the agrument of the logarithm. Then for the temperature dependence of field E, which is determined by the $\ln n_0 \sim \zeta/T$ relation and the temperature dependence of the characteristic field E_c (2) we obtain

$$E \sim \frac{x^{1/2}}{(x+x_0)^{3/2}}, \tag{16}$$

where $x \equiv 1/T$ and $x_0 \equiv 2\tau_1 k/\hbar$. Accordingly, the temperature dependence of the EL intensity I_L is given by

$$I_L \sim \frac{1}{E}\exp(-|\zeta - \varepsilon_-|x). \tag{17}$$

Figure 10 plots the temperature dependences of $V = E/d$ and I_L calculated using Eqs. (16) and (17). We set here $\varepsilon_- - \zeta = 0.2$ eV and $\tau_1 = 1.5\times 10^{-14}$ s. We readily see that the relations we have obtained are in semiquantitative agreement with experimental data. One can expect that for $\tau_1 \sim \hbar/2kT$ the characteristic fields E_{c1} and E_{c2} should be close, as this was assumed above.

At low temperatures and in a strong field, deep centers are ionized by tunneling, without participation of phonons. In agreement with Ref. 12, the probability of such tunneling-assisted ionization through a triangular potential barrier depends on the field as

$$e_E \sim \exp\left(-\frac{a\varepsilon^{3/2}}{E}\right),$$

where a is a constant, and ε is the energy reckoned from the top of the triangular barrier. Due to this tunneling effect, the electron concentration in the conduction band at low temperatures will depend only on the applied field as $n \propto \exp(-a\varepsilon^{3/2}/E)$. Figure 11 presents several points calculated using the data in Fig. 3 for the low-temperature domain, where the EL intensity is temperature independent. We see that $\ln(I_L)$ is indeed well fit by a linear dependence on $1/E$. This provides support for the above interpretation of experimental data on the EL behavior at low temperatures.

The D^--center ionization probability e depends exponentially on electric field for both high and low temperatures. Therefore a voltage pulse with a steep leading edge fed into

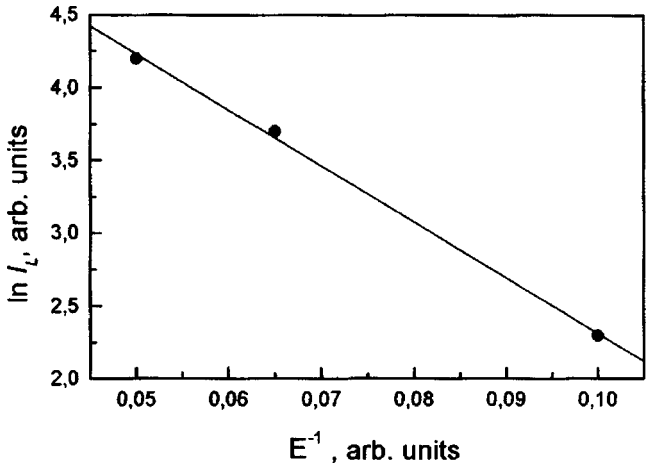

FIG. 11. Log erbium EL intensity vs electric field $1/E$ for $T=100$ K.

the structure initiates a transient process, in which the voltage across it decreases (because the free-electron concentration in the amorphous layer grows with time $\sim e^{-1}$). The time in which steady state sets in decreases with increasing voltage applied to the structure, and this accounts for the voltage pulse shape at the sample (Fig. 5).

The proposed model of erbium excitation also provides explanation for the irreversible quenching of erbium luminescence observed to occur when too high currents are passed through a structure. The corresponding high voltage favors aluminum ion diffusion from the contact into the bulk of the amorphous layer. Such phenomena were observed[13] in fields $\sim 10^5$ V/cm, which is close to the voltages used in this work. Aluminum acts as an acceptor in silicon, which results in compensation of the D^- centers (and their transformation into D^0 centers). In these conditions, ionization of D^- centers no longer takes place (the fields employed are not high enough to ionize the D^0 centers), the Auger-assisted erbium excitation becomes impossible, and the erbium luminescence dies out.

Thus we have studied the electroluminescence of amorphous hydrogenated erbium-doped silicon within the 77–300 K temperature region. It was found that the erbium luminescence intensity increases with temperature, to pass through a maximum close to room temperature.

The process underlying the mechanism of erbium-ion Auger excitation is electron capture from the conduction band by D^0 centers, with subsequent energy transfer by Coulomb interaction to the erbium-ion $4f$ electrons. The steady state is sustained by multi-phonon tunneling ionization of electrons from negatively charged dangling bonds (D^- centers) and donors created as a result of erbium doping.

The proposed theoretical model of erbium ion EL in structures based on erbium-doped amorphous hydrogenated silicon provides an adequate quantitative description of all the experimental results obtained.

Support of the Russian Fund for Fundamental Research (Grants 95-02-04163a, 96-02-1693a, and 97-02-18079), as well as of INTAS (Grant 95-IN-RU-531), Copernicus (Grant 977048-SIER), and NATO Linkage (Grant HTECH.LG 972032) is gratefully acknowledged.

[1] *Rare-Earth Doped Semiconductors I*, edited by G. S. Pomrenke, P. B. Klein, and D. W. Langer (Materials Research Society, Pittsburgh, 1993); *Rare-Earth Doped Semiconductors II*, edited by S. Coffa, A. Polman, and R. N. Schwartz (Materials Research Society, Pittsburgh, 1996).
[2] M. S. Bresler, O. B. Gusev, V. Kh. Kudoyarova, A. N. Kuznetsov, P. E. Pak, E. I. Terukov, I. N. Yassievich, B. P. Zakharchenya, W. Fuhs, and A. Sturm, Appl. Phys. Lett. **67**, 3599 (1995).
[3] J. H. Shin, R. Serna, G. N. van den Hoven, A. Polman, W. G. J. H. M. van Stark, and A. M. Vredenberg, Appl. Phys. Lett. **68**, 997 (1996).
[4] A. R. Zanatta, Z. A. Nunes, and L. R. Tessler, Appl. Phys. Lett. **70**, 511 (1997).
[5] M. S. Bresler, O. B. Gusev, B. P. Zakharchenya, V. Kh. Kudoyarova, A. N. Kuznetsov, E. I. Terukov, W. Fuhs, and I. N. Yassievich, Fiz. Tverd. Tela (St. Petersburg) **38**, 1189 (1996) [Phys. Solid State **38**, 658 (1996)]; O. B. Gusev, A. N. Kuznetsov, E. I. Terukov, M. S. Bresler, V. Kh. Kudoyarova, I. N. Yassievich, B. P. Zakharchenya, and W. Fuhs, Appl. Phys. Lett. **70**, 240 (1997).
[6] C. R. Wronski and D. E. Carlson, Solid State Commun. **23**, 421 (1977).
[7] I. N. Yassievich, M. S. Bresler, and O. B. Gusev, J. Phys.: Condens. Matter **9**, 9415 (1997).
[8] V. F. Masterov, F. S. Nasredinov, P. P. Seregin, V. Kh. Kudoyarova, A. N. Kuznetsov, and E. I. Terukov, Pis'ma Zh. Tekh. Fiz. **22**, No. 23, 25 (1996) [Tech. Phys. Lett. **22**, 960 (1996)].
[9] R. A. Street and D. K. Biegelsen, in *The Physics of Hydrogenated Amorphous Silicon*, edited by J. D. Joannopoulos and G. Lucovsky [Springer, Berlin, 1984; Mir, Moscow, 1988], p. 247.
[10] R. A. Street and D. K. Biegelsen, Solid State Commun. **33**, 1159 (1980).
[11] S. D. Ganichev, I. N. Yassievich, and W. Prettl, Fiz. Tverd. Tela (St. Petersburg) **39**, 1905 (1997) [Phys. Solid State **39**, 1703 (1997)].
[12] L. D. Landau and E. M. Lifshits, in *Quantum Mechanics* (Pergamon Press, Oxford, 1974; Nauka, Moscow, 1989), p. 223.
[13] *Electronic Phenomena in Chalcogenide Glassy Semiconductors* [in Russian], edited by K. D. Tséndin (Nauka, St. Petersburg, 1996), p. 300.

Translated by G. Skrebtsov

UV absorption of $RbAg_4I_5$-RE (Sm, Yb) thin-film systems

A. L. Despotuli and L. A. Matveeva

Institute of Microelectronics and Ultrapure Materials Technology, Russian Academy of Sciences, 142432 Chernogolovka, Moscow District, Russia

(Submitted May 15, 1998)
Fiz. Tverd. Tela (St. Petersburg) **41**, 218–222 (February 1999)

UV spectra of samples prepared by vacuum deposition of Sm and Yb thin films on 100–200-nm thick films of the $RbAg_4I_5$ solid electrolyte (SE) at 300–350 K contain strong absorption bands peaking at about 4.3 and 5.0 eV. After deposition of ~5 nm of Sm, the ionic conductivity σ of the samples decreases from σ_0 to $\approx 0.9\,\sigma_0$, and the SE lattice parameter, from 11.24 to ≈11.15 Å, with the x-ray reflection halfwidth increasing from 0.5 to 0.8°. Further growth of Sm concentration in the samples changes the x-ray diffraction pattern, the absorption at 4.3 and 5.0 eV increases, a new absorption edge forms at 3.8 eV, and σ decreases down to $\sim 10^{-2}\,\sigma_0$. It is conjectured that the strong UV absorption bands in heavily defected silver halides of the $RbAg_4I_5$-Sm(Yb) system is genetically related to the $4d^{10} \rightarrow 4d^9 5s$ electronic transitions in free Ag^+ ions. © *1999 American Institute of Physics.* [S1063-7834(99)00702-9]

1. The $RbAg_4I_5$ superionic conductor,[1–3] a solid electrolyte (SE), is a classical object of investigation in solid-state ionics.[4] Because of its record-high Ag^+ conductivity, this compound finds application in technology. The influence of impurities on the properties of $RbAg_4I_5$ have been reported in a number of publications. Some of them[5,6] dealt with the problems of superionic conduction and the stability of $RbAg_4I_5$, which still have not lost their importance. It was proposed to prepare crystalline structures with high concentrations of impurity centers and specific properties by dissolving appropriate metals in Ag^+ conduction channels in $RbAg_4I_5$.[7] The possibility of dissolving rare-earth (RE) metals in $RbAg_4I_5$ was first demonstrated in Refs. 7–9. The samples to be studied were produced by vacuum deposition of thin (~5 nm) Sm films on $RbAg_4I_5$ films at 293–350 K. The optical absorption of samples within the spectral interval $h\nu = 1.6-4.1$ eV and their ionic conductivity $\sigma\,(\approx 0.9\,\sigma_0)$ were explained as due to the formation of $RbAg_4I_5$–Sm dopants with a concentration of optically active centers (F centers) $\sim 3\times 10^{20}$ cm^{-3}. By Ref. 9, high Sm contents in the $RbAg_4I_5$–Sm system favor precipitation of a nonstoichiometric phase with $\sigma \ll \sigma_0$ and an absorption edge within the 3.6–3.8-eV interval. No data are available on UV absorption of $RbAg_4I_5$ from 4.1 to 6 eV. Preliminary experiments revealed strong absorption bands in UV spectra of $RbAg_4I_5$–RE (Sm, Yb) film systems.[10] It was conjectured that point defects (F centers) break pd valence-band hybridization in the $RbAg_4I_5$–RE silver halides, thus producing conditions favoring electronic excitations, which are similar to those in Ag^+ centers of alkali halide crystals and responsible for the strong UV absorption bands. This work reports experimental data on UV absorption in $RbAg_4I_5$–RE (Sm, Yb) silver halides. The first x-ray diffraction measurements of these objects are presented.

2. Sample preparation in a vacuum of 2×10^{-6} Torr and determination of the optical absorption and σ in the $RbAg_4I_5$–RE (Sm, Yb) system are described elsewhere.[9] X-ray characterization of $RbAg_4I_5$ films with thickness $l \approx 100-200$ nm and of $RbAg_4I_5$–Sm samples ($l \approx 100-200$ nm, $l_{Sm} \sim 5-15$ nm by weight) was performed at 293 K with Cr $K\alpha$ radiation. The x-ray diffraction patterns were obtained in the Bragg–Brentano arrangement in ≈3 h. The (110), (221), and (311) reflections in $RbAg_4I_5$ films became strong enough already at $l \approx 100$ nm. Other SE reflections were also substantially above the background at $l \sim 200$ nm. The intensity ratios of the main SE reflections were in agreement with literature data[11].

3. Figure 1 (spectra *1*, *1a*, and *2*) presents a typical UV behavior of the optical density $D(h\nu) = \log(J_{quartz}/J_{SE})$ in the starting $RbAg_4I_5$ films (quartz substrate, $l_1 \approx 100$ nm, $l_2 \approx 200$ nm, identical deposition cycles) with respect to a quartz reference. The $D(h\nu)$ spectra of the films exhibit features at about 4.3 and 5.0 eV, which cannot be associated with those of the $RbAg_4I_5$ band diagram constructed[12] using XPS data. The amplitude of the changes in $D(h\nu)$ in the region of 4.3 and 5.0 eV increases with l, i.e., it is determined by the bulk properties of the material, and is ~1/10 of the fundamental absorption.

Vacuum deposition of Sm on $RbAg_4I_5$ films gives rise to a decrease of the SE fundamental absorption and to formation of strong absorption bands in the 4.3- and 5.0-eV regions. A strong absorption tail decaying from 6 eV toward smaller $h\nu$ also becomes evident. Pairs of $RbAg_4I_5$ films with $l_1 \approx l_2$ and $D_1(h\nu) \approx D_2(h\nu)$ were used to detect the UV bands. The relative optical density of such a pair, $D_r(h\nu) = \log(J_1/J_2)$, was determined both before and after RE deposition on one of the SE films. The change in the relative optical density, $\Delta D_r(h\nu)$, at the maxima of the UV bands of $RbAg_4I_5$-Sm may be as high as ~1/5 of the fundamental absorption of $RbAg_4I_5$.

Figure 2 shows a $D_r(h\nu)$ spectrum of a $RbAg_4I_5$-Sm sample with $\sigma \approx 0.9\,\sigma_0$, the lattice parameter 11.15 ± 0.005 Å, and an x-ray reflection halfwidth ≈0.8°. The corresponding values for the pristine $RbAg_4I_5$ film are σ_0, 11.24 Å, and

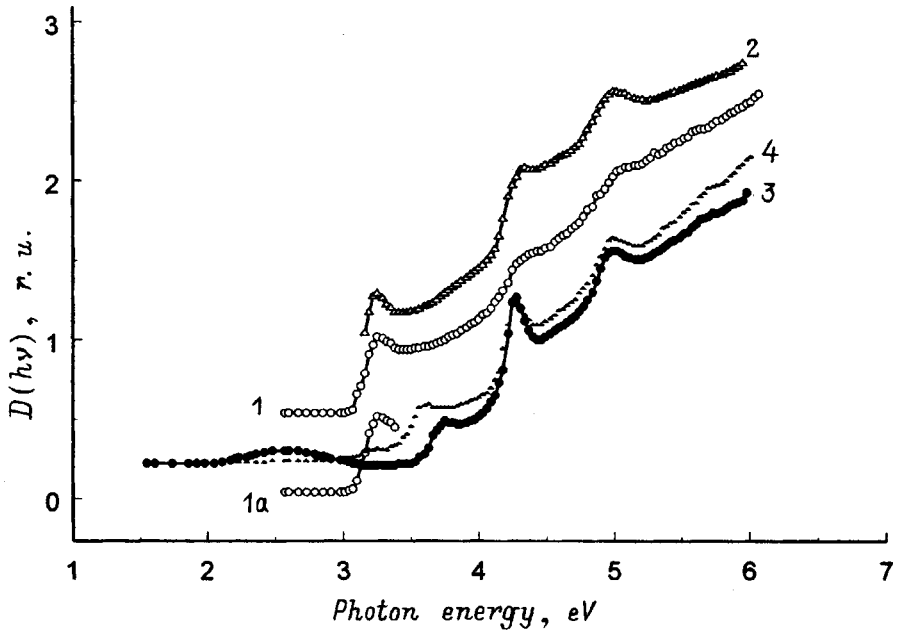

FIG. 1. $D(h\nu)$ spectra of the $RbAg_4I_5$–Sm samples obtained at 293 K. *1* — Pristine $RbAg_4I_5$ film with $l \approx 100$ nm. The vertical scale is raised by 0.5 with respect to experimental data; 1*a* - Part of spectrum 1 drawn on original scale; *2* — $RbAg_4I_5$ film with $l \approx 200$ nm. The vertical scale is raised by 0.2 with respect to experimental data; *3* — Low-σ phase: Sm layer with $l_{Sm} \approx 15$ nm deposited on $RbAg_4I_5$ (spectra *1* and *1a*) at 350 K; *4* — Sample (spectrum *3*) after 5 h storage in dry air.

0.5°. The relative intensity of the (221) and (110) or (221) and (311) reflections in $RbAg_4I_5$–Sm is approximately 1.5 that of the original $RbAg_4I_5$ film. The (221) reflection is superimposed on the strong (111) β–AgI reflection. This suggests a possibility of separating AgI in the course of RE dissolution in SE (see Ref. 9). As follows from $D(h\nu)$, σ, and x-ray diffraction measurements, $RbAg_4I_5$–RE samples recover in dry air to the original $RbAg_4I_5$ in a few days (this phenomenon is discussed in Ref. 9).

Figure 3 displays a $D(h\nu)$ spectrum of $RbAg_4I_5$–Yb in the region $h\nu = 1.6-4.1$ eV, which is similar to that of $RbAg_4I_5$–Sm (see Fig. 1 in Ref. 9) and contains a strong absorption band with a maximum at 2.4 eV in the SE transmission region (coloring). A $\Delta D_r(h\nu)$ UV spectrum of the same $RbAg_4I_5$–Yb sample with the 4.3- and 5.0-eV bands is shown in Fig. 4. The above spectra demonstrate a decrease in the SE fundamental absorption. The phenomena under study do not depend on the RE atomic number. This provides one of the necessary conditions justifying assignment of the 2.4-eV band to the *F* centers. When stored in dry air, the strong UV absorption bands of SE-RE samples become redshifted by ~ 0.05 eV, which can be associated with an increase of the lattice parameter.

Figures 5 and 6 show $D(h\nu)$ and $\Delta D_r(h\nu)$ spectra of a sample with a higher Sm content. The $D(h\nu)$ spectrum exhibits two absorption edges at 3.3 eV ($RbAg_4I_5$) and 3.6 eV [a low-σ phase coexisting with $RbAg_4I_5$:Sm (Ref. 9)].The $\Delta D_r(h\nu)$ spectrum contains a feature at the 3.6-eV absorption edge, strong absorption bands at 4.3 and 5.0 eV, and a strong-absorption tail declining from 6 eV toward smaller $h\nu$. The variation of the optical density in two-phase samples reaches $\sim 1/4$ of the fundamental absorption in $RbAg_4I_5$. The recovery of the original optical-density spectra in such samples takes more time than that in $RbAg_4I_5$:RE.

Spectra *3* and *4* in Fig. 1 were measured on a sample obtained by depositing on the starting $RbAg_4I_5$ film (spectra

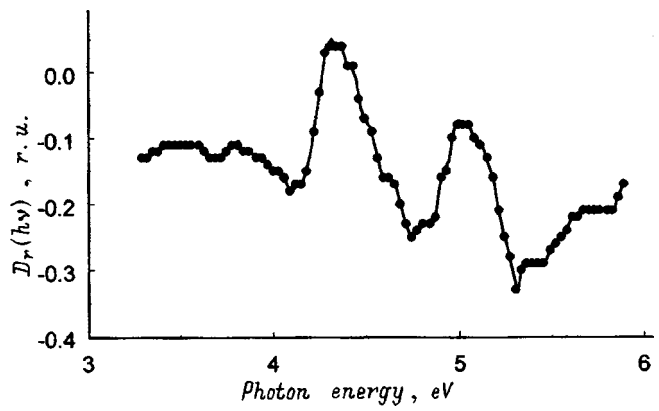

FIG. 2. $\Delta D_r(h\nu)$ spectrum of $RbAg_4I_5$:Sm and $RbAg_4I_5$ films ($l_{1,2} \approx 200$ nm) obtained at 293 K. A Sm layer with $l_{Sm} \approx 5$ nm was deposited on $RbAg_4I_5$ at 350 K.

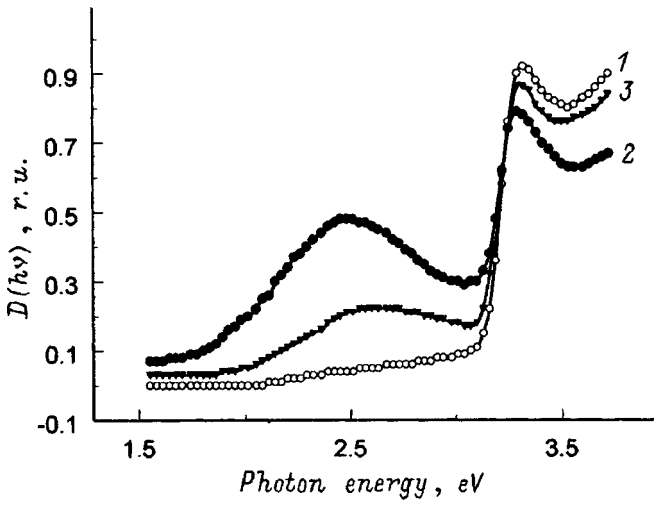

FIG. 3. $D(h\nu)$ spectra of $RbAg_4I_5$-Yb (293 K): *1* — Pristine $RbAg_4I_5$ film with $l \approx 160$ nm; *2* — An Yb layer with $l_{Yb} \approx 4$ nm was deposited on $RbAg_4I_5$ (spectrum *1*) at 350 K; *3* — Sample (spectrum *2*) after 43 h storage in dry air.

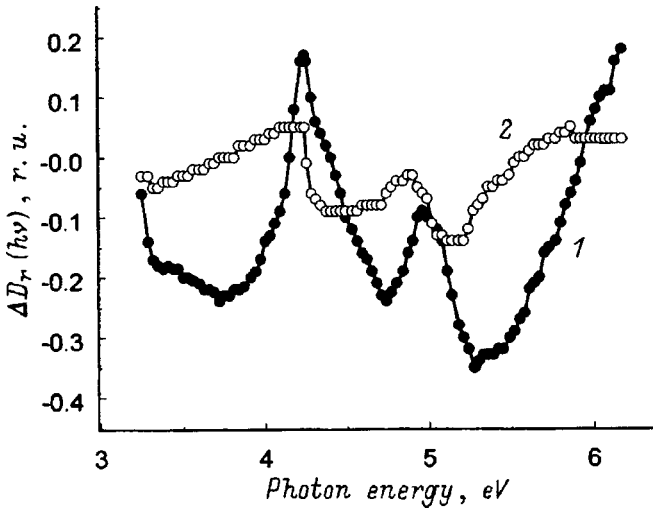

FIG. 4. $\Delta D_r(h\nu)$ spectra of $RbAg_4I_5$-Yb and $RbAg_4I_5$ ($l_{1,2}\approx 160$ nm) at 293 K. An Yb layer with $l_{Yb}\approx 4$ nm was deposited on one of the $RbAg_4I_5$ films: *1* — After Yb deposition; *2* — After 43 h storage in dry air.

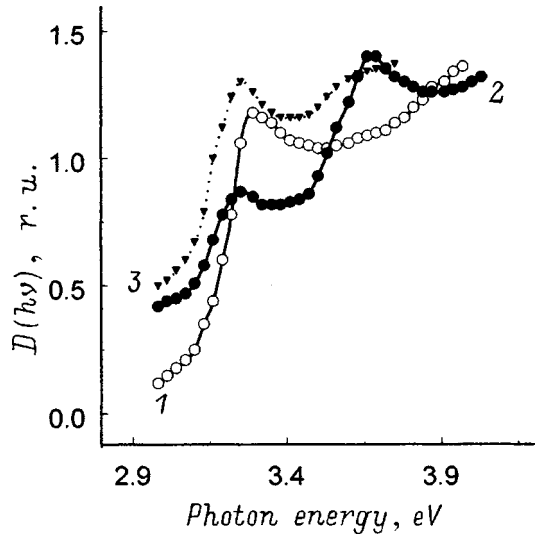

FIG. 5. $D(h\nu)$ spectra of $RbAg_4I_5$:Sm (293 K): *1* — Pristine $RbAg_4I_5$ film with $l\approx 220$ nm; *2* — Two-phase sample, with a Sm layer with $l_{Sm}\approx 8$ nm deposited on $RbAg_4I_5$ at 350 K; *3* — Two-phase sample after 10 days of storage in dry air.

1 and *1a*) a sufficiently thick Sm film (see Ref. 9). After its removal from the vacuum, measurements revealed $\sigma \sim 10^{-2}\,\sigma_0$, only one absorption edge at 3.8 eV, and UV absorption bands at 4.3 and 5.0 eV. The change in the optical density at the band maxima is as high as $\sim 1/3$ of the fundamental absorption of $RbAg_4I_5$. The x-ray diffraction of the samples with the 3.8-eV edge has a different pattern than that of $RbAg_4I_5$. There is no strong (110) reflection, there appears a reflection with $d=7.14$ Å which could be assigned to (210) Rb_2AgI_3 (see Ref. 11), but one does not observe the stronger (510), (121), (221) and (411) reflections of Rb_2AgI_3. One can see also reflections with $d=3.72$ and 3.36 Å, which correspond to the (221) and (311) reflections in $RbAg_4I_5$:Sm. The phase with $\sigma\sim 10^{-2}\,\sigma_0$ exists apparently within a certain RE concentration interval. Figure 1 shows a shift of the absorption edge of the phase to the 3.6-eV region after 5 h of sample storage in air. At the same time a weak feature at 3.3 eV corresponding to the absorption edge of $RbAg_4I_5$:Sm appears in the $D(h\nu)$ spectrum. After four days of sample storage in dry air, the $D(h\nu)$ spectrum reveals the presence of $\sim 30\%$ $RbAg_4I_5$:Sm (the lattice parameter 11.14 Å, $\sigma\sim 10^{-2}\,\sigma_0$), with the $d=7.14$-Å reflection being replaced by a diffuse one with $d=7.35$ Å, which cannot be assigned to $RbAg_4I_5$, Rb_2AgI_3, or AgI. There appears also a weak diffuse reflection with $d=7.92$ Å, which can be related to the (110) reflection of $RbAg_4I_5$:Sm. After five days, σ increases to $7\times 10^{-2}\,\sigma_0$, and the lattice parameter, to 11.16 Å. The $d=7.35$-Å reflection becomes weak to subsequently disappear. By contrast, the (110) reflection of $RbAg_4I_5$:Sm grows in intensity. As follows from the $D(h\nu)$ data, the absorption edge of the low-σ phase persists in the spectrum after eight days of the experiment, when the lattice parameter of $RbAg_4I_5$:Sm increases to 11.19 Å, and σ, to $0.5\,\sigma_0$. The 2.4-eV absorption band does not appear in the $D(h\nu)$ spectrum as the fraction of $RbAg_4I_5$:Sm in the sample increases. At the same time the high values of $D(h\nu)$, at a level of $\approx 0.2-0.3$ of the jump at the absorption edge, persist in the SE transmission region. It can therefore be conjectured that the structural transformations in $RbAg_4I_5$:Sm samples are accompanied by the formation of

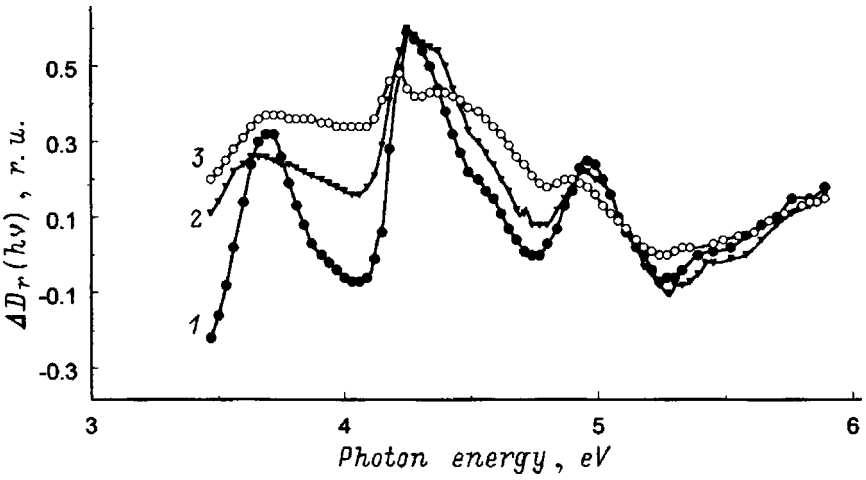

FIG. 6. $\Delta D_r(h\nu)$ spectra of the two-phase sample (Fig. 5) and of a $RbAg_4I_5$ film with $l\approx 220$ nm at 293 K: *1* — Starting two-phase sample; *2* — After 10 days of storage in dry air; *3* — After 30 days of storage in dry air.

aggregates of point defects including F centers.

Some types of solid-state current sources and electrochemical devices contain a $RbAg_4I_5$/Ag interface. Therefore in conclusion to this Section, we stress different stability of the dopants $RbAg_4I_5$:Ag (see, e.g., Ref. 13) and $RbAg_4I_5$:RE with respect to decomposition into AgI and Rb_2AgI_3. We deposited in vacuum Ag films of the same weight thickness, $l_{Ag} \approx 2$ nm, on $RbAg_4I_5$ films with $l_1 = 100$ nm and $l_2 = 200$ nm. This resulted in an irreversible appearance in $D_r(h\nu)$ spectra of a weak AgI exciton-absorption band at 3.0 eV, which signaled precipitation of this compound in the sample with l_1. While for $l_{Ag} \sim 5$ nm, AgI was found to be present in both samples, in the thinner one with l_1 its concentration reached already $\sim 50\%$. The data obtained show that the changes in the SE free energy involved in formation of the $RbAg_4I_5$:Ag and $RbAg_4I_5$:RE dopants have opposite signs.

4. The optical activity revealed in $RbAg_4I_5$ in the 2.9–3.0-eV interval was assigned to the $4d^{10} \rightarrow 4d^9 5s$ electronic transitions in Ag^+ ions.[14–16] In actual fact it was due to the AgI excitons. It was shown that AgI is nearly always present in $RbAg_4I_5$ samples.[17–19]

The strong UV absorption bands in the $RbAg_4I_5$–RE systems are close in energy to the quadrupole transitions $4d^{10} \rightarrow 4d^9 s$ ($^1S_0 - {}^1D_2$, $^3D_{1,2,3}$) in free Ag^+ ions (4.9–5.8 eV). One could also draw an analogy with the weak absorption bands ($A, \ldots, D$) of silver-doped alkali halide crystals. In this case the tail of the strong UV absorption in $RbAg_4I_5$–RE could be related to the $F, G, \ldots$ bands in silver-doped alkali halides. In alkali halides, Ag^+ ions in Ag^+ $(Hal^-)_6$ octahedral clusters can become off-centrosymmetric, and the forbiddenness on optical excitation of the $4d^{10}$ electrons can be partially lifted under dynamic or static asymmetry of the centers.[20–28] One of possible reasons for an asymmetry is a structural defect in the nearest environment of the Ag^+ ion.[22,26] As the radii of the host-lattice ions and the lattice constant increase, the absorption and luminescence of the Ag^+ ions in alkali halide crystals undergo a red shift. For instance, the D absorption band in NaCl (lattice constant 5.6 Å) peaks near 6.4 eV, while in KI (7.1 Å) the band maximum is at 5.5 eV.[22] As already pointed out, the red shift of the strong UV absorption bands in SE:RE may be associated with an increase in the lattice parameter.

No reliable data on selective optical excitation of d^{10} electrons in CuHal and AgHal are presently available.[29] According to Ref. 30, the valence-band wave functions of these compounds evolve from mixing of the Hal p functions and of the d functions of the metal. At the same time XPS data seem to suggest pd hybridization of the valence band in AgHal,[29,31–33] and strong dynamic pd hybridization[13,34] in AgCl, AgBr, and $RbAg_4I_5$. The increase of fundamental absorption in AgHal is assigned to valence-band pd hybridization.[35] As seen from Fig. 1, fundamental absorption in $RbAg_4I_5$ increases within the 3.3–6-eV interval.

The energy levels of the Ag^+ centers in alkali-halide crystals were calculated in molecular approximation,[23] with inclusion of covalent bonding of the $4d^{10}$, $4d^9 5s$, and $4d^9 5p$ configurations of Ag^+ ions with p electrons of the six nearest-neighbor Hal^- ions (see also Refs. 27 and 28). The 16 Ag^+ ions in the $RbAg_4I_5$ unit cell are distributed among 56 crystallographic sites of three types, where these ions are tetrahedrally coordinated with I^-.[3] Point defects in $RbAg_4I_5$:Sm distort the band states.[10] It is therefore conjectured[11] that valence-band pd hybridization in $RbAg_4I_5$–RE silver halides can be distorted with formation of Ag^+ centers, which include an F center. The molecular-like orbitals of such centers are assumed to be responsible for the observed strong UV absorption bands.

The possible impurity nature of the features at 4.3 and 5.0 eV in the starting $RbAg_4I_5$ films is a subject of future investigations. Note that XPS spectra of $RbAg_4I_5$ films obtained under total external reflection and carrying information on the composition of the ~ 5-nm surface layer have recently been obtained on the RFA PVO spectrometer of IPTM RAN.[36] The surface layer of the samples was found to contain $\approx 1\%$ altogether of impurities, specifically of Fe, Cu, and Br.

The authors owe their thanks to V. V. Aristov for support and to V. K. Egorov for XPS measurements on the RFA PVO spectrometer.

Support of the Russian Fund for Fundamental Research (Grants 95-02-06322a and 98-03-32739a) is gratefully acknowledged.

[1] B. B. Owens and G. R. Argue, Science **157**, 308 (1967).
[2] J. N. Bradley and P. D. Greene, Trans. Faraday Soc. **63**, 424 (1967).
[3] S. Geller, Science **157**, 310 (1967).
[4] C. Kittel, *Introduction to Solid State Physics* [Wiley, New York, 1956; Nauka, Moscow, 1978], 792 pp.
[5] A. L. Despotuli, N. V. Lichkova, F. I. Kukoz, and V. N. Zagorodnev, Fiz. Tverd. Tela (Leningrad) **26**, 2214 (1984) [Sov. Phys. Solid State **26**, 1345 (1984)].
[6] V. N. Zagorodnev, N. V. Lichkova, and E. B. Yakimov, Izv. Akad. Nauk SSSR, Neorg. Mater. **23**, 1538 (1986).
[7] A. L. Despotuli, Inform. Bull. RFFI **3**, 51 (1995).
[8] A. L. Despotuli and L. A. Despotuli, *Report on the ''Physics of Solid-State Nanostructures'' program* (FIAN, Moscow, 1996), 207 pp.
[9] A. L. Despotuli and L. A. Despotuli, Fiz. Tverd. Tela (St. Petersburg) **39**, 1544 (1997) [Phys. Solid State **39**, 1374 (1997)].
[10] A. L. Despotuli, *RFFI Project 98-03-32739a* (1997).
[11] L. Bonpunt, Y. Obaid, and Y. Haget, J. Appl. Crystallogr. **10**, 203 (1977).
[12] R. S. Bauer and B. A. Huberman, Phys. Rev. B **13**, 3344 (1976).
[13] A. V. Boris, S. I. Bredikhin, N. N. Kovaleva, and N. V. Lichkova, Fiz. Tverd. Tela (Leningrad) **31**, No. 4, 47 (1989) [Sov. Phys. Solid State **31**, 572 (1989)].
[14] S. Radhakrishna, K. Hariharan, and M. S. Jagadeesh, J. Appl. Phys. **50**, 4883 (1979).
[15] K. Hariharan, J. Phys. D **12**, 1909 (1979).
[16] M. M. Afanas'ev, V. G. Goffman, and M. E. Kompan, Zh. Éksp. Teor. Fiz. **84**, 1310 (1983) [Sov. Phys. JETP **57**, 758 (1983)].
[17] S. Chandra and V. K. Mohabey, J. Phys. D **8**, 576 (1975).
[18] V. N. Andreev and V. G. Goffman, Fiz. Tverd. Tela (Leningrad) **25**, 3480 (1983) [Sov. Phys. Solid State **25**, 2004 (1983)].
[19] I. Kh. Akopyan, B. V. Novikov, T. A. Pavlova, and S. A. Soboleva, Fiz. Tverd. Tela (St. Petersburg) **38**, 2406 (1996) [Phys. Solid State **38**, 1322 (1996)].
[20] J. M. Conway, D. A. Greenwood, J. A. Krumhansl, and W. Martienssen, J. Phys.: Condens. Matter **24**, 239 (1963).
[21] F. Seitz, Rev. Mod. Phys. **23**, 328 (1951).
[22] K. Fussgaenger, W. Martienssen, and H. Bilz, Phys. Status Solidi **12**, 383 (1965).
[23] W. Dultz, Phys. Status Solidi **34**, 95 (1969).
[24] K. Fussgaenger, Phys. Status Solidi **34**, 157 (1969).
[25] N. E. Lushchik and Ch. B. Lushchik, Opt. Spektrosk. **8**, 839 (1960).
[26] N. E. Lushchik and T. A. Kuketaev, Opt. Spektrosk. **25**, 889 (1968).

[27] N. N. Kristoffel, *Theory of Small-Radius Impurity Centers in Ionic Crystals* [in Russian] (Nauka, Moscow, 1974), 336 pp.
[28] S. Emura and S. Masunaga, Phys. Rev. B **49**, 849 (1994).
[29] F. Bassani, R. S. Knox, and W. B. Fowler, Phys. Rev. **137**, A1217 (1965).
[30] M. Cardona, Phys. Rev. **129**, 69 (1963).
[31] H. Takahashi, S. Tamaki, and Y. Waseda, Solid State Ionics **31**, 55 (1988).
[32] J. Tejeda, N. J. Shevchik, W. Braun, A. Goldmann, and M. Cardona, Phys. Rev. B **12**, 1557 (1975).
[33] M. Ostrov and A. Goldmann, Phys. Status Solidi B **95**, 509 (1979).
[34] R. S. Bauer and W. E. Spicer, Phys. Rev. Lett. **25**, 1283 (1970).
[35] M. G. Mason, Phys. Rev. B **11**, 5094 (1975).
[36] V. K. Egorov, A. P. Zuev, and B. A. Malyukov, Izv. Vyssh. Uchebn. Zaved. Tsv. Met. No 5, 54 (1997).

Translated by G. Skrebtsov

Luminescent properties of crystalline lithium triborate LiB_3O_5

I. N. Ogorodnikov and A. V. Kruzhalov

Ural State Technical University, 620002 Ekaterinburg, Russia

E. A. Radzhabov

Institute of Geochemistry, Siberian Branch of the Russian Academy of Sciences, 664033 Irkutsk, Russia

L. I. Isaenko

Single-Crystal Institute, Siberian Branch of the Russian Academy of Sciences, 630058 Novosibirsk, Russia
(Submitted June 4, 1998)
Fiz. Tverd. Tela (St. Petersburg) **41**, 223–228 (February 1999)

A study of the luminescence characteristics of crystalline lithium triborate LiB_3O_5 (LBO) is reported. Investigation of the excitation and photoluminescence spectra of nominally pure, oriented LBO crystals within broad spectral (1.2–10.5 eV) and temperature (8–500 K) regions, complemented by optical spectroscopy at the long-wavelength fundamental-absorption edge, has revealed that the broad-band LBO luminescence in the 3.5–4.5-eV region is efficiently excited by photons having energies above 7.5 eV in recombination processes and under corpuscular or x-ray irradiation. The totality of the experimental data obtained permitted a conclusion that the LBO luminescence has an intrinsic nature and that it originates from radiative decay of relaxed electronic excitations. © *1999 American Institute of Physics.* [S1063-7834(99)00802-3]

Many wide-gap insulators are characterized by strong electron-phonon coupling, which accounts for a substantial part of lattice relaxation and provides favorable conditions for self-trapping of electronic excitations (EE). One discriminates between two main channels of self-trapped exciton (STE) formation, namely, via a recombination process or by direct excitation of the resonant exciton with its subsequent relaxation. In cubic alkali-halide crystals, both mechanisms can initiate formation of STEs of the same type.[1] In lower-symmetry crystals [e.g., BeO,[2] Al_2O_3, $YAlO_3$, $Y_3Al_5O_{12}$ (Ref. 3)] STEs of two types differing in properties are observed to coexist. The fundamental reasons for this lie in different patterns of relaxation that the lattice undergoes in the cases of charged (recombination) and electrically neutral EEs in low-symmetry crystals, where charge self-trapping occurring in the first stage of STE formation in the recombination process perturbs substantially the Coulomb field of the crystal, as contrasted to the relaxation of a resonant exciton. The complex crystal structure of many low-symmetry insulators suggests existence of a large number of lattice relaxation paths, which in some cases results in stabilization of various final states[4] and makes it difficult to establish the nature of the relaxation processes in these compounds.

There is presently a considerable interest in the investigation of the dynamics of electronic excitations in nonlinear crystalline borates of some alkali metals [β-BaB_2O_4 (BBO), LiB_3O_5 (LBO), CsB_3O_5 (CBO), and $Li_2B_4O_7$), which enjoy broad application in present-day nonlinear and integrated optics as converting and waveguide optical media. Some crystals of this group [β-BaB_2O_4 (Ref. 5), $Li_2B_4O_7$ (Ref. 6)] exhibit a fairly strong short-wavelength intrinsic luminescence, which is assigned to radiative annihilation of self-trapped EEs or radiative decay of relaxed EEs at lattice defects. The luminescence of these crystals has a number of common features, and it is efficiently excited both by photons at the long-wavelength fundamental-absorption edge (LWAE) and in recombination processes. LBO crystals have been overlooked in this respect until recently, and filling in this gap would be of considerable interest from the standpoint of establishing common features in the dynamics of EEs and of the luminescence in crystals of this group and their relation with those observed in more thoroughly studied wide-gap insulators.

Lithium triborate LiB_3O_5 has a complex orthorhombic cell containing four formula units, with space group $Pn2_1a$ and lattice parameters $a=8.46$ Å, $b=5.13$ Å, and $c=7.38$ Å. Two of the three inequivalent boron atoms have a plane threefold-coordinated bond structure similar to that of B_2O_3. The third boron atom has a tetrahedral, fourfold-coordinated bond structure. There are five inequivalent oxygens. The crystal structure represents a boron-oxygen framework containing lithium atoms in open voids.[7] The LBO transmission band extends from 159 to 3500 nm.[8]

We detected earlier[9] UV luminescence of LBO crystals, which can be excited by both x-ray photons and an electron beam with an energy $E_e=0.15$ MeV. Subsequent investigation revealed some features, in particular, a complex luminescence-band profile, and participation of the main point defects in its excitation by recombination, which is to be contrasted with the absence of a clearly pronounced relation with the existence in the LBO lattice of any activator.[10,11] This gave grounds for the conjecture of the

LBO luminescence being of intrinsic origin.[12] Proving this would require, however, a comprehensive study of the excitation and photoluminescence of LBO, as well as of the LWAE.

This work was aimed at a study of the excitation and photoluminescence spectra of nominally pure LiB_3O_5 crystals within broad spectral and temperature regions, complemented by optical spectroscopy of LBO at the LWAE.

1. EXPERIMENTAL TECHNIQUES

LiB_3O_5 crystals were grown by crystallization from a Li_2O—B_2O_3—MoO_3 melt with the seed in the upper position. The starting materials of OSCh grade, up to 400 cm^3 in volume, were placed in a platinum crucible, so that the content of LiB_3O_5 in the system was 30–35 wt%. After homogenization and a pause at 850–900 °C, the melt was cooled down to the saturation temperature, and the seed crystal was brought in contact with the surface. The single crystals were grown with [010] orientation at a cooling rate of 0.1–0.2 K/h. A typical LBO crystal grown for 15–20 days varied from 70 to 120 g in weight.

We used a set of 10 nominally pure LBO crystals of optical quality in the form of polished plane-parallel plates measuring $10\times10\times1.5$ mm, with the plane perpendicular to the *X* or *Z* crystallographic axes. For brevity, they are denoted by LBO$\perp$ **X** and LBO$\perp$ **Z**, respectively.

The luminescence measurements were performed on an experimental setup including a VMR-2 vacuum monochromator with a 600-l/mm spherical grating, a high collecting-power MDR-2 monochromator with a 1200-l/mm grating, FÉU-106 and FÉU-142 PM tubes operating in the photon counting mode, a VMF-25 hydrogen lamp as a source of VUV light, an evacuated optical chamber with a LiF window provided with a low-inertia cryostat having interchangeable units for operation within a broad temperature range from 8 to 600 K, and an oil-free pumping system. The luminescence emitted in studies of excitation spectra was passed through a UFS-2 filter. The x-ray luminescence was excited with a BSV-2 tube ($U_a=30$ kV, $I_a=10$ mA, Cu anticathode). The output formatted in the CAMAC standard was interfaced to a computer providing control of the various assemblies and data acquisition and processing.

2. RESULTS OF EXPERIMENT

Measurements of LBO optical-absorption (OA) spectra showed the monotonic exponential growth of optical absorption in unirradiated crystals to start above 7.5 eV (Fig. 1), with no OA bands observed within the LBO transmission region. It was found that the real position of LWAE depends both on temperature and on the crystallographic orientation of the sample. For instance, the LWAE position in all LBO$\perp$ **Z** crystals was shifted by about 150 meV toward shorter wavelengths compared to that for LBO$\perp$ **X** crystals (Fig. 1). A change in crystal temperature from room temperature to 80 K shifts the LWAE toward shorter wavelengths in all cases by about 100 meV (Fig. 1). Irradiation of LBO by a 150-keV electron beam creates lattice defects of several types. Low-temperature defects responsible for optical absorption in the transmission region of the crystal were studied in Ref. 13. Our study reports on detection of high-temperature LBO lattice defects, which persist above 650 K and manifest themselves in OA spectra close to the LWAE (Fig. 2). The nature of the high-temperature defects remains unclear. For our present work it is essential that no photoluminescence is observed under optical excitation within the OA band of either low- or high-temperature LBO defects.

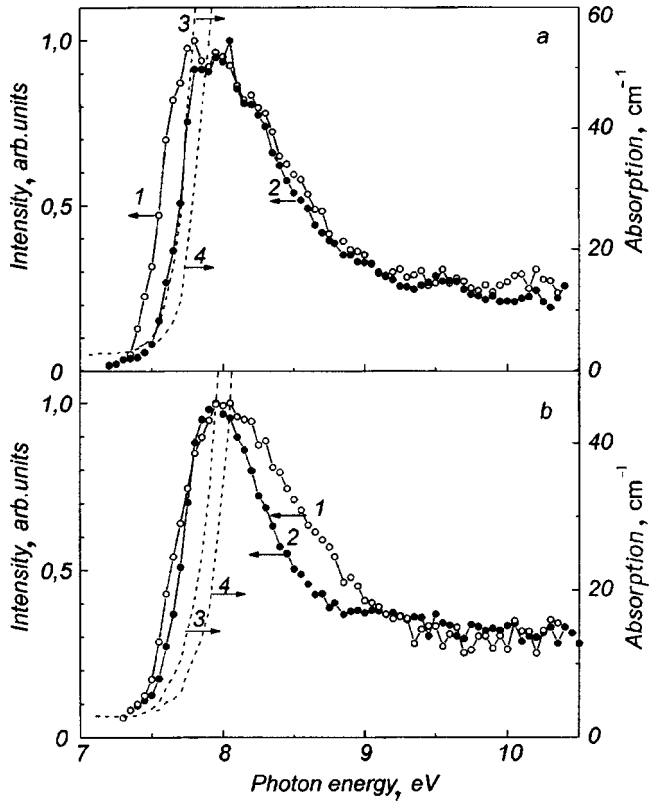

FIG. 1. Excitation spectra of (*1*,*2*) luminescence and (*3*,*4*) optical absorption of (a) LBO$\perp$ **X** sample and (b) LBO$\perp$ **Z** sample obtained at (*1*,*3*) 290 K and (*2*,*4*) 80 K.

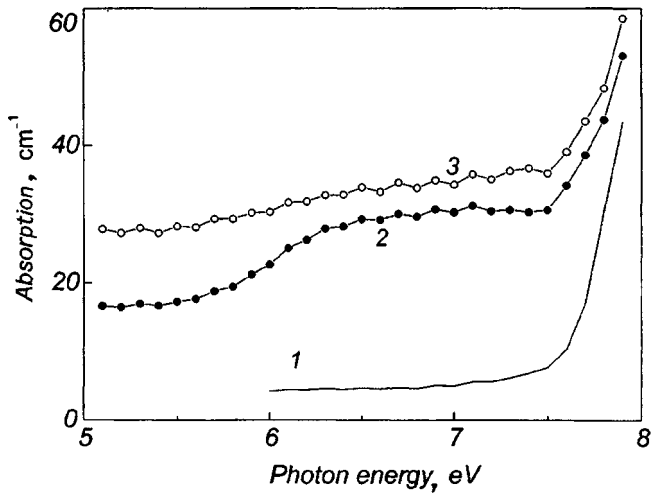

FIG. 2. Optical absorption spectra of LBO obtained at 300 K: *1* — before irradiation, *2* — after irradiation by a 150-keV electron beam, *3* — after annealing the irradiated sample in air at 650 K.

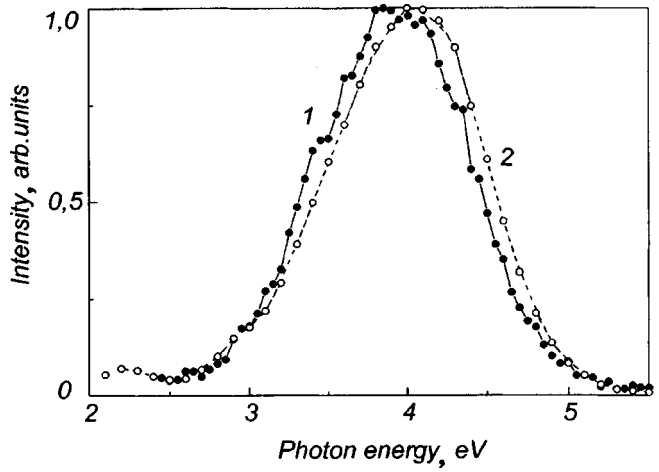

FIG. 3. Luminescence spectra of LBO obtained at 290 K under excitation with (*1*) photons with energy $E_{ex}=7.7$ eV and (*2*) x-ray photons.

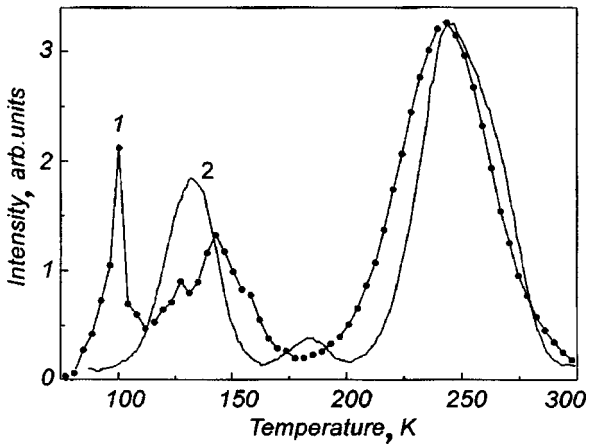

FIG. 4. (*1*) Luminescence of an unirradiated sample heated in vacuum at a rate of 5 K/s and (*2*) thermostimulated luminescence of LBO irradiated by x-rays at 77 K.

By contrast, excitation of unirradiated LBO by photons with energies above 7.5 eV gives rise to the appearance of broad-band photoluminescence (PL) within the 2.5–4.5-eV region (Fig. 3). The excitation spectrum of this luminescence is a strong band peaking near 7.9–8.0 eV. The long-wavelength edge of the excitation spectrum rises steeply in the 7.5–8.0-eV region to its maximum, followed by a smooth falloff to a constant level of 20–25% of the maximum value, to remain afterwards practically unchanged within the 9.5–10.5-eV spectral interval (Fig. 1). As seen from Fig. 1, the profile of the excitation band depends both on temperature and on the crystallographic orientation of the sample. For instance, at 80 K the excitation-band profiles measured for LBO$\perp$ **X** and LBO$\perp$ **Z** crystals coincide fairly well to form a band peaking at 8.0 eV with a FWHM of about 0.8 eV, whereas at 290 K they are noticeably broader. Also, in LBO$\perp$ **Z** crystals the broadening by about 200 meV occurs at the short-wavelength falloff of the excitation band with its long-wavelength decay remaining practically unchanged, while the situation in LBO$\perp$ **X** crystals is different, namely, a similar broadening of the excitation band takes place only at the long-wavelength decline (Fig. 1).

Most of the PL spectrum is confined to a Gaussian-shaped band with a FWHM of 1.2 eV peaking at 4.0 eV (Fig. 3). The LBO luminescence band has the same shape when excited at different points within the 7.7–10.5-eV spectral region. Figure 3 shows also an x-ray-excited LBO luminescence spectrum, which is seen to be close in shape to the PL spectrum.

It should be pointed out that the luminescence spectrum contains features in the form of weak shoulders superimposed on the main band profile (Fig. 3). These features vary in intensity and position from one sample to another, depend on the temperature regime used and other experimental conditions. For example, cooling to 77 K gives rise to a noticeable luminescence in the 2.5–4.5-eV region, which appears without any external irradiation and coincides in its main characteristics with the PL spectrum. Following a few hours' maintenance in vacuum in the dark, the spontaneous luminescence in LBO dies out completely. Note that heating an unirradiated sample within the 80–200 K interval at a rate faster than 5 K/s likewise initiates spontaneous emission, whose intensity depends on the heating rate and can become higher than that of the PL by one to two orders of magnitude. No such luminescence was observed to occur above 200 K. Interestingly, in unirradiated samples this results in generation of carriers, their localization at higher-temperature trapping centers, and subsequent thermally stimulated luminescence (TSL) near the well-known TSL peak at 240 K (Fig. 4). Such thermally induced light flashes are characteristic of many pyroelectric crystals, in particular, of lithium tetraborate.[6] Investigation of the nature of this luminescence would require an independent study involving an analysis of lattice dynamics. We shall focus out attention here on the main part of the PL spectrum, which is not affected by the above nonisothermal phenomena.

To remove these effects in measurements of the temperature dependence of the PL, we used heating and cooling rates below 0.05 K/s. PL spectra measured at 8 and 80 K coincide in shape with that obtained at room temperature (Fig. 3). The PL intensity measured at 77 K exceeds typically that taken at room temperature two times. Figure 5 displays the temperature dependence of the PL intensity in the 8–400 K range, which follows Mott's law with $E_a=290$ meV and $\omega=2.4\times10^5$ s^{-1}. The luminescence is thermally quenched above 240 K. With allowance made for the temperature-induced shift of the PL excitation band, the temperature dependence of PL was found to be the same for different energies of exciting photons.

The temperature dependence of the x-ray induced luminescence follows a somewhat different pattern. It does not typically exhibit thermally induced light emission. Above 240 K, it undergoes temperature quenching coinciding with that for the PL, whereas when cooled from 240 to 80 K, the PL intensity drops 20–25 times (Fig. 5). The reason for this lies in carrier localization at the electronic, B^{2+}, and hole, O^-, trapping centers having characteristic carrier delocalization temperatures of 130 and 240 K, respectively.

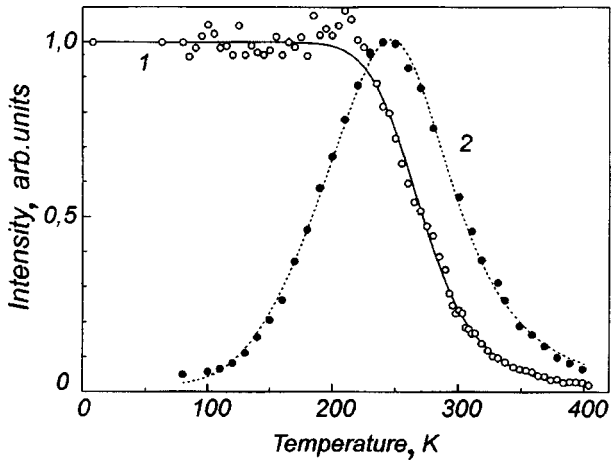

FIG. 5. Temperature dependences of (*1*) photoluminescence of unirradiated LBO samples at $E_{ex}=7.7$ eV and (*2*) x-ray luminescence. Points - experimental data, lines - assumed theoretical relations.

3. DISCUSSION OF RESULTS

The experimental data obtained reveal primarily a large, as high as 4 eV, Stokes shift of LBO photoluminescence and a correlation between the sharp increase of the crystal optical density for photon energies in excess of 7.5 eV and the profile of the long-wavelength edge of the PL excitation spectrum (Fig. 1). The increase in OA above the 7.5-eV photon energy should be assigned to fundamental absorption in LBO. Indeed, despite the fact that the exact value of E_g for LBO is still a subject of controversy, both experimental and theoretical estimates of E_g from the absorption edge yield values from 7.75 to 7.80 eV.[8,14,15] At the same time LBO band-structure calculations suggest $E_g=7.37$ eV in the Γ-Γ direction.[16] This is not contradicted by LBO reflectance-spectrum studies done for the 6–12-eV region and by the corresponding calculations[17,18], by which the energy of the $4a_2$ orbital assigned to the lower conduction band is 7.3 eV.

In this connection, experimental data (Fig. 1) permit a conclusion that the longest-wavelength fundamental-absorption peak of LBO crystals lies above 7.7 or 7.9 eV, depending on the sample crystallographic orientation. This is in full agreement with the value of 7.78 eV obtained earlier[8] for nonoriented LBO samples and accepted as an estimate of E_g. It should be pointed out that optical absorption of LBO grows steeply in the immediate vicinity of the gap edge, which differs essentially from the situation observed in other borates (BBO, CBO), where interband transitions at the extremal points are forbidden by symmetry considerations and fundamental optical absorption becomes observable at energies slightly in excess of E_g.[8] A more careful analysis of the fundamental-absorption edge at different temperatures (Fig. 1) indicates that it can be fitted well by a Lorentzian. The optical density at the maximum of this absorption band can be approximately estimated as 10^4 cm^{-1}, which is a fairly large value. Such properties can imply the presence at the LBO absorption edge of exciton-like electronic excitations, which probably overlap with interband transitions.

At the same time, in contrast to alkali-halide crystals and some binary oxides [for instance, BeO (Ref. 19)], the investigation of the LBO near the liquid-helium temperature performed in this work did not reveal any luminescence near the absorption edge that could be assigned to these states. Such pattern is typical of some simple oxides (for example, MgO and Al_2O_3) and can be realized apparently in BBO (Ref. 5) and $Li_2B_4O_7$ (Ref. 20). This interpretation is supported by the shape of the LBO luminescence excitation spectrum in the fundamental absorption region of the crystal, which is typical of crystals producing excitonic-like luminescence, as well as by its characteristic temperature dependence, the large emission band width, and a considerable Stokes shift. In this connection, LBO luminescence can be associated with radiative annihilation of relaxed exciton-like electronic excitations, as is the case with BBO (Ref. 5) and $Li_2B_4O_7$ (Ref. 20), or with the emission of relaxed excitons localized at small-scale structural distortions[21]. Additional arguments could come from studies of the electronic structure of LBO and simulation of the optical characteristics of borates.

The numerous LBO band-structure[8,14,16,22] and cluster[15] calculations, as well as XPS data obtained for this crystal[8,23] indicate unambiguously that the valence-band structure of LBO derives primarily from anionic states. Boron ions contribute comparatively little to the valence- and conduction-band states, whereas lithium-ion states do not participate in the electronic structure of the LBO valence band at all. In this connection, the electronic states of LBO are dominated by localized boron-oxygen bonds. The calculations suggest also that the LBO bands have a small dispersion in K space and that the valence band, in particular, has minigaps throughout the wave-vector variation range. As a result, the carrier effective mass is fairly large and is estimated as 0.73, 0.89, and 0.69 m_e for the conduction-band directions Γ-X, Γ-S, and Γ-Z, respectively.[16]

An analysis of possible electronic transitions from the upper valence to the lower conduction band showed them to be dominated by the electronic structure of the boron-oxygen groups, and this situation is typical of the LBO, CBO, and BBO crystals. A recent LAPW band-structure calculation[22] made for all crystals in this group showed their valence-band top to derive primarily from the oxygen orbitals, with boron ions contributing practically nothing. Note that the lowest-energy electronic transition in LBO occurs to the states evolving from the trigonally hybridized orbitals of the boron and oxygen ions forming the bottom of the conduction band. By contrast, in the other borates (CBO and BBO) the conduction-band bottom derives from the cation states, and transitions from valence-band states due to oxygen ions to purely cationic states at the conduction band-bottom have a comparatively low probability. Stronger transitions are seen at about 1 eV above the absorption edge, where mixed boron-oxygen orbitals of the CBO and BBO crystals become involved in formation of the final state of the interband transition.

Taking into account all the above-mentioned considerations, namely, that the excitation spectrum lies within the fundamental absorption region and is characterized by a higher efficiency at the long-wavelength edge, thermal stimulation of recombination processes, and the temperature dependences of x-ray and photoluminescence, one may con-

clude that the LBO luminescence is an intrinsic process originating from radiative annihilation of relaxed exciton-like electronic excitations, which can form either directly or in recombination involving the main lattice defects.

Thus the present studies of the photoluminescence and photoexcitation of LBO crystals give us grounds to associate the broad-band photoluminescence peaking at 3.75–3.8 eV with the intrinsic luminescence of LBO, which originates from radiative annihilation of relaxed exciton-like electronic excitations. Viewed from the standpoint of possible applications, this luminescence can be used in nondestructive testing of optical components made of LBO and subject to heavy laser-radiation loads.

O. I. N. and K. A. V. owe their thanks to Ch. B. Lushchik for performing some measurements at helium temperatures and for critical comments on some aspects of the work.

Support of the INCO-COPERNICUS program (Grant IC15-CT96-0721) is gratefully acknowledged.

[1] Ch. B. Lushchik and A. Ch. Lushchik, *Decay of Electronic Excitations with Formation of Defects in Solids* [In Russian] (Nauka, Moscow, 1989), 264 pp.
[2] I. N. Ogorodnikov, V. Yu. Ivanov, and A. V. Kruzhalov, Fiz. Tverd. Tela (St. Petersburg) **36**, 3287 (1994) [Phys. Solid State **36**, 1748 (1994)].
[3] A. I. Kuznetsov, V. N. Abramov, V. V. Myurk, and B. R. Namozov, Fiz. Tverd. Tela (Leningrad) **33**, 2000 (1991) [Sov. Phys. Solid State **33**, 1126 (1991)].
[4] V. Mürk and N. Yaroshevich, J. Phys.: Condens. Matter **7**, 5857 (1995).
[5] V. Kisand, R. Kink, M. Kink, J. Maksimov, M. Kirm, and I. Martinson, Physica Scripta **54**, 542 (1996).
[6] O. T. Antonyak, Ya. V. Burak, I. T. Lyseĭko, N. S. Pidzyraĭlo, and Z. A. Khapko, Opt. Spektrosk. **61**, 550 (1986) [Opt. Spectrosc. **61**, 345 (1986)].
[7] S. F. Radaev, N. I. Sorokin, and V. I. Simonov, Fiz. Tverd. Tela (Leningrad) **33**, 3597 (1991) [Sov. Phys. Solid State **33**, 2024 (1991)].
[8] R. H. French, J. W. Ling, F. S. Ohuchi, and C. T. Chen, Phys. Rev. B **44**, 8496 (1991).
[9] I. N. Ogorodnikov, V. Yu. Ivanov, A. Yu. Kuznetsov, A. V. Kruzhalov, V. A. Maslov, and L. A. Ol'khovaya, Pis'ma Zh. Tekh. Fiz. **19**, No. 2, 14 (1993) [Tech. Phys. Lett. **19**, 42 (1993)].
[10] I. N. Ogorodnikov, A. Yu. Kuznetsov, A. V. Kruzhalov, and V. A. Maslov, Radiat. Meas. **24**, 423 (1995).
[11] I. N. Ogorodnikov, A. V. Porotnikov, V. A. Pustovarov, and A. V. Kruzhalov, J. Lumin. **72-74**, 703 (1997).
[12] I. N. Ogorodnikov, V. A. Pustovarov, A. V. Porotnikov, and A. V. Kruzhalov, Nucl. Instrum. Methods Phys. Res. A **404**, 339 (1995).
[13] I. N. Ogorodnikov, A. V. Porotnikov, S. V. Kudyakov, A. V. Kruzhalov, and V. Yu. Yakovlev, Fiz. Tverd. Tela (St. Petersburg) **39**, 1535 (1997) [Phys. Solid State **39**, 1366 (1997)].
[14] W. Y. Hsu and R. V. Kasowski, J. Appl. Phys. **73**, 4101 (1993).
[15] A. B. Sobolev, A. Yu. Kuznetsov, I. N. Ogorodnikov, and A. V. Kruzhalov, Fiz. Tverd. Tela (St. Petersburg) **36**, 1517 (1994) [Phys. Solid State **36**, 829 (1994)].
[16] Y.-N. Xu and W. Y. Ching, Phys. Rev. B **41**, 5471 (1990).
[17] T.-J. Chen, R. N. Zitter, R. Tao, W. R. Hunter, and J. C. Rife, Phys. Rev. B **52**, 13703 (1995).
[18] T.-J. Chen, R. Tao, J. C. Rife, and W. R. Hunter, J. Opt. Soc. Am. B **15**, 47 (1998).
[19] I. N. Ogorodnikov and A. V. Kruzhalov, J. Lumin. **72-74**, 701 (1997).
[20] V. N. Kolobanov, J. Becker, S. Downs, B. I. Zadneprovskiĭ, I. A. Kamenskikh, A. Karl, V. V. Mikhaĭlin, V. A. Nefedov, M. Runne, D. Tikhan, I. N. Shpin'kov, and H. Zimmerer, in *Abstracts, 1st All-Russia Symposium on SSD* (Ekaterinburg, 1997), p. 94.
[21] D. Visser, G. C. Verschoor, and D. J. W. Jido, Acta Crystallogr., Sect. B: Struct. Crystallogr. Cryst. Chem. **36**, 28 (1980).
[22] J. Li, C.-g. Duan, Z.-q. Gu, and D.-s. Wang, Phys. Rev. B **57**, 6925 (1998).
[23] A. Yu. Kuznetsov, M. V. Kuznetsov, I. N. Ogorodnikov, A. V. Kruzhalov, and V. A. Maslov, Fiz. Tverd. Tela (St. Petersburg) **36**, 845 (1994) [Phys. Solid State **36**, 465 (1994)].

Translated by G. Skrebtsov

Luminescence-spectral properties and structure of optical centers in Eu- and Ce–Eu-containing quartz gel-glasses

G. E. Malashkevich

Institute of Molecular and Atomic Physics, Belarus Academy of Sciences, 220072 Minsk, Belarus

A. G. Makhanek[†)]

Institute of Physics, Belarus Academy of Sciences, 220072 Minsk, Belarus

A. V. Semchenko, V. E. Gaĭshun, I. M. Mel'nichenko, and E. N. Poddenezhnyĭ

F. Skorina Gomel' State University, 246699 Gomel', Belarus
(Submitted June 17, 1998)
Fiz. Tverd. Tela (St. Petersburg) **41**, 229–234 (February 1999)

Eu- and Ce–Eu-containing quartz glasses obtained by a direct sol–gel-glass transition are investigated. It is discovered that the conversion of a xerogel into a glass leads to lowering of the symmetry of the Eu^{3+} optical centers from hexagonal to orthorhombic and a many-fold increase in the efficiency of the excitation of their luminescence through the charge-transfer band. In the co-activated glasses, the distortion of these centers is enhanced, and compound Ce^{4+}-Eu^{3+} centers appear, in which the Eu(III) oxo complexes are characterized by cubic symmetry and by sensitization of the luminescence of the Eu^{3+} ions by photoreduced $(Ce^{4+})^{-}$ ions. Crystal-field theory shows that the coordination number of the cation in such oxo complexes is equal to 8. It is established that similar structural formations exist in annealed xerogels, but they are manifested spectroscopically only upon low-temperature shortening of the interatomic distances, as a result of which the sensitization indicated becomes possible.
 [S1063-7834(99)00902-8]

It was shown in Ref. 1 that the co-activation of Sm-containing quartz gel-glasses by cerium produces compound centers, whose luminescence-spectral characteristics differ radically from those of the centers in the monoactivated glass and which include Sm^{3+} and Ce^{4+} ions joined by an oxygen bridge. The Sm^{3+} ions in such centers are characterized on average by a local environment of higher symmetry and effective sensitization of their luminescence by photoreduced $(Ce^{4+})^{-}$ ions. A significant influence of cerium on the structure of neodymium optical centers was also discovered in similar glasses.[2] These findings prompted a more thorough investigation of the influence of cerium on the structure and properties of compound optical centers in lanthanides of similar matrices.

In the present work we made an attempt to obtain new data on the structure of such compound centers in quartz gel-glasses by employing Eu^{3+} ions as a spectroscopic probe, in which the position of the energy levels of the $4f$ configuration and the intensity of whose intraconfiguration transitions can be calculated unequivocally using the methods of crystal-field theory. A parallel attempt was made to ascertain the most efficient channels for excitation of the luminescence of these ions in cerium-monoactivated and co-activated glasses.

I. THEORY

As is generally known, in calculations of the matrix elements of the potential energy V of the $4f$ subshell of lanthanide ions in a ligand field, it is convenient to expand it into a series in irreducible tensor operators:[3,4]

$$V=\sum_{t,p} B_{tp}D_p^t, \tag{1}$$

where

$$B_{tp}=\sum_j \frac{z_j e^2}{R_j^{t+1}} C_p^t(\Theta_j\Phi_j), \tag{2}$$

$$D_p^t=\sum_i r_i^t C_p^t(\vartheta_i\varphi_i), \quad C_p^t=\left(\frac{4\pi}{2t+1}\right)^{1/2} Y_p^t; \tag{3}$$

$z_j e$ is the charge of the jth ligand with the spherical coordinates R_j, Θ_j, and Φ_j; r_i, ϑ_i, and φ_i are the spherical coordinates of the ith electron in the unfilled $4f$ subshell; and Y_p^t is a spherical function. If we regard the $B_{tp}\overline{r^t}$ (where $\overline{r^t}=\int_0^\infty r^t R^2(r) r^2\,dr$) as parameters which describe the relative energetic positions of the individual f orbitals and are subject to experimental determination, such a semiempirical crystal-field theory permits successful interpretation of the splitting of the energy levels and intensities of the lines in the spectra of lanthanides caused by transitions between sublevels of the $4f$ subshell. The relative intensities of the individual components corresponding to transitions from the $^5D_0$ state of Eu^{3+} to the ^7F_j state are described by the formula

$$I_{\mathrm{rel}}(JM)\sim\left[\sum_{t,p} B_{tp}\begin{pmatrix}1 & t & J\\ q & p & M\end{pmatrix}\right]^2, \qquad (4)$$

where $q=0$ for the π component and ± 1 for the σ component of the electric-dipole transition, and t takes the values 1, 3, 5, and 7. In this equation, the odd crystal-field parameters B_{tp} are related to the parameters A_{tp} in the expansion of the potential in operator equivalents in Stevens formalism[5] by the expression $B_{tp}=\tau_{tp}A_{tp}$, for which the values of the coefficients τ_{tp} can be found in Ref. 3. In particular, the values of τ_{40} and τ_{60} for the fourth- and sixth-order parameters are equal to 8 and 16, respectively.

II. MATERIALS AND EXPERIMENTAL METHOD

The glasses were synthesized according to a known modification of the sol-gel method, which provides bulk samples of fairly high optical quality.[6] The samples were activated by impregnating the porous xerogels with water-ethanol solutions of the chloride salts of the respective lanthanides with various concentrations C. All the reagents were of grades no poorer than ''chemically pure.'' Before the measurements, the xerogels were annealed in air for 1 h at a temperature preceding the onset of the pore-closing process ($T=1100\,^\circ$C). The glass transition was effected in air at $T=1200\,^\circ$C for 2 h followed by unaccelerated cooling. When it was necessary to alter the charge state of the activators, the glasses were subjected to annealing in a hydrogen atmosphere at $T=900\,^\circ$C for 3 h.

A Beckman UV5270 spectrophotometer was used to analyze the extinction spectra. An unactivated quartz gel-glass of identical thickness as the sample being measured was placed in the reference channel. The luminescence and luminescence excitation spectra were recorded on an SDL-2 spectrofluorometer and were corrected[7] and represented in the form of plots of the wavelength dependence of the number of photons in a unit wavelength range $dn/d\lambda$. For the purpose of improving the resolution of individual components, the luminescence spectra were recorded with cooling of the samples to 77 K. To minimize luminescence quenching, samples with a thickness which ensures an optical density less than 0.2 were used to record the luminescence excitation spectra.

III. RESULTS

Figure 1 slows the attenuation spectra of Eu- and Ce–Eu-containing quartz gel-glasses in the visible and ultraviolet regions. It can be seen that the spectrum of the monoactivated glass with $C_{\mathrm{EuCl_3}}$ [wt %] displays weak narrow bands at 395 (the $^7F_0\rightarrow{}^5L_6$ transition of Eu^{3+} ions), 460 (the $^7F_0\rightarrow{}^5D_2$ transition), and 530 nm (the $^7F_0\rightarrow{}^5D_1$ transition) and a broad intense band at 230 nm (curve *1*). Thermal treatment of this glass in hydrogen leads to appreciable weakening of the broad band and the appearance of a ''shoulder'' at 300 nm, whose long-wavelength ''wing'' stretches to 450 nm (curve *2*). The spectrum of the co-activated glass with $2C_{\mathrm{CeCl_3}}=C_{\mathrm{EuCl_3}}=1$ wt % is distinguished from the spectrum of the monoactivated glass by reduction of the relative intensity of the band at 395 nm and the presence of an intense broad band at 250 nm (curve *3*). As a result of the thermal treatment of this glass in hydrogen, this band is transformed into a relatively weak band at 320 nm, and the short-wavelength band observed for the monoactivated glass becomes noticeable (curve *4*).

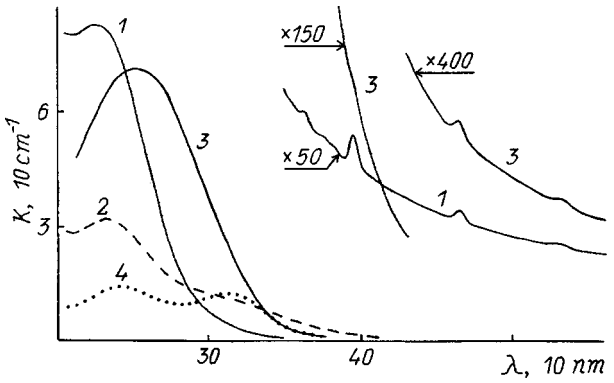

FIG. 1. Attenuation spectra of Eu- and Ce–Eu-containing quartz gel-glasses. $C_{\mathrm{CeCl_3}}$ (wt. %): 0 (*1, 2*); 0.5 (*3, 4*). $C_{\mathrm{EuCl_3}}$ (wt. %): 1 (*3, 4*); 3 (*1, 2*). *2, 4* — samples annealed in hydrogen. $T=298$ K.

Figure 2 shows the luminescence and luminescence excitation spectra of the Eu-containing xerogel and quartz gel-glass with $C_{\mathrm{EuCl_3}}=3$ wt %. It is seen that the luminescence spectrum of the xerogel with excitation at the wavelength $\lambda_{\mathrm{exc}}=395$ nm (curve *1*) consists of a series of poorly resolved narrow bands, the most intense of which lies at 615 nm (the $^5D_0\rightarrow{}^7F_2$ transition). When $\lambda_{\mathrm{exc}}=320$ nm, the narrow-band luminescence spectrum of the xerogel changes only slightly (for this reason it is not shown in Fig. 2), but a poorly resolved, intense broad band appears at 380 nm (curve *2*). The luminescence excitation spectrum of the xerogel recorded at $\lambda_{\mathrm{rec}}=615$ nm consists of narrow bands, which correspond to $f-f$ transitions of the Eu^{3+} ions, and a broad band at 270 nm (curve *3*). The luminescence spectrum

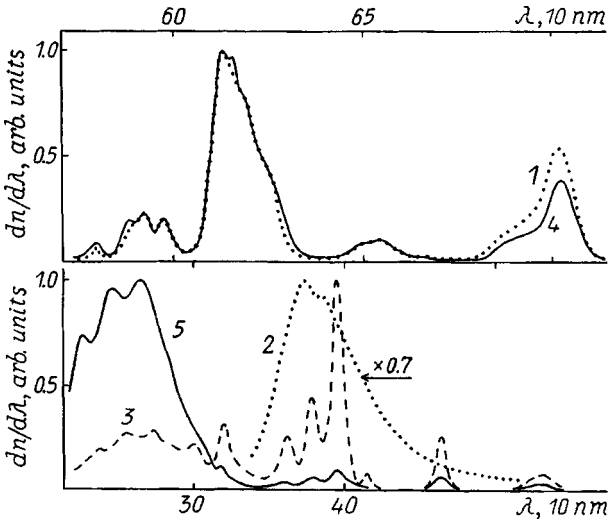

FIG. 2. Luminescence and luminescence excitation spectra of a Eu-containing xerogel (*1–3*) and quartz gel-glass (*4, 5*). $C_{\mathrm{EuCl_3}}=3$ wt %. λ_{exc} (nm): 320 (*2*), 395 (*1, 4*). $\lambda_{\mathrm{rec}}=615$ nm (*3, 5*). The intensity of band *2* is given relative to the band at 615 nm. T (K): 77 (*1, 2, 4*); 298 (*3, 5*).

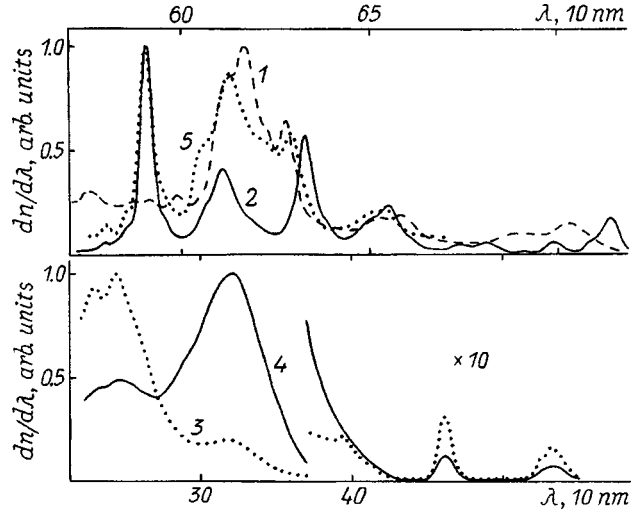

FIG. 3. Luminescence and luminescence excitation spectra of a Ce–Eu-containing quartz gel-glass (*1–4*) and xerogel (*5*). $2C_{CeCl_3}=C_{EuCl_3}=1$ wt %. λ_{exc} (nm): 320 (*2, 5*); 395 (*1*). λ_{rec} (nm): 591 (*4*); 615 (*3*). T (K): 77 (*1, 2, 5*); 298 (*3, 4*).

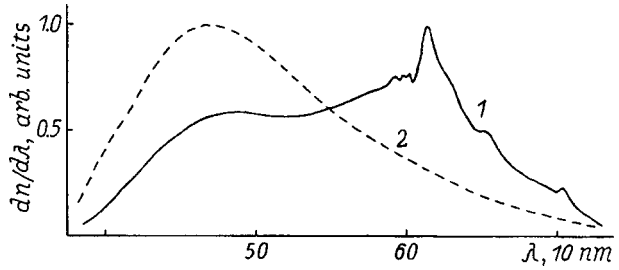

FIG. 4. Luminescence spectra of Eu- and Ce–Eu-containing quartz gel-glasses annealed in hydrogen. C_{CeCl_3} (wt. %): 0 (*1*); 0.5 (*2*). C_{EuCl_3} (wt. %): 1 (*2*); 3 (*1*). $\lambda_{exc}=320$ nm. $T=298$ K.

of the glass with $\lambda_{exc}=395$ nm (curve *4*) exhibits weakening of the relative intensity of the $^5D_0\rightarrow{}^7F_4$ band ($\lambda\sim700$ nm) and slight enhancement of the splitting of the bands assigned to $^5D_0\rightarrow{}^7F_1$ ($\lambda\sim590$ nm) and $^5D_0\rightarrow{}^7F_2$. The displacement of λ_{exc} toward shorter wavelengths is weakly manifested on the narrow-band spectrum and is accompanied by the appearance of ultraviolet luminescence, which is far less intense than for the xerogel. The luminescence excitation spectrum of the glass at $\lambda_{rec}=615$ nm (curve *5*) is distinguished from the analogous spectrum of the xerogel by an appreciable blue shift and a considerably greater relative intensity of the band at 270 nm, as well as roughly identical intensities for the $^7F_0\rightarrow{}^5L_6$ and $^7F_0\rightarrow{}^5D_2$ bands. Scanning λ_{rec} over the $^5D_0\rightarrow{}^7F_j$ bands leads to slight redistribution of the intensity in this spectrum. When C_{EuCl_3} is diminished to 0.3 wt %, no fundamental changes occur in the spectra considered.

Figure 3 shows the luminescence and luminescence excitation spectra of the Cu–Eu-containing quartz gel-glass and xerogel with $2C_{CeCl_3}=C_{EuCl_3}=1$ wt %. The narrow-band luminescence spectrum of the co-activated glass with $\lambda_{exc}=395$ nm (curve *1*) is distinguished from the corresponding spectrum of the monoactivated glass considered above by significant weakening of the $^5D_0\rightarrow{}^7F_1$ and $^5D_0\rightarrow{}^7F_4$ bands and enhancement of the splitting of the $^5D_0\rightarrow{}^7F_2$ band. The displacement of λ_{exc} toward shorter wavelengths leads to radical alteration of this spectrum. In particular, when $\lambda_{exc}=320$ nm (curve *2*), we observe many-fold enhancement of the $^5D_0\rightarrow{}^7F_1$ band and strong splitting of the $^5D_0\rightarrow{}^7F_2$ band into two components of comparable intensity, the $^5D_0\rightarrow{}^7F_0$ band ($\lambda\sim580$ nm) being almost completely absent. It is noteworthy that the relative intensity of the $^5D_0\rightarrow{}^7F_1$ band decreases by a factor of almost 2 when T is raised from 77 to 298 K. When λ_{exc} is scanned in the range 300–380 nm, the general form of the narrow-band spectrum is preserved, but the ratio between the relative intensities of the transitions to the ^7F_j states and the number of splitting components of the $^5D_0\rightarrow{}^7F_2$ band vary. We note, however, that the additional components appearing as λ_{exc} is varied have significantly smaller intensities than the principal components. When $\lambda_{exc}<280$ nm, the narrow-band luminescence spectrum begins to approximate the spectrum obtained for $\lambda_{exc}=395$ nm. When $\lambda_{rec}=615$ nm, the luminescence excitation spectrum of the glass (curve *3*) mimics the spectrum depicted in Fig. 2 by curve *5*, but when $\lambda_{rec}=591$ nm, an intense broad band with a maximum at 320 nm appears (curve *4*). The narrow-band luminescence spectrum of the co-activated xerogel recorded with $\lambda_{exc}=320$ nm at $T=298$ K differs somewhat from the analogous spectrum of the Eu-containing xerogel, but at $T=77$ K (curve *5*) it begins to approximate curve *2*.

Figure 4 shows the luminescence spectra of Eu- and Ce–Eu-containing glasses annealed in hydrogen. It can be seen that the spectrum for the monoactivated glass displays additional broad overlapping bands at 480 and 600 nm when $\lambda_{exc}=320$ nm (curve *1*). In this case the main features of the narrow-band spectrum are similar to those observed before annealing. The variation of λ_{exc} in the range 300–400 nm is accompanied by redistribution of the intensity and weak displacement of the broad bands, but it is scarcely reflected in the relative intensities and the spectral positions of the narrow bands. The narrow-band luminescence of the Eu^{3+} ions is not detected at all in the spectrum of the co-activated glass at $\lambda_{exc}=320$ nm, and only a broad band at 470 nm is observed (curve *2*).

IV. DISCUSSION

The narrow-band excitation spectra shown in Fig. 1 are typical of the $f-f$ transitions of Eu^{3+} ions. The monotonic increase in k with decreasing λ on curve *1* is associated with light scattering due to the microscopic inhomogeneity of the glass caused by the incompatibility of the highly coordinated europium-oxygen polyhedrons with the SiO_2 structural framework, and the intense band at 230 nm is most probably caused by absorption in the band assigned to charge transfer (CT) from the ligands to Eu^{3+} ions. The decrease in the intensity of this band with simultaneous broadening and the appearance of a ''shoulder'' at 300 nm as a result of the annealing of the Eu-containing glass in hydrogen (curve *2*) can be associated with the formation of stable Eu^{2+} ions in the glass. As has been reported,[8] the absorption spectra of the

latter in fused quartz glass are characterized by the presence of two broad bands at 250 and 300 nm. The appearance of the intense band at 250 nm in the spectrum of the co-activated glass (curve *3*) is caused by charge transfer from the ligands to Ce^{4+} ions.[6] The transformation of this band for the analogous glass annealed in hydrogen into a weak band at 320 nm (curve *4*) is associated with a decrease in the concentration of tetravalent cerium as a result of its reduction to trivalent cerium, which absorbs at that wavelength.[6]

Using the approach described in the theoretical part and the narrow-band luminescence spectrum of the monoactivated xerogel shown in Fig. 2 (curve *1*), we can easily show that its optical centers are characterized by a hexagonal structure, which most probably has C_{3h} or D_{3h} symmetry. The transformation of this spectrum into curve *4* upon conversion of the xerogel into a glass attests to the appearance of an appreciable rhombic (C_{2v}) distortion. In view of the weak dependence of the luminescence and luminescence excitation spectra on λ_{exc} and λ_{rec}, the fraction of other types of centers is small. On the basis of the results in Ref. 9, the intense broad luminescence band of the activated xerogel at 380 nm (curve *2*) can be assigned to CT complexes formed between the ligands (oxygen atoms and hydroxyl ions) and the activator. The dramatic weakening of this band upon conversion to the glass and the many-fold enhancement of the band at 260 nm in the excitation spectrum of its narrow-band luminescence (compare curves *5* and *3*) attest to an increase in the efficiency of energy transfer from the excited CT state to Eu^{3+} ions. In addition, the blue shift (by roughly 1500 cm^{-1}) of the position of the CT absorption band in the glass points to a decrease in the polarization of oxygen by europium.[4] Evidently, in such a case the rate of emission from the excited CT state begins to fall below the rate of return of an electron to the ligand from the ground state of the rare-earth ion, causing more efficient excitation of the latter. The quantum efficiency of such intracenter sensitization of the luminescence can be determined by comparing the intensities in the absorption and excitation spectra of the narrow-band luminescence according to the formula

$$\eta=(k_{ff}dn_{ct}/d\lambda)/(k_{ct}dn_{ff}/d\lambda), \tag{5}$$

where the subscripts ff and ct indicate that the values of the parameters being determined are taken at values of λ corresponding to $f-f$ transitions and the CT band, respectively. Using curve *5* and the spectrum obtained by subtracting the extrapolated light-scattering spectrum from the spectrum described by curve *1* in Fig. 1, we find that the value of the parameter sought lies in the range 4–8%.

An analysis of Fig. 3 with consideration of the increase in the relative intensity and splitting of the ''hypersensitive'' $^5D_0\rightarrow{}^7F_2$ transition (curve *1*) shows that enhancement of the distortion of the europium optical centers occurs in the co-activated glass and that there are additional centers of a new type (curve *2*), which are efficiently excited in a broad band at 320 nm (curve *4*). The significant intensification of the electric-dipole transitions of the Eu^{3+} ions in the additional centers as T is raised in the range 77–298 K attests to the fairly large contribution of the dynamic part of the potential of the local field to their probability and, as a consequence, to the high symmetry of such centers. On the basis of the number of very intense lines and the higher resolution of the $^5D_0\rightarrow{}^7F_1$ transition in comparison to the $^5D_0\rightarrow{}^7F_2$ electric-dipole transition, we can assume that the centers of the new type are characterized by cubic symmetry. As we know,[3,4] in the case of a cubic field the $^7F_2$ level splits into two sublevels, one of which is triply degenerate, while the other is doubly degenerate. For the coordination number $N_c=6$ the lower sublevel is a triplet with the components $B_2(|2^-\rangle)$ and $E(|\pm1\rangle)$, and for $N_c=8$ it is a doublet with the components $A_1(|0\rangle)$ and $B_1(|2^+\rangle)$. With consideration of the odd parameters B_{tp} it is not difficult to infer from formula (4) that two components with a 3:2 intensity ratio in the $|0\rangle$ and $|\pm1\rangle$ states, respectively, will be observed in the $^5D_0\rightarrow{}^7F_2$ transition when there is weak distortion of the cubic structure ($O\rightarrow C_4, C_{4v}$).

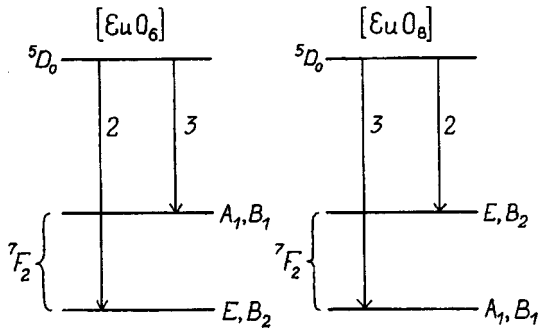

FIG. 5. Calculated intensity distribution of the components of the $^5D_0\rightarrow{}^7F_2$ transition of Eu^{3+} ions in a field of cubic symmetry for six- and eight-ligand environments.

The situation just described for the $^5D_0\rightarrow{}^7F_2$ transition in a cubic field is illustrated for both values of N_c in Fig. 5, where the numbers next to the arrows indicate the relative intensities of the transitions. It can be seen that the long-wavelength band will be more intense (by a factor of 1.5) when $N_c=6$ and that the short-wavelength band will be more intense (also by a factor of 1.5) when $N_c=8$. A comparison of the areas under the experimentally observed components of this transition (in the range 600–640 nm) for the co-activated glass at $\lambda_{exc}=320$ nm (curve *2* in Fig. 3) with the transition intensities in Fig. 5 shows that the experimental data correspond to the case where the value of N_c for the Eu^{3+} ions equals 8. However, if we take into account the inhomogeneous broadening and the fact that the experimental peak intensity of the long-wavelength component is roughly 1.4 times higher, we cannot rule out the existence of centers with $N_c=6$.

For an unequivocal choice in favor of one of the values of N_c, we utilize the results in Ref. 10, in which it was shown that Eu^{3+} ions with a six-ligand environment of O_h symmetry exhibit splitting of the $^5D_0\rightarrow{}^7F_4$ band into two groups of components, which are caused by A_{1g}, T_{1g}, and E_g Stark sublevels of similar energy (the first group) and a T_{2g} sublevel (the second group). In the case of an eight-ligand environment of the same symmetry, there is splitting into three groups, which are caused by T_{2g} and E_g (the first group), T_{1g} (the second group), and A_{1g} (the third group) sublevels. Preference should be given to optical centers with

$N_c=8$ already on the basis of this feature, since the luminescence spectrum of the co-activated glass displays three components at $\lambda\sim 680$, 699, and 714 nm for this band (curve *2* in Fig. 3). However, since the short-wavelength component can be assigned to the ${}^5D_0\rightarrow{}^7F_3$ transition, we calculated the values of the total splitting of the ${}^7F_4$ level for $N_c=6$ and 8. An intermediate calculation of the fourth- and sixth-order parameters yielded the following values (cm^{-1}):

$A_{40}=512$, $A_{60}=31$, $B_{40}=4096$, $B_{60}=496$ for $N_c=6$,

$A_{40}=-512$, $A_{60}=82$, $B_{40}=-4096$,

$B_{60}=1312$ for $N_c=8$.

We note that the values of A_{40} were obtained from experimental data on the splitting of the ${}^7F_2$ level and then the values of A_{60} were calculated using a cluster model.[3,10]

It was ultimately found that the total splitting amounts to 700 cm^{-1} for $N_c=6$ and 780 cm^{-1} for $N_c=8$. While the magnitude of the splitting between the long-wavelength and middle components equals 300 cm^{-1}, the splitting between the long-wavelength and short-wavelength components is $\geqslant 700$ cm^{-1}. Since the former value is several times less than the expected value, we can state that the short-wavelength component does, in fact, belong to the ${}^5D_0\rightarrow{}^7F_4$ band and that, therefore, $N_c=8$.

The intense broad band with a maximum at 320 nm in the luminescence excitation spectrum of the cubic Eu^{3+} centers considered (curve *4* in Fig. 3) can be associated, according to the luminescence spectra of the glasses thermally treated in hydrogen, with excitation transfer from Ce^{3+} ions. In fact, the narrow-band luminescence with a maximum at 590 nm is totally absent for such glasses, whereas only the luminescence of Ce(III) (Refs. 1 and 6) is observed for the co-activated glass (curve *2* in Fig. 4) and the luminescence of Eu^{3+} ions with a maximum at 615 nm and the broad-band luminescence of Eu(II) (Ref. 8) are observed for the monoactivated glass (curve *1* in Fig. 4). The luminescence excitation spectrum under consideration can clearly be attributed, precisely, as in the case of the Ce–Sm-containing glass in Ref. 11, to the formation of compound centers, in which Ce^{4+} ions and ions of the co-activator are joined by an oxygen bridge, and excitations are transferred to the latter from metastable photoreduced $(Ce^{4+})^-$ ions. As we know,[12] the ionic radius of tetravalent cerium is ~ 0.8 Å, and, in accordance with the geometric criterion in the Ref. 13, such ions can form cerium-containing polyhedrons with $N_c=7$ and, possibly, 6. In the latter case, according to a consequence[14] of the Pauling electrostatic valence rule, they can perform the role of buffer elements, which promote the entry of higher-coordinate lanthanide ions into the silicon-oxygen framework and thereby the formation of such compound centers. Since the minimum percentage of Eu^{3+} ions entering these centers cannot be less than the product of the quantum efficiency of the sensitization of their luminescence by $(Ce^{4+})^-$ ions and C_{CeCl_3}/C_{EuCl_3}, we can attempt to estimate it using Eq. (5) and curves *3* and *4* in Figs. 1 and 3, respectively. For this purpose the parameters with the subscript *ff* in this equation should be taken at $\lambda=530$ nm, and the parameters with the subscript *ct* should be taken at 390 nm$>\lambda>320$ nm. A simple calculation shows that the percentage amounts to $\sim 3\%$ when $2C_{CeCl_3}=C_{EuCl_3}=1$ wt%.

Finally, it should be noted that the conclusion drawn in Ref. 1 regarding the formation of compound Ce^{4+}-Ln^{3+} centers in the pore-closure stage is not entirely correct. In fact, such structural formations also exist in thermally treated xerogels, as is evidenced by the appearance of a similarity between the narrow-band luminescence spectra of the glass and xerogel cooled to 77 K at $\lambda_{exc}=320$ nm (curves *2* and *5* in Fig. 3). It can be assumed that the absence of the sensitization described due to the large interatomic distances in this intermediate matrix at $T=298$ K prevents the appearance of spectroscopic manifestations of these centers. The shortening of these distances, which occurs both when *T* is lowered and when the xerogel transforms into a glass, makes such sensitization possible and permits the confident detection of these centers.

Thus, the predominant europium-containing species in quartz gel-glasses doped by impregnation and sintering in air are rhombically distorted oxo complexes of Eu(III). This structure is essentially independent of the concentration of the europium salt introduced when the latter varies in the range 0.3–3 wt%. When Eu-containing glasses are co-activated by cerium, compound Ce^{4+}-Eu^{3+} centers also form, in which Eu(III) is characterized predominantly by cubic symmetry with a coordination number of the cation equal to 8 and effective sensitization of the luminescence by photoreduced metastable $(Ce^{4+})^-$ ions. The presence of Ce^{3+} ions not appearing in compound centers along with the Ce^{4+} ions in the co-activated glass raises the degree of distortion of the Eu(III) centers, but does not lead to radical alteration of their structure and sensitization of their luminescence. Fairly efficient excitation of the luminescence of simple Eu centers through a band assigned to charge transfer from the ligands to the Eu^{3+} ions takes place in both the monoactivated and co-activated glasses.

This work was supported by the Belarus Republican Fund for Fundamental Research (Grant No. F97-116).

†)Deceased.

[1] G. E. Malashkevich, E. N. Poddenezhnyĭ, I. M. Mel'nichenko, and A. V. Semchenko, Fiz. Tverd. Tela (St. Petersburg) **40**, 458 (1998) [Phys. Solid State **40**, 420 (1998)].
[2] G. E. Malashkevich, E. N. Poddenezhny, I. M. Melnichenko, and V. E. Gaishun, in *Proceedings of the 17th International Congress on Glass*, Beijing, China (1995), Vol. 4, p. 320.
[3] A. G. Makhanek and V. S. Korol'kov, *Analytical Methods in Quantum-Mechanical Perturbation Theory* [in Russian], Nauka i Tekhnika, Minsk (1982).
[4] M. I. Gaĭduk, V. F. Zolin, and L. S. Gaĭgerova, *Luminescence Spectra of Europium* [in Russian], Nauka, Moscow (1974), 195 pp.
[5] K. W. N. Stevens, Proc. Phys. Soc. London, Sect. A **65**, 209 (1952).
[6] G. E. Malashkevich, E. N. Poddenezhny, I. M. Melnichenko, and A. A. Boiko, J. Non-Cryst. Solids **188**, 107 (1995).
[7] C. A. Parker, *Photoluminescence of Solutions. With Applications to Photochemistry and Analytical Chemistry* (Elsevier, New York, 1968; Mir, Moscow, 1992, p. 232).
[8] V. I. Arbuzov, V. A. Bonch-Bruevich, E. I. Galant, and M. N. Tolstoĭ, Fiz. Khim. Stekla **8**, 216 (1982).
[9] J. Haas, G. Stein, and M. J. Tomkiewicz, Phys. Chem. **74**, 2258 (1970).

[10] V. S. Korol'kov and A. G. Makhanek, Zh. Prikl. Spektrosk. **48**, 975 (1988).
[11] V. I. Arbuzov, M. N. Tolstoĭ, M. A. Élerts, and Ya. S. Trokshs, Fiz. Khim. Stekla **13**, 581 (1987).
[12] *Chemistry and the Periodic Table* [Russian translation], K. Saito [Ed.], Mir, Moscow (1982), p. 179.
[13] *Modern Crystallography*, *Vol. 2: Structure of Crystals*, 2nd. ed., B. K. Vainshtein, V. M. Fridkin, and V. L. Indenbom [Eds.] (Springer-Verlag, Berlin–New York, 1995; Nauka, Moscow, 1979, 354 pp.).
[14] L. E. Ageeva, V. I. Arbuzov, E. I. Galant *et al.*, Fiz. Khim. Stekla **13**, 409 (1987).

Translated by P. Shelnitz

Temperature dependence of the second-order elastic constants of cubic crystals

B. P. Sorokin, D. A. Glushkov, and K. S. Aleksandrov

Krasnoyarsk State University, 660041 Krasnoyarsk, Russia
(Submitted February 18, 1998; resubmitted July 1, 1998)
Fiz. Tverd. Tela (St. Petersburg) **41**, 235–240 (February 1999)

A simplified phenomenological theory of the temperature dependence of the second-order elastic constants of crystals is considered. The temperature dependences of the second-order elastic constants are calculated for a series of cubic crystals with various types of predominant chemical bonding. Satisfactory agreement between the calculation results and experimental data is obtained. © *1999 American Institute of Physics.* [S1063-7834(99)01002-3]

The normal behavior of the second-order elastic constants as a function of temperature for most crystals includes a decrease with increasing temperature according to a linear law and a weak (or vanishing) dependence at low temperatures. Knowledge of these dependences is important not only from the standpoint of basic science, but also for practical problems involving crystals. The existing theories regarding the behavior of $C_{ij}(T)$ were devised on the basis of the Debye theory with allowance for anharmonicity in the vibrations of atoms in real lattices, and the temperature dependence of the number of phonons was included to obtain a correct description of $C_{ij}(T)$ over a broad temperature range.[1–9] However, the final expressions thus obtained are too cumbersome for analysis, and the behavior of $C_{ij}(T)$ is usually considered in a low- or high-temperature range. In this paper we consider a modification of a simplified phenomenological theory based on a conception of finite strains (and elastic anharmonicity), which appear in a solid during thermal expansion and the propagation of small-amplitude bulk acoustic waves under such conditions. We note that a similar method for taking into account finite strains during thermal expansion was used in Ref. 10 to analyze the temperature dependence of the resonant frequencies of quartz resonators. Since the temperature dependences of the piezoelectric and dielectric constants are not considered in our case, the results obtained can be applied to centrosymmetric crystals or to nonpiezoactive directions in acentric crystals.

1. CALCULATION OF THE TEMPERATURE DEPENDENCES OF THE SECOND-ORDER ELASTIC CONSTANTS OF CUBIC CRYSTALS

Let a crystal be subjected to the effects of a temperature change. For a mechanically free sample ($\overline{\tau}_{KL}=0$), the static strains appearing as a result of thermal expansion can be described using the relation

$$\overline{\eta}_{PQ}=S^T_{PQKL}\overline{\tau}_{KL}+\alpha_{PQ}\Delta T=\alpha_{PQ}\Delta T, \tag{1}$$

where α_{PQ} is the thermal expansion tensor and S^T_{PQKL} is the elastic compliance tensor. The corresponding equation of state for the dynamic variables has the form

$$\begin{aligned}\tilde{\tau}_{AB}&=[C^S_{ABKL}+C^S_{ABKLPQ}\overline{\eta}_{PQ}]\tilde{\eta}_{KL}\\&=[C^S_{ABKL}+C^S_{ABKLPQ}\alpha_{PQ}\Delta T]\tilde{\eta}_{KL},\end{aligned} \tag{2}$$

where C^S_{ABKL} and C^S_{ABKLPQ} are the second- and third-order elastic constants, respectively, and $\tilde{\tau}_{AB}$ and $\tilde{\eta}_{KL}$ are the dynamic elastic stresses and strains. The form of the Green–Christoffel tensor for the case of the propagation of small-amplitude elastic waves in a crystal under the action of a finite static strain has been presented, for example, in Ref. 11. Under given boundary conditions the Green–Christoffel tensor can be represented with consideration of (2) in the form

$$\Gamma_{BC}(\overline{\tau})=\overline{C}_{FC}(C^S_{ABFD}+C^S_{ABFDPQ}\alpha_{PQ}\Delta T)N_AN_D. \tag{3}$$

In (3) $\overline{C}_{FC}$ is the Green finite-static-strain tensor

$$\overline{C}_{FC}=\delta_{FC}+2\overline{\eta}_{FC}=\delta_{FC}+2\alpha_{FC}\Delta T. \tag{4}$$

Substituting (4) into (3) and assuming that $\Delta C_{ij}(T)\sim\Delta T$, we can obtain a simplified expression for the Green–Christoffel tensor, retaining only the terms which do not depend on external effects and are proportional to the first power of ΔT:

$$\begin{aligned}\Gamma_{BC}(\Delta T)&=\overline{C}_{FC}(C^S_{ABFD}+C^S_{ABFDPQ}\alpha_{PQ}\Delta T)N_AN_D\\&=(\delta_{FC}+2\alpha_{FC}\Delta T)(C^S_{ABFD}\\&\quad+C^S_{ABFDPQ}\alpha_{PQ}\Delta T)N_AN_D\\&\approx(C^S_{ABCD}+2C^S_{ABFD}\alpha_{FC}\Delta T\\&\quad+C^S_{ABCDPQ}\alpha_{PQ}\Delta T)N_AN_D\\&=[C^S_{ABCD}+(2C^S_{ABPD}\delta_{CQ}\\&\quad+C^S_{ABCDPQ})\alpha_{PQ}\Delta T]N_AN_D.\end{aligned} \tag{5}$$

Using (5) we can describe the propagation of bulk acoustic waves in the N_A direction under the conditions of a uniform static strain caused by a temperature change.

Let us consider, for example, the propagation of acoustic waves in cubic crystals of 432, $m3m$ symmetry along the [100] direction. If it is taken into account that the thermal

expansion tensor for cubic crystals is isotropic, i.e., $\alpha_{11}=\alpha_{22}=\alpha_{33}=\alpha$, the Green–Christoffel tensor (5) takes the form

$$\begin{bmatrix} \Gamma_{11} & 0 & 0 \\ 0 & \Gamma_{22} & 0 \\ 0 & 0 & \Gamma_{22} \end{bmatrix}, \tag{6}$$

where

$$\Gamma_{11}=C_{11}+(2C_{11}+C_{111}+2C_{112})\alpha\Delta T,$$
$$\Gamma_{22}=C_{44}+(2C_{44}+C_{144}+2C_{155})\alpha\Delta T. \tag{7}$$

The form of the tensor (6) for the direction under consideration coincides with its representation in the unperturbed state. This, of course, is a consequence of the Curie symmetry principle, since an isotropic influence (a temperature change) does not alter the symmetry of the medium. A longitudinal and a degenerate shear wave can clearly propagate in the direction under consideration:

$$\lambda_1=\Gamma_{11}=C_{11}+(2C_{11}+C_{111}+2C_{112})\alpha\Delta T, \quad \lambda_1^0=C_{11},$$
$$\lambda_2=\lambda_3=\Gamma_{22}=C_{44}+(2C_{44}+C_{144}+2C_{155})\alpha\Delta T,$$
$$\lambda_2^0=\lambda_3^0=C_{44}. \tag{8}$$

The temperature velocity control coefficients of bulk acoustic waves, which are determined experimentally by the slopes of the relative velocity changes as a function of temperature, are given by the expressions

$$\alpha_{v_1}=\frac{1}{2C_{11}}(2C_{11}+C_{111}+2C_{112})\alpha,$$
$$\alpha_{v_2}=\alpha_{v_3}=\frac{1}{2C_{44}}(2C_{44}+C_{144}+2C_{155})\alpha. \tag{9}$$

Using (8) and (9), we can obtain the explicit form of the temperature dependences of the elastic constants C_{11} and C_{44}:

$$\frac{dC_{11}}{dT}=(2C_{11}+C_{111}+2C_{112})\alpha,$$
$$\frac{dC_{44}}{dT}=(2C_{44}+C_{144}+2C_{155})\alpha. \tag{10}$$

In order to find the corresponding relation for C_{12}, we must consider the propagation of acoustic waves in the [110] direction, for which the Green–Christoffel tensor (5) has the form

$$\begin{bmatrix} \Gamma_{11} & \Gamma_{12} & 0 \\ \Gamma_{12} & \Gamma_{11} & 0 \\ 0 & 0 & \Gamma_{33} \end{bmatrix}, \tag{11}$$

where

$$\Gamma_{11}=\frac{1}{2}(C_{11}+C_{44})+\frac{1}{2}(2C_{11}+2C_{44}+C_{111}+2C_{112}+C_{144}+2C_{155})\alpha\Delta T,$$
$$\Gamma_{12}=\frac{1}{2}(C_{12}+C_{44})+\frac{1}{2}(2C_{12}+2C_{44}+C_{123}+2C_{112}+C_{144}+2C_{155})\alpha\Delta T,$$
$$\Gamma_{33}=C_{44}+(2C_{44}+C_{144}+2C_{155})\alpha\Delta T. \tag{12}$$

Three waves with different eigenvalues propagate in this direction:

$$\lambda_4=\Gamma_{11}+\Gamma_{12}, \quad \lambda_5=\Gamma_{11}-\Gamma_{12}, \quad \lambda_6=\Gamma_{33},$$
$$\lambda_4^0=\frac{1}{2}(C_{11}+C_{12}+2C_{44}).$$
$$\lambda_5^0=\frac{1}{2}(C_{11}-C_{12}), \quad \lambda_6^0=C_{44}. \tag{13}$$

Here λ_4 corresponds to a pure longitudinal wave, λ_5 to a shear wave with $\mathbf{U}\|[1\bar{1}0]$ polarization, and λ_6 to a pure shear wave with $\mathbf{U}\|[001]$ polarization. The control coefficients have the form

$$\alpha_{v_4}=\frac{1}{4\lambda_4(0)}[2\lambda_4(0)+C_{111}+C_{123}+4C_{112}+2C_{144}+4C_{155}]\alpha,$$
$$\alpha_{v_5}=\frac{1}{4\lambda_5(0)}[2\lambda_5(0)+C_{111}-C_{123}]\alpha,$$
$$\alpha_{v_6}=\frac{1}{4\lambda_6(0)}[2\lambda_6(0)+C_{144}+2C_{155}]\alpha. \tag{14}$$

To express the temperature dependence $C_{12}(T)$, we represent λ_1 and λ_5 in the form

$$\lambda_1=C_{11}^*=C_{11}+(2C_{11}+C_{111}+2C_{112})\alpha\Delta T,$$
$$2\lambda_5=C_{11}^*-C_{12}^*=C_{11}-C_{12}+(2C_{11}-2C_{12}+C_{111}-C_{123})\alpha\Delta T. \tag{15}$$

Subtracting the second of the relations (15) from the first, we obtain

$$\frac{dC_{12}}{dT}=(2C_{12}+C_{123}+2C_{112})\alpha. \tag{16}$$

The relation (16) together with (10) gives the temperature dependences of all the independent elastic constants of cubic crystals. Analyzing the form of these relations, we can state that the contribution of the linear elastic constants is related to the strain appearing in the material under the effect of thermal expansion and is usually positive. The contributions associated with the nonlinear elastic constants determine the change in the interatomic interaction due to anharmonicity, and when the temperature is increased, these contributions are usually negative and exceed the positive linear contribution, so that the normal temperature dependences of the elastic constants are negative in crystals. Of course, the applicability of Eqs. (10) and (16) is confined to the linear portions of the $C_{ij}(T)$ curves. Moreover, since most measurements of third-order elastic constants are performed at a fixed tem-

perature (as a rule, at room temperature), there is a real possibility of correctly comparing theoretical and experimental data only for that temperature point.

The relations (10) and (16) differ somewhat from the analogous expressions proposed in Ref. 8, which were obtained under the assumption that in a cubic crystal the ''correct'' temperature coefficients must include the effect of the isotropic phonon pressure $P_{\rm ph}$, which appears as a result of the phonon-lattice interaction:

$$\frac{dC_{11}}{dT}=(C_{11}+C_{111}+2C_{112})\alpha,$$

$$\frac{dC_{12}}{dT}=(C_{11}+3C_{12}+C_{123}+2C_{112})\alpha,$$

$$\frac{dC_{44}}{dT}=(-C_{11}+C_{12}+3C_{44}+C_{144}+2C_{166})\alpha. \qquad (17)$$

It would be interesting to compare the results of calculations using the relations (10) and (16) and the relations (17) with experimental data on the temperature dependence of the elastic constants. In addition, taking into account Shrivastava's arguments,[8] we also performed calculations using forms of (10) and (16) that were modified to take into account the phonon pressure and were obtained in the following manner. If it is assumed that the isotropic phonon pressure $P_{\rm ph}$ acts on a cubic crystal lattice from within, then, in accordance with Ref. 12, the effective elastic constants altered by such a pressure will have the form

$$C'_{11}=C_{11}-P_{\rm ph},$$

$$C'_{12}=C_{12}+P_{\rm ph},$$

$$C'_{44}=C_{44}-P_{\rm ph}. \qquad (18)$$

Differentiating (18) with respect to temperature, using the explicit forms of (10) and (16), and taking into account, according to Ref. 8, that

$$\frac{dP_{\rm ph}}{dT}=\alpha(C_{11}+2C_{12}), \qquad (19)$$

we obtain analogs of (10) and (16) modified to take into account the phonon pressure in the form

$$\frac{dC_{11}}{dT}=\alpha(C_{11}-2C_{12}+2C_{112}),$$

$$\frac{dC_{12}}{dT}=\alpha(C_{11}+4C_{12}+C_{123}+2C_{112}),$$

$$\frac{dC_{44}}{dT}=\alpha(2C_{44}-C_{11}-2C_{12}+C_{144}+2C_{155}). \qquad (20)$$

For analysis and comparison, we selected a series of cubic crystals with various types of predominant chemical bonding, which was larger than the group in Ref. 8. The results are presented in Table I. Data from Refs. 25–27 were used to compare the calculated dependences of the second-order elastic constants on T with experiment within three models: 1) the relations (10) and (16) (without consideration of the phonon pressure); 2) the relations (20) (with consideration of the phonon pressure); 3) the model from Ref. 8 with consideration of the phonon pressure [the relation (17)].

2. DISCUSSION OF RESULTS

As can be seen from Table I, for crystals having fluorite structure (CaF_2 and BaF_2) and the garnet $Y_3Al_3O_{12}$, the results obtained using the relations (20) (with allowance for the effect of the phonon pressure) are closest to the experimental values. The differences with respect to all the temperature coefficients do not exceed 15%, which can be regarded as good agreement. At the same time, the differences between the results obtained from the relations (17) and experiment for this group of crystals can reach 50% (the values of $\partial C_{44}/\partial T$ for $Y_3Al_5O_{12}$).

Considerably poorer agreement is observed for diamond within all the models considered. A possible explanation for this can be provided by the sparsity and disjointedness of the experimental data on this crystal (both the experimental temperature dependences and the data used in the calculation). For example, in Ref. 18, the third-order elastic constants were obtained in the following manner: the microscopic anharmonicity parameters were calculated from experimental dependences of optical phonon frequencies on uniaxial compression using Keating's theory,[19] and then the third-order elastic constants were calculated.

The poor agreement with experiment for semiconductor Si crystals can easily be understood, if it is realized that our calculations included only the lattice elastic nonlinearity, while the electron-phonon interaction plays a considerably more appreciable role in these crystals, as was shown in Ref. 20.

The fit between the experimental and calculated results for the group of ionic crystals should be regarded as barely satisfactory. None of the models has any advantage here. It is important, however, that models 2 and 3 predict the positive character of the temperature dependence of C_{12} for many crystals in which this anomalous dependence has been observed experimentally (NaCl, KCl, KI, KBr, RbCl, and RbBr). On the other hand, the differences in the experimental data on the temperature coefficients of $C_{\lambda,\mu}$ obtained by different investigators can be so large that values of the temperature coefficient of C_{12} having different signs were measured for the same crystal (LiF, NaF) or the differences in the absolute value of the temperature coefficient of C_{12} can be as high as hundreds of percent (KBr, NaCl). In addition, the data on the second- and third-order elastic constants which were obtained by different investigators for the same crystals and used in the calculations also differ significantly. These circumstances leave a great deal of freedom in interpreting the correctness of particular relations. We note that the differences in the original data can, most likely, be attributed to two factors: 1) systematic errors in the experiments; 2) varying and uncontrolled quality of the samples. The latter factor is especially significant for alkali halide crystal, in which the inelasticity caused by the structural nonideality (dislocations) can make a significant contribution to the irreproducibility or lead to errors in the experiments cited.

One exception among the crystals with predominant

TABLE I. Temperature coefficients of the elastic constants of crystals of cubic symmetry (in $10^7 \mathrm{Pa}\cdot\mathrm{K}^{-1}$).

No.	Crystal	$\frac{\partial C_{11}}{\partial T}$ Calc.	$\frac{\partial C_{11}}{\partial T}$ Exp.	$\frac{\partial C_{12}}{\partial T}$ Calc.	$\frac{\partial C_{12}}{\partial T}$ Exp.	$\frac{\partial C_{44}}{\partial T}$ Calc.	$\frac{\partial C_{44}}{\partial T}$ Exp.	Model	Data for calculations	Exp. data
1	2	3	4	5	6	7	8	9	10	11
1	BaF_2	−1.98	−2.00	−1.52	−1.27	−0.49	−0.72	1)	Ref. 13	Ref. 25
		−2.32		−1.18		−0.83		2)		
		−2.15		−1.26		−0.54		3)		
2	CaF_2	−3.16	−3.18	−1.81	−1.27	−0.85	−1.22	1)	Ref. 14	Ref. 25
		−3.58		−1.39		−1.28		2)		
		−3.46		−1.45		−1.01		3)		
3	$Y_3Al_5O_{12}$	−2.46	−3.00	−0.92	−0.56	−0.42	−0.81	1)	Refs. 15 and 16	Ref. 25
		−2.84		−0.54		−0.80		2)		
		−2.69		−0.61		−0.50		3)		
4	C	−0.87	−1.51	−0.41	−0.71	−0.53	−0.72	1)	Refs. 17 and 18	Ref. 26
	Diamond	−1.01		−0.27		−0.67		2)		
		−0.97		−0.29		−0.56		3)		
5	Si	−0.32	−0.87	−0.19	−0.48	−0.10	−0.33	1)	Ref. 20	Ref. 25
	(n-type)	−0.38		−0.13		−0.17		2)		
		−0.35		−0.14		−0.11		3)		
6	Si	−0.32	−1.26	−0.20	−0.16	−0.10	−0.44	1)	Ref. 20	Ref. 25
		−0.38		−0.13		−0.17		2)		
		−0.35		−0.14		−0.11		3)		
7	AgCl	−4.29	−6.06	−1.11	−1.27	−0.16	−0.27	1)	Ref. 17	Ref. 25
		−4.69		−0.72		−0.56		2)		
		−4.47		−0.83		−0.21		3)		
8	CsCl	−2.52	−1.54	−1.07	−0.84	−1.08	−1.04	1)	Ref. 21	Ref. 25
		−2.79		−0.80		−1.36		2)		
		−2.70		−0.85		−1.18		3)		
9	CsI	−1.84	−1.08	−0.96	−0.52	−0.75	−0.82	1)	Ref. 21	Ref. 25
		−2.04		−0.76		−0.95		2)		
		−1.97		−0.79		−0.81		3)		
10	LiF	−5.95	−7.39	−1.01	0.05	−1.16	−1.77	1)	Ref. 22	Ref. 25
		−6.67	−9.56	−0.28	−3.06	−1.89	−2.17	2)		Ref. 27
		−6.38		−0.43		−1.22		3)		
11	LiCl	−4.76	−3.82	−1.22	−1.14	−1.16	−0.65	1)	Ref. 8	Ref. 27
		−5.15		−0.83		−1.55		2)		
		−4.96		−0.92		−1.16		3)		
12	LiBr	−3.01	−2.86	−0.27	−0.27	−0.22	−0.67	1)	Ref. 21	Ref. 27
		−3.31		0.03		−0.52		2)		
		−3.19		−0.03		−0.25		3)		
13	NaF	−6.05	−6.21	−0.70	0.44	−0.41	−0.59	1)	Ref. 8	Ref. 25
		−6.51	−5.35	−0.24	−0.37	−0.87	−0.57	2)		Ref. 27
		−6.35		−0.32		−0.55		3)		
14	NaCl	−3.42	−3.93	−0.25	0.22	−0.34	−0.35	1)	Ref. 23	Ref. 25
		−3.71	−3.50	0.05	0.98	−0.64	−0.15	2)		Ref. 27
		−3.61		−0.01		−0.43		3)		
15	NaBr	−3.08	−3.43	−0.34	−0.50	−0.31	−0.25	1)	Ref. 8	Ref. 25
		−3.33		−0.10		−0.55		2)		
		−3.24		−0.14		−0.38		3)		
16	NaI	−2.56	−2.57	−0.31	−0.14	−0.33	−0.20	1)	Ref. 8	Ref. 27
		−2.77		−0.11		−0.53		2)		
		−2.69		−0.15		−0.38		3)		
17	KF	−3.72	−4.19	−0.25	−0.10	−0.18	−0.19	1)	Ref. 8	Ref. 27
		−4.01		0.04		−0.47		2)		
		−3.92		−0.01		−0.29		3)		
18	KCl	−3.09	−3.38	−0.10	0.39	−0.07	−0.13	1)	Ref. 17	Ref. 25
		−3.33	−3.30	0.14	0.24	−0.32	−0.12	2)		Ref. 27
		−3.27		0.11		−0.20		3)		
19	KBr	−2.45	−2.94	−0.08	0.43	−0.66	−0.12	1)	Ref. 16	Ref. 25
		−2.65	−2.76	0.12	0.12	−0.86	−0.11	2)		Ref. 27
		−2.60		0.10		−0.77		3)		
20	KI	−1.86	−2.56	0.02	0.42	−0.08	−0.08	1)	Ref. 8	Ref. 25
		−2.00		0.16		−0.22		2)		
		−1.96		0.14		−0.15		3)		
21	RbCl	−2.09	−2.90	0.03	0.25	−0.05	−0.16	1)	Ref. 8	Ref. 27
		−2.26		0.19		−0.21		2)		
		−2.21		0.17		−0.13		3)		

TABLE 1. (*Continued.*)

No.	Crystal	$\frac{\partial C_{11}}{\partial T}$ Calc.	$\frac{\partial C_{11}}{\partial T}$ Exp.	$\frac{\partial C_{12}}{\partial T}$ Calc.	$\frac{\partial C_{12}}{\partial T}$ Exp.	$\frac{\partial C_{44}}{\partial T}$ Calc.	$\frac{\partial C_{44}}{\partial T}$ Exp.	Model	Data for calculations	Exp. data
1	2	3	4	5	6	7	8	9	10	11
22	RbI	−1.76	−2.25	−0.05	0.001	−0.06	−0.05	1)	Ref. 16	Ref. 27
		−1.89		0.08		−0.18		2)		
		−1.86		0.06		−0.13		3)		
23	MgO	−5.04	−6.76	−0.08	0.95	−1.00	−1.54	1)	Ref. 24	Ref. 25
		−5.58		0.46		−1.54		2)		
		−5.37		0.35		−1.05		3)		

ionic bonding is the results for the MgO crystal, where the agreement for both the magnitude and sign of the temperature coefficients can be considered good. The best series of results is provided again by model 2 [see (20)], and a significant difference ($\sim$60%) is observed only for the absolute value of the temperature coefficient of C_{12}. From the experimental standpoint, a magnesium-oxide crystal has considerable mechanical strength in comparison to most alkali halide crystals, which can play a decisive role in the correctness and reproducibility of the results on the second- and third-order elastic constants when experiments with the application of pressure are performed.

We note that the approach developed in the present work can be used to determine the temperature dependence of the elastic constants of crystals of lower symmetry.

This work was performed with partial financial support from the Russian Fund for Fundamental Research (Grant No. 96-15-96700) and the Ministry of Education of the Russian Federation (Grant No. 97-0-7.2-117).

[1] G. Leibfried and H. Hahn, Z. Phys. **150**, 497 (1958).
[2] Y. Hiki and A. V. Granato, Phys. Rev. **144**, 411 (1966).
[3] Y. Hiki, J. F. Thomas, and A. V. Granato, Phys. Rev. **153**, 764 (1967).
[4] S. P. Nikanorov, A. A. Nran'yan, and A. V. Stepanov, Fiz. Tverd. Tela (Leningrad) **6**, 1996 (1964).
[5] J. A. Garber and A. V. Granato, Phys. Rev. B **11**, 3990 (1975).
[6] J. A. Garber and A. V. Granato, Phys. Rev. B **11**, 3998 (1975).
[7] U. C. Shrivastava, Phys. Rev. B **21**, 2602 (1980).
[8] U. C. Shrivastava, Phys. Status Solidi B **100**, 641 (1980).
[9] S. Shanker and R. K. Varshney, Phys. Status Solidi B **114**, K71 (1982).
[10] B. K. Sinha and H. F. Tiersten, J. Appl. Phys. **50**, 2732 (1979).
[11] M. P. Zaĭtseva, Yu. I. Kokorin, Yu. M. Sandler, V. M. Zrazhevskiĭ, B. P. Sorokin, and A. M. Sysoev, *Nonlinear Electromechanical Properties of Acentric Crystals* [in Russian], Nauka, Novosibirsk (1986), 177 pp.
[12] D. C. Wallace, ''Thermoelastic theory of stressed crystals and higher-order elastic constants,'' in *Solid State Physics*, H. Ehrenreich, F. Seitz, and D. Turnbull [Eds.], Academic Press, New York–London (1970), Vol. 25, pp. 301–404.
[13] D. Gerlich, Phys. Rev. **168**, 947 (1968).
[14] S. Alterovitz and D. Gerlich, Phys. Rev. **184**, 999 (1969).
[15] Y. K. Yogurtsu, A. J. Miller, and G. A. Saunders, J. Phys. C: Solid State Phys. **13**, 6585 (1980).
[16] *Landolt-Börnstein Numerical Data and Functional Relationships in Science and Technology, New Series, Group III*, Springer, Berlin (1984), Vol. 18, pp. 3–179.
[17] *Landolt-Börnstein Numerical Data and Functional Relationships in Science and Technology, New Series, Group III*, Springer, Berlin (1979), Vol. 11, pp. 9–470.
[18] M. H. Grimsditch, E. Anastassakis, and M. Cardona, Phys. Rev. **18**, 901 (1978).
[19] P. N. Keating, Phys. Rev. **149**, 674 (1966).
[20] J. J. Hall, Phys. Rev. **161**, 756 (1967).
[21] V. A. Kuchin and V. L. Ul'yanov, *Elastic and Inelastic Properties of Crystals* [in Russian], Énergoatomizdat, Moscow (1986), 136 pp.
[22] J. R. Drabble and R. E. B. Strathen, Proc. Phys. Soc. **92(4)**(578), 1090 (1967).
[23] K. D. Swartz, J. Acoust. Soc. Am. **41**, 1083 (1967).
[24] E. H. Bogardus, J. Appl. Phys. **36**, 2504 (1965).
[25] A. A. Blistanov, V. S. Bondarenko, N. V. Perelomova, F. N. Strizhevskaya, V. V. Chkalova, and M. P. Shaskol'skaya, *Acoustic Crystals. A Handbook* [in Russian], Nauka, Moscow (1982), 632 pp.
[26] H. Nakahata, K. Higaki, S. Fujii, A. Hachigo, H. Kitabayashi, K. Tanabe, Y. Seki, and S. Shikata, in *Proceedings of the 1995 IEEE Ultrasonics Symposium*, Seattle (1995), Vol. 1, p. 361.
[27] A. A. Botaki, I. N. Gyrbu, and A. V. Sharko, Fiz. Tverd. Tela (Leningrad) **13**, 3671 (1971) [Sov. Phys. Solid State **13**, 3096 (1971)].

Translated by P. Shelnitz

Employment of curvilinear coordinates in *ab initio* calculations of insulators using pseudopotentials

A. S. Fedorov

L. V. Kirenskiĭ Institute of Physics, Russian Academy of Sciences, Siberian Branch, 660036 Krasnoyarsk, Russia

(Submitted March 26, 1998; resubmitted August 19, 1998)
Fiz. Tverd. Tela (St. Petersburg) **41**, 241–246 (February 1999)

The standard *ab initio* scheme for calculating the structure of crystals using nonlocal pseudopotentials is modified for use in curvilinear coordinates. A method for solving the Poisson equation for the Coulomb potential in a curved space in the k representation is found. It is shown in the example of calculations for crystals of insulators having an NaCl structure that the employment of a curved space permits a very significant decrease in the required size of the basis set. © *1999 American Institute of Physics.* [S1063-7834(99)01102-8]

In the last decade, technological developments and a heightened interest in the description of complex microscopic and macroscopic structures have led to a need for *ab initio* calculations of complex structures with tens, hundreds, and thousands of atoms in the unit cell. The inclusion of dynamics in such calculations[1–4] using molecular dynamics, which was proposed in Ref. 5, as well as determination of the response of systems to various disturbances (calculations of phonon spectra etc.), call for the availability of simple *ab initio* calculation schemes, which can easily be modified for application to the tasks required. Unfortunately, the existing methods either were too complicated for modification (the methods based on solving the Schrödinger equation for MT spheres, viz., the LMTO method and the full-potential method) or required large amounts of machine resources (in particular, the pseudopotential method for describing atoms with large pseudopotentials required the use of a basis set consisting of more than 1000 plane waves even for simple structures consisting of several atoms).

Some new effective calculation methods have appeared in the last 5–7 years. The use of ultrasoft pseudopotentials, which was proposed in Ref. 6, significantly reduced the deficiencies of the classical pseudopotential method at the expense of only slight complication of the calculation scheme.

Another new promising method, which was proposed in Ref. 7, is a hybrid of the LMTO method and the pseudopotential method and permits avoiding many deficiencies of both methods.

At the same time, a new approach to the solution of the Kohn–Sham equations within a pseudopotential scheme was proposed within Car–Parinello molecular dynamics in Refs. 1 and 2 (as well as Refs. 3 and 4). This approach was based on replacement of the basis functions in the form of the ordinary plane waves $|k\rangle \equiv (1/\sqrt{\Omega})\, e^{i\mathbf{k}\cdot\mathbf{r}}$ by curved plane waves of the form $|k\rangle \equiv (1/\sqrt{\Omega})\, |\partial\boldsymbol{\xi}(\mathbf{r})/\partial\mathbf{r}|^{1/2} e^{i\mathbf{k}\cdot\boldsymbol{\xi}(\mathbf{r})}$. It is easy to show that such waves form an orthonormalized basis set and that the matrix elements of the Hamiltonian in this basis set transform into matrix elements that can be calculated in a basis set of ordinary plane waves, but in a special curved space that can be described by the mutually one-to-one mapping $\boldsymbol{\xi} = \boldsymbol{\xi}(\mathbf{r})$.

This paper proposes a modification of the approach just cited, which does not employ molecular dynamics, since for a small number of basis functions the latter formalism does not have any advantages over the classical direct method for diagonalization of the Hamiltonian.

I. CALCULATION SCHEME

The standard calculation scheme for the pseudopotential method described in Ref. 8 was used in the calculation algorithm. Norm-conserving pseudopotentials, which were calculated and tabulated in Ref. 9, served as the pseudopotentials. The exchange-correlation effects were taken into account within the density functional formalism [the local-density approximation (LDA)] using the approximation from Refs. 10 and 11.

All the physical quantities (wave functions, local and nonlocal parts of the potentials, Hamiltonians, and electron density) were calculated using basis functions of the form $\chi_k(\mathbf{r}) \equiv |k\rangle = (1/\sqrt{\Omega})\, |\partial\boldsymbol{\xi}(\mathbf{r})/\partial\mathbf{r}|^{1/2} e^{i\mathbf{k}\cdot\boldsymbol{\xi}(\mathbf{r})}$, which, like ordinary plane waves, are orthonormalized:[1]

$$(k|k') = \frac{1}{\Omega}\int\int\int_{\Omega} d^3r \left(\left| \frac{\partial\boldsymbol{\xi}(\mathbf{r})}{\partial\mathbf{r}} \right| e^{i(\mathbf{k}'-\mathbf{k})\boldsymbol{\xi}(\mathbf{r})} \right)$$

$$= \frac{1}{\Omega}\int\int\int_{\Omega} d^3\xi \, (e^{i(\mathbf{k}'-\mathbf{k})\boldsymbol{\xi}}) = \delta_{\mathbf{k},\mathbf{k}'}.$$

Here $|\partial\boldsymbol{\xi}(\mathbf{r})/\partial\mathbf{r}| = g_{ij}^{-1/2}$, where the metric tensor $g_{ij} = (\partial r^k/\partial\xi^i)\, \partial r^k/\partial\xi^j$.

Going over from the space $\mathbf{r}$ to the space $\boldsymbol{\xi}$ in the calculation of the matrix elements of the Hamiltonian, as well as the potentials and the electron density, in the basis set under consideration, we can easily see that the expressions for them become the same as in the case of plane waves, but in the space $\boldsymbol{\xi}$, with the exception of the forms of the Laplacian in the kinetic energy operator.

The Kohn–Sham equations in reciprocal space have the form

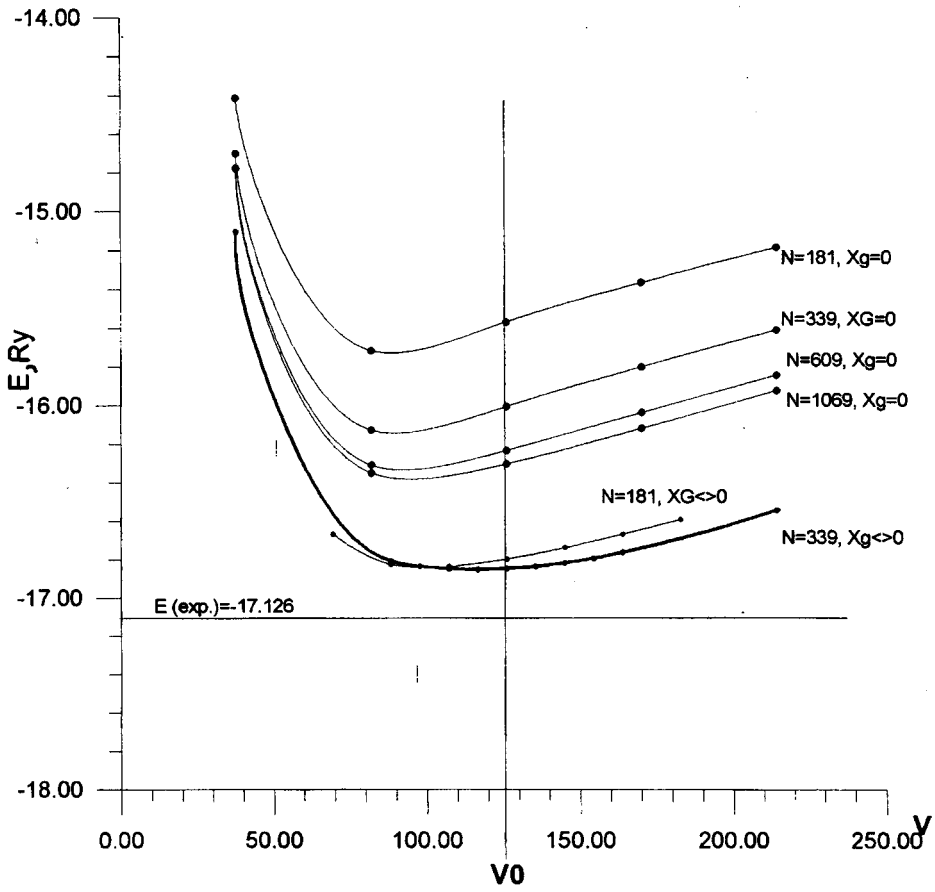

FIG. 1. Dependence of the binding energy E on the unit-cell volume V and on the number of plane waves and curved plane waves for MgO.

$$H^{\nu}(g,g')\chi^{\nu}(g')=\varepsilon^{\nu}\chi^{\nu}(g),$$

where χ^{ν} is an eigenvector (wave function), which can be expanded for each ν in the basis set $\chi^{n}_{k+g}(\mathbf{r})$ according to the formula

$$\chi^{\nu}(\boldsymbol{\xi}(\mathbf{r}))=\frac{1}{\sqrt{\Omega}}\sum_{g}\chi^{\nu}_{k}(g)\left|\frac{\partial\boldsymbol{\xi}(\mathbf{r})}{\partial\mathbf{r}}\right|^{\frac{1}{2}}e^{i(\mathbf{k}+\mathbf{g})\boldsymbol{\xi}(\mathbf{r})}, \tag{1}$$

and ε^{ν} is an eigenvalue of the Schrödinger equation with the wave function $\mathbf{k}$ and the spin σ in zone n. In (1) $\nu=\{\mathbf{k},\sigma,n\}$, $\mathbf{k}$ is the wave vector in the first Brillouin zone, $\mathbf{g}$ is the reciprocal lattice vector, and n is the number of the zone.

The matrix elements of the Hamiltonian $H=-(\hbar^2/2m)\,d^2/dr^2+\hat{V}$ in this basis set have the following form:

$$\langle q|H|q'\rangle=\langle q|T+V_{nl}|q'\rangle + \frac{1}{\Omega}\int\int\int_{\Omega}d^3\xi\,(V_l(\boldsymbol{\xi}(\mathbf{r}))e^{i(\mathbf{q}'-\mathbf{q})\boldsymbol{\xi}}),$$

$$\langle q|T|q'\rangle=\frac{1}{\Omega}\int\int\int_{\Omega}d^3\xi\left(\left(\frac{\hbar^2}{2m}[(\mathbf{q}_i-iA_i)\times g^{ij}(\mathbf{q}'_j+iA_j)]\right)e^{i(\mathbf{q}'-\mathbf{q})\boldsymbol{\xi}}\right), \tag{2}$$

where $\langle q|T|q'\rangle$ describes the Laplacian in the basis set $(1/\sqrt{\Omega})\,|\,\partial\boldsymbol{\xi}(\mathbf{r})/\partial\mathbf{r}\,|^{1/2}e^{i\mathbf{k}\cdot\boldsymbol{\xi}(\mathbf{r})}$ (see Ref. 1) and where g^{ij} denotes the tensor which is the inverse of the metric tensor g_{ij}, and the scale potential $A_i=(1/2)\partial/\partial\xi'\log|\,\partial r/\partial\xi\,|$ appears upon differentiation of the basis function. The total potential can be divided into a nonlocal part $\langle q|V_{nl}|q'\rangle$ and a local potential $V_l(q-q')\equiv\int_{\Omega}d^3r\,(V_l(\boldsymbol{\xi}(\mathbf{r}))e^{i(\mathbf{q}'-\mathbf{q})\boldsymbol{\xi}(\mathbf{r})})$. The local potential can be divided, in turn, into the Coulomb potential, the exchange-correlation potential, and the local part of the pseudopotential:

$$V_l(\boldsymbol{\xi}(\mathbf{r}))\equiv V_{\mathrm{Coul}}(\boldsymbol{\xi}(\mathbf{r}))+V_{\mathrm{xc}}(\rho(\boldsymbol{\xi}(\mathbf{r})))+V_l^{\mathrm{ps}}(\boldsymbol{\xi}(\mathbf{r})).$$

The matrix elements of the exchange-correlation potential and the local part of the pseudopotential $(k|V(\boldsymbol{\xi}(\mathbf{r}))|k')$ were calculated by Fourier transformation from the values on the uniform grid $\boldsymbol{\xi}(\mathbf{r})$.

The exchange-correlation potential V_{xc} in the local-density approximation and the exchange-correlation energy $\Phi_{\mathrm{xc}}=\int_{\Omega}d^3r\,(\varepsilon_{\mathrm{xc}}(\rho)\rho(\boldsymbol{\xi}(\mathbf{r})))$, where $\varepsilon_{\mathrm{xc}}(\rho)$, i.e., the exchange-correlation energy density, were taken from Ref. 10:

$$V_{\mathrm{xc}}(\boldsymbol{\xi}(\mathbf{r}))=\frac{\partial\Phi_{\mathrm{xc}}}{\partial\rho(\mathbf{r})}, \tag{3}$$

$$V_{\mathrm{xc}}(g)=\frac{1}{\Omega}\int\int\int_{\Omega}d^3r\,(V_{\mathrm{xc}}(\boldsymbol{\xi}(\mathbf{r}))e^{-i\mathbf{g}\boldsymbol{\xi}(\mathbf{r})}), \tag{4}$$

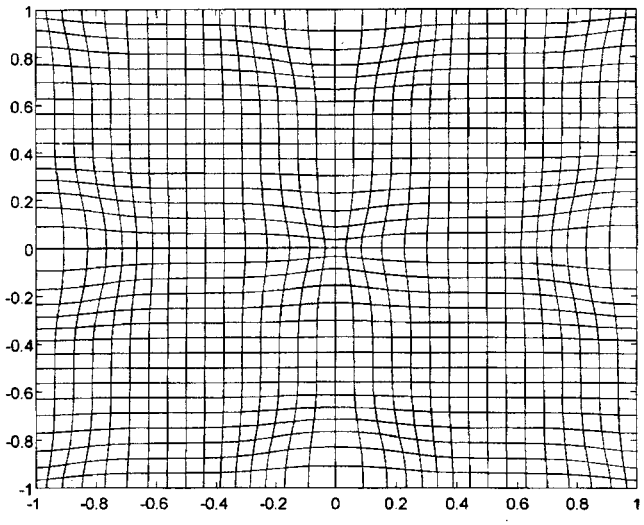

FIG. 2. Best mapping $\boldsymbol{\xi}=\boldsymbol{\xi}(\mathbf{r})$ $(N=339)$ for MgO.

$$V_l^{\mathrm{ps}}(g)=\frac{1}{\Omega}\int\int\int_{\Omega} d^3r\,(V_l^{\mathrm{ps}}(\boldsymbol{\xi}(\mathbf{r}))e^{-i\mathbf{g}\boldsymbol{\xi}(\mathbf{r})}). \tag{5}$$

The matrix elements of the nonlocal part of the pseudopotential have the form

$$(k|V_{nl}|k')=\sum_{i,l,m}(k(\boldsymbol{\xi}(\mathbf{r}))|Y_{lm}(\mathbf{r})\rangle V_{lm}(r) \times\langle Y_{lm}(\mathbf{r})|k'(\boldsymbol{\xi}(\mathbf{r})))e^{-i\mathbf{R}_i^0(\mathbf{k}-\mathbf{k}')}. \tag{6}$$

The electron density is expressed in the following manner

$$\rho(\boldsymbol{\xi}(\mathbf{r}))=\sum_{\nu}\Theta^{\nu}\lambda^{\nu *}(\boldsymbol{\xi}(\mathbf{r}))\chi^{\nu}(\boldsymbol{\xi}(\mathbf{r})), \tag{7}$$

$$\rho(g)=\sum_{\nu,g'}\Theta^{\nu}\chi^{\nu *}_{k+g'}\chi^{\nu}_{k+g+g'}. \tag{8}$$

Here and below Θ^{ν} is the occupation function of level ν.

The calculation of the Coulomb potential in the basis set $(1/\sqrt{\Omega})\,|\,\partial\boldsymbol{\xi}(\mathbf{r})/\partial\mathbf{r}\,|^{1/2}e^{i\mathbf{k}\cdot\boldsymbol{\xi}(\mathbf{r})}$ is a nontrivial problem, since while in ''flat'' space the Laplacian in the k representation has the form of a diagonal matrix $(\mathbf{k}+\mathbf{g})^2\delta_{g,g'}$, in the curved space $\boldsymbol{\xi}(\mathbf{r})$ the Laplacian has off-diagonal components [see the right-hand side of (2)]. The system of Poisson equations is written in the form

$$\sum_{k''}(k|\Delta|k'')(k''|V_{\mathrm{Coul}}|k')=-4\pi(k|\rho(\boldsymbol{\xi}(\mathbf{r}))|k') \equiv-4\pi\rho(\mathbf{k}-\mathbf{k}'). \tag{9}$$

The matrix of the Laplacian in any complete basis set has a minimum eigenvalue ε^0 equal to 0, which corresponds to the

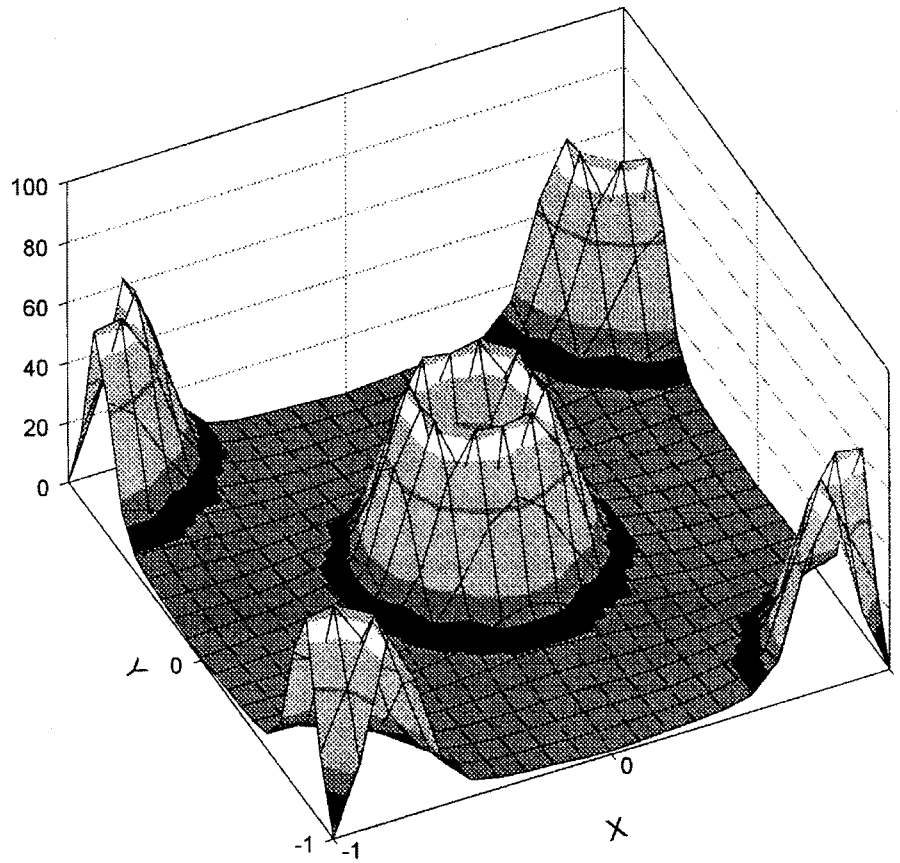

FIG. 3. Distribution of the electron density for MgO in $\boldsymbol{\xi}(\mathbf{r})$.

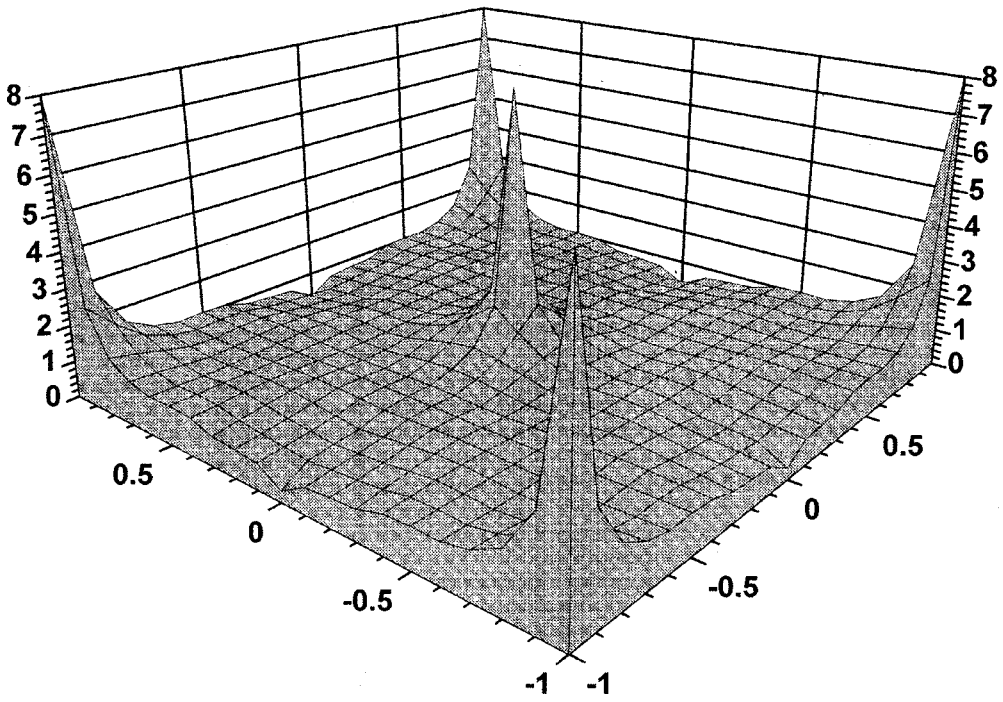

FIG. 4. Distribution of $|\partial\boldsymbol{\xi}(\mathbf{r})/\partial\mathbf{r}|$ for MgO in $\boldsymbol{\xi}(\mathbf{r})$.

solution-constant $C(\boldsymbol{\xi}(\mathbf{r}))=\text{const}$ from the degenerate subspace of eigenvectors in the space $\mathbf{r}$. Choosing $\mathbf{k}'\equiv\tilde{\mathbf{k}}'+\mathbf{g}=0$ allows the lowest eigenvector of the Laplacian ε^0 to describe the vector C. However, while the exclusion of this eigenvalue is trivial for a diagonal matrix, this is not the case for an off-diagonal matrix. To solve the system of equations, we utilize the orthogonality of the solution sought $V_{\text{Coul}}(\boldsymbol{\xi}(\mathbf{r}))$ and a vector from the degenerate subspace

$$C(\boldsymbol{\xi}(\mathbf{r}))=\sum_g C(g)\left|\frac{\partial\boldsymbol{\xi}(\mathbf{r})}{\partial\mathbf{r}}\right|e^{i\mathbf{g}\boldsymbol{\xi}(\mathbf{r})}.$$

This is a consequence of the electroneutrality of the crystal

$$\int\int\int_\Omega d^3r\,(V_{\text{Coul}}(\boldsymbol{\xi}(\mathbf{r}))+V_{\text{pseudo}}(\boldsymbol{\xi}(\mathbf{r})))=0$$

and the choice of the normalization

$$\int\int\int_\Omega d^3r\,(V_{\text{Coul}}(\boldsymbol{\xi}(\mathbf{r})))=0, \tag{10}$$

whence follows the orthogonality of V_{Coul} and the constant C. Next, choosing $\mathbf{k}'=0$ in (9) to obtain the minimum eigenvalue of the Laplacian and orthogonalizing the vector of the right-hand side relative to $C(g)(\rho\perp C)$, we can use the algorithms for solving a degenerate system of equations with a right-hand side that is orthogonal to a degenerate eigenvector (which has a unique solution) and go over from solving the system (9) to solving the system (11):

$$\sum_{k''}(k|(\Delta-\varepsilon^0)|k'')(k''|V_{\text{Coul}}|k'=0)$$
$$=-4\pi(k|\rho(\boldsymbol{\xi}(\mathbf{r}))|k'=0)\equiv-4\pi\rho(\mathbf{k}-\mathbf{0}). \tag{11}$$

In these calculations, because of the incompleteness of the basis set, we have $\varepsilon^0\approx3\times10^{-4}$, which can serve as an indirect quality factor of the basis set associated with the mapping $\boldsymbol{\xi}(\mathbf{r})$.

Although the relation (10) is satisfied, the curved space imposes the following conditions:

$$V_{\text{Coul}}(g=0)\neq0,\quad V_{\text{loc}}(g=0)\neq0.$$

The total binding energy of a crystal has the form

$$E/N=E_{\text{Mad}}/N+\frac{bZ}{\Omega}-\frac{1}{2}\sum_{\mathbf{g}}V_{\text{Coul}}(\mathbf{g})\rho(\mathbf{g})+V_{\text{Coul}}(\mathbf{g}=0)$$
$$+V_{\text{ps}}(\mathbf{g}=0)+\int\int\int_\Omega d^3r\,((\varepsilon_{\text{xc}}(\rho)$$
$$-\mu_{\text{xc}}(\rho))\rho(\mathbf{r}))+\frac{1}{N}\sum_\nu\Theta^\nu\varepsilon^\nu, \tag{12}$$

where E_{Mad} is the Madelung electrostatic energy, Z is the total charge of the unit cell, ε_F is the Fermi energy, which can be determined from the condition $Z=1/N\,\Sigma_{\varepsilon^\nu<\varepsilon_F}\Theta^\nu$, and bZ/Ω is the non-Coulomb part of the pseudopotential[12] in the limit $\mathbf{q}\to0$:

$$\frac{bZ}{\Omega}=\lim_{\mathbf{q}\to0}\left(\sum_s V_e^s(\mathbf{q})+\frac{4\pi Ze^2}{\mathbf{q}^2}\right). \tag{13}$$

TABLE I. Equilibrium parameters.

	Unit-cell parameter, Å			Bulk modulus, Mbar		
Crystal	Cartesian	curvilinear	exp.	Cartesian	curvilinear	exp.
MgO	3.74	4.18	4.21 Ref. 13	1.61	1.32	1.53 Ref. 15
BaO	4.03	5.19	5.54 Ref. 14	8.46	0.45	0.74 Ref. 16
NaCl	5.00	5.49	5.63 Ref. 15	0.530	0.238	0.245 Ref. 15
PbS	5.76	5.77	5.92 Ref. 16	0.96	0.763	0.62 Ref. 16

We note that the fictitious term associated with the space deformation energy[1–4] was not used in the Hamiltonian.

The mapping $\boldsymbol{\xi}(\mathbf{r})$ was chosen on the basis of the assumption of a correlation between $|\partial\boldsymbol{\xi}(\mathbf{r})/\partial\mathbf{r}|$ and the electron density and with the goal of describing $\boldsymbol{\xi}(\mathbf{r})$ by a small number of parameters.

On the basis of these considerations the mapping was chosen in the form of the additive sum of the contribution of each atom in the lattice, where each contribution is described by a Gaussian function of two parameters, viz., α and β:

$$\mathbf{r}=\boldsymbol{\xi}-\sum_i (\boldsymbol{\xi}-\boldsymbol{\xi}_i^0)\alpha_i e^{-\beta_i(\boldsymbol{\xi}-\boldsymbol{\xi}_i^0)^2}.$$

Here β_i characterizes the space-curving radius of action of the respective ion with the coordinate $\boldsymbol{\xi}_i^0$, and α_i describes the amplitude of the perturbation of space caused by that ion.

The total energy $E=E(\alpha_i,\beta_i)$ was minimized by direct minimization using a quasi-Newtonian minimization method.

II. RESULTS

The results obtained are presented in Figs. 1–4 and in Tables I and II.

Figure 1 shows the dependence of the binding energy E of a MgO crystal on the unit-cell volume V and on the number of basis functions for both the case of plane waves ($X_g \equiv\{\alpha_i,\beta_i\}\equiv 0$) and the case of curved plane waves ($X_g \neq 0$). It can be seen that the introduction of a curved space for any basis set is equivalent to a very significant increase in the number of basis functions in ''flat'' space. The very slow convergence of the binding energy with increasing size of the basis set in the standard approach can also be seen. The figure also shows the experimental value of the equilibrium unit-cell volume $V0$ and the binding energy from Ref. 17.

Figure 2 shows the best mapping $\boldsymbol{\xi}=\boldsymbol{\xi}(\mathbf{r})$ (for $N=339$) for a MgO crystal in the (001) plane. The figure exhibits thickening of the coordinate grid (along with an increase in the amplitude multiplier $|\partial\boldsymbol{\xi}(\mathbf{r})/\partial\mathbf{r}|^{1/2}$ of the basis functions) in the vicinity of the O ions, where the electron density reaches a maximum, and thinning of the coordinate grid in the vicinity of Mg ions. The curvature parameters for the crystals investigated are listed in Table II.

Figure 3 shows the distribution of the electron density (the coordinate Z) in the (001) plane (the coordinates X,Y) for MgO in the space $\boldsymbol{\xi}(\mathbf{r})$ within the range of nearest neighbors.

Figure 4 shows the distribution of the transition Jacobian $|\partial\boldsymbol{\xi}(\mathbf{r})/\partial\mathbf{r}|$ (the coordinate Z) in the analogous coordinates X,Y in the same space. A correlation can be seen between the electron density and the Jacobian. This correlation causes significant smoothing of the electron density in the space $\boldsymbol{\xi}(\mathbf{r})$, which leads to a decrease in the effective size of the Hamiltonian in $\boldsymbol{\xi}(\mathbf{r})$ and permits a sharp decrease in the necessary size of the basis set in this space.

Table I lists the equilibrium unit-cell parameters and the values of the bulk modulus in the crystals investigated when flat and curved spaces are used, as well as the experimental values. This table reveals significant underestimation of the unit-cell parameter and an error in the bulk modulus under the ordinary approach for all the crystals studied and considerably better agreement with experiment when curved coordinates are used.

Table II lists the curvature parameters α_i and β_i and the corresponding size of the basis set for all the crystals investigated. It can be seen that in these crystals the anions are described by positive values of α_i (which corresponds to ''thickening'' of the space at sites of larger electron density), while the cations are described by negative values (which correspond to thinning).

Thus, this method seems promising within the pseudopotential approach, since it permits significant (by 10- or more-fold) reduction in the size of the basis set. In addition, the calculation algorithm in $\boldsymbol{\xi}$ space differs only slightly from the standard algorithm. The data obtained reveal significant lowering of the energy in the calculations with a curved basis set, which is a consequence of the inaccurate description of pseudowave functions by plane waves near atoms, where the pseudopotential is most significant and where ''crushing'' of the grid cells owing to the curving of space permits a more exact description of the behavior of the pseudowave functions. Significantly better agreement with experiment can also be seen in the determination of the equilibrium unit-cell parameters.

Additional research aimed at more rapid determination of the optimal characteristics of the curved space would be desirable.

TABLE II. Curvature parameters.

Crystal	α_i	β_i	Basis set size
MgO	0.500/−0.503	0.991/0.688	339
BaO	0.476/−0.191	0.332/0.937	609
NaCl	0.172/−0.352	0.110/0.177	609
PbS	0.101/−0.220	0.992/0.497	339

We express our sincere thanks to V. I. Zinenko for some fruitful discussions.

This work was sported by the Russian Fund for Fundamental Research (Project 96-02-16542).

[1] F. Gygi, Europhys. Lett. **19**, 617 (1992).
[2] F. Gygi, Phys. Rev. B **48**, 11 692 (1993).
[3] D. R. Hamann, Phys. Rev. B **51**, 7337 (1995).
[4] D. R. Hamann, Phys. Rev. B **51**, 9508 (1995).
[5] R. Car and M. Parinello, Phys. Rev. Lett. **55**, 2471 (1985).
[6] D. Vanderbilt, Phys. Rev. B **41**, 7892 (1990).
[7] P. E. Blöchl, Phys. Rev. B **50**, 17 953 (1994).
[8] J. Ihm, A. Zunger, and M. L. Cohen, J. Phys. C **12**, 4409 (1979).
[9] G. B. Bachelet, D. R. Hamann, and M. Schlüter, Phys. Rev. B **26**, 4299 (1982).
[10] J. Perdew and A. Zunger, Phys. Rev. B **23**, 5048 (1981).
[11] D. M. Ceperley and V. J. Alder, Phys. Rev. B **18**, 3126 (1978).
[12] E. G. Brovman and Yu. M. Kagan, Usp. Fiz. Nauk **112**, 369 (1974) [Sov. Phys. Usp. **17**, 125 (1974)].
[13] G. Kalpana, B. Palanivel, and M. Rajagopalan, Phys. Rev. B **52**, 4 (1995).
[14] S. A. Chang, C. W. Tompson, E. Gurnen, and L. D. Muhlestein, J. Phys. Chem. Solids **36**, 769 (1975).
[15] C. Kittel, *Introduction to Solid State Physics*, 5th ed. (Wiley, New York, 1976; Nauka, Moscow, 1978).
[16] *Physical Constants* [in Russian], Énergoatomizdat, Moscow (1991).
[17] M. J. Mehl, R. J. Hemley, and L. L. Boyer, Phys. Rev. B **33**, 8685 (1986).

Translated by P. Shelnitz

DEFECTS, DISLOCATIONS, PHYSICS OF STRENGTH

Local order parameters at a dipolar $Gd^{3+}-O^{2-}$ center in $CsSrCl_3$ and paramagnetic resonance

V. A. Vazhenin,*) M. Yu. Artemov, and V. B. Guseva

Institute of Physics and Applied Mathematics, Ural University, 620083 Ekaterinburg, Russia
(Submitted June 22, 1998)
Fiz. Tverd. Tela (St. Petersburg) **41**, 247–251 (February 1999)

The angular dependence of the EPR spectrum of a tetragonal (in the paramagnetic phase) $Gd^{3+}-O^{2-}$ center with large initial splitting is used to determine the rotation angles of the neighboring chlorine octahedron, which are related to the components of rotation modes, in the vicinity of room temperature. Aspects of the anomalous broadening of the EPR lines near structural transformations are discussed. © *1999 American Institute of Physics.* [S1063-7834(99)01202-2]

1. In Refs. 1–6 electron paramagnetic resonance (EPR) was used to investigate and establish the sequence

$$O_h^1 \xrightarrow{[00\psi]} D_{4h}^5 \xrightarrow{[0\varphi\psi]} D_{2h}^{17} \xrightarrow{[\varphi_2\varphi_1\psi]} C_{2h}^2 \qquad (1)$$

of first-order structural transitions in $CsSrCl_3$, which occur as a result of the condensation of M_3 and R_{25} rotational modes. The probes used in those studies were Gd^{3+} ions, which replace Sr^{2+} ions within a chlorine octahedron and are compensated either nonlocally (centers of type *1*) or by a neighboring strontium vacancy (centers of type *2*). The choice of the rotation angle of the principal axes of the fourth-rank fine-structure tensor as the rotation angle of an octahedron during a structural transition (the sixth-rank parameters are determined with a large error, and the second-rank parameters contain contributions from the deformation of the octahedron caused by its rotation) showed that the values of the angles for centers of type *2* with $CA\|\psi$ or $CA\|\varphi$, where CA denotes the compensation axis, and for centers of type *1* are close and agree well with the estimates from x-ray structural investigations, while the presence of a compensator (center *2*) in the rotation plane sharply diminishes the local rotation of the octahedron.[5,6]

Similar reduction of the local rotation angle was observed in $SrTiO_3$ at Fe^{3+} centers associated with an oxygen vacancy $[\varphi(T)=(1.59\pm 0.05)\varphi_{\rm loc}(T)$ (Ref. 17)] with the one difference that the oxygen vacancy was located at a peripheral site in a neighboring octahedron, while the Sr^{2+} vacancy in $CsSrCl_3$ is located at the center of a neighboring octahedron and cannot participate in the rotation of the octahedron containing the paramagnetic ion.

The $CsSrCl_3$ crystals investigated exhibit a tetragonal spectrum with large initial splitting (a spectrum of type *3*), which should be assigned to a Gd^{3+} center with compensation by an O^{2-} ion in a chlorine position of a neighboring octahedron.[4] A comparison of the rotation of an octahedron containing a center of type *3* near structural transitions with the behavior of $Fe^{3+}-V_0$ centers in strontium titanate is complicated by the rapidly growing width of the line for center *3* (Fig. 1). The treatment of the data in Fig. 1 gives the dependence $1/T_1=10^{-5}T^5$ Hz for the spin-lattice relaxation rate.

Unlike center *3*, the signals of centers *1* and *2* scarcely broaden in the temperature range of interest (their width is $\sim$0.5 mT), and at $T<200$ K they undergo noticeable saturation at a microwave power of the order of a few milliwatts.

2. As has already been noted, near the structural transformations of $CsSrCl_3$, it is difficult to obtain information on local distortions from the ESR spectrum of the centers of type *3* because of the large linewidth. However, sufficiently resolved angular dependences of the EPR spectrum, which are suitable for estimating the local rotation angles of the octahedron, can be obtained already in the vicinity of room temperature (Figs. 2 and 3).

Samples that are essentially monodomain relative to ψ were used for the measurements. They were selected from crystals grown by A. E. Usachev and maintain their domain structure after being in the cubic phase. In the second and third low-symmetry phases there are three nonequivalent centers of type *3* with C_i symmetry. In analogy to the centers of type *2* (Ref. 6), we use the following notations:

$$\begin{aligned}
&\text{center } 3\| \text{ — } z\|\psi\|\text{CA},\ y\|\varphi_1,\ x\|\varphi_2;\\
&\text{center } 3\perp 1 \text{ — } z\|\text{CA}\|\varphi_2,\ y\|\psi,\ x\|\varphi_1;\\
&\text{center } 3\perp 2 \text{ — } z\|\text{CA}\|\varphi_1,\ y\|\psi,\ x\|\varphi_2,
\end{aligned} \qquad (2)$$

where x, y, and z are the axes of the local coordinate system. The ESR spectrum of each of these centers in an arbitrary orientation of the magnetic field is split into eight spectra differing with respect to the relationship between the signs of three order parameters.

It was shown in Refs. 5 and 6 that the determination of the local rotation angles of an octahedron requires a thorough analysis of the measured rotation angles of the principal axes of various fine-structure tensor operators, whose combined

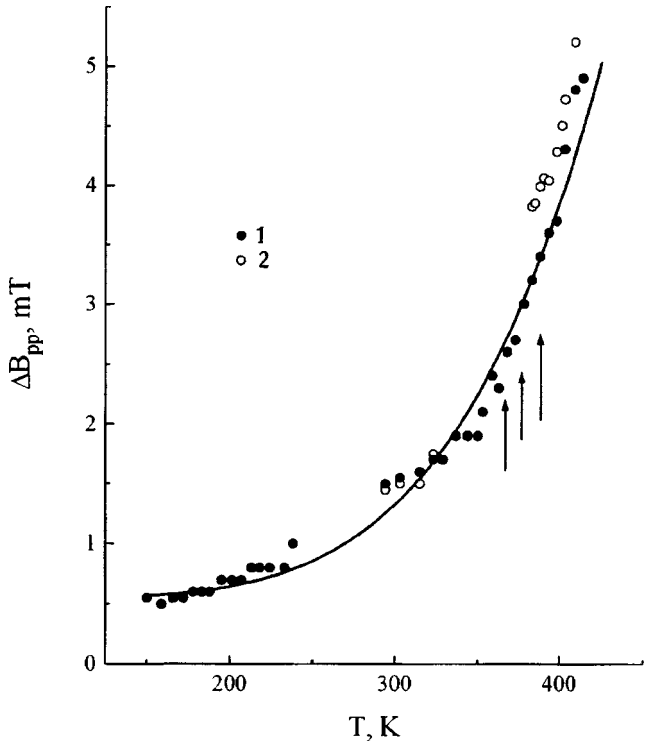

FIG. 1. Temperature dependence of the linewidth assigned to the $5\leftrightarrow6$ transition of a center of type *3* for $\mathbf{B}\|\psi\perp$ CA (points *1*; the signal investigated overlaps another signal in the range 250−300 K) and for $\theta=69.5°$ (points *2*; splitting of the signal, which is concealed in the linewidth, occurs in the range 310−380 K). The arrows indicate the temperatures of the structural transitions, and θ is the angle between **B** and the compensation axis.

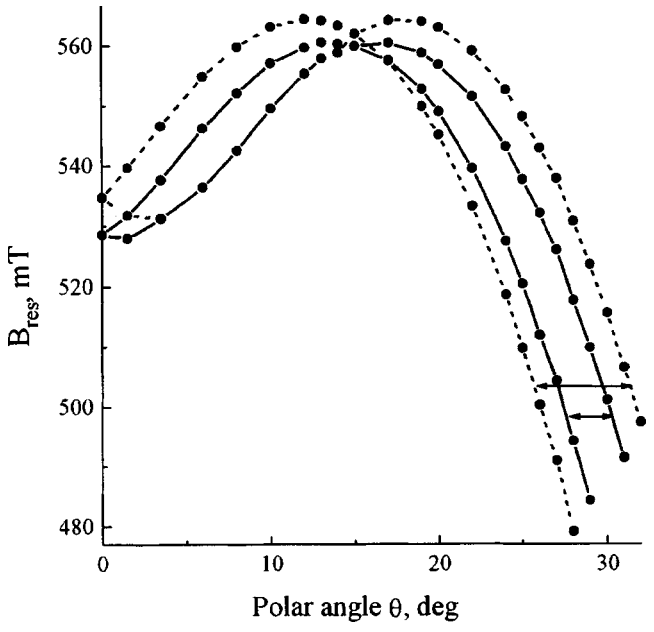

FIG. 2. Angular dependence of the resonant positions of the $5\leftrightarrow6$ transition of centers of type $3\perp$ ($T=298$ K, the azimuthal angle $\bar{\varphi}=90°$, and the minima on the plots are at $\theta=0°$ in the cubic phase).

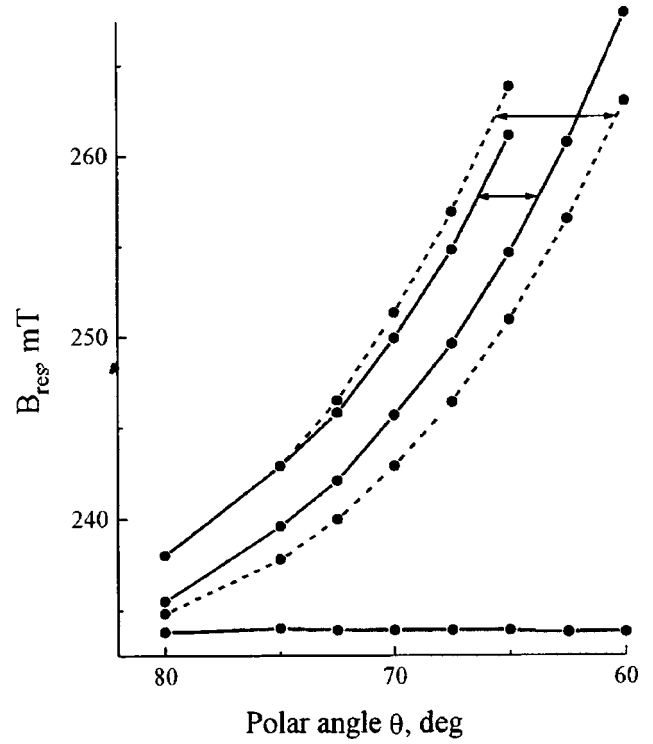

FIG. 3. Angular dependence of the resonant positions of the $5\leftrightarrow6$ transition of centers of type $3\perp$ at $T=313$ K ($\bar{\varphi}=90°$, and the horizontal plot belongs to a center which exhibits an azimuthal dependence).

action leads to low-symmetry effects (particularly, to disparity between the positions of the extrema of the angular dependences of different EPR transitions)[8] and renders the angular dependences uninformative (in the sense of direct determination of the degree of rotation of the octahedron).

Unlike the second center, a center of type *3* is essentially axial (b_{20} dominates[4]). This axis is rigidly associated with the neighboring octahedron, and the principal axes of its fourth- and sixth-rank fine-structure tensors should also be determined mainly by the orientation of the chlorine octahedron. For this reason, we can hope to determine the degree of rotation of the principal axis of the center (the compensation axis) in a plane perpendicular to the rotation axis of the octahedron by measuring the shift of the angular dependence of the EPR spectrum, as in Ref. 7, with neglect of the effects of the other order parameters.

Examples of measurements of the local rotation angles of an octahedron associated with φ_1 and φ_2 for centers of type $3\perp$ are presented in Figs. 2 and 3, where the arrows show the doubled shift (the doubled local rotation angle of the octahedron) of the angular dependence. As in Refs. 2 and 9, the behavior of the squares of the rotation angles thus measured ($b_{20}\sim\varphi^2$) far from the structural transformations is linear with respect to temperature (Fig. 4). These dependences cannot be assigned to φ_1 and φ_2 on the basis of the existing experimental data. This question was resolved by eliciting the results in Ref. 4, where it was concluded that φ_1 and φ_2 are approximately equal near the third structural transition on the basis of the temperature dependences of the positions of the EPR transitions of centers *1* and *2*. Assuming that the temperature dependence of φ_1 and φ_2 near the struc-

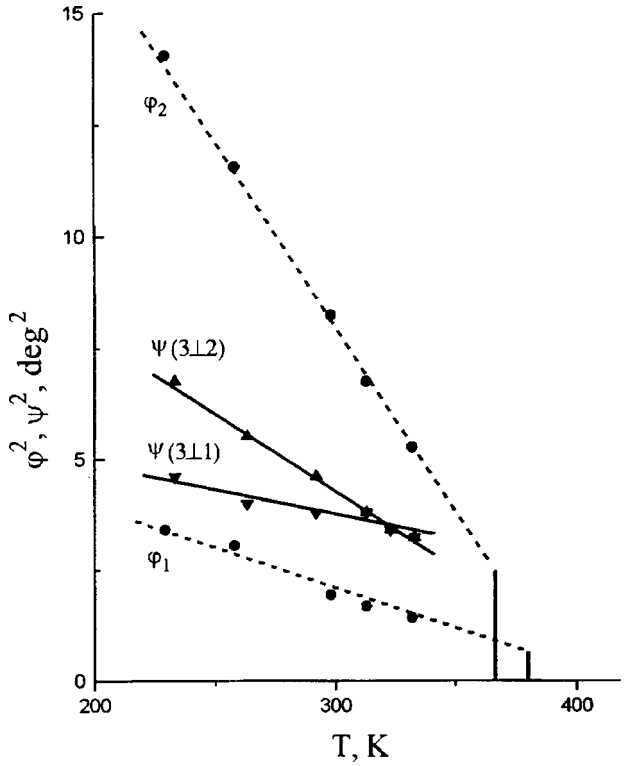

FIG. 4. Temperature dependence of the local rotation angles of the octahedron for centers of type $3\perp$ (no measurements were performed near the transition, and the dependence shown is schematic).

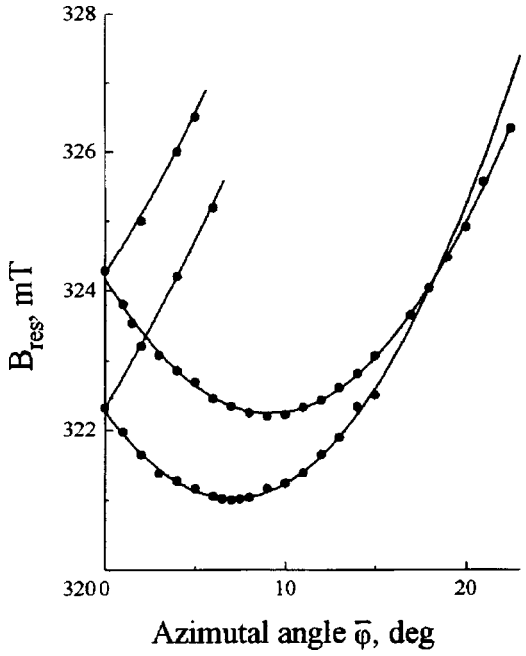

FIG. 5. Angular dependence of the resonant positions of the $5\leftrightarrow 6$ transition of a center of type *1* at room temperature. The magnetic field **B** rotates in the $\perp\psi$ plane of the dominant domain, and the two signals at $\bar{\varphi}=0°$ correspond to centers in domains with $\varphi_1\|\mathbf{B}$ and $\varphi_2\|\mathbf{B}$.

tural transitions is qualitatively the same as in Fig. 4, we obtain the predicted equality. The figure also shows plots of the local rotation angle due to the order parameter ψ for $3\perp$ centers, which were also determined from the shift of the angular dependence, but for a different orientation of the monodomain sample.

Since the rotation angles of the octahedron at center *1* in the first and second low-symmetry phases correlate well with the order parameters in the pure crystal,[5,6] and since the low-symmetry effects are weak, it is reasonable to expect that the angular dependences in Fig. 5 can serve as a source for estimating the value of ψ at room temperature ($\sim 8°$, see Table I). Figure 5 clearly shows the disparity between the positions of the extrema of the angular dependences of centers from two domains with the same orientation ψ due to the contributions of other order parameters. The estimates of φ_1 and φ_2 obtained at a previously cubic center in a different geometry are also listed in Table I.

The results of the measurements of the shift of the angular dependences (of local rotation angles of the octahedron) caused by the condensation of φ_1 and φ_2 at a $3\|$ center (the rotation due to ψ at this center cannot be measured because of its axiality) are presented in Table I and in Fig. 6. The temperature dependences obtained have appreciably larger errors than in the case of $3\perp$ primarily because of the low intensity of the EPR signals of these centers.

The weakness of the transitions of center $3\|$ is associated with the unusual (in comparison to the centers of type *2*) intensity ratio of $3\|$ and $3\perp$, which is clearly visible in Fig. 7 (similar results were obtained for other transitions). It might be theorized (Fig. 7) that the concentration of $3\|$ centers in the dominant domain is appreciably lower than the concentration of $3\perp$ centers. However, the observation, as expected, of equal intensities of the differently oriented centers of type *3* in the cubic phase and the very low probability of alteration of their orientations in the low-temperature phases forces us to reject such an hypothesis. The scarcely observable effect can be attributed to the difference between the transition probabilities, i.e., the perturbations due to structural transitions which cause the inequivalence of $3\|$ and $3\perp$ are exceedingly small. The estimation of $\Delta b_{20}(\psi,\varphi_1,\varphi_2)$ and consequently of $\Delta b_{22}(\psi,\varphi_1,\varphi_2)$ at room temperature from the data in Fig. 7 yields a value of ~ 100 MHz. The mixing of the states due to such parameters and, therefore, the changes in the transition probabilities will amount to no more than a few percent.

Incidentally, the value of $\Delta b_{20}(\psi)$ for the third center, unlike the values for centers *1* and *2*,[5,6] is negative. The positive sign of this parameter for centers *1* and *2* leads to the conclusion that the defect-containing chlorine octahedron is compressed along the rotation axis during the first phase transition. The opposite sign of $\Delta b_{20}(\psi)$ for center *3* is probably an indication of elongation of the neighboring octahe-

TABLE I. Values of the local rotation angles of the neighboring chlorine octahedron at room temperature (in degrees).

Rotation angles	Center $3\perp 1$	Center $3\perp 2$	Center $3\|$	Center $1\|$
ψ	1.9	2.1	–	8
φ_1	1.4	–	1.8	4.5
φ_2	–	2.9	2.2	6.5

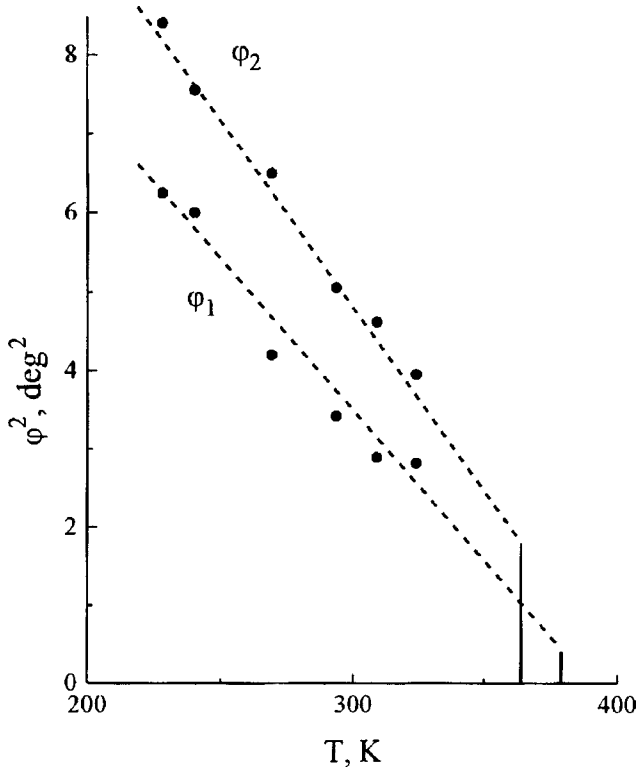

FIG. 6. Temperature behavior of the local rotation angles of the octahedron for centers of type $3\perp$.

dron, although the presence of the compensator ion in it renders the performance of a superposition analysis extremely difficult.[5,6]

The reason for the unusual intensity ratio of the $3\|$ and $3\perp$ spectra can be the small difference between the linewidths, as well as the fact that the line shape for center $3\|$ is somewhat closer to a Lorentzian than is the $3\perp$ line shape.

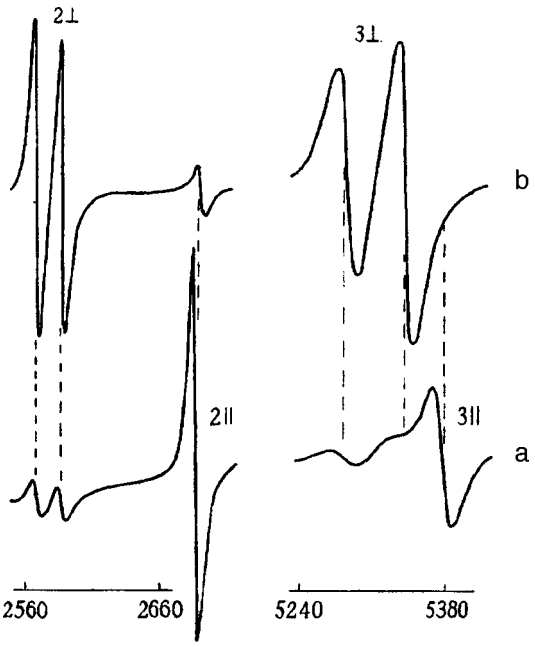

FIG. 7. EPR spectrum of centers of types *2* (the $2\leftrightarrow3$ transition) and *3* (the $5\leftrightarrow6$ transition) for CA$\|\mathbf{B}$ at room temperature. *a* — $\mathbf{B}\|\psi$ for the dominant domain, *b* — $\mathbf{B}\perp\psi$ for the dominant domain.

Thus, the presence of a charge-compensating defect (an O^{2-} ion) in the first coordination sphere of the paramagnetic Gd^{3+} ion leads to a decrease (by a factor of 2–4) in the rotation angles of the neighboring octahedron caused structural transitions, apparently without imparting additional features to the temperature behavior of these rotations.

3. The centers of types *1* and *2* do not exhibit special features in the behavior of the linewidths upon phase transitions, as was previously noted in Refs. 2 and 6. Measurement of the temperature dependence of the linewidth of center *3* for both $\mathbf{B}\|\psi\perp$CA and polar angles of the magnetic field differing from 90° (Fig. 1) likewise did not reveal any features in the vicinity of the phase transformations.

The anomalous increase in the inhomogeneous width of the EPR lines near structural transformations has been investigated most thoroughly in crystals of $SrTiO_3$ ($Fe^{3+}-V_O$),[7,10] $KTaO_3$ ($Fe^{3+}-V_O$, Fe^{3+}),[11,12] and $Pb_5Ge_3O_{11}$ (Gd^{3+}),[13] which undergo a second-order phase transition. In particular, in these studies the spin-Hamiltonian parameter, whose fluctuations contribute to the broadening of a line near a phase transition, was determined by measuring the angular dependence of the anomalous linewidth. It was presumed[11–13] or theorized[10] that the static fluctuations indicated appear as a result of the interaction of the paramagnetic ions with lattice defects through a soft mode. A significant increase in the linewidth in the vicinity of a structural transition was observed in triglycine sulfate (Cr^{3+})[14] and $(CH_3NH_2+CH_2COO^-)_3\cdot CaCl_2$ (Mn^{2+}),[15] where the effect was attributed to an anomalous increase in the spin-spin relaxation rate.

The critical broadening of EPR lines in crystals with first-order structural transitions has been discovered in $BaTiO_3$ with Mn^{2+},[16] $PbTiO_3$ with Fe^{3+},[17] $RbCaF_3$ with $Gd^{3+}-O^{2-}$,[18] $CH_3NH_3Al(SO_4)_2\cdot12H_2O$ with Cr^{3+},[19] $CH_3NH_3Ga(SO_4)_2\cdot12H_2O$ and $CH_3NH_3Al(SeO_4)_2\cdot12H_2O$ with Cr^{3+},[20] $NH_4Al(SO_4)_2\cdot12H_2O$ with Cr^{3+},[21] and $Pb_3(PO_4)_2$ with Mn^{2+} and Gd^{3+}.[22] In some cases, because of the constancy of the line shape in the temperature range investigated[19,22] or the absence of an appreciable angular dependence of the anomalous linewidth,[18,22] it can be presumed that the effect is caused by features in the behavior of the relaxation rate.

In the case of nonferroelectric first-order structural transitions the magnitude of the inhomogeneous broadening of lines in the EPR spectrum of the high-temperature phase due to modulation of the order parameter should depend on the relation between the original width ΔB and the magnitude of the jump in the EPR spectrum δB. When $\delta B>\Delta B$, because of the small probability of the formation of configurations of the paramagnetic center having spectra differing slightly from that of the most probable configuration, the inhomogeneous broadening of the lines should be very small. Such a situation is probably realized in the spectra of an isolated Gd^{3+} ion and of $Gd^{3+}-V_{Sr}$ in $CsSrCl_3$ ($\Delta B\sim0.5$ mT, and $\delta B\sim2$ mT). On the other hand, when $\Delta B\gg\delta B$ (for $Gd^{3+}-O^{2-}$ in $CsSrCl_3$ near the transition $\Delta B>3$ mT, and $\delta B<1$ mT) the broadening of the lines should also not be

large, since the anomalous width is proportional to δB in this case.

We express our sincerest thanks to A. E. Usachev for the single crystals provided.

*)E-mail: vladimir.vazhenin@usu.ru

[1] A. E. Usachev, Yu. V. Yablokov, L. A. Pozdnyakova, and K. S. Aleksandrov, Fiz. Tverd. Tela (Leningrad) **19**, 2156 (1977) [Sov. Phys. Solid State **19**, 1263 (1977)].
[2] A. E. Usachev, Yu. V. Yablokov, and S. G. L'vov, Fiz. Tverd. Tela (Leningrad) **23**, 1439 (1981) [Sov. Phys. Solid State **23**, 838 (1981)].
[3] M. V. Chernitskiĭ, V. A. Vazhenin, A. E. Nikiforov, A. E. Usachev, A. I. Krotkiĭ, and M. Yu. Artemov, Fiz. Tverd. Tela (Leningrad) **33**, 3577 (1991) [Sov. Phys. Solid State **33**, 2011 (1991)].
[4] V. A. Vazhenin, K. M. Starichenko, M. Yu. Artemov, and M. V. Chernitskiĭ, Fiz. Tverd. Tela (Leningrad) **34**, 1633 (1992) [Sov. Phys. Solid State **34**, 866 (1992)].
[5] V. A. Vazhenin, K. M. Starichenko, M. Yu. Artemov, and A. E. Nikiforov, Fiz. Tverd. Tela (St. Petersburg) **36**, 2695 (1994) [Phys. Solid State **36**, 1470 (1994)].
[6] V. A. Vazhenin and M. Yu. Artemov, Fiz. Tverd. Tela (St. Petersburg) **39**, 370 (1997) [Phys. Solid State **39**, 323 (1997)].
[7] T. Von Waldkirch, K. A. Müller, and W. Berlinger, Phys. Rev. B **5**, 4324 (1972).
[8] M. L. Meĭl'man and M. I. Samoĭlovich, *Introduction to the EPR Spectroscopy of Activated Crystals* [in Russian], Atomizdat, Moscow (1977), 270 pp.
[9] J. J. Rousseau, A. Leble, J. Y. Buzare, and J. C. Fayet, Ferroelectrics **12**, 201 (1976).
[10] G. F. Reiter, W. Berlinger, K. A. Müller, and P. Heller, Phys. Rev. B **21**, 1 (1980).
[11] B. E. Vugmeĭster, M. D. Glinchuk, A. P. Peyaenyĭ, and B. K. Krulikovskiĭ, Zh. Éksp. Teor. Fiz. **82**, 1347 (1982) [Sov. Phys. JETP **55**, 783 (1982)].
[12] B. E. Vugmeĭster, V. V. Laguta, I. P. Bykov, I. V. Kondakova, and P. P. Syrnikov, Fiz. Tverd. Tela (Leningrad) **31**(2), 54 (1989) [Sov. Phys. Solid State **31**, 205 (1989)].
[13] V. A. Vazhenin, E. L. Rumyantsev, M. Yu. Artemov, and K. M. Starichenko, Fiz. Tverd. Tela (St. Petersburg) **40**, 321 (1998) [Phys. Solid State **40**, 293 (1998)].
[14] K. Nishimura and T. Hashimoto, J. Phys. Soc. Jpn. **35**, 1699 (1973).
[15] R. Lippe, W. Windsch, G. Volkel, and W. Schulga, Solid State Commun. **19**, 587 (1976).
[16] V. V. Shapkin, B. F. Gromov, G. T. Petrov, Ya. G. Girshberg, and É. V. Bursian, Fiz. Tverd. Tela (Leningrad) **15**, 1401 (1973) [Sov. Phys. Solid State **15**, 947 (1973)].
[17] S. T. Kirillov and Yu. G. Plakhotnikov, JETP Lett. **34**, 548 (1981).
[18] J. Y. Busare and P. Simon, Ferroelectrics **54**, 115 (1984).
[19] D. E. O'Reilly and Tsang Tung, Phys. Rev. **157**, *2*, 417 (1967).
[20] R. Navalgund and L. C. Gurta, Ferroelectrics **14**, 767 (1976).
[21] F. J. Owens, Phys. Status Solidi B **79**, 623 (1977).
[22] M. Razeghi, Phys. Status Solidi B **108**, 175 (1981).

Translated by P. Shelnitz

Features of slip-band formation during the plastic straining of layered crystals

G. A. Malygin

A. F. Ioffe Physicotechnical Institute, Russian Academy of Sciences, 194021 St. Petersburg, Russia
(Submitted July 15, 1998)
Fiz. Tverd. Tela (St. Petersburg) **41**, 252–258 (February 1999)

The effects of the narrowing and branching of screw slip bands during the plastic straining of nonuniformly doped or nonuniformly irradiated (layered) crystals are discussed theoretically on the basis of the equations of dislocation kinetics. Band formation is treated as a process involving the self-organization of dislocations in a dislocation ensemble at the mesoscopic level. The distributions of the densities of mobile and immobile dislocations, as well as of the local plastic strain rate, in a slip band propagating in a layered crystal are obtained. It is found that the narrowing of bands is due to the lower rate of broadening of the bands in stiff layers than in soft layers, which have not been hardened by doping or irradiation, and that branching is due the low local strain rate in stiff layers compared with the strain rate per slip band assigned by the straining machine. In the latter case the nucleation of new bands or the branching of existing bands is required to restore the balance between these rates. © *1999 American Institute of Physics.* [S1063-7834(99)01302-7]

It has been discovered during the plastic straining of layered (nonuniformly doped[1–3] or nonuniformly irradiated[4]) single crystals that the formation of slip lines and bands in them is sensitive to the stiffness of the layers. For example, in LiF crystals which have regions (layers) with an increased concentration of Mg^{2+} or have been x irradiated, the passage of screw slip bands from ''soft'' (undoped and unirradiated) into ''stiff'' (stiffened) layers is accompanied by a considerable (five- to sixfold) increase in the density of screw dislocations[3] and the formation of unstrained dislocation-free regions within the bands.[3,4] Such ''splitting'' of the bands into individual narrower slip bands attests to the increased localization of strain in the stiff layers in comparison to the soft layers. The reverse passage of the screw bands from hardened to unhardened regions is accompanied by restoration of the disperse character of the distribution of dislocations in them. Strain localization and delocalization have been revealed by selective etching.[2–4]

It was also discovered in Refs. 2–4 that the penetration of screw bands into stiff layers does not always lead to splitting (branching) of a band into individual, narrower bands and that it can be accompanied by narrowing of the bands alone. Band narrowing is construed as a general uniform decrease in the width of a band upon its penetration into a hardened layer, as well as a small gradual decrease in the width of the band as this penetration proceeds. As for edge slip bands, their propagation from unhardened into hardened regions is not accompanied by the effects just described.[3,4] This finding indicates that strain localization and delocalization are associated with the mobility of screw dislocations in the direction transverse to the dislocation slip plane and with the ability of screw dislocations to undergo multiplication by double cross slip, whose parameters depend strongly on the doping level and irradiation dose of the crystal.[5,6]

Since the formation of slip bands is a result of the self-organization of dislocations, which takes place in a dislocation ensemble at the mesoscopic level,[7] it is clear that the observed features of the formation of slip bands in layered crystals should be explicable within a kinetic (synergetic) approach to these phenomena. This paper is intended to solve this problem. The first section presents the kinetic equations for the densities of mobile and immobile dislocations needed for this purpose and their corresponding solutions. The narrowing of slip bands as they propagate from an unhardened layer into a hardened layer is considered, and quantitative characteristics of this process are obtained in the second section. The branching of bands upon passage from soft into stiff regions is discussed in the third section of this paper.

I. EQUATIONS DESCRIBING THE EVOLUTION OF THE DISLOCATION DENSITY

The equations describing the evolution of the density of mobile $[\rho_m(x,y,t)]$ and immobile $[\rho_i(x,y,t)]$ dislocations, which characterize the formation of slip bands elongating in the direction of the x axis and broadening in the direction of the y axis, have the form[7]

$$t_m \frac{\partial \rho_m}{\partial t} = (R_x^{(m)})^2 \frac{\partial^2 \rho_m}{\partial x^2} + (R_y^{(m)})^2 \frac{\partial^2 \rho_m}{\partial y^2} + n\lambda_m + \rho_m - \beta \rho_i , \tag{1a}$$

$$\rho_i(x,y,t) = (R_x^{(i)} R_y^{(i)})^{-1} \int_x^\infty e^{-\frac{|x-x'|}{R_x^{(i)}}} dx' \times \int_y^\infty e^{-\frac{|y-y'|}{R_y^{(i)}}} \rho_m(x',y',t)\, dy' . \tag{1b}$$

Here t is the time; $t_m = \lambda_m / u$ and λ_m are, respectively, the characteristic times and the distance between acts of dislocation multiplication by a mechanism involving the double cross slip of screw dislocations; u is the dislocation velocity;

n is the density of dislocation sources of the Frank–Read type; and β is the relative immobilization coefficient of dislocations in dipoles. The parameters $R_{x,y}^{(m)}$ and $R_{x,y}^{(i)}$ specify the characteristic scales of the self-organization of mobile and immobile dislocations as a band elongates and broadens. They depend on the kinetic coefficients determining the rate of the dislocation multiplication, immobilization, and diffusion processes.[7] Doping and irradiation of a crystal strongly influence the kinetic coefficients[5,6] and, consequently, the parameters $R_{x,y}^{(m)}$ and $R_{x,y}^{(i)}$ and the relationship between them, which, in turn, have an influence on the formation of slip bands.

Equation (3) has a linear character and allows a separation of variables. We are interested in solutions of this equation of the traveling autowave type, i.e., slip bands which elongate in the x direction and broaden in the y direction:

$$\rho_m(Z_x,Z_y)=\rho_{m0}[1-\exp(Z_x+Z_y)], \quad Z_x+Z_y<0,$$
$$\rho_m(Z_x,Z_y)=0, \quad Z_x+Z_y>0; \tag{2a}$$
$$\rho_i(Z_x,Z_y)=\rho_{i0}[1-M\exp(Z_x+Z_y)],$$
$$\rho_i(Z_x,Z_y)=0, \quad Z_x+Z_y>\ln M^{-1}; \tag{2b}$$
$$Z_x=g_xX-S_x\tau, \quad Z_y=g_yY-S_y\tau,$$
$$M=\frac{a_xa_y}{(a_x-g_x)(a_y-g_y)}. \tag{2c}$$

Here $X=x/R_x^{(m)}$, $Y=y/R_y^{(m)}$, and $\tau=t/t_m$. Substituting (2a) into (1), we can find the conditions for the existence of such solutions:

$$S_x+S_y=\frac{\beta a_xa_y}{(a_x-g_x)(a_y-g_y)}-(1+g_x^2+g_y^2),$$
$$g_x<a_x, \quad g_y<a_y, \quad S_x+S_y>\beta-1, \tag{3a}$$

where

$$a_x=R_x^{(m)}/R_x^{(i)}, \quad a_y=R_y^{(m)}/R_y^{(i)},$$
$$\rho_{m0}=\frac{n\lambda_m}{\beta-1}, \quad \rho_{0i}=\frac{\delta_i}{\delta_{ai}}\rho_{m0}, \tag{3b}$$

ρ_{m0} and ρ_{i0} are the stationary densities of the mobile and immobile dislocations, and δ_i and δ_{ai} are the dislocation immobilization and screw-dipole annihilation coefficients, respectively.[7] In order for the process involving the self-organization of dislocations and the formation of spatially inhomogeneous dislocation structures to appear, the parameters of Eq. (1) must satisfy the conditions $a_x<1$, $a_y<1$, and $\beta>1$.[7] The density of immobile dislocations ρ_i was obtained by integrating (1b).

The parameters $g_{x,y}$ and $S_{x,y}$ of the solution (2) are related by (3a) and depend on the boundary conditions. The latter include the balance of plastic strains

$$\varepsilon=N(m_x\gamma_x+m_y\gamma_y)w/l_0 \tag{4a}$$

and the balance of the plastic strain rates in the crystal for a single slip

$$\dot{\varepsilon}_0=2N(m_x\dot{\gamma}_x+m_y\dot{\gamma}_y)\Delta w/l_0. \tag{4b}$$

Here N is the number of active slip bands in the crystal; m_x and m_y are orientational factors; $\gamma_x=b\lambda_m\rho_{m0}$ and $\gamma_y=b\overline{h}\rho_{m0}$ are the degrees of shear in the slip band,[7] b is the Burgers vector, $\overline{h}$ is the mean distance for emergence of the screw segment in the transverse slip plane, w is the band width, l_0 is the length of the crystal, $\dot{\varepsilon}_0$ is the plastic strain rate assigned by the straining machine, $\dot{\gamma}_{x,y}$ are the plastic strain rates associated with the dislocation motion in the original slip plane and in the transverse slip plane, respectively; and Δw is the width of the slip band edge. Because of strain hardening, the values of $\dot{\gamma}_{x,y}$ are highest on the dislocation band edge:

$$\dot{\gamma}_x=U_x(\partial\gamma_x/\partial x), \quad \gamma_x=b\lambda_m\rho_m(Z_x,Z_y),$$
$$\dot{\gamma}_y=U_y(\partial\gamma_y/\partial y), \quad \gamma_x=b\overline{h}\rho_m(Z_x,Z_y). \tag{5a}$$

Here

$$U_x=\frac{S_x}{g_x}\left(\frac{R_x^{(m)}}{\lambda_m}\right)u, \quad U_y=\frac{S_y}{g_y}\left(\frac{R_y^{(m)}}{\lambda_m}\right)u \tag{5b}$$

are the components of the slip band edge velocity according to (2). The derivatives in (5a) are found when $Z_x+Z_y=0$. As a result, we obtain the relation for determining S_x and S_y

$$m_xS_x+m_yS_y\frac{\overline{h}}{\lambda_m}=\frac{\dot{\varepsilon}_0l_0}{2N\dot{\gamma}\Delta w}, \quad \dot{\gamma}=b\rho_{m0}u. \tag{6}$$

An additional boundary condition is the condition of conservation of the planar character of the plastic flow front

$$\frac{U_y}{U_x}=\frac{S_y}{S_x}\frac{g_x}{g_y}\left(\frac{R_y^{(m)}}{R_x^{(m)}}\right)=\tan\varphi, \quad \tan\varphi=R_y^{(m)}/R_x^{(m)}, \tag{7}$$

where φ is the angle between the front surface and the crystallographic slip plane. The angle φ specifies the value of the apparent strain noncrystallographicness coefficient at the mesoscopic level and is a measure of the gradual narrowing of a slip band as it propagates. It follows from (7) that $S_y/S_x=g_y/g_x$. In view of the lack of other boundary conditions, we can set $g_x=g_y=g$. Consequently, $S_x=S_y=S\approx\dot{\varepsilon}_0l_0/2N\dot{\gamma}m_x\Delta w$, since $\overline{h}\ll\lambda_m$. Thus, all the unknown parameters of the solution (2) have been found, and their relationship to the kinetic coefficients of the original equations (1) and the plastic strain rate $\dot{\varepsilon}_0$ assigned by the loading machine has been established.

Another solution of Eq. (1) which interests us describes the broadening of a slip band with a strain front oscillating in the y direction:

$$\rho_m(X,Y,\tau)=\rho_{m0}[1-\exp(Z_x+Z_y)][1+A\cos(pY-q\tau)],$$
$$\rho_m(x,Y,\tau)=0, \quad Z_x+Z_y>0, \tag{8}$$

where A is a constant. Substituting (8) into (1), we can find the conditions for the existence of this type of solution:

$$S_x+S_y=\frac{\beta a_xa_y}{(a_x-g_x)(a_y-g_y)}-1-g_x^2-g_y^2,$$

$$q=\frac{\beta a_y p}{a_y^2+p^2},\quad p^2=1+\frac{\beta a_y^2}{a_y^2+p^2},$$

$$S_x+S_y=p^2+\frac{\beta a_x a_y(a_y-g_y)}{(a_x-g_x)[(a_y-g_y)^2+p^2]}-1-g_x^2-g_y^2,$$

$$q=\frac{\beta a_x a_y p}{(a_x-g_x)[(a_y-g_y)^2+p^2]}-2pg_y. \tag{9}$$

To determine the six unknowns $g_{x,y}$, $S_{x,y}$, p, and q, the relations (9) should be supplemented by the condition for synchronism of the stationary coordinates Z_y and $(pY-q\tau)$, i.e., $S_y/g_y=q/p$. According to (8), it implies equality to the rates of stable (U_y) and unstable (U_q) broadening of a slip band in the transverse direction:

$$U_y=\frac{S_y}{g_y}\left(\frac{R_y^{(m)}}{\lambda_m}\right)u,\quad U_q=\frac{q}{p}\left(\frac{R_y^{(m)}}{\lambda_m}\right)u. \tag{10}$$

An analysis of (9) and (10) reveals that the solution (8) exists for $g_y<0$, $S_y<0$. This means that the absolute value of the stationary coordinate Z_y should be taken in (8). The constant A is found from the boundary conditions (Sec. 3).

Thus, as in the preceding case, all the parameters of the solution (8) can be determined, and their relationship to the kinetic coefficients and the strain rate $\dot{\varepsilon}_0$ can be established. The solutions (2) and (8) will be used below to analyze, respectively, the narrowing and branching of screw slip bands during the plastic straining of layered crystals.

II. EFFECT OF SLIP-BAND NARROWING

Let us consider the propagation of a slip band in a layered crystal (Fig. 1a) from unhardened layer 1 of thickness L_1 into hardened layer 2 of thickness L_2. The balance equations of the plastic strains and the plastic strain rates in a layered crystal have the form

$$\varepsilon_0=\varepsilon_1=\varepsilon_2,\quad \varepsilon_{1,2}=N_{1,2}(m_x\gamma_x^{(1,2)}+m_y\gamma_y^{(1,2)})w_{1,2}/l_0, \tag{11a}$$

$$\dot{\varepsilon}_0=\dot{\varepsilon}_1=\dot{\varepsilon}_2,\quad \dot{\varepsilon}_{1,2}=2N_{1,2}(m_x\dot{\gamma}_x^{(1,2)}+m_y\dot{\gamma}_y^{(1,2)})\Delta w_{1,2}/l_0. \tag{11b}$$

Here $\dot{\gamma}_y^{(1,2)}\ll\dot{\gamma}_x^{(1,2)}$ and $\dot{\gamma}_x^{(1,2)}\approx\dot{\gamma}_{1,2}=b\rho_{m0}^{(1,2)}u_{1,2}$ are the plastic strain rates on the slip band edges in unhardened and hardened regions (6), and $N_{1,2}$ are the numbers of slip bands in each of these regions. In the case under consideration $N_1=N_2=N$, and the case of $N_2>N_1$ signifies band branching and is discussed in Sec. 3. According to (11), the constants g and S can be found independently of one another for soft and stiff layers.

As a result, writing the expressions for the stationary coordinates Z_x and Z_y (2) in layers 1 and 2 in dimensional form, we have

$$Z_x^{(1,2)}=(x-x_0^{(2)}-U_x^{(1,2)}t)/\Lambda_x^{(1,2)},$$

$$Z_y^{(1,2)}=(y-U_y^{(1,2)}t)/\Lambda_y^{(1,2)},$$

$$\Lambda_x^{(1,2)}=g_{1,2}^{-1}(R_x^{(m)})_{1,2},\quad \Lambda_y^{(1,2)}=g_{1,2}^{-1}(R_y^{(m)})_{1,2}. \tag{12}$$

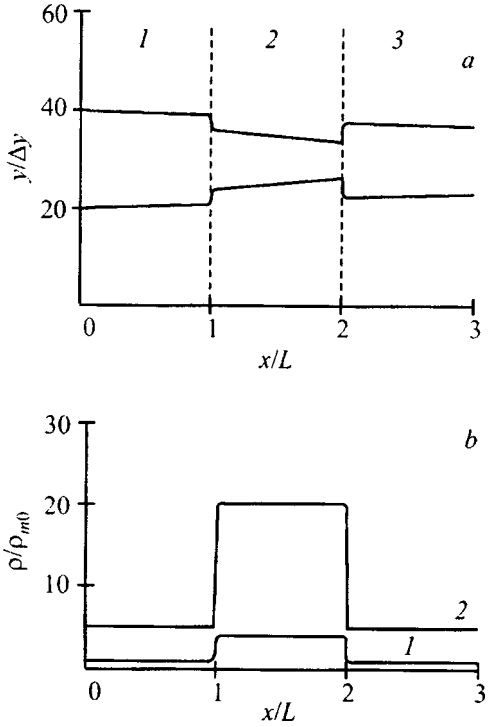

FIG. 1. Form of a slip band in a layered crystal (a) and density distribution of mobile (*1*) and immobile (*2*) dislocations (b) in unhardened (*1*, *3*) layers. The dashed lines mark the boundaries of the layers.

The subscripts 1 and 2 refer to soft and stiff layers, respectively. We henceforth assume that the thickness of the layers $L_{1,2}\gg\Lambda_{x,y}^{(1,2)}$. Since irradiation and doping significantly reduce the propagation lengths and velocities of screw dislocations between multiplication acts,[5,6] in (2), (10), and (11) we have

$$\rho_{m0}^{(2)}>\rho_{m0}^{(1)},\quad \rho_{i0}^{(2)}>\rho_{i0}^{(1)},\quad \Lambda_{x,y}^{(2)}<\Lambda_{x,y}^{(1)},$$

$$U_{x,y}^{(2)}<U_{x,y}^{(1)},\quad \dot{\gamma}_2<\dot{\gamma}_1,\quad M_2>M_1. \tag{13}$$

The constant $x_0^{(2)}$ in (12) can be found from the balance condition of the dislocation flows on the boundary between the soft and stiff layers

$$\rho_m^{(1)}u_1+\lambda_{x1}^{(m)}u_1\frac{\partial\rho_m^{(1)}}{\partial x}\bigg|_{x=I_1}=\omega^{-1}\rho_m^{(2)}u_2+\lambda_{x2}^{(m)}u_2\frac{\partial\rho_m^{(2)}}{\partial x}\bigg|_{x=I_1}. \tag{14a}$$

Here $\lambda_{x1}^{(m)}$ and $\lambda_{x2}^{(m)}$ are the characteristic diffusion lengths of dislocations in the x direction,[7] and ω is the ''transparency'' of the boundary to dislocations. The velocities $u_{1,2}$ and the dislocation density gradients are greatest on the edges of the broadening slip bands; therefore, in (1) the derivatives should be taken at $Z_y^{(1,2)}=0$ and the time $t_1=L_1/U_x^{(1)}$. As a result, we obtain

$$x_0^{(2)}=L_1-U_x^{(2)}t_1-\Lambda_x^{(2)}\ln C_2,$$

$$C_2=\left(1+\omega_{12}\frac{\lambda_{x1}^{(m)}}{\Lambda_x^{(1)}}\frac{\dot{\gamma}_1}{\dot{\gamma}_2}\right)\Big/\left(1+\omega_{12}\frac{\lambda_{x2}^{(m)}}{\Lambda_x^{(2)}}\right). \tag{14b}$$

The constants $x_0^{(3)}$ and C_3, which reconcile the dislocation flows as a slip band propagates from a stiff layer into a soft layer can be found in a similar manner ($t_2=L_2/U_x^{(2)}$):

$$x_0^{(3)}=L_2-U_x^{(1)}t_2-\Lambda_x^{(1)}\ln C_3,$$

$$C_3=\left(1+\omega_{23}\frac{\dot\gamma_2}{\dot\gamma_1^{(1)}}\frac{\lambda_{x2}^{(m)}}{\Lambda_x^{(2)}}\right)\Big/\left(1+\omega_{23}\frac{\lambda_{x1}^{(m)}}{\Lambda_x^{(1)}}\right). \qquad (14c)$$

Since $C_2>1$, $C_3<1$, and $U_y^{(2)}<U_y^{(1)}$, the penetration of a band from an unhardened region into a hardened region is accompanied by its narrowing Δy_{12}, and passage from the hardened layer into an unhardened layer is accompanied by the broadening of the band Δy_{23}, where

$$\Delta y_{12}(x,t)\approx(U_y^{(2)}-U_y^{(1)})t-(x-L)\tan\varphi_2-\Lambda_y^{(2)}\ln C_2,$$

$$\Delta y_{23}(x,t)\approx(U_y^{(1)}-U_y^{(2)})t+(x-L)\tan\varphi_2-\Lambda_y^{(1)}\ln C_3. \quad (15)$$

As can be seen from these expressions, the narrowing of the band in the stiff layer consists of three components. The first is a time-dependent component, which is associated with a slow rate of broadening of the band in the stiff layer, the second component is due to the gradual narrowing of the band at it penetrates into this layer, and, finally, there is a constant component associated with the balance of flows on the boundary between the layers (14). Since $\lambda_{x1}^{(m)}/\Lambda_x^{(1)}\approx 1$, $\lambda_{x2}^{(m)}/\Lambda_x^{(2)}\ll 1$, $\omega_{12}\approx 0.1$, and $\omega_{23}\approx 1$ in (14b) and (14c), the contribution of the constant component to the narrowing of the band is associated with the difference between the local plastic strain rates in the hardened and unhardened layers of the crystal: $\dot\gamma_2\ll\dot\gamma_1$.

Figure 1a shows the form of the cross section of a slip band propagating in a layered crystal, which was constructed according to (2) in $y/\Delta y$ vs x/L coordinates, where $\Delta y=U_y^{(1)}\Delta t$ is the increment of the band width during the time $\Delta t=L/U_x^{(1)}$ of its passage through the first (soft) layer, and $L=L_1=L_2=L_3\approx 1$ is the thickness of the layers. When the layers have the parameters

$$L/\Lambda_x^{(1)}=5,\quad L/\Lambda_x^{(2)}=20,\quad U_x^{(2)}/U_x^{(1)}=0.5,$$

$$U_y^{(2)}/U_y^{(1)}=0.8,\quad \tan\varphi_1=4\times10^{-4},\quad \tan\varphi_2=10^{-3},$$

$$t/\Delta t=5,\quad M_1=10,\quad M_2=100,\quad C_2=10^3,\ \text{and}\ C_3\approx 1,$$

a general gradual decrease in the band width is observed as it penetrates into the depth of the stiff layer with subsequent broadening upon passage into soft layer 3. As a consequence of the scale chosen ($\Delta y\approx 1$ μm, $L=1$ mm) the gradual narrowing of the slip band in layer 2 in Fig. 1a is more prominent than in the experiment.[2–4] According to the condition of balance of the values of the plastic strains of the layers (11a) and the result obtained above, the width of the slip band should be smaller in the stiff layer than in a soft layer, i.e., $w_2=(\gamma_1/\gamma_2)w_1<w_1$, since $\gamma_2/\gamma_1>1$.[5,7]

Figure 1b displays the density distribution of mobile (curve *1*) and immobile (curve *2*) dislocations along the middle of a slip band ($y/\Delta y=30$) for $\rho_{i0}^{(1)}/\rho_{m0}^{(1)}=5$, $\rho_{m0}^{(2)}/\rho_{mo}^{(1)}=4$, and $\rho_{i0}^{(2)}/\rho_{m0}^{(1)}=20$. The increased concentration

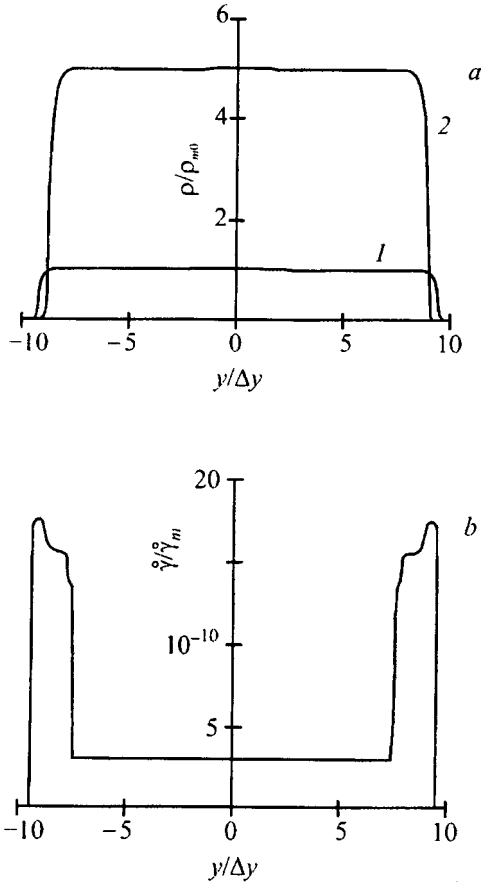

FIG. 2. Distribution of the densities of mobile (*1*) and immobile (*2*) dislocations (a) and the local plastic strain rate (b) across the width of a slip band in an unhardened layer.

of mobile and immobile dislocations in layer 2 is associated with the higher rates of dislocation multiplication and dipole formation in doped and irradiated crystals.[5,6]

Figures 2a and 3a present the distributions of the densities of mobile and immobile dislocations across the width of a slip band in unhardened ($x/L=0.5$) and hardened ($x/L=1.5$) layers , respectively. As we see, mobile dislocations predominate on the band edges, and immobile dipoles predominate in the remainder. Since their density is high, they greatly harden the crystal, and, as a result, the plastic strain rate is small in a large part of the band. It is high on the band edges in layers of thickness Δw_1 and Δw_2, respectively, without dipole hardening, ensuring a finite plastic strain rate in all the layers of an inhomogeneously hardened crystal at a given level of applied stresses, in accordance with the condition (11).

The distributions of the local plastic strain rates in the soft and stiff layers corresponding to the dislocation densities in Figs. 2a and 3a are shown in Figs. 2b and 3b. The calculation was performed in accordance with the Arrhenius expression for the plastic strain rate $\dot\gamma=b\rho_m u$, where $u=u_0\exp(-H(\sigma^*)/kT)$, T is the temperature, k is the Boltzmann constant, u_0 is the preexponential factor, $H(\sigma^*)=H_0[1-(\sigma^*/\sigma_c)^{1/2}]^2$ is the activation energy, H_0 and $\sigma_c\approx 8\sigma_f$ are the total activation energy and stress for overcoming barriers of the point type,[6] $\sigma^*=\sigma-\sigma_f-\sigma_d-\sigma_\mu$, σ^* is

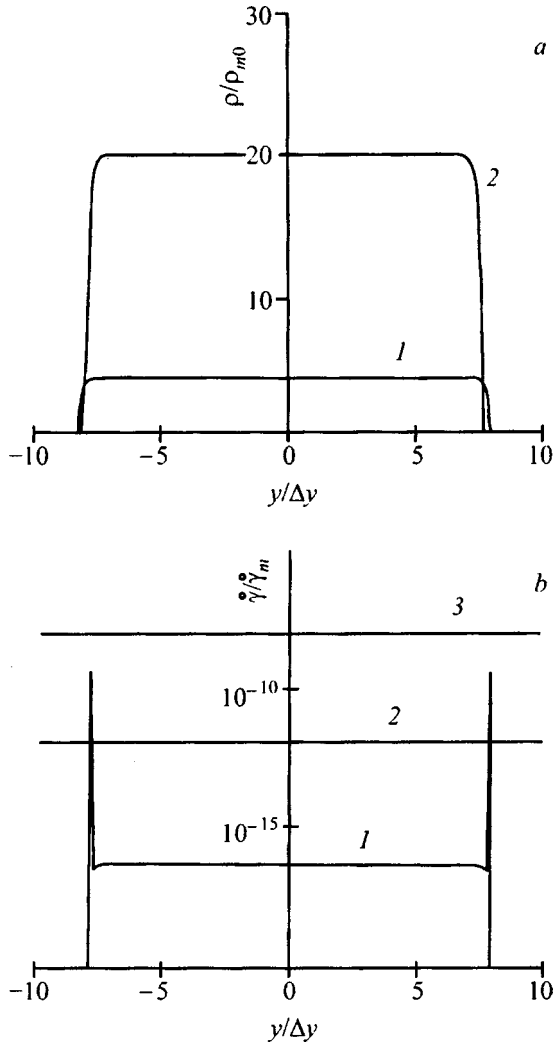

FIG. 3. Distribution of the densities of mobile (*1*) and immobile (*2*) dislocations (a) and local plastic strain rate (b) across the width of the slip band in a stiff layer.

the effective stress, $\sigma_d = 3\mu b h \rho_i$ is the hardening due to the interaction of dislocations with dipoles,[5,8] $\sigma_\mu = \alpha\mu b \rho_m^{1/2}$ is the hardening due to the interaction of dislocations with one another, and α is the interdislocation interaction constant. In accordance with the mixing rule in Ref. 4, the applied stress was $\sigma = L_1\sigma_1/(L_1+L_2) + L_2\sigma_2/(L_1+L_2)$, where $\sigma_{1,2} = \sigma^* + \sigma_f^{(1,2)} + \sigma_d^{(1,2)} + \sigma_\mu^{(1,2)}$ are the flow stresses of the respective layers.

The strain rates were calculated using the following values of the parameters for layered LiF crystals:[5] $H_0 = 1$ eV, $T = 293$ K, $\sigma = 5$ MPa, $\sigma_f^{(1)} = 1$ MPa, $\sigma_f^{(2)} = 2$ MPa, $L_1 = L_2$, $\mu = 4.3\times10^4$ MPa, $\nu = 0.75$, $b = 0.3$ nm, $\alpha = 0.2$, $\rho_{m0} = 10^{11}$ m^{-2}, and $\dot{\gamma}_m = b\rho_{m0}u_0 = 10^5$ s^{-1}. As can be seen from Figs. 2b and 3b, the plastic strain rate reaches a maximum on the edges of a broadening band. When the band propagates into a stiff layer, the strain rate decreases appreciably.

III. BRANCHING OF SLIP BANDS

In order to elucidate the cause of the branching of slip bands as they penetrate into a stiff layer, we utilize the results obtained in the preceding section.

Figure 3b presents the distribution of the local plastic strain rate $\dot{\gamma}$ (curve *1*) across the width of a band in a stiff layer with consideration of the hardening of the band due to the interaction of the mobile dislocations with dipoles and with one another. Horizontal straight lines *2* and *3* show the value of the plastic strain rate assigned by the straining machine per slip band $\dot{\varepsilon}_0/2N(\Delta w l_0)$ in the case of bilateral broadening, where N is the total number of slip bands in the crystal at a given moment in time. Two possible situations are shown. In the first case (line *2*) the number of bands N_1 is sufficiently high for the local plastic strain rates in each slip band (more precisely, on the edge of each slip band) to correspond roughly to the strain rate assigned by the loading machine per slip band $\dot{\varepsilon}_0/2N_1(\Delta w_{1,2}/l_0)$ in both the soft (Fig. 2b) and stiff layers.

In the second case (line *3*) the number of bands $N_2 < N_1$ is insufficiently high to ensure correspondence between the local strain rate in the stiff layer $\dot{\gamma}_2$ and the strain rate assigned by the straining machine $\dot{\varepsilon}_0/2N_2(\Delta w_2/l_0)$. For this correspondence to be achieved, either the nucleation of new slip bands or the branching of existing bands is required. These processes provide additional sites on the slip band edges for the development of plastic strains and thereby lower the partial rate $\dot{\varepsilon}_0/2N_2(\Delta w_2 l_0)$ to the level of the local plastic strain rate on the band edges.

Let us now examine the quantitative aspects of the question using the solution (8). Taking into account the balance of the plastic strain rates in a layered crystal (11) and the relations (5), we obtain an equation of type (6). With allowance for the fact that $\overline{h_1}/\lambda_m^{(1)} \ll 1$ (Ref. 7), we find from it the unknown constant for this solution

$$A \approx \frac{\dot{\varepsilon}_0}{2m_x S_x^{(2)} N_2 \dot{\gamma}_2 (\Delta w_2/l_0)} - 1. \tag{16}$$

Since $S_x^{(2)}$ is of the order of $a_y^{-2} > 1$, for a small number of slip bands N_2, a plastic strain rate $\dot{\gamma}_2$, which is low because of the hardening, and a width of the slip band edges Δw_2 the value of A in a stiff layer can be greater than unity.

As an example, Fig. 4a shows the character of the density distribution of mobile dislocations across the width of a slip band (only half of it is shown) according to (8) for $A = 2$ and two successive times $t_1 = 4\Delta t$ and $t_2 = 5\Delta t$. It is seen that the band consists of narrow discrete slip bands, in which the dislocation density increases with time (curves *1* and *2*). Another important circumstance demonstrated by the solution (8) is the appearance of nuclei of discrete slip bands s_1 and s_2 on the leading edge of the broadening slip band. It renders the mechanism of the branching of a band as it penetrates into a stiff layer obvious. More specifically, from the synergetic standpoint[9] it involves the successive discontinuous growth of the band by forming nuclei of new slip bands in front of it. Such discontinuous formation (''launching'') of discrete slip bands has been detected, for example, in the case of high-speed motion-picture photography of surfaces of plastically strained copper crystals following hardening by a neutron flux.[10] As follows from (8), it is a consequence of the transverse instability of the dislocation flow.

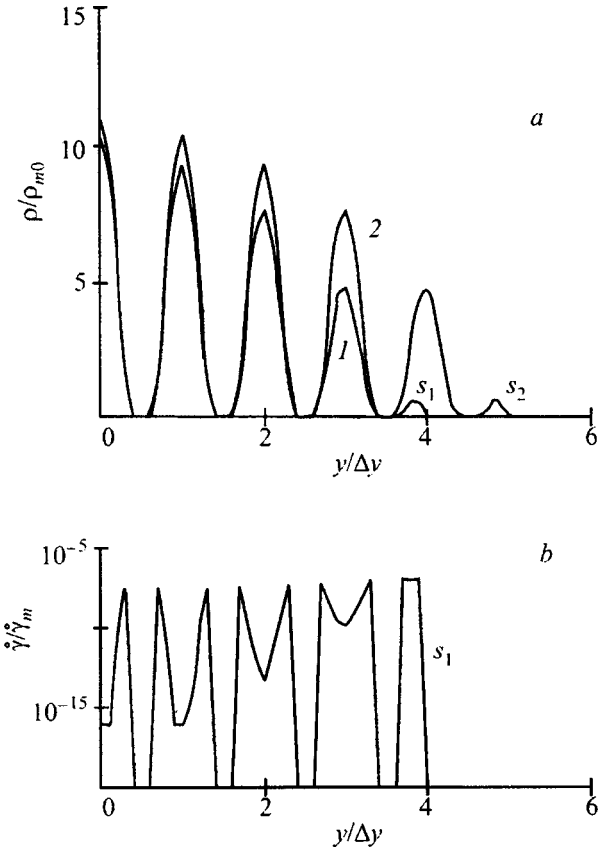

FIG. 4. Distribution of the density of mobile dislocations (a) and the local plastic strain rate (b) in a branching slip band at the times t_1 (curve *1*) and $t_2 > t_1$ (curve *2*).

It should be noted that the branching of strain bands has also been observed under the conditions of unstable inhomogeneous straining during the propagation of Lüders bands[11] and Portevin–Le Chatelier bands.[12] In the latter case, in accordance with the condition (16), an increase in the strain rate $\dot{\varepsilon}_0$ leads to the appearance of new Portevin–Le Chatelier bands, rather than an increase in the plastic strain rate in an already existing strain band.

Figure 4b shows the distribution of the local plastic strain rate $\dot{\gamma} = b\rho_m u(\rho_m, \rho_i)$ in a branching slip band in a stiff layer at the time t_1 (Fig. 4a) with consideration of the strain hardening of the band due to the interaction of the moving dislocations with dislocation dipoles and with one another. It can be seen that the strain rate is highest on the edges of the discrete slip bands and in the band nucleus s_1 and is lowest in the middle of the band because of hardening. The presence of additional active edges on discrete slip bands provides for the necessary balance between the strain rate assigned by the loading machine and the plastic strain rate of the crystal.

Thus, the results of the present work show that the formation of slip bands and the features of their formation in inhomogeneously hardened (layered) crystals are associated with the self-organization of dislocations in a dislocation ensemble of a plastically strained crystal. A synergetic approach to plastic straining based on the equations of dislocation kinetics permits consideration of the influence of the structural factors and straining conditions on the formation of various dislocation and strain structures in crystals.

We thank B. I. Smirnov and O. V. Klyavin for stimulating discussions of the questions considered in this work.

[1] A. V. Nikiforov, Yu. G. Nosov, M. B. Mukhamedzhanova, O. V. Klyavin, and P. I. Antonov, Fiz. Tverd. Tela (Leningrad) **29**, 485 (1987) [Sov. Phys. Solid State **29**, 275 (1987)].
[2] G. V. Berezhkova, N. P. Skvortsova, A. V. Nikiforov, Yu. G. Nosov, V. R. Regel', and M. A. Chernysheva, Fiz. Tverd. Tela (Leningrad) **31**(2), 252 (1989) [Sov. Phys. Solid State **31**, 321 (1989)].
[3] A. V. Nikiforov and O. V. Klyavin, Fiz. Tverd. Tela (St. Petersburg) **38**, 2744 (1996) [Phys. Solid State **38**, 1505 (1996)].
[4] B. I. Smirnov and T. S. Orlova, Fiz. Tverd. Tela (St. Petersburg) **38**, 2431 (1996) [Phys. Solid State **38**, 1336 (1996)].
[5] B. I. Smirnov, *Dislocation Structure and Hardening of Crystals* [in Russian], Nauka, Leningrad (1981), 232 pp.
[6] O. V. Klyavin, *Physics of the Plasticity of Crystals at Helium Temperatures* [in Russian], Nauka, Moscow (1987), 255 pp.
[7] G. A. Malygin, Fiz. Tverd. Tela (St. Petersburg) **37**, 3 (1995) [Phys. Solid State **37**, 1 (1995)].
[8] G. V. Bushueva and N. E. Kondorskiĭ, Fiz. Tverd. Tela (Leningrad) **31**(12), 71 (1989) [Sov. Phys. Solid State **31**, 2065 (1989)].
[9] B. S. Kerner and V. V. Osipov, Usp. Fiz. Nauk **160**(9), 1 (1990) [Sov. Phys. Usp. **33**, 679 (1990)].
[10] H. Neühauser, in *Dislocation in Solids*, F. R. N. Nabarro [Ed.], North-Holland (1983), Vol. 6, p. 319.
[11] G. T. Van Rooyen, Mater. Sci. Eng. **7**, 37 (1971).
[12] H. Dubiec, Scr. Metall. **23**, 1997 (1989).

Translated by P. Shelnitz

Recrystallization of pure and strontium-doped KCl crystals

E. B. Borisenko and B. A. Gnesin

Institute of Solid State Physics, Russian Academy of Sciences, 142432 Chernogolovka, Moscow Region, Moscow

(Submitted July 17, 1998)
Fiz. Tverd. Tela (St. Petersburg) **41**, 259–264 (February 1999)

The kinetics of microstructure transformations are studied during annealing of deformed single crystals of KCl and KCl:0.05wt %Sr^{2+} at temperatures of $(0.35-0.55)T_m$ (where T_m is the melting temperature) and during storage at room temperature. The effect of deformation rates ranging from 0.01 mm/min to 0.1 mm/min at a deformation temperature $T_d=0.5T_m$ on the crystal structure and on the recrystallization kinetics is noted. It is found experimentally that the incubation period for static recrystallization in single-crystal KCl:0.05wt %Sr^{2+} is shortened and recrystallization takes place at room temperature after deformation in this temperature range. Here, during the new recrystallization grains have a twinned orientation with respect to the initial single crystal during the first stage and to the subgrains of the deformed crystal. As the annealing temperature is raised, the stage in which twins grow in KCl:0.05wt %Sr^{2+} crystals is shortened and it is displaced by recrystallization through migration of high-angle grain boundaries of the common type. Deformation conditions which ensure prolonged (at least three months) stability of the post-deformation hardening of single crystals are found experimentally for Sr^{2+}-doped deformed single crystals. [S1063-7834(99)01402-1]

The recrystallization of alkali halide crystals has been a topic of research for the last two decades. Interest in this phenomenon in the alkali halide crystals arises mainly from the need for high mechanical strength and stability in the mechanical properties when these materials are used in laser optics. At various times studies have been made of the structure and kinetics of dynamic[1] and static recrystallization after deformation of pure and doped alkali halide crystals,[2,3] as well as of the recrystallization processes following a reversible $B1 \Leftrightarrow B2$ phase transition under pressure.[4] The observed multiplicity of recrystallization paths and studies of the general features of and differences in the structure of alkali halide crystals during recrystallization following deformation under various conditions require further investigation. As before, the important practical question of whether it is possible to retain hardening after deformation for a long time remains to be solved.

In this paper we examine the evolution of the structure of the deformation at $0.5T_m$ of single-crystal KCl and KCl:0.05wt %Sr^{2+} when held in air at room temperature $(0.3T_m)$ with isothermal annealing in a furnace at temperatures of $(0.35-0.55)T_m$, as well as the effect of post-deformation annealing on the evolution of the structure during subsequent storage.

1. MATERIALS AND TECHNIQUES

In these studies we have used KCl:0.05wt %Sr^{2+} and KCl crystals grown by the Czochralski method from OSCh (high purity) grade material. Strontium was introduced into the batch in the form of $SrCl_2$. Despite the different form of the chemical formulas, KCl and $SrCl_2$ recrystallize in a fcc structure with lattice parameters $a=6.293$ and 6.977 Å, respectively (according to data from the JCDPS card index, cards No. 4-587 and 6-537). Adding divalent valent cations of the type Ca^{2+}, Mg^{2+}, and Mn^{2+} causes substantial hardening of alkali halide crystals.[2] But then the brittleness of the alkali halide materials increases and their transparency is decreased. In this series of additives, strontium (Sr^{2+}) is unique, since its presence in KCl at a few hundredths of a percent leads to a substantial enhancement in the hardness while retaining acceptable plasticity and a transparency at the level of undoped single crystals.

The recrystallized samples were deformed in an ''Instron'' test machine in an oven at $T_d=250\,^\circ$C in air. The temperature fluctuations at the sample during the tests were less than 5 °C. The range of rates of deformation $\dot{\varepsilon}$ was 0.01 mm/min to 0.1 mm/min. The $3\times3\times7$ mm^3 samples for mechanical testing under compression (about 60 pieces, in all) were cleaved along the {100} cleavage planes. The grain structure was revealed using a 70% water solution of ethylene glycol or a 1:1 mixture of ethyl alcohol with a saturated water solution of KCl. The volume fraction of recrystallized grains was determined by the linear Rosival method.[5] The error in the measurements was calculated using relation $\delta=\sqrt{D}t$, where $\sqrt{D}$ is the root mean square deviation and t is the normalized deviation for a given confidence P in the results.[5]

Pole figures were obtained from an automated texture diffractometer by the Schultz (slope) method. Monochromatized Mo Kα radiation was used, the maximum angle of inclination was 65°, and the angular step size was $\Delta\vartheta=\Delta\varphi=5°$. The characteristic size of the illuminated spot on the sample surface was $(3-5)\times(8-16)$ mm^2. The size and

location of the spot on the sample depends, accordingly, on the angles ϑ and φ. A Soller slits were used to collimate the incident and diffracted beam. Each pole figure reflects the intensity levels in fractions of the maximum recorded over the entire pole figure with a correction for the background and defocussing. The texture was monitored using pole figures for 8 single crystals in the initial state and 18 samples after deformation and/or annealing.

2. EXPERIMENTAL RESULTS AND DISCUSSION

The KCl and KCl:Sr^{2+} samples were deformed at a temperature of 250 °C or about $0.5T_m$. A reasonable choice of T_d for the studies of static recrystallization was limited below by the brittleness of the samples, especially the doped ones. At higher (above $0.57T_m$) homologous deformation temperatures, dynamic recovery and dynamic recrystallization of the alkali halide crystals are possible.[1]

The deformation curves for the pure and strontium-doped KCl crystals have the customary form for fcc crystals. A regular increase in the yield stress and in the hardening coefficient is observed owing to doping and to an elevated deformation rate.

Figure 1a shows a typical structure of a deformed KCl crystal and Fig. 1b shows the size distribution of subgrains in a crystal of this sort. The average size of the subgrains in KCl:0.05wt %Sr^{2+} crystals was half that in the undoped KCl crystals under the same deformation conditions. Figure 2a and b show pole figures for {220} samples of KCl:0.05wt %Sr^{2+}, undeformed and deformed at a rate of 0.1 mm/min to 70%. Recording the texture using pole figures is an ''indicator'' in the sense of revealing its nonuniformity: since a scan is taken from different parts of the surface upon rotation, the nonuniformity shows up as an asymmetry in a pole figure. A comparison of the pole figure for the {200} undeformed single crystal (Fig. 2a) with that for the deformed sample (Fig. 2b) indicates that, during precipitation, the samples retained the orientation of the original single crystal $\{001\}\langle 100\rangle$, although with substantial scatter and a more nonuniform texture. Since high-angle boundaries in the deformed samples cannot be revealed by optical microscopic techniques, a combination of x-ray and metallographic data allows us to speak, specifically, of subgrains among which the disorientation builds up gradually from point to point in the samples obtained by hot deformation of single crystal KCl. As the results of the present and earlier[3] work show, the formation of the structure is qualitatively the same for all the KCl samples at deformation temperatures of $(0.4-0.5)T_m$, but as the deformation temperature is raised to $0.5T_m$, some enhancement in the uniformity of the structure can be noted after deformation and coarsening of the subgrains by roughly 25% (for the samples deformed at $\dot{\varepsilon}=0.1$ mm/min).

As Fig. 3 shows, the subgrains in deformed crystals of pure KCl coarsen with increasing storage time at room temperature. The relatively small changes observed in the pole figures and the absence of recrystallization grains suggest that coalescence is the mechanism for growth of the subgrains. Here more rapid coalescence of the subgrains is observed in crystals that have been deformed at a higher rate.

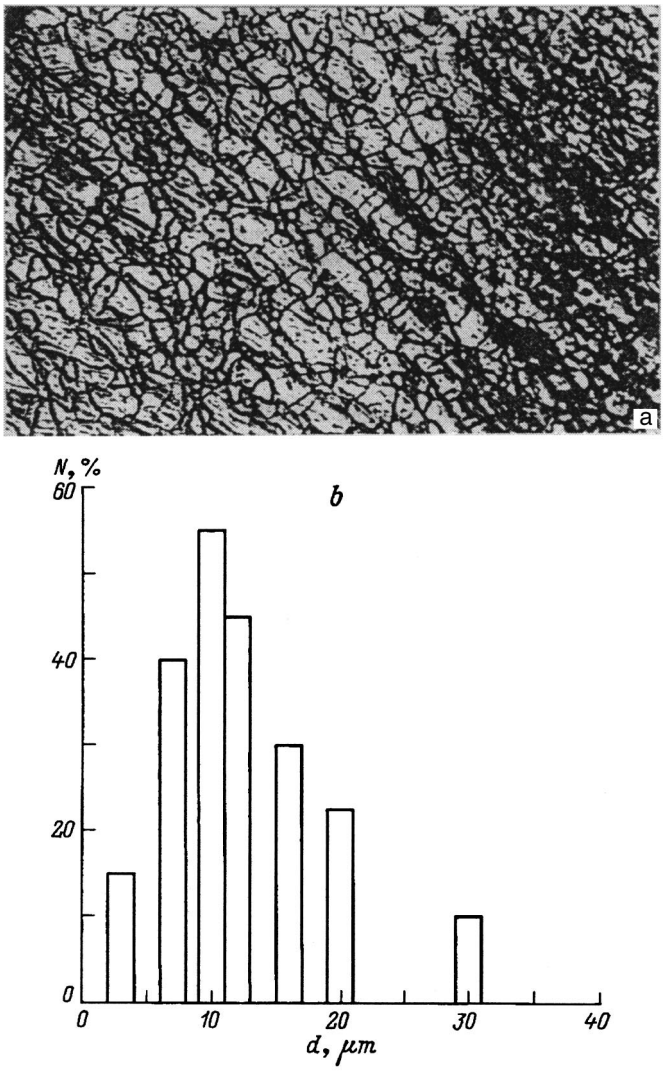

FIG. 1. KCl sample, $T_d=250$ °C, $\varepsilon=70\%$, $\dot{\varepsilon}=0.1$ mm/min: (a) structure of a deformed crystal, 400×; (b) grain size distribution.

The form of the size distribution of the grains during storage is essentially the same as that immediately after deformation, but the peak gradually is shifted to larger sizes.

The structure of Sr^{+}-doped KCl crystals changes differently during storage after deformation to $\varepsilon=70\%$. Their deformed matrix, with an average subgrain size of 8 and 4 μm for crystals precipitated at rates of 0.01 and 0.1 mm/min, respectively, remains quite stable with time. At the same time, new faceted grains appear against the background of the deformed matrix and their growth kinetics can be evaluated from the data in Figs. 4 and 5. Judging from the optical contrast in the slice, these grains are separated from the deformed matrix by high-angle boundaries. In crystals deformed at a higher rate, the volume occupied by grains of this type is greater for the same storage time following deformation (Fig. 4). In a slice parallel to the {100} plane in the original crystal, the boundaries of the new grains leave traces in the $\langle 110\rangle$, $\langle 210\rangle$, and $\langle 310\rangle$ directions (Fig. 6). In a pole figure for a crystal deformed to 70% (Fig. 7), there are regions of high intensity with twinned, relative to $\{001\}\langle 100\rangle$, and close, to those (within 5°), orientations of the type {221},

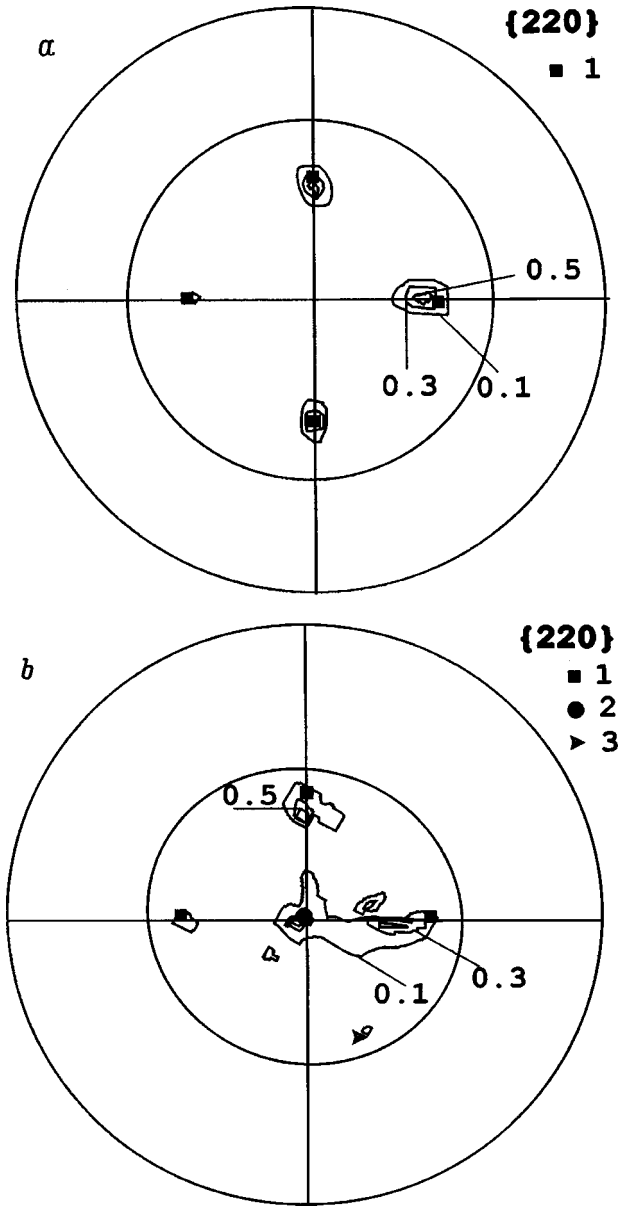

FIG. 2. {220} pole figures of a KCl:0.05wt %Sr^{2+} crystal: (*1*) {001}⟨100⟩, (*2*) {110}⟨001⟩, (*3*) twins with respect to {001}⟨100⟩: (a) undeformed sample, (b) $\dot{\varepsilon}=0.1$ mm/min, $T_d=250$ °C, $\varepsilon=70\%$.

{335}, and {332}. The twinning system is typical for fcc lattices: the plane and direction of twinning are {111} and ⟨112⟩, respectively. Experimental data indicate that after removal of a load, in KCl:0.05wt %Sr^{2+} crystals deformed at $0.5T_m$ to 70% recrystallization takes place at room temperature, with the first stage involving the nucleation and growth of grains of twins of subgrains with a {100}⟨001⟩ orientation in the deformed crystals. For longer storage times, the stage of twin growth is followed by a second stage of primary recrystallization, which is characterized by the migration of segments of the former twin boundaries into the deformed matrix. In a pole figure these changes show up as increased spread in the texture and the appearance of new orientations that are not twinned with respect to the {001}⟨100⟩ orientations. Some twins existed and continued to grow as twins for eight months of storage following deformation.

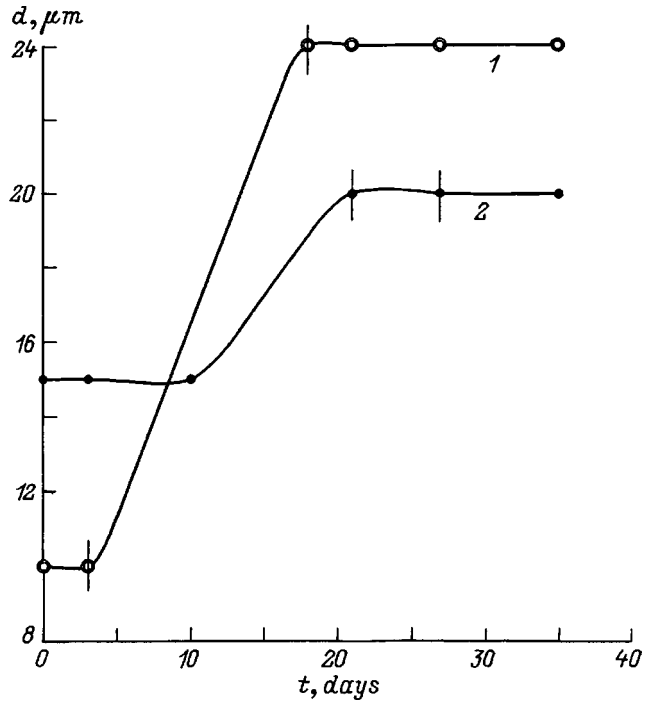

FIG. 3. Average subgrain size in KCl crystals with $T_d=250$ °C and $\varepsilon=70\%$ as a function of the time stored at room temperature: (*1*) $\dot{\varepsilon}=0.1$ mm/min; (*2*) $\dot{\varepsilon}=0.01$ mm/min. Here and in Fig. 4 the vertical lines denote the range of probable measurement error for $P=0.9$.

It is clear from Table I that adding 0.05wt %Sr^{2+} enhances the hardness of undeformed single crystal KCl by roughly 50%. But further deformation under these conditions leads to an enhancement in the hardness by 13-15% in pure and Sr-doped KCl crystals. The scatter in the values of the

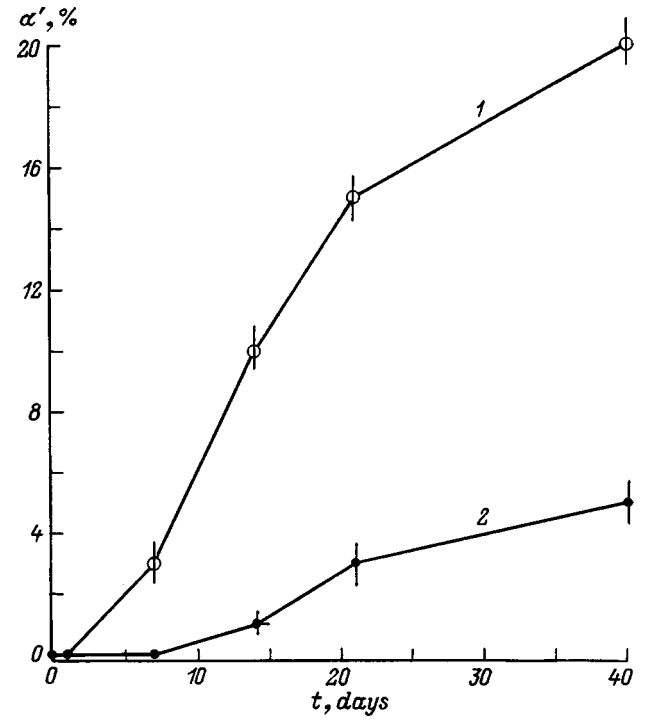

FIG. 4. Volume fraction of twins as a function of the time stored at room temperature in KCl:0.05wt %Sr^{2+} crystals deformed at $T_d=250$ °C ($\varepsilon=70\%$): (*1*) $\dot{\varepsilon}=0.1$ mm/min; (*2*) $\dot{\varepsilon}=0.01$ mm/min.

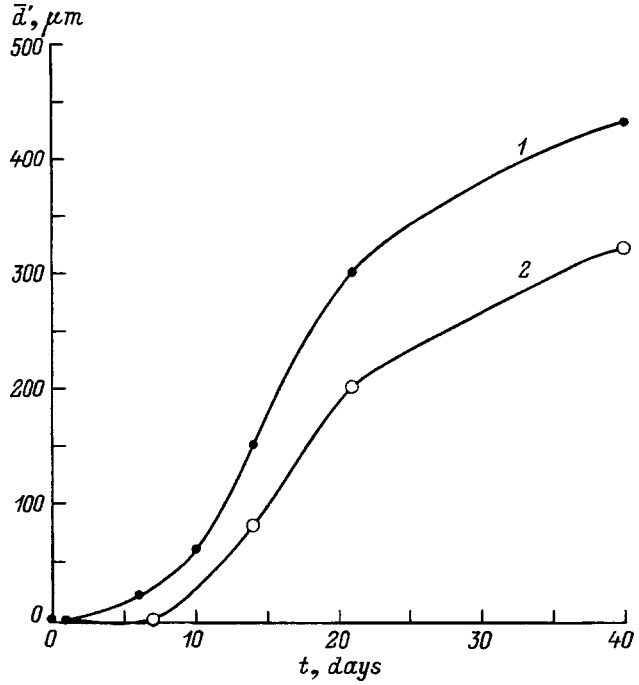

FIG. 5. Average size of grains of twinned, with respect to $\{001\}\langle 100\rangle$, orientations as a function of the storage time following deformation (T_d=250 °C, ε=70%), KCl:0.05wt %Sr^{2+}: (*1*) $\dot{\varepsilon}$=0.1 mm/min; (*2*) $\dot{\varepsilon}$ =0.01 mm/min.

microhardness, ΔH after precipitation is larger in the doped crystals. For the samples in the initial state, this indicator of the crystal nonuniformity was essentially the same. In the pure crystals stored for three weeks, caused by the increment in microhardness caused by deformation fell by a factor of two. In the doped crystals that had been deformed to 70%, the increment in hardness gained by deformation was almost completely lost during the same time.

Here the considerably greater stability in the structure and properties of KCl:0.05wt %Sr^{2+} crystals deformed to 62% should be noted. As can be seen from Table I, their microhardness hardly changed when they were stored for three months after deformation. Over that time, unlike doped

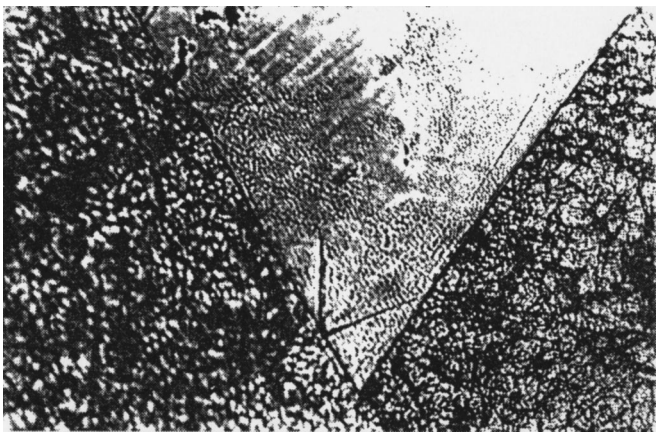

FIG. 6. Structure of a KCl:0.05wt %Sr^{2+} crystal after deformation (T_d=250 °C, ε=70%, $\dot{\varepsilon}$=0.1 mm/min) and subsequent storage at room temperature for 21 days, 200×.

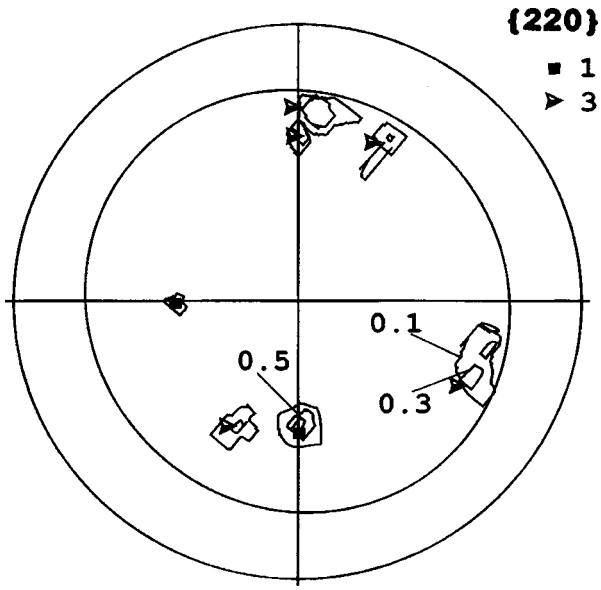

FIG. 7. {200} pole figures of KCl:0.05wt %Sr^{2+} crystals after deformation (T_d=250 °C, ε=70%, $\dot{\varepsilon}$=0.1 mm/min) and subsequent storage at room temperature for 14 days: (*1*) $\{001\}\langle 100\rangle$, (*2*) $\{110\}\langle 001\rangle$, (*3*) twins with respect to $\{001\}\langle 100\rangle$.

crystals deformed to $\varepsilon \geqslant 70\%$, no recrystallized grains were observed to appear throughout the entire sample volume. Degrees of deformation, $\varepsilon = 60-65\%$, apparently can be regarded as ''critical'' for pure and lightly doped alkali halide crystals in the sense that the structure and texture of hot-deformed single crystals are able to stabilize over time. The mechanical properties are also stable then and are close to the corresponding values for polycrystals (Table I).

The changes in the structure of hot-deformed single crystals produced by annealing in a furnace at temperatures $T_{an} = 0.35-0.55T_m$ were also studied. As can be seen from Table II, differences exist in the recrystallization of pure and Sr-doped KCl crystals, as well as of crystals that have been deformed at different rates, both during storage and after furnace annealing. Recrystallization by nucleation and growth of grains with orientations twinned with respect to $\{100\}\langle 001\rangle$ is observed mainly for short annealing times, in the initial stages of the process in Sr-doped crystals which

TABLE I. Microhardness of crystalline KCl and KCl:0.05wt %Sr^{2+}.

Material	Degree of deformation, ε,%	Deformation temperature, T_d, °C	Time* *t*, days	Hardness *H*, MPa
KCl	Without deformation			117±2
KCl:Sr^{2+}	Without deformation			173±3
KCl	70	250	0	135±5
KCl:Sr^{2+}	70	250	0	193±12
KCl:Sr^{2+}	62	250	0	195±12
KCl	70	250	21	125±5
KCl:Sr^{2+}	70	250	21	175±4
KCl:Sr^{2+}	62	250	30	195±5
KCl	70	250	52	120±3
KCl:Sr^{2+}	70	250	60	175±3
KCl:Sr^{2+}	62	250	90	195±7

*Storage time (at $0.3T_m$) after deformation.

TABLE II. Structural parameters of crystalline KCl and KCl:0.05wt %Sr^{2+}, subjected to post-deformation annealing.

Material	$\dot{\varepsilon}$, mm/min	T_d, °C	T_{an}, °C	t_{an}, min	α, %	α', %	d, μm	d', μm	Notes
KCl	0.1	250	200	10	$\leqslant 3$	$\leqslant 1$	150		
KCl	0.1	250	200	90	90	0	450		120° junctions
KCl : Sr	0.1	250	200	10	0	<10		100	
KCl : Sr	0.1	250	200	90	100	0	100		120° junctions
KCl	0.01	250	200	10	<1	3	25*	250	
KCl	0.01	250	200	90	60	40	400	400	
KCl : Sr	0.01	250	200	10	0	5	12*	80	
KCl : Sr	0.01	250	200	90	50	0	200		

*Coalescence of subgrains of the deformed matrix is observed; the ''' refers to α and d of grains which are twinned with respect to $\{100\}\langle 001\rangle$.

have been deformed to $\varepsilon = 70\%$. As the annealing time is increased, the volume fraction of recrystallized material (α) in these samples increases, mainly as a result of grains that grow by migration of high-angle boundaries of the common type. In pure KCl crystals deformed at a rate of 0.1 mm/min, during furnace annealing recrystallization proceeds from the very beginning through migration of high-angle segments of grain boundaries of the common type.

For post-deformation annealing lasting longer than 60 min at the temperatures indicated in Table II and Fig. 8, collective recrystallization was observed along with primary recrystallization. In this stage, new grains with high-angle boundaries of the common type ''ate up'' the grains of the orientations twinned with respect to $\{100\}\langle 001\rangle$ in the Sr^{2+} doped crystals. The structure of the pure and doped single

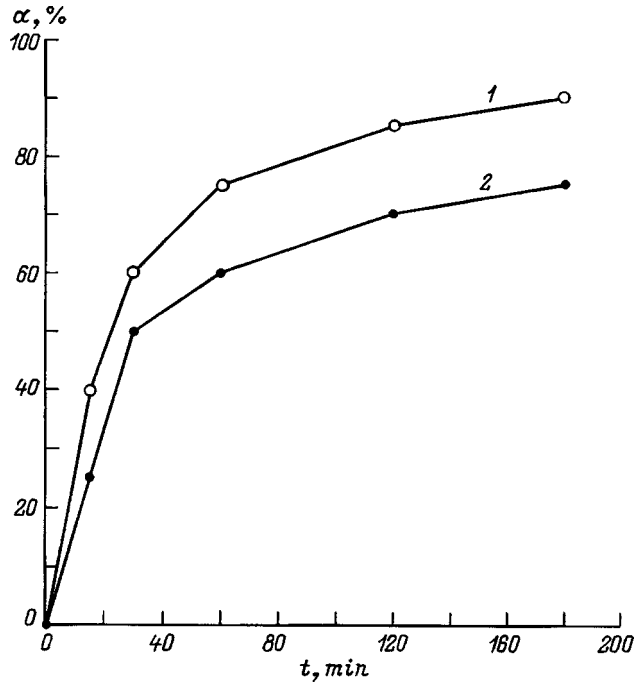

FIG. 8. Volume fraction of recrystallized material as a function of post-deformation annealing time, $T_{an}=300$ °C ($T_d=250$ °C, $\varepsilon=70\%$, $\dot{\varepsilon}=0.1$ mm/min): (1) KCl:0.05wt %Sr^{2+}; (2) KCl.

crystals that had been deformed at a rate of 0.1 mm/min consisted of equiaxial recrystallized grains after 90 min of annealing. Here it is clear (Table II) that at the end of primary recrystallization, in the stage of collective recrystallization the grains are finer in the doped than in the pure crystals. Table II and Fig. 8 imply that for the same annealing conditions, the volume fraction of recrystallized material is higher in crystals that have been deformed at a higher rate.

As the annealing temperature is raised, the differences in the recrystallization kinetics of pure and Sr-doped KCl crystals deformed at a rate of 0.1 mm/min become less noticeable. It is clear from the data of Table II and Fig. 8 that the volume fraction of recrystallized material during annealing of doped crystals can be even higher than in the pure crystals; this may be related to the influence of the additive on the structure of the principal material. The questions of the state of strontium in the solid solution and how it interacts with the structural defects require further study.

In our experiments the samples cooled in the furnace after deformation behaved qualitatively the same way during subsequent post-deformation annealing. It was, noted, however, that, during storage at room temperature, the incubation period of slowly cooled KCl:Sr^{2+} crystals is a factor of three smaller than for quenched crystals. This fact indicates the existence of a significant effect owing to recovery processes during comparatively slow post-deformation cooling of the samples on the subsequent recrystallization of potassium chloride deformed at $0.5T_m$. Evidently, these same processes can be related to the observed reduction in the incubation period for recrystallization of undoped KCl crystals when T_d is raised from $0.4T_m$ (Ref. 3) to $0.5T_m$ (the present work).

It has been reported[2] that storage for half a year after hot deformation led to a reduction in the apparent activation energy for the migration of boundaries in pure and strontium-doped (5×10^{-3}% Sr^{2+}) deformed NaCl single crystals by factors of 2 and 20, respectively. The experimental results of the present paper provide an explanation for this behavior in pure and doped alkali halide crystals. The high-angle boundaries of twins grown during post-deformation storage provide a site for nucleation, thereby easing the recrystallization of lightly doped alkali halide crystals during subsequent annealing, while the rather homogeneous subgrains (in terms of the density of defects), with their orientation close to the deformed matrix, which grow during storage of pure deformed single crystals do not provide such a powerful stimulus to recrystallization.

Relatively low-temperature annealing, in turn, does not stablize the structure: in KCl:0.05wt %Sr^{2+} crystals annealed at 100 °C for 15 min, recrystallization continues during subsequent storage at room temperature. In samples deformed at $\dot{\varepsilon}=0.1$ mm/min at $T_d=250$ °C, the volume fraction of recrystallized material after annealing in this regime was $\alpha=15\%$; with subsequent storage for two days, α rose to 30%, while without additional annealing α was less than 2% two days after deformation (Fig. 4). Here it is predominantly straight twinning boundaries that move toward the deformed matrix, but in the recrystallized region grains can be seen whose form is typical of recrystallization by migration of higher-angle boundaries.

The nucleation and growth of twins during recrystallization of alkali halide crystals has been observed[4] at room temperature in KCl undergoing a reversible $B1 \Leftrightarrow B2$ polymorphic transition at 20 kbar, following removal of the pressure. Given the undoubted differences in the structures and textures of doped KCl following uniaxial deformation and pure KCl following a phase transition under pressure, they both experience substantial hardening. The yield stresses of these samples, calculated using the Hall-Patch equation and obtained from $\sigma - \varepsilon$ curves, are roughly twice the corresponding values for pure KCl crystals after uniaxial deformation under the above conditions. This may be connected with a drop in the recrystallization temperature from $0.45T_m$ to $0.3T_m$ and with the appearance of a recrystallization mechanism in alkali halide crystals that is typical only of low temperatures.

E-mail: borisenk@issp.ac.ru

[1] M. Guillope and J. P. Poieir, J. Geophys. Res. **84**, 5557 (1979).
[2] S. N. Val'kovskiĭ, A. V. Gorbunov, and V. N. Erofeev, The effect of impurities on the properties of alkali halide crystals used in IR structural optics [in Russian], Preprint, Chernogolovka (1989), 32 pp.
[3] E. B. Borisenko, B. A. Gnesin, O. O. Likhanova, and I. B. Savchenko, Fiz. Tverd. Tela **37**, 2029 (1995) [Phys. Solid State **37**, 1105 (1995)].
[4] E. B. Borisenko and B. A. Gnesin, Textures Microstruct. **26–27**, 369 (1996).
[5] S. A. Saltykov, Stereometric Metallography [in Russian], Metallurgiya, Moscow (1970), 374 pp.

Translated by D. H. McNeill

Effect of orientation on kinking in single-crystal potassium hydrophthalate deformed in compression

V. R. Regel', N. L. Sizova, G. S. Belikova, and T. N. Turskaya

A. N. Shubnikov Institute of Crystallography, Russian Academy of Sciences, 117333 Moscow, Russia
(Submitted May 19, 1998; resubmitted July 20, 1998)
Fiz. Tverd. Tela (St. Petersburg) **41**, 265–268 (February 1999)

The effect of temperature and the rate of deformation on kinking is studied in single crystals of potassium hydrophthalate compressed along two different orientations. It is shown that the crack-formation mechanism during kinking depends on the orientation of a sample. It underscores that kinking can be regarded as a rotational deformation mode. © *1999 American Institute of Physics.* [S1063-7834(99)01502-6]

Potassium hydrophthalate $KHC_8H_4O_4$ is an organic single crystal belonging to the rhombopyramidal class of rhombic symmetry with $2mm$ point group.[1] These crystals are widely used as a dispersion element in x-ray spectroscopic devices for studying long-wavelength x rays. This crystal is characterized by highly anisotropic binding forces and, therefore, anisotropy in its elastic and plastic properties. It has been shown[2] that, depending on the direction of the axis of compression with respect to the cleavage plane, potassium hydrophthalate crystals can either deform plastically with a low yield stress or undergo brittle fracture or form kink bands. It is interesting to note that kink bands are formed in potassium hydrophthalate upon compression along two directions [100] and [010], with the latter coinciding with the polar axis of the crystal.

The effect of boundary conditions on the formation of kink bands in potassium hydrophthalate deformed by compression along the [100] direction has been studied. It was shown that the tension along the kink boundaries relaxes by forming a system of microcracks of fractal nature. The development of kink bands is an example of collective dislocation effects which develop on all scale levels when certain critical parameters are reached, such as the dislocation density, temperature, and deformation rate. In this paper we study the effect of these parameters on kink formation in potassium hydrophthalate during compression along the two directions [100] and [001] and compare the features of kink formation during compression of the samples along the two different directions which appear to be related to the anisotropy of potassium hydrophthalate. This kind of study both yields information on the mechanical properties of potassium hydrophthalate and extends our ideas regarding the variety of rotational deformation modes in anisotropic crystals with low cleavage-plane surface energies, such as potassium hydrophthalate.

The method of preparing and testing the samples has been described elsewhere.[3] The sample sizes, as before,[3] are roughly $3\times4\times12$ mm^3. Here we present the results of some experiments illustrating the effect of the deformation rate and temperature on the kinking process during compression of samples in both of the directions indicated above, together with some data on the acoustic emission and increased dislocation density near the kink boundaries which accompany this process. Then these data are discussed from the standpoint of ideas about rotational plasticity[4–6] and the dependence of kink formation on orientation is analyzed.

1. EFFECT OF DEFORMATION RATE ON KINKING IN POTASSIUM HYDROPHTHALATE AND THE ACOUSTIC EMISSION OBSERVED DURING KINK FORMATION AND DEVELOPMENT

Kinking in potassium hydrophthalate in both the [001] and [100] directions has been studied at two deformation rates, 1×10^{-6} and 1×10^{-5} m/s, on an ''Instron'' test machine. The deformation curves for the samples in both orientations show that a sample is deformed elastically at first and then, when a load of roughly 25 MPa is reached, the stress falls sharply to about 2 MPa. The drop in stress is accompanied by a readily distinguishable sharp sound. When the sample is oriented along the [100] axis, after the first kink, oscillating kinks develop within a stress interval of roughly 2 MPa with further deformation of the sample for both deformation rates. When the sample is oriented along the [001] axis, the sample undergoes fracture, generally in the region of the kink, immediately after the first major drop in stress and no oscillations in the stress are observed with small loads in this case. In this case the effect of the rate shows up in that at the higher deformation rate the sample immediately breaks up into small fragments in the region of the kink, while at the lower deformation rate it was possible to keep several samples undestroyed.

The effect of the deformation rate in both orientations also shows up as a change in the slope of the deformation curve in the elastic region. (The higher the rate, the steeper the slope.) Unfortunately, the scatter in the values of the kinking limit (τ) exceeds the expected effect of the deformation rate on τ for the range of rates examined here, so it could not be determined reliably.

In order to obtain additional information on the kinking process, we recorded the acoustic emission produced during kinking in potassium hydrophthalate deformed by compression along the [100] direction. A probe with an operating

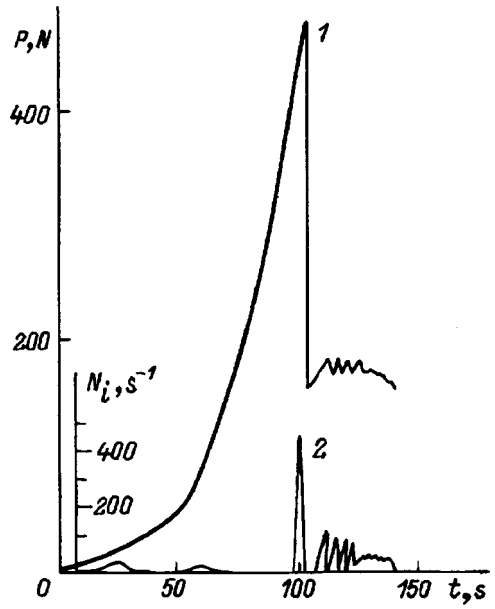

FIG. 1. (*1*) Deformation curve for a potassium hydrophthalate sample along [100] (the ordinate is P, the load in N, and the abscissa is time t in s). (*2*) A schematic representation of an acoustogram obtained with it; N_i is the number of acoustic pulses over a 10 s interval.

bandwidth of 200-500 kHz was used. Epoxy resin deposited on the end of the sample pointing toward the probe serves as a lubricant which causes kinks to form predominantly on one side as the material is moved,[3] rather than on both, as happens when there is no ''lubricant.'' The deformation curve and acoustogram shown in Fig. 1 are typical of several series of tests. The acoustograms contained a signal corresponding to the moment of kink formation, as well as two levels of periodicity in the acoustic emission after a kink band formed which apparently are related to crack formation at the boundaries of the kink. (See below.)

2. Effect of temperature on kinking in potassium hydrophthalate

Figure 2 shows the kinking limit τ for potassium hydrophthalate during compression in the [100] and [001] directions as a function of temperature. Despite the large scatter in

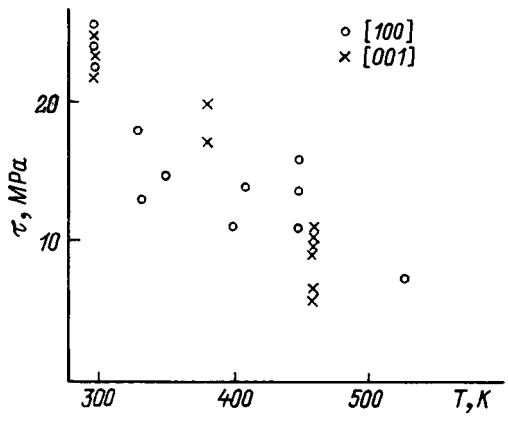

FIG. 2. The kink formation limit τ as a function of temperature for the [100] and [001] orientations of a potassium hydrophthalate single crystal.

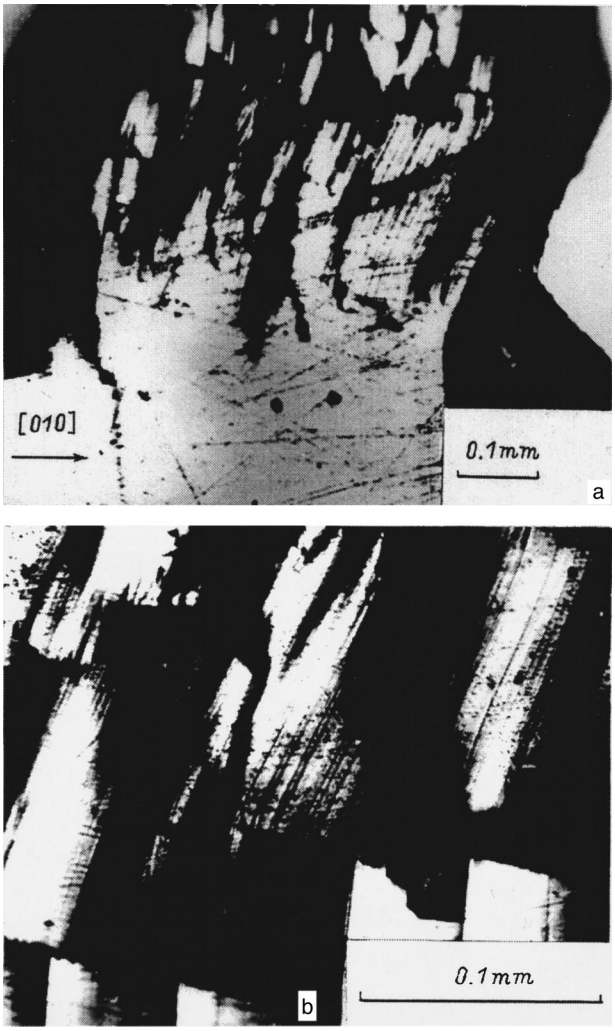

FIG. 3. (a) Overall view of a crystal after kinking during compression of potassium hydrophthalate along [001]; (b) the shape of cells in a kink band bounded by two cleavage planes (010) and (001).

the values of τ which is typical of this process,[7] a tendency for τ to decrease with increasing test temperature is still noticeable. It is interesting to note that the temperature also affects the pattern of cracks which forms in a kink band and in the crystal bulk outside a kink for different orientations of the sample. Thus, for compression along [001], the effect of temperature on kink formation is similar to that of the deformation rate: when the temperature is raised (as when the deformation rate is increased), the sample fractures in the neighborhood of the kink band. It was possible to preserve samples with [001] orientation that had been deformed at room temperature and, as noted above, with a minimal deformation rate. It is clear from Fig. 3 that immediately after the first kink forms, cracks form immediately in the kink band in two mutually perpendicular planes (010) and (001). The (010) plane is the cleavage plane in this crystal and it is characterized by a low surface energy. The (001) plane is a secondary cleavage plane and has been observed previously by indenting the (100) plane at elevated temperatures.[8] The kink region consists of cells bounded in the [010] and [001] directions with the extent of the cells in the [010] direction being roughly 3.5 times larger than in the [001] direction.

It has been shown[8] that, as the test temperature is raised, the probability of cracking of the potassium hydrophthalate along the secondary cleavage plane increases. This is related apparently to the fact that almost all the samples fracture completely in the neighborhood of the kink layer during high-temperature deformation along the [001] direction, so that further deformation is impossible. The large extent of the cells in the [010] direction appears to indicate that the (010) plane has a lower energy than the (001) plane. An analysis of resulting photographs shows that the rectangular cells are inclined at roughly 20° to the compression axis, the inclination decreases toward the upper end of the cell, and at the very end of the cell they are almost no longer inclined. In its external appearance, this pattern brings to mind the fracture regions produced during rupture of the earth's crust during an earthquake.

When potassium hydrophthalate is deformed along the [100] direction, the fractal organization of the system of cracks in the neighborhood of the kink-band boundaries observed[3] at room temperature is retained at higher temperatures. The tension along the kink boundaries relaxes by forming an hierarchical system of microcracks (Fig. 4a) with sizes $L_1, L_2, \ldots, L_i$ separated by distances $d_1, d_2, \ldots, d_i$. Over the entire range of temperatures that was studied, the ratios $L_{i+1}/L_i \approx 4 \approx d_{i+1}/d_i$. The boundaries of the kink band form a fan of low-angle dislocation walls, as shown schematically in Fig. 4b. The curvature of the lattice gradually increases as the applied stresses are raised. When this curvature reaches a critical value (corresponding to attaining the angle θ_ξ in Fig. 4b), cracks form in the region of the crystal with maximum tension. Here the inner radius of curvature of one of the parts of the crystal adjacent to the crack becomes a convex crack surface. The crystal becomes capable of being deformed to a state such that the inner radius of curvature of the crystal again reaches a critical value and the process would continue further with formation of first, second, third, etc., level cracks (Fig. 4c) until a critical concentration of cracks has built up, upon which the crystal breaks up along the plane containing these cracks, i.e., along the kink boundary.

Another source of inhomogeneity in the stresses in the neighborhood of the kinks is the possible rupture of their boundaries. These ruptures develop, as a rule, as an accommodation process, but they are already associated with the need for further deformation of the crystal in the neighborhood of the kink. This process is well known in the literature.[4] At the site of a rupture in a dislocation wall, a disclination dipole is formed in whose field a microcrack subsequently develops.

It should be noted that at all the temperatures and deformation rates studied here, kinking in potassium hydrophthalate took place near the ends, while the thickness of the bands was the same for both orientations and equal to the sample thickness. This confirms published data to the effect that, in the case of anisotropic crystals with a low specific energy of their cleavage plane, kinks have characteristic dimensions on the order of the crystal thickness and their nucleation and development require both a clearly distinct concentration of applied stresses and a macrobending moment on the scale of the entire sample, which occur together near the ends of a crystal. Similar kinks are often observed in mineral crystals.[9]

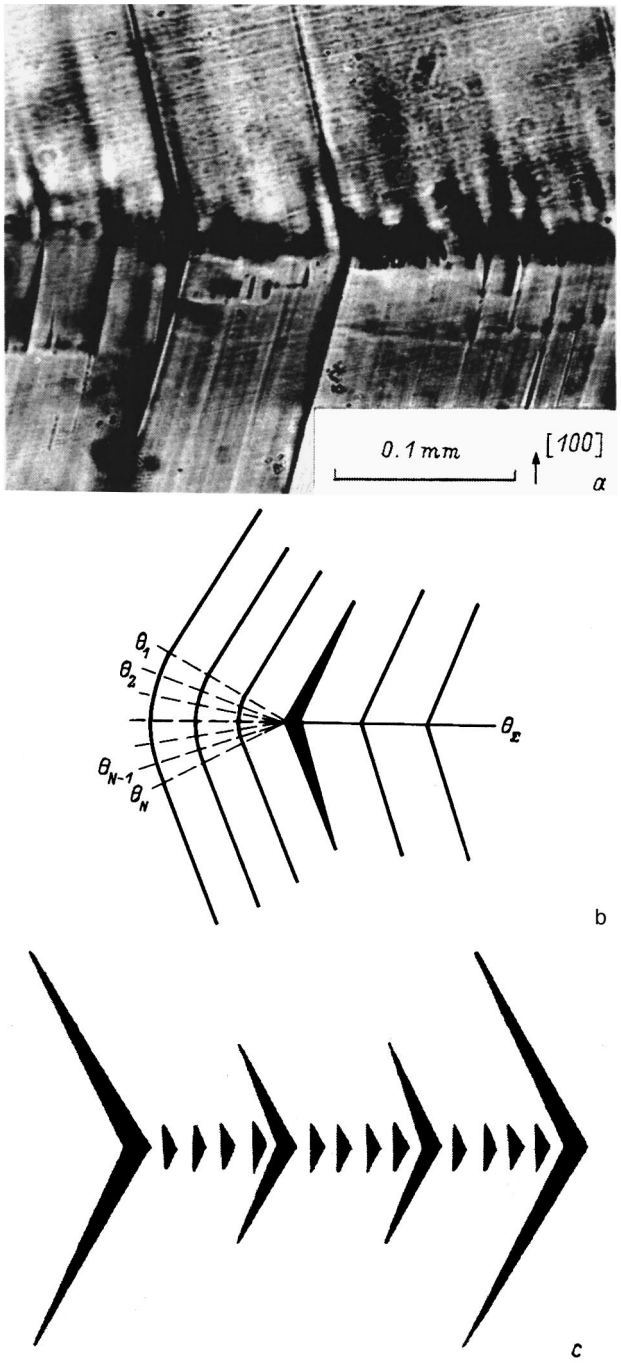

FIG. 4. (a) Picture of a kink formation region during compression of potassium hydrophthalate along [100]; (b) a sketch of the structure of a segment of a kink boundary, $d\theta_\xi$ is a high-angle boundary, θ_n is a fan of low-angle boundaries; (c) illustrating the hierarchical organization of cracks (three hierarchical levels).

3. The relation of kinking and dislocation density

One of the reasons for the appearance of secondary cleavage in potassium hydrophthalate may be the localization of residual stresses along kink boundaries. Significant internal stresses can accumulate along kink boundaries. Dur-

ing selective etching of a region adjacent to a kink band it has been found that this region is subject to more rapid selective etching than the main crystal volume to the side of the kink. A deformed sample was cracked along the cleavage plane and selective etching was performed on the fresh cleavages in dehydrated alcohol for roughly 60 s. Series of dislocations were revealed in the neighborhood of kink bands during deformation of the potassium hydrophthalate along the [100] and [001] directions. The extent of the region with an elevated density of dislocations was 3–5 mm. Thus, experiment shows that a kink band is surrounded by a region with an elevated density of dislocations.

To conclude, in this paper we have obtained new information on the features of kinking in potassium hydrophthalate crystals. It has been shown that there are two mechanisms for kinking in potassium hydrophthalate crystals, depending on the orientation of the compression axis along the [100] and [001] directions. In both cases the mechanisms for crack formation in kink bands, as well as for rotation of segments of the crystal during compression along [100], are of a dislocation-disclination character. When the stresses along a kink band relax through formation of cracks over a (010) cleavage plane with a low surface energy (compression axis [010]), the samples retain their integrity as the deformation rate and temperature are raised. In the second case (compression axis [001]), when the stresses along a kink band relax with crack formation along two planes, (010) and (001), and the secondary cleavage plane (001) has a higher surface energy than the cleavage plane (010), raising the temperature and deformation rate cause fracture of the samples. Thus, the form of the rotations and the mechanism for crack formation during kink formation in potassium hydrophthalate are determined to a substantial degree by the anisotropic properties of the material.

Both Ref. 3 and the present study were initiated by V. I. Vladimirov, who regarded kink formation as a manifestation of rotational deformation and to which he devoted several papers.[4,5] We remember our collaboration with V. I. Vladimirov with thanks.

[1] G. S. Belikova, L. M. Belyaev, Yu. V. Pisarevskiĭ, I. M. Sil'vestrova, and T. N. Turskaya, Kristallografiya **19**, 566 (1974).
[2] V. R. Regel', V. I. Vladimirov, N. L. Sizova, L. A. Lutfullaeva, M. M. Sil'vestrova, Yu. V. Pisarevskiĭ, G. S. Belikova, T. N. Turskaya, T. M. Okhrimenko, and M. A. Chernysheva, Kristallografiya **34**, 1490 (1989).
[3] V. I. Vladimirov, A. A. Birkovskiĭ, V. R. Regel', N. L. Sizova, G. S. Belikova, and T. N. Turskaya, Fiz. Tverd. Tela **31** (10), 125 (1989) [Sov. Phys. Solid State **31**, 1722 (1989)].
[4] V. I. Vladimirov and A. E. Romanov, in *Disclination in Crystals* [in Russian], Nauka, Leningrad (1986), p. 224.
[5] V. I. Vladimirov, in *The Physical Nature of Metal Fracture* [in Russian], Metallurgiya, Moscow (1984), p. 280.
[6] V. V. Rybin, in *Large Plastic Deformations and Metal Fracture* [in Russian], Metallurgiya, Moscow (1986), p. 232.
[7] G. V. Bereshkova and V. R. Regel', Kristallografiya **26**, 140 (1981).
[8] N. L. Sizova, L. A. Lutfullaeva, V. R. Regel', S. I. Dokhnovskaya, M. M. Sil'vestrova, G. S. Belikova, and T. N. Turskaya, Kristallografiya **37**, 1047 (1992).
[9] I. A. Bell, C. L. Wilson, A. C. McLaren, and M. A. Etheridge, Tectonophysics **127**, 49 (1986).

Translated by D. H. McNeill

MAGNETISM AND FERROELECTRICITY

NMR signals from 0° domain-wall magnetic inhomogeneities in cubic ferrite-garnet crystals

I. V. Vladimirov, R. A. Doroshenko, S. V. Seregin, and R. S. Fakhretdinova

Institute of Molecular and Crystal Physics, Russian Academy of Sciences, 450075 Ufa, Russia
(Submitted February 6, 1998)
Fiz. Tverd. Tela (St. Petersburg) **41**, 269-273 (February 1999)

The Fe^{57} NMR signals from 0° domain-wall magnetic inhomogeneities are studied numerically at sites where a 180° domain wall is stabilized in cubic ferrite-garnet crystals. The dependence of the NMR absorption lineshape on the induced anisotropy constants and on the magnitude of the constant magnetic field is studied.
[S1063-7834(99)01602-0]

The properties of NMR signals from nuclei localized in the region of magnetic inhomogeneities (e.g., various kinds of domain walls) of magnetically ordered crystals have, thus far, only been analyzed in materials having spatially uniform parameters which determine the structure of domain walls and other magnetic inhomogeneities.[1–3] However, the stabilization of domain walls associated with the development of anisotropies and the presence of crystal-structure defects which destroy the spatial homogeneity lead to the appearance of magnetic inhomogeneities of a new type which can change the NMR spectrum substantially.

In this paper we present results from a study of the NMR signals from in-plane magnetic inhomogeneities of the 0° domain-wall type, which develop at sites where the 180° Bloch-domain wall is stabilized in cubic crystals with a combined magnetic anisotropy. (NMR signals from magnetic inhomogeneities are produced by oscillations in the magnetization of the magnetic inhomogeneities in a longitudinal rf field.) We examine the dependence of the 0° domain-wall NMR absorption lineshape on the induced anisotropy constant and the magnitude of the constant magnetic field. The 0° domain-wall NMR signals were calculated numerically taking into account the change in structure of the magnetic inhomogeneity in the constant magnetic field.

Stabilization of a 180° Bloch-domain wall leads to the appearance of terms which depend explicitly on the spatial coordinate in the energy density of the anisotropy of a magnet. Thus, it is impossible to describe with an analytic expression the structure of a magnetic inhomogeneity that develops at the site where a domain wall is stabilized. To calculate the structure of the magnetic inhomogeneity, we have used a method[4] which essentially involves expanding the equation for rotation of the magnetization vector

$$\varphi'' - f(y,\varphi,\varphi') = 0, \tag{1}$$

in a Taylor series near an approximate solution of the form

$$\varphi''_{n+1} - \left(f(y,\varphi_n,\varphi'_n) + \frac{\partial f(y,\varphi_n,\varphi'_n)}{\partial \varphi}(\varphi_{n+1}-\varphi_n) \right) = 0, \tag{2}$$

where φ_n is an approximate solution of the equation. Writing the derivatives in the form of finite differences, we obtain a system of linear algebraic equations with a tridiagonal matrix which is solved by iteration. The resulting solution is the distribution of directions of the magnetization vector in the magnetic inhomogeneity. The direction of the magnetization in the crystal bulk coincides with the [111] direction, i.e., the boundary conditions for the problem have the form $\varphi(\pm\infty) = 0$, $\varphi'(\pm\infty) = 0$. The turning plane for the magnetization is $(1\bar{1}0)$. The energy density includes the following terms: the energies $K_1 < 0$ of the cubic anisotropy and K_u of the uniaxial (eliminating the degeneracy of the cubic axes with the symmetry axis along [111]) anisotropy, the exchange energy A, the energies of the constant magnetic field h^* and rf field with amplitude h' applied along the [111] direction, and the energies of the induced anisotropy (F and G):

$$\begin{aligned} e_{DW}/K_u = &-q\left(\frac{\sin^4\varphi}{4} + \frac{\cos^4\varphi}{3} - \frac{\sqrt{2}}{3}\sin^3\varphi\cos\varphi \right) \\ &+ \sin^2\varphi - h\cos\varphi + a(\varphi')^2 \\ &- f\Sigma_i \alpha_i^2\beta_i^2 - g\Sigma_{i\neq j}\alpha_i\alpha_j\beta_i\beta_j . \end{aligned} \tag{3}$$

Here $q = |K_1|/K_u$, $h = (h^* + h')/K_u$, $a = A/K_u$, $f = F/K_u$, $g = G/K_u$, α_i are the direction cosines of the magnetization vector, β_i are the direction cosines of the magnetization vector in the initial 180° Bloch-domain boundary [β_i depends on the angle φ_0, which describes the rotation of the magnetization vector in the 180° Bloch-domain boundary and is determined by the equation $\cot\varphi_0 = (\sqrt{4+3q}\sinh(y/\delta) + \sqrt{2}q/3)/(2(1_2q/3))$] and, φ is the angle relative to the [111] direction describing the rotation of the magnetization vector in the magnetic inhomogeneities.

The resulting solutions can be used to determine the influence of the induced anisotropy and magnetic field on the

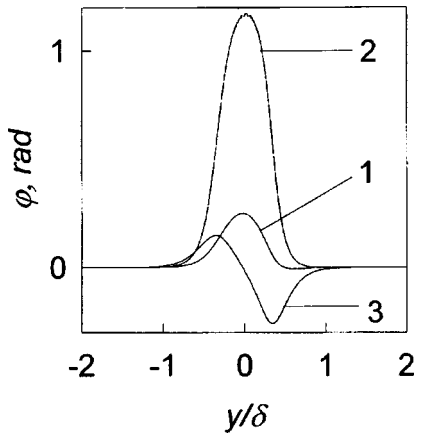

FIG. 1. Structure of a magnetic inhomogeneity for $q=100$: (*1*) $g=30$, $f=0$; (*2*) $g=70$, $f=0$; (*3*) $g=0$, $f=30$.

structure of the magnetic inhomogeneity. Figure 1 shows the structures of the magnetic inhomogeneities which develop at a site where a 180° domain wall is stabilized for various parameters g and f. The structure of the magnetic inhomogeneity originates in the nature of the induced anisotropy, which for the given turning plane of the magnetization vector can be represented as an orthorhombic anisotropy with spatially dependent parameters and, therefore, with spatially variable easy axes. Increasing the constants f and g ($0<g<66$) of the induced anisotropy which stabilizes a 180° Bloch domain wall raises the amplitude (angle of the maximum deviation from the [111] direction) of the magnetic inhomogeneity. Increasing the external magnetic field reduces the amplitude of the magnetic inhomogeneity. There is a new solution for $g>66$ in which the amplitude of the magnetic inhomogeneity increases discontinuously and the magnetization vector at the center of the magnetic inhomogeneity is oriented along a direction close to $[11\bar{1}]$ (curve *2* of Fig. 1). A constant magnetic field applied along [111] reduces the maximum deviation angle in the magnetic inhomogeneity. For magnetic inhomogeneities formed at a site where a 180° domain wall is stabilized by an induced anisotropy with $g>66$, a rise in the constant magnetic field can cause a transition between the solutions for magnetic inhomogeneities with low (curve *1* of Fig. 1) and high amplitudes (curve *2* of Fig. 1).

We now consider the 0° domain-wall NMR absorption lineshape for three groups of nuclei with orientations of the anisotropy axis of the local magnetic field along the edges of a cubic crystal lattice and for four groups, with the orientations along the body diagonals (an iron nucleus at the *d*- and *a*-sites of a ferrite-garnet). The absorption in the segment $[y,y+dy]$ of the domain wall is proportional to the square of the amplitude of the variable component of the local magnetic field at the nucleus. In this case, the NMR absorption lineshape will have the form

$$P(\nu)\propto\sum_i \int_{-\infty}^{+\infty}\langle\Delta\varphi^2\rangle dy/(\Delta^2+(\nu_i(y)-\nu)^2), \qquad (4)$$

where $i=1, 2, 3, 4, (1,2,3)$ for the *a*-sites (*d*-sites), $\Delta^2=10^{-4}$ ($\Delta^2=10^{-3}$) for the *a*-sites (*d*-sites), ν is the frequency of the rf field h', and $\langle\Delta\varphi^2\rangle$ is the average of the square of the variation in the orientation angle of the mag-

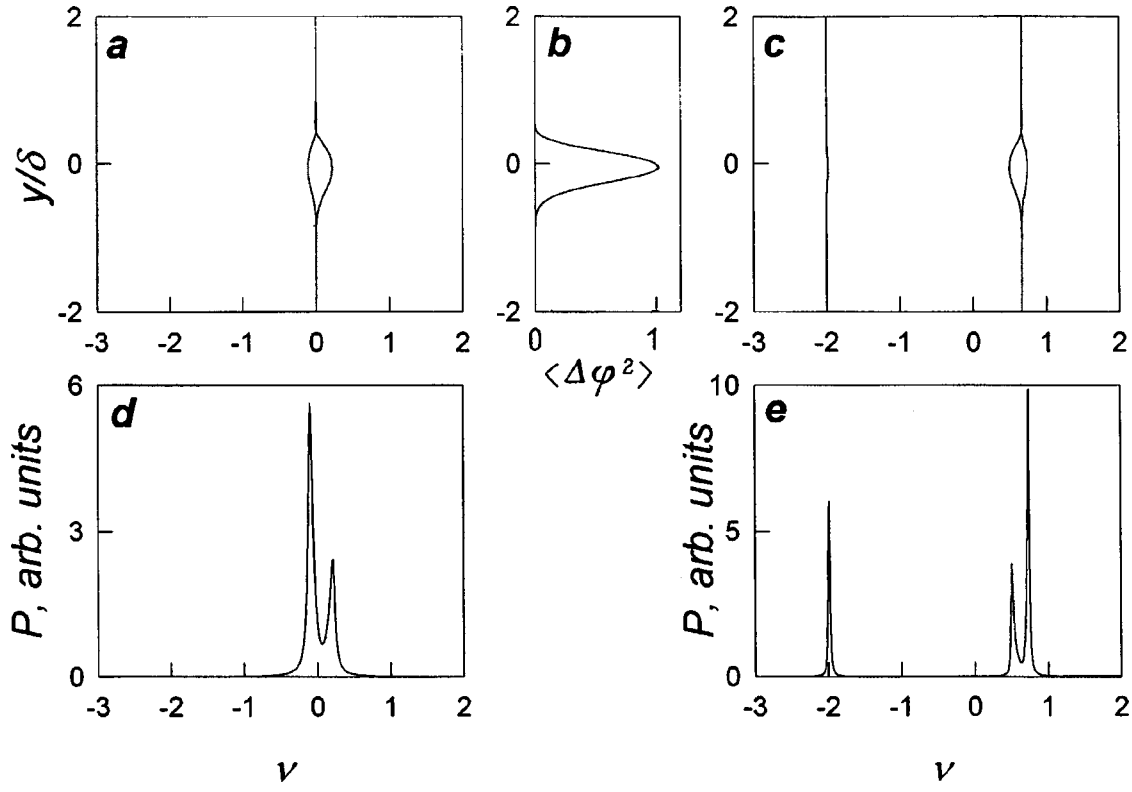

FIG. 2. The variation in the frequency (*a*, *c*) and $\langle\Delta\varphi^2\rangle$ (*b*) over the width of a magnetic inhomogeneity and the shape of the NMR absorption line (*d*, for tetrahedral sites; e for octahedral sites). The curves have been calculated for $g=30$, $f=0$, $q=100$, and $h'/K_u=0.1$.

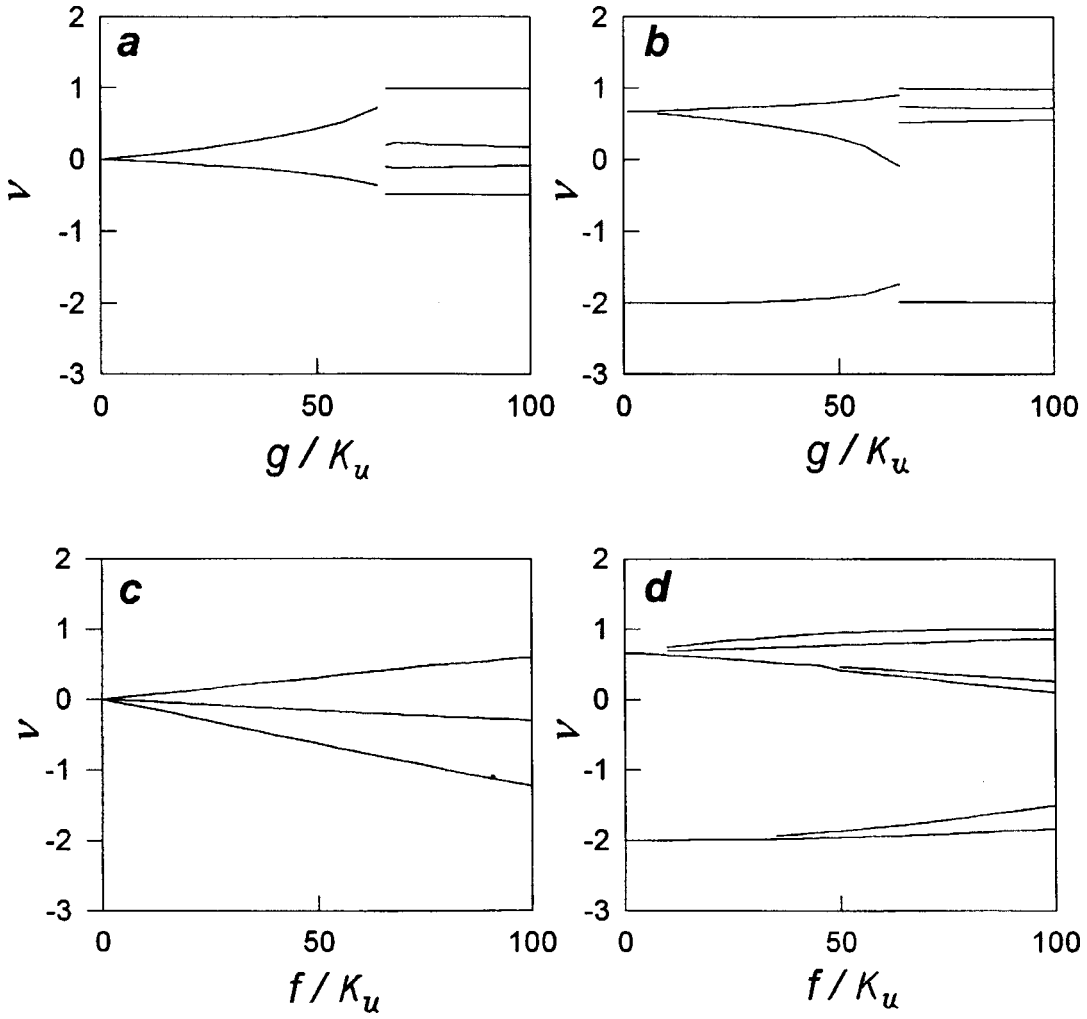

FIG. 3. The frequencies of the absorption peaks as functions of the induced anisotropy constants g (*a*, *b*) and f (*c*, *d*) for the tetrahedral (a, c) and octahedral (*b*, *d*) sublattices. The curves have been calculated for $q=100$ and $h'/K_u=0.1$.

netization vector in the magnetic inhomogeneity averaged over the period of the oscillations in the rf field. The anisotropic component of the local magnetic field is small, so it is possible to write the dependence of the NMR frequency on the orientation of the magnetic moment in the form

$$\nu_i(y)=1-3\cos^2\Phi_i, \tag{5}$$

where Φ_i is the angle between the *i*-th local anisotropy axes at the nucleus and the direction of the magnetization in the magnetic inhomogeneity and $\nu_i(y)$ is the reduced frequency.

It is known[1] that the main contribution to the formation of the peaks in the NMR absorption of magnetic inhomogeneities is from the segments of the walls with a maximum spectral density, i.e., for which $d\nu_i(y)/dy=0$. Since the maximum deviation angles from the [111] direction increase when the induced anisotropy constants in the magnetic inhomogeneity become larger, this leads to a change in the frequency dependence over the width of the magnetic inhomogeneity.

The NMR signals of a volume uniformly magnetized along the [111] direction ($f=0$ and $g=0$) from tetrahedral sites of iron nuclei appear at $\nu=0$ and those from octahedral sites, at $\nu=-2$ and $\nu=2/3$.[5,6] The effect of the induced anisotropy on the NMR signals of magnetic inhomogeneities from sites where 180° domain walls are stabilized shows up as an splitting of the signals and a change in the absorption amplitude. Let us examine the effect of the components of the induced anisotropy on the NMR signals.

g-component. We shall examine two domains of variation in g, $0<g<66$ and $66<g<100$.

1. $0<g<66$, $f=0$. It is clear in Fig. 2b that the maximum of $\langle\Delta\varphi^2\rangle$ lies in the central part of the magnetic inhomogeneity. This is because, for a given value of the anisotropy constant g, the magnetization vector in the central portion of the magnetic inhomogeneity is directed along an intermediate crystallographic direction. Thus, a low amplitude magnetic field causes a significant shift in the orientation of the magnetization at the center of the magnetic inhomogeneity.

According to Eq. (5), the spatial dependence of the orientation of the magnetization vector in the magnetic inhomogeneity leads to a frequency $\nu_i(y)$ dependence over the width of the inhomogeneity (Figs. 2a and 2c). Since the inhomogeneity under study is a 0° domain wall inhomogeneity, the maximum spectral density will always lie at layers

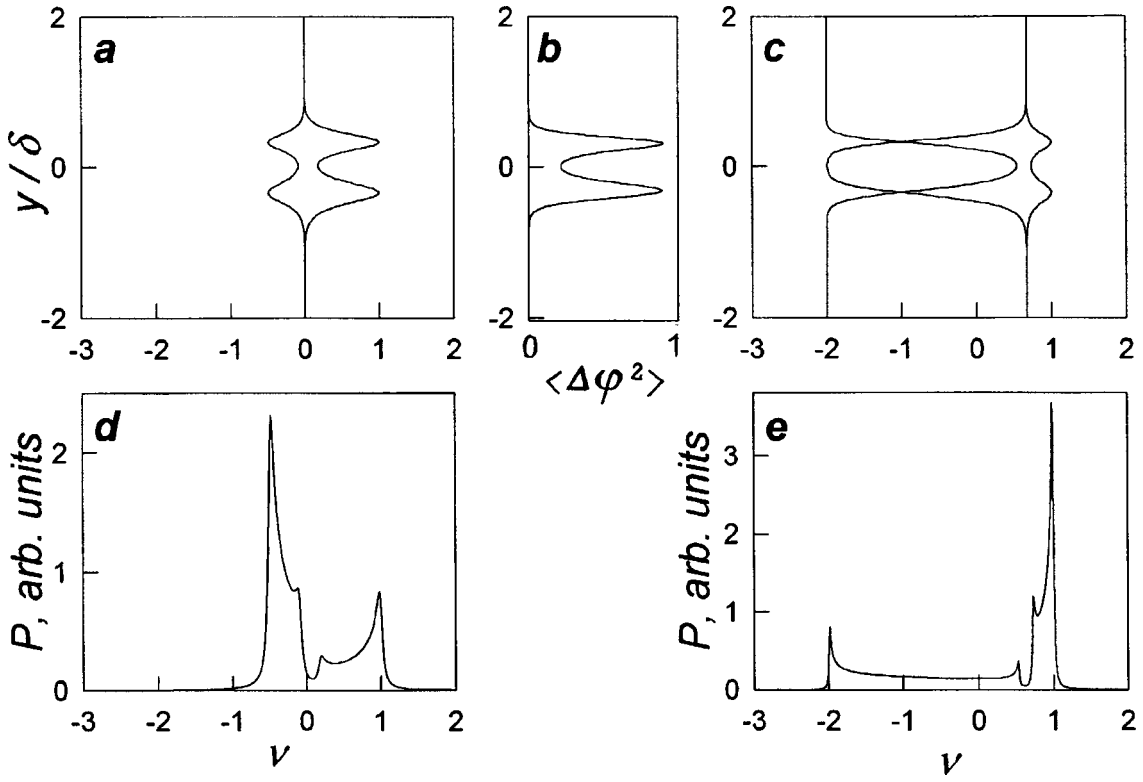

FIG. 4. The variation in the frequency (*a*, *c*) and $\langle \Delta\varphi^2 \rangle$ (*b*) over the width of a magnetic inhomogeneity and the shape of the NMR absorption line (*d*, for tetrahedral sites; e for octahedral sites). Curves *a*-*e* have been calculated for $g=70$, $f=0$, $q=100$, and $h'/K_u=0.1$.

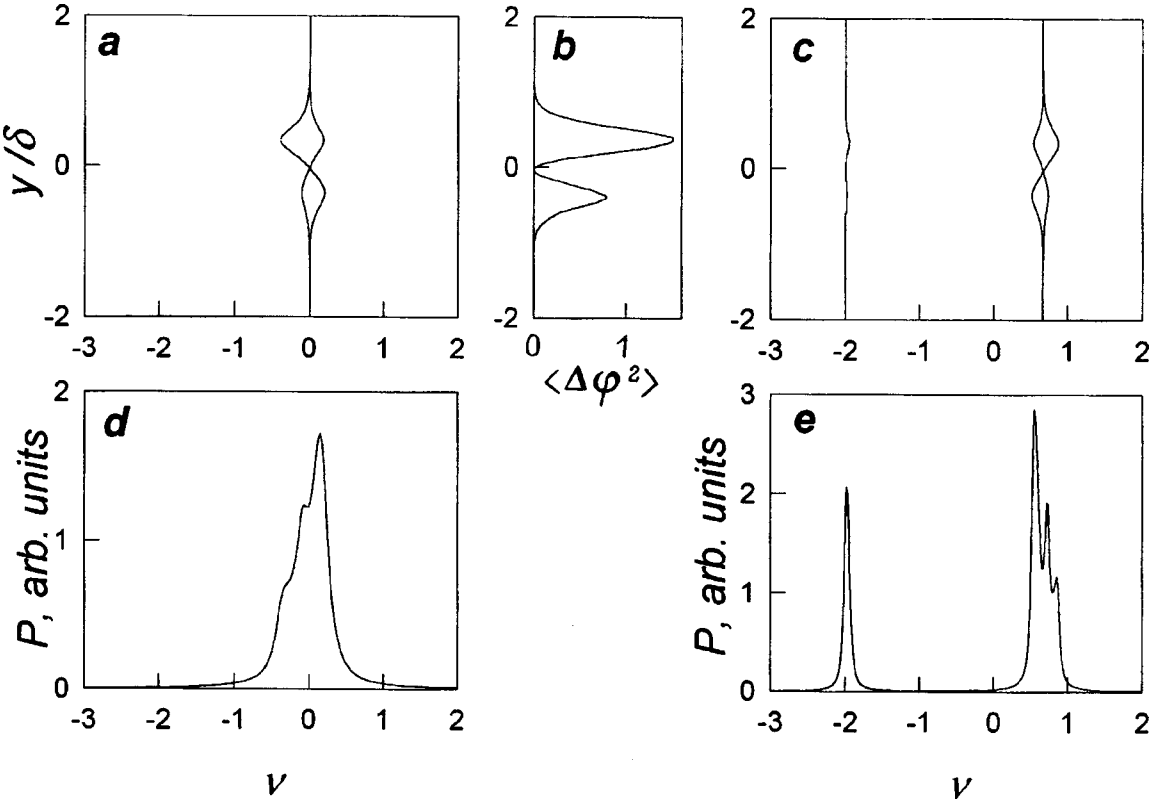

FIG. 5. The variation in the frequency (*a*, *c*) and $\langle \Delta\varphi^2 \rangle$ (*b*) over the width of a magnetic inhomogeneity and the shape of the NMR absorption line (*d*, for tetrahedral sites; e for octahedral sites). Curves *a*-*e* have been calculated for $g=0$, $f=30$, $q=100$, and $h'/K_u=0.1$.

with a maximum deviation angle from the direction of the magnetization vector in sample bulk. Thus, all the absorption peaks from *a* (Fig. 2d) and *d* sites (Fig. 2e) are formed by the central layer of the magnetic inhomogeneity. An increase in g leads, as stated above, to an increase in the maximum deviation angle in the magnetic inhomogeneity and, therefore, to a change in the frequencies of the NMR absorption peaks (Figs. 3a and 3b). The increased change in the central layer of the magnetic inhomogeneity with rising g leads to an increase in the NMR absorption amplitude at all resonance frequencies, for both the *a* and *d* sublattices.

2. $66<g<100$, $f=0$. For this range of values of g in the central part of the magnetic inhomogeneity the magnetization vector is oriented along directions close to $[11\bar{1}]$. The effect of the magnetic rf field induces small changes in the center of the magnetic inhomogeneity compared to the layers with a magnetization direction along [110] (Fig. 4b). In Figs. 4a and 4c it is clear that the condition of a maximum in the spectral density is satisfied for 4 frequencies in the *d* and *a* sublattices. The corresponding NMR spectra (Figs. 4d and 4e) consist of 4 absorption peaks. In Figs. 3a and 3b the frequencies of the absorption peaks remain essentially unchanged with increasing g (for the range of values considered here); this is because of a negligible change in the structure of the magnetic inhomogeneity. The amplitudes of the peaks over the entire absorption band for the *a* and *d* sites decrease owing to an absolute decrease in $\langle \Delta\varphi^2 \rangle$.

f-component ($g=0$). The more complicated structure of magnetic inhomogeneities that form at a site where a 180° domain wall is stabilized by a magnetic anisotropy with an f component (curve *3* of Fig. 1) lead to complicated variations in the frequency and $\langle \Delta\varphi^2 \rangle$ over the width of the inhomogeneity. The spatial variation dependence of $\langle \Delta\varphi^2 \rangle$ has two maxima and a minimum corresponding to a change in the orientation of the magnetization at the center of the magnetic inhomogeneity (Fig. 5b). Figures 5a and 5c shows plots of $\nu_i(y)$ for the *d* and *a* sublattices, respectively. The spectrum of the *d* sites (Fig. 5d) consists of three maxima and the absorption band broadens with increasing f (Fig. 3c), while the amplitudes of the absorption peaks increase (for $f \in [0;100]$). $\nu_i(y)$ for the *a* sublattices contains seven frequencies for which the condition for a maximum spectral density is satisfied. In the central layer of the magnetic inhomogeneity (frequency $\nu=-2$) the condition for a maximum spectral density is satisfied, but, since $\langle \Delta\varphi^2 \rangle = 0$ at the center of the magnetic inhomogeneity, there is no signal. The absorption lineshape for the *a* sites of iron nuclei from the magnetic inhomogeneity consists of four absorption maxima. The maximum on the left hand edge of the absorption band, as well as the signal with the highest absorption amplitude consist of two signals that are close in amplitude. With increasing f, there is a small shift in the absorption band to higher frequencies (Fig. 3d) and the signals undergo splitting. The amplitudes of the absorption maxima then increase at all the resonance frequencies and there is also a change in the relationships among the maxima.

When a constant magnetic field is applied parallel to the magnetization in the sample bulk, the deviation angles of the magnetization in the magnetic inhomogeneity become smaller and, because of this, the resonance frequencies of the absorption maxima change. For magnetic inhomogeneities formed from places where 180° domain walls are stabilized by an f ($g=0$) or g ($0<g<66$, $f=0$) component, there is typically a reduction in $\langle \Delta\varphi^2 \rangle$ over the entire width of the magnetic inhomogeneity and a drop in the absorption amplitude at all the resonance frequencies. For magnetic inhomogeneities formed from places where 180° domain walls are stabilized by a g component with $66<g<100$ ($f=0$), there is typically a sharp rise in $\langle \Delta\varphi^2 \rangle$ over the width of the inhomogeneity and, therefore, an increase in the amplitude over the entire NMR absorption band. When the external field amplitude is raised in this range of g a maximum begins to appear at $\nu=-2$ for two reasons: an increase in the width of the boundary layer with $\nu=-2$ and an increase in $\langle \Delta\varphi^2 \rangle$ for this layer.

These studies show the following: at places where 180° domain walls are stabilized, magnetic inhomogeneities of a 0° domain-wall type are formed whose structures depend both on the components of the induced anisotropy and on the strength of the constant magnetic field. The NMR spectra of magnetic inhomogeneities differ from those of uniform magnetized samples and samples containing Bloch domain walls.[7–9] The NMR lineshapes for the signals from magnetic inhomogeneities for the *a* and *d* sublattices are determined by the magnitudes of the components f and g of the induced anisotropy and by the strength of the constant magnetic field.

This work was supported by the Russian Fund for Fundamental Research (96-02-19255).

[1] G. A. Murray and W. Murshall, Proc. Phys. Soc. **86**, 315 (1965).
[2] E. A. Turov, A. P. Tankeev, and M. I. Kurkin, Fiz. Tverd. Tela **28**, 385 (1969) [*sic*].
[3] E. A. Turov, A. P. Tankeev, and M. I. Kurkin, Fiz. Tverd. Tela **29**, 747 (1970) [*sic*].
[4] V. G. Veselago, I. V. Vladimirov, and R. A. Doroshenko, Tr. IOFAN **44**, 92 (1993).
[5] V. A. Borodin, V. D. Doroshev, V. A. Klochan, N. M. Kovtun, R. Z. Levitin, and A. S. Markosyan, Zh. Éksp. Teor. Fiz. **70**, 1363 (1976) [Sov. Phys. JETP **43**, 711 (1976)].
[6] F. Boutron and C. Robert, Compt. Rend. **253**, 433 (1961).
[7] R. A. Doroshenko, S. V. Seregin, and R. S. Fakhretdinova, *Statics and Dynamics of Ordered Media* [in Russian, Ufa (1994), p. 54].
[8] R. A. Doroshenko, S. V. Seregin, and R. S. Fakhretdinova, Fiz. Tverd. Tela **38**, 3642 (1996) [Phys. Solid State **38**, 1985 (1996)].
[9] S. V. Seregin, R. A. Doroshenko, and R. S. Fakhretdinova, JETP Lett. **50**, 142 (1989).

Translated by D. H. McNeill

Dynamics of interphase domain walls during a Morin-type phase transition

V. S. Gerasimchuk

Donbas State Academy of Construction and Architecture, 339023 Makeevka, Ukraine

A. L. Sukstanskiĭ

Donetsk Physicotechnical Institute, Ukrainian Academy of Sciences, 340114 Donetsk, Ukraine
(Submitted June 9, 1998)
Fiz. Tverd. Tela (St. Petersburg) **41**, 274–282 (February 1999)

The dynamics of 90-degree interphase domain walls during a first-order Morin-type spin-reorientation phase transition is studied theoretically. It is shown that an oscillatory motion of the walls with an amplitude that depends linearly on the field amplitude, as well as a drift motion of the wall at a velocity proportional to the square of the field amplitude, are driven by an external oscillating magnetic field. Drift of the entire domain structure as a whole is predicted to be possible. © *1999 American Institute of Physics.* [S1063-7834(99)01702-5]

It is well known that in a number of weak ferromagnetic materials spin-reorientation phase transitions take place from a weakly ferromagnetic phase to an antiferromagnetic phase, the so-called Morin-type phase transitions. A classical example of this type of phase transition is the transition in dysprosium orthoferrite ($DyFeO_3$) when the temperature is reduced to 40 K,[1,2] during which the antiferromagnetism vector is reoriented from the crystal *a* axis to the *b* axis.

Experimental observations[2–4] of a Morin transition in $DyFeO_3$ indicate that this transition is a first-order phase transition and an intermediate state develops in the transition region in the form of a domain structure consisting of alternating weakly ferromagnetic and antiferromagnetic domains. Here it should be noted that a coherent domain structure appears only when an external constant magnetic field is applied to the magnet. (In experiments[4,5] this field was oriented along the crystal *b* axis.)

A large number of papers have been devoted to the theoretical study of Morin-type transitions. (See Refs. 1–4, for example.) In these, primary attention has been devoted to studying the intermediate state which arises in the phase transition region, symmetry analysis, the construction of phase diagrams, etc. The dynamical properties of the interphase domain walls, which separate the antiferromagnetic and weakly ferromagnetic domains that coexist during this spin-reorientation phase transition, have been studied much less.

In a Morin phase transition the interphase domain walls are 90-degree domain walls. The dynamic properties of 90-degree domain walls differ greatly from the corresponding properties of 180-degree walls. In particular, it has been shown[6] that the limiting steady-state velocity of a 90-degree interphase domain wall is determined by relativistic interactions, while that of 180-degree domain walls in an antiferromagnetic material is determined only by exchange interactions.[7]

The uniform motion of an interphase 90-degree domain wall which occurs during a temperature phase transition has been studied[8] and it was shown that the velocity of the interphase domain wall is determined by the balance between the ''pressure force'' owing to the deviation of the system from phase equilibrium and the ''frictional force'' owing to dissipative processes. The dynamic properties of an interphase-domain wall in an antiferromagnetic material in an external magnetic field during a spin-flop phase transition have been studied.[9] The steady and oscillatory motions of an interphase-domain wall in rhombic ferroelectric-ferromagnetic materials acted on by an external electric field have been examined.[10]

The characteristic features of the dynamical properties of interphase domain walls in dysprosium orthoferrite in a pulsed magnetic field with a short risetime have been observed experimentally.[11–13] These features show up, in particular, in a nonlinear dependence of the wall velocity on the field amplitude and in the asymmetry of this dependence with respect to the direction of the pulsed field.

The purpose of this paper is to study theoretically the dynamical properties of isolated 90-degree interphase domain walls in weak ferromagnetic materials such as the rare-earth orthoferrites during Morin-type phase transitions under the action of a variable external magnetic field. An analogous problem has been solved[14] for the interphase boundaries in the region of a spin-flop spin-reorientation phase transition in antiferromagnetic materials. The important difference between these problems is that a Dzyaloshinskii-exchange relativistic interaction exists in the rare-earth orthoferrites and creates a weak ferromagnetic moment in one of the phases between which a Morin phase transition takes place. As has been shown for the example of 180-degree domain walls in weak ferromagnets,[15] including the Dzyaloshinskii interaction leads to significant differences between the dynamic characteristics of the walls in weak ferromagnets and the corresponding characteristics of ''pure'' antiferromagnets. Thus, one should expect that the Dzyaloshinskii interaction should be just as fundamental for the interphase domain walls in the rare-earth orthoferrites of interest to us in this paper.

As is known from the example of 180-degree domain

walls in different magnetically ordered crystals, in an oscillating magnetic field the domain walls oscillate at the frequency of the field and, in addition, they drift, i.e., there is a constant component of the velocity.[15–18] It will be shown below that these types of motion are also typical for the 90-degree interphase domain walls separating the antiferromagnetic and weakly ferromagnetic phases during a Morin phase transition.

1. BASIC EQUATIONS

We shall, examine therefore, a two-sublattice weak ferromagnet of the rare-earth orthoferrite type, including substances with the chemical formula $MFeO_3$, where M is a rare-earth element or yttrium. The crystal symmetry group is D_{2h}^{16}. We shall proceed from the standard expression for the energy of a rare-earth orthoferrite, expressed in terms of the weak ferromagnetism vector $\mathbf{M}=\mathbf{M}_1+\mathbf{M}_2$ and the antiferromagnetism vector $\mathbf{L}=\mathbf{M}_1-\mathbf{M}_2$ (where $\mathbf{M}_1$ and $\mathbf{M}_2$ are the magnetization vectors of the sublattices)[1,2]

$$W=\int d\mathbf{r}\left\{\frac{\delta}{2}\mathbf{M}^2+\frac{\alpha}{2}(\nabla\cdot\mathbf{L})^2+\mathbf{d}\cdot[\mathbf{M}\times\mathbf{L}]+w_a(\mathbf{L})-\mathbf{M}\cdot\mathbf{H}\right\}, \tag{1}$$

where α and δ are the nonuniform and uniform exchange interaction constants, respectively, w_a is the magnetic anisotropy energy density, and $\mathbf{H}$ is the external magnetic field. We choose the axes (X,Y,Z) of the cartesian coordinate system to coincide, respectively, with the *a*, *b*, and *c* axes of the crystal. The rare-earth orthoferrites are characterized by a rhombic magnetic symmetry of type $2_x^-2_z^-$. Here the principal even axis is the Y axis and $\mathbf{d}=d\mathbf{e}_y$, where d is the Dzyaloshinskii-exchange relativistic-interaction constant, and $\mathbf{e}_y$ is the unit vector along the corresponding axis. In this geometry, the weakly ferromagnetic phase corresponds to an orientation of the vectors $\mathbf{L}$ and $\mathbf{M}$ along the *a* and *c* axes of the rare-earth orthoferrite, respectively (the F_xG_x phase according to the terminology used by Turov[19]). In the antiferromagnetic phase the antiferromagnetism vector $\mathbf{L}$ is oriented along the *b* axis (G_y phase, $\mathbf{M}=0$).

It should be noted that the symmetry of the rare-earth orthoferrites allows the invariants M_xL_z and M_zL_x separately. Thus, the more general expression for the energy of an rare-earth orthoferrite contains two constants describing the Dzyaloshinskii interaction, $d_1M_xL_z$ and $d_3M_zL_x$, with $d_1\neq d_3$. However, the difference between the constants d_1 and d_3 is purely relativistic in origin and is, therefore, much smaller than either d_1 or d_3 ($|d_1-d_3|\sim10^{-2}d_{1,3}$, see Refs. 1–3). This circumstance makes it possible to use the approximation $d_1\approx d_3=d$ in describing the dynamics of the rare earth orthoferrites. (The effect of the difference between the constants d_1 and d_3 becomes extremely important for analyzing the relaxation properties of the domain walls in the rare earth orthoferrites).[20]

We write the energy of the magnetic anisotropy in an rare-earth orthoferrite in the form

$$w_a=M_0^2\left[\frac{1}{2}(\beta_1l_z^2+\beta_2l_y^2)+\frac{1}{4}(\beta_1'l_z^4+\beta_2'l_y^2l_z^2+\beta_3'l_y^4)\right], \tag{2}$$

where $\mathbf{l}=\mathbf{L}/|\mathbf{L}|$, β_1 and β_2 are the second-order anisotropy constants, β_1', β_2', and β_3' are those of fourth order, and $M_0=|M_{1,2}|$ is the magnitude of the magnetization vectors of the sublattices.

The static and dynamical properties of two-sublattice antiferromagnetic materials (including weak ferromagnets such as the rare earth orthoferrites) can be studied in terms of a standard system of equations of motion for the magnetization vectors of the sublattices (the Landau-Lifshitz equations) or an equivalent system of equations for the vectors $\mathbf{M}$ and $\mathbf{L}$. However, it has been shown[21,22] that the problem can be greatly simplified if we use the fact that the exchange antiferromagnetic interaction between the sublattices is large ($\delta\gg1$), so the turning angle of the sublattice magnetization vectors $\mathbf{M}_1$ and $\mathbf{M}_2$ are small. Here the inequality $|\mathbf{M}|\ll|\mathbf{L}|\sim2\mathbf{M}_0$ holds and can be used t express the weak ferromagnetism vector $\mathbf{M}$ in terms of the unit anitferromagnetism vector $\mathbf{1}$,

$$\mathbf{M}=\frac{2}{\delta}\left\{[\mathbf{l}\times[\mathbf{H}\times\mathbf{l}]]+\frac{2}{g}[\dot{\mathbf{l}}\times\mathbf{l}]+M_0[\mathbf{d}\times\mathbf{l}]\right\} \tag{3}$$

(g is the gyromagnetic ratio and a dot over a symbol denotes the time derivative) and to write down a closed equation for the vector $\mathbf{1}$ which is an Euler–Lagrange variational equation for the effective lagrangian $L(\mathbf{1})$.[22] For the rare earth orthoferrite being considered here, the density of the effective lagrangian has the form

$$L=M_0^2\left\{\frac{\alpha}{2}\left[\frac{1}{c^2}\dot{\mathbf{l}}^2-(\nabla\mathbf{l})^2\right]-\tfrac{1}{2}(\beta_1l_z^2+\tilde{\beta}_2l_y^2)+\tfrac{1}{4}(\beta_1'l_z^4+\beta_2'l_y^2l_z^2+\beta_3'l_y^4)+\frac{4}{\delta g M_0^2}[\mathbf{H}\times[\dot{\mathbf{l}}\times\mathbf{l}]]-\frac{2}{\delta M_0^2}(\mathbf{l}\cdot\mathbf{H})^2+\frac{2d}{\delta M_0}(l_xH_z-l_zH_x)\right\}, \tag{4}$$

where $c=gM_0(\alpha\delta)^{1/2}/2$ is a characteristic velocity equal to the minimum phase velocity of spin waves in the absence of a magnetic field and $\tilde{\beta}_2=\beta_2+d^2/\delta$. Note that this description of the dynamics of an antiferromagnetic material is valid in external magnetic fields much lower than the exchange field $H_e=\delta M_0$. We shall describe the dynamic braking of the domain walls owing to different relaxation processes with the aid of the dissipation function Q,

$$Q=\frac{\lambda M_0}{2g}\dot{\mathbf{l}}^2. \tag{5}$$

In terms of the two independent angular variables parametrizing the unit vector $\mathbf{l}$,

$$l_x+il_y=\sin\theta\exp(i\varphi),\quad l_z=\cos\theta, \tag{6}$$

the equations of motion, including the dissipative terms, have the form

$$\alpha\left(\Delta\theta-\frac{l}{c^2}\ddot{\theta}\right)+\sin\theta\cos\theta\left[\alpha\left(\frac{l}{c^2}\dot{\varphi}^2-(\nabla\varphi)^2\right)+\beta_1-\tilde{\beta}_2\sin^2\varphi+\beta_1'\cos^2\theta-\beta_3'\sin^2\theta\sin^4\varphi-\frac{\beta_2'}{2}\cos 2\theta\sin^2\varphi\right]-\frac{2d}{\delta M_0}(H_z\cos\theta\cos\varphi+H_x\sin\theta)-\frac{4}{\delta M_0^2}(H_z\cos\theta+H_y\sin\theta\sin\varphi+H_x\sin\theta\cos\varphi)\times(H_y\cos\theta\sin\varphi-H_z\sin\theta+H_x\cos\theta\cos\varphi)+\frac{4}{\delta g M_0^2}[\dot{H}_y\cos\varphi-\dot{H}_x\sin\varphi-2\dot{\varphi}\sin^2\theta(H_y\sin\varphi+H_x\cos\varphi)-H_z\dot{\varphi}\sin 2\theta]=\frac{\lambda}{gM_0}\dot{\theta}, \tag{7}$$

and

$$\alpha\nabla(\sin^2\theta(\nabla\varphi))-\frac{\alpha}{c^2}(\sin^2\theta\dot{\varphi})-\sin^2\theta\sin\varphi\cos\varphi\times\left(\tilde{\beta}_2+\frac{\beta_2'}{2}\cos^2\theta+\beta_3'\sin^2\theta\sin^2\varphi\right)+\frac{4}{\delta g M_0^2}\left[-\frac{1}{2}\sin 2\theta(\dot{H}_y\sin\varphi+\dot{H}_x\cos\varphi)+\dot{H}_z\sin^2\theta+2\dot{\theta}\sin^2\theta(H_y\sin\varphi+H_x\cos\varphi)+H_z\dot{\theta}\sin 2\theta\right]-\frac{4\sin\theta}{\delta M_0^2}(H_z\cos\theta+H_y\sin\theta\sin\varphi+H_x\sin\theta\cos\varphi)(H_y\cos\varphi-H_x\sin\varphi)+\frac{2d}{\delta M_0}H_z\sin\theta\cos\theta=\frac{\lambda}{gM_0}\dot{\varphi}\sin^2\theta. \tag{8}$$

If $\beta_1>0$ and $\tilde{\beta}_2>0$, then without an external magnetic field a weak ferromagnet in the F_xG_z phase is realized, where the antiferromagnetism vector **l** in the ground state is collinear with the easy axis X and the weak ferromagnetism vector **M**, with the Z axis. When the temperature is reduced, the effective anisotropy constant $\tilde{\beta}_2$ changes sign; for $\tilde{\beta}_2<0$ the light axis becomes the Y axis to which the antiferromagnetism vector **l** reorients itself. Then, as can easily be seen from Eq. (3), the weak ferromagnetism vector **M** in the ground state equals zero and the antiferromagnetic G_y phase results.

As noted above, in a spontaneous spin-reorienting transition of this sort, a coherent domain structure is not formed because of the kinetics of this process.[3,4] In fact, in the initial weakly ferromagnetic (''high temperature'') phase the unique nuclei for the antiferromagnetic phase are the 180-degree domain walls between domains with opposite orientations of the antiferromagnetism vector (parallel and antiparallel to the X axis), in which the vector **1** is rotated in the XY plane (in the center of these walls the vector **1** is oriented along the Y axis). As the phase transition point is approached the thickness of the walls increases, and this ultimately leads to the actual decay of the original 180-degree wall into two 90-degree interphase boundaries which separate the domains with **1** oriented along the X and Y axes. A coherent domain structure (an intermediate state) could also form as a result of this process. However, the demagnetizing fields prevent expansion of the 180-degree wall; its breakup into two 90-degree walls is possible only when the energy of the two 90-degree walls is lower than that of the 180-degree wall. Thus, the transition to the antiferromagnetic phase is incoherent and no intermediate state appears. If, however, a weak external constant magnetic field along the Y axis is applied to the magnet, then it stimulates breakup of the 180-degree wall into two 90-degree walls with formation of a coherent domain structure.[3,4] In this regard, we shall also assume that the external magnetic field $\mathbf{H}=\mathbf{H}_e+\tilde{\mathbf{H}}(t)$, where $\mathbf{H}_e=H_c\mathbf{e}_y$ is a constant external field and $\tilde{\mathbf{H}}(t)$ is an external oscillating magnetic field with all three components nonzero. We shall assume, as well, that the different components of the oscillating field have, in general, arbitrary phase shifts among themselves, i.e.,

$$\tilde{H}_z=\tilde{H}_{0z}\cos\omega t,\quad \tilde{H}_x=\tilde{H}_{0x}\cos(\omega t+\chi),\quad \tilde{H}_y=\tilde{H}_{0y}\cos(\omega t+\chi_1). \tag{9}$$

(As will be shown below, the drift velocity of the wall depends significantly on χ_1 and χ_2.)

For $\tilde{\mathbf{H}}(t)=0$ the equations of motion (7) and (8) imply that the domain wall in which the antiferromagnetism vector **1** is turned in the XY plane corresponds to $\theta=\theta_0=\pi/2$, while the angular variable $\varphi=\varphi_0(y)$ satisfies the condition

$$\alpha\varphi_0''-\left(\tilde{\beta}_2(T)+\frac{4H_c^2}{\delta M_0^2}\right)\sin\varphi_0\cos\varphi_0-\beta_3'\sin^3\varphi_0\cos\varphi_0=0. \tag{10}$$

(We assume that the distribution of the magnetization in the domain wall is nonuniform along the Y axis; a prime denotes differentiation with respect to this coordinate.)

It is known[1–3] that if the fourth-order anisotropy constant $\beta_3'<0$, then a Morin-type phase transition is a first-order phase transition whose temperature $T=T_M$ is determined by the equation

$$\beta'(T_M)\equiv\tilde{\beta}_2(T_M)+\frac{4H_c^2}{\delta M_0^2}=\frac{|\beta_3'|}{2}. \tag{11}$$

(The external constant field H_c shifts the transition temperature slightly.[1]) At the phase transition point (i.e., for $\beta'=|\beta_3'|/2$), where weakly ferromagnetic and antiferromagnetic phases coexist, the solution of Eq. (10) for a 90-degree interphase domain wall that satisfies the boundary conditions

$$\varphi_0(-\infty)=0,\quad \varphi_0(+\infty)=\pi/2,\quad \text{and } \varphi_0'(\pm\infty)=0, \tag{12}$$

is given by the equations

$$\varphi_0'=\frac{1}{2y_0}\sin 2\varphi_0=\frac{1}{2y_0}\operatorname{sech}\left(\frac{y}{y_0}\right),$$

$$\cos 2\varphi_0=-\tanh\left(\frac{y}{y_0}\right), \tag{13}$$

where $y_0=(\alpha/\beta')^{1/2}$ is the effective thickness of the 90-degree wall. Note that the effective thickness of the interphase wall is substantially greater than that of ordinary 180-degree walls because the fourth order anisotropy constants are small compared to the second order anisotropy constants.

It follows from Eqs. (3) and (13) that the distribution of the magnetization vector $\mathbf{M}$ in the interphase wall for $\tilde{\mathbf{H}}(t)=0$ has the form

$$M_x=-\frac{H_c}{\delta}\sin 2\varphi_0=-\frac{H_c}{\delta}\operatorname{sech}\left(\frac{y}{y_0}\right),$$

$$M_y=\frac{2H_c}{\delta}\cos^2\varphi_0=\frac{H_c}{\delta}\left[1-\tanh\left(\frac{y}{y_0}\right)\right],$$

$$M_z=-\frac{2dM_0}{\delta}\cos\varphi_0-\frac{2dM_0}{\delta}\left[1+\exp\left(\frac{2y}{y_0}\right)\right]^{-1/2}. \tag{14}$$

Therefore, when $H_c=0$ the vector $\mathbf{M}$ in the interphase wall is parallel to the Z axis and changes only in magnitude–from $2dM_0/\delta$ (absolute value) in the weakly ferromagnetic phase (for $y\to-\infty$) to 0 in the antiferromagnetic phase (for $y\to+\infty$). If, however, the external magnetic field H_c is not zero, then all three components of $\mathbf{M}$ in the interphase wall are nonzero.

If an additional external magnetic field along the Z axis is applied to an already existing interphase domain wall, then it destroys the energy balance of the two phases and the wall begins to move toward a more energy-favorable phase. Then the maximum rate of movement is determined by the maximum attainable magnitude of the additional field. (This limitation exists because the total field must remain within the lability region of the phases separated by the interphase wall.) If the additional field is variable, then the motion of the interphase wall will be nonsteady-state and, in particular, in the case of an oscillating field, the wall will oscillate at the frequency of the field with the amplitude of the oscillations directly proportional to that of the variable field (a first-order effect). In addition (see below), the wall will drift at a certain velocity proportional to the square of the amplitude of the variable field (a second order effect).

2. FIRST-ORDER PERTURBATION THEORY: OSCILLATIONS OF AN INTERPHASE DOMAIN WALL

Assuming that the oscillating field is quite weak and following a general scheme for analysis of the dynamics of domain walls in a variable field based on a version of perturbation theory for solitons,[14–18] we introduce a collective variable $Y(t)$ representing the coordinate of the domain wall at time t and shall seek a solution of the equations of motion (7) and (8) in the form

$$\theta=\frac{\pi}{2}+\vartheta(\xi,t),\quad \text{and } \vartheta=\vartheta_0(\xi)+\psi(\xi,t), \tag{15}$$

where $\xi=y-Y(t)$. The function $\varphi_0(\xi)$ describes the motion of the undistorted wall (the structure of $\varphi_0(\xi)$ is the same as that of the function $\varphi_0(y)$ in the static solution (1300, while the functions $\psi(\xi)$ and $\vartheta(\xi)$ correspond to distortions of the wall shape. The drift velocity of the domain wall is defined as the average value of the instantaneous domain wall velocity $V(t)=\dot{Y}(t)$ over the period of the oscillations, i.e., $V_{dr}=\overline{V(t)}$, where the overline denotes averaging over the period of the oscillations in the external field.

We seek the functions $\psi(\xi)$ and $\vartheta(\xi)$ which describe the distortion of the domain wall shape, as well as the wall velocity $V(t)$ in the form of series in powers of the field amplitude, keeping in mind that we are only interested in the forced motion of the domain wall,

$$\vartheta(\xi,t)=\vartheta_1(\xi,t)+\vartheta_2(\xi,t)+\ldots,$$

$$\psi(\xi,t)=\psi_1(\xi,t)+\psi_2(\xi,t)+\ldots,$$

$$V=V_1+V_2+\ldots, \tag{16}$$

where the subscripts $n=1,2,\ldots$ denote the order of smallness of the quantity with respect to the field amplitude, i.e., ψ_n, ϑ_n, $V_n\propto h^n$.

We substitute the expansion (16) in Eqs. (7)–(8) and isolate the terms of different orders of smallness. Evidently, in the zeroth approximation we obtain Eq. (10) for an interphase domain wall at rest.

The equations for the first approximation in the external variable field can be written in the form

$$(\hat{L}+\hat{T})\psi_1-2\frac{h_c g M_0}{\tilde{\omega}_0^2}\dot{\vartheta}_1\sin\vartheta_0=\frac{d}{2}\left(\frac{gM_0}{\tilde{\omega}_0}\right)^2 h_z\sin\vartheta_0$$
$$+\left(\frac{gM_0}{\tilde{\omega}_0^2}\right)\dot{h}_z+\frac{\sin 2\varphi_0}{2y_0\tilde{\omega}_0^2}(\dot{V}_1+\omega_r V_1)$$
$$-\left(\frac{gM_0}{\tilde{\omega}_0}\right)^2 h_c[h_x\cos 2\varphi_0+h_y\sin 2\varphi_0], \tag{17}$$

and

$$(\hat{L}'+\hat{T}+\sigma)\vartheta_1+2\frac{h_c g M_0}{\tilde{\omega}_0^2}\dot{\psi}_1\sin\varphi_0$$
$$=-\frac{d(gM_0)^2}{2\tilde{\omega}_0^2}h_x+\left(\frac{gM_0}{\tilde{\omega}_0}\right)^2 h_c h_z\sin\varphi_0$$
$$+\frac{gM_0}{\tilde{\omega}_0^2}\left[\dot{h}_y\cos\varphi_0\right.$$
$$\left.-\dot{h}_x\sin\varphi_0+\frac{V_1}{y_0}h_c\sin\varphi_0\sin 2\varphi_0\right]. \tag{18}$$

Here we have introduced the notation $\mathbf{h}(t)=\tilde{\mathbf{H}}(t)/M_0$, $h_c=H_c/M_0$, $\sigma=(1-k^{-1})\omega_0^2/\tilde{\omega}_0^2$, $k=\beta_1/\beta'$, and

$$\hat{T}=\frac{1}{\tilde{\omega}_0^2}\frac{d^2}{dt^2}+\frac{\omega_r}{\tilde{\omega}_0^2}\frac{d}{dt}, \tag{19}$$

where $\omega_0=gM_0(\beta_1\delta)^{1/2}/2$ and $\tilde{\omega}_0=c/y_0=\omega_0(\beta'/\beta_1)^{1/2}\ll\omega_0$ are the activation frequencies for the volume branch of spin waves in the magnet far from the phase transition temperature T_M and at $T=T_M$, respectively, and $\omega_r=\lambda\delta gM_0/4$ is the characteristic relaxation frequency.

The operator $\hat{L}$ in Eq. (17) has the form of a Schrödinger operator with a nonreflecting potential

$$\hat{L}=-y_0^2\frac{d^2}{d\xi^2}+1-\frac{2}{\cosh^2(\xi/y_0)}. \tag{20}$$

The spectrum and wave functions of the operator $\hat{L}$ (20) are well known. It has a single discrete level $\lambda_0=0$ corresponding to a localized wave function

$$f_0(\xi)=\frac{1}{(2y_0)^{1/2}\cosh(\xi/y_0)}, \tag{21}$$

as well as a continuous spectrum $\lambda_k=1+(ky_0)^2$ which has the eigenfunctions

$$f_k(\xi)=\frac{1}{b_kL^{1/2}}(\tanh(\xi/y_0)-iky_0)\,e^{ik\xi}, \tag{22}$$

where $b_k=[1+(ky_0)^2]^{1/2}$ and L is the length of the crystal.

The operator $\hat{L}'$ in Eq. (18) has the form

$$\hat{L}'=\hat{L}+\frac{5}{4\cosh^2(\xi/y_0)}+\left(1+\frac{\beta_2'}{|\beta_3'|}\right)\frac{\exp(\xi/y_0)}{2\cosh(\xi/y_0)}. \tag{23}$$

As opposed to the operator $\hat{L}$, the operator $\hat{L}'$ (23) does not posses the nonreflecting property. Its spectrum and eigenfunctions are unknown and this makes the analysis of a 90-degree domain wall more complicated than the analogous problem for 180-degree walls. (For the models of magnets in Refs. 15–18 only the nonreflecting operator $\hat{L}$ shows up in the first-order equations analogous to Eqs. (17) and (18).) Thus, in solving the first-order equations we used the fact that previously[5,11–13] frequencies $\omega\sim10^6-10^7\,\mathrm{s}^{-1}$ of the variable external magnetic field were used; this is much lower than the characteristic frequencies ω_0 and $\tilde{\omega}_0$ (for typical rare earth orthoferrites $\omega_0\sim10^{11}\,\mathrm{s}^{-1}$ and $\tilde{\omega}_0\sim10^9-10^{10}\,\mathrm{s}^{-1}$). Here, as can easily be seen, the parameter σ which appears in Eq. (18) obeys $\sigma\sim(\omega_0/\tilde{\omega}_0)^2\gg1$, so in this equation we can neglect the terms $(\hat{L}'+\hat{T})\vartheta_1$ compared to $\sigma\vartheta_1$ and express the function $\vartheta_1(\xi,t)$ in terms of the function $\psi_1(\xi,t)$ as

$$\begin{aligned}\vartheta_1=&-2\frac{h_cgM_0}{\omega_0^2}\,\dot{\psi}_1\sin\varphi_0-\frac{d(gM_0)^2}{2\omega_0^2}h_x\\&+4\left(\frac{gM_0}{\omega_0}\right)^2h_ch_z\sin\varphi_0+\frac{gM_0}{\omega_0^2}\left[\dot{h}_y\cos\varphi_0-\dot{h}_x\sin\varphi_0\right.\\&\left.+\frac{V_1}{y_0}h_c\sin\varphi_0\sin2\varphi_0\right].\end{aligned} \tag{24}$$

Substituting the expression for ϑ_1 in Eq. (17) and neglecting terms that are small compared to the parameter $\omega/\tilde{\omega}_0\gg1$, we obtain an equation for the function $\psi_1(\xi,t)$ of the form

$$\begin{aligned}(\hat{L}+\hat{T})\psi_1=&\frac{\sin2\varphi_0}{2y_0\tilde{\omega}_0^2}(\dot{V}_1+\omega_rV_1)\\&-\frac{2(gM_0)^3}{(\omega_0\tilde{\omega}_0)^2}h_c\sin\varphi_0\left[\frac{d}{2}\dot{h}_x-4h_c\dot{h}_z\sin\varphi_0\right]\\&+\left(\frac{gM_0}{\tilde{\omega}_0}\right)^2\left[\frac{d}{2}h_z\sin\varphi_0-h_c(h_x\cos2\varphi_0\right.\\&\left.+h_y\sin2\varphi_0)\right]+\frac{gM_0}{\tilde{\omega}_0^2}\dot{h}_z.\end{aligned} \tag{25}$$

We shall seek a solution to Eq. (24) in the form of an expansion in the eigenfunctions of the operator $\hat{L}$ (20), which form a complete orthonormal set. For a monochromatic field of frequency ω we set

$$\psi_1(\xi,t)=\mathrm{Re}\left\{\left[\sum_k d_kf_k(\xi)+d_0f_0(\xi)\right]e^{i\omega t}\right\}. \tag{26}$$

The expansion coefficients d_k and d_0 in the expansion (26) are found in the standard way by multiplying the right hand side of Eq. (25) by $f_k^*(\xi)$ or $f_0^*(\xi)$, respectively, and integrating over the variable ξ.

The first-order equations (17) and (18) describe the excitation of linear spin waves against the background of a domain wall. Here the last terms in the expansion (26) corresponds to a shear (Goldstone) mode, which describes the motion of a domain wall as a whole. However, the corresponding degree of freedom has already been taken into account with the aid of the collective coordinate $Y(t)$ in the definition of the variable ξ, so the Goldstone mode in Eq. (26) should be left out, i.e., we must require that the corresponding coefficient $d_0=0$. (See a discussion of this question elsewhere.[24]) The absence of the Goldstone mode in the expansion (26) is a condition equivalent to requiring orthogonality of the right hand side of Eq. (25) to the function $f_0(\xi)$, which then determines the equation for the velocity of the interphase domain wall $V_1(t)$ in the linear approximation in the field,

$$\begin{aligned}\dot{V}_1+\omega_rV_1=&y_0gM_0\left[2h_c\left(\frac{gM_0}{\omega_0}\right)^2(d\dot{h}_x-2\pi h_c\dot{h}_z)\right.\\&\left.+gM_0(2h_ch_y-dh_z)-\pi\dot{h}_z\right].\end{aligned} \tag{27}$$

Equation (27) is integrable in an elementary fashion and for a monochromatic field of frequency ω we have

$$V_1(t)=\frac{y_0 g M_0}{\omega^2+\omega_r^2}\Big\{ gM_0(2h_c h_{0y}-dh_{0z})(\omega\sin\omega t + \omega_r\cos\omega t)+\omega(\omega\cos\omega t-\omega_r\sin\omega t) \times\left[\left(\frac{gM_0}{\omega_0}\right)^2 2h_c(dh_{0x}-2\pi h_c h_{0z})-\pi h_{0z}\right]\Big\}. \quad (28)$$

Equation (28) describes the oscillations of an interphase domain wall in an oscillating external field and, as can easily be seen, does not lead to drift of the wall, as $\overline{V_1(t)}=0$.

Note that for $\omega=0$, i.e., in the case of a static field, Eq. (28) describes the motion of an interphase-domain boundary at a constant velocity.[8] Similar equations have been obtained[10] for the velocity of interphase-domain walls formed during Morin phase transitions in rhombic ferroelectric-ferromagnetic materials in an external electric field.

On determining the coefficients d_k in the expansion (26), we obtain a solution of the first-order equation (in the approximation $\omega\gg\omega_0$),

$$\psi_1(\xi,t)=\mathrm{Re}\{a_x(t)\cos 2\varphi_0(\xi)+a_z(t)U(\xi)\},$$

$$\vartheta_1(\xi,t)=\left(\frac{gM_0}{\omega_0}\right)^2\mathrm{Re}[b_x(t)\sin\varphi_0(\xi)\cos 2\varphi_0(\xi) + b_z(t)\sin\varphi_0(\xi)+c_x(t)+(c_z(t) + b_y(t))\sin^2\varphi_0(\xi)\cos\varphi_0(\xi) + c_y(t)\cos\varphi_0(\xi)], \quad (29)$$

where we have introduced the notation

$$a_x(t)=-h_c h_{0x}e^{i\omega t},\quad a_z(t)=\left(\frac{gM_0}{\tilde{\omega}_0}\right)^2\frac{d}{4\pi}h_{0z}e^{i\omega t},$$

$$b_x(t)=2i\left(\frac{\omega}{gM_0}\right)h_c^2 h_{0x}e^{i\omega t},\quad b_y(t)=4\left(\frac{gM_0}{\omega_r}\right)h_c^2 h_{0y}e^{i\omega t},$$

$$b_z(t)=4h_c h_{0z}e^{i\omega t},\quad c_x(t)=-\frac{d}{2}h_{0x}e^{i\omega t},$$

$$c_y(t)=i\left(\frac{\omega}{gM_0}\right)h_{0y}e^{i\omega t},\quad c_z(t)=-2\left(\frac{gM_0}{\omega_r}\right)dh_c h_{0z}e^{i\omega t},$$

and

$$U(\xi)=Lf_k(\xi)\int_{-\infty}^{+\infty}\int_{-\infty}^{+\infty}dk\,d\tilde{\xi}\,\frac{f_k^*(\tilde{\xi})\sin\varphi_0(\tilde{\xi})}{\lambda_k}.$$

Therefore, in a linear approximation in the amplitude of a variable external field an interphase domain wall oscillates at the frequency of the field (28) and the wall shape is distorted in a way described by Eqs. (29).

3. SECOND-ORDER PERTURBATION THEORY: DRIFT OF THE INTERPHASE DOMAIN WALL

We now proceed to analyze the equations in the second approximation in the amplitude of an external oscillating magnetic field.

We shall not write down the corresponding system of equations in the second approximation in their general form, but only give those equations which follow from Eq. (4),

$$\hat{L}\psi_2=\frac{\sin 2\varphi_0}{2y_0\tilde{\omega}_0^2}(\dot{V}_2+\omega_r V_2)+N(\xi,t), \quad (30)$$

where the function $N(\xi,t)$ is defined by the equation

$$N(\xi,t)=\frac{1}{\tilde{\omega}_0^2}(\dot{V}_1+\omega_r V_1)\psi_1'+\sin 2\varphi_0(5\cos^2\varphi_0-1)\psi_1^2 - \frac{1}{4}\left(\frac{V_1}{c}\right)^2\sin 4\varphi_0-y_0\sin 2\varphi_0\vartheta_1\vartheta_1' - \vartheta_1^2\left(\sin^2\varphi_0+\frac{\beta_2'}{2\beta_3'}\right)\sin 2\varphi_0-\left(\frac{gM_0}{\tilde{\omega}_0^2}\right) \times[(\dot{h}_x\cos\varphi_0+\dot{h}_y\sin\varphi_0)\vartheta_1+2(h_x\cos\varphi_0 + h_y\sin\varphi_0)\dot{\vartheta}_1+2h_c(\psi_1\dot{\vartheta}_1\cos\varphi_0 - V_1\vartheta_1'\sin\varphi_0)]-\left(\frac{gM_0}{\tilde{\omega}_0}\right)^2\Big[h_x h_y\cos 2\varphi_0 + \frac{1}{2}(h_y^2-h_x^2)\sin 2\varphi_0-2h_c\Big(h_x\psi_1\sin 2\varphi_0 + h_y\psi_1\cos 2\varphi_0-\frac{1}{2}h_z\vartheta_1\cos\varphi_0\Big)\Big] + \frac{1}{2}\left(\frac{gM_0}{\tilde{\omega}_0}\right)^2 dh_z\psi_1\cos\varphi_0. \quad (31)$$

The equation for the second approximation for the function $\vartheta_2(\xi,t)$ has a similar structure, but does not contain a second order term in the expansion for the velocity of the domain wall (V_2), so it is of no further interest to us.

We shall also seek a solution of Eq. (31) in the form of an expansion over the complete orthonormal set of eigenfunctions $\{f_0(\xi),f_k(\xi)\}$ of the operator $\hat{L}$,

$$\psi_2(\xi,t)=\mathrm{Re}\left\{\left[\sum_k d_k^{(2)}f_k(\xi)+d_0^{(2)}f_0(\xi)\right]e^{i\omega t}\right\}. \quad (32)$$

Here, as in the first-order equation, we must require that there be no shear mode in the expansion of $\psi_2(\xi,t)$, i.e., it is necessary that the right hand side of Eq. (31) be orthogonal to the function $f_0(\xi)$ and the coefficient $d_0^{(2)}=0$. This requirement leads to an equation for the second-order term V_2 in the expansion of the wall velocity,

$$\dot{V}_2+\omega_r V_2=-\tilde{\omega}_0^2\int_{-\infty}^{+\infty}d\xi\,N(\xi,t)\sin 2\varphi_0. \quad (33)$$

Substituting the functions $\psi_1(\xi,t)$ and $\vartheta_1(\xi,t)$ calculated in the previous section in Eq. (31), taking the average over the period of the oscillations, and integrating in Eq. (33), after some simple, but quite cumbersome calculations, we obtain the following expression for the drift velocity $V_{dr}=\overline{V_2(t)}$:

$$V_{dr}=\sum_{ij}\ \nu_{ij}(\omega;\chi,\chi_1)\,\tilde{H}_{0i}\tilde{H}_{0j}\,. \tag{34}$$

The coefficients ν_{ij} are functions of the frequency of the field and the phase shifts that have the significance of nonlinear mobilities of the interphase wall,

$$\nu_{xx}=-\nu_0\left[1+h_c^2\left(\frac{gM_0}{\tilde{\omega}_0}\right)^2\right],$$

$$\nu_{yy}=\nu_0\left[1+\frac{32}{15}h_c^4\left(\frac{gM_0}{\omega_0}\right)^2\left(\frac{gM_0}{\omega_r}\right)^2\left(\frac{\tilde{\omega}_0}{\omega_0}\right)^2\right],$$

$$\nu_{zz}=\nu_0\left[-\frac{d^2}{32}\left(\frac{gM_0}{\tilde{\omega}_0}\right)^2\eta+4h_c^2\left(\frac{gM_0}{\omega_0}\right)^2\left(-1+\frac{\pi}{16}d\left(\frac{gM_0}{\omega_r}\right)\right)\right],$$

$$\nu_{xy}=-2\pi\nu_0h_c^2\left(\frac{gM_0}{\tilde{\omega}_0}\right)^2\cos\chi,$$

$$\nu_{yz}=\nu_0\left(\frac{gM_0}{\omega_0}\right)^2h_c\left[\frac{2\eta_1}{\pi}dh_c^2\left(\frac{gM_0}{\tilde{\omega}_0}\right)^2\left(\frac{\omega}{\omega_r}\right)\sin(\chi-\chi_1)+\left(\frac{5}{16}d\left(\frac{\omega_0}{\tilde{\omega}_0}\right)^2-\frac{\pi}{2}h_c^2\left(\frac{gM_0}{\omega_r}\right)-\frac{32}{15}dh_c^2\left(\frac{gM_0}{\omega_r}\right)^2\left(\frac{\tilde{\omega}_0}{\omega_0}\right)^2+\frac{13}{2}\pi h_c^2\left(\frac{gM_0}{\omega_r}\right)\times\left(\frac{\tilde{\omega}_0}{\omega_0}\right)^2\right)\cos(\chi-\chi_1)\right],$$

and

$$\nu_{xz}=\nu_0\left(\frac{gM_0}{\tilde{\omega}_0}\right)^2h_c\left[d\left(\eta_2+\left(\frac{\tilde{\omega}_0}{\omega_0}\right)^2\right)\cos\chi_1-\frac{\pi^2}{2}\left(\frac{\omega}{gM_0}\right)\times\left(1+4h_c^2\left(\frac{gM_0}{\omega_0}\right)^2\right)\sin\chi_1\right], \tag{35}$$

where $\nu_0=y_0g^2/2\omega_r$ and η, η_1, and η_2 are numerical coefficients of order unity.

It should be noted that, as opposed to the 180-degree domain walls in weak ferromagnetic materials studied in Ref. 15, interphase 90-degree domain walls can drift even when there is only one component of the external oscillating magnetic field. (In the case of 180-degree walls, only the nondiagonal components of the nonlinear mobility tensor are nonzero.) An analogous result hods for 90-degree interphase walls during spin-flop transitions.[14]

In typical rare-earth orthoferrites, the sublattice magnetization is $M_0\sim10^2$ Oe so, for external constant fields of order $H_c\sim10$ Oe, we can neglect all terms in the nonlinear mobility tensor proportional to h_c. Here all the nondiagonal coefficients ν_{ij}, $i\neq j$, go to zero and the only nonzero nonlinear mobilities are

$$\nu_{xx}=-\nu_0,\quad \nu_{yy}=\nu_0,\quad \text{and}\quad \nu_{zz}=-\nu_0\frac{d^2\eta}{32}\left(\frac{gM_0}{\tilde{\omega}_0}\right)^2, \tag{36}$$

which, within the frequency range $\omega\ll\tilde{\omega}_0$ of interest, are essentially independent of the frequency of the oscillating external field.

For an estimate of the components of the nonlinear mobility tensor we use the following typical parameter values: $y_0\sim10^{-5}$ cm, $g\sim10^7$ $(\text{s}\cdot\text{Oe})^{-1}$, and $\omega_r\sim10^{10}$ s^{-1}. (The typical value of the relaxation frequency in an rare-earth orthoferrite is rather high since the relaxation constant λ in it has been enhanced by exchange.) Here ν_0 is on the order of 10^{-1} cm/$(\text{s}\cdot\text{Oe}^2)$. Given also that, in typical rare-earth orthoferrites $d\sim10^2$ and $\tilde{\omega}_0\sim10^{10}$ s^{-1}, we find that the nonlinear mobility coefficient ν_{zz}, which is proportional to the square of the Dzyaloshinskii-interaction constant, turns out to be substantially larger than ν_{xx} and ν_{yy}: $\nu_{xx}\sim\nu_{yy}\sim10^{-1}$ cm/$(\text{s}\cdot\text{Oe}^2)$, while $\nu_{zz}=1-10$ cm/$(\text{s}\cdot\text{Oe}^2)$. Therefore, for an external field with an amplitude on the order of 1 Oe, the drift velocity of an interphase-domain wall can reach 0.1 cm/s with the variable field oriented in the XY plane and $1-10$ cm/s when the oscillating component has a Z component.

As already noted above, the nondiagonal components of the nonlinear mobility tensor are nonzero only when the constant external field has a Y component. Taking $H_c\sim10$ Oe $(h_c\sim0.1)$, we find that, for example, the coefficient ν_{xy} is of order 10^{-2} cm/$(\text{s}\cdot\text{Oe}^2)$, which is substantially smaller than the diagonal coefficients.

Note also the significant dependence of some components of the nonlinear mobility tensor on the phase shift (χ and χ_1) between the corresponding components of the external field.

4. DRIFT OF A TWO-PHASE DOMAIN STRUCTURE

As noted above, the experimentally observed Morin-type transition[3,4] in the presence of a weak constant external magnetic field oriented along the Y axis is accompanied by the formation of a coherent, two-phase domain structure (intermediate state). Thus, it is natural to ask about the possibility of drift of the entire domain structure as a whole. (A similar problem concerning the drift of an intermediate state formed during spin-flop transitions in uniaxial antiferromagnetic materials has been examined in Ref. 14.)

Like the intermediate state in a spin-flop phase transition, the coherent domain structure that develops during a Morin transition consists of alternating domains of a weakly ferromagnetic phase, in which the anitferromagnetism vector **l** is oriented parallel or antiparallel to the X axis (while the weak ferromagnetism vector **m** is, correspondingly parallel or antiparallel to the Z axis), and domains of an antiferromagnetic phase, in which **l** is parallel or antiparallel to the Y axis (while $\mathbf{m}=0$).

It is easy to see that in a two-phase structure of this type, there can be eight types of 90-degree interphase domain walls, which separate domains with different orientations of **l** and, in addition, differ in the direction of rotation of the

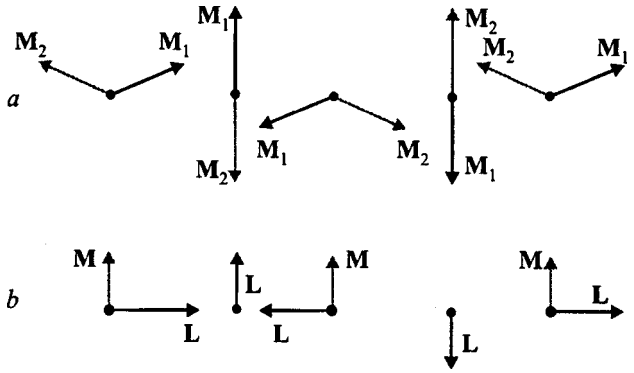

FIG. 1. The relative orientation of the (a) sublattice magnetization vectors $\mathbf{M}_1$ and $\mathbf{M}_2$ and (b) weak ferromagnetism $\mathbf{M}$ and antiferromagnetism $\mathbf{L}$ vectors in domains corresponding to a domain structure which can drift as a unified whole.

vector during a transition from a left to a right domain. It is perfectly natural that the domain structure in the intermediate state should drift as an intact whole only when the entire domain wall in the structure drifts to one side with one and the same drift velocity.

In the preceding section we examined the drift of an isolated interphase domain wall with fully specific orientation of the antiferromagnetism vector $\mathbf{l}$ in right and left domains, and, in particular, when solving Eq. (10) for the domain-wall structure, we used the boundary conditions $\varphi_0(-\infty)=0$ $\varphi_0(+\infty)=\pi/2$, i.e., we assumed that $\mathbf{1}$ is oriented along the X axis in a left domain (for $y\to-\infty$) and along the Y axis in a right domain (for $y\to+\infty$).

An analysis of the dynamics of all the other possible interphase domain walls in this structure shows that the drift velocity of all types of domain walls is given by

$$V_{dr}=\rho\sum_{ij}\ \nu_{ij}(\omega;\chi,\chi_1)\tilde{H}_{0i}\tilde{H}_{0j}, \tag{37}$$

which differs from Eq. (34) only in having an additional factor $\rho=\pm1$, which determines the ''spirality'' of the wall: $\rho=\pm1$ if $\varphi_0'>0$ in a given domain wall, i.e., $\mathbf{1}$ rotates counterclockwise on going from a left into a right domain, and $\rho=-1$ if $\varphi_0'=0$, i.e., with $\mathbf{1}$ rotating clockwise. Therefore, in a given oscillating external magnetic field all the walls drift with one and the same speed, but the direction of the drift depends on the mutual orientation of $\mathbf{1}$ in the domains separated by an interphase wall. All the walls with the same direction of rotation of $\mathbf{l}$, i.e., those at which the sign of the derivative φ_0' is the same, move to one and the same side. For example, walls for which $\varphi_0'>0$, i.e., such that on going from a left to a right domain $\mathbf{1}$ turns counterclockwise, will move to the same side as the specific interphase domain wall studied above. A structure of this type is illustrated in Fig. 1.

At present there is no convincing experimental data on whether a domain structure of this sort develops during a Morin-type phase transition, but, as with a spin-flop phase transition, the required structure can be created in a special way: the principles for organizing it have been presented elsewhere.[25,26]

We are sincerely grateful to S. L. Gnatchenko and A. B. Chizhik for acquainting us with yet unpublished experimental data on interphase domain wall drift and to K. I. Primak for help in this work.

This work was partially supported by the International Soros Program for support in the exact sciences (ISSEP) and the International ''Renaissance'' foundation (grant N APU 062018).

[1)]Note that the presence of a oscillating magnetic field also causes a shift in the phase transition temperature,[23] but here this effect will be of no interest to us.

[1] S. V. Vonsovskiĭ, *Magnetism* [in Russian], Nauka, Moscow (1971).
[2] K. P. Belov, A. K. Zvezdin, A. M. Kadomtseva, and R. Z. Levitin, *Orientational Phase Trasitions in Rare Earth Magnetic Materials* [in Russian], Nauka, Moscow (1979), 317 pp.
[3] V. V. Eremenko, N. F. Kharchenko, and Yu. G. Litvinenko, *Magnetooptics and Spectroscopy of Antiferromagnetic Materials* [in Russian], Naukova Dumka, Kiev (1989), 264 pp.
[4] S. L. Gnatchenko, N. F. Kharchenko, K. Petrovski, G. Shimchak, and R. Shimchak, Zh. Éksp. Teor. Fiz. **99**, 874 (1991) [Sov. Phys. JETP **72**, 485 (1991)].
[5] S. L. Gnatchenko and A. B. Chizhik, personal communication.
[6] B. A. Ivanov, Zh. Éksp. Teor. Fiz. **79**, 581 (1980) [Sov. Phys. JETP **52**, 293 (1980)].
[7] V. G. Bar'yakhtar, B. A. Ivanov, and M. V. Chetkin, Usp. Fiz. Nauk **146**, 417 (1985).
[8] T. K. Soboleva, E. P. Stefanovskiĭ, and A. L. Sukstanskiĭ, Pis'ma Zh. Éksp. Teor. Fiz. **42**, 59 (1985) [JETP Lett. **42**, 68 (1985)].
[9] A. K. Zvezdin and A. A. Mukhin, Kratkie soobshcheniya po fizike FIAN (6), 11 (1985).
[10] T. K. Soboleva, E. P. Stefanovskiĭ, and A. L. Sukstanskiĭ, Fiz. Tverd. Tela **26**, 2725 (1984) [Sov. Phys. Solid State **26**, 1651 (1984)].
[11] S. L. Gnatchenko, N. F. Kharchenko, and A. B. Chizhik, Fiz. Nizk. Temp. **12**, 1111 (1986) [Sov. J. Low Temp. Phys. **12**, 628 (1986)].
[12] S. L. Gnatchenko, A. B. Chizhik, and N. F. Kharchenko, Fiz. Nizk. Temp. **15**, 304 (1989) [*sic*].
[13] S. L. Gnatchenko, A. B. Chizhik, and N. F. Kharchenko, Pis'ma Zh. Éksp. Teor. Fiz. **51**, 282 (1990) [JETP Lett. **51**, 324 (1990)].
[14] V. S. Gerasimchuk and A. L. Sukstanskiĭ, Zh. Éksp. Teor. Fiz. **112**, 1374 (1997) [JETP **85**, 748 (1997)].
[15] V. S. Gerasimchuk and A. L. Sukstanskiĭ, Zh. Éksp. Teor. Fiz. **103**, 151 (1993) [JETP **76**, 82 (1993)].
[16] V. G. Bar'yakhtar, Yu. I. Gorobets, and S. I. Denisov, Zh. Éksp. Teor. Fiz. **98**, 1345 (1990) [Sov. Phys. JETP **20**, 751 (1990)].
[17] V. S. Gerasimchuk and A. L. Sukstanskiĭ, Fiz. Nizk. Temp. **20**, 142 (1994) [Low Temp. Phys. **20**, 114 (1994)].
[18] V. S. Gerasimchuk and A. L. Sukstanskii, J. Magn. Magn. Mater. **146**, 323 (1995).
[19] E. A. Turov, *Physical Properties of Magnetically Ordered Crystals* [in Russian], Izd-vo AN SSSR, Moscow 91962), 224 pp.
[20] B. A. Ivanov and A. L. Sukstanskiĭ, Zh. Éksp. Teor. Fiz. **94**, 204 (1988) [Sov. Phys. JETP **67**, 981 (1988)].
[21] I. V. Bar'yakhtar and B. A. Ivanov, Fiz. Nizk. Temp. **5**, 759 (1979) [Sov. J. Low Temp. Phys. **5**, 361 (1979)].
[22] V. G. Bar'yakhtyar, B. A. Ivanov, and A. L. Sukstanskiĭ, Zh. Éksp. Teor. Fiz. **78**, 1509 (1980) [Sov. Phys. JETP **51**, 757 (1980)].
[23] V. S. Gerasimchuk and Yu. I. Gorobets, Fiz. Nizk. Temp. **5**, 753 (1979) [Sov. J. Low Temp. Phys. **5**, 358 (1979)].
[24] R. Rajaraman, *Solitons and Instantons in Quantum Field Theory*, North-Holland, Amsterdam (1982).
[25] N. F. Kharchenko and V. A. Bedarev, Pis'ma Zh. Éksp. Teor. Fiz. **56**, 360 (1992) [JETP Lett. **56**, 345 (1992)].
[26] N. F. Kharchenko and V. A. Bedarev, Fiz. Nizk. Temp. **19**, 72 (1993) [Low Temp. Phys. **19**, 52 (1993)].

Translated by D. H. McNeill

Magnetic phases in quasi-binary $(Fe_{1-x}Co_x)Ge_2$ intermetallic compounds

A. Z. Men'shikov, Yu. A. Dorofeev, and A. E. Teplykh

Institute of Metal Physics, Ural Branch of the Russian Academy of Sciences, 620219 Ekaterinburg, Russia
(Submitted April 7, 1998; resubmitted June 30, 1998)
Fiz. Tverd. Tela (St. Petersburg) **41**, 283–289 (February 1999)

Magnetic neutron diffractometry revealed the existence in $(Fe_{1-x}Co_x)Ge_2$ solid solutions ($x<0.5$) with $C16$ structure of only two magnetic phases, namely, low-temperature (AFI) and high-temperature (AFII). A third magnetic phase, AFIII, suggested by earlier magnetic measurements, has not been found. The AFI and AFII phases have a commensurate and an incommensurate antiferromagnetic structure with the wave vectors $\mathbf{k}_0=2\pi/a\,(1,0,0)$ and $\mathbf{k}=\mathbf{k}_0+\delta\mathbf{k}$, respectively. The regions of their existence are shown in the magnetic phase diagram. Neutron diffraction measurements yielded the concentration dependence of the average magnetic moment per atom in the antiferromagnetic sublattice of a $3d$ metal, which, similarly to the dependence of the Néel point on x, was found to be nonlinear. An analysis of these dependences suggests that substitution of cobalt for iron is accompanied, on the one hand, by a decrease of the local spin density on the iron atoms in the nearest environment of a cobalt atom and, on the other hand, by an increase of the effective exchange integral between the nearest-neighbor iron atoms located along the tetragonal axis. © *1999 American Institute of Physics.* [S1063-7834(99)01802-X]

The intermetallic compound $FeGe_2$ having a tetragonal $C16$-type cell (space group $14/mcm$), with $a=5.908$ Å and $c=4.955$ Å, exhibits a strong difference in the distances between the nearest iron atoms along the c axis (2.48 Å) and in the basal plane (4.2 Å), which are equal, respectively, to the radii of the first and second coordination spheres. This results in strongly anisotropic magnetic properties of this compound.

According to recent neutron diffraction studies,[1–3] the magnetic ground state of $FeGe_2$ is described by a commensurate collinear structure with a wave vector $\mathbf{k}_0=2\pi/a\,(1,0,0)$, where the iron magnetic moments are ordered antiferromagnetically in the basal plane and ferromagnetically along the c axis (the AFI phase). This structure persists up to a temperature $T_1=263$ K to transfer thereafter to an incommensurate spiral magnetic structure (the AFII phase), where the iron magnetic moments retain ferromagnetic order along the $\langle 001\rangle$ axis while forming a simple helical structure in the basal plane.

Investigation of the spin dynamics of this compound revealed a large anisotropy in the dispersion of spin waves measured along the tetragonal axis and in the basal plane.[4] It was found that the velocity of ferromagnetic spin waves with small wave vectors propagating along the c axis is larger by more than an order of magnitude than that for antiferromagnetic spin waves in the basal plane. Rough estimates of the ratio of the absolute values of exchange integrals in the first, $I^{(1)}_{\mathrm{FeFe}}$, and second, $I^{(2)}_{\mathrm{FeFe}}$, coordination spheres yield about 20. This permits one to consider $FeGa_2$ as a quasi-one-dimensional spin system, which can be pictorially conceived as wall bars with stanchions representing the ferromagnetic chains with spins directed perpendicular to the c axis, and the bars, the weak antiferromagnetic bonds along the $\langle 110\rangle$ directions. When such a spin system is heated to the temperature T_1, the collinear antiferromagnetic order between the chains disappears, but the correlated turns of the chains are retained up to T_N. As for the ferromagnetic order along the c axis, it does not change above T_N, which becomes evident in the existence of weakly damping ferromagnetic spin waves for $T\gg T_N$.[4] Measurements of magnetoresistance in different directions in the basal plane made on such a system placed in a magnetic field showed that up to $H=15$ T the Néel temperature T_N decreases by 2 K only, and the commensurate-incommensurate transition temperature T_1 increases by more than 7 K.[5]

Because the magnetic ordering in $FeGa_2$ is quasi-one-dimensional, it seemed especially interesting to study the effect of substituting iron by other elements, which would influence the pattern of exchange interaction both within the ferromagnetic spin chain and between the chains. The first study of this kind used the $(Fe_{1-x}Co_x)Ge_2$ alloy system by measuring the temperature dependences of magnetic susceptibility.[6] A few of the $\chi(T)$ curves taken from Ref. 6 are presented in Fig. 1, where the features at T_1 and T_N marked by arrows were identified with the AFI$\rightarrow AF$II and AFII$\rightarrow P$ transitions, respectively. One more feature observed at $T=T_x$ in alloys with $x=0.3-0.45$ was assigned to the transition to a third phase, AFIII.[6] The existence of these phases was not confirmed, however, by direct neutron diffraction measurements, so that the matter of the magnetic states and the magnetic phase diagram of the $(Fe_{1-x}Co_x)Ge_2$ alloys remained open. The objective of this work was to fill in this gap, as well as to deepen our understanding of the quasi-one-dimensional magnetism of $FeGa_2$ using elastic magnetic scattering of neutrons.

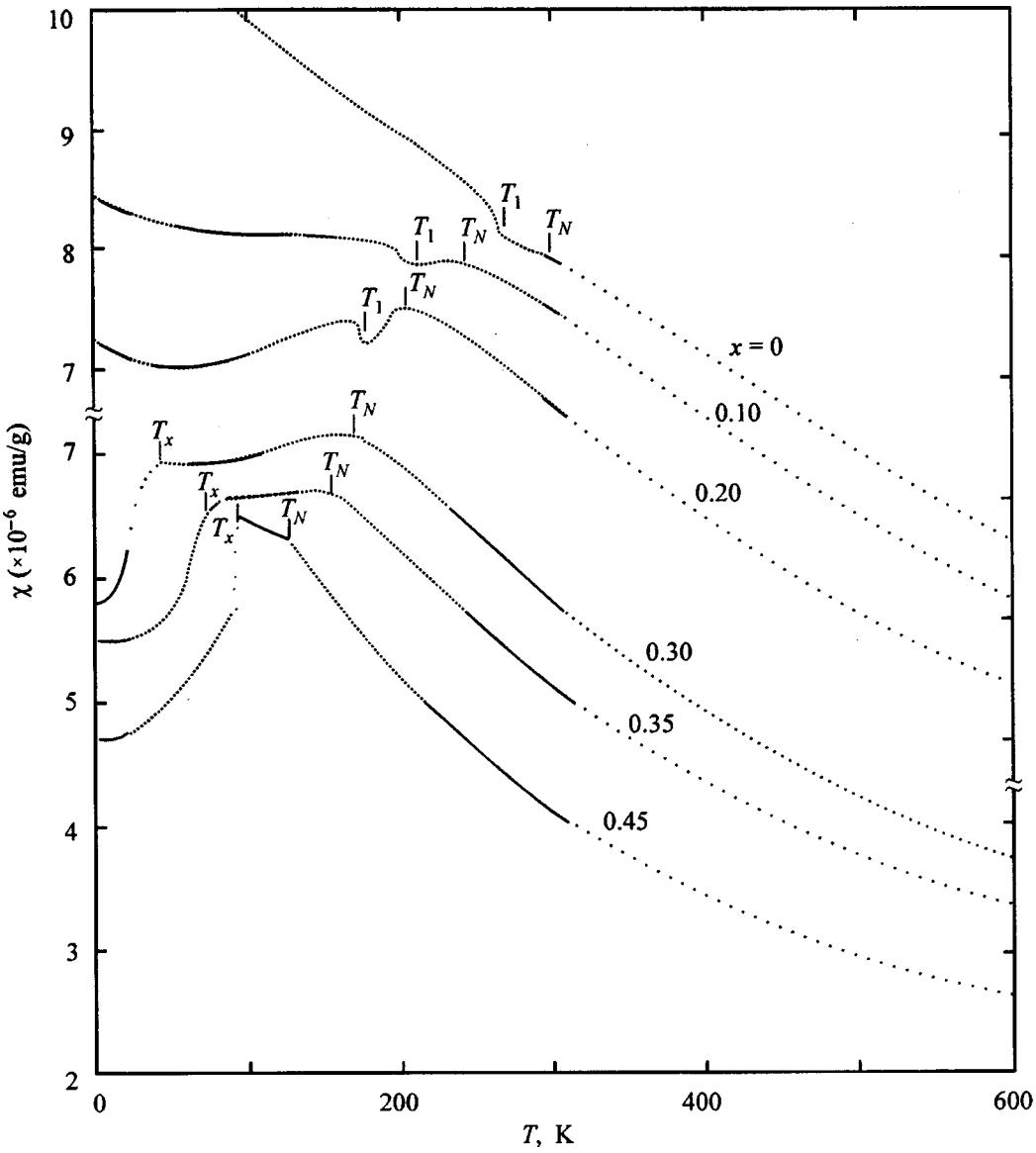

FIG. 1. Temperature dependences of the magnetic susceptibility of $(Fe_{1-x}Co_x)Ge_2$ alloys (from Ref. 6).

1. EXPERIMENTAL TECHNIQUES

We used $(Fe_{1-x}Co_x)Ge_2$ quasi-binary compounds in our neutron diffraction experiment with $x=0$, 0.03, 0.05, 0.1, 0.3, 0.35, and 0.45. The single crystals of the first four compositions were melt grown by the Czochralski method in the General Physics Department of the Ural Technical University (Ekaterinburg). Large single crystals were used to cut samples measuring approximately $5\times5\times10$ mm along the edges of the tetragonal lattice. The remainder of the ingots was ground to powder with grain size $\sim1-10\,\mu$m. The last three compositions were studied in the form of fine powder with about the same grain size on which the magnetic susceptibility measurements[6] had been made previously.

Magnetic neutron scattering studies were carried out on a D-2 neutron diffractometer mounted on one of the horizontal channels of the IWW-2M reactor. The scans were made in a helium cryostat in the 4.2–300 K temperature range within the angular region $2\theta=16-100°$. The $\lambda=1.81$-Å monochromatic neutron beam used in the measurements was obtained by successive reflection from the (111) plane of a deformed germanium single crystal and the (004) plane of pyrolytic graphite. This geometry of the experiment permitted us to exclude completely the $\lambda/2$ contributions and to obtain an adequate resolution ($\sim10^{-2}$) for large scattering angles.

The sample temperature was monitored by copper-iron-copper and copper-constantan thermocouples to within ±1 K.

2. EXPERIMENTAL RESULTS

2.1. Atomic structure

In order to establish the parameters of the atomic structure and the pattern of cobalt-atom distribution in the $3d$-metal sublattice, one studied nuclear elastic scattering of neutrons at room temperature and at 4.2 K, where all the alloys under investigation were, respectively, in the paramagnetic and magnetically ordered states. These experiments

TABLE I. Lattice parameters a and c of $(Fe_{1-x}Co_x)Ge_2$ alloys ($T=4.2$ K) obtained from neutron diffraction measurements, as well as calculated using the FULLPROF code for the probability P_{Co} for cobalt atoms in the $3d$-metal sublattice filling the positional parameter X_{Ge}.

x	a, Å	c, Å	P_{Co}	X_{Ge}	R_B, %	R_f, %
0	5.890(2)	4.936(1)	0	0.1538	4.2	2.6
0.03	5.889(2)	4.934(1)	0.03	0.1568	2.1	1.6
0.05	5.887(3)	4.944(4)	0.06	0.1549	2.7	2.0
0.10	5.878(1)	4.947(3)	0.11	0.1550	2.4	2.0
0.30	5.844(2)	4.979(1)	0.29	0.1557	2.9	2.8
0.35	5.835(2)	4.984(1)	0.35	0.1561	2.8	3.1
0.45	5.820(2)	4.998(5)	0.44	0.1576	2.9	3.2

Note: R_B and R_f are the convergence factors obtained taking into account only the integrated reflection intensity (R_B) and the total reflection profile (R_f).

showed that the crystal structure $C16$ remained unaffected in all the samples studied. As x was increased, the lattice parameter along the a axis decreased, and that along c increased, in good agreement with the room-temperature results quoted in Ref. 6. Data on the lattice parameter changes at 4.2 K are given in Table I.

The Rietveld refinement procedure incorporated in the FULLPROF program yielded the positional parameter X_{Ge} for different samples, as well as the probabilities for occupation of iron sites by cobalt atoms, P_{Co}. The best convergence factors R_b and R_f (within 5%) were obtained for a random distribution of cobalt atoms in the $3d$-metal sublattice (Table I).

2.2. Low-temperature magnetic state (*AF*I phase)

The low-temperature magnetic state of the alloys was derived from elastic neutron-scattering measurements made on powder samples at 4.2 K. Figure 2 displays typical neutron diffraction patterns of this kind normalized to the (211) nuclear-reflection intensity, which is due to germanium atoms only. All compositions are seen to exhibit the same antiferromagnetic reflections, $(100)_m$ and $(210)_m$, characteristic of these scattering angles. No additional magnetic reflections besides those seen in the neutron diffractogram for pure $FeGe_2$ were detected for larger angles either. This implies that the magnetic structure of all the alloys under study is described at low temperatures by the same wave vector $\mathbf{k}_0=2\pi/a(1,0,0)$ corresponding to the *AF*I phase state.

To check the possibility of existence of the magnetic phase *AF*III in $x\geqslant 0.3$ compositions at low temperatures, which was suggested earlier in Ref. 6, we carried out thorough measurements of the temperature dependences of the intensity of the $(100)_m$ and $(210)_m$ reflections, as well as of their FWHMs. These dependences are plotted in Fig. 3 for the $(100)_m$ reflection for the $x=0.3$ alloy against reduced temperature T/T_N. No signs of an anomalous behavior of the intensity or diffraction-reflection FWHM are seen to exist at $T_x/T_N=0.2$. Thus the assumption[6] of a new antiferromagnetic phase existing for $T<T_x$ is not supported, which implies that all $(Fe_{1-x}Co_x)Ge_2$ alloys with $x\leqslant 0.45$ have only one magnetic state (of the *AF*I type) at low temperatures.

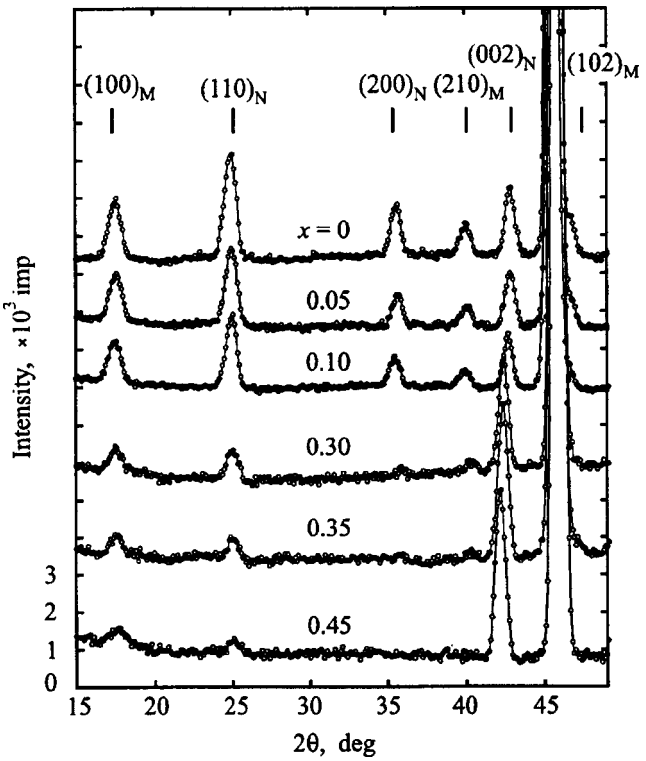

FIG. 2. Neutron diffraction patterns of $(Fe_{1-x}Co_x)Ge_2$ alloys obtained at 4.2 K. The M and N symbols refer, respectively, to magnetic and nuclear reflections.

2.3. High-temperature magnetic state (*AF*II phase)

To check the existence of an incommensurate (IC) magnetic structure in the *AF*II phase, temperature dependences of the $(100)_m$ reflection were measured on $x<0.3$ single-crystal samples. This reflection was found to split at $T=T_1$

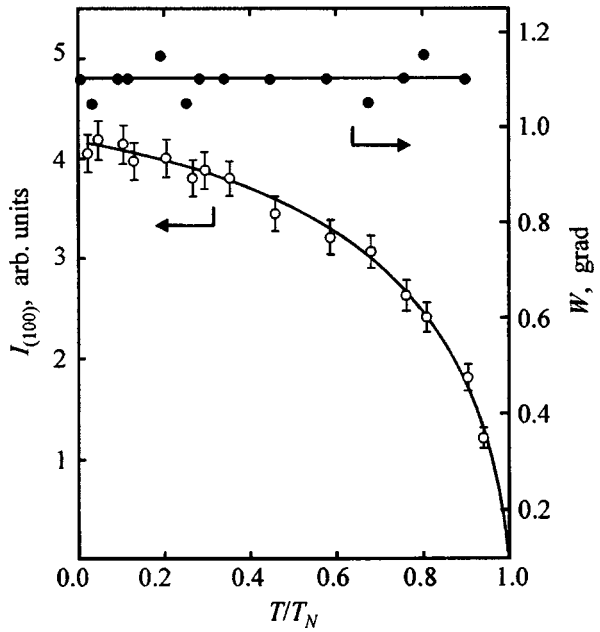

FIG. 3. The intensity I of the $(100)_M$ reflection (open circles) and its FWHM W (filled circles) as functions of reduced temperature. No features are seen at $T_x/T_N\sim 0.2$.

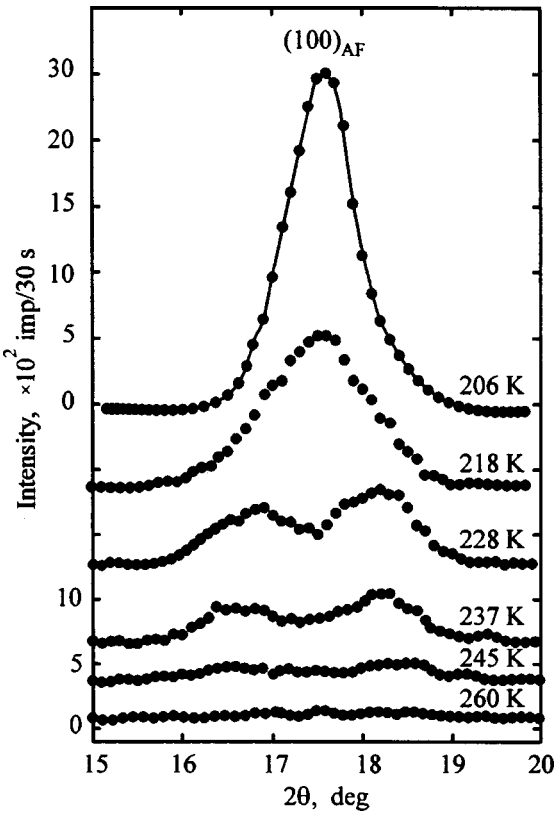

FIG. 4. Neutron diffraction patterns in the vicinity of the $(100)_m$ reflection obtained on a $Fe_{0.9}Co_{0.1}Ge_2$ single crystal near the T_1 and T_N phase-transition temperatures.

into two satellites, which is the main feature of a spiral. The angular positions of these satellites, as well as their intensities, depended both on concentration and on temperature. For illustration, Fig. 4 presents neutron diffraction patterns of the $Fe_{0.9}Co_{0.1}Ge_2$ alloy obtained at different temperatures in the region of the transition from the commensurate to an IC structure described by the wave vector $\mathbf{k}=\mathbf{k}_0+\delta\mathbf{k}$, where $\delta\mathbf{k}=(2\pi/a)\mu$. The measurements were used to construct the temperature dependence of δk in the region of existence of the IC phase, which was subsequently compared with a similar dependence obtained for pure $FeGe_2$ (Fig. 5). We readily see that the cobalt-containing alloys exhibit, besides a decrease in the lock-in phase-transition temperature, a smoother $\delta k\,(T)$ dependence as well.

Thus the assumption[6] of the features in the temperature dependences $\chi\,(T)$ observed to occur at T_1 and T_N being associated with transitions to the AFI and AFII phases is correct. This gave us grounds to construct a magnetic phase diagram for the $(Fe_{1-x}Co_x)Ge_2$ alloys based on our present measurements of T_1 and T_N, as well as on the temperature dependences of magnetic susceptibility of these alloys,[6] which contains only two magnetic phases, AFI and AFII (Fig. 6). The existence of a third magnetic phase has not been confirmed throughout the region where solid solutions with a $C16$-type crystal structure are observed.

3. DISCUSSION OF RESULTS

Consider now the effect of cobalt atoms on the quasi-one-dimensional spin system in $FeGe_2$. As follows from our

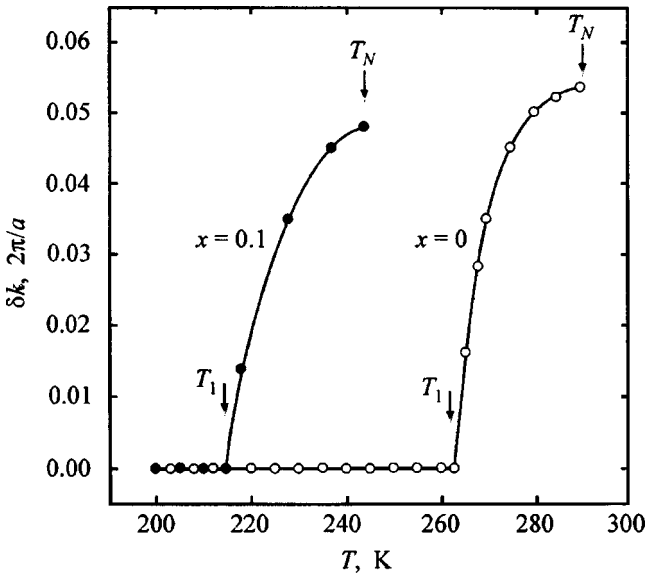

FIG. 5. Temperature dependence of the wave vector of the IC magnetic structure δk for $(Fe_{1-x}Co_x)Ge_2$ alloys. The arrows identify the transition temperatures to the lock-in phase (T_1) and the paramagnetic state T_N.

measurements, cobalt atoms substitute in a random manner for iron atoms on the $3d$-transition metal sublattice. In the process, the wave vector of the ground-state magnetic structure of $(Fe_{1-x}Co_x)Ge_2$ alloys remains unchanged, which argues for the pattern of exchange interaction along the c axis

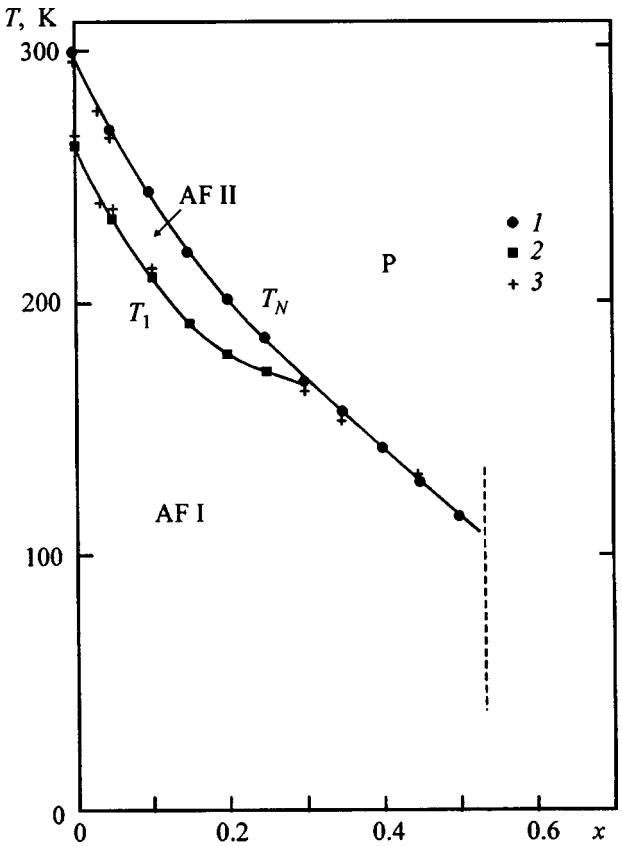

FIG. 6. Magnetic phase diagram of $(Fe_{1-x}Co_x)Ge_2$ alloys. The filled circles and squares refer to the data derived from magnetic susceptibility measurements[6], and the crosses, to neutron diffraction data (this work).

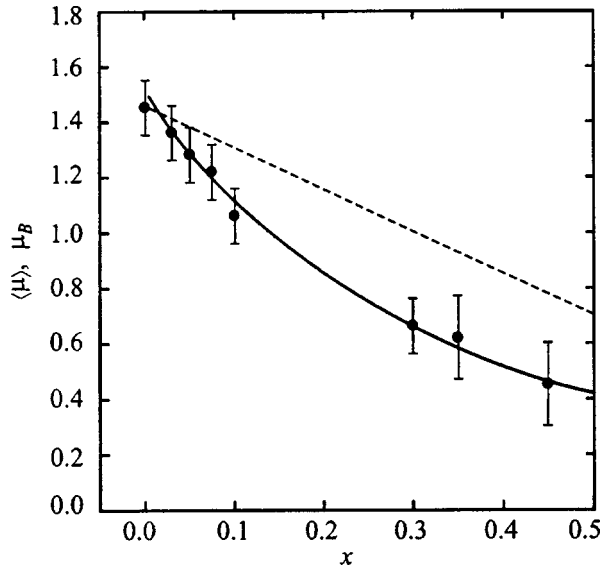

FIG. 7. Concentration dependence of the average magnetic moment in $(Fe_{1-x}Co_x)Ge_2$ alloys: points - present data, the solid line shows the plot of the fitting curve $\langle\mu\rangle=\mu_{Fe}(1-x)^{-\delta\mu x}$, and the dashed line corresponds to the case of $\langle\mu\rangle=\mu_{Fe}(1-x)$.

and in the basal plane being retained. At the same time the observed concentration dependences of the average magnetic moment $\langle\mu\rangle(x)$ and of the Néel point $T_N(x)$ indicate a change in the electronic state of the iron atoms.

Indeed, the magnetic-reflection intensities measured at 4.2 K permitted calculation of the experimental value of the average magnetic moment $\langle\mu\rangle$ per $3d$-metal atom in $(Fe_{1-x}Co_x)Ge_2$ compounds. As follows from its concentration dependence shown graphically in Fig. 7, for small x one observes a fairly large change in $\langle\mu\rangle$, which falls off smoothly with increasing x. Such a nonlinear behavior of $\langle\mu\rangle(x)$ implies that atoms of cobalt suppress the spin density at the nearest-neighbor iron atoms. Indeed, if there were no such effect, the average magnetic moment in the case of randomly distributed cobalt atoms on the $3d$-metal sublattice would change with concentration by the rule of mixture

$$\langle\mu\rangle=\mu_{Fe}(1-x)\pm\mu_{Co}x\,, \tag{1}$$

where μ_{Fe} and μ_{Co} are the local magnetic moments on the iron and cobalt atoms, respectively. Here the plus sign refers to the case where exchange interaction between the iron and cobalt atoms along the c axis is ferromagnetic ($J^{(1)}_{FeCo}>0$), and the minus sign, where it is antiferromagnetic ($J^{(1)}_{FeCo}<0$). The linear law of $\langle\mu\rangle$ variation allows also the case of nonlocalized moment on the cobalt atom ($\mu_{Co}=0$). But because the experimental $\langle\mu\rangle(x)$ curve is nonlinear and deviates from a plot constructed under the assumption of a ''magnetic hole,'' as is the case in Fig. 7, it appears only natural to assume that a cloud with negative spin polarization $\delta\mu$ forms around the iron atoms located nearest to the cobalts. In other words, the local magnetic moment of the iron atoms adjoining atoms of cobalt becomes smaller than that in pure $FeGe_2$. But then the expression for the magnetization of one sublattice of an antiferromagnet can be recast, taking into account the effect of neighboring cobalt atoms, in the form

$$\langle\mu\rangle_{Fe}(x)=\mu_{Fe}(1-x)-x^n\,\delta\mu\,, \tag{2}$$

where x^n is the concentration of cobalt atoms capable of creating around them a cloud with negative spin polarization with respect to the spin density at the iron atoms, and $\delta\mu$ is the magnetic moment per this cloud.

It was found that Eq. (2) can be fit to experimental values of $\langle\mu\rangle_{Fe}(x)$ for $n=0.5$ and $\delta\mu=0.4\,\mu_B$ (see solid line in Fig. 7).

Thus the fraction of magnetization associated with the formation of negative spin polarization around cobalt atoms is a result of the change in the electronic structure of the nearest-neighbor iron atoms, and this change follows a power-law relation $\Delta\langle\mu_{Fe}\rangle\sim x^n$ with $n=1/2$.

As seen from Fig. 6, the Néel temperature in the $(Fe_{1-x}Co_x)Ge_2$ alloys decreases with concentration x also by a nonlinear law, which implies that cobalt atoms cannot be identified with the magnetic hole, because otherwise, according to molecular-field theory[7], the Néel temperature would have obeyed a linear relation $T_N(x)\sim(1-x)$. Because cobalt atoms do not have a localized moment, however, it appears natural to assume that the Néel temperature is determined only by the exchange energy per iron atom, i.e., that $kT_N=E_{Fe}$, with the total exchange energy being $E=N(1-x)E_{Fe}$. Expressing E through the exchange energy between a pair of atoms in the first, ($N^{(1)}_{FeFe}=\frac{1}{2}NZ_1$), and the second, ($N^{(2)}_{FeFe}=\frac{1}{2}NZ_2$), coordination spheres, and using Eq. (2) for the average magnetic moment of iron, we come to

$$kT_N=\frac{1}{4(1-x)}[\mu_{Fe}(1-x)-\delta\mu/x]^2[J^{(1)}_{FeFe}+2|J^{(2)}_{FeFe}|]\,, \tag{3}$$

where $J^{(1)}_{FeFe}$ and $J^{(2)}_{FeFe}$ are the effective exchange integrals between iron-iron atoms in the first and second coordination spheres with the number of atoms $Z_1=2$ and $Z_2=4$, respectively. Taking into account that $J^{(1)}_{FeFe}/J^{(2)}_{FeFe}\sim 20$, one can fit numerically this expression to the $T_N(x)/T_N(x=0)$ experimental data (Fig. 8). This was found to be possible in the case where the exchange integral $J^{(1)}_{FeFe}$ varies with concentration as

$$J^{(1)}_{FeFe}(x)=J^{(1)}_{FeFe}(x=0)[1+(2x)^2]\,. \tag{4}$$

If we recall now that an increase of x entails a linear increase of the interatomic spacing $r^{(1)}_{FeFe}$, for which the second horizontal scale in Fig. 8 is appropriate, it becomes clear that the increase of the exchange integral $J^{(1)}_{FeFe}$ with interatomic distance increasing from 2.477 to 2.5 Å follows the trend observed in fcc and bcc iron alloys. In particular, the interatomic spacing $r_{Fe\text{-}Fe}$ in pure α Fe, which is a good ferromagnet, is 2.52 Å.

As follows from this experimental study of the magnetic phase state of the $(Fe_{1-x}Co_x)Ge_2$ solid solutions, substitution of cobalt for iron to a concentration $x=0.25$ leaves the $AF\text{I}\rightarrow AF\text{II}\rightarrow P$ magnetic phase-transition pattern practically as it is in pure $FeGe_2$. The only result is a decrease of the T_1 and T_N transition temperatures. For $x>0.25$, however,

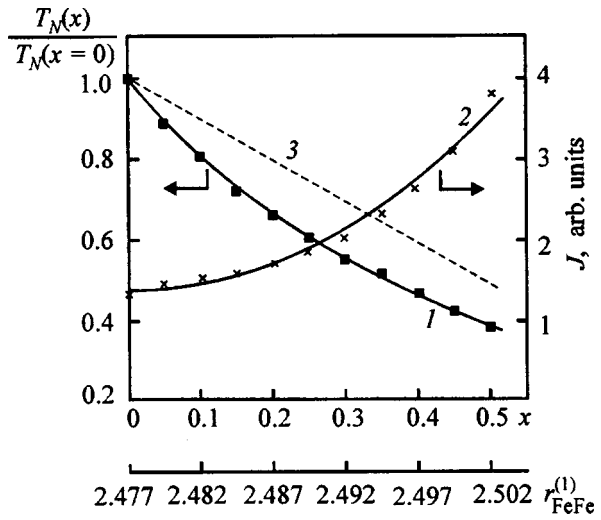

FIG. 8. Reduced Néel temperature and effective exchange integral I_{FeFe} *vs* concentration: filled squares refer to the experiment, and the crosses, to data derived from the experiment. The dashed line is a plot of the $T_N(x)/T_N(x=0)$ relation obtained under the assumption of a magnetic hole in place of a cobalt atom.

the *AF*II phase disappears, and all alloys are in the *AF*I magnetic state. This is due to a large extent to the fact that no local magnetic moment forms on cobalt atoms and, moreover, that the local spin density on the iron atoms that are in nearest neighbors of cobalt atoms undergoes a change. The magnetic state of the alloys is affected also substantially by the increase of the Fe–Fe spacing along the tetragonal axis, which results in an increase of the effective exchange integral $J^{(1)}_{\mathrm{FeFe}}$ with increasing cobalt concentration in alloys. These conclusions have been drawn naturally only from an analysis of experimental data on the concentration dependences of the average magnetic moment and of the Néel point. More rigorous support for the above conclusions must come from theoretical calculations of the electron energy spectrum of the $(Fe_{1-x}Co_x)Ge_2$ intermetallic compounds. Unfortunately, the latter can be obtained only by averaging the electronic states for the iron and cobalt atoms.

The authors owe sincere thanks to Professor H. Shiraishi for providing the samples with $x=0.3$, 0.35, and 0.45.

Support of the Russian Fund for Fundamental Research (Grant 98-02-16165) and of the State Research and Development Program ''Neutron Studies of Matter'' is gratefully acknowledged.

[1] L. M. Corliss, J. M. Hastings, W. Kunnmann, R. Thomas, J. Zhuang, R. Butera, and D. Mukamel, Phys. Rev. B **31**, 4337 (1985).
[2] Yu. A. Dorofeev, A. Z. Men'shikov, G. L. Budrina, and V. N. Syromyatnikov, Fiz. Met. Metalloved. **63**, 1110 (1987).
[3] A. Z. Menshikov, Yu. A. Dorofeyev, G. L. Budrina, and V. N. Syromyatnikov, J. Magn. Magn. Mater. **73**, 211 (1988).
[4] T. M. Holden, A. Z. Menshikov, and E. Fawcett, J. Phys.: Condens. Matter **8**, L291 (1996).
[5] C. P. Adams, T. E. Mason, S. A. M. Mentink, and E. Fawcett, J. Phys.: Condens. Matter **9**, 1347 (1997).
[6] H. Shiraishi, T. Hori, and K. Kanematsu, Jpn. J. Appl. Phys. **32**, S 32-3, 263 (1993).
[7] A. Z. Menshikov, Yu. M. Dorofeev, N. A. Mironova, and M. V. Medvedev, Solid State Commun. **98**, 839 (1996).

Translated by G. Skrebtsov

Splitting of NMR signals in parallel fields in the easy-plane antiferromagnet $FeBO_3$

Kh. G. Bogdanova,*) V. E. Leont'ev, and M. M. Shakirzyanov

Kazan Physicotechnical Institute, Russian Academy of Sciences, 420029 Kazan, Russia
(Submitted June 26, 1998)
Fiz. Tverd. Tela (St. Petersburg) **41**, 290–292 (February 1999)

Experimental observations are reported of the splitting of NMR lines of ^{57}Fe into two absorption peaks in a static magnetic field $\mathbf{H}_0$ parallel to a variable field $\mathbf{H}_1$ in the basis plane. The field dependence of the intensity and the variation in the resonance frequencies of the absorption peaks with H_0 are studied. These results can be used to explain some features of the layered domain structure of iron borate. © *1999 American Institute of Physics.* [S1063-7834(99)01902-4]

In a study of NMR in the easy-plane antiferromagnet $FeBO_3$, it has been demonstrated experimentally[1] that the NMR signal from ^{57}Fe nuclei for parallel rf ($\mathbf{H}_1$) and constant ($\mathbf{H}_0$) magnetic fields applied in the ''easy'' basis plane (111) vanishes when $H_0 > H_{sat}$ ($H_{sat} \cong 16$ Oe in $FeBO_3$). This result was explained by the fact that, as the domain walls vanish in fields $H_0 > H_{sat}$, the main contribution to the NMR signal disappears since the signal from nuclei located in domain walls greatly exceeds the contributions from nuclei inside the domains, as well as by the fact that in a single-domain sample at high fields the gain coefficient for the signal for $\mathbf{H}_1 \| \mathbf{H}_0$ approaches zero with increasing H_0.[1,2] Based on this, it was assumed that an iron borate sample forms a single domain in fields $H_0 \cong H_{sat}$. Later on, however, based on NMR data in perpendicular fields ($\mathbf{H}_1 \perp \mathbf{H}_0$), it was shown that only a certain type of domain walls vanishes in the sample for $H_0 \geqslant 16$ Oe (a Neel-type wall), but layer domains with a different direction of the antiferromagnetism vector in the easy plane survive. We believe this causes the experimentally observed splitting of the NMR signal into three absorption peaks in fields $H_0 > H_{sat}$. In our experiments, the sample transformed fully to a single domain in fields $H_0 \sim 200$ Oe, as indicated by the disappearance of the side peaks and an increase in the intensity of the central absorption peak consistent with theoretical calculations. It should be noted that these effects were observed in high power rf fields.

In this paper we present the results of some experiments on NMR of ^{57}Fe for a geometry in which the vectors $\mathbf{H}_0$ and $\mathbf{H}_1$ were parallel and lay in the easy (111) magnetization plane of the sample. Our results show that features of the domain structure of $FeBO_3$ during single domain formation in a magnetic field show up in the NMR signals in this case as well.

According to magnetooptical studies,[4,5] for $T \leqslant 77$ K, the domain structure of $FeBO_3$, a two-sublattice easy-plane antiferromagnet with weak ferromagnetism, consists of split 120°-Bloch walls ($S_\parallel$) parallel to the easy plane, layer-domains with different directions of the antiferromagnetism vector $\mathbf{L}^{(k)} = \mathbf{M}_1^{(k)} - \mathbf{M}_2^{(k)}$.[1,5] ($\mathbf{M}_{1,2}^{(k)}$ are the sublattice magnetizations and $k = 1,2,3$ are the numbers of the domain layers). The vector $\mathbf{L}^{(k)}$ in an individual layer-domain is perpendicular to the second order C_2 axis lying in the easy plane.[6,7] Each plane, in turn, contains domains separated by 180°-Néel walls ($S_\perp$) perpendicular to the basis plane. The Néel walls manifest substantial mobility in very weak magnetic fields H_0 applied in the basis plane and completely vanish for $H_0 = H_{sat} \equiv H_{H1} \sim 16$ Oe.[1] A further rise in H_0 causes the Bloch walls between the layers to vanish because of the rotation of the vectors $\mathbf{M}^{(k)} = \mathbf{M}_1^{(k)} - \mathbf{M}_2^{(k)}$ to states $\mathbf{M}^{(k)} \| \mathbf{H}_0$ in all the layer-domains.[1,3,4,8] It should be noted that the effective spontaneous magnetostriction fields, which also determine the orientation of the magnetizations of the sublattices in the layer-domains,[4,9] are of magnitude $H_{H2} \sim 200$ Oe in the $FeBO_3$ crystal.[10] This implies that one can speak of the disappearance of Bloch walls and the transformation of a sample to a single domain only in fields H_0 exceeding H_{H2}. Thus, the magnetic structure of $FeBO_3$ in sufficiently low fields ($H_{H1} < H_0 \ll H_{H2}$) can be represented schematically as shown in Fig. 1, where the xy plane is the easy basis plane (111). In the case $\mathbf{H}_0 \| x \| \mathbf{M}^{(1)}$ (corresponding to the experiment), the angle between $\mathbf{M}^{(2)}$, $\mathbf{M}^{(3)}$ and $\mathbf{H}_0$ equals $\alpha < \pi/2$ and α approaches zero as $\mathbf{H}_0$ increases.

As mentioned above, one characteristic feature of strong magnets is that in very weak fields $H_0 < H_{H1}$ the main contribution to the NMR signal is from nuclei situated in domain walls, since the gain coefficient for them is much (by roughly 10^2 times) greater than the gain for nuclei in the domains.[11] With increasing H_0 and the vanishing of the domain walls for $H_0 > H_{H1}$, the main contribution to the signal must come from nuclei lying in the layer-domains, for which the gain depends on the mutual orientation of the vectors $\mathbf{M}_i^{(k)}$ and $\mathbf{H}_0$, as well as of the vectors $\mathbf{H}_1$ and $\mathbf{H}_0$. The NMR gains in an individual layer-domain[2] for $\mathbf{H}_1 \| \mathbf{H}_0$ and $\mathbf{H}_1 \perp \mathbf{H}_0$ are given by

$$\eta_\parallel^{(k)} = \left| \frac{H_n \cos \xi^{(k)}}{H_0 \sin \xi^{(k)} + \Delta H_a} \right|, \quad \mathbf{H}_1 \| \mathbf{H}_0,$$

$$\eta_\perp^{(k)} = \left| \frac{H_n \sin \xi^{(k)}}{H_0 \sin \xi^{(k)} + \Delta H_a} \right|, \quad \mathbf{H}_1 \perp \mathbf{H}_0, \qquad (1)$$

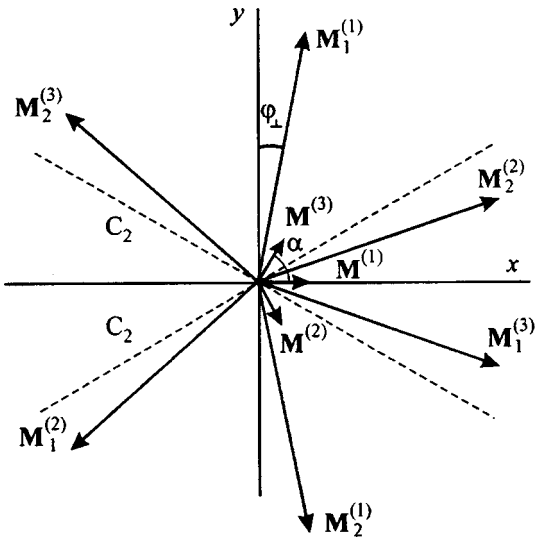

FIG. 1. The orientations of magnetizations in iron-borate-layer domains for $H_0 > 16$ Oe.

where $\xi^{(k)}$ is the angle between the direction of $\mathbf{H}_0$ and that of the magnetization in the sublattice of the k-th domain, and ΔH_a is the exchange-enhanced effective field of the magnetic anisotropy and of the spontaneous magnetostriction in the basis plane. Equation (1) implies that for $\mathbf{H}_0 \| \mathbf{M}^{(1)}$ the NMR gains from the intradomain nuclei are large enough only in layer-domains 2 and 3, while $\eta_\parallel^{(1)} \sim 0$ because $\xi^{(1)} \cong \pi/2$ and $\cos\xi^{(1)} \cong 0$.

The NMR frequencies ($\omega_i^{(k)}$) given by the following expressions for $H_0 > H_{H1}$ ($\mathbf{H}_0 \| x \| \mathbf{M}^{(1)}$, see Ref. 1) have a similarly important dependence on both the magnitude and mutual orientation of the vectors $\mathbf{M}_i^{(k)}$ and $\mathbf{H}_0$:[3]

$$\omega_1^{(1)} = \omega_n - \gamma_n H_0 \sin\varphi_\perp, \quad \omega_1^{(2)} = \omega_n + \gamma_n H_0 \sin(\alpha - \varphi_\perp),$$

$$\omega_1^{(3)} = \omega_n - \gamma_n H_0 \sin(\alpha + \varphi_\perp), \quad \omega_2^{(1)} = \omega_n - \gamma_n H_0 \sin\varphi_\perp,$$

$$\omega_2^{(2)} = \omega_n - \gamma_n H_0 \sin(\alpha + \varphi_\perp),$$

$$\omega_2^{(3)} = \omega_n + \gamma_n H_0 \sin(\alpha - \varphi_\perp),$$

$$\omega_1^{(1)} = \omega_2^{(1)} \equiv \omega_0, \quad \omega_1^{(2)} = \omega_2^{(3)} \equiv \omega_+,$$

$$\omega_1^{(3)} = \omega_2^{(2)} \equiv \omega_-, \quad \alpha < \pi/2, \qquad (2)$$

where γ_n is the nuclear gyromagnetic ratio, $\omega_{n1} = \omega_{n2} = \omega_n$ is the NMR frequency in the hyperfine field H_n, φ is the slope ($\sin\varphi \approx \varphi \approx (H_0 + H_D)/H_E$), which is determined by the deviation of the sublattice magnetizations from strict antiparallelism and characterizes the weak ferromagnetism of $FeBO_3$, H_D is the Dzyaloshinskii field, and H_E is the exchange field. Here the frequency difference $\Delta\omega = \omega_0 - \omega_\pm$, $\Delta\omega = \omega_+ - \omega_-$ are greater than the NMR linewidth ($\delta\omega_n/\gamma_n \cong 20$ Oe) of a single-domain sample, even for small $H_0 > H_{H1}$. Thus, if this model of the single-domain formation process for iron borate in a constant field, which has been confirmed by experiment for $\mathbf{H}_1 \perp \mathbf{H}_0$, is true, then in the case of parallel orientation of $\mathbf{H}_0$ and $\mathbf{H}_1$ ($\mathbf{H}_1 \| \mathbf{H}_0$) a splitting of the NMR signal into two absorption peaks which spread apart for higher H_0 should be observed when $H_0 > H_{H1}$. An important difference between this case of parallel $\mathbf{H}_0$ and $\mathbf{H}_1$ in the basis plane and the $\mathbf{H}_1 \perp \mathbf{H}_0$ case is the following: with complete transformation of the sample into a single domain, because the angles $\xi^{(2)}$ and $\chi^{(3)}$ approach $\chi^{(1)} \cong \pi/2$, the gains for $\mathbf{H}_1 \| \mathbf{H}_0$ in the corresponding layer-domains, $\eta_\parallel^{(2)}$ and $\eta_\parallel^{(3)}$, fall off rapidly, so the NMR signal should vanish ($\eta_\parallel^k \to 0$), while for $\mathbf{H}_1 \perp \mathbf{H}_0$ only the lateral peaks disappear and the intensity of the central peak increases, since, on one hand, $\sin\xi^{(2)} = \sin\xi^{(3)} \Rightarrow \sin\xi^{(1)} \cong \pi/2$ and, on the other, according to Eq. (2) the frequencies $\omega_\pm$ approach ω_0, since the angle $\alpha \to 0$ owing to the rotation of $\mathbf{M}^{(2)}$ and $\mathbf{M}^{(3)}$ to a state $\mathbf{M}^{(k)} \| \mathbf{H}_0$.[3]

EXPERIMENTAL RESULTS AND DISCUSSION

We have investigated the dependence on the magnitude H_0 of the external magnetic field of the drop in the free induction and its frequency spectrum after Fourier transformation.

The measurements were made with parallel rf and constant fields ($\mathbf{H}_1 \| \mathbf{H}_0$) with the vectors $\mathbf{H}_0$ and $\mathbf{H}_1$ lying in the easy magnetization plane (111).

Preparation of the samples and their characteristics, as well as the measurement techniques, have been discussed in detail elsewhere.[12–14]

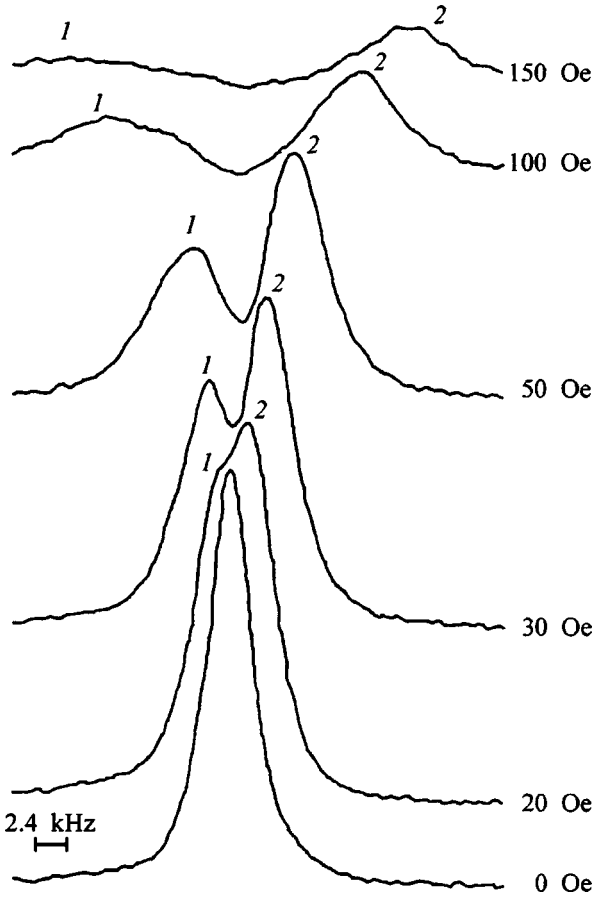

FIG. 2. NMR spectra of ^{57}Fe for different fields H_0 (power attenuation $\Delta P = -20$ dB).

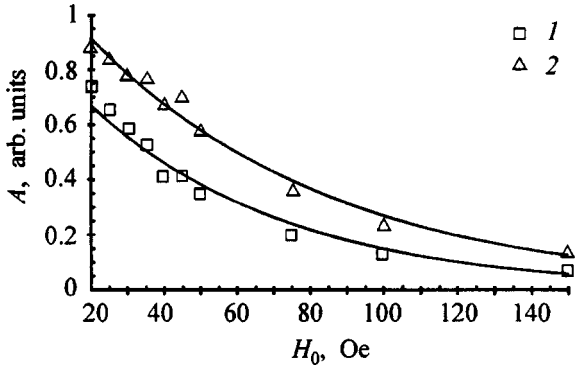

FIG. 3. The drop in free inductance as a function of field ($\Delta P = -20$ dB).

In this case, the NMR signal of the ^{57}Fe nuclei in $FeBO_3$ was observed in fields $H_0 \geqslant 20$ Oe with $H_1 \geqslant H_{1cr}$ to split into two absorption peaks at frequencies close to the zero field NMR frequency $\omega = \omega_n$ ($\omega_n/2\pi = 75.395$ MHz) (Fig. 2). Both absorption signals showed up throughout the entire range of rf field intensities $H_1 \geqslant H_{1cr}$ with an almost monotonic dependence of the amplitude of both signals on H_0 (Fig. 3). The change in the resonance frequencies of these lines, $\Delta\nu_{\pm} = \Delta\omega_{\pm}/2\pi = (\omega_{\pm} - \omega_n)/2\pi$, depends linearly on H_0 (Fig. 4). Here H_{1cr} is the magnitude of the variable magnetic field at which absorption peaks first appear for the given $H_0 \geqslant 20$ Oe. $H_{1\,cr}$ corresponds to an attenuation of the transmitter output power by 39 dB ($P_{max} \cong 1$ kW).

We believe that splitting of the NMR signal was observed only at high powers because of the following: the gains $\eta_{\parallel}^{(k)}$ fall off rapidly with increasing H_0, not only as $1/H_0$, but also because the vectors $\mathbf{M}^{(k)}$ turn toward the direction of $\mathbf{H}_0$ ($\xi^{(k)} \to \pi/2$, $\cos\xi^{(k)} \to 0$, Eq. (1)). At the same time, it is well known[14] that observing an NMR signal requires that the angle of deviation of the nuclear magnetization from the equilibrium position, which is determined by $\eta_{\parallel}^{(k)} H_1$, be close to $\pi/2$. This implies that, in order to compensate the reduction in the gain with increasing H_0, there must be a significant enhancement in the amplitude H_1 of the variable field. It is evidently this factor which prevented the observation of the NMR splitting effects described here and in Ref. 3 in an earlier study[1] of NMR in $FeBO_3$ at low rf powers.

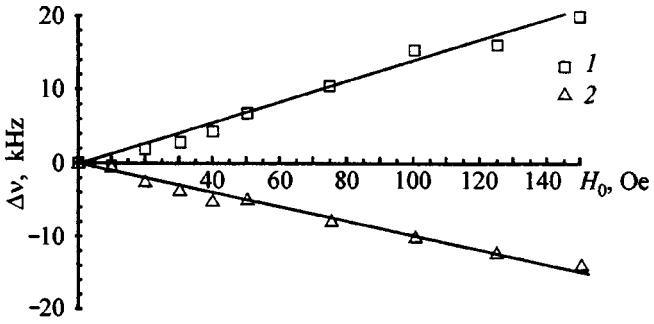

FIG. 4. The change in frequency of the absorption peaks (*1*, *2*) as a function of the field H_0. The points are experimental data; the smooth curves correspond to the points 2.

In conclusion, we note that the present results, like the earlier ones[3] confirming the domain structure model for iron borate and the dynamics of the single domain formation process in a constant field, make it possible to employ the proposed NMR experimental technique, which uses high rf fields, for studying the domain structure of magnetically ordered materials.

This work was supported by the Russian Fund for Fundamental Research (96-02-16-489).

*)E-mail: bogdanova@dionis.kfti.kcn.ru

[1] N. M. Salanskiĭ, E. A. Glozman, and V. N. Seleznev, Zh. Éksp. Teor. Fiz. **68**, 1413 (1975) [Sov. Phys. JETP **41**, 704 (1975)].
[2] D. H. Anderson, Phys. Rev. **151**, *1*, 247 (1966).
[3] Kh. G. Bogdanova, V. A. Golenishchev-Kutuzov, L. I. Medvedev, and M. M. Shakirzyanov, Fiz. Tverd. Tela **33**, 379 (1991) [Sov. Phys. Solid State **33**, 219 (1991)].
[4] D. E. Lacklison, J. Chadwick, and J. L. Page, Appl. Phys. **D5**, *1*, 810 (1972).
[5] J. Haisma and W. T. Stacy, J. Appl. Phys. **44**, 3367 (1973).
[6] V. D. Doroshev, I. M. Krygin, S. N. Lukin, A. N. Molchanov, A. D. Prokhorov, V. V. Rudenko, and V. N. Seleznev, Pis'ma Zh. Éksp. Teor. Fiz. **29**, 286 (1979) [Sov. Phys. JETP **29**, 257 (1979)].
[7] T. K. Soboleva and E. F. Stefanovskiĭ, Fiz. Nizk. Temp. **6**, 1314 (1980) [Sov. Phys. Low Temp. Phys. **6**, 640 (1980)].
[8] A. G. Gurevich, *Magnetic Resonance in Ferrites and Antiferromagnetic Materials* [in Russian], Nauka, Moscow (1973), 591 pp.
[9] E. A. Turov and V. G. Shavrov, Usp. Fiz. Nauk **140**, 429 (1983).
[10] R. Diehl, W. Jantz, B. I. Nolang, and W. Wettling, Current Topics in Mater. Sci., Ed. E. Kadlis. **11**, 242 (1986).
[11] E. A. Turov and M. P. Petrov, *Nuclear Magnetic Resonance in Ferro- and Antiferromagnetic Materials* [in Russian], Nauka, Moscow (1969), 260 pp.
[12] R. A. Bagautdinov, Kh. G. Bogdanova, V. A. Golenishchev-Kutuzov, G. R. Enikeeva, and L. I. Medvedev, Fiz. Tverd. Tela **28**, 924 (1986) [Sov. Phys. Solid State **28**, 518 (1986)].
[13] Kh. G. Bogdanova, V. A. Golenishchev-Kutuzov, L. I. Medvedev, M. I. Kurkin, and E. A. Turov, Zh. Éksp. Teor. Fiz. **95**, 613 (1989) [Sov. Phys. JETP **68**, 345 (1989)].
[14] M. I. Kurkin and E. A. Turov, *NMR in Magnetically Ordered Substances and its Applications* [in Russian], Nauka, Moscow (1990), 244 pp.

Translated by D. H. McNeill

Magnetic and electrical properties of $Mg_{1-x}Cu_xO$ solid solutions and magnetic shielding in $Cu-Mg_{1-x}Cu_xO$ structures

A. A. Samokhvalov, T. I. Arbuzova, N. A. Viglin, V. V. Osipov, N. I. Solin, and S. V. Naumov

Institute of Metal Physics, Urals Branch of the Russian Academy of Sciences, 620219 Ekaterinburg, Russia

V. G. Bamburov, N. I. Lobachevskaya, and O. G. Reznitskikh

Institute of Solid State Chemistry, Urals Branch of the Russian Academy of Sciences, 620219 Ekaterinburg, Russia

(Submitted July 14, 1998)
Fiz. Tverd. Tela (St. Petersburg) **41**, 293-296 (February 1999)

$Mg_{1-x}Cu_xO$ solid solutions having an NaCl structure with $0 \leqslant x \leqslant 0.20$ are synthesized and $Cu-Mg_{1-x}Cu_xO$ structures are prepared for superconductivity studies. The magnetic susceptibility χ, electron paramagnetic resonance (EPR), and electrical conductivity of the solid solutions are studied at temperatures of 5–550 K. It is shown that $\chi^{-1}(T)$ obeys the Curie–Weiss law with a paramagnetic Curie temperature Θ close to zero and an effective magnetic moment $\mu_{\text{eff}} = 1.9\mu_B$, close to the $1.73\mu_B$ of a Cu^{2+} ion with spin $S = 1/2$. The width ΔH of the EPR line depends weakly on temperature and increases as x is raised. The volume narrowing of the EPR linewidth ΔH is used to estimate the exchange interaction parameter, 3×10^{-4} eV. The g-factor is close to 2 and is temperature independent. The electrical conductivity of $Mg_{1-x}Cu_xO$ at $T = 300$ K is $\approx 10^{-11} - 10^{-12} \Omega^{-1}\text{cm}^{-1}$ for $x = 0$ and increases to $10^{-5} - 10^{-6} \Omega^{-1}\text{cm}^{-1}$ for $x = 0.15 - 0.20$. The conductivity is p-type. Magnetic shielding is observed in $Cu-Mg_{1-x}Cu_xO$ structures with $x = 0.15$ and 0.20. The possible connection of this phenomenon with interference superconductivity in the contact layer of the structure is discussed.
 [S1063-7834(99)02002-X]

Establishing the feasibility of raising the critical temperature T_c of high-temperature superconductors is an important problem in modern physics. Certain information in this area can be provided by studies of the localized (impurity) superconductivity with T_c up to 200–300 K which is often observed in cuprate superconductors along with the main superconducting phase with $T_c \approx 100$ K.[1] This sort of localized superconductivity is also observed in partially reduced copper monoxide and a number of heterophase systems based on CuO, such as ''copper-single crystal CuO films.''[2,3] Of the likely reasons for the appearance of localized superconductivity with a high T_c, the most often discussed is the possible formation of impurity CuO having an NaCl structure, which favors HTSC for a number of reasons.[4] Unfortunately, attempts to synthesize CuO with an NaCl structure have not been successful yet. Some preliminary information on this hypothetical CuO can be obtained, however, from studies of $Mg_{1-x}Cu_xO$ solid solutions having an NaCl structure which can exist for $0 \leqslant x \leqslant 0.20$. In this regard, we have synthesized these solid solutions and studied their magnetic susceptibility, electron paramagnetic resonance, and electrical conductivity. $Cu-Mg_{1-x}Cu_xO$ structures have also been created from the solid solutions and magnetic shielding has been observed in them when an electric field is applied.

1. SAMPLES AND MEASUREMENT TECHNIQUES

Samples of $Mg_{1-x}Cu_xO$ solid solutions with $0 \leqslant x \leqslant 0.20$ were prepared from a mixture of the principal carbonate of magnesium $Mg_4(OH)_2(CO_3)_3 \cdot 3H_2O$ and chemically pure (KhCh grade) copper oxide CuO. The mixture was carefully mixed and then annealed for 8–10 hours in an air atmosphere at 400 °C. After remixing, a second anneal was carried out for 12–24 hours at 850 °C. The samples were examined by x-ray structure and x-ray phase analysis. It was found that single-phase samples of the solid solutions with an NaCl structure are formed at concentrations within $0 \leqslant x \leqslant 0.20$. The crystal lattice parameters of the synthesized $Mg_{1-x}Cu_xO$ samples varied linearly from 4.212 ± 0.001 Å for MgO to 4.218 ± 0.001 Å when $x = 0.20$. $Cu-Mg_{1-x}Cu_xO$ structures were prepared by depositing copper films onto pressed samples of $Mg_{1-x}Cu_xO$ with $x = 0.15$ and 0.20. The magnetic susceptibilities were measured on a Faraday magnetic balance with a sensitivity of 5×10^{-8} cm^3g^{-1} for $H \leqslant 1.5$ T. The EPR measurements used an ERS-231 spectrometer in the X-band. The electrical conductivity of the $Cu-Mg_{1-x}Cu_xO$ structures was measured by applying an electrical potential in a device that has been described in detail elsewhere.[2]

2. RESULTS

Figure 1 shows the magnetic susceptibilities χ as a function of temperature for $Mg_{1-x}Cu_xO$ solid solutions. It is

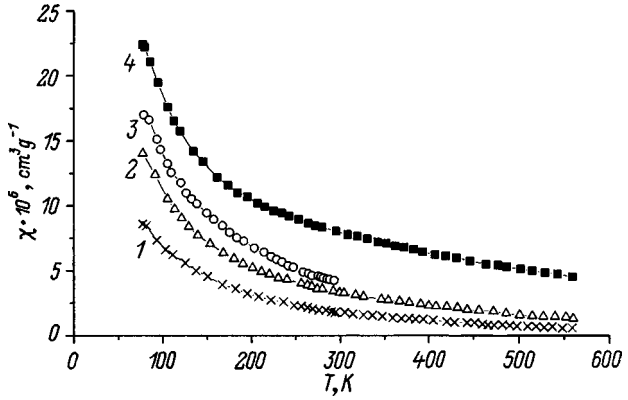

FIG. 1. Temperature dependence of the magnetic susceptibility of $Mg_{1-x}Cu_xO$ solid solutions: (*1*) $x=0.04$, (*2*) $x=0.10$, (*3*) $x=0.15$, and (*4*) $x=0.20$.

clear that, on the whole, $\chi(T)$ has a paramagnetic form and that χ increases monotonically as x is raised. An analysis of the temperature dependence of the reciprocal magnetic susceptibility $\chi^{-1}(T)$ taking the contributions of the MgO matrix and the impurities in it into account shows that for all the compositions, $\chi^{-1}(T)$ obeys the Curie–Weiss law for $T \geqslant 300$ K with a paramagnetic Curie temperature Θ close to 0 K. Here the effective magnetic moment at a copper ion is $\mu_{\text{eff}}=1.9\pm0.2\mu_B$, close to the $1.73\mu_B$ for a Cu^{2+} ion with spin $S=1/2$. For $T<300$ K, when the contributions from impurities to the susceptibility are taken into account, there is ''diamagnetic'' anomaly, i.e., a reduction in χ as the temperature is lowered against the background of the common paramagnetic temperature dependence of $\chi(T)$ in solid solutions.

Figure 2 shows the measured temperature dependence of the EPR linewidth ΔH for $Mg_{1-x}Cu_xO$ solid solutions. For all the compositions ΔH lies between 135 Oe for $x=0.005$ and 640 Oe for $x=0.20$ and depends comparatively weakly on temperature. Although the changes in $\Delta H(T)$ are comparatively small, it is clear from the figure that as the temperature is reduced ΔH decreases linearly, passes through a broad minimum, and then increases as the temperature is reduced further. At 300 K, ΔH depends linearly on the concentration of Cu^{2+} ions in the solid solutions. Measurements

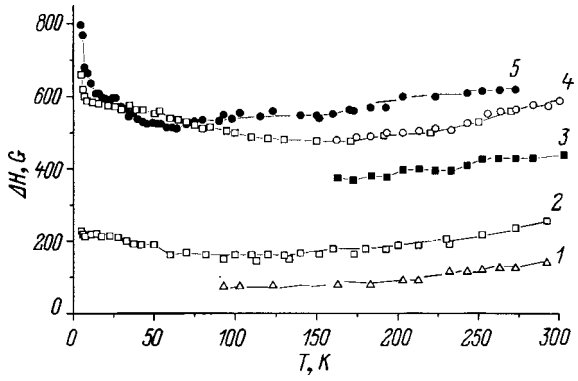

FIG. 2. Temperature dependence of the EPR linewidths of $Mg_{1-x}Cu_xO$ solid solutions: (*1*) $x=0.005$, (*2*) $x=0.04$, (*3*) $x=0.10$, (*4*) $x=0.15$, and (*5*) $x=0.20$.

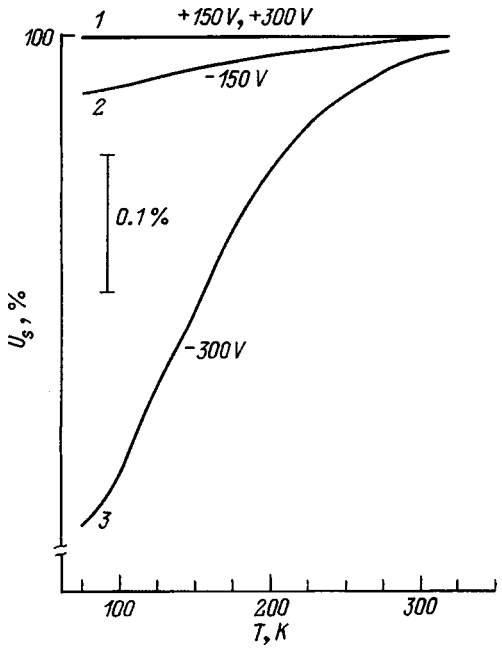

FIG. 3. Temperature dependence of the magnetic shielding of $Cu-Mg_{0.85}Cu_{0.15}O$ structures with applied electrical potentials of 150 V and 300 V.

of the g factor showed that it lies within $g=2.13-2.16$ for all compositions, which is typical of Cu^{2+} ions, and is temperature independent.

Measurements of the conductivity σ of the $Mg_{1-x}Cu_xO$ solid solutions showed that at 300 K, $\sigma \leqslant 10^{-11}\Omega^{-1}\text{cm}^{-1}$ for MgO, while σ increases monotonically to $10^{-6}-10^{-5}\Omega^{-1}\text{cm}^{-1}$ for the compositions with $x=0.15$ and 0.20. Here the activation energy for the electrical conductivity, ΔE_σ, falls from 1.76 eV for MgO to 0.96 eV for $x=0.10$, to 0.84 eV for $x=0.15$, and to 0.28 eV for $x=0.20$. According to the sign of the thermal emf coefficient, the conductivity is *p*-type. During the measurements of the temperature dependence of ρ, in some of the solid solutions an electrical instability involving sharp jumps in ρ (drops) was observed near $T=230-270$ K.

The measured current-voltage characteristics of the solid solutions with $x=0.15$ and 0.20 indicated the existence of a diode effect in the samples.

Figure 3 shows the temperature dependence of the magnetic shielding effect found in the $Cu-Mg_{1-x}Cu_xO$ structures with $x=0.15$ and 0.20 when a negative potential was applied to the copper. The straight line *1* corresponding to applying a positive potential to the copper is temperature independent and indicates the absence of a shielding effect. When a negative potential of 150 V (curve *2*) or 300 V (curve *3*) is applied to the copper, a magnetic shielding effect is observed which depends on the magnitude of the potential applied to the structure. Shielding sets in a $T\approx310$ K. At this same temperature, the ''diamagnetic'' anomaly in the magnetic susceptibility of the solid solutions against the background of the paramagnetic $\chi(T)$ dependence begins to show up in the $\chi^{-1}(T)$ curves. As the temperature is lowered, the shielding gradually increases. The magnitude of the shielding effect measured 6 months after preparation of the

solid solutions (see Fig. 3) corresponds to $10^{-1}-1\%$ by volume of an impurity superconducting phase in the sample. It should be noted that measurements of the shielding on the same sample 3 months after it had been prepared indicated a substantially larger effect, by up to 10%. These results are indicative of an aging effect in the samples. An aging effect was also observed in the measurements of ρ; for samples with $x=0.15$ and 0.20, 12 months after they were prepared, ρ increased from $10^5-10^6\Omega\cdot$cm by 2–3 orders of magnitude. Repeated measurements of the magnetic susceptibility 3 months after preparation of the samples revealed no noticeable changes in its magnitude or temperature dependence. The solid solutions studied here may be said to be quite satisfactorily stable compared to partially reduced CuO.[2]

3. DISCUSSION OF RESULTS

Our studies of magnetic susceptibility and electron paramagnetic resonance (EPR linewidth and g factor) show that $Mg_{1-x}Cu_xO$ solid solutions are paramagnetic with a paramagnetic Curie temperature Θ near 0 K and an effective magnetic moment at the copper ion of $1.9\pm0.2\mu_B$, close to the theoretical value of $1.73\mu_B$ for a Cu^{2+} ion with spin $S=1/2$. The valence of the Cu^{2+} ion and $S=1/2$ are confirmed by the measured g factor, which is close to 2.

It should be noted that, according to previous studies,[2,3] localized high-T_c superconductivity is observed only in those copper-oxide systems which have a paramagnetic temperature dependence of the magnetic susceptibility. The presence of an impurity paramagnetic phase (or fragments) in antiferromagnetic copper oxide is a necessary condition for realization of impurity localized high-T_c superconductivity. Strong spin correlations and antiferromagnetic ordering in copper oxide compounds, for example, in stoichiometric CuO with a monoclinic structure, inhibits superconductivity.

Applying the theory of exchange narrowing of paramagnetic resonance lines[5] to our measurements of the EPR ΔH made it possible to obtain a preliminary estimate of the exchange interaction parameter J in the $Mg_{1-x}Cu_xO$ solid solutions: 3×10^{-4} eV. The paramagnetic Curie temperatures calculated from this value of J for the solid solutions studied here should lie within the interval of 0.2–4 K. These values are consistent with the magnetic susceptibility and EPR data, in which no evidence of magnetic ordering was observed at or above 5 K. This sort of ordering, however, is entirely probable below 5 K.

As for the electrical properties of $Mg_{1-x}Cu_xO$, the rather strong effect of introducing Cu^{2+} ions on the conductivity is noteworthy. The enhancement in the conductivity by 6–7 orders of magnitude for $x=0.15-0.20$ may indicate that Cu^{2+} ions are acceptors with a relatively low activation energy, i.e., are located relatively close to the bottom of the oxygen valence band. (According to the sign of the coefficient of thermal emf, the charge carriers in $Mg_{1-x}Cu_xO$ are holes.) Another feature of the electrical conductivity of $Mg_{1-x}Cu_xO$ is an electrical instability, in the form of sharp drops in ρ at 230–270 K, observed in several samples. These instabilities have been observed before in partially reduced CuO and may indicate the presence of a superconducting impurity in the samples.[6] It should also be noted that over 1 year, ρ in the most highly conducting compositions with $x=0.15$ and 0.20 increased by 2–3 orders of magnitude over the value measured immediately after production. This indicates that aging is not too strong an effect in the solid solutions tested. The observation of magnetic shielding in $Cu-Mg_{1-x}Cu_xO$ structures when a potential of a certain polarity is applied to them and the absence of this effect with the opposite polarity suggests that, in this case, a localized interference superconducting layer analogous to that observed previously in Cu–CuO and $Cu-YBa_2Cu_3O_7$ structures[2,7] is formed in the layer of $Mg_{1-x}Cu_xO$ which contacts the copper.

Therefore, these $Mg_{1-x}Cu_xO$ ($0\leqslant x\leqslant0.20$) solid solutions with an NaCl crystal structure at temperatures of 5–550 K are paramagnetic p-type semiconductors. The existence of a diode effect in a $Cu-Mg_{1-x}Cu_xO$ structure and the corresponding possibility of creating a layer enriched with charge carriers in the region of the solid solution which comes into contact with the copper with p-type conductivity when a negative potential is applied to the copper, the paramagnetism of a copper containing solid solution with an NaCl crystal structure, and a diamagnetic anomaly in the paramagnetic susceptibility in the same temperature region (below 310 K) where magnetic shielding is observed, as well as the entire set of results, some of which have been published before for structures of this type, all suggest that the observed magnetic shielding effect is related to the formation of superconducting fragments in the interface of the $Cu-Mg_{1-x}Cu_xO$ structure.

This work was performed as part of the Federal Program on ''Surface Atomic Structures,'' Project No. 95-2.10.

[1] A. V. Mitin, Perspektivnye Tekhnologii **3** (17), 7 (1996).
[2] A. A. Samokhvalov, T. I. Arbuzova, V. V. Osipov, N. A. Viglin, S. V. Naumov, N. I. Solin, B. A. Gizhevskiĭ, I. B. Smolyak, V. A. Teplov, and V. P. Pilyugin, Fiz. Tverd. Tela **38**, 3277 (1996) [Phys. Solid State **38**, 1788 (1996)].
[3] A. A. Samokhvalov, T. I. Arbuzova, N. A. Viglin, S. V. Naumov, V. R. Galakhov, D. A. Zatsepin, Yu. A. Kotov, O. M. Samatov, and D. G. Kleshchev, Fiz. Tverd. Tela **40**, 795 (1998) [Phys. Solid State **40**, 268 (1998)].
[4] M. V. Krasin'kova and B. Ya. Moĭzhes, Pis'ma Zh. Tekh. Fiz. **17** (7), 1 (1991) [Sov. Phys. Tech. Phys. **17**, 459 (1991)].
[5] P. W. Anderson and P. R. Weiss, Rev. Mod. Phys. **25**, 269 (1953).
[6] C. B. Azzoni, G. B. Paravicini, G. Samogia, P. Ferloni, and F. Parmigiani, Z. Naturforsch. **45a**, 790 (1990).
[7] V. V. Osipov, O. G. Reznitskikh, and A. A. Samokhvalov, *Book of Abstracts, II International Conference Ternary and Multinary Compounds*, England (1997), Abstract P2-66.

Translated by D. H. McNeill

Magnetoacoustic resonance on nuclear spin waves in the cubic antiferromagnet $RbMnF_3$

Kh. G. Bogdanova,*) V. A. Golenishchev-Kutuzova, M. R. Nazipov, and M. M. Shakirzyanov

Kazan Physicotechnical Institute, Russian Academy of Sciences, 420029 Kazan, Russia

S. V. Petrov

P. L. Kapitsa Institute of Physical Problems, Russian Academy of Sciences, 117973 Moscow, Russia
(Submitted July 23, 1998)
Fiz. Tverd. Tela (St. Petersburg) **41**, 297–300 (February 1999)

Magnetoacoustic resonance on nuclear spin waves is measured in the cubic antiferromagnet $RbMnF_3$. A resonance change with respect to a constant magnetic field H_0 with maximum damping at $H_0 \approx 4\times 10^3$ Oe is observed in the amplitude of an acoustic pulse passing through a sample owing to excitation of nuclear spin waves under nuclear magnetoacoustic resonance conditions. A study of the angular dependence of the damping revealed a 90° periodicity consistent with the fact that the [001] direction, around which the rotation takes place, is a four-fold axis of the crystal. An analysis of the dispersion law for nuclear spin waves shows that longitudinal ultrasound propagating along the [001] axis perpendicular to $\mathbf{H}_0$ excites a branch of nuclear spin waves whose frequency depends on the magnitude of the constant magnetic field. [S1063-7834(99)02102-4]

1. Acoustic excitation of nuclear spin waves under nuclear magnetoacoustic resonance conditions has been reported[1] in the spin system of ^{55}Mn nuclei in the easy-plane antiferromagnet $KMnF_3$. This paper is devoted to an experimental study of the conditions for acoustic excitation of nuclear spin waves in the spin system of ^{55}Mn nuclei in the cubic antiferromagnet $RbMnF_3$. The existence of nuclear spin waves in the two-sublattice antiferromagnet $RbMnF_3$ is determined by an effective oblique interaction of the magnetic moments of nuclei, $\mathbf{m}_i$ and $\mathbf{m}_i'$, through magnons whose radii $r(i)$ $(i=1,2)$ attain macroscopic sizes for both branches of the magnon spectrum ($r \approx (10^3-10^4)a$, where a is the interatomic separation in the crystal).[2] This ensures formation of two branches ($\omega_{n_i}(\mathbf{q})$) of nuclear spin waves at liquid-helium temperatures, when the spin system of the ^{55}Mn nuclei is in a disordered paramagnetic state.[2] The wide nuclear-spin-wave band (compared to the NMR linewidth)[2,3] and an efficient magnetoacoustic interaction[3] allow us to hope for the possibility of observing a nuclear magnetoacoustic resonance and the acoustic excitation of nuclear spin waves in $RbMnF_3$, as well. Since the experimental technique is based on measuring the damping coefficient of an ultrasound pulse as it passes through a sample under nuclear magnetoacoustic resonance conditions, the direction of propagation of the longitudinal sound and the orientation of the constant magnetic field $\mathbf{H}_0$ were chosen in advance so as to exclude the resonance absorption of elastic energy in the uniform oscillations of the nuclear magnetization at NMR frequencies ($\omega_{n_i}(0)$) (the nuclear-acoustic-resonance effect). The nuclear-acoustic-resonance effect in this compound has been investigated in detail, both theoretically and experimentally.[3]

2. An experimental study was made of the dependence of the damping coefficient of longitudinal sound with a frequency $\nu_s = 640$ MHz propagating along the four-fold [001] axis ($\mathbf{k} \| [001]$, where $\mathbf{k}$ is the wave vector of the sound) on the magnitude and direction of a constant magnetic field $\mathbf{H}_0$ applied in the (001) plane ($\mathbf{H}_0 \perp \mathbf{k}$). The apparatus and measurement techniques have been discussed in detail elsewhere.[1,4]

The single crystals of $RbMnF_3$ on which the measurements were done were prepared in the form of parallelepipeds with dimensions of $4\times 4\times 5$ mm^3 whose edges coincided with the principal crystal axes [100], [010], and [001]. The end surfaces were flat and mutually parallel to within 1/5 of the acoustic wavelength. Ultrasonic waves were excited in a pulsed mode at one of the end surfaces (001) of the sample and detected at the opposite end. The measurements were made at $T = 4.2$ K. The helium cryostat with the sample was rotated about its R axis, always perpendicular to $\mathbf{H}_0$. The angle between the R axis and the wave vector $\mathbf{k}$ was set to be 0°. The magnitude of the constant magnetic field was varied from 0 to 8000 Oe. An acoustic pulse that passed through the sample once was used. The ratio of its amplitude (U) to the amplitude of the incident sound (U_0) determines the damping coefficient $\alpha = U/U_0$ measured in the experiment.

During the study of the dependence of the damping of the ultrasound on the magnitude of the magnetic field applied in the (001) plane, a resonant variation, with respect to the field, was found in the damping coefficient α (Fig. 1). The maximum damping was observed at $H_0 \approx 4000$ Oe. The half width of the line was about $\Delta H \approx 1000$ Oe. An investigation of the angular dependence of the damping coefficient α on the direction of the field in the (001) plane for $H_0 = 4000$ Oe

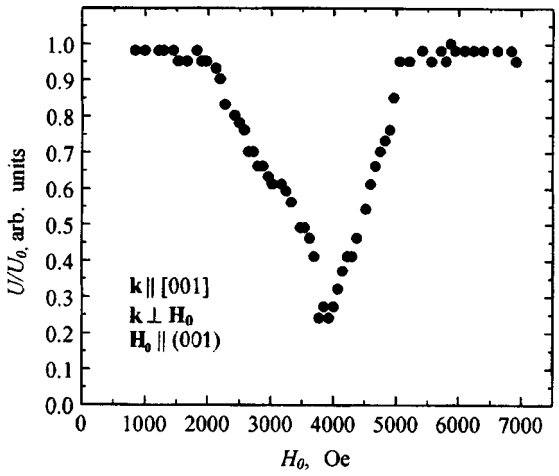

FIG. 1. The ratio U/U_0 as a function of the constant magnetic field H_0.

(by rotating the sample about the R axis of the cryostat $\|[001]$) revealed the expected 90° periodicity consistent with the fact that the [001] direction is a 4-th order axis (Fig. 2). For certain directions of the constant magnetic field, there was no damping of the ultrasound, whatever ($\alpha=1$). The angle between the maximum and minimum of the damping coefficient was 45°. We may assume from considerations of symmetry that the extrema in the angular dependence are associated with directions of $\mathbf{H}_0$ parallel to crystallographic axes of type [110] and [010] and planes (001). This is explained primarily by the fact that the position of the sublattice magnetizations in sufficiently high fields depend on the direction of $\mathbf{H}_0$, which, in turn, determines the components of the magnetoelastic interaction.

3. In the case being considered here, the magnetoelastic interaction of longitudinal acoustic oscillations propagating along the $[001]\|\mathbf{k}$ axis with sublattice magnetizations $\mathbf{M}_i$ ($i=1,2$) in a cubic antiferromagnet having a coordinate system with axes $x\|[100]$, $y\|[010]$, and $z\|[001]$ can be written in the form[3,5]

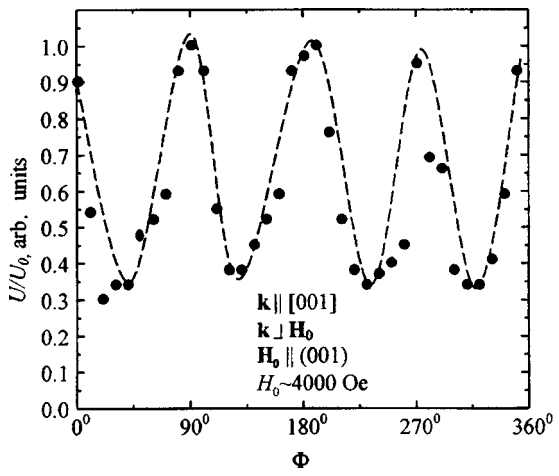

FIG. 2. The angular variation of the ratio U/U_0 at a frequency of 664 MHz.

$$V_{ME}=\frac{B_1}{M_0^2}(M_{1z}^2+M_{2z}^2)U_{zz}(z,t)+\frac{B_3}{M_0^2}M_{1z}M_{2z}U_{zz}(z,t), \tag{1}$$

where B_1 and B_3 are the magnetoelastic constants, $M_0=|M_1|=|M_2|$ are the equilibrium values of the sublattice magnetizations, $U_z(z,t)$ are the elastic displacements caused by the external acoustic field, and $U_{zz}(z,t)$ is the corresponding component of the elastic deformations, given by $U_{zz}(z,t)=\partial U_z(z,t)/\partial z$. In the constant magnetic field $H_0=H_{01}\approx 4000$ Oe, at which a resonant variation in the damping coefficient $\alpha(H_0)$ is observed, the antiferromagnetic compound $RbMnF_3$ at helium temperatures is in a state where the ferromagnetism vector $\mathbf{M}=(\mathbf{M}_1+\mathbf{M}_2)\|\mathbf{H}_0$, while the antiferromagnetism vector $\mathbf{L}=(\mathbf{M}_1-\mathbf{M}_2)\perp\mathbf{H}_0$ (''spin-flop'' phase[3,6]). A cubic antiferromagnet is in a ''spin-flop'' phase if the inequality $H_0^2>2H_EH_A$ is satisfied, where H_E is the exchange field and H_A is the cubic anisotropy field. For the known magnitudes of the exchange field $H_E\approx 0.82\times 10^6$ Oe and anisotropy field $H_A\approx 4.6$ Oe in crystalline $RbMnF_3$,[3] this inequality is easily satisfied, even in fields $H_0\geqslant 3000$ Oe. The magnitude of the vector $\mathbf{M}$, given by $|\mathbf{M}|=2M_2\sin(H_0/2H_E)$, is very small in these fields and $|\mathbf{L}|\gg|\mathbf{M}|$. Given this inequality, Eq. (1) for the magnetoelastic interaction can be written in the form

$$V_{ME}=\frac{B}{2M_0^2}L_z^2U_{zz}(z,t). \tag{2}$$

In a polar coordinate system, where θ is the polar angle of the vector $\mathbf{L}$ measured from the [001] direction and φ is the azimuthal angle measured from the [100] direction, $\mathbf{L}$ is characterized by the components

$$L_x=L_0\cos\varphi\sin\theta,\quad L_y=L_0\sin\theta\sin\varphi,$$

and

$$L_z=L_0\cos\theta,\quad L_0=2M_0,$$

and the magnetoacoustic interaction is given by

$$V_{ME}=2B\cos^2\theta U_{zz}(z,t). \tag{3}$$

The acoustic waves act on the nuclear spin system in magnetic materials through magnetoelastic fields $\mathbf{h}_{iu}$ ($i=1,2$) which are defined as variational derivatives of the magnetoelastic energy $\mathbf{h}_{iu}(z,t)=\delta V_{ME}(z,t)/\delta\mathbf{M}_i$ and caused by oscillations in the sublattice magnetizations $\mathbf{M}_i$ (or in the vectors $\mathbf{L}$ and $\mathbf{M}$).[7] In our case, the small oscillations in $\mathbf{L}$ caused by the field of elastic deformations $U_{zz}(z,t)$ are characterized by small changes in the angle θ ($\Delta\theta$, $\theta=\theta_0+\Delta\theta$), where θ_0 is the equilibrium value of θ. Taking the deformations U_{zz} to be small and expanding Eq. (3) in powers of $\Delta\theta$, to within terms of second order in smallness we have

$$V_{ME}\approx 2B\sin 2\theta_0\Delta\theta U_{zz}(z,t). \tag{4}$$

Equation (4) for the magnetoelastic interaction does not have an explicit dependence on the angle φ. However, it is known[6,8] that in a ''spin-flop'' phase the vector $\mathbf{L}$ lies in a plane perpendicular to $\mathbf{H}_0$ and changes its equilibrium posi-

tion from a state with $\mathbf{L}\|[010]$ ($\theta_0=\pi/2$) for $\mathbf{H}_0\|[100]$ to a state with $\mathbf{L}\|[111]$ ($\theta_0=\arcsin 2/3$ in the (110) plane) for $\mathbf{H}_0\|[110]$ and from this state to a state with $\mathbf{L}\|[100]$ ($\theta_0=\pi/2$) for $\mathbf{H}_0\|[010]$. Thus, if we take the angle Φ, which characterizes the direction of $\mathbf{H}_0$ in the (001) plane (taken from the [100] direction), then when Φ varies in the interval $0\leqslant\Phi\leqslant\pi/4$, the angle θ_0 varies from $\theta_0=\pi/2$ to $\theta_0=\arcsin 2/3$ and from $\theta_0=\arcsin 2/3$ to $\theta_0=\pi/2$ when Φ varies over the interval $\pi/4\leqslant\Phi\leqslant\pi/2$ (similarly for $\mathbf{H}_0$ lying in the other quadrants formed in the (001) plane by the [100] and [010] axes). It is evident that the angle θ_0 is a function of the angle Φ. However, it was possible to obtain an analytic expression for the function $\theta_0(\Phi)$ only in the special cases mentioned above, where the direction of $\mathbf{H}_0$ coincides with the crystallographic axes of a cubic crystal. The numerical calculations require knowledge of these necessary parameters.

At the same time, it is possible to explain the major aspects of the angular dependence of the damping coefficient α on the direction of $\mathbf{H}_0$. According to Eq. (4), the above remarks imply that the longitudinal acoustic oscillations propagating along the [001] axis do not interact with the oscillations of the sublattice magnetizations for $\mathbf{H}_0\|[100]$ and $\mathbf{H}_0\|[010]$, and that the magnetoelastic interaction is greatest when $\mathbf{H}_0\|[110]$. This conclusion is consistent with the data of Refs. 3 and 5. Thus, we can say that the damping peak observed in the experiment corresponds to a direction of the field $\mathbf{H}_0\|[100]$ and that for $\mathbf{H}_0\|[010]$ or [100], $\alpha=1$. That is, the acoustic pulse travels through the sample without attenuation.

Calculations[3] show that the absorption coefficient for ultrasound energy owing to resonance transitions between energy levels in the spin system of the ^{55}Mn nuclei (nuclear acoustic resonance effect) is zero when $\mathbf{H}\|[110]$. Therefore, the resonance change, with respect to the magnetic field, in the sound intensity within this range of frequencies ($\nu_s\approx 640$ MHz) is caused by other factors. We believe that the observed resonance damping effect is, as in crystalline $KMnF_3$,[3] related to the excitation of nuclear spin waves by the acoustic field near the point where the dispersion curves for sound and nuclear spin waves intersect, i.e., under nuclear magnetoacoustic resonance conditions.

An analysis of the nuclear spin wave frequency spectrum[9,3] in cubic $RbMnF_3$ shows that for $H_0\approx 4000$ Oe at a frequency of ($\nu_s\approx 640$ MHz) only one of the nuclear spin wave branches $\nu_{ni}(\mathbf{q})$ can intersect the dispersion curve $\nu(\mathbf{k})$ for sound. This branch of the nuclear spin waves is associated with a field dependent branch of the magnon spectrum corresponding to oscillations of $\mathbf{L}$ in a vertical plane passing through the [001] axis.[8] The frequency of this nuclear spin wave branch is given by[9]

$$\nu_{n1}(\mathbf{q})\approx\nu_n\left\{1-\frac{2H_EH_N}{\gamma_e^{-2}\omega_{e1}^2(0)+H_E^2(a\mathbf{q})^2/12}\right\}^{1/2},$$

$$\nu_n=\gamma_nH_n, \tag{5}$$

where γ_e and γ_n are the gyromagnetic ratios for the electrons and nuclei, H_n and H_N are the hyperfine fields at, respectively, the nuclei and electrons, $\mathbf{q}$ is the wave vector of the nuclear spin waves, and $\omega_{e1}(0)$ is the homogeneous antiferromagnetic resonance frequency, which equals

$$\omega_{e1}^2(\theta)=\gamma_e^2(H_0^2+3B(\theta_H,\Phi)H_EH_A+2H_EH_N). \tag{6}$$

The coefficient $B(\theta_H,\Phi)$ in Eq. (6) depends on the orientation of the constant magnetic field relative to the crystallographic [100], [010], and [001] axes and, in the case where $\mathbf{H}_0$ lies in the (001) plane, is given by the expression[8] (θ_H is the polar and Φ is the azimuthal angle of the vector $\mathbf{H}_0$)

$$B(\pi/2,\Phi)=-4\cos 4\Phi/(7+\cos 4\Phi),\quad \theta_H=\pi/2. \tag{7}$$

For $\Phi=\pi/4$, $B(\Phi)$ has a maximum, $B(\Phi)=2/3$. In this case the NMR frequency corresponding to uniform oscillations of the nuclear magnetization with $\mathbf{q}=0$ also has a maximum (see Eq. (6)) and, for fields $H_0=4000$ Oe, $H_E=0.82\times 10^6$ Oe, $H_A=4.6$ Oe, and $H_N=9.43/T$ ($T=4.2$ K),[3] is approximately $\nu_{n1}(0)\approx 635$ MHz.

Therefore, the nuclear spin wave frequency that matches the sound frequency ν_s lies in a region of $\nu_{n1}(\mathbf{q})$ with high dispersion. The wave vector $\mathbf{q}$ of the nuclear spin waves given by Eq. (6) for $\nu_{n1}(\mathbf{q})=640$ MHz, $\gamma_nH_n/2\pi$, and $a=3\times 10^{-8}$ cm has essentially the same magnitude as the acoustic wave vector, $|\mathbf{k}|$ calculated from the condition $\nu_s=Vk$ for a sound speed $V=5.51\times 10^5$ cm·s^{-1}. This implies that at the point where the dispersion curves of the sound and nuclear spin waves intersect, a condition for a magnetoacoustic resonance in the nuclear spin waves, analogous to the magnetoacoustic resonance effect in magnons,[10] is satisfied. Here a coupled magnetoelastic wave, characterized by magnetic and elastic components at each point, propagates in the sample. And it is obvious that the reduction in the intensity of the acoustic component observed under nuclear magnetoacoustic resonance conditions is related to the conversion of elastic energy into magnetic energy of a nuclear spin wave.[10] The resonance character of the acoustic damping with respect to the magnetic field is caused by the fact that, as H_0 increases, the intersection of the dispersion curves approaches the frequency of the sound excited in the sample owing to the change in $\nu_{n1}(\mathbf{q})$ (Fig. 3).

Note that acoustic excitation of the second (field-independent[3]) branch of the nuclear spin waves is impossible for the given geometry of the vectors $\mathbf{k}$ and $\mathbf{H}_0$ ($\mathbf{k}\perp\mathbf{H}_0$, $\mathbf{k}\|[001]$) and the given frequency. On one hand, this branch of nuclear spin waves is associated with oscillations of $\mathbf{L}$ in a plane parallel to (001) that are characterized by variation in the azimuthal angle φ. Excitation of this type of oscillations in $\mathbf{L}$ by the elastic field requires a change in the mutual orientation of the vectors $\mathbf{k}$ and $\mathbf{H}_0$.[1,3] On the other hand, the frequency of the second branch of the nuclear spin waves is given by[2,3]

$$\nu_{n2}(\mathbf{q})=\nu_n\left\{1-\frac{2H_EH_N}{\gamma_e^{-2}\omega_{e2}^2(0)+H_E^2(aq)^2/12}\right\}^{1/2}, \tag{8}$$

and

$$\omega_{e2}(0)=\gamma_e(2H_EH_N+3C(\theta_H,\Phi)H_EH_A)^{1/2}, \tag{9}$$

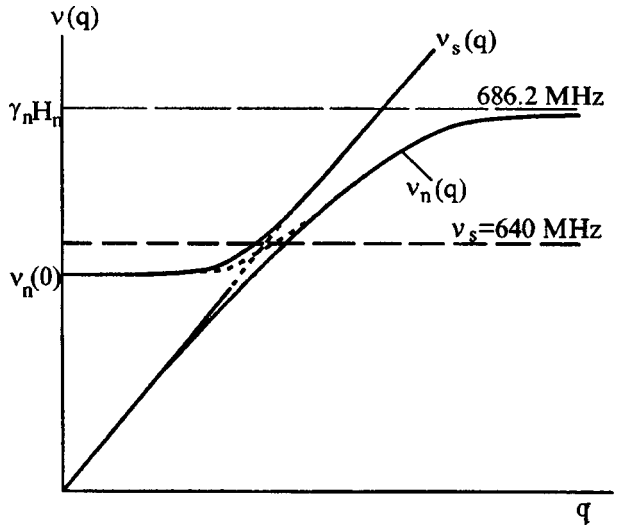

FIG. 3. Spectra of nuclear magnetoelastic waves under conditions such that nuclear spin waves exist.

where $\omega_{e2}(0)$ is the uniform antiferromagnetic-resonance frequency corresponding to the field independent mode of the magnon spectrum.[11] The coefficient $C(\theta_H,\Phi)$ in the expression for $\omega_{e2}(0)$, like the coefficient $B(\theta_H,\Phi)$, depends on the orientation of the constant magnetic field $\mathbf{H}_0$ with respect to the crystallographic axes, and for $\mathbf{H}_{0\|}[110]$, $C(\pi/2,\pi/4)=2/3$.[11] Substituting the known values of the frequencies and fields (see above) in Eqs. (8) and (9), we obtain $\nu_{n2}(0)\approx 561.7$ MHz for $|\mathbf{q}|=0$. This implies that a much lower ultrasound frequency than $\nu_s=640$ MHz would have to be used to satisfy the conditions for a nuclear magnetoacoustic resonance at the second branch of the nuclear-spin waves for the given acoustic dispersion relation $\nu_s=Vk$.

In conclusion, it should be noted that a complete theoretical description of the acoustic excitation of nuclear spin waves under nuclear-magnetoacoustic-resonance conditions requires solution of the combined equations of motion for the electron and nuclear magnetizations and the equations of the theory of elasticity including the hyperfine and magnetoelastic interactions. This kind of calculation has been carried out in a study of the acoustic excitation of nuclear spin waves in the easy-plane antiferromagnet $KMnF_3$.[1,12] We have not set ourselves this task in this paper and have limited ourselves to analyzing the feasibility of acoustic excitation of nuclear spin waves in the cubic antiferromagnet $RbMnF_3$ under nuclear-magnetoacoustic-resonance conditions. In the future we plan to perform a detailed theoretical calculation for this phenomenon, along with an experimental study of the conditions for excitation of both nuclear spin wave branches.

This work has been supported by the Russian Fund for Fundamental Research (Grant No. 96-02-16489).

*)E-mail: bogdanova@dionis.kfti.kcn.ru

[1] Kh. G. Bogdanova, V. A. Golenishchev-Kutuzov, M. I. Kurkin, V. E. Ľeont'ev, M. R. Nazipov, V. V. Nikolaev, and M. M. Shakirzyanov, Zh. Éksp. Teor. Fiz. **112**, **5(11)**, 1830 (1997) [JETP **85**, 1001 (1997)].
[2] M. I. Kurkin and E. A. Turov, *NMR in Magnetically Ordered Materials and its Applications* [in Russian], Nauka, Moscow (1990), 244 pp.
[3] J. B. Merry and D. I. Bolef, Phys. Rev. **B4**, 1572 (1971).
[4] Kh. G. Bogdanova, V. A. Golenishchev-Kutuzov, V. E. Leont'ev, M. R. Nazipov, and M. M. Shakirzyanov, PTÉ **4**, 60 (1997).
[5] R. L. Melcher and D. I. Bolef, Phys. Rev. **186**, 491 (1969).
[6] P. H. Cole and W. J. Ince, Phys. Rev. **150**, 377 (1966).
[7] V. I. Ozhogin and V. L. Preobrazhenskiĭ, Usp. Fiz. Nauk **155**, 593 (1988).
[8] Dale T. Teany, M. J. Freiser, and R. W. H. Stevenson, Phys. Rev. Lett. **9**, 212 (1962).
[9] E. A. Turov and M. P. Petrov, *Nuclear Magnetic Resonance in Ferro- and Antiferromagnetic Materials* [in Russian], Nauka, Moscow (1969), 260 pp.
[10] A. I. Akhiezer, V. G. Bar'yakhtar, and S. V. Peletminskiĭ, *Spin Waves* [in Russian], Nauka, Moscow (1967), 368 pp.
[11] M. J. Freiser, P. E. Seideu, and Dale T. Teaney, Phys. Rev. Lett. **10**, 293 (1963).
[12] Kh. G. Bogdanova, V. A. Golenishev-Kutuzov, V. E. Leont'yev, M. I. Kurkin, M. R. Nazipov, and M. M. Shakirzyanov, Appl. Phys. A: Solids Surf. **14**, (4) (1998).

Translated by D. H. McNeill

Barkhausen effect in stepped motion of a plane domain boundary in gadolinium molybdate

V. Ya. Shur,*) E. L. Rumyantsev, V. P. Kuminov, A. L. Subbotin, and V. L. Kozhevnikov

Institute of Physics and Applied Mathematics, Ural State University, 620083 Ekaterinburg, Russia
(Submitted June 4, 1998)
Fiz. Tverd. Tela (St. Petersburg) **41**, 301–305 (February 1999)

Barkhausen pulses generated in stepped motion of a single plane domain boundary (PDB) are investigated experimentally in single-crystalline wafers of the extrinsic ferroelastic ferroelectric gadolinium molybdate containing artificial pinning centers of the ''field inhomogeneity'' type near the edges of the sample. Two scenarios of the evolution of a PDB in interaction with ''defects'' are proposed on the basis of analyzing the shape of the pulses in a linearly increasing field: small changes of the pulse shape in a weak field and the generation of wedge domains in a strong field. The proposed mechanism of PDB motion due to the generation of steps near the edge of the sample and their longitudinal motion provides a means for explaining the experimentally observed linear field dependence of the PDB velocity and for determining the velocity of the steps. © *1999 American Institute of Physics.* [S1063-7834(99)02202-9]

The domain-structure kinetics of polarization switching covers the complex process of nucleation, growth, and coalescence of an ensemble of separate domains. The experimental investigation of domain kinetics is usually carried out by indirect methods, the most popular of which is the measurement of switching currents. The results of such measurements contain statistical information about the evolution of domain structure, and such information can be extracted once the relationship has been established between the specific stages of the domain kinetics and the corresponding responses (switching currents). A special role is played by deviations of the switching current from monotonic behavior (Barkhausen jumps), which are usually identified with nucleation, individual domain growth, and pinning (interaction of the boundaries with defects).[1–3] It is of utmost importance to establish in detail the relationship between the shape of the current step and specific nature of the evolution of domains, particularly in connection with the interaction of plane domain boundaries (as an elementary process of domain structure kinetics) with defects that can be monitored (pinning centers).

Plane domain boundaries are stable in ferroelastic ferroelectrics throughout a wide range of external influences, making them superior model materials for investigating plane domain boundaries (PDBs). We have chosen the extrinsic ferroelastic ferroelectric $Gd_2(MoO_4)_3$ (GMO), because its physical properties and domain structure have been thoroughly investigated.[4–6] Barkhausen pulses have been observed in GMO as an accompaniment to the nonmonotonic motion of domain boundaries.[7]

The present study is devoted to a detailed analysis in GMO of the shape of Barkhausen pulses generated in the stepped motion of a solitary PDB upon interaction with controllable pinning centers of the ''field inhomogeneity'' type.

1. EXPERIMENT

The investigated samples were single-crystal, rectangular GMO wafers (with typical dimensions $0.39\times 2\times 7$ mm^3) cut perpendicular to the polar axis, their side faces parallel to the coherent orientations of the PDBs. All faces of the wafers were ground and polished with diamond pastes. Transparent In_2O_3:Sn electrodes were deposited on the polar faces by reactive sputtering. Prior to the measurements, a single PDB parallel to the smaller face of the plate was formed by a machining process, and the sample was fastened to the substrate. Strips of electrodes (Fig. 1a) limited the range of movement of the PDB and prevented it from vanishing. One of the electrodes was specially shaped (Fig. 1b) to create pinning centers (of the ''field inhomogeneity'' type), imparting nonmonotonic motion to the PDB with accompanying Barkhausen jumps. An alternating voltage of amplitude up to 300 V and frequency 30–100 Hz, varying according to a sinusoidal or linear law, was applied for cyclic motion of the PDB. For one hour before the start of the measurements the sample was switched in an alternating field of maximum amplitude. The switching currents in a linearly increasing field were recorded and analyzed by means of an IBM personal computer. Frequencies higher than 33 kHz were eliminated by digital filtering to reduce the influence of recording system noise.

2. BARKHAUSEN JUMPS

In contrast with measurements made during smooth motion of the boundary in a homogeneous field,[8] the switching currents were not reproduced in successive measurement cycles. The field (time) dependence of the averaged current $\langle j\rangle$ and its variance $\langle \Delta j^2\rangle$, determined by statistical processing of the results of 50 successive measurement cycles in a linearly increasing field, are shown in Figs. 2a and 3a, respectively.

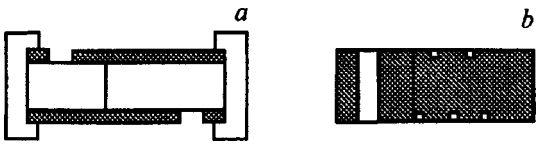

FIG. 1. Configuration of the electrodes.

The current pulse was divided into three intervals on the basis of the variance (Fig. 3a). In the first interval ($E < 2.15$ kV/cm) the variance is small (being determined solely by recording system noise), indicating that the motion of the PDB is reproducible. In the second interval (2.15 kV/cm $< E < 3.2$ kV/cm) the variance is much greater than the initial level. Beginning with $E = 3.2$ kV/cm, the variance rises sharply, and at the same time the field dependence of the average switching charge $\langle Q \rangle$, determined by the numerical integration of $\langle j \rangle$, undergoes a qualitative change (Fig. 3b).

The first interval is naturally identified with smooth motion of the PDB in a homogeneous field without pinning centers. It will be shown below that the differences between the currents in the second and third intervals are attributable to a change in the interaction of the PDB with the pinning centers (field inhomogeneities).

To describe the field dependence of the switching charge, we bear in mind that the switching current during the motion of a PDB in a rectangular sample is proportional to the lateral velocity v, and a linear field dependence of the velocity is observed over a wide range of fields in GMO[4]:

$$v(E) = \mu(E - E_{st}), \tag{1}$$

where E_{st} is the starting field, and μ is the mobility of the PDB.

During motion of the PDB in a linearly increasing field $Q(E)$ now has the form

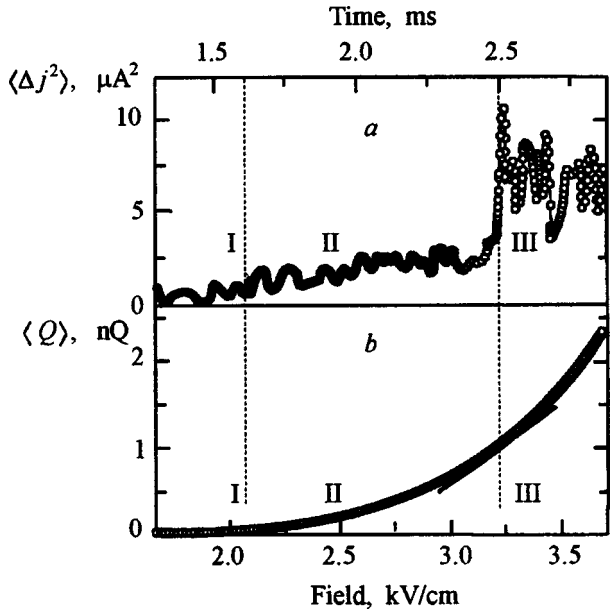

FIG. 3. Field dependences of the variance of the switching current $\langle \Delta j^2 \rangle$ (a) and the switched charge $\langle Q \rangle$ (b).

$$Q(E) = P_s b \mu (E - E_{st})^2, \tag{2}$$

where P_s is the spontaneous polarization, and b is the width of the sample.

Smooth, uniformly accelerated motion of the PDB is observed only in the first interval:

$$j(t) \sim (t - t_0). \tag{3}$$

We regard the prominent features of the nonmonotonic motion in the second and third intervals as deviations from uniformly accelerated motion. Figure 4b shows the devia-

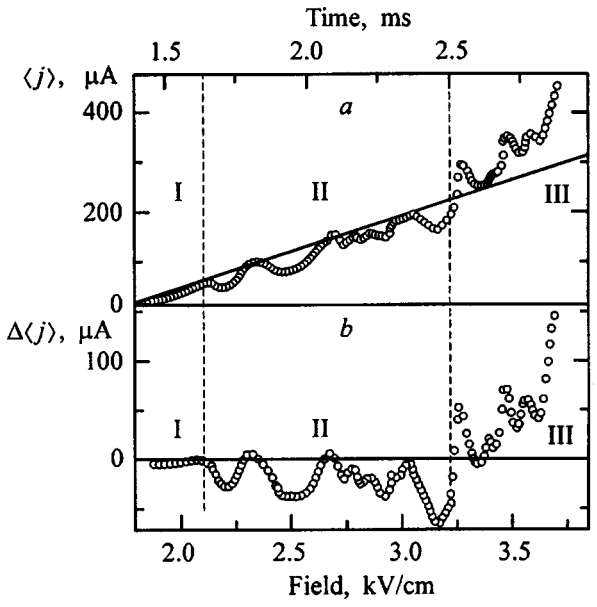

FIG. 2. Field dependences of the averaged switching current $\langle j \rangle$ (the straight line is interpolated from the linear field dependence determined in the first interval) (a) and the deviation of the current from the interpolation (b).

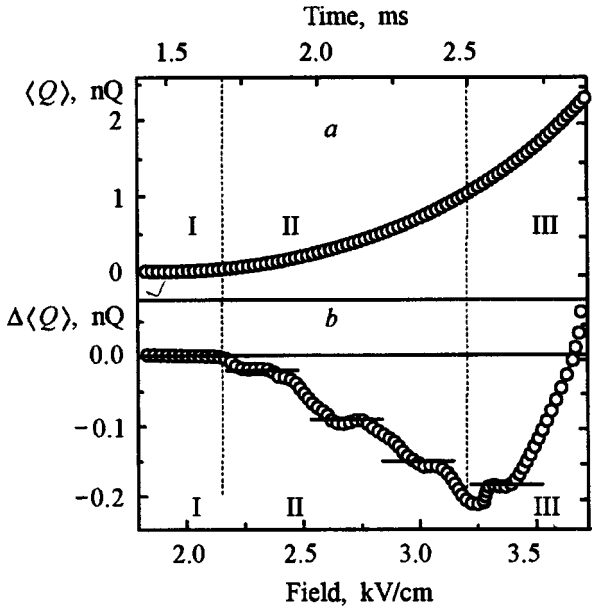

FIG. 4. Interpolation of the field dependence of the switched charge by Eq. (2) with the parameters determined in the first interval (a) and the deviation from the interpolation (b) (the line segments delimit individual stages corresponding to smooth, uniformly accelerated PDB motion).

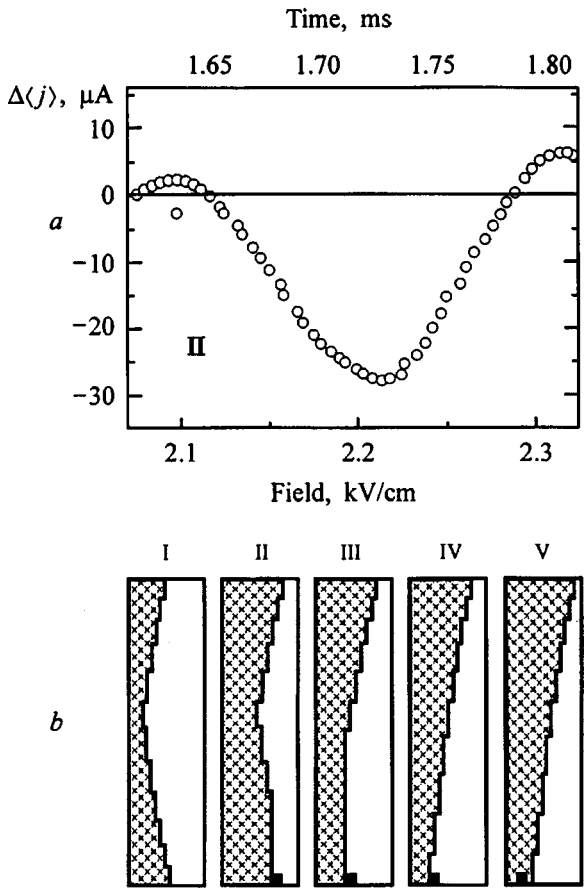

FIG. 5. Negative Barkhausen jump (a) and the corresponding diagram showing the evolution of the shape of the PDB (b).

tions of the experimental values of $\langle Q(E)\rangle$ from the interpolation of the first interval (Fig. 4a). In the second interval (Fig. 4b) we distinguish separate stages (indicated by line segments) corresponding to smooth, uniformly accelerated motion of the PDB. It is evident that interaction with pinning centers merely slows down the PDB, and the current deviations can be characterized by a sequence of negative Barkhausen jumps of different amplitudes (Fig. 2b). Positive Barkhausen jumps occur only in the third interval.

3. MOTION OF A PLANE DOMAIN BOUNDARY IN A CONSTANT FIELD

To analyze the observed features, we consider the motion of a PDB in a constant electric field. Any ferroelectric domain boundary is known to be set in motion by the formation of one-dimensional (1D) and two-dimensional (2D) nuclei in the boundary zone.[9,10] The PDB is unique in that it moves by virtue of layered growth, i.e., the motion of steps along the domain boundary.[11,12]

Let steps be formed by the generation of 2D nuclei at the intersection of the domain boundary with an edge of the sample (step generation center) and move as a result of the formation of 1D nuclei (Fig. 5b). The step generation rate dn/dt is determined by the local field $E_{\rm loc}$ at the generation center, and the velocity of the steps $v_{\rm st}$ is determined by the local field ahead of the moving step.

Allowance for the delay in screening of the depolarizing fields[13] created during the nucleation process produces a nonuniform spatial distribution of local fields. For a finite screening time $\tau_{\rm scr}$ a vestigial stub of ''uncompensated'' bound charge is formed and moves behind the step.[13,14] The unscreened part of the depolarizing field $\Delta E_{\rm dep}(x,t)$ reduces the local field in the vicinity of a step:

$$E_{\rm loc}(x,t)=E_{\rm ex}-\Delta E_{\rm dep}(x,t). \tag{4}$$

We assume that the probability of step generation has a threshold-type field dependence

$$p_s=\begin{cases}1 & \text{for} \quad E_{\rm loc}>E_{\rm th}\\ 0 & \text{for} \quad E_{\rm loc}<E_{\rm th}\end{cases}. \tag{5}$$

With the advent of a 2D nucleus (step generation) the field in the generation center falls below the threshold level because of an increase in the contribution $\Delta E_{\rm dep}$, and step generation ceases. In the subsequent motion of the step (as a result of 1D nucleation) the depolarizing field increases, and the influence of $\Delta E_{\rm dep}$ gradually diminishes strictly as a result of screening. The magnitude of the local field in the step generation center attains the threshold level when the step moves away from the edge of the sample to a distance Δl, which can be determined from the relation

$$E_{\rm ex}-\Delta E_{\rm dep}(\Delta l)=E_{\rm th}. \tag{6}$$

Under the stated assumptions, the motion of the steps always begins when the local field is equal to the threshold value. As a result, the velocity of the steps does not depend on the external field. As the field increases, the number of steps on the boundary increases (Δl decreases). When the length of the step is much greater than the length of the stub ($l_{\rm tr}=v_{\rm st}\cdot\tau_{\rm scr}$), the following approximate field dependence $\Delta l(E)$ can be obtained from Eq. (6)[15]:

$$\Delta l\sim(E_{\rm ex}-E_{\rm st})^{-1}. \tag{7}$$

If the invariance of the step velocity is taken into account, the postulated mechanism can be used to account for the experimentally observed[4] linear field dependence of the PDB velocity (1).

The following equation for the field dependence of the switching current can be written on the basis of the approach described here:

$$j(E)=2P_saN(E)v_{\rm st}=2P_sab\cdot dn/dt(E), \tag{8}$$

where a is the step thickness, which is approximately equal to the width of the domain boundary (in GMO, seven times the lattice constant[16]), and N is the number of steps at the boundary.

During motion of the PDB in a homogeneous field, steps are generated near the edges of the sample, move in opposite directions toward each other, and are annihilated in the middle (Fig. 5b). In the presence of field inhomogeneities near the edge of the sample, the step generation rate and, accordingly, the number of steps on the boundary change.

4. DISCUSSION OF RESULTS

In a linearly increasing field, the step velocity depends on the time. The initial velocity is constant, being governed only by the threshold field (as in a constant field), and the velocity increases during motion as a result of the increase in the external field, so that the final velocity is determined by the step lifetime (from the instant of generation until annihilation or arrival at the opposite edge of the sample).

Our experimental results can be explained if we assume that two different mechanisms underlie the influence of the pinning centers (field inhomogeneities) on the motion of the PDB.

In a weak field (second current interval), as the PDB passes through a ''defect'' (reduced-field zone), the current decreases and then increases to a value corresponding to the uniformly accelerated motion (3) but never exceeding it. As a result, the number of steps decreases, because the step generation rate is cut in half and annihilation continues at the same rate (Fig. 5b, II).

A typical negative Barkhausen jump is shown in Fig. 5a. In the approach used here, the current minimum corresponds to the instant at which the annihilation of steps ceases (Fig. 5b, III). In the subsequent motion of the PDB the steps move in the direction of the ''defect'' and bypass it (Fig. 5b, V). The observed difference in the current decay and rise times is readily attributed to acceleration of the steps as a result of the increase in their lifetime without annihilation. The average step velocity can be determined by analyzing the form of the jump: $v_{st} \approx 300$ m/s.

Positive Barkhausen jumps emerge in a strong field (in the third interval with $E > 3.15$ kV/cm) (Fig. 6a); they can be attributed to a change in the shape of the PDB. It is obvious that the increase in the number of steps as the field increases has the effect of increasing the deviation of the moving PDB from the coherent direction. A wedge-shaped domain forms in the region of the PDB where the deviation attains a critical value.[17,18] New steps are not generated when the wedge appears, but the velocity of some of the steps increases considerably, and the current increases. The kinetics of the process is shown schematically in Fig. 6b. We should note that we have previously[18] observed in GMO a loss of stability of the PDB and the formation of wedge domains under the influence of a spatially inhomogeneous field.

In summary, by investigating the motion of a solitary PDB in GMO in samples with artificially created pinning centers (field inhomogeneities) we have been able to determine the relationship of the form of the Barkhausen jumps to distinctive characteristics of the nucleation process. We have proposed two scenarios of evolution of the PDB, corresponding to different intervals of the external fields. The specific mechanism of the motion of a PDB due to the formation of steps on the domain boundary and their longitudinal displacement has provided a means for explaining the observed results. We have determined the velocity of the steps from an analysis of the form of the current jumps. Not only can the proposed approach be used to investigate the details of domain boundary dynamics in GMO, but it affords the possibility of investigating the distinctive features of the jump kinetics of domains and phase boundaries from an analysis of the form of the Barkhausen jumps in other ferroelectrics.

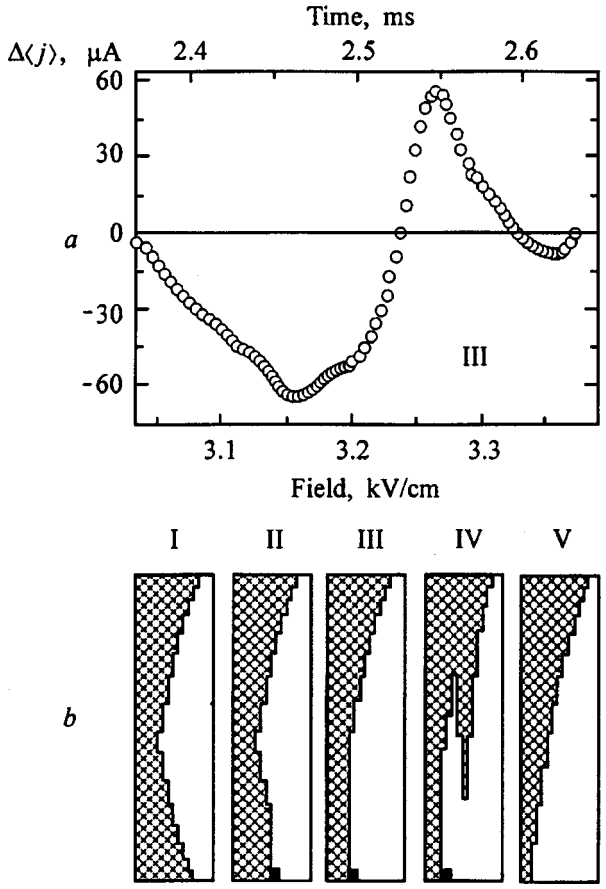

FIG. 6. Positive Barkhausen jump (a) and the corresponding diagram showing the evolution of the shape of the PDB (b).

This work has received partial support from the Russian Fund for Fundamental Research (Grant No. 96-02-19588).

*)E-mail: Vladimir.Shur@usu.ru

[1] A. G. Chynoweth, J. Appl. Phys. **30**, 280 (1959).
[2] M. E. Lines and A. M. Glass, *Principles and Applications of Ferroelectrics and Related Materials* (Clarendon Press, Oxford, 1977; Mir, Moscow, 1981, 736 pp.).
[3] V. M. Rudyak, *Switching Processes in Nonlinear Crystals* [in Russian] (Nauka, Moscow, 1986), 243 pp.
[4] A. Kamada, Phys. Rev. A **30**, 186 (1969).
[5] H. J. Borchardt and P. E. Bierstedt, J. Appl. Phys. **38**, 2057 (1967).
[6] A. N. Alekseev, M. V. Zlokazov, A. L. Proklov, N. A. Tikhomirova, and L. A. Shuvalov, Izv. Ross. Akad. Nauk, Ser. Fiz. **48**, 1123 (1984).
[7] N. N. Bol'shakova, N. S. Komlyakova, G. M. Nekrasova, T. M. Polkhovskaya, and V. M. Rudyak, Izv. Ross. Akad. Nauk, Ser. Fiz. **45**, 1666 (1981).
[8] V. Ya. Shur, A. L. Gruverman, V. P. Kuminov, and N. A. Tonkachyova, Ferroelectrics **111**, 197 (1990).
[9] E. Fatuzzo and W. J. Merz, *Ferroelectricity* (North-Holland, Amsterdam, 1967), p. 241.
[10] M. J. Hayashi, J. Phys. Soc. Jpn. **33**, 616 (1972).
[11] V. Ya. Shur, A. L. Gruverman, and E. L. Rumyanstev, Ferroelectrics **111**, 123 (1990).
[12] V. Ya. Shur, in *Ferroelectric Thin Films: Synthesis and Basic Properties*, Vol. 10, edited by S. A. Paz de Araujo, J. F. Scott, and G. W. Taylor (Gordon and Breach, New York, 1996), Chap. 6, p. 153.
[13] V. Ya. Shur and E. L. Rumyantsev, Ferroelectrics **191**, 319 (1997).
[14] M. E. Drougard and R. Landauer, J. Appl. Phys. **30**, 1663 (1959).

[15] V. Ya. Shur, E. L. Rumyantsev, V. L. Kozhevnikov, E. V. Nikolaeva, and E. I. Shishkin, Appl. Phys. (in press).
[16] E. K. H. Salje, A. Buckley, G. van Tendeloo, and Y. Ishibashi, Am. Mineral. (1998) (in press).
[17] A. L. Roĭtburd, JETP Lett. **47**, 171 (1988).
[18] V. Ya. Shur, V. V. Letuchev, E. L. Rumyantsev, and T. B. Charikova, Fiz. Tverd. Tela (Leningrad) **28**, 2829 (1986) [Sov. Phys. Solid State **28**, 1583 (1986)].

Translated by James S. Wood

Evolution of the fractal surface of amorphous lead zirconate-titanate films during crystallization

V. Ya. Shur,*) S. A. Negashev, A. L. Subbotin, D. V. Pelegov, E. A. Borisova, and E. B. Blankova

Institute of Physics and Applied Mathematics, Ural State University, 620083 Ekaterinburg, Russia

S. Trolier-McKinstry

Intercollege Material Research Laboratory, Pennsylvania State University, University Park, PA 16802, USA
(Submitted June 22, 1998)
Fiz. Tverd. Tela (St. Petersburg) **41**, 306–309 (February 1999)

The recrystallization kinetics of amorphous lead zirconate-titanate films prepared by sol-gel technology are investigated experimentally using elastic scattering of light. Sequences of elastic dependences of the scattered light intensity are recorded directly during thermal annealing. The evolution of the morphology of the film surface during annealing is described in terms of the variation of their fractal dimensionalities D_s. The experimental dependences $D_s(t)$ are compared with the results of a computer simulation of the phase transition kinetics in a thin plate (film). © *1999 American Institute of Physics.* [S1063-7834(99)02302-3]

The preparation of ferroelectric thin films of lead zirconate titanate (PZT) is of considerable interest for practical applications, most importantly the production of energy-independent ferroelectric memory. The most popular of the several technologies used in the preparation of PZT films is the sol-gel method. A film with the required phase composition is formed in two stages: An amorphous film of the necessary chemical composition is first obtained by pyrolysis, and then the required crystal structure is created by high-temperature annealing. It has been established that the ferroelectric parameters and structure of the films are dictated by the annealing conditions.[1–3]

The annealing process is complicated by the ability of PZT to form different crystal phases. The amorphous films crystallize at temperatures of 400–500 °C with the formation of a pyrochlore phase. At higher temperatures (600–700 °C) a ferroelectric perovskite phase is formed. It has been shown that textured films have the maximum spontaneous polarization and the minimum coercive field.[4] The texture of the films is uniquely determined by the crystallization kinetics (nucleation and growth of crystallites), which, in turn, depends on the type of substrate, the temperature, and the heating rate. It has been established that films having the highest degree of structural perfection can be obtained by rapid thermal annealing with a high heating rate ($dT/dt > 100$ °C/s).[5]

The investigation of the crystallization kinetics (especially in rapid annealing) with sufficient time resolution poses a complex experimental problem. The method of recording the instantaneous angular dependence of the light scattering intensity[6,7] has high time resolution (to 10 ms), offering possibilities for *in situ* studies of the crystallization processes within times of the order of seconds.

1. EXPERIMENTAL PROCEDURE

We have investigated the crystallization kinetics of thin sol-gel films of lead zirconate titanate $Pb(Zr_{0.5}Ti_{0.5})O_3$ (PZT) with zero lead excess.[8,9] X-ray-amorphous PZT films of thickness $0.4-0.6\,\mu$m were prepared on $Pt/Ti/SiO_2/Si$ substrates (the epitaxial platinum layer having a thickness of approximately $0.2\,\mu$m) at pyrolysis temperatures of 230–420 °C.

The annealing kinetics depended strongly on the pyrolysis temperature and the specific characteristics of the technological regime; the plate was therefore separated into several sections, which were then annealed under different conditions. Both conventional annealing at a slow heating rate ($dT/dt \leqslant 1.5$ °C/s) and rapid annealing at a heating rate up to 200 °C/s were used in the study. Sequences of instantaneous angular dependences of the scattering intensity of light reflected from the surface of the film were recorded during the annealing process.

X-ray diffraction data were obtained on partially crystallized films in the $\Theta-2\Theta$ regime with Co Kα radiation in the interval of angles 20–65° at room temperature. The intensity of the ''texture maximum'' [the (111) maximum corresponding to the type of texture formed] was measured as a function of the annealing temperature and time.

The optical system used in recording the angular dependences of the elastic scattering of light in the annealing of amorphous films is shown in Fig. 1. The beam from a helium-neon laser *1* ($\lambda = 0.63\,\mu$m) having a power of approximately 1 mW, with controlled orientation of the light polarization, served as a probe for measurements in reflected light, so that the films could be investigated on any substrate with any type of lower electrode. The diameter of the light spot on the surface of the sample in the annealing furnace *2* was approximately 1 mm. The scattered light was incident on the spinning disk of an angular modulator *3* and was focused by a lens onto the photodetector *4*. The frequency of recording of the instantaneous angular dependences of the scattered light intensity was governed by the frequency of rotation of the modulator disk. The duration of one measurement cycle

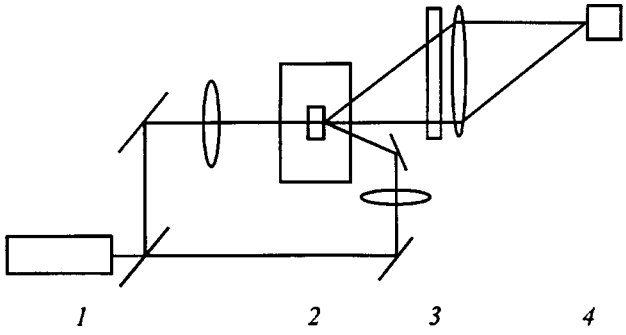

FIG. 1. Optical system for *in situ* recording of the instantaneous angular dependences of the light scattering intensity in crystallization: (*1*) laser; (*2*) furnace containing the sample; (*3*) angular modulator; (*4*) photodetector.

in the angular range 0.5–30° with an angular resolution to 10′ did not exceed 30 ms.

The difference in the refractive indices of the perovskite and pyrochlore phases could be exploited to monitor the spatial distribution of the phases in the partially annealed samples under an optical microscope.[10] Comparisons of the results of scattered-light measurements with images of the film surface obtained by optical and electron microscopy showed that: 1) the scattering of light by the interface between the lower electrode and the film and in the bulk of the film is negligible; 2) the measured angular dependences are sensitive only to changes in the surface morphology in crystallization;[7] 3) the details of the surface relief exhibit a distribution of scales over a wide range, so that fractal formalism can be used in processing experimental data on the angular dependence of scattering.[11]

2. EXPERIMENTAL RESULTS

We have investigated the pyrochlore-perovskite transition kinetics during annealing. The angular dependences of the light scattering intensity in rapid thermal annealing (Fig. 2a) and in annealing at a constant heating rate (Fig. 2b) exhibit a behavior typical of fractal objects (a straight-line segment is observed in log-log scale).[12,13] The dependence of the light intensity scattered by a fractal surface on the scattering vector is known to be described by the relation[10]

$$I(q) \sim q^{-m}, \tag{1}$$

where $q = 4\pi/\lambda \sin(\phi/2)$ is the scattering vector, λ is the light wavelength, and ϕ is the scattering angle. In scattering by ''bulk'' fractals the slope m is equal to the fractal dimensionality D, and in scattering by a fractal surface $m = 6 - D_s$, where D_s is the fractal dimensionality of the surface.[13,14]

Figure 3 shows the temperature (time) dependences, measured in annealing at a constant heating rate, of: 1) the intensity of the texture maximum $S(T)$; 2) the total scattered light intensity $I(T)$; 3) the slope $m(T)$. It is evident from a comparison of the dependences $S(T)$ and $I(T)$ that the increase in the total scattered light intensity at a temperature above 600 °C correlates with the increase in the volume of the perovskite phase, i.e., the surface relief changes significantly in transition from the pyrochlore to the perovskite phase.

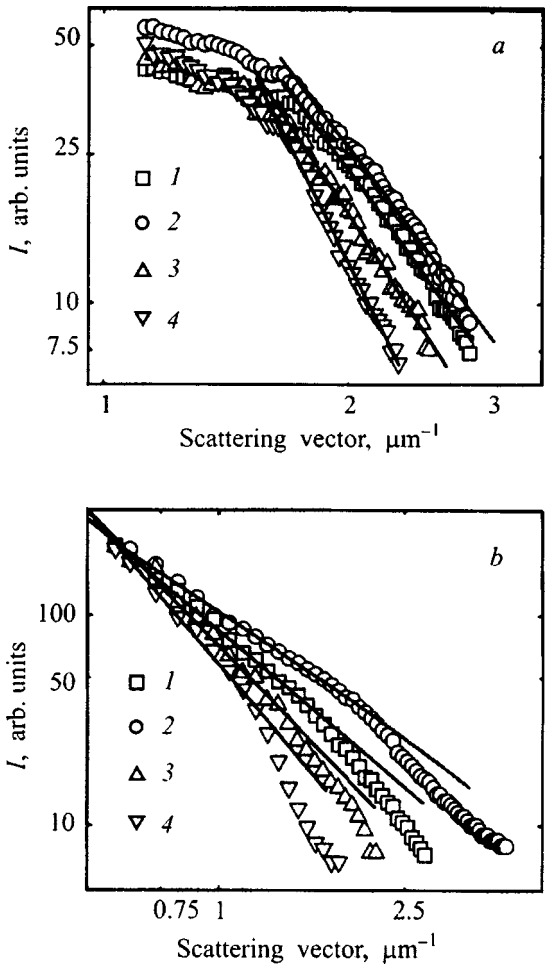

FIG. 2. Variation of the angular dependence of the scattered light intensity: (a) in annealing at a constant heating rate ($dT/dt = 0.4$ °C/s), final anneal temperature: (*1*) 642 °C; (*2*) 663 °C; (*3*) 731 °C; (*4*) 742 °C; (b) in rapid thermal annealing ($dT/dt = 100$ °C/s), $T = 500$ °C, anneal time: (*1*) 90 s; (*2*) 60 s; (*3*) 55 s; (*4*) 30 s. The experimental points are approximated by the functional relation (1).

In analyzing the form of the dependence $I(t)$, we have assumed that scattering by three types of surfaces is observed, with different scattering coefficients: 1) minimum scattering from the smooth surface of the pyrochlore phase ($K_0 \approx 0$); 2) maximum scattering from the side faces of the crystallites ($K_1 \approx 1$); 3) scattering from the surfaces of recrystallized regions of the perovskite phase ($0 < K < 1$). Then

$$I(t) \sim \Delta t \, dS(t)/dt + KS(t), \tag{2}$$

where Δt is a constant.

The dependence $S(t)$ can be approximated by the Kolmogorov–Avrami equation[15,16] for the kinetics of the increase in volume of the perovskite phase in phase transition at a constant heating rate[17]:

$$S(t) \sim 1 - \exp\left[-\left(\frac{t - \Delta t}{t_0} \right)^4 \right]. \tag{3}$$

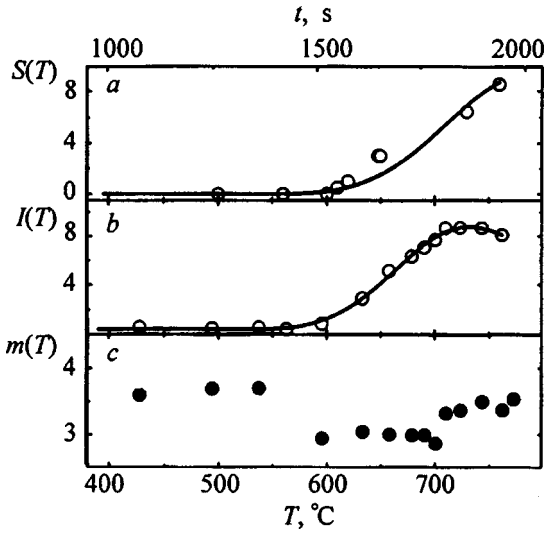

FIG. 3. Temperature dependences of: (a) the intensity of the texture maximum $S(T)$; (b) the total light scattering intensity $I(T)$; (c) the slope $m(T)$. The experimental points are approximated by relations (2) and (3).

The approximation of $I(t)$ by Eq. (2) (Fig. 3b) shows that the formation kinetics of the perovskite phase at a constant heating rate conforms to the β model,[15] i.e., the growth of nuclei formed in pyrolysis. Relation (3), with the same value of t_0, has been used to approximate $S(t)$ (Fig. 3a). Our analysis has enabled us to determine the threshold temperature of the onset of formation of the perovskite phase, $\Delta T = 530\,^{\circ}\mathrm{C}$.

As the temperature increases, the slope m also changes in transition to the perovskite phase (Fig. 3c). The increase of D_s in the temperature interval 540–600 °C corresponds to the transition from the ''smooth'' surface of the homogeneous pyrochlore phase to the fractal surface of a heterophase state. Smoothing of the film is observed only in the final stage of crystallization.

The time variation of the fractal dimensionality in rapid thermal annealing ($dT/dt = 100\,^{\circ}\mathrm{C/s}$, $T = 650\,^{\circ}\mathrm{C}$) is shown in Fig. 4. The results are approximated by a functional relation describing the decrease in the uncrystallized volume of the film in the α process:

$$D(t) = D_{\infty} + \Delta D \exp\left[-\left(\frac{t - \Delta t}{t_0} \right)^3 \right], \tag{4}$$

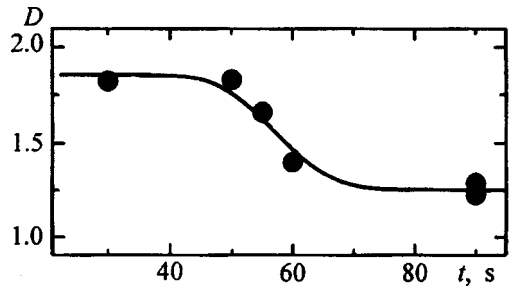

FIG. 4. Variation of the fractal dimensionality in rapid thermal annealing. The experimental points are approximated by relation (4).

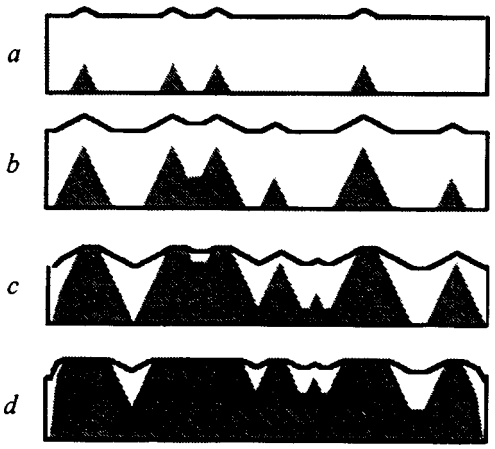

FIG. 5. Diagram used in computer simulation to represent successive phases in the variation of the surface relief of the film during crystallization.

where D_{∞} is the fractal dimensionality of the crystallized film.

It is important to note that the variation (decrease) of D takes place within a 10-s period (from 50 s to 60 s after the start of annealing). This behavior of the fractal dimensionality shows that crystallization is very rapid following a comparatively protracted stage of heating and precrystallization.

To analyze the behavior of the resulting experimental dependences of the fractal dimensionalities, we have performed a computer simulation of the crystallization kinetics in a bounded volume.

3. COMPUTER SIMULATION

The computer simulation is carried out for the phase transition in a three-dimensional volume with strong anisotropy of the dimensions $257 \times 257 \times (5-48)$ of the plate or film. The crystallization process is treated as the isotropic (in the plane) growth of new-phase crystallites nucleated at the lower face (i.e., at the film-substrate interface).[18] The isolated growing crystallites are modeled by cones, whose axes are perpendicular to the lower face. Crystallites that reach the top face (free surface) acquire the shape of truncated cones (Fig. 5).

Three models of new-phase formation are used to describe the phase transition kinetics[15]: 1) the α model with a constant nucleation rate; 2) the β model with the growth of nuclei formed at the initial time; 3) the $\beta + \alpha$ model, which combines the first two.

The Kolmogorov method[11] is used to determine D_s. The dimensionalities are averaged over a sequence of independent realizations.

The simulation results show that the variation of D_s described in the different models of phase formation differs, but an extremum associated with the growth of crystallites through the entire film is observed in every case. The position of the maximum of D_s as a function of the fraction of growing phase (Fig. 6a) depends on the film thickness (i.e., on the time to grow through the entire film).

The fractal dimensionality is known to be dependent on the method by which it is determined and cannot be used as

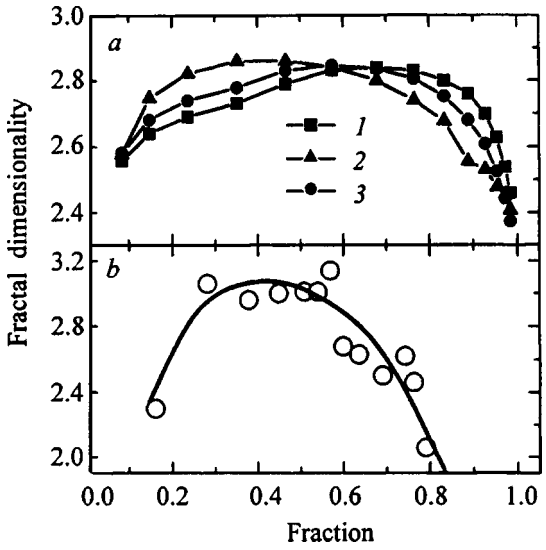

FIG. 6. Dependence of the fractal dimensionality on the fraction of crystallized phase: (a) results of computer simulation for various plate thicknesses (β process), d (arbitrary units): (*1*) 5; (*2*) 10; (*3*) 15; (b) comparison of experimental results on crystallization at a constant annealing rate ($dT/dt=0.49$ °C/s) with the simulation results (β process, $d=5$).

a unique characteristic of the process.[11] On the other hand, our investigations show that the form of the dependence of D_s on the fraction of crystallized volume p is totally unique. A comparison of the computer simulation results with the experimental scattering results not only exhibits qualitative agreement in the general behavior of $D_s(p)$ (Fig. 6b), but can also be used to estimate the full growth time. It should be mentioned that D_s has been renormalized for comparison with experiment.

We have thus used experiments involving measurements of the angular dependence of light scattering during crystallization and computer simulation to show that the instantaneous fractal dimensionality in finite systems changes significantly upon phase transition. The bounded range of self-similarity (scaling) in real systems makes it difficult to determine uniquely the dimensionality. As a result, the values obtained for D_s depend on the method used to process the experimental data. The computer simulation results suggest that the nature of the variation of the dimensionality and the positions of the extrema of $D_s(t)$ can serve as stable characteristics of the type of kinetic process involved. It should be noted that the method developed here for investigating the phase transition kinetics, combined with the proposed mathematical processing of the results of light scattering measurements, is easily implemented and universal.

This work has received partial support from Grant No. 96-02-19588 of the Russian Fund for Fundamental Research.

*)E-mail: Vladimir.Shur@usu.ru

[1] K. G. Brooks, I. M. Reaney, R. Klissurska, Y. Huang, L. Bursill, and N. Setter, J. Mater. Res. **9**, 2540 (1994).
[2] S. Trolier-McKinstry, J. Chen, K. Vedam, and R. E. Newnham, J. Am. Ceram. Soc. **78**, 1907 (1995).
[3] M. Huffman, F. D. Gealy, L. Kammerdiner, P. Zurcher, J. G. Zhu, M. Al-Jassim, and C. J. Echer, Ferroelectrics **134**, 303 (1992).
[4] M. Klee and P. K. Larsen, Ferroelectrics **133**, 91 (1992).
[5] C. V. R. Vasant Kumar, R. Pascual, and M. Sayer, J. Appl. Phys. **71**, 864 (1992).
[6] V. Ya. Shur, S. A. Negashev, E. L. Rumyantsev, A. L. Subbotin, and S. D. Makarov, Ferroelectrics **169**, 63 (1995).
[7] V. Ya. Shur, E. B. Blankova, S. A. Negashev, A. L. Subbotin, E. A. Borisova, D. V. Pelegov, and S. Trolier-McKinstry, in *Abstract Book of the Ninth International Meeting on Ferroelectricity* (Seoul, Korea, 1997), p. 249.
[8] V. Ya. Shur, S. A. Negashev, A. L. Subbotin, E. A. Borisova, and S. Trolier-McKinstry, Mater. Res. Soc. Symp. Proc. **433**, 351 (1996).
[9] V. Yu. Shur, S. A. Negashev, A. L. Subbotin, and E. A. Borisova, Ferroelectrics **196**, 183 (1997).
[10] I. P. Pronin, N. V. Zaĭtsev, E. Yu. Kaptelov, and V. P. Afans'ev, Izv. Ross. Akad. Nauk, Ser. Fiz. **61**, 379 (1997).
[11] J. C. Russ, *Fractal Surfaces* (New York, 1994), 309 pp.
[12] J. Feder, *Fractals* (Plenum Press, New York, 1988; Mir, Moscow, 1991), 254 pp.
[13] S. K. Sinha, Physica D **38**, 310 (1989).
[14] H. D. Bale and P. W. Schmidt, Phys. Rev. Lett. **53**, 596 (1984).
[15] A. N. Kolmogorov, Izv. Akad. Nauk SSSR Ser. Mat. **3**, 355 (1937).
[16] M. Avrami, Chem. Phys. **7**, 1103 (1939).
[17] V. Ya. Shur, E. L. Rumyantsev, S. D. Makarov, A. L. Subbotin, and V. V. Volegov, Integr. Ferroelectr. **10**, 223 (1995).
[18] E. M. Griswold, L. Weaver, D. S. McIntyre, M. Sayer, and I. D. Cadler, Integr. Ferroelectr. **10**, 123 (1995).

Translated by James S. Wood

LOW DIMENSIONAL SYSTEMS AND SURFACE PHYSICS

Size effects in the exciton energy and first-order phase transitions in CuCl nanocrystals in glass

P. M. Valov*) and V. I. Leĭman

St. Petersburg State Technological University of Plant Polymers, 198095 St. Petersburg, Russia
(Submitted March 3, 1998; resubmitted June 18, 1998)
Fiz. Tverd. Tela (St. Petersburg) **41**, 310–318 (February 1999)

The absorption spectra and the melting and crystallization kinetics of CuCl nanocrystals in glass are investigated in the range of particle radii 1–30 nm. Three discontinuities are found on the curves representing the size dependence of the melting point $T_m(R)$ and the crystallization point $T_c(R)$. As the particle radius gradually decreases from 30 nm in the range $R \leqslant 12.4$ nm there is a sudden 60° drop in the temperature T_c in connection with the radius of the critical CuCl nucleus in the melt. A 30° drop in T_m is observed at $R = 2.1$ nm, and a second drop of 16° in the temperature T_c is observed for CuCl particles of radius 1.8 nm. The last two drops are associated with changes in the equilibrium shape of the nanoparticles. In the range of smaller particles, $R \leqslant 1.34$ nm the $T_c(R)$ curve is observed to merge with the $T_m(R)$ curve, owing to the disappearance of the work of formation of the crystal surface during crystallization of the melt as a result of the zero surface tension of CuCl particles of radii commensurate with the thickness of the effective surface layer. An increase in the size shift of the exciton energy is observed in this same range of CuCl particle radii (1–1.8 nm). The size dependence of the melting and crystallization temperatures of the nanoparticles is attributed to variation of the free energy in the surface layer of a particle. © *1999 American Institute of Physics.* [S1063-7834(99)02402-8]

Research on the optical and physical properties of nanocrystals comprises the subject of a growing number of scientific publications, as shown by a recent survey.[1] Far less attention is given to the thermodynamics of small particles, owing to the complexity of conducting investigations in the vicinity of their melting point.[2,3] Theoretical and experimental solutions have been found for many problems in the thermodynamics of phase transitions.[4–6] Still today, however, certain fundamental questions regarding the properties of the ultradisperse phase are in the process of investigation and discussion.

One such question is the size of the critical crystal nucleus in the melt during crystallization, because experimental methods have yet to be developed for determining its radius.

A second question is more concerned with the properties of small particles and is related to the size dependence of surface tension. In the calculations of Gibbs,[4] Tolman,[7] and Rusanov[8] it is assumed that the surface tension of the phase tends to zero as its size decreases. In the opinion of many, the phase itself can vanish. According to a remark by Gibbs,[4] however, the surface tension of a particle can become equal to zero before the ''inhomogeneity of the phase'' vanishes. For small sizes, the shape of the particle can have an influence on the effective surface tension.[8] These phenomena should appear to some extent in a size dependence of the thermodynamic parameters of the ultradisperse phase (UDP), which influence the small-particle melting and crystallization temperatures.

Recent studies of size effects in semiconductor nanocrystals in glass[9–13] have disclosed a ''blue'' shift of the energy levels as the particle size decreases,[9] along with lowering of their melting and crystallization temperatures.[10–13]

In a previous paper[12] we have shown that when the energy has a certain value E_0 equal to the energy parameter in the Urbach relation[14] describing the long-wavelength decay of the exciton absorption band, the absorption coefficient of CuCl nanocrystals having radii of 10 nm and 2.6 nm is independent of the temperature in the range from 300 K up to the melting point of the crystal. Here E_0 is close to the $Z_{1,2}$-exciton energy measured at helium temperatures.[9] Proceeding from this result, we have postulated[12,13] that the energy E_0 determined at high temperatures represents the $Z_{1,2}$-exciton ground state, and the absorption at the energy E_0 can be regarded as a direct optical transition to this state without any involvement of the phonon subsystem. As a result of the quantum size effect[9] E_0 provides a means for investigating in detail the melting of nanocrystals and the crystallization of nanomelts by the probing of exciton states.

The present article is a continuation of our work[12,13] on ultradisperse CuCl crystals in the size range 1–30 nm. We investigate size effects in greater detail at particle radii of 1–2 nm, where two new discontinuities are discovered in the first-order phase transition parameters. We submit a possible interpretation of the observed sudden drops in the nanopar-

ticle melting and crystallization points. We calculate the size dependences of the small-particle melting and crystallization temperatures, based on the assumption of an exponential dependence on the reciprocal free-energy range in the surface layer of a particle and, accordingly, on the surface tension.

1. EXPERIMENTAL PROCEDURE

Glass samples in the form of plates with a continuous distribution of an average CuCl nanocrystal radius of 1 nm to 30 nm were prepared by annealing in a gradient furnace. Thick plates ($4\times14\times60$ mm) were heat-treated for three hours in the temperature range 500 °C to 720 °C in steps of approximately 2.5 °C/mm, and then a middle section of the plate was cut out with a thickness of 0.6 mm. Under these heat-treatment conditions there is a third, competing UDP growth stage[1,10,15]; according to recondensation theory,[15] the average radius R_a in the ensemble of UDP particles in this case depends on the time t and the annealing temperature T_a:

$$R_a^3=\frac{4}{9}\alpha t D_0 \exp\left(-\frac{U}{kT_a}\right), \tag{1}$$

where α is the UDP-glass coefficient of surface tension, D_0 and U are the diffusion parameter and the activation energy for new-phase formation, and k is the Boltzmann constant. The distribution of R_a along the sample was calculated from Eq. (1) with the parameters $\frac{4}{9}\alpha t D_0=1.5\times10^{19}$ nm^3 and $U=47\times10^{-20}$ J. These parameters have been determined from experimental data[10] for glasses having a similar composition. Control samples were prepared at selected temperatures for determining the nanocrystal size by small-angle x-ray scattering (SAXS) and measuring the parameters T_m and T_c. The results validated the choice of parameters for Eq. (1). The reliability of determining CuCl particle radii smaller than 2 nm by SAXS dropped sharply as a result of the increased contribution to x-ray scattering from inhomogeneities of the glass matrix. Consequently, the CuCl nanocrystal radii calculated from Eq. (1) in the range of R_a smaller than 2 nm must be regarded as approximate.

The optical absorption in each zone of the glass was measured by means of an energy-adjustable light probe of width 0.1 mm and height 2 mm (the sample height was 14 mm). It follows, therefore, that the average radius of the ensemble of nanocrystals was scanned with sufficient size resolution.

The absorption spectra and temperature dependence of the absorption at the energy E_0, i.e., the $K(E_0, T)$ curve, were measured on a computer-controlled spectral assembly. The optical probe energy E_0 for each zone of the sample (with the corresponding average CuCl nanocrystal radius) was determined from the ''nodal point'' [12] of intersection of several absorption spectra recorded at various temperatures.

The typical temperature dependence (in linear heating) of the $K(E_0, T)$ curve for a glass sample containing CuCl nanocrystals at $R_a=30$ nm (defect-free) is represented by curve *1* in Fig. 1a. The absorption actually remains invariant up to 350 °C and then decays on account of melting of the CuCl nanocrystals [10, 13].

As the UDP melt cools, the absorption begins to rise sharply below 300 °C as a result of crystallization of the UDP and the precipitation of CuCl crystals. The absorption does not return to its previous level, owing to the large number of ''frozen-in'' thermal defects at the instant of CuCl crystallization due to pronounced supercooling (by 80 K) of the UDP melt at that instant. The temperature dependence of the $K(E_0, T)$ curve of an unannealed glass sample containing ''defective'' CuCl nanocrystals (curve *2* inn Fig. 1a) shows a drop in the absorption at 315 °C as a result of these defects.

Curve *3* in Fig. 1a represents the first derivative $dK(E_0, T)/dT$, which reflects the rate of phase transition in melting or crystallization of the annealed sample. The peaks of curve *3* with maxima at 370 °C and 290 °C reflect the melting or crystallization of CuCl particles with an average radius of 30 nm.

The behavior of the $K(E_0, T)$ and $dK(E_0, T)/dT$ curves for CuCl nanocrystals of radius 1.8 nm (Fig. 1b) exhibit more than a 100-K decrease in the temperature interval between the melting and crystallization points. The crystallization peak of the $dK(E_0, T)/dT$ curve (curve *3*) is seen as a structure consisting of two peaks at 150 °C and 170 °C, indicating the greater degree of information when the phase transitions are represented by their rate curves $dK(E_0, T)dT$ as opposed to the $K(E_0, T)$ curves.

A holdup of the temperature in the vicinity of the melting (crystallization) point during heating of the sample causes the melting (crystallization) process to stop, i.e., the descent (ascent) of the $K(E_0, T)$ curve is observed to stop. Consequently, the behavior of the $K(E_0, T)$ and the width of the peaks of the phase transition rate $dK(E_0, T)/dT$ for large nanocrystal radii are governed more by the dispersion of the melting and crystallization temperatures in the ensemble of CuCl particles, whose size distribution has a certain width.[15] The maxima of the $dK(E_0, T)/dT$ curves correspond to the melting point T_m or the crystallization point T_c of particles at the maximum of the distribution with $R=R_a$.

2. EXPERIMENTAL RESULTS

Figure 2 shows curves of the phase transition rate $dK(E_0, T)/dT$ on the plane of the coordinates {temperature vs average radius} of the CuCl particles. The left scale indicates the corresponding anneal temperature T_a of the sample zone. As the CuCl particle radius R_a in the glass decreases (as the anneal temperature T_a is lowered), we observe a general shift toward lower temperatures and broadening of the phase transition peaks, along with a decrease in their intensity as the result of a decrease in the quantity of precipitated CuCl phase during heat treatment.

There is a noticeable 60° drop (I) in the position of the crystallization peak (T_c) in the vicinity of $R_a\approx13$ nm, along with anomalies in the size variations of the melting peak (T_m, drop II) and the crystallization peak (drop III) in the vicinities of $R_a\approx2$ nm and 1.8 nm, respectively.

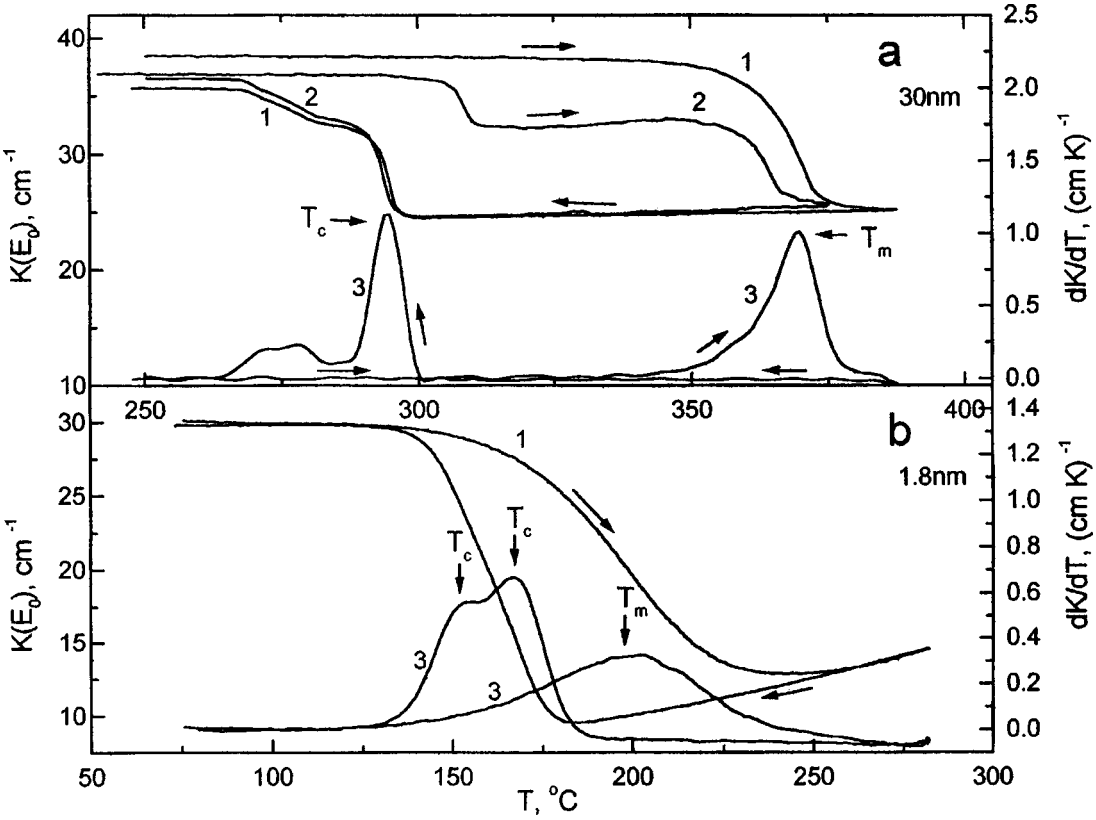

FIG. 1. Variation of the absorption of CuCl nanocrystals of radius 30 nm (a) and 1.8 nm (b) at the energy E_0 (graphs *1* and *2*) and their first derivatives (*3*) in the vicinity of the melting and crystallization temperatures: (*1*) sample annealed 0.5 h at 350 °C; (*2*) unannealed sample; photon energies: (a) $E_0 = 3.248$ eV; (b) $E_0 = 345$ eV.

Figure 3 shows in closer detail the size variations in the melting peak in the vicinity of the drop II and in the crystallization peak in the vicinity of the drop III. The graphs indicate how the melting (crystallization) peak shifts as the particle radius decreases. A redistribution of the peak takes place from a peak with one position of the maximum to a peak with a maximum situated 30 K lower (drop II) and to a peak with the maximum 16 K lower (drop III). The corresponding maxima of the phase transition peaks (temperatures T_m and T_c, respectively) before and after the drop are found by expanding the curves in Fig. 3 on the basis of the relation for the particle-size distribution.[15]

Figure 4 shows summary data on the size shift of the maximum of the melting and crystallization peaks, along with the size shift of the $Z_{1,2}$-exciton energy of CuCl nanocrystals in glass. It is evident from curves *1* and *2* in Fig. 4a that the same supercool $\Delta T = T_m - T_c$ of the UDP melt during its crystallization is observed in the interval where the nanocrystal radii decrease from 30 nm to 13 nm. This behavior is explained[13] by the invariance of the radius R_z of the critical nucleus of a CuCl crystal in the UDP melt. In the vicinity of 12–13 nm the crystallization temperature undergoes the 67-K drop I from $T_c = 557$ K to $T_c = 490$ K, implying an increase in the supercool of the UDP to $\Delta T = 140$ K during crystallization. The temperature T_m essentially remains constant in this case. The drop I of the crystallization temperature has been discussed in a previous paper,[13] where it was identified with transition of the UDP radius through the radius of the critical nucleus R_z ($R_z = 12.4$ nm for CuCl).

As the size of the CuCl nanocrystals decreases below 12.4 nm, the temperature T_m drops more and more rapidly (curve *1* in Fig. 4a), whereas T_c is essentially invariant (curve *3* in Fig. 4a). In the vicinity of nanocrystal radii equal to 2.1 nm and 1.8 nm curves *1* and *3* clearly exhibit the drops noted in Figs. 2 and 3 above: the drop II in the size dependence of T_m and the drop III in the size dependence of T_c.

Below the drop II T_m continues to decrease significantly (curve *1* in Fig. 4a), and below the drop III T_c begins to decrease abruptly (curve *4* in Fig. 4a).

The size dependence $T_c(R)$ then coincides with the dependence $T_m(R)$. The gradual disappearance of hysteresis from the melting and crystallization curves and, accordingly, the merging of the peaks of the melting (T_m) and crystallization (T_c) rates for CuCl particles with radii from 1.4 nm to 1.15 nm can be traced in Figs. 5a and 5b, respectively. We actually have $T_c = T_m$ along curve *2*. The approximate average radius of the ensemble of such CuCl particles from a calculation according to Eq. (1) is $R_\delta = 1.34$ nm.

Previously this coincidence of the melting and crystallization temperatures has been observed only for small metal particles.[2] We have performed the first-time direct measurements of the phase transition process and absorption spectrum for such small particles, for which, as predicted in Ref. 6, the size dependences of T_c and T_m merge.

Check tests have shown that the behavior of the $T_m(R)$ and $T_c(R)$ curves and the positions of the indicated drops in

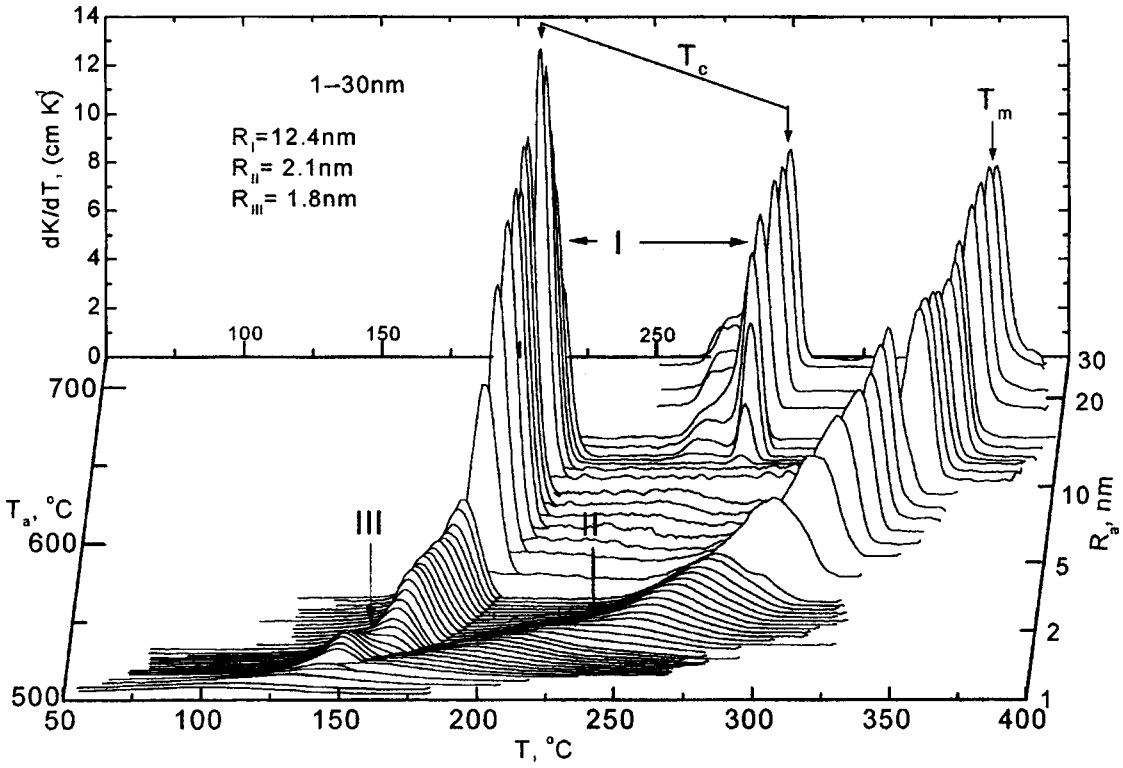

FIG. 2. Size variations in the curves representing the rate of first-order phase transitions in CuCl nanocrystals in glass as a function of the average radius R_a of the CuCl particles (and, accordingly, the annealing temperature T_a of part of the sample; T_m and T_c are the temperatures at which the maxima of the melting and crystallization peaks occur; the Roman numerals I, II, and III indicate the intervals of drops in the melting and crystallization parameters; R_a has been calculated from Fig. 1.

Figs. 2, 3, and 4a are not associated with any temperature variations of the diffusion characteristics of the components of the CuCl phase in glass or with the properties of the glass matrix, because after a tenfold increase or decrease of the anneal time of the control samples the $T_m(R)$ and $T_c(R)$ curves and the intervals of the drops shift more than 15° toward lower or higher anneal temperatures, respectively.

Figure 4b shows the size variations of the $Z_{1,2}$-exciton energy of CuCl nanocrystals over the entire range of sizes in the coordinates $\{E, \log(R)\}$. In the interval were R_a decreases from 30 nm to 3 nm the maximum E_m of the exciton-phonon absorption band and the ground state energy E_0 increase almost linearly as $\log(R)$ decreases. It is important to note the stark increase in the size shift of the exciton energy in the range of radii below 2 nm. In the final analysis, for the smallest observed average radius of the ensemble of CuCl particles (approximately $R=1.15$ nm) with T_m equal to T_c, E_m attains 3.54 eV, and we have the energy $E_0=3.40$ eV.

3. DISCUSSION

We now consider possible explanations of the size dependence of the melting and crystallization temperatures of the ultradisperse phase in glass containing CuCl nanocrystals. For the macrosystems we assume that the melting process takes place without an energy barrier when the specific free energies of the crystal $F_c(T)$ and the melt $F_m(T)$ are equal[16] at the point of intersection of their temperature curves. If we rely on Thomson's concept of melting in a thin surface layer, the energies $F_c(T)$ and $F_m(T)$ must be represented as the specific free energies in the surface layers of the macrocrystal and the macromelt, respectively.

The $F_c(T)$ and $F_m(T)$ curves for macrocrystals with a flat surface ($R=\infty$) intersect at the temperature T_0 (Fig. 6). As the particle size decreases, the free energy of the surface layers of the crystal and the melt vary on account of the curvature of the surface by the amount ΔF_c for the crystal and by the amount ΔF_m for the melt. As a consequence, the intersection point of the free energy $F_c(T, R)$ of the surface layer of a crystal of radius R and the corresponding energy $F_m(T, R)$ of the melt layer shifts, and the particle melting point T_m changes (Fig. 6). When the phase transition temperature is attained, for $F_c(T, R)=F_m(T, R)$, the surface of particles of a certain size melts, and a crystal beneath the melt layer is now smaller in size and can melt at a lower temperature. This process has the effect that all crystals of one size completely melt all at once by a kind of ''trigger'' mechanism.

The energy shift ΔF of the point of intersection of the $F_c(T, R)$ and $F_m(T, R)$ curves relative to the $F_c(T)$ and $F_m(T)$ curves (for a flat surface) is determined as the difference between ΔF_c and ΔF_m (Fig. 6):

$$\Delta F=\Delta F_c-\Delta F_m. \tag{2}$$

In the case of a macroparticle, on the other hand, for a temperature variation ΔT in the vicinity of T_0 the difference between the specific free energies ΔF in the crystal and liquid states is described by the well-known relation

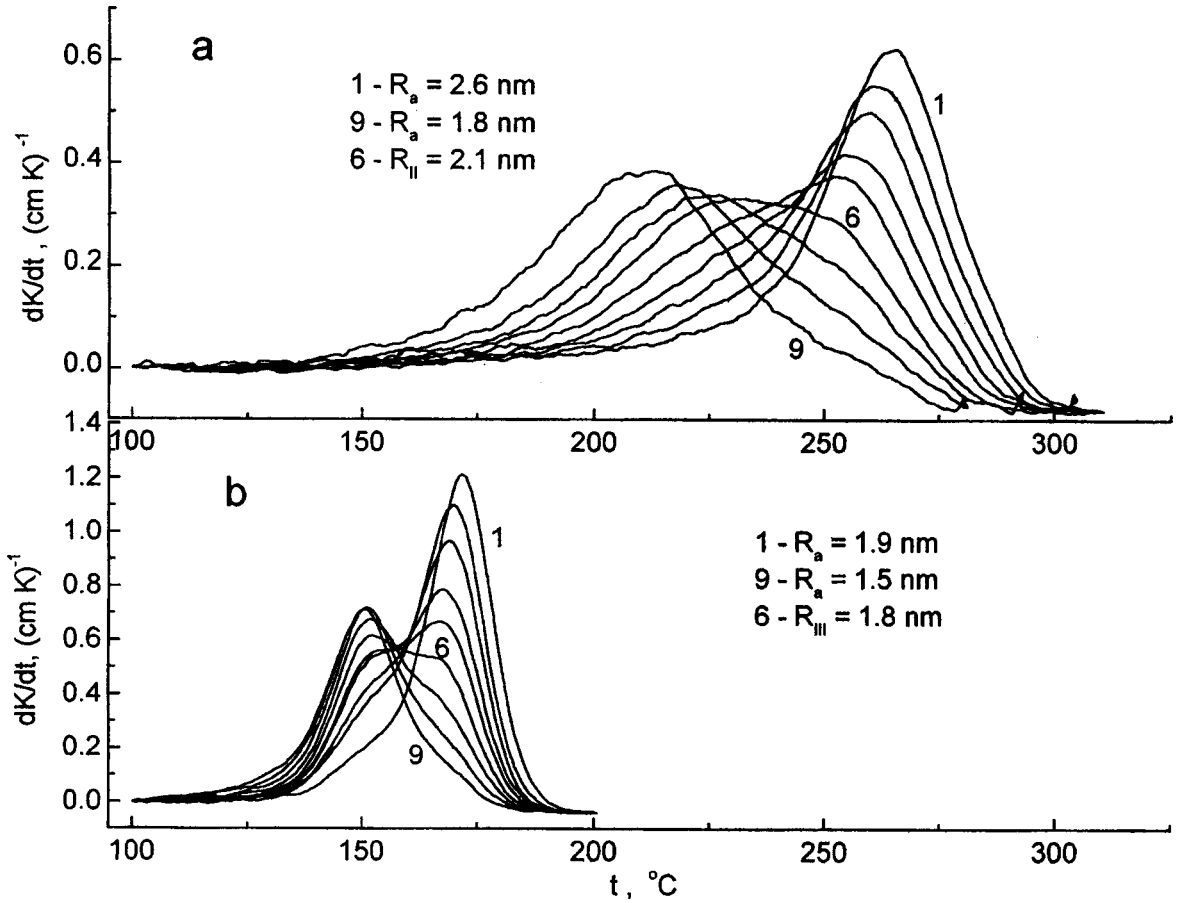

FIG. 3. Size variations in the curves representing the rate of first-order phase transitions in CuCl nanocrystals in the vicinity of the drops II (a) and III (b): (a) melting peaks for average nanocrystal radii of 1.9–2.6 nm; (b) crystallization peaks for average nanocrystal radii of 1.5–1.9 nm.

$$\Delta F=\rho\Delta L\frac{\Delta T}{T_0}, \tag{3}$$

where ρ is the density of the phase, ΔL is the latent specific heat of crystallization, and T_0 is the melting point for a crystal with a flat surface.

The increments ΔF_c and ΔF_m depend on the particle radius. The general behavior of the experimental $T_m(R)$ curve (curve *1* in Fig. 3a) can be described if the specific free energies of the surface layers of the crystalline particle $F_c(T, R)$ and its melt $F_m(T, R)$ are assumed to be exponential functions of $1/R$:

$$F_c=F_{c,\infty}\exp\left(-\frac{A}{R}\right),\quad F_m=F_{m,\infty}\exp\left(-\frac{B}{R}\right), \tag{4}$$

where $F_{c,\infty}$ and $F_{m,\infty}$ are the specific free energies of the surface layers of the macroparticle in the crystalline and molten phases, respectively, and A and B are parameters of the crystal and the melt.

We calculate the size variation of the melting point as $T_m=T_0-\Delta T$. Ultimately, making use of relations (2), (3), and (4), we obtain a relation for the size dependence of the melting point:

$$T_m=T_0\left(1-\frac{\Delta F_c-\Delta F_m}{\rho\Delta L}\right), \tag{5}$$

$$\Delta F_c=F_{c,\infty}-F_c,\quad \Delta F_m=F_{m,\infty}-F_m. \tag{6}$$

Satisfactory agreement with the experimental dependence (dots on curve *1* in Fig. 4a) is obtained when the function $T_m=f(R)$ is calculated from Eq. (5) (solid curve *1* in Fig. 4a) with the parameters $T_0=650$ K, $F_{c,\infty}=0.41\,J/m^3$, and $F_{m,\infty}=0.09$ J/m^3. The constants have the values $A=1$ nm and $B=3$ nm.

The experimental results begin to deviate from the calculated function $T_m=f(R)$ in the vicinity of CuCl particle radii around 2 nm, where the drop II is observed (curve *1* in Fig. 4a). This drop in T_m for $R=2.1$ nm can be attributed to the size dependence of the equilibrium shape (faceting) of the CuCl nanocrystal, so that F_c and, accordingly, ΔF_c change.

The experiments show that the size dependence of the $Z_{1,2}$-exciton energy parameters E_m and E_0 (curves *1* and *2* in Fig. 4b) does not exhibit any appreciable variations in this interval of radii. In the case of CuCl nanocrystals, therefore, the change in the shape of the crystal at $R_{II}=2.1$ nm takes place without any significant change in its crystal structure.

The interpretation is more complicated in regard to the experimental dependence of the crystallization temperature $T_c(R)$ (curves *2–4* in Fig. 3a). The observed constancy of the melt supercool $\Delta T=T_m-T_c$ in the crystallization of an ultradisperse phase having a radius greater than 13 nm (curve

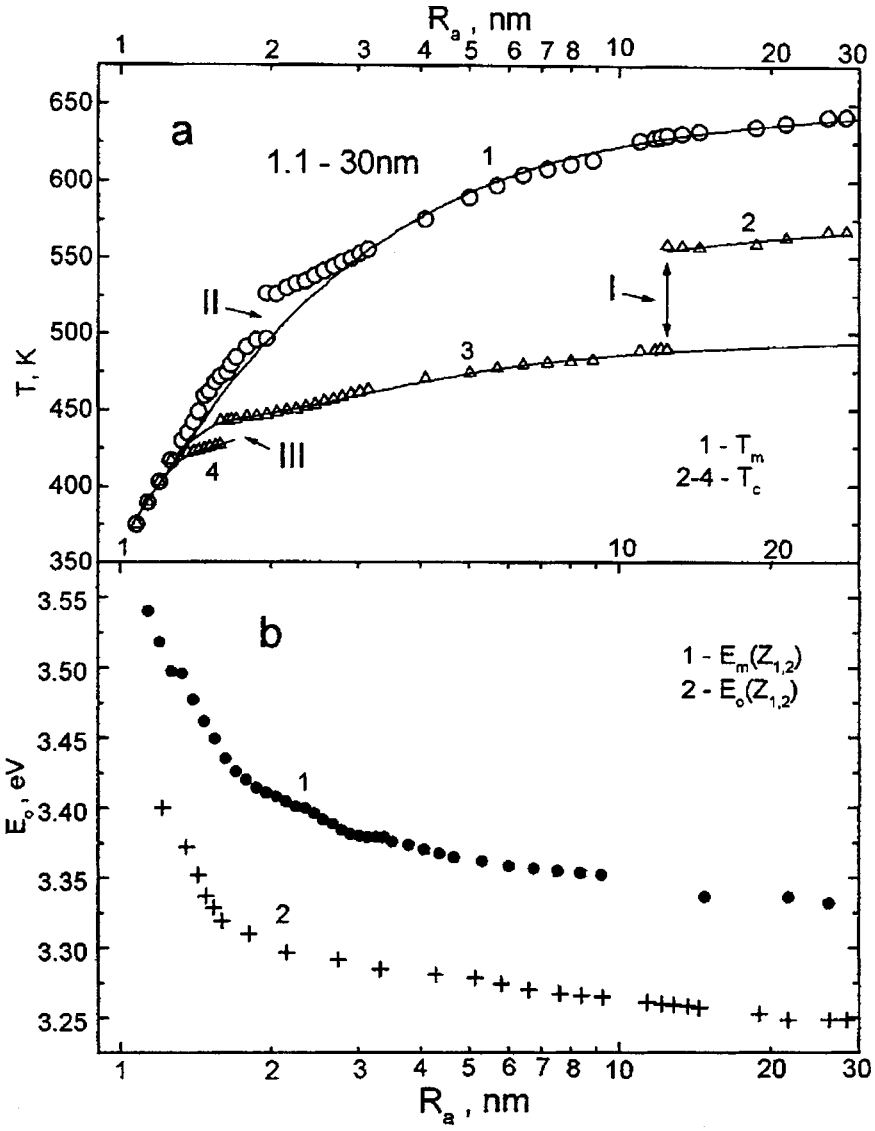

FIG. 4. Size dependences of: (a) the melting (*1*) and crystallization (*2–4*) temperatures; (b) the energies of the absorption maximum E_m (*1*) and the ground state E_0 of a $Z_{1,2}$-exciton in CuCl nanocrystals in glass. The points on curves *1–4* represent experimental data. The solid curves represent the calculated dependence of the melting point (curve *1*) according to Eq. (5)) and the crystallization point (curves *2–4*) according to Eq. (10); the Roman numerals I, II, and III indicate the intervals of size drops in the first-order phase transition parameters.

2) is explained[13] on the basis of crystallization theory[4–6] by the invariance of the size of the critical CuCl nucleus in the UDP melt.

The crystallization mechanism differs when the radius of the UDP is smaller than R_z. The CuCl crystal no longer nucleates in the melt, but immediately at the free surface. The size dependence of the temperature T_c for such particles can be described theoretically, if the expression for the crystallization energy is written in the form

$$\Delta W=(\sigma_c-\sigma_m)S-\Delta F_v. \tag{7}$$

The first term represents the work of formation of new surface of the crystal $\sigma_c S$ minus the vanishing surface energy of the melt $\sigma_m S$. The second term characterizes the gain in the free energy during crystallization and, as in Eq. (3), is governed by the supercool of the melt ΔT. Crystallization takes place when $\Delta W\approx 0$. Then, finding ΔF_v in terms of ΔT as in (3) and replacing T_0 by T_m (T_m is the temperature at which the free energies of the crystal and the melt are equal to $R<\infty$), we obtain an equation for the supercool of the melt in crystallization:

$$\Delta T=\frac{(\sigma_c-\sigma_m)S}{V\rho\Delta L}T_m. \tag{8}$$

Equation (8) can be used to describe the experimental dependence $T_c(R)$ for radii smaller than R_z, subject to certain assumptions. Above all, the volume V in the expression for ΔF_v and in Eq. (8) must be interpreted as the volume V_s of an effective surface layer of thickness δ_0 wherein the variations of the free energy cancel the work of formation of the crystal surface. We then have $V_s=S\delta_0$.

We also know that the surface tension[4,8] and, hence, the work of formation of the crystal surface decrease as the particle radius decreases. As first remarked by Gibbs[4] and demonstrated by our experiments, the work of formation of the new-phase surface can become equal to zero at some finite particle radius δ (the merging of curves *1* and *4* in Fig. 4a for $R=1.34$ nm). In accordance with the foregoing, the experiment is described by means of the following empirical relation for the size dependence of the particle surface tension, interpreted here as the work of formation of unit new-phase surface:

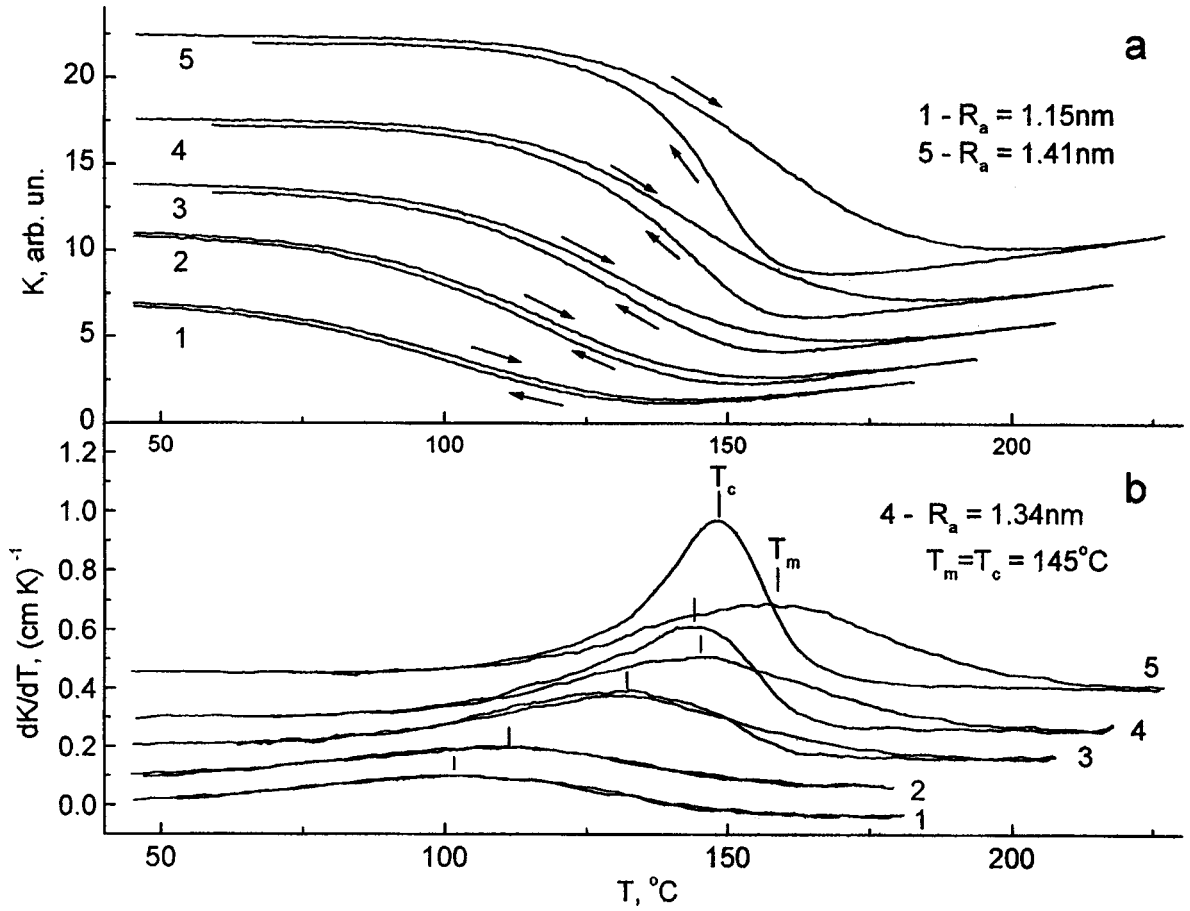

FIG. 5. Size variations in the melting-crystallization curves (a) and their first derivatives (b) for CuCl nanocrystals in the zero-supercool interval. The average nanocrystal radii are less than or equal to $R_\delta = 1.34$ nm.

$$\sigma = \sigma_\infty \exp\left(-\frac{A_1 \cdot \delta}{R-\delta}\right), \tag{9}$$

where σ_∞ is the surface tension on a flat surface, and A_1 is a constant. In the large-size approximation ($R \gg \delta$), when the expansion of the exponential function can be limited to the first two terms, Eq. (9) almost coincides with Tolman's equation.[7] Any possible variation of the particle is disregarded here, so that σ must be interpreted as an effective surface tension.

The quantities ρ and ΔL can exhibit a size dependence. However, lacking theoretical treatments of these parameters, we must resort to an empirical description of the function

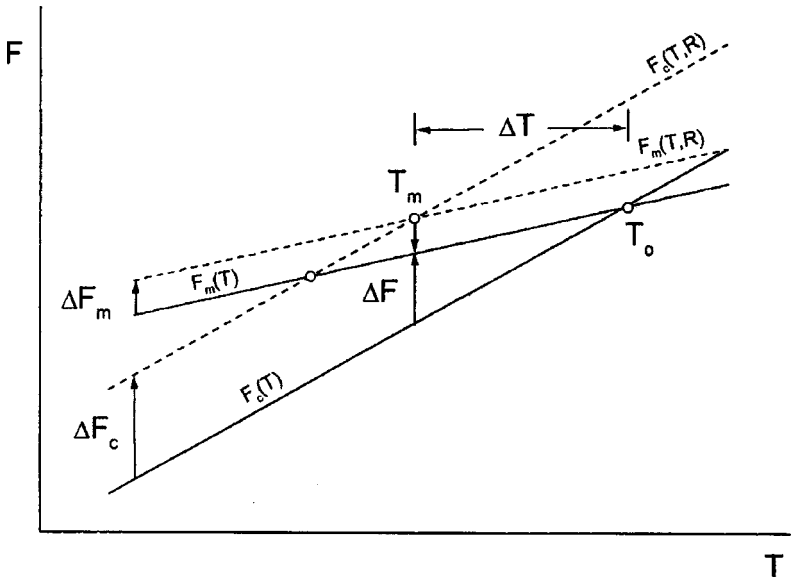

FIG. 6. Diagram showing the variation of the specific free energies in the surface layer of a crystal $F_c(T)$ and melt $F_m(T)$ with a flat surface and the same $F_c(T, R)$ and $F_m(T, R)$ for a curved surface in the vicinity of the crystal melting point; ΔF_c and ΔF_m are the size shifts of the surface layer energy of the crystal and melt, respectively, and ΔT is the shift of the melting point T_m of a particle of radius R relative to the melting point T_0 of a particle with $R = \infty$.

$T_c = f(R)$ based on reasonable approximations.

Expressing σ_c and σ_m in terms of Eq. (9) and using V_s as the volume of the surface layer, we obtain relations similar to (5) for $T_c = T_m - \Delta T$:

$$T_c = T_m\left(1 - \frac{\sigma_c - \sigma_m}{\delta_0 \rho \Delta L}\right), \tag{10}$$

$$\sigma_c = \sigma_{c,\infty} \exp\left(-\frac{A_1 \cdot \delta_c}{R - \delta_c}\right),$$

$$\sigma_m = \sigma_{m,\infty} \exp\left(-\frac{B_1 \cdot \delta_m}{R - \delta_m}\right). \tag{11}$$

The subscripts m and c refer to the melt and the crystal, respectively. In calculations using Eq. (10) T_m is calculated as the melting point of a crystal of radius R_a in accordance with Eq. (5).

The best agreement between the experimental determination (points on curve *3* in Fig. 4a) and the calculation of $T_c = f(R)$ according to Eq. (10) (solid curve *3* in Fig. 4a) is obtained for $\sigma_{c,\infty}/\delta_0 = 0.157\ \mathrm{J/m^2}$, $\sigma_{m,\infty}/\delta_0 = 0.07\ \mathrm{J/m^2}$, $\delta_m = 1.3$ nm, and $\delta_c = 1.2$ nm. The parameters A_1 and B_1 are equal to 0.97 and 1.45, respectively. The experimental $T_c(R)$ curve deviates from the calculated curve in the vicinity of the drop III for the particle radius $R_{\mathrm{III}} = 1.8$ nm and proceeds along curve *4*. This drop can be identified with the abrupt disappearance of surface tension of the nanomelt or with a change in the structure of its clusters. The behavior of the $T_c(R)$ curve below the drop III can be described by Eq. (10) if, for example, the crystal parameter δ_c decreases to 1.14 nm, the parameter A_1 is assumed to be equal to 0.8, and the surface tension of the melt $\sigma_m = 0$.

When the radii of the CuCl nanocrystals are smaller than $R_\delta = 1.34$ nm, the crystallization temperature $T_c(R)$ varies along the $T_m(R)$ curve, and supercooling of the melt therefore vanishes: $\Delta T = 0$. Gibbs has hypothesized that this effect is associated with vanishing of the work of formation of new-phase surface. The crystal structure of such particles is evinced by the distinct emergence of exciton absorption and the presence of melting and crystallization phase transitions (curves *2–5* in Fig. 5). An anomaly of these particles is the drastic increase in the size shift of the exciton energy states (curves *1* and *2* in Fig. 4b).

As mentioned, the shift of the exciton energy levels in nanocrystals is associated with the quantum-size effect.[9] In the range of particle radii smaller than 1.8 nm the exciton energy increases more rapidly with decreasing particle size than predicted by the quantum size effect. According to Ref. 17, this result could be attributed to a transition at the critical particle radius $a_c = 2a_{\mathrm{ex}}$ (a_{ex} is the exciton radius) from a bulk exciton at $R > a_c$ to an exciton in a potential well at $R < a_c$.

To summarize, we have found that the method of exciton-thermal analysis carried out in the probing of exciton states at the energy E_0 is an effective tool for the investigation of first-order phase transitions in CuCl nanocrystals in glass. From the melting and crystallization curves we have succeeded in carrying out a detailed investigation of the size dependence of the phase transition parameters. We have discovered a sudden drop in the supercooling temperature increment of the ultradisperse phase in crystallization, due to transition of the size of the UDP through the radius of the critical nucleus (12.4 nm for CuCl), along with two drops that are probably associated with changes in the equilibrium shapes of ultrasmall particles in the crystalline and liquid states with radii of 2.1 nm and 1.8 nm. We have also shown that the surface tension of the crystal (melt) becomes equal to zero for CuCl particles of radius $R \leqslant 1.34$ nm, whereupon the melting and crystallization curves are observed to coincide.

We have corroborated Gibbs's remark as to the possible existence of a physical heterogeneity (UDP) with zero work of formation.[4] We have seen that this condition refers to special type of crystals, whose chief property is zero surface tension. However, these particles have aggregate states and are inherently endowed with a stronger size dependence of the exciton energy states.

We are grateful to V. V. Golubkov for conducting the SAXS measurements of R_a for the control samples.

This work has received support from the Russian Fund for Fundamental Research (Grant No. 96-02-16966).

*)E-mail: pmv@upp.cit.spb.su

[1] C. V. Gaponenko, Fiz. Tekh. Poluprovodn. **30**, 577 (1996) [Semiconductors **30**, 315 (1996)].
[2] G. L. Zhdanov, Izv. Ross. Akad. Nauk, Ser. Fiz. **41**, 1004 (1977).
[3] V. V. Pogosov, Fiz. Tverd. Tela (St. Petersburg) **36**, 2521 (1994) [Phys. Solid State **36**, 1371 (1994)].
[4] *The Collected Works of J. Willard Gibbs* (Longmans, Green and Co., London-New York-Toronto, 1928; Goskhimizdat, Moscow, 1950), 438 pp.
[5] M. Vollmer, *Kinetik der Phasenbildung* (Steinkopff, Dresden, 1939; Nauka, Moscow, 1986), 300 pp.
[6] V. P. Skripov and V. P. Kaverda, *Spontaneous Crystallization of Supercooled Melts* [in Russian] (Nauka, Moscow, 1984), 230 pp.
[7] R. C. Tolman, J. Chem. Phys. **17**, 333 (1949).
[8] A. I. Rusanov, *Phase Equilibria and Surface Phenomena* [in Russian] (Khimiya, 1967), 388 pp.
[9] A. I. Ekimov, Phys. Scr. **T39**, 217 (1991).
[10] V. V. Golubkov, A. I. Ekimov, A. A. Onushchenko, and V. A. Tsekhomskiĭ, Fiz. Khim. Stekla **7**, 397 (1981).
[11] A. A. Onushchenko and G. T. Petrovskii, J. Non-Cryst. Solids **196**, 73 (1996).
[12] P. M. Valov, L. V. Gracheva, V. I. Leĭman, and T. A. Negovorova, Fiz. Tverd. Tela (St. Petersburg) **36**, 1743 (1994) [Phys. Solid State **36**, 954 (1994)].
[13] P. M. Valov, L. V. Gracheva, and V. I. Leĭman, Fiz. Khim. Stekla **23**, 187 (1997).
[14] M. V. Kurik, Phys. Status Solidi A **8**, 9 (1971).
[15] I. M. Lifshits and V. V. Slezov, Zh. Eksp. Teor. Fiz. **35**, 479 (1958) [Sov. Phys. JETP **8**, 331 (1958)].
[16] C. A. Croxton, *Introduction to Liquid State Physics* (Wiley, New York-London, 1975; Mir, Moscow, 1978), 400 pp.
[17] S. I. Pokutniĭ, Fiz. Tekh. Poluprovodn. **30**, 1952 (1996) [Semiconductors **30**, 1015 (1996)].

Translated by James S. Wood

Anomalous two-phonon absorption in diamond nanocrystals embedded in amorphous carbon

V. I. Ivanov-Omskiĭ, T. K. Zvonareva, and G. S. Frolova

A. F. Ioffe Physicotechnical Institute, Russian Academy of Sciences, 194021 St. Petersburg, Russia
(Submitted June 6, 1998)
Fiz. Tverd. Tela (St. Petersburg) **41**, 319–324 (February 1999)

Observation of anomalously strong IR absorption are reported in the region of two-phonon diamond frequencies in amorphous hydrogenated carbon films grown by cosputtering graphite and copper in a plasma. Up to five structural elements of bands having frequencies close to or coinciding with the figures quoted in the literature for two-phonon absorption bands in bulk diamond were observed. This suggests the presence of diamond nanocrystals in the grown layers. Observation of two-phonon absorption in thin films is in itself remarkable because of the smallness of its coefficient in bulk diamond. An estimate of the absorption coefficient in the dominant band at 2140 cm^{-1} yields about 200 cm^{-1}, which exceeds by more than an order of magnitude that for bulk diamond. This can be assigned to an anomalous enhancement of the two-phonon absorption coefficient due to phonon confinement in the small diamond particles nucleated in the amorphous carbon matrix. An estimate of these inclusions from the band width yields about 20 Å. The reasons for the catalytic activity of copper in diamond nucleation are analyzed. [S1063-7834(99)02502-2]

Symmetry considerations allow only two-phonon absorption in diamond-like crystals.[1] It would seem that the small intensity of this process must impose severe constraints on the analytical potential of two-phonon spectroscopy, specifically on the size of particles to be detected. It was found, however, that there exists a mechanism of anomalous enhancement of two-phonon absorption. We are reporting observation of two-phonon absorption by diamond nanocrystals, which is substantially stronger than could be expected from the known[1] bulk-diamond data. We believe this to be the first successful application of two-phonon spectroscopy for detection of nucleation of diamond nanocrystals in fairly thin amorphous-carbon films containing copper nanoclusters. This result is of a crucial significance, because the closeness of copper and diamond in lattice parameters complicates detection of nanosized diamonds in a medium enriched in copper nanocrystals. The same applies to other metals used as catalysts in diamond synthesis [for instance, Co (Ref. 2)]. We present experimental evidence that, in the case of small diamond particles incorporated in amorphous hydrogenated carbon, two-phonon absorption is capable of competing successfully with Raman spectroscopy used traditionally for diamond detection due to an anomalous enhancement of the two-phonon absorption coefficient, which is attributed to the phenomenon of phonon confinement.

1. EXPERIMENTAL TECHNIQUE

a-C:H:Cu films were prepared by dc planar-magnetron cosputtering of a graphite and a copper target in an argon-hydrogen plasma (80%Ar + 20%H). A planetary substrate-rotation system was provided to improve layer uniformity. The target was a plane ring-shaped graphite cathode with copper plates distributed uniformly over its surface. SIMS measurements showed the copper content to be proportional, to within 2%, to the copper/graphite surface-area ratio with a coefficient of proportionality of 1.5. The copper concentration could be controlled by properly varying this ratio. *a*-C:H:Cu layers with copper concentration ranging from 9 to 24 at.% were prepared. The layers were deposited on (100)Si substrates. The initial substrate temperature was about 200 °C. The sputtering was carried out in a flow of the working gas at pressures from 5 to 15 mTorr and at magnetron power varied within the 0.35–0.45-kW interval. Two main film growth regimes were used, namely, *G* (magnetron voltage 420–450 V, working mixture pressure 12–14 mTorr), in which the graphite-like component of *a*-C:H is primarily produced (trigonal carbon), and *D* (voltage 360–380 V, gas pressure 8–9 mTorr), which enriches the layer in the diamond-like component (tetrahedral carbon).[3] It was found possible to grow in such conditions *a*-C:H:Cu layers with thickness of 0.1 to 4.0 μm. The grown layers were annealed in vacuum for one hour at 220 °C.

The layers were characterized by IR absorption and Raman spectroscopy at the excitation wavelength of 4840 Å. Figure 1 shows a Raman scattering spectrum obtained for an *a*-C:H:Cu (9%) layer, which is essentially a typical spectrum of amorphous carbon without any signs of the presence of the diamond phase.[4] The optical absorption of *a*-C:H:Cu films was measured with a Specord 75IR double-beam IR spectrometer in the region of the carbon-hydrogen bond vibrational frequencies in *a*-C:H. Besides normal-incidence measurements (single-pass absorption), double-pass absorption at an incidence angle of 45° was studied in reflection geometry in order to improve the contrast. To prevent radiation losses, the sample was mounted on the mirror.

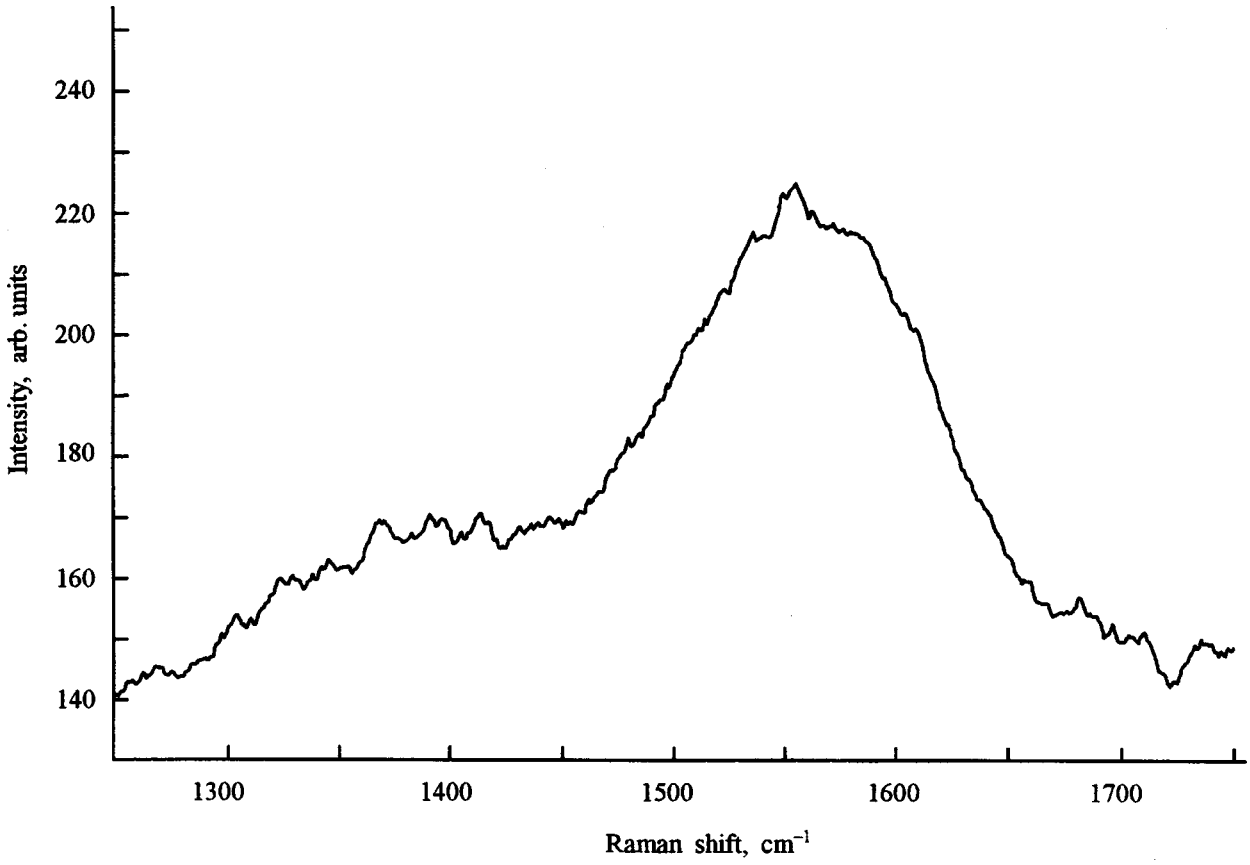

FIG. 1. Raman scattering spectrum of an *a*-C:H:Cu(9%) layer.

2. EXPERIMENTAL RESULTS

Figure 2 presents two fragments of *a*-C:H:Cu transmission spectra obtained in the frequency regions of interest here. The high-frequency fragment contains the strongest two-phonon diamond-absorption bands (1900–2300 cm^{-1}).[1] A direct comparison of spectrum *a* with spectra *b* and *c* shows that addition of copper activates the absorption of *a*-C:H films in this frequency region, which is particularly clearly seen in the *D* regime enriching the layer in tetrahedral (diamond-like) carbon phase. In the layer prepared by the *G* regime, absorption becomes evident practically only after an additional anneal. The low-frequency fragment of the spectrum in Fig. 2 includes the graphite Raman-scattering bands, whose activation in the optical spectra of *a*-C:H:Cu by finely dispersed copper was reported[5] earlier. Figure 3 displays parts of double-pass optical-transmission spectra in the region of two-phonon absorption of diamond, which were obtained for three layers grown in the *D* regime but differing in thickness or atomic concentration of copper. The bands contain features specified by arrows and labeled by Roman numerals. One can discriminate here up to five structural elements, whose frequencies are listed in Table I together with literature data for the two-phonon absorption bands in bulk diamond. One sees also that annealing at 220 °C, a temperature only slightly exceeding that of the substrate under sputtering, substantially increases the intensity of the copper-initiated absorption bands.

The coincidence of the two-phonon absorption frequen-

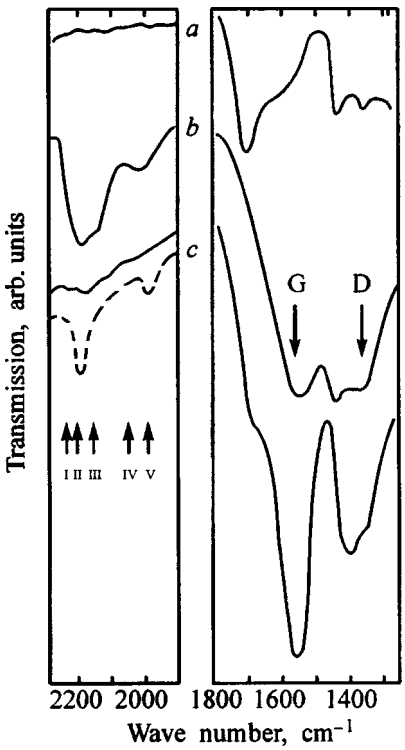

FIG. 2. Fragments of double-pass transmission spectra of the layers: (a) *a*-C:H, regime *D*; (b) *a*-C:H:Cu(9%), regime *D*; (c) *a*-C:H:Cu(9%), regime *G*. Solid lines: before, and dashed lines, after annealing. The Roman numerals identify spectral features (see Table I).

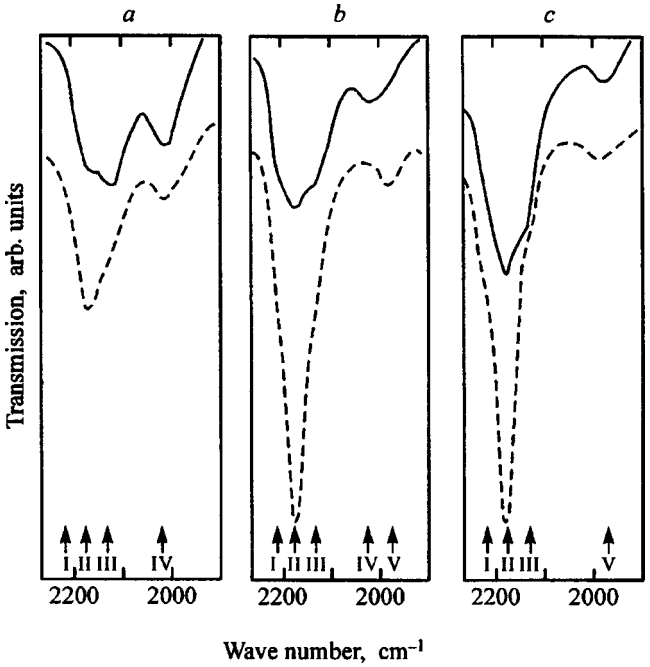

FIG. 3. Fragments of double-pass transmission spectra of *a*-C:H:Cu layers. (a) 9%Cu, ''thin''; (b) 9%Cu, ''thick''; (c) 14%Cu, ''thick.'' Solid lines: before, and dashed lines, after annealing. The Roman numerals identify spectral features (see Table I).

cies of bulk diamond with the frequencies of the bands observed in *a*-C:H:Cu layers suggests the presence in the latter of a diamond phase or at least of a phase in which the carbon atoms are coupled by the diamond σ bonds, i.e., of the tetrahedral-carbon phase. This suggestion might seem to be in conflict with the preceding analysis of the Raman spectra. This paradox, however, can be explained if one takes into account that (i) the coefficient of two-phonon absorption by the diamond phase incorporated in the amorphous-carbon matrix which contains finely dispersed copper is extremely high, and (ii) the resonance effect enhances many times the Raman scattering cross section by amorphous carbon compared to that for crystalline diamond.[6] This is why Raman scattering, whose spectrum is dominated by signals due to amorphous carbon, turns out in our case to be less sensitive to nanosized diamond inclusions than optical absorption.

The above optical measurements evidence nucleation of a diamond phase in amorphous carbon at 200 °C in the course of cosputtering of copper and graphite. We reported earlier on similar results obtained with films having the same parameters and prepared in the same reactor, but without copper cosputtering.[3] There is, however, an essential difference between the two cases, namely, in the presence of copper diamonds were observed to nucleate always, and without copper, only occasionally.

3. DISCUSSION OF RESULTS

3.1. Enhancement of two-phonon absorption

Considering the small coefficient of two-phonon absorption in bulk diamond, observation of this process in such thin films appears a remarkable phenomenon in itself. The dramatic difference between the two-phonon absorption coefficients in bulk diamond and the *a*-C:H:Cu films studied suggests that the absorption in the latter undergoes enhancement by some mechanism. Indeed, estimates of the absorption coefficient at the maximum of the 2140-cm^{-1} band yield about 200 cm^{-1}, whereas that at the strongest two-phonon band of bulk diamond does not exceed 14 cm^{-1}.[1] It should be noted that the above estimate is only a lower limit, because the size ratio of the diamond inclusions and of the amorphous carbon phases is unknown. One may consider as a possible reason for the observed enhancement spatial confinement of phonons in small crystalline diamond particles nucleated in the amorphous carbon matrix. As follows from earlier elec-

TABLE I. Characteristic features of the two-phonon absorption bands of copper-containing amorphous hydrogenated carbon films.

		Band No.				
		I	II	III	IV	V
		Frequency, cm^{-1}				
Layer composition and thickness, d, μ	Thermal annealing	2210	2177	2137	2024	1977
9%Cu, d=0.4	No	Break	Shoulder	Peak	Peak	–
Thin No.	Yes	Break	Peak	Break	Peak	–
9%Cu, d=1.9	No	Break	Peak	Shoulder	Peak	–
Thick	Yes	Break	Peak	Break	–	Peak
14%Cu, d=4.0	No	Break	Peak	Shoulder	–	Peak
Thick	Yes	Break	Peak	Shoulder	–	Peak
		Literature data[1,9]				
Frequency, cm^{-1}		2210	2177	2153	2024	1968
Features		Break	Break	Peak	Peak	Peak
Origin of band		$TO+TA$ (W)	?	$LO+LA$ (L)	$TO+TA$ (L)	L^*+TA (X)

*LO and LA branches at the zone X point.

tron microscopy studies, the average size of the diamonds forming in the amorphous carbon matrix in magnetron sputtering of graphite in a plasma with the same parameters and in the same reactor but without cosputtering of copper is about 3–4 nm.[3] Accepting the fluctuation mechanism of diamond nucleation in amorphous carbon proposed in Ref. 3, it can be expected that the characteristic size of the fluctuations depends only on the inherent properties of the diamond and of the medium, so that the average size of the nucleating diamond nanocrystals should not be affected substantially by the presence of copper. Because the presence of copper clusters makes reliable determination of the size of diamond nanocrystals by diffraction methods rather difficult, we shall attempt this from the width of the observed bands. As seen from Fig. 3, the bands overlap too strongly to permit evaluation of their individual width in almost all spectra. An exception is band II dominating the spectra of both thick samples after annealing, and its width can be used to estimate the diamond nanocluster dimensions if we note that it decreases with increasing copper concentration from $\delta\omega \approx 30$ to ≈ 23 cm^{-1}. We shall use the dispersion relation for LO phonons propagating in the diamond lattice along the Δ direction toward the zone-edge X point, which is available in an analytic form.[7] Disregarding the nature of the phonons in the combination responsible for band II, we shall assume for an order-of-magnitude estimate that the phonon dispersion is the same for all branches at the boundary of the Brillouin zone. Then Eq. 5 of Ref. 7 yields

$$\frac{d\omega}{dq} = \frac{4\mu \sin \pi q - \pi\alpha \sin \dfrac{\pi q}{2}}{M\omega_{LO}}, \tag{1}$$

where q is the dimensionless phonon momentum in units of $q_{\max}$ at zone edge, ω is the phonon frequency, μ and α are the main Born force constants for interaction with the first- and second-nearest neighbors, respectively, and M is the carbon atom mass. The dispersion relation (5) in Ref. 7 permits one also to obtain another expression for the zone edge ($q=1$):

$$\mu = \frac{M}{32}(2\omega_{LO}^2 - \omega_{Ra}^2), \tag{2}$$

where ω_{Ra} is the Raman frequency for diamond (1332 cm^{-1}), and ω_{LO} is the band frequency; combining this with the relation[7] $\alpha = 7.28\,\mu$, we can now estimate the dispersion ratio $\delta q/\delta\omega$ for LO phonons at zone edge, which in this case was found to be 2.14×10^{-3}. The dimensions δx of diamond nanocrystals can be evaluated from the uncertainty relation $\delta x\ \delta q = \delta x\ \delta\omega \cdot 4\times 10^{-3} \approx 1$, which immediately yields two estimates for nanocrystal dimensions based on the above line halfwidths $\delta\omega_1$ and $\delta\omega_2$, namely, $\delta x_1 \approx 18$ Å and $\delta x_2 \approx 23$ Å. The first estimate relates to the lower copper concentration, which suggests a trend to an increase of diamond nanocrystals in size with increasing copper concentration.

The nanocrystals are sufficiently small to make the contribution of surface phonon modes substantial, as well as to enhance local electromagnetic field effects. Besides, as follows from molecular dynamics calculations,[8] the increase of the contribution of quasi-free surface with decreasing particle size gives rise to an increase of phonon anharmonicity as a result of surface-atom relaxation, thus enhancing two-phonon absorption[1]. Any one of these factors or their combined action can be responsible for the anomalously strong two-phonon absorption observed by us.

3.2. Influence of thermal annealing and layer thickness

As seen from Table I, the characteristic features in the transmission spectra of *a*-C:H:Cu films are affected by their thickness and thermal annealing. Remarkably, an increase in layer thickness and additional annealing appear equivalent. Indeed, an increase in layer thickness entails a longer time the layer resides in conditions of radiation annealing by the sputtered atoms and ions. For this reason the thermal annealing and growth duration (layer thickness) are essentially equivalent factors, a conclusion borne out by Table I and Figs. 2 and 3. As follows, in particular, from Table I and Fig. 3, band IV decreases in intensity after an anneal in a thin sample (9%Cu) and disappears completely in a thick one (9%Cu), whereas in the 14%Cu sample band IV is seen neither before nor after the anneal. By contrast, band V is absent in the thin sample with 9%Cu to appear in the thick one only after the anneal, while the 14%Cu sample exhibits this band both before and after the anneal. The spectrum is dominated by band II, except for the thin sample before the anneal. One can therefore maintain that the intensity of band II increases under annealing together with increasing thickness and Cu concentration, and that this increase in thick samples after the anneal becomes so strong as to wash out the other features in the band wings. Note that, as evident from Table I, this band can be identified in the spectrum of bulk diamond only with the shoulder in the neighboring band, and that there is still no unambiguous interpretation of its nature.[9] The dominance of this band in the spectra of diamond nanocrystals incorporated in copper-enriched amorphous carbon, as contrasted by its weakness in bulk diamond, suggests its being associated with local phonon modes enhanced by the confinement effects. As for the nature of the two-phonon combination responsible for band II, it is apparently arranged so that its resultant dipole moment is normal to the nanodiamond surface. In this case the copper-modified dielectric properties of the medium[10] and, as a consequence, a local enhancement of electromagnetic field at the diamond nanocrystal interface could increase two-phonon absorption. Note that both an increase in copper concentration and thermal annealing, as well as the additional exposure of the layer to ion-beam treatment associated with the increase of its thickness, may favor this modification. Band V resembles in behavior to a certain extent band II, while being weaker in intensity. At the same time band IV behaves in an opposite manner.

Observation of the behavior of the Raman bands of copper-activated graphite and of the two-phonon absorption bands of diamond (Fig. 2) generated in differently grown layers reveals some aspects of how copper influences the structure of *a*-C:H:Cu layers. One can readily see that the so-called *G* band at 1575 cm^{-1}, which is dominant in the *G*

layer, compares in intensity with band *D* in the *D* layer. These trends evidence a decrease of graphite-like fragments in the *a*-C:H structure grown in regime *D* in size (Ref. 3) and support the previous suggestions that this regime enriches the layer in the nanophase of tetrahedral carbon, and the *G* regime, in the trigonal-carbon nanophase. Activation of the graphite Raman bands in optical absorption spectra of *a*-C:H:Cu layers is assigned to the graphite-like fragments being intercalated by atomically dispersed copper.[5,11] Obviously enough, the *G* band intensity should be proportional to the number of states accessible to intercalation and, hence, to the size of the graphite-like fragments of the structure. This conjecture correlates with the noticeable decrease in intensity of the *G* band in the layer grown in the *D* regime, where the fairly strong diamond two-phonon band is observed in an as-grown layer. By contrast, the relative increase of the *G* band intensity in the *G*-grown layer accords with the increasing size and number of graphite-like fragments, as can be judged from the relative *G* and *D* band intensities (Fig. 2). Note that the diamond bands become noticeable only after a thermal anneal.

3.3. Effect of copper nanoclusters

The optical measurements described above argue for nucleation at 200 °C of nanosized diamonds in the amorphous carbon matrix under magnetron cosputtering of graphite and copper. Diamond nucleation in amorphous carbon layers was observed to occur before.[12] We also reported a similar result obtained in a plasma with the same parameters and in the same reactor, but without copper cosputtering.[5] These two cases differ substantially in that, in the presence of copper, diamonds nucleate always while without it, only occasionally. In this connection it should be pointed out that cosputtering of copper and graphite brings about formation of copper nanoclusters in *a*-C:H:Cu.[11] Copper nanoclusters can apparently act as catalysts for diamond nucleation. Copper was known to behave in this way, but only at high temperatures.[13] It may be conjectured that it is the nanoscale size of the copper clusters that is responsible for the enhanced catalytic activity of copper, which manifests itself in a decrease of the diamond nucleation temperature. One cannot exclude, however, the possible effect of atomically dispersed copper intercalating the graphite-like fragments in *a*-C:H:Cu. This would affect the electronic structure of the graphite-like fragment,[14] and this could shift the equilibrium point in the graphite-diamond phase transition.

The authors owe their thanks to I. I. Novak for Raman measurements.

Support of the Russian Fund for Fundamental Research (Grant 97-02-18110) and, partially, of the Arizona University is gratefully acknowledged.

[1] F. A. Johnson, in *Progress in Semiconductors*, Vol. 9, edited by A. F. Gibson and R. E. Burgess, (Heywood Books, London, 1965), p. 179.
[2] W. Liu, D. A. Tucker, P. Yang, and J. T. Glass, J. Appl. Phys. **78**, 1291 (1995).
[3] V. I. Ivanov-Omskii, V. I. Siklitsky, A. A. Sitnikova, A. A. Suvorova, A. V. Tolmachev, T. K. Zvonariova, and S. G. Yastrebov, Philos. Mag. B **76**, 973 (1997).
[4] M. Yoshikawa, G. Katagiri, H. Ishida, A. Ishitani, M. Ono, and K. Matsumura, Appl. Phys. Lett. **55**, 2608 (1989).
[5] V. I. Ivanov-Omskiĭ and G. S. Frolova, Zh. Tekh. Fiz. **65**, No. 9, 186 (1995) [Tech. Phys. **40**, 966 (1995)].
[6] S. Matsumuma, Thin Solid Films **306**, 17 (1997).
[7] R. Tubino and J. L. Birman, Phys. Rev. B **15**, 5843 (1977).
[8] J. M. Dickey and A. Paskin, Phys. Rev. B **1**, 851 (1970).
[9] J. L. Warren, J. L. Yarnell, G. Dolling, and R. A. Cowley, Phys. Rev. **158**, 805 (1967).
[10] V. I. Ivanov-Omskii, A. V. Tolmachev, and S. G. Yastrebov, Philos. Mag. B **73**, 715 (1996).
[11] V. I. Ivanov-Omskii, in *Diamond-Based Composites and Related Materials*, NATO ASI Series 3, Vol. 38, edited by M. Prelas, A. Benedictus, L.-T. S. Lin, G. Popovici, and P. Gielisse (Kluwer, Dordrecht, 1997), p. 171.
[12] M. Kitabake and L. Wasa, J. Vac. Sci. Technol. A **6**, 1793 (1988).
[13] R. Roy, H. S. Dewan, and C. Langlade, Mater. Lett. **25**, 191 (1995).
[14] E. A. Smorgonskaya and V. I. Ivanov-Omskii, in *Diamond-Based Composites and Related Materials*, NATO ASI Series 3, Vol. 38, edited by M. Prelas, A. Benedictus, L.-T. S. Lin, G. Popovici, and P. Gielisse (Kluwer, Dordrecht, 1997), p. 203.

Translated by G. Skrebtsov

Manifestation of collective properties of spatially indirect excitons in GaAs/AlGaAs asymmetric double quantum wells

V. V. Krivolapchuk, E. S. Moskalenko, and A. L. Zhmodikov

A. F. Ioffe Physicotechnical Institute, Russian Academy of Sciences, 194021 St. Petersburg, Russia

T. S. Cheng and C. T. Foxon

Physics Department, Nottingham University, NG7-2RD, Great Britain
(Submitted July 1, 1998)
Fiz. Tverd. Tela (St. Petersburg) **41**, 325–329 (February 1999)

Low-temperature ($T=1.8$, 4.2 K) luminescence of GaAs/$Al_{0.3}Ga_{0.7}As$ double-coupled asymmetric quantum wells (DQW) is observed under variation of an electric field V_{dc} applied along the normal to the DQW plane. The FWHM of the indirect exciton (IX) emission line was found to undergo, within a certain interval of V_{dc}, a strong (up to a factor 3.5) narrowing, accompanied by anomalously large IX intensity fluctuations in time within the V_{dc} region where a strong decrease (or increase) of the FWHM is observed to occur. The dependence of the FWHM on the pumping level I_p also exhibits a substantial decrease of the FWHM within a certain I_p interval. The results obtained are discussed in the frame of an assumption which relates the observed phenomena to the onset of a condensed state in the interacting ensemble of spatially indirect excitons in DQWs. © *1999 American Institute of Physics.* [S1063-7834(99)02602-7]

The properties of double quantum wells (DQW) are attracting presently considerable interest by both theoreticians and experimenters.

A distinctive feature of DQWs is their spatially indirect excitons (IX), which consist of an electron (e) and a hole (h) localized in different quantum wells of a DQW. Because the e and h are spatially separated, the IX has a considerably longer lifetime (recombination time) than a direct exciton DX formed of an e and an h in the same well in a DQW. This it makes possible to obtain at low temperatures a thermalized IX gas of fairly high concentrations ($\sim 10^{10}$ cm^{-2}) even at comparatively low optical-pumping densities (~ 1 W cm^{-2}). As a consequence, one may expect formation of theoretically predicted[1–3] phases of collectively interacting excitons. A recent comprehensive analysis of the IX system in a DQW established the conditions of existence of a stable liquid IX phase and predicted the possibility of a transition of the IX system to a superfluid state.[4]

Recent experiments[5–8] demonstrate unusual properties of two-dimensional excitons, which can be qualitatively described within models including collective interaction effects. For instance, one observed a considerable narrowing of the IX radiative-recombination line of a GaAs/$Al_{0.3}Ga_{0.7}As$ coupled DQW under variation of an external electric field and temperature, which was assigned to the formation in the IX system of a new ordered condensed phase.[6] The existence of this phase is supported by observation of anomalously large fluctuations in the IX line intensity in a GaAs/AlGaAs DQW with time. These fluctuations, observed to occur only in a strong magnetic field applied perpendicular to the DQW plane, were interpreted within the model of condensed-state domains, whose formation is assisted by the magnetic field.[7] Anomalously large fluctuations of the IX line intensity in a magnetic field were recently observed also in GaAs/$Al_{0.33}Ga_{0.67}As$ asymmetric DQWs.[8] At the same time, the above features can be due apparently also to other processes, which are not connected with formation of a condensed-exciton state. For example, the narrowing of the IX luminescence line with decreasing temperature was associated[9] with the inhomogeneous nature of the linewidth, which is due to imperfection of the interfaces and to specific features of the IX distribution over the inhomogeneously broadened ensemble of states originating from the IX excitons having dipole moments. The onset of low-frequency fluctuations in DQW emission could be connected with the strong instability and screening of electric fields at a DQW, which results from electron buildup in one of the wells.[10] Thus the existence of spatially indirect excitons in a condensed state requires further investigation. Because a condensed state assumes a certain equilibrium exciton concentration and a certain boundary separating different phases, it is essential to find the conditions favoring the onset and breakdown of the condensed state before a conclusion regarding the existence of a condensate can be drawn.

The objective of this work was to study the evolution of an ensemble of spatially indirect excitons in a DQW under variation of external parameters, viz. the electric field V_{dc} applied to the DQW, optical excitation density I_p, and of the sample (bath) temperature T_b. These parameters govern to a considerable extent the conditions in which a condensed exciton state appear in DQWs.[4] In contrast to the preceding studies, our investigation was performed on a slightly asymmetric DQW of sufficient perfection (small amplitude of the random potential producing inhomogeneous spectral-line

broadening). Because the condensed state should manifest itself the strongest at low temperatures, all measurements were carried out at $T_b = 1.8$ and 4.2 K. One studied the line shape of IX photoluminescence (PL) in a GaAs/$Al_{0.33}Ga_{0.67}As$ DQW for various fixed optical pumping densities I_p under continuous variation of an external electric field V_{dc} normal to the DQW plane. By applying an electric field which shifts the *e* and *h* positions in the wells one can control efficiently the IX lifetime (which depends on the *e* and *h* wave-function overlap in the IX in the structure-growth direction) and, hence, the IX concentration, which is essential for creating the conditions favorable for the onset of the exciton condensed state.

By continuously varying V_{dc} and I_p, we observed a strong decrease in the IX line FWHM within a certain interval of V_{dc} and I_p. Besides, in the transition region of V_{dc}, where the linewidth changes abruptly (by decreasing or increasing), anomalously large low-frequency fluctuations in the IX line intensity were seen to set in. Investigation of the IX properties under variation of V_{dc}, I_p, and T_b is important to establish the regions where different exciton-state phases exist (the phase diagram). The results obtained are discussed within the frame of the assumption that a condensed state forms in the spatially indirect exciton system in a DQW.

1. SAMPLES AND EXPERIMENT

The samples to be studied (NU1117) were MBE-grown at Nottingham University (Great Britain) at $T = 630\,^\circ$C on a 0.4-mm thick GaAs(001) substrate. The structure consisted of a GaAs buffer layer (1 μm) followed by three pairs of consecutively grown, slightly asymmetric quantum wells (QW) with thicknesses (QW/$Al_{0.33}Ga_{0.67}As$ barrier/QW in nm) of 20.07/3.82/1.95, 10.18/3.82/9.61, and 8.20/3.82/7.63, and a GaAs cap layer (5 nm) on the face side of the sample. The DQWs were separated from one another and from the buffer layer by 20-nm thick $Al_{0.33}Ga_{0.67}As$ barriers. The measurements were made on the 10.18/3.82/9.61 DQW. A dc electric voltage V_{dc} was applied to two indium contacts deposited on the substrate and the DQW side of the sample (Fig. 1a). The photoluminescence (PL) was excited and measured through a small hole (0.2×0.2 mm^2) in the contact on the DQW side (Fig. 1a). The sample was illuminated by a cw Ti:Sp laser ($P<10$ mW, $\lambda = 765.2$ nm, laser light focused to a dia. 100–200 μm spot on the sample) to produce under-barrier DQW excitation. The DQW luminescence spectra were measured with a DFS-52 double-grating spectrometer operating in a gated photon-counting regime.

The luminescence spectrum of the 10.18/3.82/9.61 DQW of our NU1117 sample and the effect on it of an external voltage V_{dc} were described in detail in Ref. 11 presenting also the energy diagram of direct (DX) and indirect (IX) excitons in this DQW. In the present work, the V_{dc} polarity (with the substrate biased positively) provided operation in the ''indirect mode'' (Fig. 1b), which corresponds to the lowest energy position of the indirect exciton IX (with the electron localized in the wide, and the hole, in the narrow QW) with respect to the transition energy of the direct exciton DX (with the electron and the hole in the wide well) in PL. Within the V_{dc} interval studied, the photocurrent throughout the sample was very small ($\sim$100 nA).

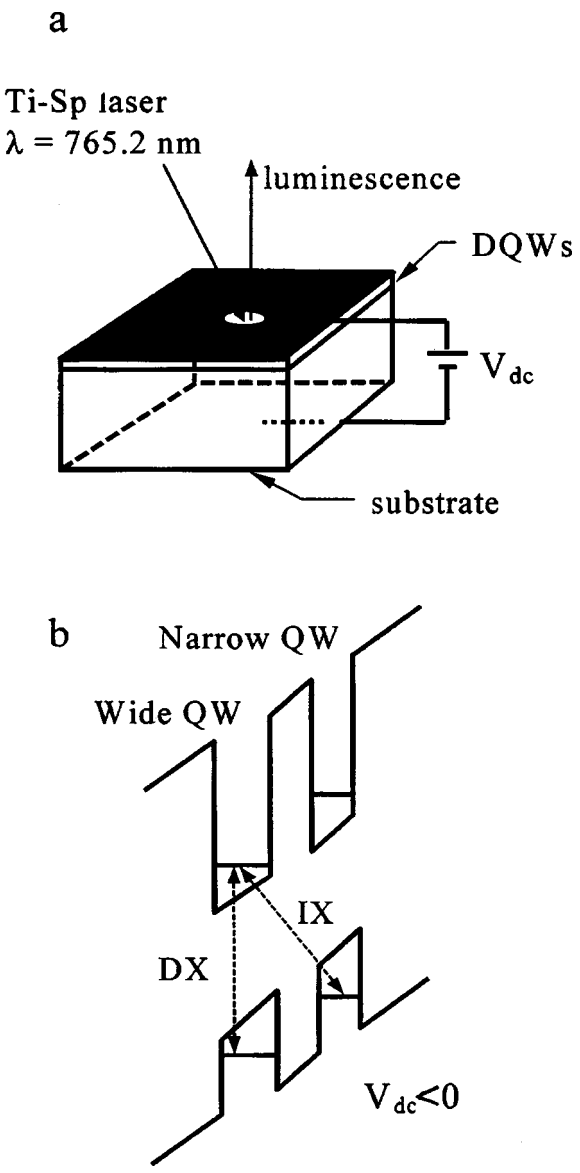

FIG. 1. (a) Scheme of experiment and (b) energy diagram for ''indirect'' regime.

2. RESULTS OF MEASUREMENTS

Figure 2 displays PL spectra obtained at $I_p = 2.5$ W cm^{-2} and $T_b = 1.8$ K for different values of V_{dc}. For $V_{dc} = 0$ (Fig. 2a), the spectrum consists of two lines produced by direct-exciton emission (DX) from the narrow ($E = 1.559$ eV) and the wide ($E = 1.555$ eV) well. The spectrum in Fig. 2a is close to a DQW flat-band spectrum, and its observation at $V_{dc} = 0$ indicates that the built-in electric field V_0 here is very small. It should be noted that V_0 depends on the position of the region under study on the sample surface, and that, in other regions of the sample, the built-in electric field may have different signs, which requires application of the corresponding compensating voltage V_{dc}. For not too high applied electric fields ($<10^5$ V/cm), where the quadratic Stark effect may be neglected, the spectral position of

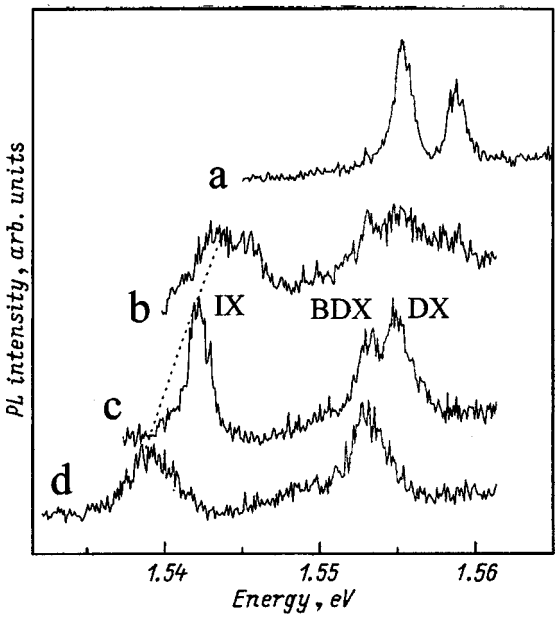

FIG. 2. PL spectra obtained at $I_p=2.5$ W cm^{-2}, $T_b=1.8$ K, and V_{dc}(V): (a) 0, (b) -0.8, (c) -1.3, (d) -1.6.

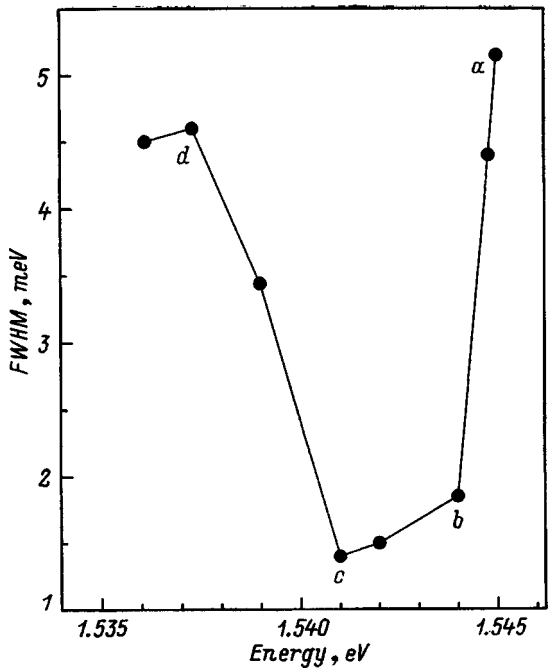

FIG. 3. FWHM of the IX line as a function of its position, which is governed by the electric field applied to a DQW. $T_b=1.8$ K and $I_p=2.5$ W cm^{-2}.

the direct-exciton line is independent of the electric field across the structure. At the same time, the position of the IX indirect exciton line depends substantially on electric field, which is shown schematically in Fig. 1b. Indeed, for a nonzero V_{dc}, the IX line appears in the PL spectrum and shifts strongly toward lower energies with increasing V_{dc} (Fig. 2b–2d). The spectral position E_{IX} of the IX line reflects the resultant electric field applied to the DQW and characterizes the DQW exciton-state diagram,[11] including the indirect excitons under study here. Thus the directly measured value of E_{IX} is a convenient experimental parameter which is related unambiguously to the DQW energy level diagram in different experimental conditions.

As seen from Fig. 2, at nonzero V_{dc} there is no DX emission from the narrow well ($E=1.559$ eV). The disappearance of the direct-exciton line from the narrow well accompanied by the appearance of the indirect exciton IX, which consists in this particular case of an electron localized in the wide well and a hole in the narrow well (Fig. 1b), implies that the electronic states in the narrow well are not filled. This redistribution of the population of DQW excitonic states in an electric field is caused by the fast relaxation processes involved in electron tunneling between wells.[11] Note also that the spectrum obtained at $V_{dc}\neq 0$ has a BDX line, which corresponds to the emission of an impurity-bound direct exciton from the wide well,[12] and that the position of this line, as that of the DX line, does not depend on the magnitude of V_{dc} (Fig. 2b–2d).

It is essential that, as the applied electric voltage V_{dc} is monotonically increased, the FWHM of the IX line shifting toward longer wavelengths undergoes a dramatic change (Fig. 3). At a certain position of the line determined by V_{dc} the FWHM decreases abruptly by a few (up to 3.5) times. The narrow width remains practically unchanged within some E_{IX} interval (i.e., within a certain interval of applied fields), to increase thereafter sharply to a value comparable to the original width (Fig. 3). All data presented in Figs. 2 and 3 relate to the same fixed optical-pumping density $I_p=2.5$ W cm^{-2}. A number of PL spectra were measured in a similar way for different applied voltages V_{dc} and other fixed pumping densities within the $0.6<I_p<12.5$ W cm^{-2} range. These experiments revealed also a narrowing of the IX emission line, whose position depended however not only on the voltage applied to the sample but on the pumping level I_p as well (the latter indicates a change in the real field applied to the DQW with changing optical excitation density). Figure 4 presents for different pumping levels I_p the FWHMs of the IX line occupying the same position $E_{IX}=1.543$ eV in the PL spectra. The data displayed in Fig. 4 reflect obviously the behavior of the IX excitons in a DQW with fixed energy parameters of the IX (and of other exciton states as well) depending on the IX concentration, which varies with the pumping level. We readily see that the IX-line FWHM decreases strongly with increasing pumping level within a certain I_p interval, to increase again afterwards. Besides, one observes in the region of the strong FWHM variation (the *a-b* and *c-d* regions in Fig. 3) giant fluctuations of the IX PL-line intensity, whose typical pattern is shown in Fig. 5. A similar behavior of the IX line was observed experimentally at $T=4.2$ K.

3. DISCUSSION

In our analysis of the line shape of IX indirect-exciton emission in a DQW, which is the main goal of our investigation, we first note the well-known part played by the complex spatial relief of the potential acting on the IX in a DQW. This random potential is generated both by thickness fluctua-

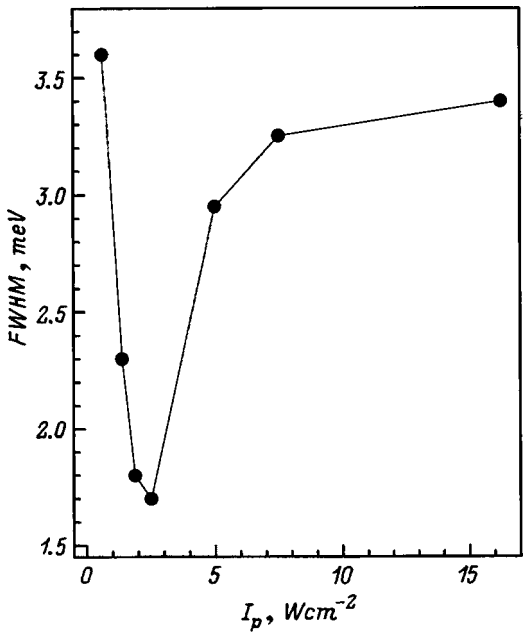

FIG. 4. FWHM of the IX line *vs* optical pumping density I_p for $E_{IX}=1.543$ eV and $T_b=1.8$ K.

tions within one or two monolayers of the QWs and of the barriers making up the DQW, and by the electric field of impurities present in the barriers. For fluctuations with a characteristic size L exceeding the IX-exciton radius a_{ex} ($L>a_{ex}$), excitons localize at low temperatures at potential fluctuations, and the inhomogeneous broadening of the IX line is accounted for by the spread in energy of the photons emitted in the IX radiative recombination. In our case, the width of this profile is approximately 5 meV (Fig. 3). The observation of a strong (down to ~ 1.5 meV) narrowing of the IX-exciton emission line under variation of the electric field applied to a DQW, which occurs in a specific (for a given optical pumping level) field interval, argues convincingly for a sharp change in the state of the emitting IX-exciton ensemble in this field interval bounded on both sides.

The behavior of an exciton system consisting of spatially separated electrons and holes (this situation applies to our case of the IX excitons in a DQW) with concentration has recently been studied theoretically.[4] Because e and h are spatially separated, such an exciton possesses a constant electric dipole moment eD oriented perpendicular to the layers (here D is the distance between the layers containing the electrons and holes). Therefore the dipole-dipole repulsion between excitons with identically oriented dipole moments affects to a large extent the behavior of the exciton system. It was shown that as the exciton concentration n increases, the exciton gas should transfer to a two-layer exciton liquid within a certain interval of n, provided D is small enough ($D<1.1\,a_{ex}$).[4] For large D ($D>1.9\,a_{ex}$) however, the gas phase is always stable, and in these conditions a gas-liquid transition in the D parameter is possible.

Comparing our experimental results with the conclusions drawn in Ref. 4, we point out that the new state of a system of spatially indirect excitons characterized by a narrow emission line sets in in our experiments when the electric field applied to the DQW and affecting strongly the parameters of the IX excitons is increased. Indeed, an increase of the field entails an increase in the IX recombination time (due to the decreasing overlap of the e and h wave functions occurring as the electrons and holes shift in opposite directions in the corresponding wells), which should give rise to an increase in the IX concentration n (for a fixed pumping level). Our estimates suggest that for a pumping density $I_p=2.5$ W cm^{-2} the IX concentration can reach fairly high values $\sim 10^{10}-10^{11}$ cm^{-2}. At the same time the field-induced increase in the e-h separation results in an increase of the dipole moment of indirect excitons and an increase of their repulsion. According to Ref. 4, this growth of n and D should qualitatively result in the new liquid phase becoming stable within a limited electric-field interval, and this is ex-

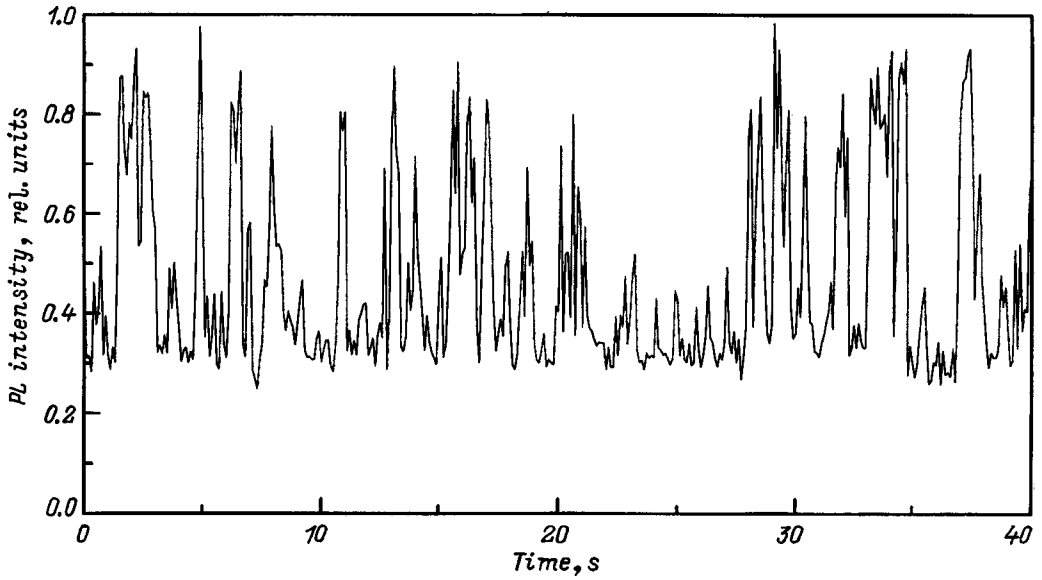

FIG. 5. IX-line intensity fluctuations with time measured within the *c*-*d* interval in Fig. 3.

actly what is seen experimentally (Fig. 3). Therefore it appears natural to consider the fluctuations in the IX line intensity (Fig. 5) observed within the regions where the FWHM undergoes substantial changes (i.e. in the regions where the IX system transfers from one stable phase to another) as critical fluctuations in the vicinity of a phase transition.

The observation of the line narrowing under variation of the optical pumping density I_p determining the IX-exciton concentration (Fig. 4), where this effect occurs within a limited interval of I_p, is also in qualitative agreement with Ref. 4. The observed strong narrowing of the IX emission line indicates suppression of the strong inhomogeneous broadening of this line and is probably a consequence of the DQW potential relief becoming averaged out over a substantial area as a result of the large size of the ordered phase.

In this way, the above experimental data on the dependence of the FWHM on electric field (for a fixed I_p) and on I_p (for a fixed eD), as well as the existence of anomalously large fluctuations in the IX-line intensity within the region of abrupt variation of the IX line halfwidth, permit a conclusion that spatially indirect excitons in a DQW transfer to a condensed state for $T \leqslant 4.2$ K, and that the behavior of the line halfwidth essentially reflects the phase diagram of indirect excitons in a DQW.

The authors owe their sincere thanks to Prof. A. A. Kaplyanskiĭ for support and fruitful discussions, and to S. A. Permogorov, Yu. E. Lozovik, and V. B. Timofeev for valuable criticisms.

Support of the Russian Fund for Fundamental Research (Grant 98-02-18296) is gratefully acknowledged.

[1] Yu. E. Lozovik and V. I. Yudson, Zh. Éksp. Teor. Fiz. **71**, 738 (1976) [Sov. Phys. JETP **44**, 389 (1976)].
[2] I. V. Lerner and Yu. E. Lozovik, Zh. Éksp. Teor. Fiz. **80**, 1488 (1981) [Sov. Phys. JETP **53**, 763 (1981)].
[3] D. Yoshioka and A. H. MacDonald, J. Phys. Soc. Jpn. **59**, 4211 (1990).
[4] Yu. E. Lozovik and O. L. Berman, Zh. Éksp. Teor. Fiz. **111**, 1879 (1997) [JETP **84**, 1027 (1997)].
[5] L. V. Butov and V. D. Kulakovskiĭ, JETP Lett. **53**, 466 (1991).
[6] T. Fukuzawa, E. E. Mendez, and J. M. Hong, Phys. Rev. Lett. **64**, 3066 (1990).
[7] L. V. Butov, A. Zrenner, G. Abstreiter, G. Böhm, and G. Weimann, Phys. Rev. Lett. **73**, 304 (1994).
[8] V. V. Krivolapchuk, A. L. Zhmodikov, D. A. Mazurenko, E. S. Moskalenko, N. K. Poletaev, T. S. Cheng, and C. T. Foxon, Fiz. Tverd. Tela (St. Petersburg) **40**, 803 (1998) [Phys. Solid State **40**, 737 (1998)].
[9] J. A. Kash, M. Zachau, E. E. Mendez, J. M. Hong, and T. Fukuzawa, Phys. Rev. Lett. **66**, 2247 (1991).
[10] V. B. Timofeev, A. V. Larionov, J. Zeman, G. Martinez, J. Hvam, D. Birkedal, and K. Soerensen, Usp. Fiz. Nauk **168**, 117 (1998) [*sic*].
[11] A. V. Akimov, E. S. Moskalenko, A. L. Zhmodikov, D. A. Mazurenko, A. A. Kaplyanskii, L. J. Challis, T. S. Cheng, and C. T. Foxon, Fiz. Tverd. Tela (St. Petersburg) **39**, 735 (1997) [Phys. Solid State **39**, 649 (1997)].
[12] E. S. Moskalenko, A. L. Zhmodikov, A. V. Akimov, A. A. Kaplyanskii, L. J. Challis, T. S. Cheng, and O. H. Hughes, Ann. Phys. **4**, 127 (1995).

Translated by G. Skrebtsov

Resonance elastic scattering of light by a quantum well with statistically uneven boundaries

V. A. Kosobukin*)

A. F. Ioffe Physicotechnical Institute, Russian Academy of Sciences, 194021 St. Petersburg, Russia
(Submitted July 21, 1998)
Fiz. Tverd. Tela (St. Petersburg) **41**, 330–336 (February 1999)

A theory is formulated for the elastic scattering of light through quasi-two-dimensional exciton states in a quantum well with randomly uneven walls. The nonlocal exciton susceptibility is expressed in terms of random functions describing the shape of the quantum well boundaries up to and including linear terms in the unevenness height. The resonance elastic scattering cross sections in the presence of arbitrary statistical unevenness are calculated in the Born approximation for all channels in which the initial and final states are represented by an electromagnetic TM or TE mode. The spectral and angular dependences of the scattering probability are calculated with the unevenness characterized by Gaussian correlation functions. It follows from numerical estimates that elastic scattering in quantum wells should be observed for unevenness having an rms height of the order of the thickness of an atomic monolayer. © *1999 American Institute of Physics.* [S1063-7834(99)02702-1]

Many optical properties of low-dimensional excitons in structures containing quantum wells can be explained on the assumption of ideally plane heterointerfaces.[1–3] In this case the secondary emission can deviate only in specular directions relative to the incident wave, because the component of the wave vector in the plane of the quantum well is preserved. The reflection and transmission of light are described by the transfer matrix method developed in Ref. 3 with allowance for the nonlocal character of the exciton response to quantum wells. However, real quantum wells have nonremovable structural imperfections, most significantly random deviations of the heterointerfaces from the plane.[4] The interface unevenness in a quantum well makes its width and polarization field randomly inhomogeneous and is, therefore, a source of light scattering.

Relatively few papers have been devoted to theoretical investigations of the role of statistically uneven heterointerfaces in exciton optics, and those have been concerned primarily with nonuniform broadening of the exciton spectra in quantum-well structures,[5] light transmission,[6] the time-resolved spectroscopy of exciton luminescence,[7] and the elastic scattering of light.[8] Unevenness effects are usually[5–7] discussed in terms of a random ''potential'' affecting the center-of-mass motion of an exciton, with observable quantities being expressed in terms of the statistical characteristics of such a potential. In view of the physical indeterminacy of the latter, as a rule, important questions are left unanswered in regard to the localization of excitons and the relationship between the statistical parameters of the heterointerfaces and the exciton potential energy.

The objective of this paper is to formulate a theory of steady-state resonance elastic scattering of light by excitons of a quantum well with uneven walls. Instead of introducing a random potential acting on an exciton, we propose a model generalization of exciton susceptibility whereby the geometry of the uneven heterointerfaces of the quantum well are explicitly taken into account.[8] We assume that the unevenness has small heights and a large correlation length in the plane of the quantum well, its influence on the transition frequency and exciton wave function being regarded as a perturbation. This model of large-scale fluctuations of the shape of the boundaries of a quantum well is largely analogous to the model used to explain the elastic scattering of light by the rough surface of a semiconductor in the vicinity of its exciton resonances.[9]

1. DESCRIPTION OF THE MODEL

A quantum well with randomly uneven boundaries is treated as a set of regions known as islands, where the width of the well can be assumed to be constant within each island. The dimensions of the islands in the lateral directions can range from tens to hundreds of angstroms.[4] Consequently, the transverse cross section of a light beam in an optical experiment simultaneously covers a large number of islands, which therefore form a statistical ensemble. The above-indicated structural peculiarities of a quantum well with statistically nonequivalent interfaces[4] are reflected in the model shown in Fig. 1. The shape of the interfaces of the quantum well is described by the equations $z=-\overline{L}/2+\xi_1(\mathbf{R})$ and $z=\overline{L}/2+\xi_2(\mathbf{R})$, where $\mathbf{R}=(x,y)$, $\mathbf{r}=(\mathbf{R},z)$, and $\overline{L}$ is the average width of the well. The random functions $\xi_n(\mathbf{R})$ describing the shape of the nth interface $(n=1,2)$ have the average value $\langle\xi_n(\mathbf{R})\rangle=0$, where the angle brackets signify averaging over the ensemble $\{\xi_n(\mathbf{R})\}$. The functions

$$\xi_\pm(\mathbf{R})=\xi_2(\mathbf{R})\pm\xi_1(\mathbf{R}) \tag{1}$$

locally describe the width of the quantum well

$$L(\mathbf{R})=\overline{L}+\xi_-(\mathbf{R}) \tag{2}$$

and the position of its center $Z=\xi_+(\mathbf{R})/2$.

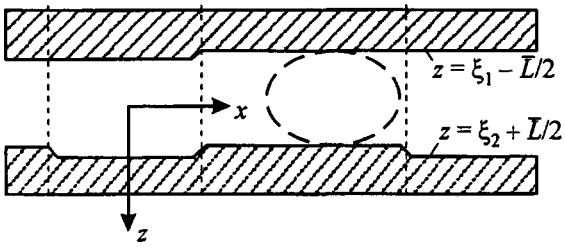

FIG. 1. Schematic diagram of an uneven-walled quantum well. The constant-width sections of the well are separated by vertical lines, and an exciton is conditionally shown in one of the sections.

If the transverse correlation radius of the microasperities in the plane of the well exceed the Bohr exciton radius, the quasi-two-dimensional (quasi-2D) exciton preserves its individuality with respect to an unbounded quantum well of the same width. The constitutive equation relating the exciton polarization $\mathbf{P}$ to the electric field $\mathbf{E}$ at a given frequency ω (Refs. 10 and 11) is generalized as follows:

$$4\pi P_\alpha(z,\mathbf{R};\omega)=\frac{A_\alpha}{\omega_0(\mathbf{R})-\omega-i\gamma}\psi\left(z-\frac{\xi_+(\mathbf{R})}{2}\right)\times\int dz'\,\psi\left(z'-\frac{\xi_+(\mathbf{R})}{2}\right)E_\alpha(z',\mathbf{R};\omega). \tag{3}$$

Here we have introduced slow parametric dependences of the exciton transition frequency $\omega_0(\mathbf{R})$ and the envelope of the exciton wave function $\psi(z-\xi_+/2)$ on $\mathbf{R}$; the envelope describes bending of the quantum well. In Eq. (3) we have $\psi(z)=\psi(-z)$ for the exciton ground state, γ is the nonradiative exciton damping parameter, and A_α is proportional to the anisotropic transition oscillator strength,[10] whose dependence on L (Ref. 12) is ignored.

As a result of applying the Fourier transform

$$\mathbf{E}(z;\mathbf{K},\omega)=\int d^2R\,\exp(-i\mathbf{K}\cdot\mathbf{R})\mathbf{E}(z;\mathbf{R},\omega) \tag{4}$$

we obtain the following relation from Eq. (3):

$$4\pi P_\alpha(z;\mathbf{K},\omega)=\int dz'\int\frac{d^2K'}{(2\pi)^2}\chi^{(\alpha)}(z,z';\mathbf{K}-\mathbf{K}',\omega)\times E_\alpha(z';\mathbf{K}',\omega), \tag{5}$$

where

$$\chi^{(\alpha)}(z,z';\mathbf{K}-\mathbf{K}',\omega)=(2\pi)^2\delta(\mathbf{K}-\mathbf{K}')\psi(z)\chi_0^{(\alpha)}(\omega)\psi(z')+\delta\chi^{(\alpha)}(z,z';\mathbf{K}-\mathbf{K}',\omega). \tag{6}$$

Here we have separated out the part having translation symmetry in $\mathbf{R}$, in which

$$\chi_0^{(0)}(\omega)=\frac{A_\alpha}{\bar{\omega}_0-\omega-i\gamma}\equiv\frac{A_\alpha}{\Delta_0(\omega)} \tag{7}$$

describes the resonance response of an ''average'' quantum well with plane surfaces $z=\pm\bar{L}/2$ and frequency $\bar{\omega}_0$.

For small roughness heights, $\langle\xi_n^2\rangle^{1/2}\ll\bar{L}$ the quantity $\delta\chi^{(\alpha)}$ in Eq. (6) is conveniently expanded in $\xi_\pm$ up to and including linear terms; this operation requires satisfaction of the auxiliary condition $\langle\delta\omega_0^2\rangle^{1/2}<\gamma$, where

$$\delta\omega_0(\mathbf{R})=\omega_0(\mathbf{R})-\bar{\omega}_0. \tag{8}$$

The random correction (8) to the frequency $\bar{\omega}_0$ due to the variation of the width of the quantum well (2) is determined from the equation

$$\delta\omega_0(\mathbf{R})\approx\{\partial\omega_0/\partial L\}_{L=\bar{L}}\xi_-(\mathbf{R})=-\Omega\xi_-(\mathbf{R})/\bar{L}, \tag{9}$$

which is valid for $\langle\delta\omega_0^2\rangle^{1/2}\ll\bar{\omega}_0$. Taking Eqs. (7)–(9) into account, we find that in Eq. (6)

$$\delta\chi^{(\alpha)}(z,z';\mathbf{K}-\mathbf{K}';\omega)=\chi_0^{(\alpha)}(\omega)\sum_\sigma a_\sigma(\omega)F_\sigma(z,z')\frac{\xi_\sigma(\mathbf{K}-\mathbf{K}')}{\bar{L}}. \tag{10}$$

Here $\xi_\sigma(\mathbf{K})$ is the result of applying the Fourier transform (4) to the function $\xi_\sigma(\mathbf{R})$, σ denotes $(+)$ or $(-)$ in accordance with Eq. (1),

$$a_-=\Omega/\Delta_0(\omega),\quad F_-(z,z')=\psi(z)\psi(z'), \tag{11}$$

$$a_+=-1,$$

$$F_+(z,z')=\frac{\bar{L}}{2}\left\{\psi(z)\frac{d\psi(z')}{dz'}+\frac{d\psi(z)}{dz}\psi(z')\right\}. \tag{12}$$

In Eq. (3) the exciton transition energy, which depends on the local width of the quantum well (2), is equal to

$$\hbar\omega_0(L)=E_{\rm gap}+E_{\rm conf}(L)-E_{\rm bind}(L). \tag{13}$$

Here $E_{\rm gap}$ is the width of the band gap of the semiconductor, $E_{\rm conf}$ is the total energy of spatial quantization of the unbound electron and the unbound hole, and $E_{\rm bind}$ is their binding energy in the exciton. For a region of the quantum well (island) with dimensions $D_X\times D_Y\times L$ in the model of infinitely high barriers the energy of the lowest level of size quantization of carriers is given by the expression

$$E_{\rm conf}(L)=(\pi\hbar)^2\beta/(2\mu L^2).$$

Here μ is the normalized electron-hole mass, and the dimensionally dependent constant β has values between $\beta=1$ (unbounded well with $D_X\to\infty$ and $D_Y\to\infty$) and $\beta=3$ (cubical well with $D_X=D_Y=L$). Hence

$$\hbar\Omega_{\rm conf}=(\pi\hbar)^2\beta/(\mu\bar{L}^2)=2\pi^2\beta E_B(a_B/\bar{L})^2, \tag{14}$$

where E_B and a_B are the energy and radius of the bulk exciton. In an unbounded quantum well with infinite barriers the exciton binding energy $E_{\rm bind}(L)$ as a function of L decays monotonically from $E_{\rm bind}(0)=4E_B$ to $E_{\rm bind}(\infty)=E_B$, where $\hbar\Omega_{\rm bind}\approx E_B$. Consequently, $\Omega_{\rm bind}\ll\Omega_{\rm conf}$ for $\bar{L}\approx a_B$, and $\Omega\approx\Omega_{\rm conf}$ in Eq. (9). In GaAs quantum wells for a $1e-1hh$ heavy-hole exciton the quantity $\hbar\Omega_{\rm conf}$ decreases approximately from 1.5×10^2 meV for $\bar{L}=100$ Å to 20 meV for $\bar{L}=300$ Å, and for a $1e-1lh$ light-hole exciton it is larger by the approximate factor $\mu_{hh}/\mu_{lh}\approx1.4$. In the interval $100\,\text{Å}<\bar{L}<300\,\text{Å}$, on the other hand, we have $\hbar\Omega_{\rm bind}$

≈ 2 meV for a $1e-1hh$ exciton and a value approximately $\mu_{hh}/\mu_{lh}\approx 1.4$ times larger for the $1e-1lh$ state. These conclusions are also readily confirmed for barriers of finite height with the aid of the functions $\hbar\Omega_{\rm bind}(L)$ from Ref. 13 and the corresponding functions $\hbar\Omega_{\rm conf}(L)$, but the quantity Ω in Eq. (9) is diminished somewhat by carrier tunneling below the barrier. We also note that the resonance denominator of Eq. (3) lacks the term associated with spatial dispersion of excitons, $\hbar\kappa^2/[2(m_e+m_h)]$, which is small in comparison with $\langle\delta\omega_0^2\rangle^{1/2}$.

We have thus formulated a model in which the exciton susceptibility of a quantum well and the observable optical variables associated with it are expressed directly in terms of statistical characteristics of the heterointerfaces. In the ensuing discussion we treat the susceptibility (6) as a perturbation, incorporating the contribution (7) into it self-consistently and including the contribution (10) in the first perturbation approximation with respect to the unevenness height.

2. ELECTRODYNAMICS OF THE "AVERAGE" QUANTUM WELL

We assume that a monochromatic (with frequency ω) wave is incident on a quantum well at an angle θ relative to the normal (z axis) in a medium with a background dielectric constant ε_b; the electric field of the wave is

$$\mathbf{E}^0(\mathbf{r},t)=\mathbf{e}_\lambda\cdot E_\lambda^{\rm inc}\exp[-i\omega t+i(\kappa x+k_z z)]. \tag{15}$$

Here $\mathbf{K}=\kappa\mathbf{e}_x$, $\kappa=\sqrt{\varepsilon_b}\,k_0\sin\theta$, and $k_z(\kappa)=\sqrt{\varepsilon_b k_0^2-\kappa^2}$, $k_0=\omega/c$, and c is the speed of light. The subscript λ designates the linear polarizations p (TM mode) or s (TE mode), for which the unit vectors $\mathbf{e}_\lambda$ in Eq. (15) are equal to $\mathbf{e}_p=(\cos\theta,0,-\sin\theta)$ and $\mathbf{e}_s=(0,1,0)$, respectively.

We solve the electrodynamic equations for the electric field $\mathbf{E}(z;\mathbf{K},\omega)$ and the Green's function $G_{\alpha\beta}(z,z';\mathbf{K},\omega)$ self-consistently, taking into account the nonlocal response (6) for $\delta\chi^{(\alpha)}=0$ and following the customary procedure.[3,11,14] The result, in particular, is the complex frequency $\omega_\alpha(\kappa)-i\Gamma_\alpha(\kappa)-i\gamma$ of a quasi-2D exciton with allowance for electromagnetic renormalization. The radiative exciton decay rate is expressed in the form[14]

$$\Gamma_\alpha(\kappa)=\Gamma_\alpha^0 f_\alpha(\kappa),$$
$$\mathbf{f}=\{|\cos\theta|,|\cos\theta|^{-1},|\cos\theta|^{-1}-|\cos\theta|\}I_c^2(\kappa)/I_c^2(0), \tag{16}$$

where Γ_α^0 are the radiative exciton decay rates at normal incidence, whose anisotropy is taken into account in the form $\Gamma_X^0=\Gamma_Y^0=\Gamma_\parallel^0\neq\Gamma_\perp^0=\Gamma_Z^0$ (Refs. 10 and 11). The radiative shifts of the corresponding exciton transition frequencies $\omega_\alpha(\kappa)$ relative to $\overline{\omega_0}$ are insignificant[3,14]; from now on, therefore, we take into account only the frequency splitting $\omega_Z-\omega_X=2\Gamma_Z^0 I_0/[\sqrt{\varepsilon_b}\,k_0 I_c^2(0)]$, which is electromagnetic in origin. Here $I_c(\kappa)=\int dz\cos[k_z(\kappa)z]\psi(z)=\int dz\times\exp[\pm ik_z z]\psi(z)$, and $I_0=\int dz\,\psi^2(z)$, where $I_c(\kappa)/I_c(0)\approx 1$ in the long-wavelength approximation $k_z\overline{L}\ll 1$ of the scattering problem treated below.

3. LIGHT SCATTERING BY INTERFACE UNEVENNESS

Using Eq. (1) in the first perturbation approximation with respect to ξ_n (Born approximation), we obtain the following relation for the electric field of the scattered light:

$$\mathcal{E}_\alpha(\mathbf{r},\omega)=-k_0^2\sum_\beta\chi_0^{(\beta)}(\omega)\int\frac{d^2K'}{(2\pi)^2}\exp(i\mathbf{K}'\cdot\mathbf{R})$$
$$\times\sum_\sigma a_\sigma\frac{\xi_\sigma(\mathbf{K}'-\mathbf{K})}{\overline{L}}\int dz'G_{\alpha\beta}(z,z';\mathbf{K}',\omega)$$
$$\times\int dz''F_\sigma(z',z'')E_\beta(z'';\mathbf{K},\omega). \tag{17}$$

Here $\mathbf{K}=\mathbf{e}_x\kappa$ and $\mathbf{K}'=(\mathbf{e}_x\cos\varphi'+\mathbf{e}_y\sin\varphi')\kappa'$ are the 2D components of the wave vectors of incident and scattered plane waves with $(\kappa,\kappa')=\sqrt{\varepsilon_b}\,k_0(\sin\theta,\sin\theta')$, respectively, and $G_{\alpha\beta}(z,z';\mathbf{K}',\omega)$ denotes the components of the tensor Green's function discussed in Sec. 2.

We now calculate the Poynting vector for the scattered-light field (17) and average the result over the ensemble of realizations $\{\xi_n\}$. In the asymptotic region $|z|\to\infty$ this procedure gives

$$\langle\mathbf{S}(\mathbf{r})\rangle=\frac{c\sqrt{\varepsilon_b}k_0^4}{8\pi}Re\left\{\int\frac{d^2K'}{(2\pi)^2}\mathbf{N}(\mathbf{K}')\right.$$
$$\times\sum_{\alpha,\beta,\gamma}\int dz_1\ldots dz_4G_{\alpha\beta}(z,z_1;\mathbf{K}')\chi_0^{(\beta)}$$
$$\times E_\beta(z_3;\mathbf{K})[G_{\alpha\gamma}(z,z_2;\mathbf{K}')\cdot\chi_0^{(\gamma)}$$
$$\cdot E_\gamma(z_4;\mathbf{K})]^*\sum_{\sigma,\tau}\frac{Q_{\sigma\tau}(\mathbf{K}'-\mathbf{K})}{\overline{L}^2}a_\sigma a_\tau^*F_\sigma(z_1,z_3)$$
$$\left.\times F_\tau(z_2,z_4)\right\}, \tag{18}$$

where $\mathbf{N}(\mathbf{K})=\{\mathbf{K}/(\sqrt{\varepsilon_b}\,k_0+\mathbf{e}_z|\cos\theta|\mathrm{sgn}(z)\}$. The matrix elements $Q_{\sigma\tau}(\mathbf{K})$ are expressed in terms of the functions $g_{mn}(|\mathbf{K}|)$ encountered in the Fourier components

$$\langle\xi_m(\mathbf{K}')\xi_n(\mathbf{K})\rangle=h_m h_n g_{mn}(|\mathbf{K}|)(2\pi)^2\delta(\mathbf{K}'-\mathbf{K}) \tag{19}$$

of the correlation functions

$$\langle\xi_m(\mathbf{R})\xi_n(\mathbf{R}')\rangle=h_m h_n g_{mn}(|\mathbf{R}-\mathbf{R}'|). \tag{20}$$

Equations (19) and (20) rest on the assumption that the quantum well interface unevenness, on the average, is homogeneous and isotropic in the plane of the quantum well. In Eq. (20) $h_n^2=\langle\xi_n^2(\mathbf{R})\rangle$, and $g_{mn}(|\mathbf{R}|)=\langle\xi_m(\mathbf{R})\xi_n(0)\rangle/h_m h_n$ are the variance of the unevenness heights and the correlation function of profile of the microasperities, where $\int d^2K g_{mn}(\mathbf{K})/(2\pi)^2=1$ for the Fourier components.

An analysis of Eq. (18) shows[8] that the scattering contribution due to bending of the quantum well can become significant only for $\xi_1=\xi_2$, i.e., in the presence of correlated interfaces. In general, $\xi_1\neq\xi_2$ the dominant scattering contribution is associated with spatial variation of the width of the quantum well (energy of size quantization of carriers). Indeed, first of all, in the vicinity of the resonance frequency

we have $|\Delta_\alpha| \approx \gamma + \Gamma_\alpha \ll \Omega$, so that $|a_-/a_+| \approx \Omega/\gamma \gg 1$ in Eqs. (11) and (12) (far from resonance the increase of $|\Delta_\alpha|$ is limited by the same denominators of the functions E_α and $G_{\alpha\beta}$ occurring in Eq. (18). Second, the contribution with $\sigma=(+)$ in (17) has an additional smallness parameter $\sim\sqrt{\varepsilon_b}\,k_0\overline{L} \ll 1$, which emerges in the convolution of electromagnetic field functions having the phase factors $\exp(\pm ik_z z)$ with the functions $d\psi(z)/dz$ from Eq. (12).

Following Refs. 9 and 15, we now look at the differential quantity (18) and normalize it to the modulus of the Poynting vector of the incident wave $S_\lambda^{\rm inc} = c\sqrt{\varepsilon_b}\,|E_\lambda^{\rm inc}|^2 \times \cos\theta/(8\pi)$. Here we take into account only the contribution associated with the variation of the width of the quantum well, i.e., $\sigma=\tau=(-)$ in (18). Then for the dimensionless differential light-scattering cross sections from the initial state $(\lambda,\mathbf{K})$ to the final state $(\lambda',\mathbf{K}')$ we obtain

$$\frac{dw(s\to s)}{d\Omega'} = |L_Y(\kappa')|^2 |L_Y(\kappa)|^2 W(\mathbf{K}',\mathbf{K})\cos^2\varphi', \quad (21)$$

$$\frac{dw(s\to p)}{d\Omega'} = |L_X(\kappa')|^2 |L_Y(\kappa)|^2 W(\mathbf{K}',\mathbf{K})\sin^2\varphi', \quad (22)$$

$$\frac{dw(p\to s)}{d\Omega'} = |L_Y(\kappa)'|^2 |L_X(\kappa)|^2 W(\mathbf{K}',\mathbf{K})\sin^2\varphi', \quad (23)$$

$$\begin{aligned}\frac{dw(p\to p)}{d\Omega'} = \{&|L_X(\kappa')|^2|L_X(\kappa)|^2\cos^2\varphi' \\ &+ |L_Z(\kappa')|^2|L_Z(\kappa)|^2 \\ &+ 2Re[L_X(\kappa')L_Z^*(\kappa')L_X(\kappa)L_Z^*(\kappa)] \\ &\times \mathrm{sgn}(z)\cos\varphi'\}W(\mathbf{K}',\mathbf{K}). \end{aligned} \quad (24)$$

Here $d\Omega' = \sin\theta' d\theta' d\varphi'$ is an element of solid angle for scattering, and the functions

$$L_\alpha(\kappa,\omega) = \frac{\sqrt{\Omega\cdot\Gamma_\alpha(\kappa)}}{\omega_\alpha(\kappa) - i\Gamma_\alpha(\kappa) - i\gamma - \omega} \equiv \frac{\sqrt{\Omega\cdot\Gamma_\alpha(\kappa)}}{\Delta_\alpha(\kappa,\omega)} \quad (25)$$

with the parameters defined in Sec. 2 describe the resonance features of the excitation of quasi-2D excitons and the radiation of photons.

The statistical characteristics of the unevenness enter into the quantities

$$\begin{aligned}W(\mathbf{K}',\mathbf{K}) = \frac{1}{4\pi^2}&\left(\frac{\sqrt{\varepsilon_b}k_0}{\overline{L}}\right)^2 \{h_1^2 g_{11} + h_2^2 g_{22} \\ &- h_1 h_2[g_{12}+g_{21}]\}, \end{aligned} \quad (26)$$

where $g_{mn}(|\mathbf{K}'-\mathbf{K}|)$ are functions given in Eq. (19).

4. INFLUENCE OF THE SAMPLE SURFACE

In experimental work the samples are finite, light is incident from vacuum, and the secondary emission is recorded in the same vacuum. Of the waves discussed above, only those which satisfy the conditions $\theta,\ \theta' < \arcsin\sqrt{1/\varepsilon_b}$ are accessible for measurements in vacuum. We now consider the real situation in which a quantum well centered at $z=0$ is situated close to the interface $z=-D$ between a dielectric (vacuum) and a semiconductor, which are characterized by the background dielectric constants $\varepsilon_1 (z<-D)$ and $\varepsilon_2 = \varepsilon_b (z>-D)$, respectively. In this case, for example, if only the width variations of the well are taken into account, Eq. (21) corresponds to the expression

$$\begin{aligned}\frac{d\tilde{w}(s\to s)}{d\tilde{\Omega}'} = &\frac{\cos\theta|\cos\theta'|}{\cos\tilde{\theta}|\cos\tilde{\theta}'|}|t_s(\kappa')|^2|t_s(\kappa)|^2 \\ &\times \frac{\Omega\Gamma_Y(\kappa')}{|\tilde{\Delta}_Y(\kappa')|^2}\frac{\Omega\Gamma_Y(\kappa)}{|\tilde{\Delta}_Y(\kappa)|^2} W(\mathbf{K}',\mathbf{K})\cos^2\varphi', \end{aligned} \quad (27)$$

which refers to scattering of the type $s\to s$ from the semiconductor. In Eq. (27) $d\tilde{\Omega}' = \sin\tilde{\theta}' d\tilde{\theta}' d\varphi'$, where the polar angle $\tilde{\theta}$ of the wave propagating in the dielectric is related to the angle θ of the same wave in the semiconductor by the optical refraction law $\kappa/k_0 = \sqrt{\varepsilon_b}\sin\theta = \sqrt{\varepsilon_1}\sin\tilde{\theta}$, $k_n(\kappa) = \sqrt{\varepsilon_n k_0^2 - \kappa^2}$ (where $n=1,2$), and $t_s(\kappa) = 2k_1/(k_1+k_2)$ is the transmission coefficient of an *s*-polarized wave through the surface of the semiconductor. In the resonance denominators occurring in Eq. (27)

$$\tilde{\Delta}_Y(\kappa) = \Delta_Y(\kappa) + i\Gamma_Y(\kappa) r_s(\kappa)\exp(2ik_2 D) \quad (28)$$

the second term includes other radiation corrections to the exciton frequency and damping in addition to the denominator $\Delta_Y(\kappa)$ from Eq. (25). These corrections are attributable to the interference field between the quantum well and the surface of the sample, and their values are determined by the reflection coefficient $r_s(\kappa) = (k_1-k_2)/(k_1+k_2)$. As a consequence, the exciton resonance frequency and radiative damping, which determine the positions and intensities of the spectral peaks in accordance with (27), can undergo oscillations of amplitude comparable with Γ_Y^0. The period of these oscillations depends on the phase $2k_2 D = 2k_0 D\sqrt{\varepsilon_b - \varepsilon_1\sin^2\tilde{\theta}}$, i.e., on the angle of incidence $\tilde{\theta}$ (scattering $\tilde{\theta}'$) of light and the distance D between the quantum well and the sample surface. This effect is modified as a result of variation of the light reflection coefficient in the case of the *p-polarized component.*

5. DISCUSSION OF THE RESULTS

A fundamentally important distinction of the above-derived equations (21)–(24) and (27) is their dependence on the unevenness parameters by way of the correlation functions (19), (20), and (26). These equations are formally applicable to small heights for arbitrary statistics. For real heterointerfaces, however, the type of statistics is unknown, so that estimates are based on Gaussian correlation functions with

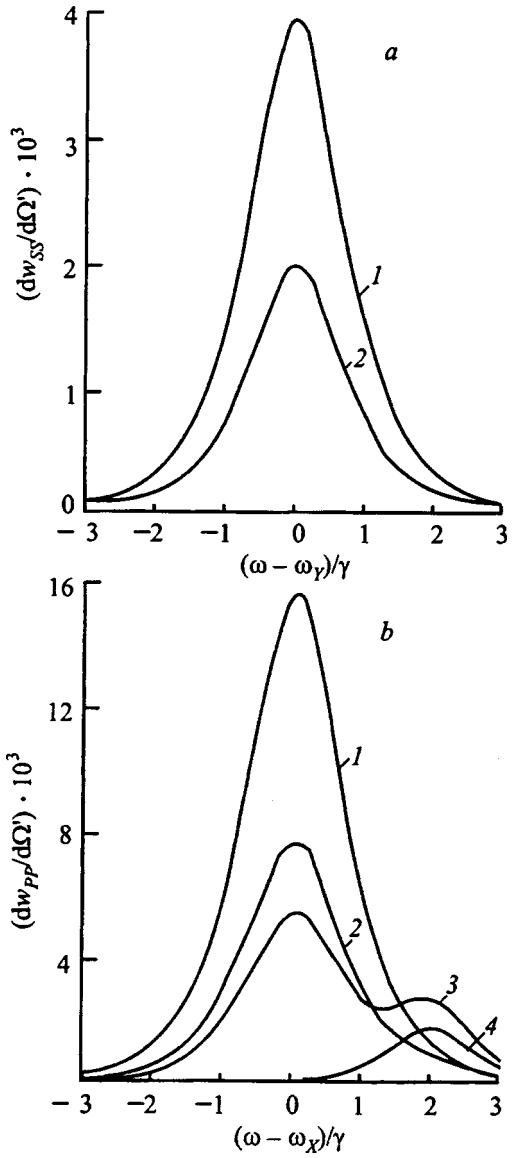

FIG. 2. Dimensionless elastic scattering cross sections $dw/d\Omega'$ of the type $s \to s$ versus $(\omega - \omega_Y)/\gamma$ for $\Lambda = 500$ Å (a) and of the type $p \to p$ versus $(\omega - \omega_X)/\gamma$ for $\Lambda = 1000$ Å (b), calculated for $\hbar\Omega = 50$ meV, $h = 2$ Å, $\overline{L} = 140$ Å, and $U = 0$ in Eq. (30. The curves correspond to the following sets of angles $(\theta, \theta', \varphi')$ in degrees: (a): (*1*) (0, 5, 0); (*2*) (0, 5, 45); (b): (*1*) (5, 10, 0); (*2*) (10, 10, 45); (*3*) (10, 30, 45); (*4*) (10, 30, 90). The following parameters are used for a $1e-1lh$ light-hole exciton in a GaAs/AlGaAs quantum well: $\hbar\gamma = 1$ meV; $\hbar(\omega_Z - \omega_X) = 2$ meV, $\hbar\Gamma_X^0 = \hbar\Gamma_Y^0 = \hbar\Gamma_Z^0/4 = 0.25$ meV (for $\theta = \theta' = 0$), and $\varepsilon_b = 12.5$.

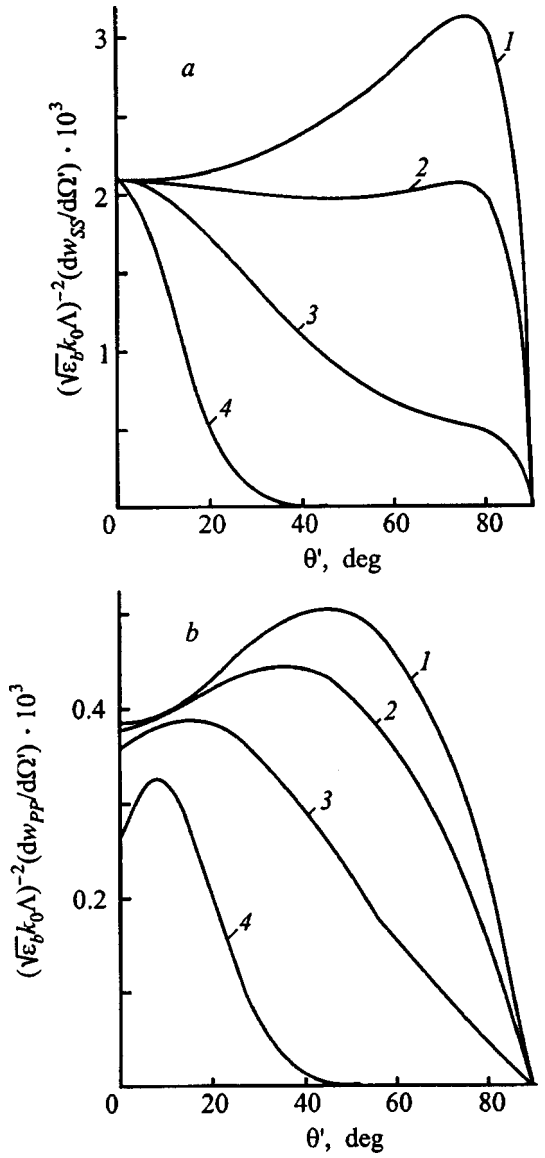

FIG. 3. Dependence on the angle θ' of the normalized dimensionless scattering cross sections $(\sqrt{\varepsilon_b} k_0 \Lambda)^{-2} dw/d\Omega'$ of the type $s \to s$ for $\omega = \omega_Y$, $\theta = 0$, $\varphi' = 0$ (a) and of the type $p \to p$ for $\omega = (\omega_X + \omega_Z)/2$, $\theta = 10°$, $\varphi' = 45°$ (b). The curves correspond to the following values of the parameter $\sqrt{\varepsilon_b} k_0 \Lambda$: (*1*) 0.42 ($\Lambda = 150$ Å); (*2*) 1.4 ($\Lambda = 500$ Å); (*3*) 2.8 ($\Lambda = 1000$ Å); (*4*) 7 ($\Lambda = 2500$ Å). All other parameters are the same as in Fig. 2.

$$g_{mn}(|\mathbf{R} - \mathbf{R}'|) = \exp(-|\mathbf{R} - \mathbf{R}'|^2/\Lambda_{mn}^2), \tag{29}$$

where Λ_{mn} is the transverse correlation length. Gaussian statistics are typical of systems having a large number of independent weak scatterers. Moreover, an investigation of the elastic scattering of light in the vicinity of exciton resonances has shown[9] that Gaussian statistics are suitable for describing the growth-roughened surfaces of semiconductors. Using Eq. (29) in (19) and (20) and assuming for simplicity that $g_{mm} = g$, $g_{mn} = gU$, $h_n = h$, and $\Lambda_{mn} = \Lambda$, we obtain the quantity (26) in the form

$$W_G(\mathbf{K}', \mathbf{K}) = \frac{1}{2\pi}\left(\frac{\sqrt{\varepsilon_b} k_0 h \Lambda}{\overline{L}}\right)^2 \times \exp\left(-\frac{|\mathbf{K} - \mathbf{K}'|^2 \Lambda^2}{4}\right)(1 - U). \tag{30}$$

Figures 2 and 3 show the results of numerical calculations of the cross sections $dw((\lambda \to \lambda)/d\Omega'$ using Eqs. (21) for $s \to s$ and (24) for $p \to p$ light scattering by GaAs/AlGaAs quantum wells. The role of $W(\mathbf{K}', \mathbf{K})$ is taken by the functions (30) with $U = 0$ corresponding to uncorrelated quantum well interfaces, for which $\langle \xi_m \xi_n \rangle = 0$ if $m \neq n$. The quantities shown in Fig. 2 refer to scattering through the $1e-1hh$ light-hole exciton state, for which $\Gamma_Z^0 \neq 0$, as opposed to the

$1e-1hh$ exciton state, for which $\Gamma_Z^0 \equiv 0$ (Refs. 10 and 11). The scattering spectra (Fig. 2) have resonance features at the exciton frequencies, where two resonance states with frequencies $\omega_X \neq \omega_Z$ are possible in the case of $p \to p$ scattering (Fig. 2b), but the second resonance vanishes in the limit $\theta \to 0$ or $\theta' \to 0$ as $\Gamma_Z(\kappa) \to 0$ in accordance with Eq. (16).

The intensity of secondary emission as a function of the polar scattering angle θ' (Fig. 3) depends strongly both on the polarization ($s \to s$ in Fig. 3a or $p \to p$ in Fig. 3b) and on the transverse correlation length of the unevenness Λ. For $\Lambda < 1/k_0$ the scattering is highly isotropic with respect to θ', and the main part of the backscattered light stays in the semiconductor, being reflected into it from the plane surface. For $\Lambda > 1/k_0$, on the other hand, the emission is concentrated within a comparatively small angle about the specular direction, and the main part of it can exist therefore outside the semiconductor.

It is instructive to compare the numerical scattering probabilities (Fig. 2) with the results of measurements of the analogous exciton spectra for statistically rough surfaces of semiconductors.[9] A comparison leads to the conclusion that the phenomena discussed above should be observable through the intensity for quantum wells having an unevenness rms height larger than 1 Å. The theoretical estimates of the scattering probability can be improved significantly by increasing the factor $(h\Lambda/\overline{L})^2$ in Eq. (30), but without losing sight of the fundamental condition $\Omega h/\overline{L} \ll \gamma$ underlying the validity of the above-formulated perturbation theory. The violation of this condition would signal the need to switch to a model of nonresonance (localized in the plane of the quantum well) exciton polariton states.

We have thus expressed the nonlocal exciton susceptibility and the intensity of resonance elastic scattering of light directly in statistical terms characterizing the rough interfaces of quantum wells. In the proposed theory, the random unevenness effects responsible for the onset of elastic scattering of light are distinct from the ''average'' quantum-well effects manifested in the reflection and transmission of light.[3] We have shown that only the first of the two scattering mechanisms discussed above, one associated with variation of the width of the quantum well, and the other with its bending, is valid in the general case. It follows from the numerical estimates that the differential cross section (probability) of elastic scattering of light in a quantum well can greatly exceed the existing level of experimental observability[9] if the unevenness is characterized by an atomic-scale rms height. Inasmuch as the contributions of the individual heterointerface unevenness are summed (with allowance for phase factors), strong enhancement of the above-described phenomena can be expected in structures containing many quantum wells.

This work has been supported by the Russian Fund for Fundamental Research (Grant No. 96-02-17929).

*)E-mail: Vladimir@polar.ioffe.rssi.ru

[1] S. Schmitt-Rink, D. S. Chemla, and D. A. B. Miller, Adv. Phys. **38**, 89 (1989).
[2] E. L. Ivchenko and G. E. Pikus, *Superlattices and Other Heterostructures: Symmetry and Optical Phenomena* (*Springer Series in Solid State Sciences*, Vol. 110), Springer-Verlag, Berlin-New York (1995).
[3] V. A. Kosobukin, Fiz. Tverd. Tela (Leningrad) **34**, 3107 (1992) [Sov. Phys. Solid State **34**, 1662 (1992)]; E. L. Ivchenko, A. I. Nesvizhskiĭ, and S. Jorda, Fiz. Tverd. Tela (St. Petersburg) **36**, 2118 (1994) [Phys. Solid State **36**, 1156 (1994)].
[4] F. Bechstedt and R. Enderlein, *Semiconductor Surfaces and Interfaces: Their Atomic and Electronic Structure* (Akademie-Verlag, Berlin, 1988; Mir, Moscow, 1990); J. Singh, K. K. Bajaj, and S. Chaudhuri, Appl. Phys. Lett. **44**, 804 (1984).
[5] J. Humlíček, E. Schmidt, L. Bočánek, R. Švehla, and K. Ploog, Phys. Rev. B **48**, 5241 (1993); S. Glutsch and F. Bechstedt, Phys. Rev. B **50**, 7733 (1994).
[6] T. Stroucken, A. Knorr, C. Anthony, A. Schulze, P. Thomas, S. W. Koch, M. Koch, S. T. Cundiff, J. Feldmann, and E. O. Göbel, Phys. Rev. Lett. **74**, 2391 (1995).
[7] R. Zimmermann, Nuovo Cimento D **17**, 1801 (1995); D. S. Citrin, Phys. Rev. B **54**, 14572 (1996); R. Zimmermann, E. Runge, and F. Grosse, in *Proceedings of the 23rd Conference on the Physics of Semiconductors*, edited by M. Scheffler and R. Zimmermann (World Scientific, 1996), p. 1935.
[8] V. A. Kosobukin, Solid State Commun. **108**, 83 (1998).
[9] V. A. Kosobukin and A. V. Sel'kin, JETP Lett. **44**, 483 (1986); Solid State Commun. **66**, 313 (1988); V. A. Kosobukin, M. I. Sazhin, and A. V. Sel'kin, Fiz. Tverd. Tela (Leningrad) **32**, 1023 (1990) [Sov. Phys. Solid State **32**, 602 (1990)]; Solid State Commun. **94**, 947 (1995).
[10] L. C. Andreani and F. Bassani, Phys. Rev. B **41**, 7536 (1991).
[11] E. L. Ivchenko, Fiz. Tverd. Tela (Leningrad) **33**, 2388 (1991) [Sov. Phys. Solid State **33**, 1344 (1991)].
[12] E. L. Ivchenko, V. P. Kochereshko, P. S. Kop'ev, V. A. Kosobukin, I. N. Uraltsev, and D. R. Yakovlev, Solid State Commun. **70**, 529 (1989).
[13] G. Bastard, E. E. Mendez, L. L. Chang, and L. Esaki, Phys. Rev. B **26**, 1974 (1982); R. L. Greene, K. K. Bajaj, and D. E. Phelps, Phys. Rev. B **29**, 1807 (1984); M. Matsuura and Y. Shinozuka, J. Phys. Soc. Jpn. **53**, 3138 (1984).
[14] V. A. Kosobukin, Phys. Status Solidi B **208**, 271 (1998).
[15] A. A. Maradudin and D. L. Mills, Phys. Rev. B **11**, 1392 (1975); D. L. Mills and A. A. Maradudin, Phys. Rev. B **12**, 2943 (1975).

Translated by James S. Wood

A new type of local polariton at the interface of gyrotropic enantiomorphic crystals

O. A. Dubovskiĭ and A. V. Orlov

Institute of Physics and Power Engineering, 249020 Obninsk, Kaluga Oblast', Russia
(Submitted April 13, 1998)
Fiz. Tverd. Tela (St. Petersburg) **41**, 337–340 (February 1999)

It is shown that a new type of local polariton can propagate at the interface of enantiomorphic twins—gyrotropic crystals with left-handed and right-handed rotation of the polarization plane. The wave function of these local polaritons oscillates strongly, with changes of sign, over lengths of the order of the lattice constant near the interface, and the period of the spatial oscillations grows with increasing distance from the interface. The local polariton term is detached from the band of delocalized states toward higher frequencies. Calculations of the radiation broadening of this term show that, for a local polariton, the effect of a giant increase of the decay (''superradiance'') is possible. The magnitude of the polarization rotation due to a local polariton has been found. © *1999 American Institute of Physics.* [S1063-7834(99)02802-6]

The study of exciton and vibrational excitations localized at various defects of the crystal lattice—impurities, vacancies, dislocations, and crystal boundaries—has attracted attention in connection with the possibility of their utility in various optical devices and in the solution of problems pertaining to the stability of various solid-state materials. The corresponding wave functions of various types of localized exciton and phonon states usually fall off monotonically with distance from the defect, and the radius of the local state, depending on the magnitude of the parameter describing the defect, e.g., the isotope shift for an isotopic impurity,[1,2] usually exceeds the lattice constant by a substantial amount. In work on gyrotropic crystals,[3,4] including liquid crystals rotating the polarization plane,[5] local polaritons (mixed exciton–photon modes) of a new type were found, propagating along their own kind of defect—the interface of differently rotating gyrotropic enantiomorphic crystals of quartz type—twins with left-handed and right-handed rotation. The existence of these local polaritons (LP) within the context of phenomenological electrodynamics with additional boundary conditions (ABC) is closely linked to the effect of spatial dispersion.[6] A number of unusual trends are observed in the behavior of their dispersion curves and spatial decay parameters. Note that these local polaritons have been found only in crystals of the class C_{2v} of the rhombic system and the class D_{2d} of the tetragonal system. The question remains open of a microscopic study of the possible existence of local states of such type in other crystal classes by testing the corresponding classes and additional boundary conditions, which fundamentally determine the very possibility of the existence of local polaritons and their parameters. In the present work, within the framework of a microscopic theory, we examine a system, accessible for an initial study, of contacting left-handed and right-handed one-dimensional crystals. Our results can be applied directly to follow-on studies of two-dimensional and three-dimensional crystal systems. Real systems of this type can be gyrotropic polymer chains and biological chains such as those investigated experimentally and theoretically in a number of studies.[7] A new, specific type of local polariton state has been found, having a rapidly sign-changing, spatially decaying wave function and a term of the local state detached from the band of delocalized states. This result shows that local polaritons of the type found in Refs. 3 and 4 and in the present work can exist not only in crystals of the classes C_{2v} and D_{2d}, but also in twins of other crystal groups. Note that quartz, for example, has symmetry D_3.

The inset to Fig. 1 depicts schematically what is in some sense a continuation of the simple, two-oscillator Kuhn model[8]—a crystal chain of periodically arrayed dipole oscillators of the corresponding monomers, oriented perpendicular to the chain axis, with left-handed rotation by an angle of $2\pi/3$ over the lattice constant for the sites $n \leqslant 0$ and with right-handed rotation for the sites $n \geqslant 0$. In the numbering of the sites $n = \ldots -2,-1,0,+1,+2 \ldots$ the value $n=0$ corresponds to the central oscillator dividing the two regions of left-handed and right-handed rotation.

The use of the corresponding microscopic theory,[1] which includes an account of translational motion of the excitons and also the exciton–photon retarding interaction within the framework of the second-quantization representation leads, after diagonalization of the corresponding Hamiltonian, to the following system of secular equations for the wave function Ψ_n of the symmetric polarized state $\Psi_n = \Psi_{-n}$ with energy $\hbar\omega$

$$(\omega^2-\omega_0^2)\Psi_n=\frac{2\omega_0|\mathbf{P}|^2}{\hbar a^3}\sum_{m\geqslant 0}\left[(1-\delta_{nm})\varphi(\omega,(n-m))+(1-\delta_{m0})\varphi(\omega,(n+m))\right]\times\cos\left(\frac{2\pi}{3}|n-m|\right)\Psi_m, \tag{1a}$$

$$\varphi(\omega,|n\pm m|)=\left[\frac{1}{|n\pm m|^3}-i\frac{((\omega/c)a)}{|n\pm m|^2}-\frac{((\omega/c)a)^2}{|n\pm m|}\right]\exp\left[i\left(\frac{\omega}{c}a\right)|n\pm m|\right],$$

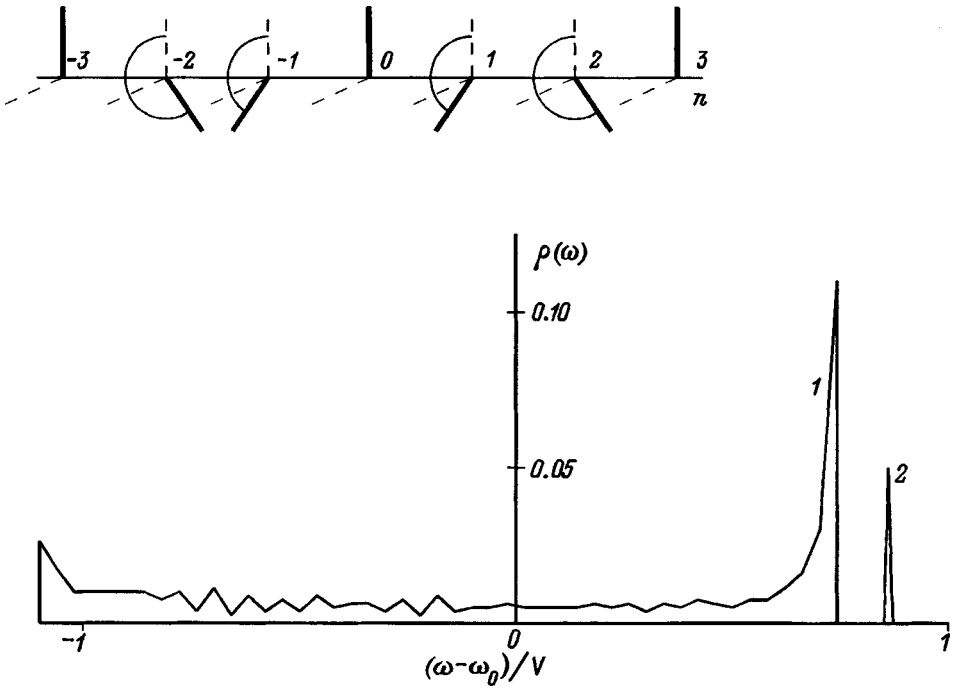

FIG. 1. Density of the polariton states of contacting enantiomorphic crystals. *1* — band of delocalized states, *2* — local polariton term. Inset shows a model chain of dipole oscillators.

$$0 \leqslant n \leqslant N. \tag{1b}$$

In Eq. (1) ω_0 is the frequency of the dipole transition in an isolated molecule, $\mathbf{P}$ is the corresponding matrix element of the dipole moment operator, a is the chain constant, self-action has been excluded ($n \neq m$), the second term on the right-hand side of Eq. (1a) describes the interaction of the enantiomorphous crystals, the first term on the right-hand side of Eq. (1b) describes the Coulomb interaction at close range, the third term—the interaction in the wave zone, and the second term describes the interaction in the intermediate region, and $2N+1$ is the number of chain sites. To find an exact solution of this complicated system of equations, where we set $\omega = \omega' - i\omega'$ and $\Psi_n = \Psi'_n + i\Psi''_n$, is quite a difficult task since ω appears on the right-hand side in a very complicated way. Note that this task can be completed in a follow-up work using the procedure employed in Ref. 9 of solving the ''inverse'' problem by finding $|\mathbf{P}|^2/\hbar a^3$ as the corresponding ''eigenvalue'' for fixed ω' and ω''.

We first carried out a preliminary calculation of the eigenfunctions and eigenenergies of an exciton in such a system ignoring the retarding interaction, i.e., for $c \to \infty$, $\omega/c \to 0$, so that in Eq. (1) only the Coulomb dipole–dipole interaction $\sim 1/|n \pm m|^3$ remains. Calculation of the spectrum of frequencies and wave functions of this system showed that above the upper edge of the band of delocalized exciton states there exists a term of the local state detached from the edge in frequency by the distance $\sim 0.12|\mathbf{P}|^2/\hbar a^3$ (as in Fig. 1) with a rapidly oscillating and decaying wave function (as in Fig. 2). A distinguishing feature of this state is the fact that near the interface oscillations with change of sign take place over the length of the lattice constant, and the period of the spatial oscillations gradually increases with distance away from the interface. The radius of the local state r, estimated from the formula $\Psi_n \cong \Psi_0 \exp[-(|n|a/r)](-1)^4$, is $r \cong 10a$. Results of a treatment taking into account only the Coulomb interaction pointed to the fundamental possibility of the existence of local polaritons, and the full matrix corresponding to system of equations (1) was then diagonalized. On the right-hand side of Eq. (1a), we set $\omega = \omega_0$ to simplify the calculations in the Heitler–London approximation. The value of the optical parameter $(\omega_0/c)a$ was set equal to 10^{-3}, which is a typical value for various crystals. The calculations yielded values of the frequency ω'_l and decay ω''_l of the polariton in units of $V \equiv |\mathbf{P}|^2/\hbar a^3$ as well as its wave function $\Psi_n^{(l)\prime} = \Psi_n^{(l)\prime} + i\Psi_n^{(l)\prime\prime}$ with the defining features of its spatial behavior indicated above.

Figure 1 depicts the band of delocalized states 1 in the form of a graph of the density of states calculated using the obtained values of the eigenvalues for a chain of 801 sites for $(\omega_0/c)a = 10^{-3}$. The behavior of the density of states in this band is typical for a linear crystal, note, however, with maxima of different height at the boundaries of the band. The solitary term of the local polariton state, detached by the frequency distance $0.12|\mathbf{P}|^2/\hbar a^3$ from the upper boundary of the band, is nominally represented as peak 2. The radiation broadening of this term of the local polariton, ω''_l, is substantially less than the detachment of this term from the upper edge of the band, their ratio is very small: $\hbar\omega''_l/(\hbar\omega'_l - \hbar\omega_{\max}) = 10^{-5}$, and the graphical representation of the broadening of this peak in Fig. 1 is only for illustrative purposes. At the same time, the calculated absolute value of the broadening of the local state substantially exceeds the value of the broadening of an isolated monomer $\omega''_l \cong (10 - 100|\mathbf{P}|^2)(\omega_0/c)^3/\hbar$ for $\omega_0 a/c \cong 10^{-3} - 10^{-4}$. The absolute value of the radiation broadening of the local-polariton term can be estimated numerically using typical experimen-

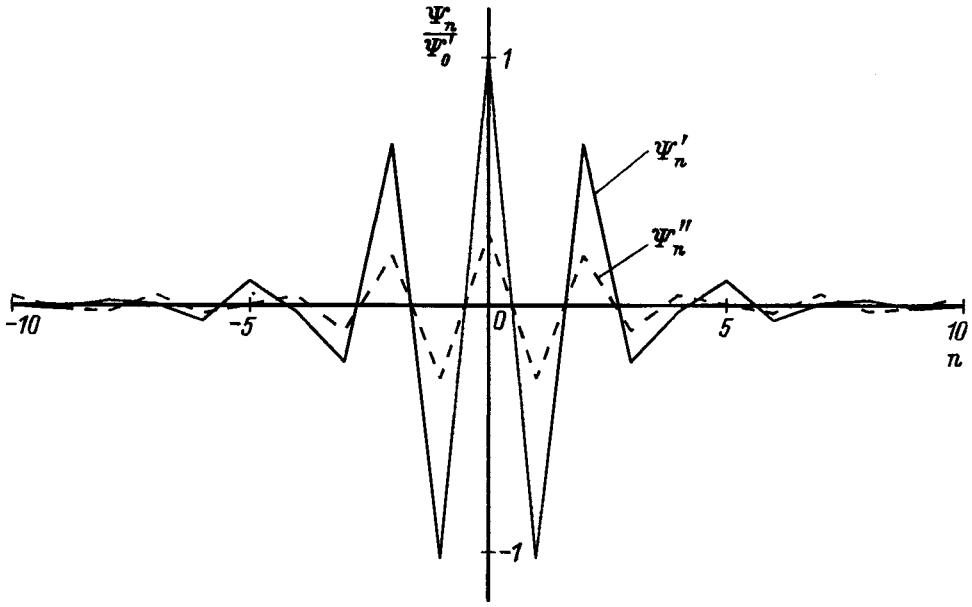

FIG. 2. Spatial dependence of the wave function of a local polariton $\Psi_n^{(l)}=\Psi_n^{(l)\prime}+i\Psi_n^{(l)\prime\prime}$. Solid line — $\Psi_n^{(l)\prime}$, Dashed line — $\Psi_n^{(l)\prime\prime}$.

tal values of the corresponding energy parameters $\hbar\omega_0\cong 1$ eV, $|\mathbf{P}|=0.2\,\text{Å}\cdot e$, $\omega_0 a/c\cong 10^{-3}$, and the width of the exciton band $|\mathbf{P}|^2/a^3\cong 0.1$ eV. Here the radiative decay of an isolated monomer $\hbar\gamma_0=|\mathbf{P}|^2(\omega_0/c)^3$ is equal to $\hbar\omega_0 \cong 10^{-10}$ eV, and the broadening of the local-polariton term $\hbar\omega_l''\cong 10^{-9}-10^{-8}$ eV for $\omega_0 a/c\cong 10^{-3}-10^{-4}$. The presence already in the one-dimensional system of a significant radiation broadening of the local-polariton terms indicates that, for a local state of the new type, it should be possible to observe the effect of a giant increase in the broadening (''superradiance'') in two-dimensional and three-dimensional twin crystal systems. Such an effect was first studied theoretically in Ref. 10 for one-dimensional and two-dimensional uniform crystals and was later observed experimentally.[11,12] Here the large factor $(c/\omega_0 a)\approx 10^3$ for the two-dimensional and for the three-dimensional twins $[(c/\omega_0 a)^2\approx 10^6]$ twins[10] can increase the radiation broadening to experimentally observable values on the order of $10^{-3}-1$ meV.

Figure 2 plots the wave function of the local state $\Psi_n^{(l)}=\Psi_n^{(l)\prime}+i\Psi_n^{(l)\prime\prime}$. It can be seen that $\Psi_n^{(l)\prime}$ (solid curve) has strong oscillations with change of sign across a distance of length a near the interface, and with distance away from the boundary this length grows. The wave function decays at a distance $\sim 10a$ [judging from an approximation using the function $\exp[-\chi na](-1)^n$]. The imaginary part $\Psi_n^{(l)\prime\prime}$ (dashed curve), magnified in Fig. 2 by a factor of 10^7, has similar decay and oscillations.

It would seem at first glance that oscillations of the wave function across a distance of length a should lead to a substantial decrease in the corresponding matrix elements defining the intensity of the various dynamic processes with decay and excitation of this local state. However, the analogous oscillatory behavior (again over a distance a) of the biphonon wave functions, for example,[13] for a given relation between the signs of the anharmonism constant and the effective mass, not only does not lead to a substantial decrease in the cross section of fission of the biphonons by neutrons, but, on the contrary, for a given relation between these two signs, gives the same value of the cross section as for a non-oscillating, monotonically decreasing wave function, which is evidence of some kind of universality as has been noted earlier by other authors. The way that this pertains to the new type of local polariton requires further study.

In this vein, in connection with the question of the rotation of the polarization plane, which is important with regard to gyrotropic crystals, the question of the polarization of the radiation emitted upon decay of the newly discovered local state is also of interest. The electric field vector $\mathbf{E}$ at the point $\mathbf{R}$ of the wave zone of the given crystal system of radiating oscillators is given by the following expression:

$$\mathbf{E}(\mathbf{R})=-\sum_n \frac{(\omega^2/c^2)}{|\mathbf{R}_n|^3}[\mathbf{R}_n[\mathbf{R}_n\mathbf{P}_n]]\exp\left(i\frac{\omega_l}{c}|\mathbf{R}_n|\right),$$

$$\mathbf{R}_n=\mathbf{R}-\mathbf{j}na,\quad \mathbf{P}_n=|\mathbf{P}|\Psi_n^{(l)}\mathbf{e}_n, \tag{2}$$

where $\mathbf{j}$ is the unit vector of the chain axis, $\mathbf{e}_n$ are the unit vectors of the corresponding dipole moments. To simplify the calculations, we used the approximating wave functions of the local state $\tilde{\Psi}_n^{(l)}=\Psi_0\exp[-\chi na](-1)^n$. Substitution of this function in expression (2) gives the following value for the electric field vector $\mathbf{E}$ assuming strong decay $\chi a>1$:

$$\mathbf{E}(\mathbf{R})=-\frac{(\omega^2/c^2)}{|\mathbf{R}|^3}[\mathbf{R}[\mathbf{R}(\mathbf{P}_0+\sqrt{3}e^{-\chi a}[\mathbf{j}\mathbf{P}_0])]]$$

$$\times\exp\left[i\frac{\omega_l}{c}|\mathbf{R}|\right]. \tag{3}$$

It is clear from expression (3) that the effective dipole moment of the system is rotated relative to the central dipole moment to the right, toward the vector $[\mathbf{j}\mathbf{P}_0]$, and the magnitude of this rotation is determined by the decay factor

$\exp(-\chi a)$. Of course, the use of exact values for Φ_n (Fig. 2) numerically alters the magnitude of the corresponding rotations.

Local polaritons of the newly discovered type also exist, obviously, in crystal systems of larger dimensionality. Further study of this question in application to a two-dimensional system of contacting enantiomorphic half-planes with a one-dimensional interface is of interest.

In conclusion, we would like to express our sincere gratitude to V. M. Agranovich for helpful discussions.

This work was carried out with the support of the Russian State Scientific–Technical Program ''Promising Directions in the Physics of Condensed Media'' under the heading ''Neutron Studies of Matter.'' The first author thanks the Volkswagen Foundation for partial support (Grant No. 1/69928).

[1] V. M. Agranovich, *Theory of Excitons* [in Russian] (Nauka, Moscow, 1969).
[2] V. M. Agranovich and O. A. Dubovsky, *Optical Properties of Mixed Crystals* (North-Holland, Amsterdam, 1988), p. 297.
[3] V. M. Agranovich and O. A. Dubovskiĭ, JETP Lett. **26**, 488 (1977).
[4] V. M. Agranovich and O. A. Dubovskiĭ, Fiz. Tverd. Tela (Leningrad) **20**, 3237 (1978) [Sov. Phys. Solid State **20**, 1867 (1978)].
[5] Ya. B. Zel'dovich, Zh. Éksp. Teor. Fiz. **67**, 2357 (1974) [Sov. Phys. JETP **40**, 1170 (1975)].
[6] V. M. Agranovich and V. L. Ginzburg, *Crystal Optics with Spatial Dispersion, and Excitons* (Springer-Verlag, New York, 1984, Nauka, Moscow, 1979) 432 pp.
[7] W. Moffitt, J. Chem. Phys. **23**, 467 (1956).
[8] M. V. Vol'kenshteiĭn, *Molecular Optics* [in Russian] (Gostekhizdat, Moscow, 1951), 744 pp.
[9] V. M. Agranovich, O. A. Dubovsky, and D. Basko, J. Chem. Phys. **106**, 3896 (1997).
[10] V. M. Agranovich and O. A. Dubovskiĭ, Pis'ma Zh. Éksp. Teor. Fiz. **3**, 345 (1966) [JETP Lett. **3**, 223 (1966)].
[11] Ya. Aaviksoo, Ya. Lipmaa, and T. Reĭnot, Opt. Spektrosk. **62**, 419 (1987) [Opt. Spectrosc. **62**, 250 (1987)].
[12] B. Deveaud, F. Clérot, N. Roy, K. Satake, B. Sermage, and D. S. Katzer, Phys. Rev. Lett. **67**, 2355 (1991).
[13] O. A. Dubovskiĭ and A. V. Orlov, Fiz. Tverd. Tela (St. Petersburg), **41**, in press (1999) [Phys. Solid State **41**, in press (1999)].

Translated by Paul F. Schippnick

POLYMERS. LIQUID CRYSTALS

The effect of surface roughness of a solid substrate on its wetting by a smectic-*A* structure in the nematic phase of a liquid crystal

L. V. Mirantsev and A. V. Zakharov

Institute of Problems of Machine Building, Russian Academy of Sciences, 199178 St. Petersburg, Russia

V. G. Korsakov

St. Petersburg State Technological University, 195251 St. Petersburg, Russia
(Submitted April 17, 1998)
Opticheskiĭ Zhurnal **41**, 341–347 (February 1999)

The effect of regular wavy microrelief of a substrate surface on the formation of a smectic-*A* (Sm*A*) surface structure in a nematic liquid crystal (NLC) near the nematic–smectic-*A* second-order phase transition temperature has been investigated theoretically. Within the framework of the Ginzburg–Landau model we have obtained the dependence of the surface smectic-order parameter and the penetration depth of a Sm*A* surface structure into the NLC on the amplitude and period of the substrate microrelief. The effect of surface roughness on wetting by a Sm*A* structure in the nematic phase of the liquid crystal is investigated. It is shown that the wetting of a rough surface by the smectic phase is always incomplete. It is also shown that sufficiently sharp microrelief of a substrate surface can suppress the Sm*A* surface structure almost completely. © *1999 American Institute of Physics.* [S1063-7834(99)02902-0]

It is well known that the surface properties of liquid crystals (LC) differ significantly from their bulk properties.[1,2] The interaction of LC molecules with the bounding surface (a free surface, the surface of a solid substrate) leads to a substantial change in the degree of orientational order in the surface layer of the nematic phase[3–8] and can even induce some orientational order in the near-surface region of the isotropic phase of a liquid crystal.[9–12] The bounding surface can also induce layered smectic structures in the near-boundary region of a nematic liquid crystal (NLC). In other words, the bounding surfaces of positionally disordered liquid-crystal phases can be wetted by a smectic phase possessing uniform translational order.[13] At present, the existence of surface-induced smectic structures in the isotropic phase and the nematic phase of a liquid crystal is a firmly established fact; they are objects of intense experimental[14–21] and theoretical[22–25] study.

One of the more important problems arising in the study of surface smectic structures is the effect of microrelief (roughness) of the surface of a solid substrate on its wetting by these structures. The point is that only the free surface of the liquid crystal can be assumed to be an ideally smooth bounding surface. In the overwhelming majority of experimentally realized situations, a solid substrate surface possesses some microrelief. In addition, surface relief of various geometrical shapes can be created artificially, e.g., by sputtering thin films of various oxides (SiO, GeO, etc.)[26] onto the solid substrate surface, as well as photolithographically.[27–29] In Ref. 30 it was shown that a sufficiently strong deformation of a solid substrate surface lowers the orientational order in the surface layer of a nematic. Obviously, surface microrelief deforming the nearby smectic layers should also have a negative effect on the formation of a surface smectic structure in a liquid crystal, and this effect should be much stronger than in the case of a pure nematic since the deformation energy of the smectic layers significantly exceeds the energy of bending deformations in a NLC.[13] Note that the overwhelming majority of experimental data on surface smectic structures was obtained with the help of small-angle x-ray scattering measurements from the free surface of the liquid crystal. In this situation, near nematic–smectic-*A* (N–Sm*A*) second-order phase transitions[14,15,17,18,20] the penetration depth of the surface smectic structure into the NLC reached a macroscopic value ($\sim 0.1\,\mu$m), which speaks of complete wetting of the free surface of the NLC by the smectic-*A* phase. In the vicinity of isotropic phase–smectic-*A* (I – Sm*A*) first-order phase transitions,[19,20] this depth did not exceed a thickness of several smectic layers (~ 100 Å), which speaks of a partial or incomplete wetting by the Sm*A* phase of the free surface of the isotropic phase of a liquid crystal. As for the nematic (isotropic) phase–solid substrate interface, the number of experiments demonstrating its wetting by the surface smectic structure[16,21] is significantly less than the number of analogous experiments for the free surface. This fact receives especial note in the review on surface effects in liquid crystals contained in Ref. 2. In this same article it is suggested that such a ''quasi-absence'' of experimentally revealed surface smectic structures near the LC–solid substrate interface may be due to surface roughness of the substrate. However, at present, the effect of microrelief

of a solid substrate on the smectic structures induced by it in the liquid crystal has not been examined in detail, and theoretical works on surface smectic structures[22–25] have considered only the case of an ideally smooth bounding surface. One consequence of this is the absence of any estimates of the quality of surface treatment of a solid substrate needed for it to be wetted by a surface smectic structure at a temperature above the transition temperature to the Sm*A* phase in the bulk of the liquid crystal.

In the present paper we present a theoretical description of a Sm*A* structure in a NLC induced by a solid substrate surface with regular microrelief in the vicinity of the $N-$Sm*A* second-order phase transition temperature. For simplicity, the microrelief is represented in the form of a uniform harmonic function with period much larger than the atomic scale. The dependences of the surface smectic-order parameter and the penetration depth of the Sm*A* surface structure into the NLC as functions of the amplitude and period of the microrelief of the substrate are obtained. The effect of surface roughness of the substrate surface on its wetting by a Sm*A* structure in the nematic phase of the LC is investigated. It is shown that wetting of a rough surface by the Sm*A* phase is always incomplete. It is also shown that the existence of sufficiently rough microrelief on a substrate surface can lead to almost complete suppression of the surface Sm*A* structure.

1. BASIC EQUATIONS OF THE MODEL

Let us consider a layer of NLC in contact with the surface of a solid substrate with wavy microrelief described by the one-dimensional harmonic function

$$U_0(x)=U_0\cos((2\pi/d)x), \tag{1}$$

where U_0 is the amplitude and d is the period of the wavy microrelief. We assume that the NLC layer is oriented homeotropically (the director **n** in the bulk of the sample is parallel to the z axis, which is perpendicular to the substrate surface). We also assume that we find ourselves in the vicinity of the $N-$Sm*A* second-order phase-transition temperature (temperature of the NLC slightly above the transition temperature) and, in the sample under study, there exists uniform orientational order, close to ideal (the orientational order parameter S does not depend on the coordinates and is equal to 1, i.e., the long axes of all the molecules are oriented parallel to the director **n**). This latter assumption is entirely reasonable since, in the majority of liquid crystals, $N-$Sm*A* second-order phase transitions occur quite far from the clearing point, and in a nematic almost ideal orientational order is achieved ($S\approx 1$).

We assume that, thanks to the interaction of the NLC molecules with the surface, a translationally ordered, layered Sm*A* phase with period equal to the length of a molecule l is induced near the surface (for simplicity we assume the surface smectic structure to be a monolayer classical Sm*A* phase). If the substrate surface is ideally smooth, then the molecules inside the smectic layers will be strictly perpendicular to the surface, and the layers themselves will be parallel to it. If it is assumed that the molecules in the first near-surface layer rigidly adhere to the surface, then this layer is distorted with the same period as that of the wavy deformation of the substrate surface and this deformation, due to the small transverse compressibility of the smectic layers, is transmitted along a chain of neighboring layers, gradually attenuating with depth into the sample. Obviously, such a deformation of the near-surface smectic phase should have an effect on the degree of translational order of that phase, i.e., on the magnitude of the smectic order parameter. On the other hand, the depth of propagation of a deformation induced by the substrate surface into a LC layer depends on the bulk modulus B of the near-surface smectic layers, which is determined by their translational order.[31] Thus, for a complete description of the state of the near-surface region of the NLC it is necessary to determine the profile of the smectic order parameter for a given surface deformation and describe the propagation of the surface-generated wavy deformation $U(x,z)$ into the NLC with allowance for the existence of a near-surface Sm*A* structure.

To solve the problem formulated above, it is necessary to know an expression for the free-energy density in the deformed near-surface layer of the NLC. Obviously, this expression should contain two terms. The first of these terms is the Oseen–Frank free energy density in the deformed NLC, associated with the director gradients[13,31]

$$f_N=(K_1/2)(\operatorname{div}\mathbf{n})^2+(K_2/2)(\mathbf{n}\cdot\operatorname{curl}\mathbf{n})^2 +(K_3/2)(\mathbf{n}\times\operatorname{curl}\mathbf{n})^2, \tag{2}$$

where K_1, K_2, and K_3 are the Frank elastic moduli for the deformations of transverse bending, twisting, and longitudinal bending, respectively. If it is assumed that the wavy microrelief of the substrate surface is weak enough $[(2\pi/d)U_0\ll 1]$, then the components of the director **n** are related to the displacement of the smectic layers $U(x,z)$ by the following equations:

$$n_x\approx-\partial U/\partial x,\quad n_y=0,\quad n_z\approx 1. \tag{3}$$

Substituting these relations into Eq. (2), it is not hard to obtain

$$f_N\approx(K_1/2)(\partial^2U/\partial x^2)^2+(K_3/2)(\partial^2U/\partial x\partial z)^2. \tag{4}$$

The second contribution to the free-energy density in the near-surface layer is the free-energy density of the surface-induced smectic Sm*A* phase, which is also deformed thanks to the surface microrelief. If $\sigma(z)$ is the smectic order parameter, and $U(x,z)$ is the displacement of the smectic layers due to the regular surface microrelief, then the Sm*A* phase induced by this surface in the vicinity of the $N-$Sm*A* second-order transition is described by the wavy microdensity[31]

$$\rho(x,z)=\rho_0[1+\sigma(z)\cos(2\pi(z-U(x,z))/l)], \tag{5}$$

where ρ_0 is the mean density of the LC. Here the free energy density of such a Sm*A* structure is given by the following expression of Ginzburg–Landau type:

$$f_{SmA}=(A/2)\sigma^2+(C/4)\sigma^4 +(L/2)(d\sigma/dz)^2+(B/2)(\partial U/\partial z)^2, \tag{6}$$

where $A=\alpha(T-T_{NA})$, α is a constant, T is the temperature of the system, T_{NA} is the $N-\mathrm{Sm}A$ second-order transition temperature, C is a constant, and L is an elastic constant which determines within the context of the mean-field theory the longitudinal correlation length ξ of the fluctuations of the smectic order in the nematic phase in the vicinity of the $N-\mathrm{Sm}A$ second-order transition, thus[31]

$$\xi=(L/A)^{1/2}. \tag{7}$$

The first three terms of expression (6) describe the free energy density of an undeformed SmA structures induced by a perfectly smooth surface, and the fourth term defines the contribution to the free-energy density of the surface layer of the LC due to deformation of the smectic layers. According to Ref. 31, the bulk modulus of the smectic layers B is proportional to the square of the smectic-order parameter σ, and can be written as

$$B=B_0\sigma^2, \tag{8}$$

where the elastic constant B_0 is related to the elastic constant L by the formula $B_0=L(2\pi/l)^2$. Combining Eqs. (4) and (6) and noting relation (8), we obtain the following expression for the free-energy density of the LC layer near the deformed substrate surface:

$$\begin{aligned} f=f_N+f_{\mathrm{Sm}A}&=(K_1/2)(\partial^2U/\partial x^2)^2\\ &+(K_3/2)(\partial^2U/\partial x\partial z)^2+(A/2)\sigma^2+(C/4)\sigma^4\\ &+(L/2)(d\sigma/dz)^2+(B_0/2)\sigma^2(\partial U/\partial z)^2. \end{aligned} \tag{9}$$

To obtain the total free energy of the near-surface region of the NLC, it is necessary to integrate expression (9) over the half-space above the substrate surface and add the energy of the direct interaction of the LC molecules with the substrate to the obtained result. If we assume for simplicity that this interaction reduces to short-range attraction forces, then the corresponding potential for a substrate surface with microrelief $U_0(x)$ can be represented in the form

$$G(z)=-G_0\delta(z-U_0(x)), \tag{10}$$

where G_0 is the interaction constant of the LC molecules with the substrate. Thus, the energy of the direct interaction of the LC molecules with the substrate per unit area of its surface turns out to be equal to

$$F_s=\int_0^\infty G(z)\rho(x,z)dz=-G_0\rho_0-G_0\rho_0\sigma_0, \tag{11}$$

where σ_0 is the value of the smectic order parameter on the substrate surface. Finally, the total free energy of the near-surface LC layer per unit area of the substrate can be represented in the form

$$F=\int_0^\infty \overline{f}(z)dz-G_0\rho_0-G_0\rho_0\sigma_0, \tag{12}$$

where $\overline{f}(z)$ is the free energy density (9) of the near-surface LC layer after averaging over the XY plane. If we seek the dependence of the displacement of the smectic layers on the coordinates $U(x,z)$ in the form

$$U(x,z)=U(z)\cos((2\pi/d)x),$$

$$U(z)\big|_{z=0}=U_0, \tag{13}$$

then we find that such averaging yields the following expression for $\overline{f}(z)$:

$$\begin{aligned} \overline{f}&=(A/2)\sigma^2+(C/4)\sigma^4+(L/2)(d\sigma/dz)^2\\ &+(B_0/4)\sigma^4(dU/dz)^2+(K_1/4)(2\pi/d)^4U^2\\ &+(K_3/4)(2\pi/d)^2(dU/dz)^2. \end{aligned} \tag{14}$$

After substituting expression (14) in Eq. (12) we must minimize the free energy functional (12) over the variables $\sigma(z)$, $U(z)$, and σ_0. The standard minimization procedure leads us to the Euler–Lagrange equations

$$L(d^2\sigma/dz^2)-A\sigma-C\sigma^3-(B_0/2)\sigma(dU/dz)^2=0, \tag{15}$$

$$\begin{aligned} &\frac{d}{dz}((B_0/2)\sigma^2(dU/dz))+(K_3/2)(2\pi/d)^2(d^2U/dz^2)\\ &\quad-(K_1/2)(2\pi/d)^4U=0 \end{aligned} \tag{16}$$

and the boundary condition

$$\left.\frac{\partial\overline{f}}{\partial(\partial\sigma/\partial z)}\right|_{z=0}=-G_0\rho_0. \tag{17}$$

Simultaneous solution of Eqs. (15) and (16) together with the boundary condition (17) and the condition of total decay in the bulk of the sample of both the smectic order and the deformations induced by the substrate surface ($\sigma\to0$, $d\sigma/dz\to0$, $U\to0$, $dU/dz\to0$ as $z\to\infty$) yields the profile of the smectic order parameter and determines the propagation of deformations into the depth of a non-uniform LC layer with surface SmA structure. These equations are nonlinear second-order differential equations with cross terms, and their exact solution can be obtained only numerically. Let us attempt to obtain an approximate solution of Eqs. (15) and (16). Here we can make use of the following arguments. Even in the case of an ideally smooth surface the smectic order induced by it decays in the bulk of the NLC at a distance on the order of the longitudinal correlation length ξ (Ref. 17). According to the experimental data,[32] at a temperature roughly 0.1 K above the $N-\mathrm{Sm}A$ second-order transition temperature $\xi\sim0.1\,\mu$m. On the other hand, if the period of the wavy microrelief of the substrate surface $d\sim1\,\mu$m, then the depth of propagation of the deformations induced by this microrelief even in a pure NLC (without allowance for the near-surface smectic structure) should be $\sim d\sim1\,\mu$m (Ref. 13), i.e., an order of magnitude greater than ξ. Consequently, it is entirely reasonable to assume that the smectic-order parameter $\sigma(z)$ is a rapidly decaying function of the distance z to the substrate surface in comparison with $U(z)$. Thus, in the third term of Eq. (16) U can be taken to be constant and we can approximately set it equal to U_0. Then it is possible to integrate the approximate equation obtained in this way over any interval z_2-z_1 within the limits of the existence region of the SmA phase. As a result we obtain

$$[B_0\sigma^2(z_1)+K_3(2\pi/d)^2](dU/dz_1)$$
$$\approx[B_0\sigma^2(z_2)+K_3(2\pi/d)^2](dU/dz_2)$$
$$-K_1(2\pi/d)^4U_0(z_2-z_1). \quad (18)$$

If as z_2 we take the point at which the surface smectic order can be considered to a significant degree to have already decayed $[\sigma(z_2\approx 0)]$, then dU/dz_2 can be found from the equation

$$dU/dz_2=-(K_1/K_3)^{1/2}(2\pi/d)U, \quad (19)$$

describing the decay of the wavy deformation in a homeotropically ordered NLC.[13] Hence it follows that

$$[B_0\sigma^2(z_1)+K_3(2\pi/d)^2](dU/dz_1)$$
$$\approx-(K_1K_3)^{1/2}(2\pi/d)^3U_0-K_1(2\pi/d)^4U_0(z_2-z_1). \quad (20)$$

Here the ratio of the second term on the right-hand side of Eq. (20) to the first term is equal to $(K_1/K_3)^{1/2}[2\pi(z_2-z_1)/d]$. Since the depth of propagation of the surface smectic order into the NLC is an order of magnitude smaller than the period d, and near the $N-$SmA second-order phase transition the longitudinal bending modulus of the nematic K_3 is significantly greater than the transverse bending modulus K_1 (Refs. 13 and 31), the value of this ratio should be much less than unity. Thus, the second term on the right-hand side of the equation can be omitted and we obtain

$$(dU/dz)\approx-\frac{(K_1/K_3)^{1/2}(2\pi/d)^3U_0}{[B_0\sigma^2(z)+K_3(2\pi/d)^2]}. \quad (21)$$

Substituting the approximate expression obtained for (dU/dz) into Eq. (15), we can integrate it once. If we make use here of the condition of total decay of the near-surface smectic structure in the bulk of the NLC, we obtain the following solution:

$$(d\sigma/dz)\approx-\sqrt{W(\sigma,U_0,d)}, \quad (22)$$

where

$$W(\sigma,U_0,d)=\xi^{-2}\sigma^2+C^*\sigma^4+(K_1/2L)(2\pi/d)^4U_0^2$$
$$\times\{1-[(B_0/K_3)(d/2\pi)^2\sigma^2+1]^{-1}\}, \quad (23)$$

and $C^*=C/2L$. Equation (22) directly yields the equation

$$z=\int_{\sigma(z)}^{\sigma_0}\frac{d\sigma}{\sqrt{W(\sigma,U_0,d)}}, \quad (24)$$

defining the profile of the smectic order parameter $\sigma(z)$. Here the magnitude of the smectic order parameter at the surface σ_0 can be found from a combination of Eq. (22) and the boundary condition (17). Taking into account that

$$\left.\frac{\partial\overline{f}}{\partial(\partial\sigma/\partial z)}\right|_{z=0}=L\left.\frac{d\sigma}{dz}\right|_{z=0}, \quad (25)$$

it is not hard to obtain the algebraic equation

$$W(\sigma_0,U_0,d)=(G_0\rho_0/L)^2, \quad (26)$$

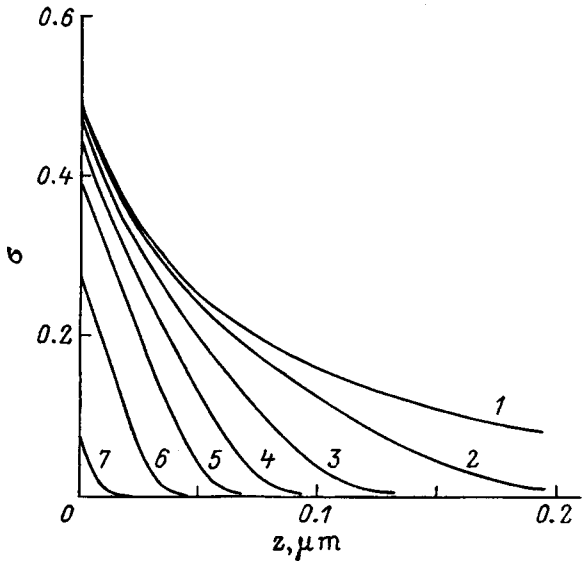

FIG. 1. Profile of the surface smectic-order parameter for different values of the amplitude of the wavy microrelief of the substrate surface. $d=1$ μm. U_0(μm): *1* — 0, *2* — 0.01, *3* — 0.02, *4* — 0.03, *5* — 0.04, *6* — 0.05, *7* — 0.06.

determining the value of σ_0.

Since we are interested in the effect of the surface microrelief of a solid substrate on its wetting by the surface Sm A structure at a temperature above the transition temperature to the SmA phase in the bulk of the LC, it is necessary to determine the adsorption coefficient Γ of the SmA structure for such a surface. According to Ref. 2, this coefficient is equal to

$$\Gamma=\int_0^\infty\sigma(z)dz. \quad (27)$$

If $\Gamma=0$, then the substrate surface is not wetted by the SmA phase. If $\Gamma\neq 0$, but remains finite as $T\to T_{NA}$, then incomplete wetting takes place. Finally, if $\Gamma\to\infty$ as $T\to T_{NA}$, then it is possible to speak of complete wetting of the substrate surface by the SmA structure above the transition temperature to the SmA phase in the bulk of the LC. It can be easily seen that taking Eq. (22) into account, Eq. (27) can be reduced to the form

$$\Gamma=\int_0^{\sigma_0}\frac{\sigma d\sigma}{\sqrt{W(\sigma,U_0,d)}}, \quad (28)$$

which is more suitable for numerical calculation.

2. RESULTS OF NUMERICAL CALCULATIONS AND DISCUSSION

The relations obtained allow us to determine profiles for the order parameter describing the SmA structure induced in a nematic LC by a solid substrate surface with wavy microrelief in the vicinity of the $N-$SmA second-order phase transition temperature. These profiles, obtained for several values of the microrelief amplitude U_0 with fixed period $d=1$ μm, are shown in Fig. 1. Here we used the following values of the necessary parameters: $(T-T_{NA})/T_{NA}=10^{-4}$,

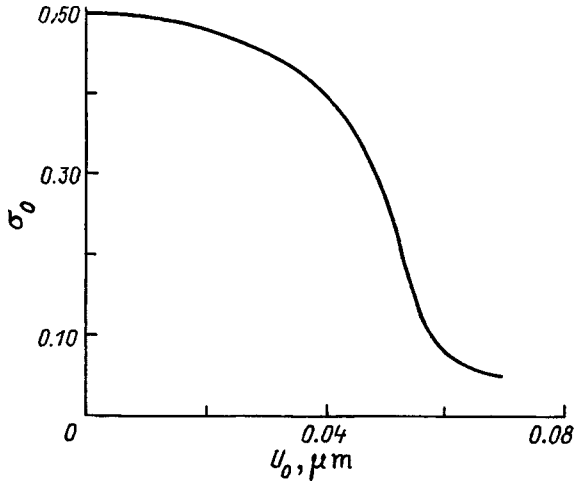

FIG. 2. Dependence of the smectic-order parameter of the substrate surface on the amplitude of the wavy surface microrelief. $d=1$ μm.

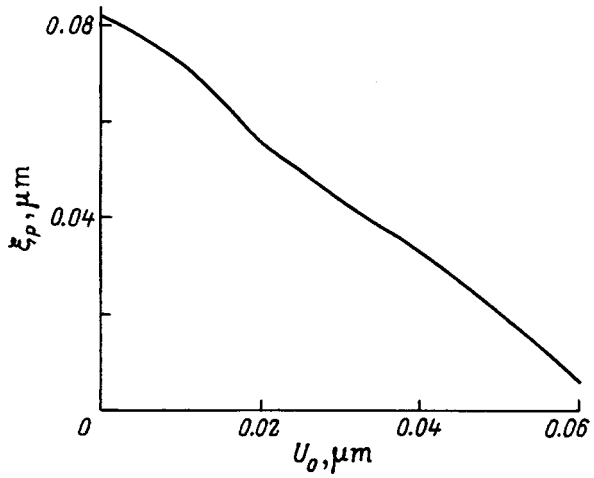

FIG. 3. Penetration depth of the surface smectic order into the NLC versus the amplitude of the wavy surface microrelief. $d=1$ μm. $(T-T_{NA})/T_{NA}=10^{-4}$.

$T_{NA}\approx 307$ K, $\xi=0.16$ μm, $K_1=10^{-6}$ dyn, $l=3\times10^{-7}$ cm (data for the liquid crystal 8 CB from Ref. 32), and $C^*\approx 1200$ (Ref. 33). The quantity B_0 was determined with the help of the relation $B_0/K_1\approx 1/l^2$ (Refs. 13 and 31). It was also assumed that the elastic moduli K_3 and K_1 are related as

$$K_3/K_1\approx 1+(K_BT/6)(\pi\xi l^2K_1), \tag{29}$$

where K_B is the Boltzmann constant. This relation can be derived using the results of Ref. 34, which studied the effect of fluctuations of smectic short-range order in the bulk nematic phase on the longitudinal bending modulus of the NLC K_3 near the $N-$SmA second-order phase transition. As for the values of the parameter $G_0\rho_0/L$, its choice is entirely arbitrary in view of the absence of any detailed information regarding the direct interaction of the LC molecules with the substrate surface. Therefore we have chosen it so as to obtain a reasonable value, e.g., $\sigma_0=0.5$ for the smectic order parameter at the surface of an ideally smooth substrate ($U_0=0$). It can been seen from Fig. 1 that the presence of wavy microrelief on the surface of the substrate leads to suppression of the surface SmA structure, and the sharper the microrelief (the larger the amplitude U_0 for a fixed value of the period d), the ''weaker'' is the surface smectic structure. Here, both the absolute value σ_0 of the smectic-order parameter at the substrate surface (Fig. 2) and the ''penetration depth'' of smectic order into the NLC (as this depth ξ_P we take the distance from the substrate surface at which the smectic order parameter has decreased by a factor of e in comparison with its value at the surface σ_0). It can be seen from Fig. 3 that the depth ξ_P falls off almost linearly with growth of U_0 almost linearly.

As has already been mentioned, the wettability of the solid substrate—NLC interface by the SmA-structure near the $N-$SmA second-order phase transition point is determined by the magnitude of the adsorption coefficient Γ. Figure 4 plots temperature curves of this coefficient, calculated numerically according to Eq. (28) for different values of the amplitude U_0 of the wavy microrelief (its period was taken as fixed and equal to $d=1$ μm). It can be seen from the figure that for an ideally smooth substrate (curve *1*) as the phase transition temperature T_{NA} is approached the temperature dependence of Γ in the bulk of the LC asymptotically approaches a linear dependence on $-\ln((T-T_{NA})/T_{NA})$ (the asymptote is shown in the figure as a dashed line). It is not hard to convince oneself of the validity of this result considering that for $U_0=0$ the integral (28) behaves analytically and as $T\to+T_{NA}$ it is possible to obtain the following asymptotic relation:

$$\Gamma=(1/2)C^{*-1/2}\ln(4G_0\rho_0C^{*-1/2}A^{-1}). \tag{30}$$

Since $A=\alpha(T-T_{NA})$, as $T\to+T_{NA}$ $\Gamma\sim\ln((T-T_{NA})/T_{NA})\to\infty$. Consequently, the surface SmA structure should completely wet an ideal smooth solid substrate near the $N-$SmA second-order phase transition. However, it follows from Fig. 4 that the existence of even a very ''shallow'' microrelief leads to a substantial deviation from the

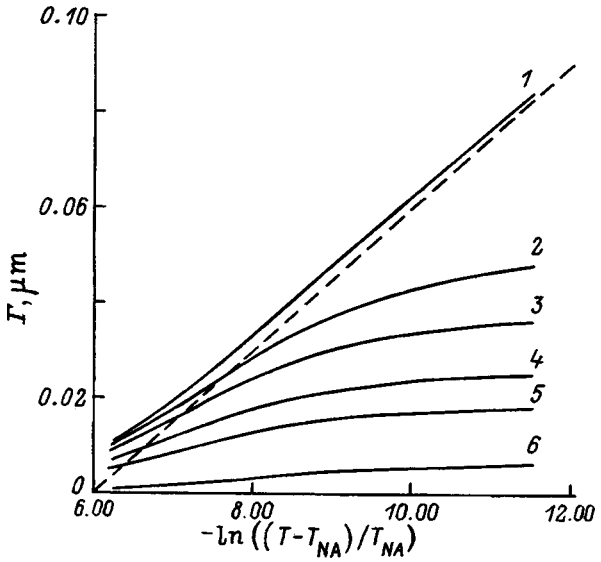

FIG. 4. Temperature dependence of the adsorption coefficient of a SmA structure at the solid substrate–NLC interface for different amplitudes of the wavy microrelief of the substrate surface. $d=1$ μm. $U_0(\mu m)$: *1* — 0, *2* — 0.005, *3* — 0.01, *4* — 0.02, *5* — 0.03, *6* — 0.05.

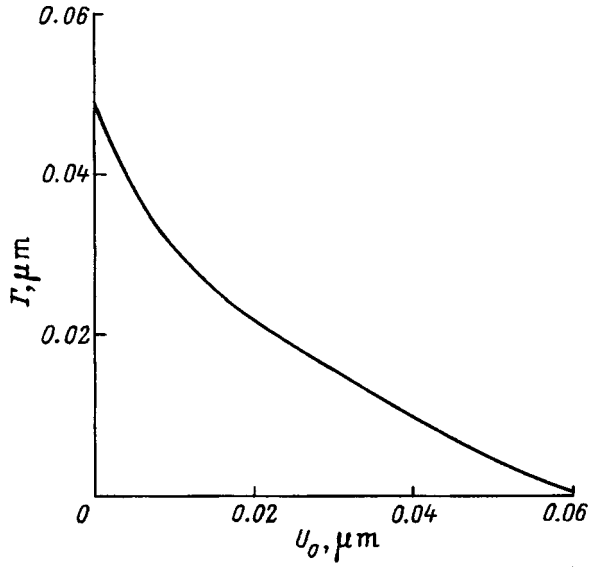

FIG. 5. Dependence of the adsorption coefficient Γ on the amplitude of surface microrelief. $d=1\ \mu$m. $(T-T_{NA})/T_{NA}=1.1\times10^{-4}$.

asymptotic dependence (30). It is easy to see that in the presence of an arbitrarily weak deformation of the surface the dependence of Γ on $\ln((T-T_{NA})/T_{NA})$ saturates and the adsorption coefficient of the surface Sm*A* structure should remain finite no matter how closely the $N-$Sm*A* phase transition temperature is approached. In other words, wetting of a rough substrate surface by a Sm*A* structure above the transition temperature to the Sm*A* phase in the bulk of a LC is always incomplete. It can also be seen from Fig. 4 that the larger the amplitude U_0 of the surface microrelief, the faster the temperature dependence of the adsorption coefficient saturates and the smaller will be the absolute value of Γ. Figure 5 plots the dependence of the adsorption coefficient on the amplitude of the microrelief U_0 at a fixed temperature slightly above the $N-$Sm*A* transition temperature in the bulk of the LC $[(T-T_{NA})/T_{NA}=1.1\times10^{-4}]$ for a fixed value of the period ($d=1\ \mu$m). It can be seen that for $U_0\approx0.06\ \mu$m Γ is essentially zero. Consequently, the surface of a solid substrate with sufficiently sharp microrelief generally can not be wetted by the Sm*A* phase all the way down to its appearance in the bulk of the LC.

The above theoretical results are of extraordinary significance for two reasons. First, they fully confirm the assumption made in Ref. 2 that the number of experiments demonstrating effects of formation of a smectic layered structure in nematics near solid surfaces is significantly less than the number of analogous experiments for the free surface of the liquid crystal is roughness of the substrate surfaces. Second, the theory developed above allows one to formulate clearly the requirements for the quality of substrate surfaces needed to observe a smectic structure in the nematic phase of the liquid crystal. Thus, for example, it follows from the data presented in Figs. 1 and 5 that, if periodic microrelief with amplitude $U_0\sim0.05-0.06\ \mu$m and period $d\sim1\ \mu$m remains on the substrate surface as a result of imperfect polishing (here its shape need not be wavy), then near such a surface it is unlikely that a surface Sm*A* structure will be observed in the nematic above the $N-$Sm*A* transition temperature. The severity of such requirements on the quality of the substrate surface can be illustrated in the following way. The authors of Ref. 30 theoretically investigated the influence of of wavy relief of the substrate surface on the degree of orientational order of a NLC near this surface. They showed that the orientational distortions in the nematic induced by such microrelief lead to a substantial decrease of the orientational order parameter if the condition $U_0(2\pi/d)^2\xi_N\sim1$, where ξ_N is the correlation length of the fluctuations of the nematic order in the vicinity of the $I-N$ phase transition. Taking, as in Ref. 30, $\xi_N\sim0.01\ \mu$m, and setting the period of the microrelief $d=1\ \mu$m, we find that to achieve a substantial decrease of the orientational order parameter the amplitude of the microrelief U_0 should be $\sim2.5\ \mu$m, which is roughly 40–50 times greater than the amplitude sufficient for almost complete suppression of surface smectic order in the nematic phase. In other words, the orientational order should be completely insensitive to the surface microrelief completely suppressing surface smectic order. Consequently, the quality of the substrate surface needed for a surface smectic structure to exist in the nematic phase should be, at a minimum, an order of magnitude higher than the surface quality needed not to disrupt the orientational order. This is so because a microrelief-induced deformation of the smectic layers leads to much bigger energy losses than do orientational distortions in the nematic phase.

This work was carried out with the financial support of the Foundation of Natural Sciences (Grant No. 97-9.3-37).

[1] L. M. Blinov, E. I. Kats, and A. A. Sonin, Usp. Fiz. Nauk **152**, 449 (1987) [Sov. Phys. Usp. **30**, 604 (1987).
[2] B. Jerome, Rep. Prog. Phys. **54**, *3*, 391 (1991).
[3] H. Mada and S. Kobayashi, Appl. Phys. Lett. **35**, *1*, 4 (1979).
[4] H. Mada and S. Kobayashi, Mol. Cryst. Liq. Cryst. **66**, *1*, 57 (1981).
[5] H. A. van Sprang, Mol. Cryst. Liq. Cryst. **97**, *1*, 255 (1983).
[6] I. A. Kleĭnman and I. E. Tomashevskiĭ, Kristallografiya **29**, 1214 (1984) [Sov. Phys. Crystallogr. , (1984)].
[7] J. P. Nicholson, J. Phys. (Paris) **49**, *12*, 2111 (1988).
[8] W. Chen, L. J. Martinez-Miranda, H. Hsiung, and Y. R. Shen, Phys. Rev. Lett. **62**, 1860 (1989).
[9] K. Miyano, J. Chem. Phys. **71**, 4108 (1979).
[10] J. C. Tarczon and K. Miyano, J. Chem. Phys. **73**, 1994 (1980).
[11] H. Yokoyama, S. Kobayashi, and H. Kamei, Appl. Phys. Lett. **41**, 438 (1982).
[12] D. Beaglehole, Mol. Cryst. Liq. Cryst. **89**, *2*, 319 (1982).
[13] P. De Gennes and J. Prost, *The Physics of Liquid Crystals* (Clarendon Press, Oxford, 1993; Mir, Moscow, 1977) 400 pp.
[14] J. Als-Nielsen, F. Chrstensen, and P. S. Pershan, Phys. Rev. Lett. **48**, 1107 (1982).
[15] P. S. Pershan and J. Als-Nielsen, Phys. Rev. Lett. **52**, 759 (1984).
[16] C. Rosenblatt, Phys. Rev. Lett. **53**, 791 (1984).
[17] J. Als-Nielsen, Physica A **140**, 376 (1986).
[18] P. S. Pershan, A. Braslau, A. H. Weiss, and J. Als-Nielsen, Phys. Rev. A **35**, 4800 (1987).
[19] B. M. Ocko, A. Braslau, P. S. Pershan, J. Als-Nielsen, and M. Deutsch, Phys. Rev. Lett. **57**, 94 (1986).
[20] P. S. Pershan, J. Phys. (Paris) **50**, *Coll. 7*, 1 (1989).
[21] B. M. Ocko, Phys. Rev. Lett. **64**, 2160 (1990).
[22] J. V. Selinger and D. R. Nelson, Phys. Rev. A **37**, 1736 (1988).
[23] Z. Pawlowska, G. F. Kventsel, and T. J. Sluckin, Phys. Rev. A **38**, 5342 (1988).
[24] L. Mederos and D. E. Sullivan, Phys. Rev. A **46**, 7700 (1992).

[25] A. M. Somoza, L. Mederos, and D. E. Sullivan, Phys. Rev. Lett. **72**, 3674 (1994).
[26] Zh. Kon'yar, *Orientation of Nematic Liquid Crystals and Their Mixtures* [in Russian] (Belorussian State Univ. Press, Minsk, 1986), p. 101.
[27] H. V. Kanel, J. D. Leister, J. Melngalis, and H. I. Smith, Phys. Rev. A **24**, 2713 (1981).
[28] G. Barbero, Nuovo Cimento Lett. **29**, *17*, 553 (1980).
[29] A. Suiamura and T. Kawamura, Jpn. J. Appl. Phys. **23**, *2*, 137 (1984).
[30] G. Barbero and G. Durand, J. Phys. (Paris) II **1**, *6*, 651 (1991).
[31] S. Chandrasekhar, *Liquid Crystals* (Cambridge University Press, Cambridge, 1977; Mir, Moscow, 1980) 344 pp.
[32] J. D. Litster, J. Als-Nielsen, R. J. Birgeneau, S. S. Dana, D. Davidov F. Garcia-Golding, M. Kaplan, C. R. Safinya, and R. Schaetzing, J. Phys. (France) **40**, 339 (1979).
[33] I. Lelidis and G. Durand, Phys. Rev. Lett. **73**, 672 (1994).
[34] P. G. De Gennes, Solid State Commun. **10**, 753 (1972).

Translated by Paul F. Schippnick

FULLERENES AND ATOMIC CLUSTERS

Coherent effects in regular three-dimensional lattices of insulator nanocrystals in an opal matrix

B. N. Bogomolov, N. F. Kartenko, D. A. Kurdyukov, L. S. Parfen'eva, A. A. Sysoeva, N. V. Sharenkova, and I. A. Smirnov

A. F. Ioffe Physicotechnical Institute, Russian Academy of Sciences, 194021 St. Petersburg, Russia

H. Miserek, J. Mucha, and A. Jeżowski

Institute of Low Temperature and Structure Research, Polish Academy of Sciences, 50-950 Wrocław, Poland

(Submitted June 23, 1998)
Fiz. Tverd. Tela (St. Petersburg) **41**, 348–353 (February 1999)

Samples of the nanocomposite opal + NaCl with 100% filling of first-order voids in the opal by NaCl have been obtained. The thermal conductivity of the nanocomposite has been measured in the temperature interval 4.2 − 300 K. It is shown that NaCl, introduced into opal, forms a regular ''matrix quasilattice'' of microcrystals, which leads to suppression of coherent effects and, as a consequence, of properties characteristic of massive crystals. © *1999 American Institute of Physics.* [S1063-7834(99)03002-6]

This work is a continuation of a series of studies on the thermal conductivity of nanocomposites with regular structure (semiconductors and insulators injected into the voids of synthetic opals) initiated by the authors in 1995.[1–5]

The present work investigates the thermal conductivity of the nanocomposite opal + NaCl.

The crystal structure of fractal-type opals was described in detail in Refs. 6 and 7 and in our previous papers.[1–5] However, as an aid to understanding the experimental data obtained in the present work, we shall briefly recall the main points of the unusual crystal structure of opals. Opals are formed from close-packed spheres of amorphous SiO_2 of diameter $\sim 2000-2500$ Å (first-order spheres). The spheres themselves are made up from densely packed spheres of smaller diameter $\sim 300-400$ Å (second-order spheres), which in turn are made up of close-packed spheres with diameter of the order of 100 Å (third-order spheres).

It is well known from crystallography that lattices of close-packed spheres contain octahedral and tetrahedral voids. In opal, such voids arise between spheres of all three orders. The voids are interlinked by ''channels''—thin bridges. The first-order voids (and also the first-order SiO_2 spheres) form a regular cubic lattice with period $a \sim 3000-4000$ Å. The diameters of the octahedral and tetrahedral voids and ''channels'' in the first-order structure in opals are equal, respectively, to 800, 400, and 300 Å.[1)] The total theoretical porosity of opal is equal to 59% (the first-, second-, and third-order porosities are, respectively, 26, 19, and 14%). The actual total porosity of the opals we grew, as was shown earlier, was $\sim 46-50\%$.[2,8] Here the volume of the first-order voids (and this is very important) remains equal to its theoretical value $\sim 26\%$.

Also note that the thermal conductivity of synthetic opals corresponds in its magnitude and temperature dependence to the thermal conductivity of amorphous or ''semicrystalline'' solids.[1,2]

In our foregoing works[3,5] we showed that semiconductors and insulators injected into the first-order voids of opals under certain conditions form a regular ''matrix quasilattice''[2)] of microcrystals, which leads to the appearance of coherent effects and, as a consequence, to the appearance of properties characteristic of bulk crystals.

The purpose of the present work is to expand the set of opal-based nanocomposites in which it would be possible to confirm the above conclusions on the basis of studies of their thermal conductivity. It was of interest to inject the opal with a filler material having a high thermal conductivity.

As the object for study we chose the nanocomposite opal + NaCl.[3)] The first-order voids were completely filled with NaCl. We used chemically pure NaCl. The filling process took place in two steps. First, a sample of pure opal (with dimensions $1\times 2.2\times 8$ mm) was immersed in a saturated solution of NaCl at room temperature. In this step the first-order voids were partially filled with NaCl.[4] Then this sample was immersed in a NaCl melt at $T=900\pm 5$ °C. In contact with the NaCl melt, a partial crystallization of SiO_2 took place on the surface of the voids (pores) in the form of crystoballite, as was confirmed by x-ray studies (Fig. 1), which were performed on a DRON-2 generator (Cu $K\alpha$ radiation). The lattice constant a turned out to equal 5.642(4) Å, and texture is observed along the (110) face. For NaCl bulk crystals $a=5.640$ Å.

According to the results of density measurements of the obtained nanocomposite, it can be concluded that all of the first-order voids (and channels between them) ($\sim 26\%$ of the volume of the sample) were completely filled with NaCl.

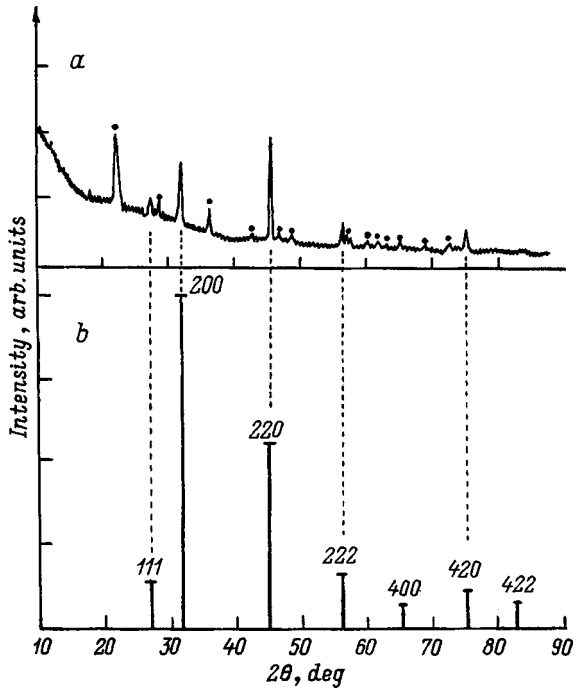

FIG. 1. Diffraction curves for the nanocomposite opal + NaCl (a) and a bulk NaCl crystal (b). The filled circles in Fig. 1(a) are reflections characteristic of crystoballite.

The thermal conductivity was measured in the temperature interval 4.2−300 K in vacuum $\sim 10^{-5}$ mm Hg on an instrument similar to the one described in Ref. 9. Since opal and NaCl are insulators, the measured thermal conductivity of the nanocomposite ($\varkappa_{\rm eff}^{\rm exp}$) is the thermal conductivity of the crystal lattice.

The experimental results for $\varkappa_{\rm eff}^{\rm exp}(T)$ in the nanocomposite opal + NaCl are plotted in Fig. 2. Figure 2 also plots $\varkappa_m^0(T)$ data for the opal-1 matrix.[1,2] Since amorphous SiO_2 crystallized on the surface of the voids with formation of crystoballite during the filling process, it was necessary to determine the thermal conductivity $\varkappa_m'(T)$ of this altered matrix. Toward this end, the nanocomposite opal + NaCl was immersed in water and kept there until the NaCl had completely dissolved out, which was confirmed by x-ray measurements. The thermal conductivity of the partially crystallized matrix, turned out, as expected, to be higher than that of opal-1. Data for $\varkappa_m'(T)$ appear as curve *3* in Fig. 2.

It turned out that the thermal conductivity of the matrix $\varkappa_m'$ is roughly an order of magnitude smaller than that of the nanocomposite $\varkappa_{\rm eff}^{\rm exp}$ (curve *1*, Fig. 2). This is very important to bear in mind in the following discussion of obtained results.

Figure 3 compares the thermal conductivity of the nanocomposite opal + NaCl, $\varkappa_{\rm eff}^{\rm exp}(T)$, opal-1 $\varkappa_m^0(T)$, and the matrix $\varkappa_m'(T)$ with the thermal conductivity $\varkappa(T)$ of a pure bulk single crystal of NaCl.[10] At low temperatures the thermal conductivity of the nanocomposite $\varkappa_{\rm eff}^{\rm exp}$ is less than that of NaCl, and at all temperatures the thermal conductivity of the matrix $\varkappa_m'$ is much less than that of bulk NaCl, $\varkappa$.

To describe the behavior of the thermal conductivity of composites, there is a large set of relations in the literature

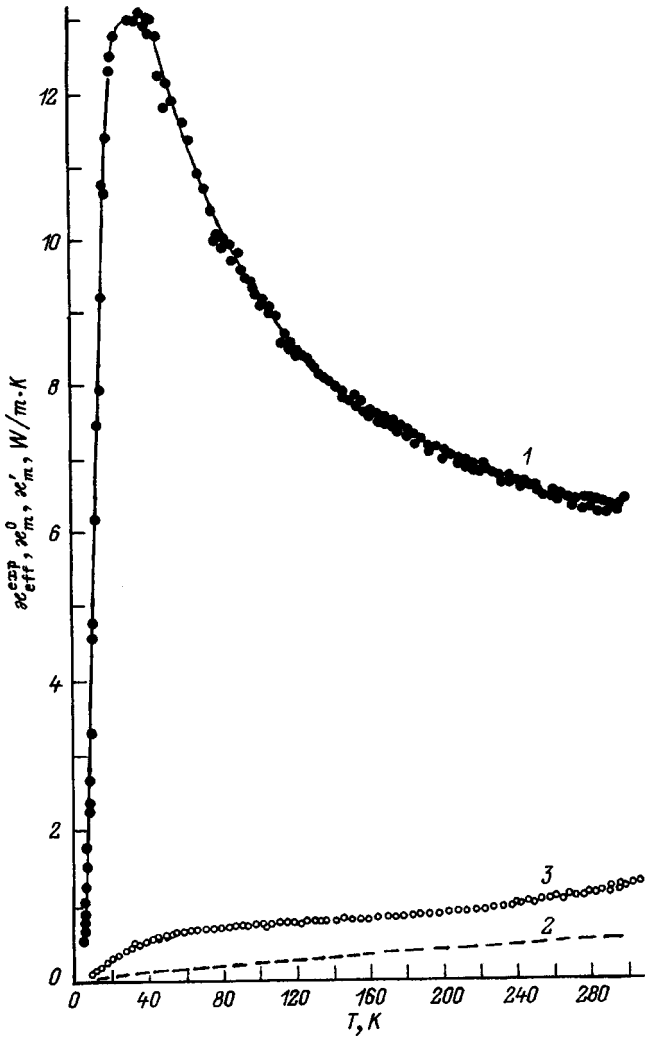

FIG. 2. Temperature dependence of the thermal conductivity: *1* — $\varkappa_{\rm eff}^{\rm exp}$ of the nanocomposite opal + NaCl (100% filling of first-order voids in the opal); *2* — $\varkappa_m^0$ of opal-1 (Refs. 1 and 2); *3* — $\varkappa_m'$ of a sample of opal, obtained from nanocomposite *1* after dissolving out the NaCl in water.

which, when calculated for certain models, give quite good agreement with experiment.[11–13]

Calculated values $\varkappa_{\rm eff}^{\rm calc}(T)$ for some models of composites along with experimental data for opal + NaCl, $\varkappa_{\rm eff}^{\rm exp}(T)$ are plotted in Fig. 4.

As can be seen, none of the models considered could describe $\varkappa_{\rm eff}^{\rm exp}$ for the nanocomposite in question.

Let us consider the calculated results in more detail. Curve *2* in Fig. 4 was obtained by calculating $\varkappa_{\rm eff}^{\rm calc}(T)$ according to the equation of Odolevskiĭ[11 4)] under the assumption that the spheres of filler, isolated from one another by the matrix, are located randomly or regularly in the matrix

$$\frac{\varkappa_{\rm eff}^{\rm calc}}{\varkappa_m} = 1 - \frac{m_2}{1/(1-\nu) - (1-m_2)/3}, \tag{1}$$

where $\nu = (\varkappa_f/\varkappa_m)$; $\varkappa_f$ and $\varkappa_m$ are respectively the thermal conductivities of the filler and matrix (in our case NaCl and $\varkappa_m'$);[5)] and m_2 is the volume occupied by the filler (in our case $m_2 = 0.26$).

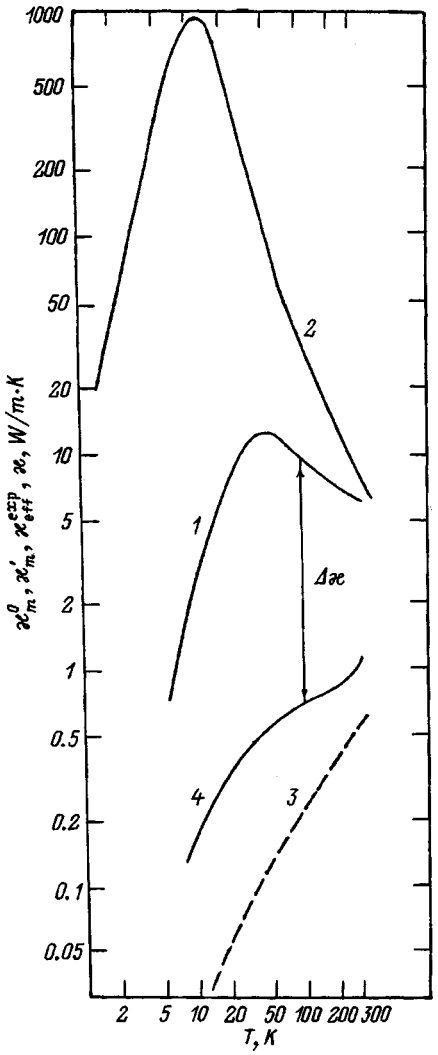

FIG. 3. Temperature dependence of the thermal conductivity: *1* — $\varkappa_{\text{eff}}^{\text{exp}}$ for the investigated nanocomposite opal + NaCl; *2* — $\varkappa$ for NaCl bulk crystal (Ref. 10); *3* — $\varkappa_m^0$ opal-1 (Refs. 1 and 2); *4* — $\varkappa_m'$ for opal obtained from nanocomposite (*1*) by dissolving out the NaCl in water. For an explanation of the $\Delta\varkappa$ values, see text and caption to Fig. 7.

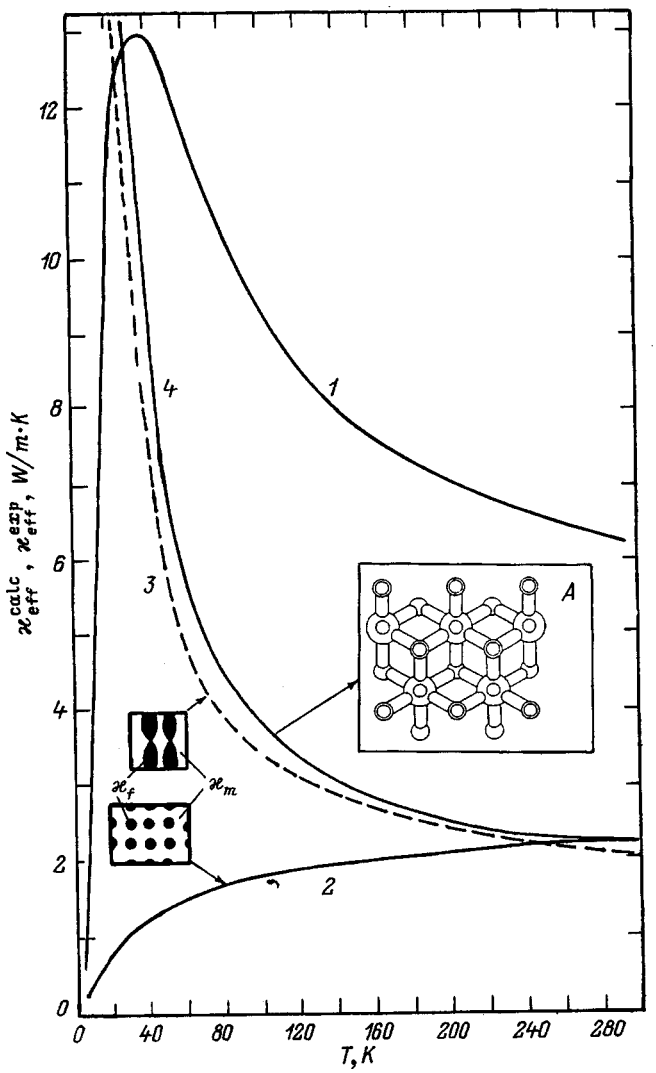

FIG. 4. Calculated ($\varkappa_{\text{eff}}^{\text{calc}}$) and experimental ($\varkappa_{\text{eff}}^{\text{exp}}$) curves of the temperature dependence of the thermal conductivity for the nanocomposite opal + NaCl (100% filling of first-order voids): *1* — experimental values of $\varkappa_{\text{eff}}^{\text{exp}}$ for the nanocomposite opal + NaCl (100% filling of first-order voids); *2* — $\varkappa_{\text{eff}}^{\text{calc}}$ calculated according to Eq. (1) (Ref. 11); *3* — $\varkappa_{\text{eff}}^{\text{calc}}$ calculated according to Eq. (2) (Ref. 11); *4* — $\varkappa_{\text{eff}}^{\text{calc}}$ calculated according to Eq. (4), based on geometrical calculations of an actual lattice (inset *A*) of opal voids. Inset *A* — lattice of first-order voids.[6]

The calculated values $\varkappa_{\text{eff}}^{\text{calc}}$ turned out to be much smaller than those obtained experimentally.

Reference 11 considers a model that is quite similar to the investigated nanocomposite: unclosed interacting pores with interconnecting necks, filled with a filler having thermal conductivity $\varkappa_f$. For this model, the authors of Ref. 11 suggest the following formula to calculate $\varkappa_{\text{eff}}^{\text{calc}}(T)$:

$$\varkappa_{\text{eff}}^{\text{calc}} = \varkappa_m \left[A^2\nu + (0.75-A) + \frac{(0.5-2A^2)\nu}{\nu+1} + \frac{A}{\left[\frac{A}{\nu}(\nu-1)\right]} \right], \tag{2}$$

where ν and m_2 have the same meaning as in Eq. (1).

A^2 is the cross-sectional area of a contact neck of the impregnations. Equation (2) is valid for

$$0.125 \leqslant m_2 \leqslant 0.5, \quad 0 \leqslant A \leqslant 0.5.$$

Curve *3* in Fig. 4 plots $\varkappa_{\text{eff}}^{\text{calc}}(T)$ calculated according to formula (2). Again, $\varkappa_{\text{eff}}^{\text{calc}}(T)$ could not describe $\varkappa_{\text{eff}}^{\text{exp}}(T)$.

The actually existing lattice of voids in opal (inset *A*, Fig. 4) can also be represented in the form of a set of ''threads'' running through the opal matrix.[6,7] Thus it may be supposed that end-to-end heat transfer from the hot end of the sample to the cold end is possible in the nanocomposite via the NaCl ''threads.''

Let us attempt to estimate the contribution to $\varkappa_{\text{eff}}^{\text{exp}}$ from such a mechanism of heat transfer.

We estimate the phonon mean free path (l) for bulk NaCl according to the Eq. (3)

$$l = \frac{3\varkappa}{C_v \overline{v}}, \tag{3}$$

where C_v is the thermal conductivity at constant volume, $\overline{\mathbf{v}}$ is the mean sound velocity $\overline{\mathbf{v}} = (2v_\perp + v_\parallel/3)$, where $v_\perp$ and $v_\parallel$

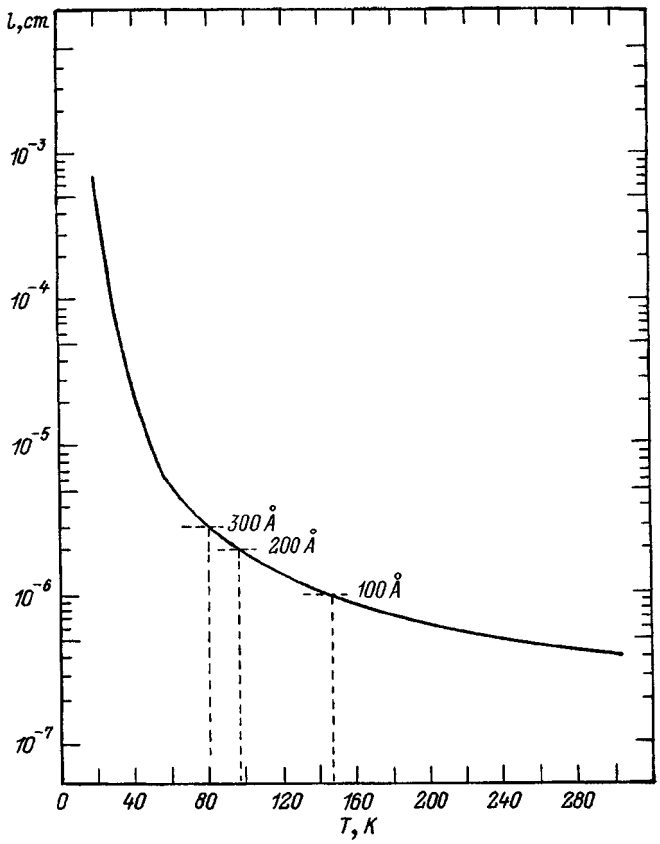

FIG. 5. Temperature dependence of the phonon mean free path in NaCl bulk crystals.

are, respectively, the transverse and longitudinal sound velocities, and $\varkappa$ is the thermal conductivity of bulk NaCl. The values for $\varphi(T)$ were taken from Ref. 10 (curve *2*, Fig. 3), for C_v from Refs. 15–17, and for $\overline{\mathbf{v}}$ from Refs. 18 and 19. The calculated results are plotted in Fig. 5.

For an ideal lattice of voids filled with NaCl, the diameter of a ''thread,'' which limits the phonon mean free path for end-to-end heat transfer in the sample, could correspond to the smallest diameter of a channel joining the large octahedral first-order voids (Fig. 4 in Ref. 6). According to Ref. 6 this diameter is ~ 300 Å. However, because of possible sintering of the opal matrix the diameter of the channel can also be smaller. For a channel with a diameter ~ 300 Å we should have observed a maximum for $\varkappa_{\text{eff}}^{\text{exp}}$ of the nanocomposite opal + NaCl, arising from a size effect limiting the phonon mean free path somewhere in the vicinity of 80 K (or higher) (Fig. 5). However, in the experiment, the maximum of $\varkappa_{\text{eff}}^{\text{exp}}(T)$ for the investigated nanocomposite is found approximately at 35 K.[6] This can serve, to first order, as evidence that the effect related to heat transfer by ''threads'' of NaCl in the nanocomposite is either absent or is quite small.

We derived an empirical dependence for $\varkappa_{\text{eff}}^{\text{calc}}(T)$ for the nanocomposite opal + NaCl, based on geometrical parameters of the actual lattice of first-order voids in opal filled with a filler material (the lattice in inset *A* in Fig. 4), which takes account of the end-to-end heat flux along NaCl ''threads.''

The empirical relation has the form

$$\varkappa_{\text{eff}}^{\text{calc}} = \varkappa_{\text{NaCl}} \cdot 0.148 + \varkappa_m' \cdot 0.852. \tag{4}$$

The second term in (4) takes account of the heat flux along the matrix. The coefficient of $\varkappa_{\text{NaCl}}$ turns out to be close to the coefficient obtained for model experiments on measuring the electrical conductivity of a solution of the NaCl injected into the first-order voids of the opal matrix.

Calculation of $\varkappa_{\text{eff}}^{\text{calc}}(T)$ according to Eq. (4) (curve *4*, Fig. 4) led to a result similar to the result calculated using Eq. (2), but in this case as well it could not explain the experiment.

Thus, the equations for thermal conductivity of composite materials could not describe $\varkappa_{\text{eff}}^{\text{exp}}(T)$ of the investigated nanocomposite.

To explain the obtained results, we must assume that, along with the standard mechanism of heat transfer, which operates in a typical composite consisting of a matrix and a filler, in the nanocomposite opal + NaCl some additional mechanism is present which is peculiar to ordinary crystalline solids. For this purpose it is necessary to assume that the NaCl injected into the cubic lattice of first-order voids of the opal matrix forms a matrix quasilattice of microcrystals, which leads to the appearance of coherent effects and properties characteristic of bulk crystals.

Thus, the nanocomposite based on opals with a regular structure of voids (in which the fillers fill 100% of the first-order voids of the opal matrix) is a unique physical object, whose thermal conductivity depends on the thermal conductivity of two subsystems.

The first is the filler (in our case NaCl) and the matrix with their own individual properties in the system of the standard composite, and the second is a new ''matrix quasilattice,'' made up of NaCl microcrystals with ''heavy atomic mass'' (''atomic mass'' here means the tetrahedral void ~ 800 Å filled with filler) and a huge crystal lattice constant $a \sim 3000-4000$ Å.

In conclusion, let us try to separate from $\varkappa_{\text{eff}}^{\text{exp}}$ of the investigated composite opal + NaCl the thermal conductivity belonging to the matrix quasicrystal. We consider again $\varkappa_{\text{eff}}^{\text{calc}}(T)$ calculated with the help of formula (4). It is represented by curve *4* in Fig. 4 and curve *3* in Fig. 6 for the temperature intervals $25-300$ K and $4.2-300$ K, respectively. For $T \lesssim 30$ K, $\varkappa_{\text{eff}}^{\text{calc}}$ begins to exceed the values obtained experimentally for the investigated nanocomposite (Figs. 4 and 6). What can this be due to? As was noted above, Eq. (4) allows for end-to-end heat flux along ''threads'' of the lattice of first-order voids of opal filled with NaCl. In the calculations we used data for the thermal conductivity of bulk NaCl. In so doing, we ignored the fact that a limitation of the phonon mean free path for NaCl takes place in the ''threads'' because of the size effect. If we assume that the minimum diameter of the channels (and consequently of the ''threads'') connecting the tetrahedral voids of the opal matrix is ~ 300 Å, then $\varkappa(T)$ for NaCl (calculated according to Eq. (3) including the mean-free-path data plotted in Fig. 5, under the assumption that for

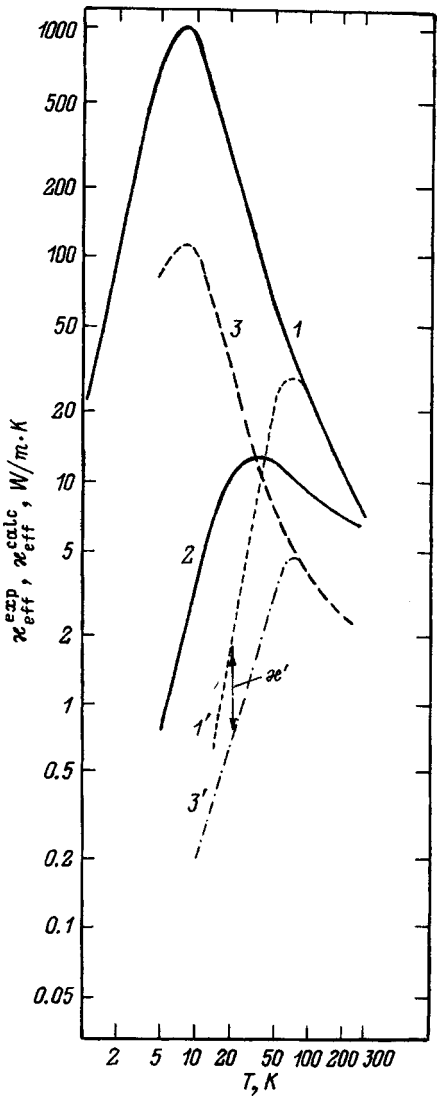

FIG. 6. Experimental and calculated curves of the temperature dependence of the thermal conductivity: *1* — $\varkappa$ for NaCl; *2* — $\varkappa_{\rm eff}^{\rm calc}(T)$ for the nanocomposite opal + NaCl (100% filling of first-order voids); *3* — $\varkappa_{\rm eff}^{\rm calc}$ calculated according to formula (4). Explanation of curves *1′* and *3′* given in text.

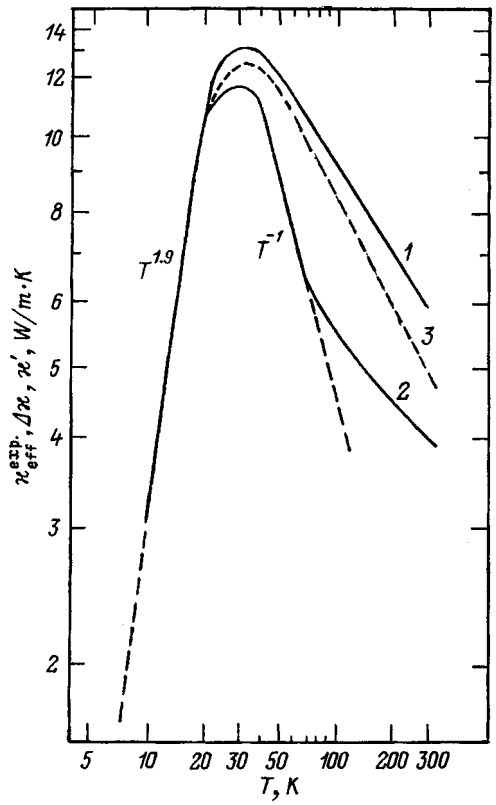

FIG. 7. Temperature dependence of the thermal conductivity: *1* — $\varkappa_{\rm eff}^{\rm exp}$ for the nanocomposite opal + NaCl (100% filling of first-order voids); *2, 3* — $\varkappa_{\rm cryst}$ for a NaCl matrix quasicrystal. *2* — $\varkappa_{\rm cryst}=\varkappa'=\varkappa_{\rm eff}^{\rm exp}$ (opal + NaCl) — $\varkappa_{\rm eff}^{\rm calc}$ (curves *3* and *3′* in Fig. 6). *3* — $\Delta\varkappa=\varkappa_{\rm cryst}=\varkappa_{\rm eff}^{\rm exp}$ (opal + NaCl) — $\varkappa_m'$ (see Fig. 3).

$T<80$ K, $l\sim$const) takes the form represented in Fig. 6 by the dependence *1′* with maximum in the vicinity of 80 K.

Calculation of $\varkappa_{\rm eff}^{\rm calc}(T)$ according to Eq. (4), taking into account the values of the thermal conductivity for NaCl, $\varkappa(T)$, corresponding to curve *1′* in Fig. 6, leads to the effective thermal conductivity of the composite $\varkappa_{\rm eff}^{\rm calc}(T)$ represented by curve *3′* in Fig. 6.

Now we can try to separate out from the experimental values $\varkappa_{\rm eff}^{\rm exp}(T)$ of the nanocomposite the thermal conductivity belonging to the matrix quasicrystal ($\varkappa_{\rm cryst}$) (Fig. 6)

$$\varkappa'=\varkappa_{\rm cryst}=\varkappa_{\rm eff}^{\rm exp}(T)(\text{curve } 2) - \varkappa_{\rm eff}^{\rm calc}(T)(\text{curves } 3, 3'). \quad (5)$$

The value of $\varkappa_{\rm cryst}$ obtained from Eq. (5) is plotted as curve *2* in Fig. 7. The thermal conductivity of the matrix quasicrystal, determined with the help of the above-described procedure, behaves similarly to a standard crystal with an ordinary atomic mass and an ordinary lattice constant: at low temperatures $\varkappa_{\rm cryst}\sim T^{1.9}$, and for $T>T_{\max}$ $\varkappa_{\rm cryst}\sim T^{-1}$.

As was already mentioned, for the investigated nanocomposite, $\varkappa_m'\ll\varkappa_{\rm eff}^{\rm exp}$. Therefore, we could try to estimate the thermal conductivity of the matrix quasicrystal by simply subtracting the value $\varkappa_m'$ (obtained noting the remarks made in footnote 5) (Fig. 3) from the experimentally measured value $\varkappa_{\rm eff}^{\rm exp}(T)$

$$\Delta\varkappa=\varkappa_{\rm cryst}=\varkappa_{\rm eff}^{\rm exp}(\text{opal}+\text{NaCl})-\varkappa_m'. \quad (6)$$

The results calculated using Eq. (6) are plotted as curve 3 in Fig. 7. As can be seen, no fundamental difference is seen in the behavior of $\varkappa_{\rm cryst}(T)$ calculated using Eqs. (5) and (6).

The work presented in this paper was supported by a grant from the Russian Fund for Fundamental Research (Grant No. 96-03-32458a).

[1)] For simplicity and ease of visualization the voids are customarily approximated as spheres interlinked by cylindrical ''channels.'' A diagram of a cubic lattice of first-order voids is shown below in Fig. 5 (*A*).[6]

[2)] This term was introduced by us. We hope that it will survive in the literature to describe the new structures under consideration since their properties are partly similar to those of classical quasicrystals.

[3)] As the matrix we used ''single-crystal'' opal-1 (Ref. 2). Here we preserve the terminology adopted in Refs. 1 and 2.

[4)] Analogous results were also obtained using the equations of Meredith and Tobias.[13,14]

[5)] In all the calculations, to determine the true value of $\varkappa_m'$ (with allowance for the fact that not all of the voids are filled with NaCl) we used the

equation of Ref. 12 and the procedure suggested in Ref. 3. In the calculations of $\varkappa_{\text{eff}}^{\text{calc}}$ using Eq. (1) and subsequent calculations using Eqs. (2), (3), and (4) we used data for $\varkappa$ of pure NaCl, Ref. 10 (see curve *2* in Fig. 3)

[6)]The nature of the appearance of the maximum in $\varkappa_{\text{eff}}^{\text{exp}}(T)$ for the nanocomposite opal + NaCl remains unclear.

[1] V. N. Bogomolov, L. S. Parfen'eva, A. V. Prokof'ev, I. A. Smirnov, S. M. Samoĭlovich, A. Jeżowski, J. Mucha, and H. Miserek, Fiz. Tverd. Tela (St. Petersburg) **37**, 3411 (1995) [Phys. Solid State **37**, 1874 (1995)].

[2] V. N. Bogomolov, D. A. Kurdyukov, L. S. Parfen'eva, A. V. Prokof'ev, S. M. Samoĭlovich, I. A. Smirnov, A. Jeżowski, J. Mucha, and H. Miserek, Fiz. Tverd. Tela (St. Petersburg) **39**, 392 (1997) [Phys. Solid State **39**, 341 (1997)].

[3] L. I. Artyunyan, V. N. Bogomolov, N. F. Kartenko, D. A. Kurdyukov, V. V. Popov, A. V. Prokof'ev, I. A. Smirnov, and N. V. Sharenkova, Fiz. Tverd. Tela (St. Petersburg) **39**, 586 (1997) [Phys. Solid State **39**, 510 (1997)].

[4] L. I. Artyunyan, V. N. Bogomolov, N. F. Kartenko, D. A. Kurdyukov, L. S. Parfen'eva, I. A. Smirnov, N. V. Sharenkova, A. Jeżowski, J. Mucha, and H. Miserek, Fiz. Tverd. Tela (St. Petersburg) **40**, 379 (1998) [Phys. Solid State **40**, 348 (1998)].

[5] V. N. Bogomolov, N. F. Kartenko, L. S. Parfen'eva, A. V. Prokof'ev, I. A. Smirnov, H. Miserek, J. Mucha, and A. Jeżowski, Fiz. Tverd. Tela (St. Petersburg) **40**, 573 (1998) [Phys. Solid State **40**, 528 (1998)].

[6] V. N. Bogomolov and T. M. Pavlova, Fiz. Tekh. Poluprovodn. **29**, 826 (1995) [Semiconductors **29**, 428 (1995)].

[7] V. G. Balakirev, V. N. Bogomolov, V. V. Zhuravlev, Yu. A. Kumzerov, V. P. Petranovskiĭ, S. G. Romanov, and L. A. Samoĭlovich, Kristallografiya **38**, *3*, 111 (1993) [Crystallogr. Rep. **38**, 348 (1993)].

[8] V. V. Ratnikov, Fiz. Tverd. Tela (St. Petersburg) **39**, 956 (1997) [Phys. Solid State **39**, 856 (1997)].

[9] A. Jeżowski, J. Mucha, and G. Pompe, J. Phys. D **20**, 1500 (1987).

[10] *Handbook of Thermal Conductivity of Solids* [in Russian], edited by A. S. Okhotin (Energoatomizdat, Moscow, 1984) 320 pp.

[11] G. N. Dul'nev and Yu. P. Zarichnyak, *Thermal Conductivity of Mixtures and Composite Materials* [in Russian] (Énergiya, Leningrad, 1974) 264 pp.

[12] E. Ya. Litovskiĭ, Izv. Akad. Nauk SSSR, Neorg. Mater. **16**, *3*, 559 (1980).

[13] K. W. Garrett and H. M. Rosenberg, J. Phys. D **7**, 1247 (1974).

[14] R. E. Meredith and C. W. Tobias, J. Appl. Phys. **31**, 1270 (1960).

[15] K. Clusius, J. Goldmann, and A. Perlick, Z. Naturforsch. **4a**, 424 (1949).

[16] J. H. Barkman, R. L. Anderson, and T. E. Brackett, J. Chem. Phys. **42**, 1112 (1965).

[17] T. H. Kwon and J. H. Henkel, Can. J. Psychol. **49**, 20 (1970).

[18] R. Q. Fugate and D. E. Schuele, J. Phys. Chem. Solids **27**, 493 (1966).

[19] *Acoustic Crystals* [in Russian], edited by M. P. Shaskol'skiĭ (Nauka, Moscow, 1982) 632 pp.

Translated by Paul F. Schippnick

Oriented growth of oxygen-free C_{60} crystallites on silicon substrates

T. L. Makarova and A. Ya. Vul'

A. F. Ioffe Physicotechnical Institute, Russian Academy of Sciences, 194021 St. Petersburg, Russia

I. B. Zakharova and T. I. Zubkova

St. Petersburg State Technical University, 195251 St. Petersburg, Russia
(Submitted May 15, 1998)
Fiz. Tverd. Tela (St. Petersburg) **41**, 354–359 (February 1999)

This is the first report of preparation of C_{60} fullerite films on silicon substrates coated by a layer of natural oxide. The crystallites are about 1 μm in size. The films were found to have an enhanced stability to atmospheric oxygen. The films were obtained by a modified method of discrete evaporation in a quasi-closed volume. The principal features of the method are the quasi-equilibrium condensation conditions, a high substrate temperature (up to 300 °C), and alternation of deposition with recrystallization in a single technological cycle. The method is characterized by high film condensation rates (up to 2000 Å/min) and an economical expenditure of the starting material. A study has been made of the surface structure and morphology, and of the depth profile of the film optical constants and elemental composition. © *1999 American Institute of Physics.* [S1063-7834(99)03102-0]

Development of methods of growing crystalline-fullerene films on silicon is a key problem in application of fullerenes in electronics. Fullerite films were obtained up to now by vacuum sublimation,[1–6] sublimation in a closed gradient furnace,[7] by hot wall,[8,9] laser[10] and jet[11] deposition, as well as by MBE[12–14]. All of the above studies reported fabrication of crystalline films only on layered substrates having an appropriate geometrical structure factor [mica,[4] GeS,[12] MoS_2 (Ref. 14)], or on specially treated large-misfit substrates[13]. Preparation of films whose structure is dominated by weak van der Waals forces imposes special requirements on maintaining equilibrium condensation conditions which would provide growth in energetically favorable directions. When obtaining films by thermal evaporation in vacuum, such requirements can be met by using closed and quasi-closed evaporation chambers, so films condense at a high vapor pressure, and a small difference exists between the substrate and evaporator temperatures. Information on the preparation of fullerite films by quasi-equilibrium methods is presently very scarce.[7–9]

A new method of condensation of fullerite films on amorphous and crystalline substrates has recently been proposed.[15] This work reports on the use for this purpose of nonorienting silicon substrates, a case more complex from the standpoint of growing crystalline films while being at the same time most promising for applications.

1. EXPERIMENT

The C_{60} films were obtained by a modified quasi-closed volume method (MQCV). High-purity C_{60} fullerene (99.98%) was used as starting material. The evaporation chamber was described in detail elsewhere.[15] The closed volume of the evaporation chamber is formed by a hollow quartz cylinder with two graphite bases. The substrates are mounted close to the top base. The evaporator, the substrates, and the quartz cylinder are heated by tungsten furnaces and maintained at the temperatures T, T_s, and $T_w = 0.7\,T$, respectively. The material used for the substrates was KDB-4.5 commercial (100) silicon coated by natural oxide. The structure of the films and the surface morphology were studied by x-ray diffraction on D/max-B Rigaku generator (1.54 μm Cu $K\alpha$, $\lambda = 1.54$ Å) and by scanning electron microscopy (SEM). The depth profile of the optical constants and of the elemental composition of the films were derived from spectral ellipsometry and Rutherford backscattering data[16].

2. RESULTS AND DISCUSSION

2.1. Film growth rate

The diagram in Fig. 1 exhibits the main characteristics of film condensation. The film growth rates lie typically within the 200–2000-Å/min range. Increasing the evaporator temperature brings about a sharp increase in the film growth rate following the relation $V = V_0 \exp(-E_a/kT)$, where E_a, the film condensation activation energy, was found to be 1.9 eV. This value is close to the activation energy of the C_{60} saturated vapor pressure *vs* temperature relation,[17] which evidences complete transport of evaporated material on the substrate. An increase in the substrate temperature reduces the growth rate, because the probability of reevaporation increases with temperature. A comparison with the available literature data listed in Table I shows that the growth rates obtained exceeded by several orders of magnitude those reached by the other methods employed up to now (1–30 Å/min).

The conditions favoring the growth of fullerite films from the physical and technological standpoints are a low

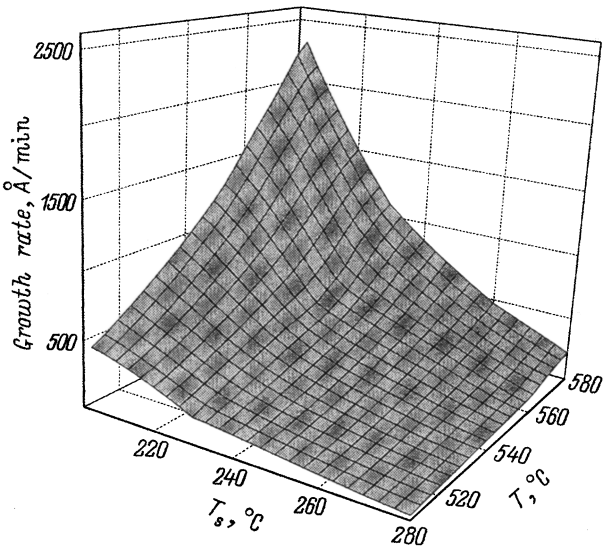

FIG. 1. Rate of condensation of C_{60} films *vs* evaporation, T_1, and condensation, T_s, temperature.

supersaturation of the vapor phase and a fairly high condensation rate under intense reevaporation.

Vacuum sublimation from open sources involves condensation from a molecular cluster beam at a high supersaturation of the vapor phase (10^5-10^7), with the maximum substrate temperature at which the film still continues to grow not exceeding 200 °C. In the modified, closed-volume method used here the film condenses under near-equilibrium conditions, at a high vapor pressure and a low supersaturation (10^2-10^3), i.e., with a small difference between the substrate and evaporator temperatures. Film growth on a substrate maintained at a high temperature is accompanied by intense exchange interaction of the growing condensate with the vapor phase, with simultaneous recrystallization through coalescence of nuclei, by defect annealing, and diffusion of adsorbed atoms and molecules over the substrate surface.

An analysis of x-ray diffraction patterns obtained with different substrates showed that, if condensation occurs below 200 °C, the crystalline phase exists only in films grown on an orienting substrate, in our case, mica.[15] X-ray diffractograms of C_{60} on silicon show only an amorphous halo at 15–17°, which corresponds to reflection from individual clusters (the lower curve in Fig. 2a). The strong interaction of C_{60} with the substrate does not favor formation of epitaxial layers. Fullerite films growing on hydrogen-treated silicon surfaces interact only weakly with the substrate, and therefore physical absorption gives rise to growth of (111) crystalline films, whereas silicon coated by natural oxide stimulates chemical absorption suppressing the ordering of the first monolayers to form, which favors growth of amorphous films in the same conditions.[2]

Increasing the oxidized-silicon substrate temperature from 200 to 265 °C results in the appearance in the films of a crystalline fullerene phase with peaks corresponding to the (111), (220), and (311) reflections. These observations are supported by surface morphology studies with a scanning electron microscope (Fig. 3). The surface with rounded-off hillocks seen in Fig. 3a is characteristic of an amorphous film, while Fig. 3b exhibits the presence of a polycrystalline phase, with (111) preferred orientation parallel to the substrate. The unusually high crystallinity of the film obtained on oxidized silicon is associated apparently not with the surface diffusion of clusters, which is impeded by the high cluster molecular mass, but rather with intense reevaporation of weakly bound clusters under a high cluster flux impinging on the surface.

TABLE I. Comparison of the characteristics of fullerite films obtained by different techniques.

	Condensation parameters			Film characteristics		
Method of preparation	p_0, Torr	T_s, °C	V_{cond}, Å/min	Substrates	Crystallite size d, μm	Ref.
Vacuum sublimation	10^{-6}		5–20	Glass	0.01	1
		20	15	Si, SiO_2	0.03 Amorphous	2
	10^{-6}	20–200	10	Mica	0.1	3
				Si, SiO_2	Amorphous	
	10^{-6}	100	15	NaCl, Mica	0.01 0.05	4
	10^{-6}	240	5	KI(001)	0.3	5
	10^{-6}	20	20	Si(100)	0.02	6
MBE	10^{-9}	200	0.1	Mica, NaCl, MoS_2	0.4 0.2 1	14
	10^{-9}	20–200	0.3–1	GeS(001)	Epitaxial	12
	10^{-9}	200	0.5	Si(111) (7×7)	0.1	13
Sublimation in closed temperature-gradient furnace	6×10^{-7}	200	7	Glass	1	7
Hot wall	10^{-7}	140	1.3	Mica	0.05–0.1	8,9
MQCV	10^{-7}	200–300	20–2000	Si(100)	0.5–1	present work

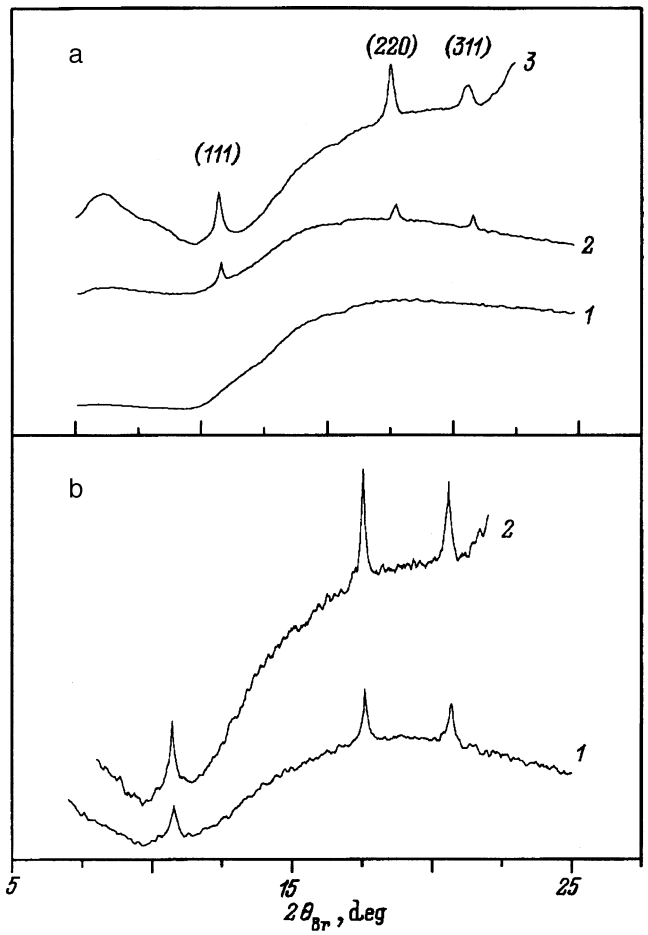

FIG. 2. X-ray diffraction patterns of C_{60} films on oxidized silicon. (a) One-stage process; condensation temperatures T_s (°C): *1* — 190, *2* — 230, *3* — 265; (b) Multi-stage process, $T_s = 250$ °C; *1* — two stages, *2* — three stages.

2.2. Multistage film growth

It could be expected that the merits of the quasi-equilibrium growth of films bonded by weak van der Waals forces on large-lattice-misfit substrates would become best seen if condensation took place on the substrate precoated by a C_{60} layer. Such passivation would reduce the effect of the substrate-induced active condensation centers. This suggestion was tested by using a multi-stage method, with the deposition and recrystallization alternating in a continuous vacuum cycle. In the first stage, a C_{60} buffer layer, 500–600-Å thick, is deposited on a silicon substrate at a high condensation temperature $T_s = 280 - 300$ °C. This is followed, without impairing the vacuum, by annealing at 10–20 °C above the condensation temperature. In these conditions, the condensate undergoes intense reevaporation and recrystallization to form blocks separated by boundaries, which pass at 90 and 120° and are clearly seen in SEM images (Fig. 3c and 3d).

The deposition in the second stage takes place on the modified first C_{60} layer under conditions in which the first layer was formed, with subsequent vacuum annealing for recrystallization of the second layer. The x-ray diffraction patterns presented in Fig. 2b show a substantially increased crystallinity of the film. Electron photomicrographs (Fig. 3c and 3d) reveal the presence of coarse-grained growth figures at the block boundaries. The crystallite diameter was found to be of the order of 1 μm, which exceeds literature data considerably (see Table I), and the filaments may be as long as 30–50 μm. The nucleation and growth of crystallites in the second layer occur obviously at the active block boundaries of the first recrystallized layer, and the subsequent thermal vacuum anneal of the second layer stimulates autocoalescence of nonequilibrium crystallites to produce large faceted crystals, which may join to create growth patterns of different shapes. In the third stage of deposition, performed under the same conditions, it is the growth figures that act as centers for the crystallization and recrystallization. This results in a random growth of faceted cubic crystals, whose shape is fairly close to the equilibrium one (Fig. 3e and 3f).

2.3. Oxygen content in the films

It is known that as-deposited fullerite films interact actively with oxygen, which degrades rapidly their electrical and optical characteristics.[18–20] The interaction of thin films with oxygen reduces to intercalation and physisorption, with formation on the surface of crystallites of a charged O_2^- layer. Obviously enough, the stability of films against oxygen depends substantially on their structure (amorphous, finely or coarse-grained), which is determined by the actual conditions of condensation. It is known, for example, that large fullerite crystals (a few mm in size) are stable with respect to oxygen, i.e. the instability of most of the films is associated with the large total crystallite surface area and the high rate of oxygen diffusion over the interfaces.[19]

A careful analysis reveals that most of the films described in the literature (see Table I) cannot be considered to have been obtained under high-vacuum conditions. Indeed, it can be shown that a monolayer of oxygen adsorbs on a substrate in a residual pressure of 10^{-6} Torr in three to four seconds,[21] whereas the growth of a C_{60} monolayer takes 5–60 s. Taking into account the low substrate temperatures which do not favor oxygen desorption, it becomes clear that such conditions of preparation, first, impair the epitaxial growth regime and, second, lead to condensation of films already saturated by oxygen to a considerable extent. This is corroborated by the report[19] that condensation of C_{60} at an oxygen pressure of the order of 10^{-6} Torr produces intercalated films with an O_2 content of 0.5 at.%. It could be added that deposition of most metals at such oxygen pressures and growth rates of 10–100 Å/min produces stoichiometric metal oxides.[21] Hence oxygen-free films can be obtained either at residual pressures of $10^{-8} - 10^{-9}$ Torr or at high condensation rates.

The films prepared by us by the modified closed-volume method condense with a rate of 5–10 C_{60} monolayers per sec at high temperatures favoring desorption of impurities, and have coarse-grained structure with crystallites about 1 μm in size. Such films could be expected to have a higher stability with respect to oxygen.

To check this assumption, we carried out a comparative study of the depth profile of optical constants (the refractive

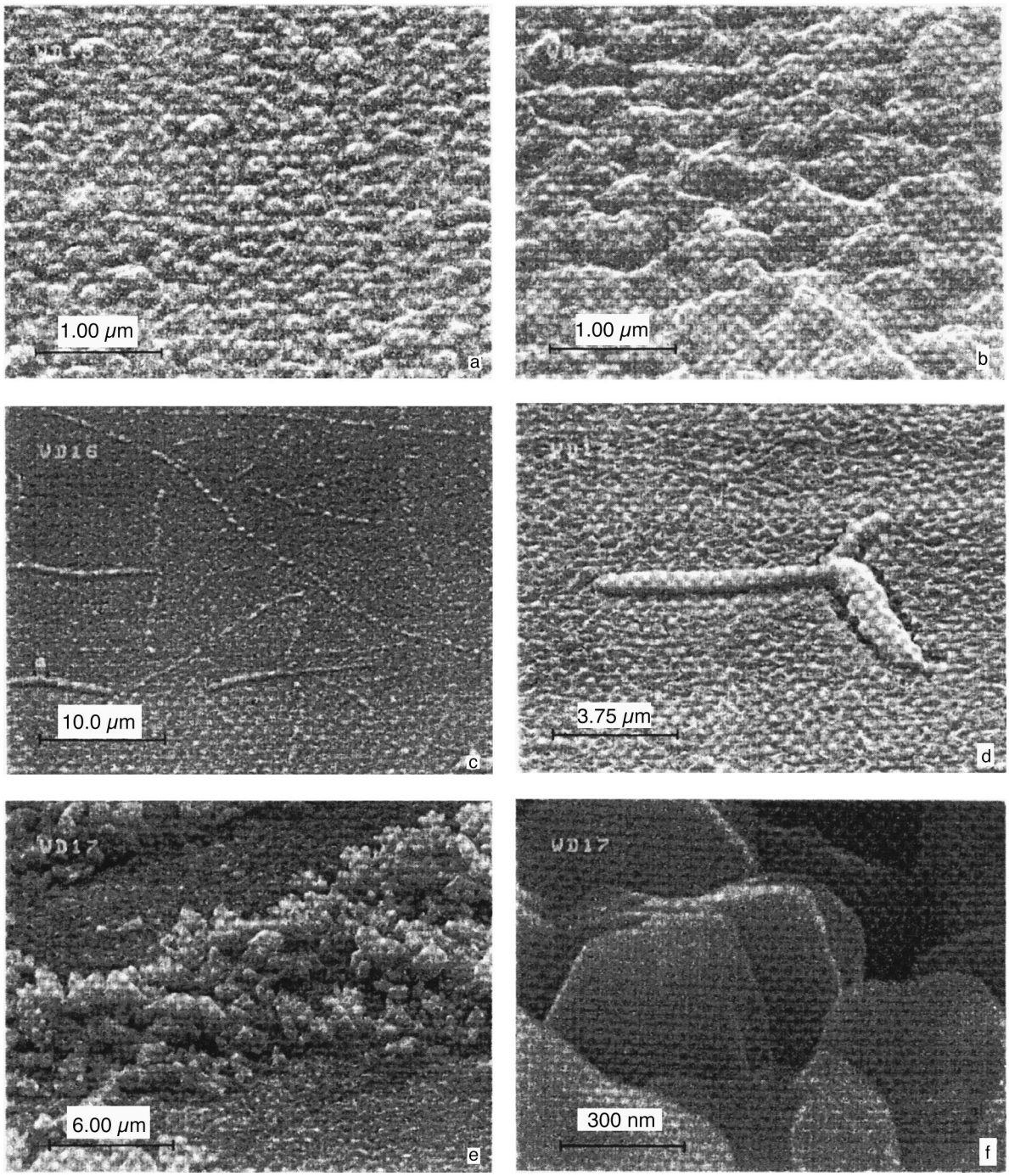

FIG. 3. Morphology of C_{60} films on oxidized silicon. (a,b) One-stage growth, $T_s = 200\,^{\circ}C$ (a) and $T_s = 265\,^{\circ}C$ (b); (c–f) Multi-stage growth, $T_s = 250\,^{\circ}C$, (c,d) two stages, (e,f) three stages.

index n and absorption coefficient k) in the films obtained by the above technique and by standard molecular-beam condensation by the technique described in Ref. 6. The measurements were made by spectral ellipsometry in the 1.96–2.80-eV region. As seen from Fig. 4, a common feature of the films obtained by the two techniques is the presence of a surface layer with a carbon/oxygen content ratio C:O = 10:1 ($C_{60}O_6$), thickness of 150 Å, and refractive index $n = 1.5$. This layer forms in air in several minutes and does not change in optical parameters thereafter during several months of storage. Films grown by molecular-beam condensation[6] are optically inhomogeneous, with a gradient of optical constants observed to exist throughout their thickness. The values of n and k indicate an enhanced oxygen content at the film surface.[20]

The films grown by MQCV with a condensation rate of 800 Å/min have a thinner surface layer, are optically homogeneous throughout the remainder of the thickness, and stable when stored in air for six months.

An analysis of MQCV-grown films by Rutherford backscattering also revealed the presence of a surface layer with the $C_{60}O_6$ stoichiometry. The volume concentration of car-

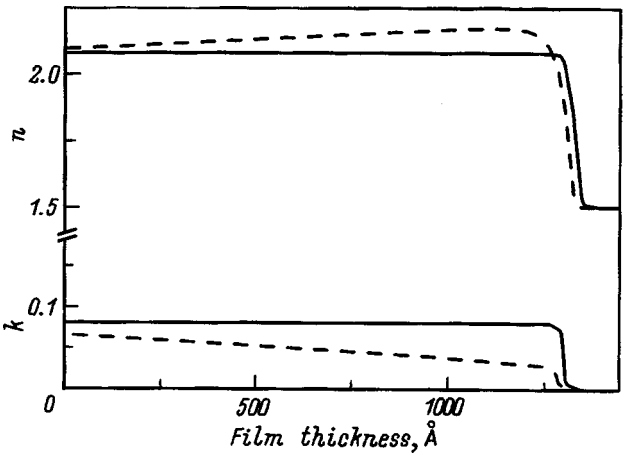

FIG. 4. Depth profile of optical constants ($h\nu = 2.8$ eV) of fullerite films obtained by different techniques. Solid line — MQCV, dashed line — vacuum sublimation.

bon atoms derived from the energy spectra of backscattered ions and the film thickness extracted from ellipsometric measurements permitted us to calculate the film density, $\rho = 1.58$ g/cm^3, which is close to the value $\rho = 1.65$ g/cm^3 for bulk crystals.

Thus interaction of a fullerite film with oxygen produces a surface layer enriched in oxygen. In heavily defected, fine-grained and amorphous films, diffusion of oxygen over the interfaces continues and results in optical inhomogeneities and unstable film properties. In a coarse-grained, structurally perfect film such a layer passivates the surface and inhibits further diffusion of oxygen into the bulk of the film.

Thus our studies have demonstrated the possibility of growing coarse-grained, structurally-perfect, optically homogeneous and stable, oriented fullerite films with uniquely large crystallites and a low oxygen content by a technologically simple vacuum method. The results of our studies broaden considerably the possibilities of investigation and the applications potential of fullerite-based films and structures.

The authors owe their thanks to I. T. Serenkov and V. I. Sakharov for the Rutherford backscattering measurements, and to N. I. Nemchuk for making SEM images.

Support of the Russian Fund for Fundamental Research (Grant 96-02-17926), Federal program ''Integration'' (Grant 75), and ''Fullerenes and Atomic Clusters'' program (Grant 98059) is gratefully acknowledged.

[1] A. F. Hebard, R.C. Haddon, R. M. Fleming, and A. R. Kortan, Appl. Phys. Lett. **59**, 2109 (1991).
[2] A. F. Hebard, O. Zhou, Q. Zhong, R. M. Fleming, and R. C. Haddon, Thin Solid Films **257**, 147 (1995).
[3] A. Richter and R. Smith, Wiss. Beiträge **1**, 72 (1996).
[4] W. Krakow, N. M. Rivera, R. A. Roy, R. S. Ruoff, and J. J. Cuomo, Appl. Phys. A: Solids Surf. **56**, 185 (1993).
[5] H. Yanagi and T. Sasaki, Appl. Phys. Lett. **65**, 1222 (1994).
[6] Yu. F. Biryulin, A. Ya. Vul', I. K. Ionova, O. I. Kon'kov, T. L. Makarova, V. P. Mikheev, D. A. Sakseev, E. I. Terukov, and V. A. Shul'bakh, Fiz. Tverd. Tela (St. Petersburg) **37**, 3124 (1995) [Phys. Solid State **37**, 1722 (1995)].
[7] A. F. Hebard, T. T. M. Palstra, R. C. Haddon, and R. M. Fleming, Phys. Rev. B **48**, 9945 (1993).
[8] J. E. Fisher, E. Werwa, and P. A. Heiney, Appl. Phys. A: Solids Surf. **56**, 193 (1993).
[9] T. Nguen Mahn, H. Sitter, and D. Stifter, in *Proceedings of the International Winterschool on Electronic Properties of Novel Materials*, edited by H. Kuzmany, J. Fink, M. Mehring, and S. Roth (World Scientific, Singapore, 1996), p. 430.
[10] G. Meijer and D. S. Bethune, J. Chem. Phys. **93**, 7800 (1990).
[11] D. Wang, G. Ke, S. Qian, W. Peng, and Z. Yu, Chin. Phys. Lett. **12**, 717 (1995).
[12] G. Gensterblum, L.-M. Yu, J.-J. Pireaux, P. A. Thiry, and R. Caudiano, in *Electronic Properties of Fullerenes*, edited by H. Kuzmany, J. Fink, M. Mehring, and S. Roth (Springer, Berlin, 1994), p. 195.
[13] D. M. Chen, H. Xu, W. N. Creager, and P. Burnett, J. Vac. Sci. Technol. B **12**, 1910 (1994).
[14] K. Tanigaki, S. Kuroshima, J. Fujita, and T. W. Ebbessen, Appl. Phys. Lett. **63**, 2351 (1993).
[15] T. L. Makarova, N. V. Seleznev, I. B. Zakharova, and T. I. Zubkova, Mol. Mater. **10**, 105 (1998).
[16] T. L. Makarova, V. I. Sakharov, I. T. Serenkov, and A. Ya. Vul', Fiz. Tverd. Tela (St. Petersburg) (to be published).
[17] J. Abrefah, D. R. Olander, M. Balooch, and W. J. Siekhaus, Appl. Phys. Lett. **60**, 1313 (1992).
[18] H. Werner, M. Wohlers, D. Bublak, J. Blöcker, and R. Schlögl, Fullerene Sci. Technol. **1**, 457 (1993).
[19] H. Werner, Th. Schedel-Niedrig, M. Wohlers, D. Herein, B. Herzog, R. Schlögl, M. Keil, A. M. Bradshaw, and J. Kirschner, J. Chem. Soc., Faraday Trans. **90**, 403 (1994).
[20] T. L. Makarova, Mol. Mater. **7**, 199 (1996).
[21] L. Maissel and R. Glang, *Handbook of Thin Film Technology* (McGraw-Hill, New York, 1970).

Translated by G. Skrebtsov

Calorimetric studies of $C_{70}S_{48}$ crystals

V. M. Egorov, B. I. Smirnov, A. V. Talyzin, A. B. Sherman, and M. El Ghalobzouri

A. F. Ioffe Physicotechnical Institute, Russian Academy of Sciences, 194021 St. Petersburg, Russia
(Submitted June 17, 1998)
Fiz. Tverd. Tela (St. Petersburg) **41**, 360–363 (February 1999)

A comparative study of the thermodynamic properties of the C_{70} fullerene, sulfur, and $C_{70}S_{48}$ crystals has been made by differential scanning calorimetry. It is shown that only $C_{70}S_{48}$ has an endothermic δ phase transition with a peak at 430 K, which lies in the temperature region exhibiting conductivity and dielectric anomalies. A correlation between the behavior of the sulfur sublattice in the $C_{70}S_{48}$ crystals and the thermodynamic parameters of the transition has been established. © *1999 American Institute of Physics.* [S1063-7834(99)03202-5]

It was shown[1,2] that, in the range from 100 K to room temperature, the $C_{70}S_{48}$ lattice exists with the polar space group $Amm2$. This means that $C_{70}S_{48}$ crystals possess spontaneous polarization and belong to the class of pyroelectrics. In principle, these crystals could be expected to transform to an unpolar phase with increasing temperature (ferroelectric phase transition). It was shown, however, that no such transition takes place up to 450–500 K.[3] At the same time it was found that the relatively slow increase in the conductivity of $C_{70}S_{48}$ samples observed with increasing temperature is replaced near 400 K by an abrupt (by several orders of magnitude) and irreversible growth. Such a sharp increase in conductivity is characteristic of a transition to the superionic state.[4]

The present work studies the specific features in the thermodynamic behavior of $C_{70}S_{48}$ crystals by differential scanning calorimetry (DSC).

1. EXPERIMENTAL TECHNIQUE

$C_{70}S_{48}$ single crystals were grown by slow evaporation of a stoichiometric mixture of sulfur and C_{70} solutions, but, in contrast to Refs. 1,2, the solvent was benzene C_6H_6 rather than CS_2. The method of growing these single crystals is described elsewhere.[5] By properly monitoring the rate and temperature of crystallization during the growth that lasted two to three weeks, we succeeded in obtaining crystals of up to $10\times1\times0.1$ mm in size. The crystals exhibit needle-like habits and have a scaly structure with layers parallel to (100). X-ray diffraction revealed, besides (100)-type reflections with orders of up to 20–30, reflections from other planes as well, which implies that large needles consist of differently oriented blocks making up a (100)-type texture. The structure of the crystals is orthorhombic with unit cell parameters $a=38.0$, $b=20.23$, and $c=10.7$ Å, which is in a good agreement with the results quoted in Ref. 2 ($a=37.953, b=20.241, c=10.226$ Å).

The thermal effects were studied on a DSC-2 Perkin-Elmer differential scanning calorimeter within the 220–500 K range by the well-known technique[6,7]. The temperature scale was calibrated against the melting points of indium (430 K) and ice (273.1 K). The samples to be measured ($C_{70}S_{48}$ crystallites or C_{70} and sulfur powder) were placed in air-tight aluminum ampoules and heated or cooled in nitrogen flow together with a reference (a corundum crystal) kept in the reference cell. The heating or cooling (temperature scanning) were carried out at a constant rate, and the energy required to maintain the sample and the reference at the same temperature was measured. DSC curves record the heat flux absorbed or released by a sample per unit time, dH/dt, where H is the total enthalpy.

2. EXPERIMENTAL RESULTS AND THEIR DISCUSSION

In addition to a calorimetric study of the $C_{70}S_{48}$ compound, we performed also a preliminary calorimetric investigation of powder samples of C_{70} and sulfur (OSCh grade). No thermal effects were found in the DSC curve of C_{70} within the 350–500 K region, while the DSC curve of sulfur exhibits three endothermic peaks at about 390, 400, and 470 K (curve *1* in Fig. 1). The temperatures 390 and 400 K are the melting points of orthorhombic (385.9 K) and monoclinic (392.1 K) sulfur phases, and the slight excess of the experimental temperatures of the endothermic peaks can be assigned to the DSC-2 thermal response.

Figure 1 presents also a DSC curve for $C_{70}S_{48}$. A strong endothermic peak is observed here at 430 K, which is clearly different from the peak temperatures in the sulfur DSC curve. The enthalpy derived from the peak area $\Delta H = 16$ J/g. A small peak seen in this curve at 390 K evidences the presence in $C_{70}S_{48}$ crystals of inclusions of pure sulfur in rhombic phase. No noticeable thermal effects (peaks or anomalies) are seen in the DSC curves of $C_{70}S_{48}$ obtained under cooling from 500 to 293 K.

It should be pointed out that the DSC peak of $C_{70}S_{48}$ lies within the temperature region where dielectric and resistivity anomalies were observed[3] earlier (Fig. 2). As seen from the figure, the dc resistance of samples decreases rapidly above 400 K. This is paralleled by a steep growth of the capacity, which is accompanied by a peak in dielectric losses. The relations presented in graphical form in Fig. 2 were measured on samples which were not subjected to any preliminary thermal treatment. Subsequent cooling reveals noticeable irreversibility in the temperature course of the measured

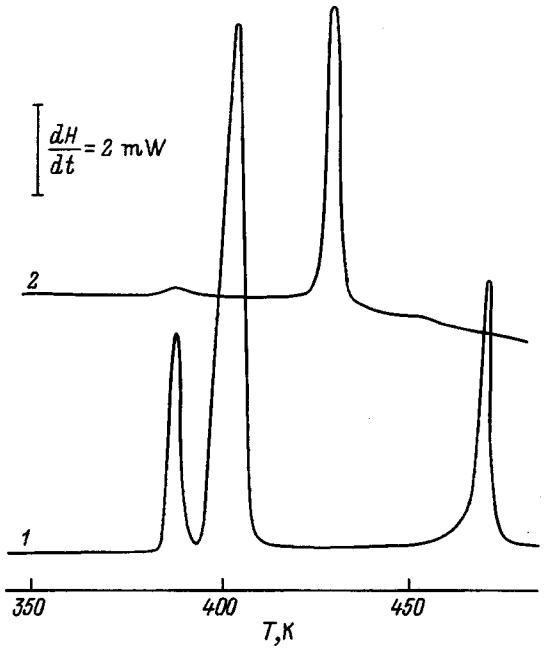

FIG. 1. DSC heating curves of (*1*) sulfur and (*2*) $C_{70}S_{48}$. Heating rate 10 K/min.

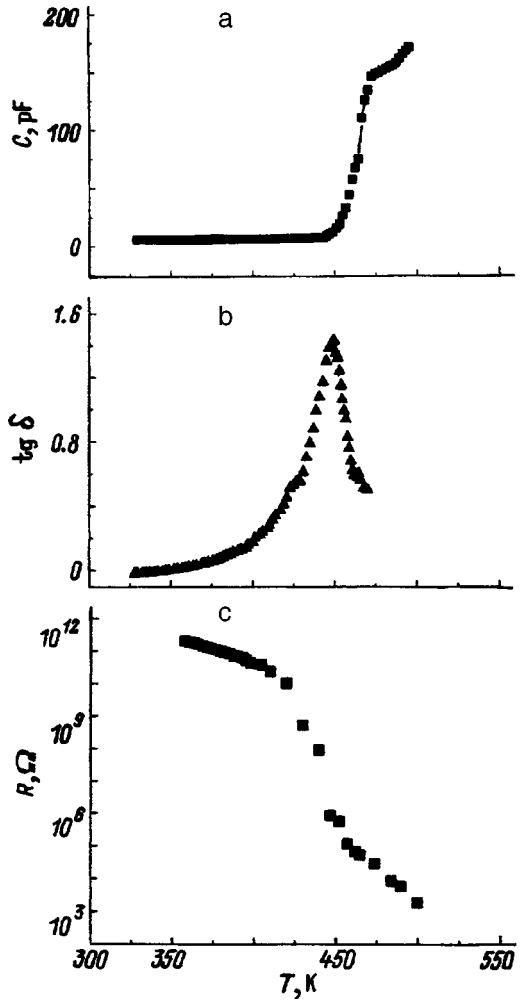

FIG. 2. Temperature dependences of (a) capacity C, (b) dielectric losses tan δ at 1 MHz , and (c) dc resistance R of $C_{70}S_{48}$ single crystals.

quantities, namely, the capacity, dielectric losses, and resistance. The temperature hysteresis is not the same for different samples and can become as large as 50 K.

It was also found that the parameters of the main DSC peak of a $C_{70}S_{48}$ sample depend to a considerable extent on its thermal prehistory (Fig. 3). For instance, preliminary heating of a sample up to 435 K followed by cooling to 293 K reduces the height of the peak by an order of magnitude, and its area, by a few times. Note that the change of the peak parameters observed under fast cooling (quenching) is larger (curve *3*) than that under slow one (curve *2*). Finally, the endothermic peak at 430 K in the sample preheated to 730 K and cooled thereafter to 293 K disappears completely (curve *4*), and subsequent prolonged (up to two months) holdup of the sample at room temperature results not only in a partial recovery of the 430 K peak but in the reappearance of the endothermic peak (curve *5*) corresponding in position to the melting peak of the rhombic phase of free sulfur. The 390 K peak again disappears after the sample was heated to 435 K, and the DSC curve exhibits in this case only the endothermic peak due to the phase transition in $C_{70}S_{48}$ (curve *6*).

Consider briefly the possible nature of the thermal instability of $C_{70}S_{48}$, in particular, the formation of the 430 K endothermic peak and its evolution under various thermal-cycling conditions. Because the $C_{70}S_{48}$ structure can be represented by two weakly coupled sublattices of C_{70} and of sulfur,[2] the temperature-induced variations in these sublattices may be assumed to be independent. The crystal structure of C_{70} is known[8] to be fairly stable above 340 K and does not undergo any substantial structural transformations. Accordingly, the C_{70} sublattice can also remain sufficiently stable within the temperature range under study (above 340 K). Free sulfur, the ''free analog'' of the sulfur sublattice in $C_{70}S_{48}$, exhibits in this temperature range a diverse thermodynamic behavior. It may be conjectured that the sulfur sublattice in $C_{70}S_{48}$ (which consists, like sulfur, of crown-shaped S_8 molecules) could undergo structural transformations close in pattern to those occurring in free sulfur.

To test this idea, free sulfur was subjected to a more comprehensive calorimetric investigation. Powder samples of chemically pure sulfur were studied in the starting and quenched (preheated to 490 K and cooled rapidly) states (Fig. 4). As already mentioned, the DSC curve of the starting sulfur exhibits two endothermic peaks at about 400 K. As for the prequenched sulfur, its DSC curve reveals thermal effects of opposite signs, namely, an exothermic one within a broad temperature region of 290–330 K, and an endothermic one at the melting point of the rhombic phase.

It is known[9] that quenched sulfur undergoes a partial amorphization to become the so-called plastic sulfur, which transforms to the rhombic phase under prolonged storage at room temperature. The plastic (amorphous) phase has typically a higher defect concentration. The transformation of the plastic to rhombic sulfur under heating accounts for the disappearance of these defects, which is signaled by a broad exothermic feature in the DSC curve at 290–330 K. If the processes responsible for the formation of the crystalline sul-

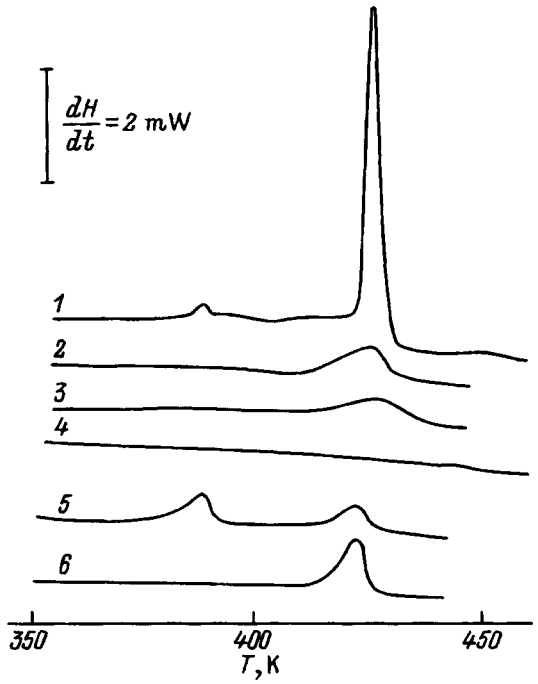

FIG. 3. DSC heating curves for (*1*) original and (*2–6*) pretreated $C_{70}S_{48}$ samples: (*2*) heating to 435 K followed by cooling to 293 K with a rate $V_c = 1.25$ K/min; (*3*) heating to 435 K followed by rapid cooling (320 K/min) to 293 K; (*4*) heating to 730 K with subsequent cooling to 293 K, $V_c = 320$ K/min; (*5*) heating to 730 K and cooling to 293 K at $V_c = 320$ K/min with subsequent storage for two months; (*6*) heating of sample 5 to 435 K and cooling to 293 K with $V_c = 1.25$ K/min. Heating rate 10 K/min.

fur sublattice in $C_{70}S_{48}$ and of the free-sulfur lattice are identical, then the parameters of the endothermic peak in $C_{70}S_{48}$ crystals should depend both on the temperatures to which they were heated (above the phase-transition point) and on the prehistory of the crystals below the phase-transition temperature (Fig. 3).

A partial support for this conjecture may come from a comparison of curves *2* and *3* in Fig. 3, which reveals a

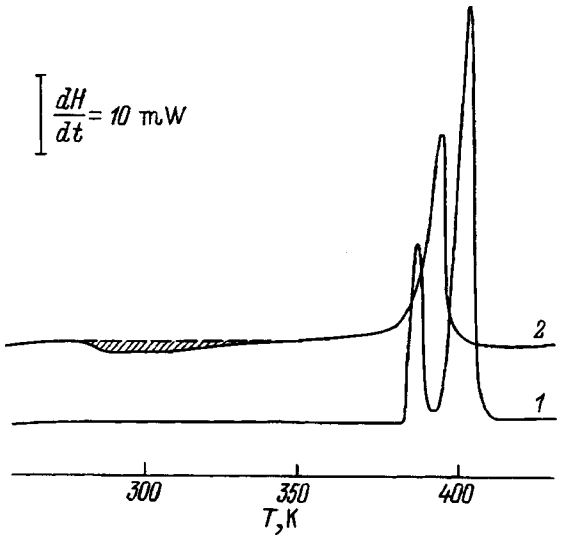

FIG. 4. DSC curves of sulfur in (*1*) initial state and (*2*) quenched ($V_c = 320$ K/min) from 490 K. Heating rate 10 K/min.

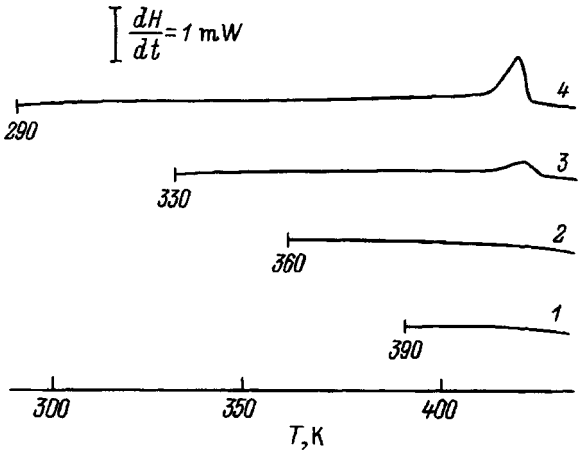

FIG. 5. DSC heating curves of $C_{70}S_{48}$ samples precooled from 435 K at a rate of 10 K/min to (*1*) 390 K, (*2*) 360 K, (*3*) 330 K, and (*4*) 290 K. Heating rate 10 K/min.

difference between the cases of fast and slow cooling of $C_{70}S_{48}$ samples preheated to the same temperature.

To determine the temperature region within which a $C_{70}S_{48}$ sample has to be maintained after a heating to 435 K in order for their transition parameters to change, the following experiments were carried out. Figure 5 shows DSC heating curves of samples obtained after their thermal cycling. Each cycle was terminated at 435 K, a temperature above the phase-transition point. On reaching this temperature, the sample was cooled in each cycle to one of the following temperatures, namely, 390, 360, 330, or 290 K, to be heated again thereafter to 435 K. No noticeable thermal features in the form of peaks or anomalies were observed under cooling. No thermal effects are seen either in the DSC curves measured after cooling the crystals to 390 or 360 K (curves *1* and *2*). By contrast, the DSC curves of the samples cooled preliminarily to 330 and 290 K reveal an endothermic phase-transition peak (curves *3* and *4*, respectively), which is weakly pronounced in the first case and close in intensity to the original effect (curve *6* in Fig. 2), in the second. Thus we witness apparently in the 330–290 K interval recovery (at least, partial) of the $C_{70}S_{48}$ structure. As follows from experiments with pure sulfur (Fig. 4), within the same interval the defects in plastic sulfur are annealed to transfer it to the rhombic phase. This coincidence gives us grounds to believe that both the formation of the $C_{70}S_{48}$ lattice and the appearance in it of thermally induced defects are associated primarily with the annealing or, conversely, creation of defects in the sulfur sublattice. These defects can give rise to relaxation phenomena. Indeed, it is such a relaxation pattern that was evident[3] in the dielectric anomalies in $C_{70}S_{48}$ under heating.

Thus our present studies, combined with the results of an investigation of the temperature dependences of capacity, dielectric losses, and resistivity reported in Ref. 3, may be considered as evidence for the existence of a phase transition at 430 K in $C_{70}S_{48}$ crystals, which, judging from the abrupt drop of the resistivity, has a superionic nature and is apparently associated with melting of the sulfur sublattice.

The authors owe their thanks to V. V. Lemanov for interest in this work and fruitful discussions.

Support of the ''Fullerenes and Atomic Clusters'' project (Grant 98065) is gratefully acknowledged.

[1] G. Roth and P. Adelman, J. Phys. I **2**, 1541 (1992).
[2] H. B. Buergi, P. Venugopalan, D. Schwarzenbach, F. Diederich, and C. Thilgen, Helv. Chim Acta **76**, 2155 (1993).
[3] V. V. Lemanov, A. V. Talyzin, A. B. Sherman, and M. El Gholabzouri, in *Fullerenes*, Vol. 4 *Recent advances in the Chemistry and Physics of Fullerenes and Related Materials* (Electrochemical Society, Pennington, 1997), p. 1217.
[4] M. B. Salamon, in *Physics of Superionic Conductors*, edited by M. B. Salamon (Zinatne, Riga, 1982), p. 123.
[5] A. V. Talyzin, V. V. Ratnikov, and P. P. Syrnikov, Fiz. Tverd. Tela (St. Petersburg) **38**, 2263 (1996) [Phys. Solid State **38**, 1248 (1996)].
[6] V. M. Egorov, V. V. Shpeĭzman, and I. P. Kremenskaya, Pis'ma Zh. Tekh. Fiz. **19**, No. 19, 49 (1993) [Tech. Phys. Lett. **19**, 621 (1993)].
[7] V. M. Egorov, B. I. Smirnov, V. V. Shpeĭzman, and R. K. Nikolaev, Fiz. Tverd. Tela (St. Petersburg) **38**, 2214 (1996) [Phys. Solid State **38**, 1219 (1996)].
[8] T. Mitsuki, Y. Ono, H. Horiuchi, J. Li, N. Kino, K. Kishio, and K. Kitazawa, Jpn. J. Appl. Phys. **33**, Pt. 1, 6281 (1994).
[9] *Thermodynamic Properties of Substances* [in Russian], Vol. 1, edited by V. P. Glushko (Nauka, Moscow, 1962), 1016 pp.

Translated by G. Skrebtsov

ERRATA

ERRATUM: Low-temperature photoluminescence determination of dislocation slip systems in CdSe single crystals [Phys. Solid State 40, No. 10, 1672–1675 (October 1998)]

N. I. Tarbaev

Institute of Semiconductor Physics, Ukrainian Academy of Sciences, 252650 Kiev, Ukraine
Fiz. Tverd. Tela (St. Petersburg) **41**, 364 (February 1999)

[S1063-7834(99)03502-9]

The title of this paper should read as follows: ''Low-temperature photoluminescence determination of dislocation slip systems in CdSe single crystals.''

Translated by M. E. Alferieff

Rules for authors preparing articles for the journal ''Fizika tverdogo tela''

The editorial board of the journal requests authors submitting articles for publication to adhere to the following rules.

Articles ignoring these rules will be rejected.

• The article should indicate the address of the institution where the work was performed. The manuscript should be signed by the author (coauthors) whose last name, name, patronymic, home address, place of employment, and telephone numbers should be indicated. The individual(s) to whom correspondence is to be directed should be indicated. The authors may suggest possible referees. Proofs are not provided.

• The journal publishes original articles and invited reviews on various aspects of solid-state physics. Two copies of the article, typed double-spaced and one-sided with a 12- or 14-point font, should be submitted. The left-hand margin should be at least 4 cm. Handwritten insertions are not allowed. All pages should be numbered.

The following should be indicated on a *separate* sheet:

— title of the article;

— initials and last names of the authors (initials placed before the last name);

— name of the institution (no abbreviations or acronyms) submitting the article and the address of the institution (postal code, city, country);

— e-mail address.

The text of the article should be preceded by an abstract not exceeding 0.5 typewritten pages in length. The abstract should not repeat the introductory and concluding sections. The institution financing the work described in the article (grant No.) should be indicated at the end of the abstract.

• The exposition should be clear and succinct without intermediate equations and calculations and complicated mathematical expressions. Data given in tables, plots, and figures should not be repeated in the text of the article. Presentation of numerical results in tables and figures simultaneously should also be avoided. If sections are not provided with headings, they should be numbered. Abbreviations used by the authors should be defined in the text.

Latin letters should be used for dimensions of quantities and notations (in the text, tables, and figures).

• Two copies of each figure should be submitted. The minimum number of figures with a limited number of details should be used. Inscriptions in the figures should be in English.

Line drawings should be drawn using India ink on white or tracing paper.

Half-tone figures should be submitted in the form of glossy photographs. The second copy of the photographs should not contain letter or numberical labels (only the picture). The notation ''top'' should be written on the back using a soft pencil. Photographs should not be glued on. Clips should not be used.

Figures *composed on a computer* should be of high quality.

The last names of the authors, the title of the article, and the figure number should be indicated on the back of the figures.

Figure captions should be presented on a separate sheet of paper. Graphical elements (circles, crosses, and so on) are not allowed in figure captions.

• Tables should be printed on separate sheets of paper and should have headings. The units of measurement should be indicated.

• Equations should be inserted in large type, loosely, and clearly. The equations should be numbered continuously throughout the article (not by sections).

In the first copy of the manuscript the *equations* and *notations* should be marked according to the following rules:

— Greek letters should be underlined in red;

— handwritten letters should be circled using a green pencil;

— Gothic letters should be circled using a yellow pencil;

— vectors should be underscored with a blue underbar (not with an overarrow!);

— indices and exponents should be indicated by carats on top and bottom using an ordinary pencil;

— upper- and lower-case letters having similar outlines (C, c; K, k; P, p; O, o), the letters I (i) and J (j), the letter I and the Roman numeral 1, the Arabic number 1 and the Roman numeral I, the vertical bar (|), 1, and a stroke in indices, and ℓ (Latin ell) and *e*, should be indicated clearly;

— upper-case letters should be marked with two underbars ($\underline{\underline{C}}$) using pencil and lowercase letters should be marked with two overbars ($\bar{\bar{c}}$).

In in-line equations a slash should be used to indicate division. The notation exp should be used for the exponential function.

• Special attention should be given to composing the list of references:

for books — initials and last names of *all* authors, title of the book, publisher, location of publication, year of publication,

volume, edition, total number of pages (54 p.); if a citation is made to a specific page, the number of this page should be indicated after the year of publication: p. 54 (not 54 p.);

for periodicals — initials and last names of *all* authors, name of the journal, volume, issue number, number of the first page of the article, year of publication;

Examples:

1. B. P. Aduev, É. D. Aluker, V. V. Gavrilov, R. G. Deĭch, and S. A. Chernov, Fiz. Tverd. Tela **38**, *12*, 3521 (1996).
2. V. J. Emery, Phys. Rev. B **14**, *3*, 2989 (1976).
3. L. D. Landau and E. M. Lifshitz, *Quantum Mechanics*, Nauka, M. (1989).

Citations to Russian editions should be given in Russian.

The references should be numbered in the order in which they appear in the text.

• In accordance with an agreement between the publishers of the journal ''Fizika tverdogo tela'' and the American Institute of Physics, the journal is translated into English and distributed outside Russia.

Authors desiring to publish their article in the journal ''Fizika tverdogo tela'' should send a letter to the editorial board in the following form:

We, the undersigned authors, ... give the publishers and the editorial board of the journal ''Fizika tverdogo tela'' the right to publish the article ..... in Russian and in English.

We affirm that this publication does not violate any copyrights of other individuals or organizations.

Signature

Date

The authors retain their rights as owners of the articles.

Translated by M. E. Alferieff